Transactions of the ASME

Technical Editor, L. B. FREUND

APPLIED MECHANICS DIVISION

Chairman, WILLIAM G. GOTTENBERG
Secretary, CHARLES R. STEELE
Associate Editors, J. D. ACHENBACH
S. T. ARIARATNAM
T. BELYTSCHKO
D. B. BOGY
R. J. CLIFTON
L. B. FREUND
MAURICE HOLT
W. D. IWAN
T. R. KANE
A. S. KOBAYASHI
S. LEIBOVICH
L. E. MALVERN
R. P. NORDGREN
R. H. PLAUT
R. T. SHIELD
C. T. SUN
J. S. WALKER
G. A. WEMPNER

BOARD ON COMMUNICATIONS
Chairman and Vice-President
M. J. RABINS

Members-at-Large
W. BEGELL
J. CALLAHAN
H. C. REEDER
D. KOENIG
M. KUTZ
F. LANDIS
J. W. LOCKE
J. E. ORTLOFF
C. PHILLIPS
K. REID

President, SERGE GRATCH
Exec. Dir.
PAUL ALLMENDINGER
Treasurer, ROBERT A. BENNETT

PUBLISHING STAFF
Mng. Dir., Pub., J. J. FREY
Dep. Mng. Dir., Pub.
JOS. SANSONE
Managing Editor,
CORNELIA MONAHAN
Production Editor, SUZANNE MAGIDA
Prod. Asst., BETH DARCHI

The Journal of Applied Mechanics (ISSN 0021-8936) is published quarterly for $72 per year by The American Society of Mechanical Engineers, 345 East 47th Street, New York, NY 10017. *Second class postage paid at New York, NY and additional mailing offices.* POSTMASTER: Send address changes to The Journal of Applied Mechanics, c/o THE AMERICAN SOCIETY OF MECHANICAL ENGINEERS, P.O. Box 3199, Grand Central Station, New York, NY 10163.

CHANGES OF ADDRESS must be received at Society headquarters seven weeks before they are to be effective. Please send old label and new address.

PRICES: To members, $36.00, annually; to *nonmembers, $72.00. Single copies, $24.00 each.* Add $6.00 for postage to countries outside the United States and Canada.

STATEMENT from By-Laws. The Society shall not be responsible for statements or opinions advanced in papers or . . . printed in its publications (B7.1, Par. 3).

COPYRIGHT © 1983 by the American Society of Mechanical Engineers. Reprints from this publication may be made on condition that full credit be given the TRANSACTIONS OF THE ASME, JOURNAL OF APPLIED MECHANICS, and the author, and date of publication be stated.

INDEXED by the Engineering Index, Inc.

Journal of Applied Mechanics

Published Quarterly by The American Society of Mechanical Engineers

VOLUME 50 • NUMBER 2 • JUNE 1983

TECHNICAL PAPERS

(Contents continued on Inside Back Cover)

Downloaded 04 May 2010 to 171.66.16.34. Redistribution subject to ASME license or copyright; see http://www.asme.org/terms/Terms_Use.cfm

CONTENTS (CONTINUED)

DESIGN DATA AND METHODS

BRIEF NOTES

DISCUSSIONS

BOOK REVIEWS

Downloaded 04 May 2010 to 171.66.16.34. Redistribution subject to ASME license or copyright; see http://www.asme.org/terms/Terms_Use.cfm

M. Holt
Department of Mechanical Engineering,
University of California,
Berkeley, Calif. 94720
Mem. ASME

W.-S. Yeung
Department of Mechanical Engineering,
University of Lowell,
Lowell, Mass. 01854
Assoc. Mem. ASME

A Numerical Investigation for Curved Pipe Flow at High Reynolds Number

A numerical scheme for solving the curved pipe flow at high Reynolds number is presented in considerable detail. This paper complements an earlier paper presenting mainly numerical results. An efficient scheme based on the conventional Telenin method is developed to solve the general three-dimensional Laplace equation subject to Dirichlet, Neumann, or mixed boundary conditions.

1 Introduction

Numerous investigations of curved pipe flow have been carried out since the first theoretical studies due to Dean [1, 2]. A brief survey of the more important work on this topic is given by Yeung [3], which is also the major source of the present work.

A numerical investigation is made of the flow of an incompressible fluid in the entry region of a circular curved pipe at very large Reynolds number. The three-dimensional flow field is divided into two parts, namely, the boundary layer region near the inner pipe surface and an irrotational core. The Method of Integral Relations (MIR) is used to solve the appropriate boundary layer equations while a modified version of Telenin's method is applied in the irrotational core region. The general equations of motion are the usual Navier-Stokes equations written in toroidal coordinates as shown in Fig. 1.

The equations of motion, respectively, governing the inviscid and boundary layer flows are solved as a coupled system. This composite method was applied to flow in a 90 deg elbow with ratio of pipe radius to elbow radius equal to 0.1 with Reynolds number 10^4. The results of the application are given in Yeung [4]. The present paper deals with the details of the numerical technique employed.

2 Irrotational Core

Since the core region is assumed irrotational, we can define a potential function Ω such that

$$\frac{\partial^2\Omega}{\partial r_0^2}+\frac{\partial\Omega}{\partial r_0}\left[\frac{1}{r_0}+\frac{\alpha\cos\psi_0}{1+\alpha r_0\cos\psi_0}\right]+\frac{1}{r_0^2}\frac{\partial^2\Omega}{\partial\psi_0^2}$$

$$-\frac{\alpha\sin\psi_0}{1+\alpha r_0\cos\psi_0}\frac{\partial\Omega}{\partial\psi_0}+\frac{\alpha^2}{(1+\alpha r_0\cos\psi_0)^2}\frac{\partial^2\Omega}{\partial s_0^2}=0. \quad (1)$$

Equation (1) is written in toroidal coordinates shown in Fig. 1. The pipe is generated by rotating the circle, radius a, about the y axis. The angular coordinate ϕ is in the main stream direction (following the mean radius of the curved pipe) while r and ψ are polar coordinates in the cross-flow plane. The ratio of the pipe radius a to the pipe radius of curvature R is denoted by α; r_0 is nondimensionalized with respect to a and (r_0, ψ_0, s_0) are the coordinates for the core region. The corresponding velocity components, relative to the constant entry velocity W_i, are given by

$$U_0=\frac{1}{\alpha}\frac{\partial\Omega}{\partial r_0},\quad V_0=\frac{1}{\alpha r_0}\frac{\partial\Omega}{\partial\psi_0},\quad W_0=\frac{1}{1+\alpha r_0\cos\psi_0}\frac{\partial\Omega}{\partial s_0}. \quad (2)$$

We restrict ourselves to the following boundary conditions:

$$\frac{\partial\Omega}{\partial s_0}=1+\alpha r_0\cos\psi_0 \quad \text{at} \quad s_0=0 \quad (3)$$

corresponding to uniform flow at the entry, and

$$\Omega=g(\psi_0,r_0) \quad \text{at} \quad s_0=\pi/2 \quad (4)$$

corresponding to a prescribed variation of the potential at the exit. In addition, the radial velocity is prescribed at the pipe boundary,

$$\frac{\partial\Omega}{\partial r_0}=f_3(\psi_0,s_0) \quad \text{at} \quad r_0=1. \quad (5)$$

The function f_3 is the main interaction term between the boundary layer region and the core region, as we shall see later.

Telenin's method, which is described in full in Holt [5], is chosen to solve equation (1). In short, Ω is represented by appropriate interpolating functions in r_0 and ψ_0. This makes possible the calculation of the corresponding partial derivatives, and eventually replaces equation (1) with a system of ordinary differential equations in s_0. The principal advantage of Telenin's method over conventional finite difference schemes lies in the flexibility in choice of the interpolating functions. Thus, when certain functional properties of the unknowns are known (for example, the

Contributed by the Applied Mechanics Division for presentation at the 1983 ASME Applied Mechanics, Bioengineering, and Fluids Engineering Conference, Houston, Texas, June 20-22, 1983 of THE AMERICAN SOCIETY OF MECHANICAL ENGINEERS.

Discussion on this paper should be addressed to the Editorial Department, ASME, United Engineering Center, 345 East 47th Street, New York, N.Y. 10017, and will be accepted until two months after final publication of the paper itself in the JOURNAL OF APPLIED MECHANICS. Manuscript received by ASME Applied Mechanics Division, November, 1981; final revision, October, 1982. Paper No. 83-APM-18.

Copies will be available until February, 1984.

Copyright © 1983 by ASME
Downloaded 02 May 2010 to 171.66.16.246. Redistribution subject to ASME license or copyright; see http://www.asme.org/terms/Terms_Use.cfm

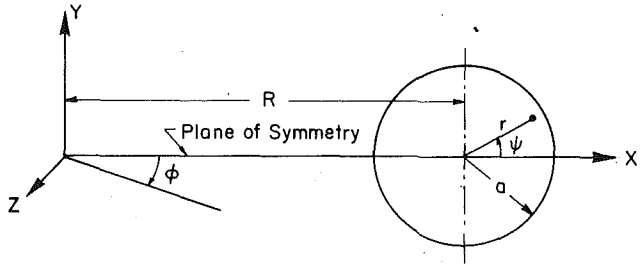

Fig. 1 Toroidal coordinate system

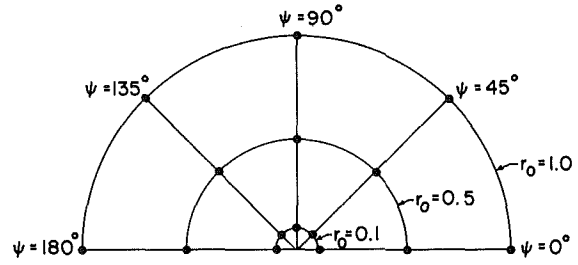

Fig. 2 Grid system and nodal point coordinates in the core region

functions may be odd, even, or periodic), one can easily choose appropriate functions that exhibit those properties, thereby improving the accuracy of the numerical results. Furthermore, some boundary conditions can be carefully incorporated into such chosen functions, thus eliminating the need to consider the boundary points separately, as is required in finite difference formulations.

The cross-flow plane is discretized according to Fig. 2. Changing from Cartesian to toroidal coordinates introduces an artificial singularity in the solution of equation (1) at $r_0 = 0$. This is avoided in numerical work by taking the inner boundary of the integration on the circle $r_0 = 0.1$ rather than the center $r_0 = 0$. The resulting numerical solution can be extrapolated uniformly to $r_0 = 0$. Let (i,k) represent the coordinates of the nodes, i.e., at the point (i,k), $r_0 = r_{0,i}$ and $\psi_0 = \psi_{0,k}$. The value of any function $f(r_0,\psi_0,s_0)$ at the node (i,k) will be denoted by $f_{ik}(s_0)$. Note that f_{ik} is only a function of s_0.

On planes of constant ψ_0, $\psi_0 = \psi_{0,k}$, we approximate Ω by a Lagrangian polynomial in the r_0 direction:

$$\Omega = \sum_{j=1}^{NX1+1} \Omega_j^0 r_0^{j-1} \tag{6}$$

where $NX1$ is the number of nodes in the r_0 direction and Ω_j^0 depends only on ψ_0 and s_0. Normally, one can only fit a $(NX1-1)$ degree polynomial to $NX1$ points. However, due to the derivative boundary condition at $r_0 = 1$, one has an extra degree of freedom in fitting a polynomial through $NX1$ points, i.e., one can fit an $NX1$ degree polynomial through the $NX1$ points. Rewrite (6) as

$$\Omega = \sum_{j=1}^{NX1} \Omega_1^0 r_0^{j-1} + \Omega_{NX1+1}^0 r_0^{NX1}. \tag{7}$$

Applying the boundary condition at $r_0 = 1$ from equation (5) we finally obtain

$$\bar{\Omega} = \Omega_i^0 + \sum_{j=2}^{NX1} \Omega_j^0 \left\{ r_0^{j-1} - \frac{j-1}{NX1} r_0^{NX1} \right\}, \tag{8}$$

where $\bar{\Omega}$ is defined as

$$\bar{\Omega} = \Omega - \frac{f_3(\psi_0,s_0) r_0^{NX1}}{NX1}. \tag{9}$$

The interpolating coefficients $\Omega_1^0, \Omega_2^0, \ldots$ can be solved in terms of the nodal values of $\bar{\Omega}$. Thus, if we apply (8) to the $NX1$ points in the r_0 direction, we have

$$\bar{\Omega}_{ik} = \sum_{j=1}^{NX1} A_{ij} \Omega_j^0, \quad i = 1,2, \ldots, NX1, \tag{10}$$

where A_{ij} is given by

$$A_{ij} = 1 \quad \text{when} \quad j = 1$$

and

$$A_{ij} = r_{0,i}^{j-1} - \frac{(j-1)}{NX1}, \quad \text{otherwise.} \tag{11}$$

Solving (10), we obtain

$$\Omega_i^0 = \sum_{j=1}^{NX1} A_{ij}^{-1} \bar{\Omega}_{jk}, \quad i = 1,2, \ldots, NX1. \tag{12}$$

The partial derivatives in the r_0 direction are then given by

$$\frac{\partial \bar{\Omega}_{ik}}{\partial r_0} = \sum_{j=1}^{NX1} C1_{ij} \bar{\Omega}_{jk}$$

where

$$C1_{ij} = \sum_{\ell=2}^{NX1} (\ell-1) A_{\ell j}^{-1} (r_{0,i}^{\ell-2} - r_{0,i}^{NX1-1}) \tag{13}$$

and

$$\frac{\partial^2 \bar{\Omega}_{ik}}{\partial r_0^2} = \sum_{j=1}^{NX1} D1_{ij} \bar{\Omega}_{jk}$$

where

$$D1_{ij} = \sum_{\ell=2}^{NX1} (\ell-1) A_{\ell j}^{-1} [(\ell-2) r_{0,i}^{\ell-3} - (NX1-1) r_{0,i}^{NX1-2}]. \tag{14}$$

Similarly, on contours of constant r_0, Ω is expressed in cosine series (because of its symmetry property) as follows,

$$\Omega = \sum_{j=1}^{NX2} \Omega_j^{00} \cos(j-1)\psi_{0,j}, \tag{15}$$

where $NX2$ is the number of nodes in the ψ_0 direction. As before, Ω_j^{00}, which is now a function of r_0 and s_0 only, is a linear combination of the values of Ω on the $NX2$ points. If a matrix B is defined as

$$B_{kj} = \cos(j-1)\psi_{0,k}, \quad k, j = 1, \ldots, NX2, \tag{16}$$

it can be shown that the following holds,

$$\Omega_j^{00} = \sum_{\ell=1}^{NX2} B_{j\ell}^{-1} \Omega_{i\ell}, \quad j = 1, \ldots, NX2, \tag{17}$$

$$\frac{\partial \Omega_{ik}}{\partial \psi_0} = \sum_{j=1}^{NX2} C2_{kj} \Omega_{ij},$$

where

$$C2_{kj} = -\sum_{\ell=2}^{NX2} (\ell-1) B_{\ell j}^{-1} \sin(\ell-1)\psi_{0,k}, \tag{18}$$

and

$$\frac{\partial^2 \Omega_{ik}}{\partial \psi_0^2} = \sum_{j=1}^{NX2} D2_{kj} \Omega_{ij},$$

Downloaded 02 May 2010 to 171.66.16.246. Redistribution subject to ASME license or copyright; see http://www.asme.org/terms/Terms_Use.cfm

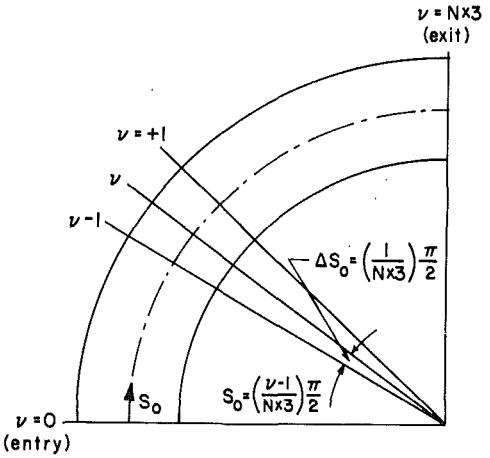

Fig. 3 Notation of the mesh size in the streamwise direction in the core region

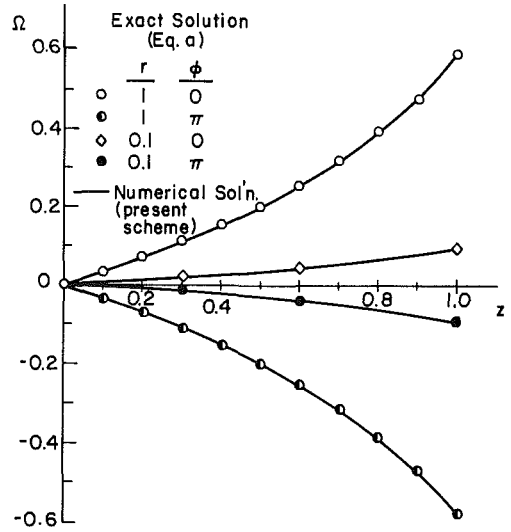

Fig. 4 Comparison of numerical solution by the modified Telenin method to the exact analytical solution of Laplace's equation in a circular cylinder

where

$$D2_{kj} = -\sum_{\ell=2}^{NX2} (\ell-1)^2 B_{\ell j}^{-1} \cos(\ell-1)\psi_{0,k}. \tag{19}$$

Substituting the partial derivatives in r_0 and ψ_0 directions into equation (1), Laplace's equation reduces to the following system of second-order ordinary differential equations in s_0:

$$\left.\begin{aligned} &\frac{d^2\Omega_{ik}}{ds_0^2} = \mathcal{F}_{ik}(\Omega_{nm}, f_3), \qquad i=1,\ldots,NX1,\quad k=1,\ldots,NX2 \\ &\text{where } \mathcal{F}_{ik} \text{ is given by} \\ &\mathcal{F}_{ik} = -\frac{(J_{ik})^2}{\alpha_2}\left\{\frac{\partial^2\Omega_{ik}}{\partial r_0^2} + \left(\frac{1}{r_{0,i}} + \frac{\alpha\cos\psi_{0,k}}{J_{ik}}\right)\frac{\partial\Omega_{ik}}{\partial r_0} + \frac{1}{r_{0,i}^2}\frac{\partial^2\Omega_{ik}}{\partial\psi_0^2} - \frac{\alpha\sin\psi_{0,k}}{J_{ik}}\frac{\partial\Omega_{ik}}{\partial\psi_0}\right\} \end{aligned}\right\} \tag{20}$$

with

$$J_{ik} = 1 + \alpha r_{0,i}\cos\psi_{0,k}. \tag{21}$$

The dependence on f_3 is derived from equation (9).

The boundary conditions for (20) can be derived from (3) and (4) as

$$\frac{d\Omega_{ik}}{ds_0} = 1 + \alpha r_{0,i}\cos\psi_{0,k} \quad \text{at} \quad s_0 = 0 \tag{22a}$$

and

$$\Omega_{ik}^0 = g(\psi_{0,k}, r_{0,i}) \quad \text{at} \quad s_0 = \pi/2. \tag{22b}$$

The conventional Telenin method transforms the boundary value problem into an initial value problem by guessing enough initial conditions to start the integration. Mathematically, this is equivalent to solving an elliptic problem by assigning Cauchy data along an initial line. This approach suffers from so-called Hadamard instability [6]. Indeed, when this shooting technique was applied to (20) with (22*a*,*b*), the solutions increased without limit and it was not possible to obtain convergent results.

A different approach is sought by taking advantage of the linearity of equation (20). Since Hadamard instability arises only when we try to cast the elliptic problem into a Cauchy initial value problem, numerical schemes based on the direct solution of (20) should eliminate this instability. To do so, let us divide the curved pipe into $NX3$ equal parts in the direction of increasing s_0, as shown in Fig. 3. Denote the value of Ω at the point (i,k) on the plane $s_0 = (\nu/NX3)\,\pi/2$, where $\nu = 0,1,\ldots,NX3$, by Ω_{ik}^{ν}. Equation (20) is then approximated by replacing the second derivative by a central difference formula. For the derivative boundary condition at $s_0 = 0$, we imagine a fictitious plane $s_0 = -(1/NX3)\cdot\pi/2$, and denote the values of Ω at this plane by Ω_{ik}^{-1}. In the case when a derivative condition is also prescribed at $s_0 = \pi/2$, it can be treated in similar fashion. The resulting finite difference system of equation (20) is

$$\left.\begin{aligned} &\frac{\Omega_{ik}^{\nu-1} - 2\Omega_{ik}^{\nu} + \Omega_{ik}^{\nu+1}}{h^2} = F_{ik}(\Omega_{nm}^{\nu}, f_3), \\ &\frac{\Omega_{ik}^{1} - \Omega_{ik}^{-1}}{2h} = (f_1)_{ik}, \\ &i=1,\ldots,NX1, \quad k=1,\ldots,NX2, \quad \nu=0,1,\ldots,NX3, \end{aligned}\right\} \tag{23}$$

where $h = (1/NX3)\,\pi/2$ is the step size in the present problem.

The linear system (23) has a very interesting property. Rearrangement of the equations enables us to write it in the following form

$$\mathbf{A}\,\mathbf{X} = \mathbf{C}, \tag{24}$$

where $\mathbf{A}$ turns out to be a block tridiagonal matrix with the following special property,

$$\mathbf{A} = \begin{bmatrix} \mathbf{A}_0 & 2\mathbf{I} & & & \\ \mathbf{I} & \mathbf{A}_1 & \mathbf{I} & & \\ & & \mathbf{A} & & \\ & & & \mathbf{I} & \mathbf{A}_{NX3} \end{bmatrix} \tag{25}$$

with $\mathbf{A}_0 = \mathbf{A}_1 = \ldots = \mathbf{A}_{NX3}$ and $\mathbf{I}$ being the identity matrix. The order of each matrix element is $NX1 \cdot NX2$ by $NX1 \cdot NX2$. The transpose of $\mathbf{X}$ is given by

$$\mathbf{X}^T = \{X_0, X_1, \ldots, X_{NX3}\}, \tag{26}$$

where X_ν is a column vector containing Ω_{ik}^{ν}, $i = 1, NX1$, $k = 1, NX2$. Finally, $\mathbf{C}$ contains the corresponding inhomogeneous term that depends on the boundary conditions.

Downloaded 02 May 2010 to 171.66.16.246. Redistribution subject to ASME license or copyright; see http://www.asme.org/terms/Terms_Use.cfm

The special structure of the coefficient matrix **A** improves the efficiency of the present numerical scheme for solving equation (1) tremendously. Thus, one can easily transform **A** into a lower and upper triangular matrix as one does for an ordinary tridiagonal matrix [7]. The order of systems that need to be solved during the course of the LU decomposition is at most $NX1 \cdot NX2$, as compared to the original order of $NX1 \cdot NX2 \cdot (NX3+1)$ in (23). Moreover, many matrix multiplications are saved since the lower and upper diagonal elements of **A** are multiples of the identity matrix **I**.

The present modified version of Telenin's method has been applied to solve Laplace's equation in a circular cylinder with prescribed Neumann boundary conditions, as shown in Fig. 4. The numerical results agree well with the exact analytical solution indicated. Other boundary conditions, mostly mixed Neumann-Dirichlet conditions for the same problem, have been tried and in all cases there is close agreement between the numerical and exact solutions. Hence there is no doubt that the present modified scheme is more efficient than the conventional Telenin method, at least when applied to a linear problem.

For equation (1), different forms of $g(r_0,\psi_0)$ have been tried and the corresponding solutions do not differ significantly over most of the curved pipe downstream of the entry plane. This is in conformity with a simple perturbation analysis [3]. In view of this we take g = constant for the rest of the paper. It now remains to specify f_3, the boundary condition at $r_0 = 1$. The value of f_3 is determined from the radial outflow of the boundary layer region and, consequently, provides the interaction between the core and the boundary layer region, as mentioned earlier.

3 Boundary Layer Region

In this region, the governing equations are of the usual boundary layer type [3]. The Method of Integral Relations (MIR) has been applied to reduce the original parabolic equations to a system of first-order hyperbolic partial differential equations. The derivation of the basic integral relations is given elsewhere [3, 4]. The final forms of the basic integral relations are as follows,

$$\left.\begin{aligned}
&\frac{1}{1+\alpha\cos\psi}\left\{\frac{\partial b_{01}}{\partial s}\int_0^1 \frac{Wg_k(W)}{1-W}\,dW+\frac{\partial b_{j1}}{\partial s}\right\}=C(k)\\
&\quad-\int_0^1\left(V\frac{\partial Z}{\partial\psi}+Z\frac{\partial V}{\partial\psi}\right)g_k(W)\,dW \quad k=1,2,\ldots,N=1,\\
&\frac{1}{1+\alpha\cos\psi}\frac{\partial b_{01}}{\partial s}\int_0^1\frac{Wg_N(W)}{1-W}\,dW\\
&\quad=C(N)-\int_0^1\left(V\frac{\partial Z}{\partial\psi}+Z\frac{\partial V}{\partial\psi}\right)g_N(W)\,dW,
\end{aligned}\right\} \tag{27}$$

$$\frac{1}{1+\alpha\cos\psi}\frac{\partial b_{k2}}{\partial s}=D(k)-\int_0^1 V\frac{\partial V}{\partial\psi}h_k(W)\,dW, \quad k=1,2,\ldots,N, \tag{28}$$

where

$$V=\frac{v}{w_e},\quad W=\frac{w}{w_e},\quad s=\frac{\phi}{\alpha},\quad Z=\left(\frac{\partial W}{\partial\eta}\right)^{-1},$$
$$\eta=(a-r)R_e^{1/2}\alpha^{1/4}/a,\quad R_e=W_{ia}/\nu. \tag{29}$$

Here, w_e is the streamwise velocity component at the boundary layer edge, b_{j1}, $j = 0, \ldots, N-1$ are the parameters for the Z profile, b_{j2}, $j = 1, \ldots, N$ are the parameters for the V profile, $g_k(W)$ and $h_k(W)$ are appropriate weighting functions, and $C(k)$ and $D(k)$ are complex expressions that do not contain any s or ψ derivatives of b_{j1} or b_{j2}. The coordinates for the boundary layer are (r,ψ,s).

On the plane $\psi = 0$ the following integral relations are used

$$\frac{1}{1+\alpha}\frac{db_{01}}{ds}\int_0^1\frac{Wg_N(W)}{1-W}\,dW=\tilde{C}(N),$$

$$\frac{1}{1+\alpha}\left\{\frac{db_{01}}{ds}\int_0^1\frac{Wg_k(W)}{1-W}\,dW+\frac{db_{j1}}{ds}\right\}=\tilde{C}(k), \quad k=1,\ldots,N=1, \tag{30}$$

$$\frac{1}{1+\alpha}\frac{de_k}{ds}=\tilde{D}(k),\quad k=1,\ldots,N, \tag{31}$$

where $e_j, j = 1, \ldots, N$ are the parameters for the profile $S \equiv \partial V/\partial\psi$ and $\tilde{C}(k)$ and $\tilde{D}(k)$ are again complex expressions not containing any s or ψ derivatives of b_{j1} or e_j. $C,D,\tilde{C}$, and $\tilde{D}$ are given in the Appendix.

The appropriate initial conditions can be obtained from the solution of a uniform entry into a straight tube. As a first approximation, the Blasius solution with a free stream velocity equal to W_i was used. It is well known that a similarity solution exists in this case and equation (27) yields a system of nonlinear coupled algebraic equations given by [3]

$$\tfrac{1}{2}\bar{A}_0\int_0^1\frac{Wg_N}{1-W}\,dW=S(N),$$

$$\tfrac{1}{2}\left\{\bar{A}_k+\bar{A}_0\int_0^1\frac{Wg_k}{1-W}dW\right\}=S(k),\quad k=1,\ldots,N-1, \tag{32}$$

where $\bar{A}_k$ is related to b_{k1} by

$$b_{k1}=\alpha^{1/4}\bar{A}_k\sqrt{s_i} \tag{33}$$

and s_i is an initial station taken as 0.0025 at present. $S(k)$ is given in the Appendix. Equation (32) has been solved iteratively for $\bar{A}_k$'s. Since the flow is approximately axisymmetric at s_i,

$$b_{j2}=e_j=0,\quad j=1,\ldots,N. \tag{34}$$

A simple method based on the Method of Lines [5] was used to solve equations (27) and (28). The ψ domain is divided into ℓ equal intervals and the ψ derivatives of either Z or V at the nodal point $\psi_k = k\pi/\ell$, $k = 1,2, \ldots, (\ell-1)$ is approximated by a backward difference formula

$$\left(\frac{\partial U}{\partial\psi}\right)_k=\frac{U_k-U_{k-1}}{\Delta\psi}, \tag{35}$$

where U is either Z or V and $\Delta\psi$ is simply π/ℓ. It should be mentioned that the backward difference scheme produced stable results for the present problem. The conventional Telenin method has been tried and found to yield oscillatory results in the streamwise direction.

The solution procedure in the boundary layer region was to integrate equations (30) and (31) directly subject to the appropriate initial conditions at s_i. Solutions at $\psi = 0$ were used to calculate the ψ derivatives of the next plane, $\psi = \pi/\ell$; equations (27) and (28) were then integrated to yield results at $\psi = \pi/\ell$. This procedure was continued until $\psi = \pi$ was reached. It should be noted that it is possible to decouple each ψ = constant plane only because of the simple backward difference scheme used. If a general finite difference formula were used in place of (35), $2N\ell$ coupled ordinary differential equations would be generated by equations (27) and (28). An available ODE solver package has been used for the integration.

Downloaded 02 May 2010 to 171.66.16.246. Redistribution subject to ASME license or copyright; see http://www.asme.org/terms/Terms_Use.cfm

4 Interaction Between the Core and Boundary Layer Regions

A computer program was written for each of the solution procedures described in Sections 2 and 3. A simple iteration scheme was used to account for the interaction between the two regions. The core flow was initially represented by a two-dimensional point vortex to provide the necessary functional values at the boundary layer edge. In general, a five-point Lagrangian interpolation scheme was used to calculate the values at a particular point in space. From the boundary layer solution, a new estimate for the outward radial velocity, and hence f_3, could be calculated and the core region reevaluated. If f_3^n and f_3^{n-1} are the estimates of f_3 from the current nth boundary layer calculation and the previous $(n-1)$th calculation, respectively, then the new estimate of f_3 is evaluated as

$$f_3^{(\text{new})} = f_3^{n-1} + \omega(f_3^n - f_3^{n-1}), \quad 0 < \omega < 1 \tag{36}$$

f_3^{n-1} is then updated as

$$f_3^{n-1} = f_3^{(\text{new})} \tag{37}$$

for the next iteration.

5 Results and Discussion

The overall accuracy of the present model is restricted by the accuracy of the boundary layer calculation, which is of first order in ψ by virtue of equation (35). All numerical calculations were carried out on a CDC 7600 computer. In the first approximation (corresponding to $N = 1$ in the Method of Integral Relations (equations (27) and (28)), the computing time for the boundary layer calculation requires about twice as much time as for the core calculation, which needs about 1 sec. The computation time increases rather rapidly as the order of approximation, N, increases. The present calculation is limited to the second-order approximation, $N = 2$. Five points were calculated in the ψ direction and three points were taken in the v direction. A typical calculation requires about 40 iterations or 5 min of computation time, which is to be compared with 50 sec for the first approximation. Also, the converged solution for the core region from the first approximation was used to initiate the iteration process for the second approximation. As a result, comparatively large values of ω can be used ($\omega = 0.1$ at present) which speeds up the iteration process. Typical results have been presented in [4].

6 Conclusion

A numerical scheme has been presented in detail for the solution concerning the steady laminar flow of an incompressible fluid in the entry region of a circular curved pipe at very high Reynolds number. A special feature of the numerical scheme is to eliminate as much finite difference formulation as possible. The present scheme is restricted to the second approximation due to the large number of ordinary differential equations arising in the boundary layer calculations.

References

1 Dean, W. R., "Note on the Motion of Fluid in a Curved Pipe," *Philosophical Magazine*, Vol. 4, 1927, pp. 208-223.

2 Dean, W. R., "The Streamline Motion of Fluid in a Curved Pipe," *Philosophical Magazine*, Vol. 5, 1928, pp. 673-695.

3 Yeung, W. S., "Gas-Particle in the Entry Region of a Curved Pipe," Ph.D. Thesis, Report LBL-9905, Lawrence Berkeley Laboratory, University of California, Berkeley, Calif., 1979.

4 Yeung, W. S., "Laminar Boundary-Layer Flow Near the Entry of a Curved Circular Pipe," ASME JOURNAL OF APPLIED MECHANICS, Vol. 47, 1980, pp. 697-702.

5 Holt, M., *Numerical Methods in Fluid Dynamics*, Springer-Verlag, Berlin, Heidelberg, New York, 1977.

6 Garabedian, P. R., *Partial Differential Equations*, Wiley, New York, 1964.

7 Issacson, E., and Keller, H. B., *Analysis of Numerical Methods*, Wiley, New York, 1966.

APPENDIX

Expressions for $C(k)$, $D(k)$, $\tilde{C}(k)$, $\tilde{D}(k)$, and $S(k)$ from reference [3]

$$C(k) = \frac{\sin}{1+\alpha\cos\psi} - \frac{1}{W_e}\frac{\partial W_e}{\partial \psi}\int_0^1 [(VW - V_e)g_k' + Vg_k]Z\,dW + \frac{1}{1+\alpha\cos\psi}\frac{1}{W_e}\frac{\partial W_e}{\partial s}\int_0^1 [(1-W^2)g_k - Wg_k]Z\,dW - \frac{\sqrt{\alpha}}{W_e}\frac{g_k'(0)}{Z_0} - \frac{\sqrt{\alpha}}{W_e}\int_0^1 \frac{g_k''}{Z}\,dW$$

$$D(k) = \frac{1}{W_e}\frac{\partial W_e}{\partial \psi}\int_0^1 \left\{(V_e^2 - V^2) - \frac{\partial V}{\partial W}(V_e - VW)\right\}h_k(W)\,dW + \frac{1}{1+\alpha\cos\psi}\frac{1}{W_e}\frac{\partial W_e}{\partial s}\int_0^1 \left\{V_e - WV - \frac{\partial V}{\partial W}(1-W^2)\right\}h_k\,dW + \frac{\alpha\sin\psi}{1+\alpha\cos\psi}\int_0^1 \left\{(1-W^2) - \frac{\partial V}{\partial W}(VW - V_e)\right\}h_k\,dW + \left(V_e\frac{\partial V_e}{\partial \psi} + \frac{1}{1+\alpha\cos\psi}\frac{\partial V_e}{\partial s}\int_0^1 h_k\,dW + \frac{\sqrt{\alpha}}{W_e}\int_0^1 \frac{\partial^2 V}{\partial W^2}\frac{1}{Z^2}h_k\,dW,$$

$$\tilde{C}(k) = -\int_0^1 ZSg_k\,dW + \frac{1}{1+\alpha\cos\psi}\frac{1}{W_e}\frac{dW_e}{ds}\int_0^1 [(1-W^2)g_k' - Wg_k]Z\,dW - \frac{\sqrt{\alpha}\,g_k'(0)}{W_eZ_0} - \frac{\sqrt{\alpha}}{W_e}\int_0^1 \frac{g_k''}{Z}\,dW,$$

$$\tilde{D}(k) = -\int_0^1 S^2h_k\,dW + \frac{1}{1+\alpha\cos\psi}\frac{1}{W_e}\frac{dW_e}{s}\int_0^1 \left[(S_e - WS) - \frac{\partial S}{\partial W}(1-W^2)\right]h_k\,dW + \frac{\alpha\cos\psi}{1+\alpha\cos\psi}\int_0^1 (1-W^2)h_k\,dW + \left(S_e^2 + \frac{1}{1+\alpha\cos\psi}\frac{dS_e}{ds}\int_0^1 h_k\,dW + \frac{\sqrt{\alpha}}{W_e}\int_0^1 \frac{\partial^2 S}{\partial W^2}\frac{1}{Z^2}h_k\,dW,$$

$$S(k) = -\frac{g_k(0)}{\theta_0} - \int_0^1 \frac{g_k''}{\theta(W)}\,dW,$$

where the prime denotes differentiation with respect to W, and θ is related to $\bar{A}_k$ (equation (33)) by

$$\theta(W) = \left\{\bar{A}_0 + \sum_{j=1}^{N-1}\bar{A}_j g_j(W)\right\}/(1-W).$$

Downloaded 02 May 2010 to 171.66.16.246. Redistribution subject to ASME license or copyright; see http://www.asme.org/terms/Terms_Use.cfm

On Transverse Secondary Flows in Wave Channels

R. E. Johnson
Assistant Professor,
Department of Theoretical and Applied Mechanics,
University of Illinois at Urbana-Champaign,
Urbana, Ill.

The viscous boundary layer analysis for the sidewalls of a wave tank is presented for the case of two-dimensional waves of small amplitude traveling along the channel length. The second-order transverse streaming motion induced in the interior of the channel by the sidewall layers is determined. The calculations extend the work of Mei and Liu [1] which examined the effect of sidewalls on the longitudinal streaming motion. The intensity of the transverse streaming flow is found to increase as the depth to wavelength ratio decreases, and is found to be significant for typical wave tanks that generally have a depth to width ratio between one-half and one-fourth. The present results are useful if accurate conclusions concerning mass transport in the open ocean are to be made from laboratory studies. Furthermore, the results may offer an explanation for some of the laboratory observations already in the literature.

Introduction

The fundamental theory of mass transport in water waves is due to Longuet-Higgins [2]. In that work the classical two-dimensional inviscid, irrotational water wave theory was modified to satisfy the no-slip condition at the water bottom and the shear-free condition at the free surface. This was accomplished by including in the solution viscous boundary layers at the water bottom and free surface. One of the principal results found is that the nonlinear effect of Reynolds stresses cause a second-order steady streaming motion in the boundary layers which in turn drives a steady circulation or current in the interior or core of the fluid. Although the existence of a mass transport velocity had already been predicted by Stokes [3] based on inviscid, irrotational theory, the presence of the viscous boundary layers was found to have a substantial effect on the mass transport.

The pioneering work of Longuet-Higgins has been followed by a great number of studies on wave-induced mass transport. The majority of these studies have been concerned with purely two-dimensional flow fields. Summaries of the work on two-dimensional waves are available in the introductions to [4–6].

One of the only studies of three-dimensional effects is presented by Mei and Liu [1] in a MIT report. In that report, Mei and Liu consider the effect of wave tank sidewalls on the streaming motion induced in the direction of wave propagation by waves traveling along the channel length. They made no calculations, however, of the induced transverse streaming motion in the cross-section plane of the channel. The present study will extend the work of Mei and Liu by examining the transverse motion. The viscous boundary layers at the wave tank sidewalls which, along with the bottom and free-surface boundary layers, drive the steady motion in the interior of the channel will be examined. The boundary layer analysis is similar to that of Mei and Liu, except an Eulerian description is used here as opposed to the Lagrangian description used by Mei and Liu. The present version is believed to be somewhat simpler. The results are in agreement with those of Mei and Liu, and the analysis will be presented in an appendix since their work is not readily available in its present form. The present study will also estimate the attenuation coefficient of the wave motion due to the viscous dissipation in the sidewall layers. This result is in agreement with that obtained previously by Mei and Liu [7]. In the somewhat similar situation involving closed basins, the linear wave damping due to the sidewalls has been examined by a number of researchers [7–10]. Note that in this connection it has been pointed out that sidewall capillary effects can contribute significantly to the damping. This effect, however, is not considered here.

The primary result of the present investigation will be the determination of the transverse streaming motion that is established in the interior of the channel. This will be found for the case of very small amplitude waves when the streaming motion is governed by the Stokes equations. This case is referred to as the conduction-limit and implies that the steady streaming Reynolds number $R_s = a^2\ \omega/\nu$ is small (a is the wave amplitude, ν the kinematic viscosity, and ω the wave frequency). Although this restriction is severe, Mei and Liu [1] indicate that experimental results have shown qualitative agreement with such a theory under various conditions. They also point out that in the natural environment the eddy viscosity ν_e should replace the much smaller laminar viscosity

Contributed by the Applied Mechanics Division for presentation at the 1983 ASME Applied Mechanics, Bioengineering, and Fluids Engineering Conference, Houston, Texas, June 20–22, 1983 of THE AMERICAN SOCIETY OF MECHANICAL ENGINEERS.

Discussion on this paper should be addressed to the Editorial Department, ASME, United Engineering Center, 345 East 47th Street, New York, N.Y. 10017, and will be accepted until two months after final publication of the paper itself in the JOURNAL OF APPLIED MECHANICS. Manuscript received by ASME Applied Mechanics Division, August, 1982; final revision, October, 1982. Paper No. 83-APM-26.

Copies will be available until February, 1984.

Copyright © 1983 by ASME
Downloaded 02 May 2010 to 171.66.16.246. Redistribution subject to ASME license or copyright; see http://www.asme.org/terms/Terms_Use.cfm

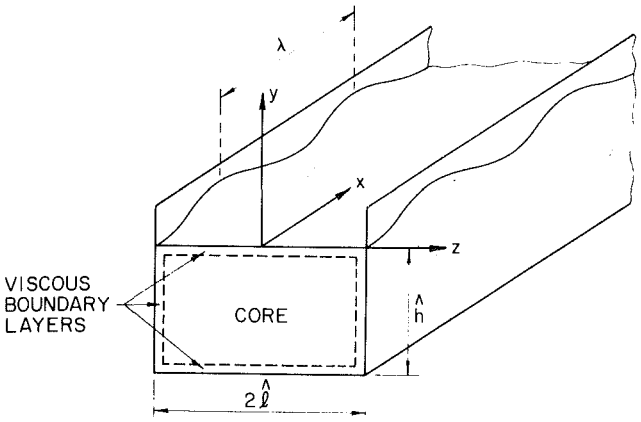

Fig. 1 Cross-sectional view of a wave channel

ν in which case this limit may be very realistic. Furthermore, it should be noted that numerous applications of the conduction-limit have been made in purely two-dimensional flows and that the results have often been useful.

For the two-dimensional case, studies have recently examined the problem when $R_s >> 1$ [4, 6]. For these large streaming Reynolds numbers the analysis results in a double-boundary layer theory in which the boundary layer of the type previously discussed, often referred to as a Stokes layer, is embedded within a thicker outer boundary layer. The theory is analogous to that developed by Stuart [11] for an oscillating cylinder. Similar attempts in the present problem have unfortunately not yet been successful. The difficulty is primarily due to the increased complexity associated with the three-dimensional character of the present problem.

Formulation

We consider a wave channel of width $2\hat{l}$ and constant mean depth $\hat{h}$ in which small amplitude, two-dimensional waves are propagating along the channel length. The wave disturbance is given to leading order by

$$\hat{y} = a\cos(k\hat{x} - \omega\hat{t}),$$

where a is the wave amplitude, $k = 2\pi/\lambda$ is the wave number, λ the wave length, $\hat{x}$ the direction of wave propagation, $\hat{y}$ the vertical direction, and ω the wave frequency. The $\hat{z}$ axis is taken to be in the cross-channel direction (see Fig. 1).

In the governing equations the velocity $\hat{\mathbf{u}}$, pressure $\hat{p}$, time $\hat{t}$, and position $\hat{\mathbf{x}} = (\hat{x},\hat{y},\hat{z})$ are nondimensionalized according to

$$\mathbf{u} = \hat{\mathbf{u}}/\omega a, \quad p = \hat{p}/\rho\omega^2 a\lambda, \quad t = \omega\hat{t},$$
$$\mathbf{x} = \hat{\mathbf{x}}/\lambda, \quad l = \hat{l}/\lambda, \quad h = \hat{h}/\lambda,$$

giving the equations of momentum and mass conservation as

$$\frac{\partial \mathbf{u}}{\partial t} + \epsilon(\mathbf{u}\cdot\nabla)\mathbf{u} = -\nabla(p+\alpha y) + \mathrm{Re}^{-1}\nabla^2\mathbf{u}, \quad \nabla\cdot\mathbf{u} = 0. \tag{1}$$

Here $\alpha = g/\omega^2 a$, g is the constant gravitational acceleration, $\epsilon = a/\lambda$ is the amplitude parameter which is assumed small, and $\mathrm{Re} = \omega\lambda^2/\nu$ is a Reynolds number. The boundary conditions are as follows. The velocity vanishes at the bottom and sidewalls of the channel. At the free surface the shear stress vanishes, the normal stress equals the ambient atmospheric pressure, and the flux of fluid across the surface is zero. The effects of surface tension and/or surface films are neglected at the free surface.

We restrict attention to $\mathrm{Re} >> 1$ in which case it is well known that near the solid boundaries (bottom and sidewalls) and free surface there will be thin regions where viscous effects become important, i.e., the viscous boundary layers. The thickness of these layers is of order $\delta = \sqrt{\nu/\omega}$ where δ is the characteristic length scale associated with momentum diffusion. The viscous regions are thin because the Reynolds number is assumed large and $\delta/\lambda = \mathrm{Re}^{-1/2} << 1$. Consequently, we determine the solution within these viscous boundary layers and match the solution to the core solution valid in the interior of the channel. Within the core the flow field is given at leading order by the classical two-dimensional, inviscid, irrotational water wave theory. Deviation from this potential flow are found at second order due to the matching with the motion in the boundary layers. In the boundary layers, however, the flow field differs from the two-dimensional potential flow at leading order so that the boundary conditions may be satisfied. That is, at leading order the boundary layer solution is given by the two-dimensional potential flow plus a correction term that vanishes outside the boundary layer.

Although it has been popular in previous studies to use a Lagrangian formulation, here the problem is formulated in terms of the Eulerian velocity.

Consideration of the Core

The solution valid in the core has the form

$$\begin{aligned}
u &= u^{(P0)} + \epsilon(u^{(P1)} + u^*) + \ldots, \\
v &= v^{(P0)} + \epsilon(v^{(P1)} + v^*) + \ldots, \\
w &= \epsilon w^* + \ldots, \\
P &= p + \alpha y = P^{(P0)} + \epsilon(P^{(P1)} + \mathrm{Re}^{-1}P^*) + \ldots \\
y &= \epsilon Y^{(0)} + \epsilon^2 Y^{(1)} + \ldots = \epsilon\cos(2\pi x - t) + \epsilon^2 Y^{(1)} + \ldots,
\end{aligned} \tag{2}$$

where $(u,v,w,)$ are the (x,y,z) components of velocity, and the last equation is the free-surface profile which contains a perturbation at second order. $\mathbf{u}^{(PK)} = (u^{(PK)}, v^{(PK)}, 0)$, $P^{(PK)}$ and $Y^{(K)}$, $K = 0,1$, are the first and second-order potential flow solutions of classical water wave theory. This potential part of the core solution is unaffected by the viscous boundary layers, including the sidewalls. $\mathbf{u}^*$, p^* are the rotational velocity and pressure fields which must be added to the potential flow in the core so that the core solution can match to the boundary layer solutions.

The potential flow terms satisfy the governing equations of inviscid, irrotational flow. The viscous terms of order Re^{-1} in the momentum equations are neglected and there is zero vorticity, giving the following heirarch of equations.

$$\begin{aligned}
&\frac{\partial \mathbf{u}^{(P0)}}{\partial t} = -\nabla P^{(P0)}, \\
&\nabla\cdot\mathbf{u}^{(P0)} = 0, \quad \nabla\times\mathbf{u}^{(P0)} = 0, \\
&\frac{\partial \mathbf{u}^{(P1)}}{\partial t} + (\mathbf{u}^{(P0)}\cdot\nabla)\mathbf{u}^{(P0)} = -\nabla P^{(P1)}, \\
&\nabla\cdot\mathbf{u}^{(P1)} = 0, \quad \nabla\times\mathbf{u}^{(P1)} = 0.
\end{aligned} \tag{3}$$

The potential part of the core solution is thus given by the classical two-dimensional water wave solution,

$$u^{(P0)} = \cos\theta\,\frac{\cosh 2\pi(h+y)}{\sinh 2\pi h},$$

Downloaded 02 May 2010 to 171.66.16.246. Redistribution subject to ASME license or copyright; see http://www.asme.org/terms/Terms_Use.cfm

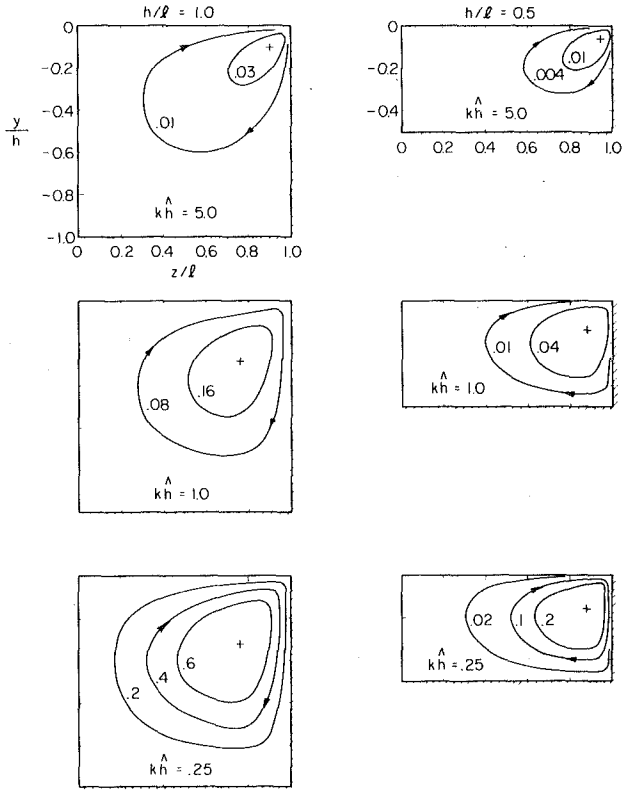

Fig. 2 Streamlines (ψ = constant) in the cross section plane of the channel. Depth to half-width ratio h/l = 1.0 and 0.5 in the figures on the left and right, respectively. $k\hat{h}$ = 5.0, 1.0, and 0.25 in the top, middle, and bottom figures, respectively.

$$
\begin{aligned}
v^{(P0)} &= \sin\theta \frac{\sinh 2\pi(h+y)}{\sinh 2\pi h},\\
P^{(P0)} &= \cos\theta \frac{\cosh 2\pi(h+y)}{2\pi \sinh 2\pi h},\\
u^{(P1)} &= \frac{3}{2}\pi A^2 \cosh 4\pi(h+y)\cos 2\theta,\\
v^{(P1)} &= \frac{3}{2}\pi A^2 \sinh 4\pi(h+y)\sin 2\theta,\\
P^{(P1)} &= \frac{A}{4}\{1-\cosh 4\pi(h+y)\\
&\quad +\cos 2\theta[3\cosh 4\pi(h+y)-1]\},\\
Y^{(1)} &= \frac{1}{2}\coth 2\pi h\left(1+\frac{3}{2\sinh^2 2\pi h}\right)\cos 2\theta,
\end{aligned}
\tag{4}
$$

$$\theta = 2\pi x - t, \quad A = \frac{1}{\sinh^2 2\pi h}.$$

This motion is purely periodic and lies in a plane parallel to the sidewalls.

Next we consider the governing equations for the velocity $\mathbf{u}^*$ and pressure P^*. This part of the core velocity is affected by the presence of the viscous boundary layers. The quantity of practical interest is the steady streaming motion in the core, and therefore we will only consider the time average of the velocity $\mathbf{u}^*$ averaged over one wave period. As discussed in the Introduction, this may be determined in the conduction limit of Longuet-Higgins [2], namely when $\epsilon^2 << \mathrm{Re}^{-1}$. (This being equivalent to $R_s << 1$ discussed in the Introduction.) In this limit the governing equations for the time average velocity and pressure have a particularly simple form,

$$
\begin{aligned}
\nabla^2 \bar{\mathbf{u}}^* &= \nabla \bar{P}^*,\\
\nabla \cdot \bar{\mathbf{u}}^* &= 0,
\end{aligned}
\tag{5}
$$

where an overbar denotes a time average over one wave period.

The core problem is completed with the followed boundary values which are derived from the boundary layer solutions (see Appendix 1),

$$
\begin{aligned}
&\text{Sides:} \quad \bar{u}^* = \bar{w}^* = 0, \ \bar{v}^* = V(y) \quad \text{at} \quad z = \pm l,\\
&\text{Surface:} \quad \frac{\partial \bar{u}^*}{\partial y} = \tau, \ \bar{v}^* = \frac{\partial \bar{w}^*}{\partial y} = 0 \quad \text{at} \quad y = 0,\\
&\text{Bottom:} \quad \bar{u}^* = U, \ \bar{v}^* = \bar{w}^* = 0 \quad \text{at} \quad y = -h.
\end{aligned}
\tag{6}
$$

$V(y)$, τ, and U are given in Appendix 1 by equations (a), (b), and (c), respectively.

Since the boundary conditions are independent of x, we consider solutions for the velocity field $\bar{\mathbf{u}}^*$ which are functions only of y and z. Consequently, the motion in the x-direction decouples from the motion in the cross-section plane. The problem for $\bar{u}^*$, i.e., the streaming motion in the direction of wave propagation, is therefore,

$$\frac{\partial^2 \bar{u}^*}{\partial y^2} + \frac{\partial^2 \bar{u}^*}{\partial z^2} = \frac{\partial \bar{P}^*}{\partial x} \equiv G, \tag{7}$$

with the boundary conditions

$$
\begin{aligned}
&\bar{u}^*(y, \pm l) = 0,\\
&\frac{\partial \bar{u}^*}{\partial y}(0, z) = \tau,\\
&\bar{u}^*(-h, z) = U.
\end{aligned}
\tag{8}
$$

The motion in the cross-section plane is governed by

$$
\begin{aligned}
&\frac{\partial^2 \bar{v}^*}{\partial y^2} + \frac{\partial^2 \bar{v}^*}{\partial z^2} = \frac{\partial P^*}{\partial y},\\
&\frac{\partial^2 \bar{w}^*}{\partial y^2} + \frac{\partial^2 \bar{w}^*}{\partial z^2} = \frac{\partial \bar{P}^*}{\partial z},\\
&\frac{\partial \bar{v}^*}{\partial y} + \frac{\partial \bar{w}^*}{\partial z} = 0,
\end{aligned}
\tag{9}
$$

with the boundary conditions

$$
\begin{aligned}
&\bar{v}^*(y, \pm l) = V(y), \quad \bar{w}^*(y, \pm l) = 0,\\
&\bar{v}^*(0, z) = \frac{\partial \bar{w}^*}{\partial y}(0, z) = 0,\\
&\bar{v}^*(-h, z) = \bar{w}^*(-h, z) = 0.
\end{aligned}
\tag{10}
$$

Note that a velocity field $\bar{\mathbf{u}}^*$ which is independent of x requires that the pressure gradient in the x-direction be a constant G, i.e., independent of y and z. Furthermore, such a solution is likely only to be valid away from the ends of the wave tank.

The motion in the direction of wave propagation has been previously considered by Mei and Liu [1] and therefore it will not be examined here. For the motion in the cross-section plane it is convenient to introduce the stream function ψ defined as

$$\bar{v}^* = \frac{\partial \psi}{\partial z}, \quad \bar{w}^* = -\frac{\partial \psi}{\partial y}, \tag{11}$$

which has the governing equation,

$$\left(\frac{\partial^2}{\partial y^2} + \frac{\partial^2}{\partial z^2}\right)^2 \psi = 0. \tag{12}$$

Due to the flow symmetry about the channel centerline, it is

Downloaded 02 May 2010 to 171.66.16.246. Redistribution subject to ASME license or copyright; see http://www.asme.org/terms/Terms_Use.cfm

sufficient to solve the problem in the region $0 \le z \le +l$. Using the symmetry condition at the channel centerline $z = 0$ the boundary conditions on the stream function become

$$\psi = \frac{\partial^2 \psi}{\partial z^2} = 0, \quad z = 0,$$

$$\psi = 0, \quad \frac{\partial \psi}{\partial z} = V(y), \quad z = l,$$

$$\psi = \frac{\partial^2 \psi}{\partial y^2} = 0, \quad y = 0,$$

$$\psi = \frac{\partial \psi}{\partial y} = 0, \quad y = -h. \tag{13}$$

The solution for ψ is

$$\psi = \sum_{m=1}^{\infty} b_m \psi_m,$$

$$\psi_m = \sin \beta_m y \left[\frac{z}{l} \tanh \beta_m l \cosh \beta_m z - \sinh \beta_m z \right]$$

$$+ \sum_{n=1}^{\infty} B_{mn} \sin \alpha_n z \left[\frac{y}{h} \tanh \alpha_n h \cosh \alpha_n y - \sinh \alpha_n y \right],$$

$$\beta_m = \frac{m\pi}{h}, \quad \alpha_n = \frac{n\pi}{l}.$$

b_m and B_{mn} are constants determined from the boundary conditions, the details of which are given in the Appendix 2.

Discussion

Shown in Fig. 2 are streamlines (ψ = constant) in the cross-section plane of a channel ($0 \le z \le l$, $-h \le y \le 0$) for the depth to half-width ratios $h/l = 1$, 1/2 and $k\hat{h} = 0.25$, 1.0, 5.0 ($h = \hat{h}/\lambda$, $l = \hat{l}/\lambda$). These curves represent a cross-sectional veiw of the stream surfaces since there is an additional superposed flow in the direction of wave propagation. Furthermore, a duplicate pattern is present in the other half of the cross-sectional plane, $-l \le z \le 0$, due to the flow symmetry. The motion in Fig. 2 is clockwise; toward the sidewall near the free surface and then down along the sidewall. Note that it is easy to verify that the components of the Lagrangian or mass transport velocity in the cross-sectional plane of the channel are equal to the Eulerian velocity components $\bar{v}^*$, $\bar{w}^*$. Consequently, the streamlines in Fig. 2 describe the mass transport in the transverse direction. Furthermore, if we combine this motion with the drift motion in the direction of wave propagation, we find that fluid particles typically move in a spiral-like fashion.

From Fig. 2 we observe that this transverse streaming motion intensifies as $k\hat{h}$ decreases, i.e., as the wavelength increases for fixed depth. This relatively strong circulation in the cross-section plane at small values of $k\hat{h}$ may partially explain why experimentalists have encountered difficulty attempting to measure mass transport, which was believed to be only in the direction of wave propagation [12, 13]. On the other hand, there is very little direct quantitative measurements of motion in the cross-sectional plane. This may be due to the fact that the majority of the experimental work has been directed at sediment transport near the bottom where the transverse velocity $\bar{w}^*$ vanishes. In addition, velocity measurements taken across the depth of the channel are usually performed along the channel center line where the transverse motion also vanishes. Russell and Osorio [12] state that for $k\hat{h} < 0.3$ the flow patterns varied unsymmetrically and " . . . usually involved flows in directions other than in the direction of wave propagation." Whether the present analysis pertains to what they observed is unclear, especially since they claim that sidewall effects in the experiment were unimportant. Furthermore, the experiments of Russell and Osorio were strongly affected by surface contamination which is neglected here. The unsystematic or erratic motion which has been reported for small $k\hat{h}$ suggests that these flows may be unstable. Craik [5] found that the two-dimensional drift motion in the direction of wave propagation is unstable to spanwise-periodic disturbances. A similar stability analysis for the transverse streaming motion discussed here would be useful.

The only experiments giving a good qualitative description of an observed transverse flow are due to Carter [14]. Carter observed two cells near each sidewall separated at about the half depth point with the flow down along the wall in each cell. With the exception of the direction of flow near the wall, clearly such a pattern is in poor agreement with the single cell predicted here. Unfortunately, the range of flow conditions for which the double cell structure is observed is not made clear. This pattern again raises the question of stability. We should note that extending the theory to include large streaming Reynolds numbers R_s is not likely to explain the two cell pattern. However, a large R_s theory might be a more realistic flow on which to consider the stability of laboratory scale experiments.

I am most grateful to Professor S. Stewart for his comments concerning the original manuscript. This work was partially supported by the National Science Foundation (MEA 81-07564).

References

1 Mei, C. C., and Liu, P. L-F., "Mass Transport in Water Waves. Part I: Theory," Ralph M. Parsons Lab. Water Resources Hydrodyn., MIT Report No. 146, 1972.

2 Longuet-Higgins, M. S., "Mass Transport in Water Waves," *Phil. Trans.*, Series *A*, Vol. 245, 1953, pp. 535-581.

3 Stokes, G. G., "On the Theory of Oscillatory Waves," *Trans. Camb. Phil. Soc.*, Vol. 8, 1847, pp. 441-455.

4 Liu, A-K., and Davis, S. H., "Viscous Attenuation of Mean Drift in Water Waves," *J. Fluid Mech.*, Vol. 81, 1977, pp. 63-84.

5 Craik, A. D. D., "The Drift Velocity of Water Waves," *J. Fluid Mech.*, Vol. 116, 1982, pp. 187-205.

6 Dore, B. D., "On Mass Transport Velocity Due to Progressive Waves," *Q.J. Mech. Appl. Math.*, Vol. 30, 1977, pp. 157-173.

7 Mei, C. C., and Liu, L. F., "The Damping of Surface Gravity Waves in a Bounded Liquid," *J. Fluid Mech.*, Vol. 59, 1973, pp. 239-256.

8 Miles, J. W., "Surface-Wave Damping in Closed Basins," *Proc. Roy. Soc. London*, Series *A*, Vol. 297, 1967, pp. 459-475.

9 Keulegan, G. H., "Energy Dissipation in Standing Waves in Rectangular Basins," *J. Fluid Mech.*, Vol. 6, 1959, pp. 33-50.

10 Case, K. M., and Parkinson, W. C., "Damping of Surface Waves in an Incompressible Liquid," *J. Fluid Mech.*, Vol. 2, 1957, pp. 172-184.

11 Stuart, J. T., "Double Boundary Layers in Oscillatory Viscous Flow," *J. Fluid Mech.*, Vol. 24, 1966, pp. 673-687.

12 Russell, R. C. H., and Osorio, J. D. C., "An Experimental Investigation of Drift Profiles in a Closed Channel," *Proc. 6th Conf. on Coastal Eng.*, 1957, pp. 171-193.

13 Allen, J., and Gibson, D. H., "Experiments on the Displacement of Water by Waves of Various Heights and Frequencies," *Min. Proc. Instn. Civ. Engrs.*, Vol. 13, 1959, pp. 363-386.

14 Carter, T. G., "Mass Transport in Water Waves, Part II: Experiments," Ralph M. Parsons Lab. Water Resources Hydrodyn., MIT Report No. 146, 1972.

15 Phillips, O. M., *The Dynamics of the Upper Ocean*, Cambridge Univ. Press, London, 1977.

APPENDIX 1

(a) Consideration of the Boundary Layers

For the viscous layers near the wave channel sidewalls, we rescale the distance normal to the wall by introducing the

Downloaded 02 May 2010 to 171.66.16.246. Redistribution subject to ASME license or copyright; see http://www.asme.org/terms/Terms_Use.cfm

inner variable $Z = \mathrm{Re}^{1/2}(l \pm z)$, the + and − being for the sidewalls at $z = -l$ and $+l$, respectively. With this rescaling the momentum equation in the direction normal to the wall gives the familiar result that the pressure P is approximately constant across the boundary layer, i.e., $\partial P/\partial Z = 0$, with an error of order $\mathrm{Re}^{-1/2}$ w, w being the boundary layer velocity normal to the wall. Consequently, the pressure within the boundary layer is given by the core pressure evaluated at the sidewalls $z = \pm l$, the leading order terms of which are simply the potential flow pressure field

$$P = P^{(P0)}(x,y,t) + \epsilon P^{(P1)}(x,y,t) + \ldots$$

For the velocity field within the sidewall boundary layers we have

$$\begin{aligned} u &= u^{(P0)}(x,y,t) + u^{(B0)}(x,y,Z,t) + \\ &\quad \epsilon[u^{(P1)}(x,y,t) + u^{(B1)}(x,y,Z,t)] + \ldots \\ v &= v^{(P0)}(x,y,t) + v^{(B0)}(x,y,Z,t) + \\ &\quad \epsilon[v^{(P1)}(x,y,t) + v^{(B1)}(x,y,Z,t)] + \ldots \\ w &= \mathrm{Re}^{-1/2} w^{(B0)}(x,y,Z,t) + \epsilon\,\mathrm{Re}^{-1/2} w^{(B1)}(x,y,Z,t) + \ldots \end{aligned}$$

Here $\mathbf{u}^{(PK)}$ $(K = 0,1)$ are equal to the two-dimensional potential flow velocity present in the core (equations (4)), and $\mathbf{u}^{(BK)}$ $(K = 0,1)$ are the deviations from the potential flow which are necessary to satisfy the no-slip condition on the sidewalls. Note that the $\mathrm{Re}^{-1/2}$ appearing in the expansion for the Z-component of velocity is a consequence of the rescaled form of the continuity equation which must be satisfied.

After expressing the remaining governing equations in terms of the inner variable Z, and using the fact that the potential flow solution $\mathbf{u}^{(P0)}$, $P^{(P0)}$ are functions only of x and y and satisfy the equations (3), we obtain the following equations for the leading-order boundary layer correction $\mathbf{u}^{(B0)}$,

$$\frac{\partial u^{(B0)}}{\partial t} = \frac{\partial^2 u^{(B0)}}{\partial Z^2}, \qquad \frac{\partial v^{(B0)}}{\partial t} = \frac{\partial^2 v^{(B0)}}{\partial Z^2}$$

$$\frac{\partial u^{(B0)}}{\partial x} + \frac{\partial v^{(B0)}}{\partial y} + \frac{\partial w^{(B0)}}{\partial Z} = 0$$

At this order the no-slip and matching conditions require

$$\left.\begin{aligned} u^{(B0)} &= -u^{(P0)} \\ v^{(B0)} &= -v^{(P0)} \\ w^{(B0)} &= 0 \end{aligned}\right\} \quad \text{on} \quad Z = 0,$$

$$\left.\begin{aligned} u^{(B0)} &\to 0 \\ v^{(B0)} &\to 0 \\ w^{(B0)} &\to 0 \end{aligned}\right\} \quad \text{as} \quad Z \to \infty,$$

and the solution is found to be

$$u^{(B0)} = -\frac{\cosh 2\pi(h+y)}{\sinh 2\pi h} e^{-Z/\sqrt{2}} \cos(\theta + Z/\sqrt{2}),$$

$$v^{(B0)} = -\frac{\sinh 2\pi(h+y)}{\sinh 2\pi h} e^{-Z/\sqrt{2}} \sin(\theta + Z/\sqrt{2}),$$

$$w^{(B0)} = 0, \quad \theta = 2\pi x - t.$$

In a similar fashion we obtain the governing equations for the second-order boundary layer velocity $\mathbf{u}^{(B1)}$ as

$$\frac{\partial u^{(B1)}}{\partial t} + \frac{\partial}{\partial x}[2u^{(P0)}u^{(B0)} + u^{(B0)^2}] +$$

$$\frac{\partial}{\partial y}[u^{(P0)}v^{(B0)} + v^{(P0)}u^{(B0)} + u^{(B0)}v^{(B0)}] = \frac{\partial^2 u^{(B1)}}{\partial Z^2},$$

$$\frac{\partial v^{(B1)}}{\partial t} + \frac{\partial}{\partial x}[u^{(P0)}v^{(B0)} + v^{(P0)}u^{(B0)} + u^{(B0)}v^{(B0)}] +$$

$$\frac{\partial}{\partial y}[2v^{(P0)}v^{(B0)} + v^{(B0)^2}] = \frac{\partial^2 v^{(B1)}}{\partial Z^2}$$

$$\frac{\partial u^{(B1)}}{\partial x} + \frac{\partial v^{(B1)}}{\partial y} + \frac{\partial w^{(B1)}}{\partial Z} = 0.$$

In obtaining the preceding equations, we have used the continuity equation satisfied by the leading-order solution to express the Reynolds-stress terms in a convenient form. As already discussed, we are primarily interested in the time-average velocity at second order. Consequently, after substituting $\mathbf{u}^{(P0)}$ and $\mathbf{u}^{(B0)}$ into the equations for $\mathbf{u}^{(B1)}$ and taking the time average over one wave period, we obtain

$$\frac{\partial^2 \bar{u}^{(B1)}}{\partial Z^2} = 0,$$

$$\frac{\partial^2 \bar{v}^{(B1)}}{\partial Z^2} = -4V(y)\left[\frac{1}{2} e^{-\sqrt{2}Z} - e^{-Z/\sqrt{2}}\cos(Z/\sqrt{2})\right],$$

$$\frac{\partial \bar{u}^{(B1)}}{\partial x} + \frac{\partial \bar{v}^{(B1)}}{\partial y} + \frac{\partial \bar{w}^{(B1)}}{\partial Z} = 0,$$

$$V(y) = -\pi \frac{\sinh 2\pi(h+y)\cosh 2\pi(h+y)}{\sinh^2 2\pi h}$$

The no-slip boundary condition requires

$$\bar{u}^{(B1)} = \bar{v}^{(B1)} = \bar{w}^{(B1)} = 0 \quad \text{on} \quad Z = 0,$$

and as $Z \to \infty$ the matching with the core solution at order ϵ gives

$$\begin{aligned} \bar{u}^*(x,y,\pm l) &= \bar{u}^{(B1)}(x,y,Z \to \infty), \\ \bar{v}^*(x,y,\pm l) &= \bar{v}^{(B1)}(x,y,Z \to \infty), \\ \bar{w}^*(x,y,\pm l) &= 0. \end{aligned}$$

Recall that the Z component of velocity in the boundary layer is of order $\epsilon\mathrm{Re}^{-1/2}$; hence, the zero on the right-hand side of the last equation. With these conditions, the boundary layer solution is found to be,

$$\begin{aligned} \bar{u}^{(B1)} &= 0, \\ \bar{v}^{(B1)} &= V(y)[1 - e^{-\sqrt{2}Z} - 4e^{-Z/\sqrt{2}}\sin(Z/\sqrt{2})]. \end{aligned}$$

$\bar{w}^{(B1)}$ can be obtained from the continuity equation, but since its effect on the core is of higher order it is not presented. Therefore, at the sidewalls the matching conditions for the core become,

$$u^*(x,y,\pm l) = w^*(x,y,\pm l) = 0,$$

$$v^*(x,y,\pm l) = V(y) = -\frac{\pi \sinh 2\pi(h+y)\cosh 2\pi(h+y)}{\sinh^2 2\pi h} \qquad (a)$$

For the bottom and free-surface boundary layers the analysis follows that of Longuet-Higgins [2] with a minor modification. Here we must include an additional component of velocity in the cross-channel or z-direction. However, there will be no leading-order term in this component of velocity. The flow is being driven by a two-dimensional wave motion in the $x - y$ plane, i.e., $\mathbf{u}^{(P0)} = (u^{(P0)}, v^{(P0)}, 0)$. Since $w^{(P0)}$ is zero, the boundary conditions will be satisfied at leading order without requiring a correction to the z-component of velocity in the boundary layer. The first nontrivial contribution to the boundary layer velocity in the z-direction appears at second order due to the matching with the $0(\epsilon)$ velocity in the core. Furthermore, in the boundary layers the z-momentum equation decouples from the equations in the $x - y$ plane. This is because the leading-order velocity in the z-

Downloaded 02 May 2010 to 171.66.16.246. Redistribution subject to ASME license or copyright; see http://www.asme.org/terms/Terms_Use.cfm

direction is zero. Consequently, the Reynolds stress terms, $\epsilon \mathbf{u} \cdot \nabla \mathbf{u}$, which appear in the governing equations at second order due to the leading-order solution, are identical to the two-dimensional case of Longuet-Higgins [2]. That is, at second order no Reynolds stress term is present in the z-momentum equation and the momentum equations in the $x - y$ plane are the same as those given by Longuet-Higgins.

In particular, in the surface and bottom layers the z-component of velocity has the form

$$w = \epsilon w^{(B1)} + \ldots .$$

In both of these boundary layers the time-average velocity satisfies

$$\frac{\partial^2 \bar{w}^{(B1)}}{\partial N^2} = 0.$$

where the boundary layer variable $N = \mathrm{Re}^{1/2} n$, n being the position in the flow field measured along the normal to the surface (i.e., at the bottom $y = -h$, $N = Y = \mathrm{Re}^{1/2}(y + h)$. The boundary conditions on $\bar{w}^{(B1)}$ at the free-surface (shear-free) and bottom (no-slip) are, respectively,

$$\frac{\partial \bar{w}^{(B1)}}{\partial N} = 0 \quad \text{at} \quad N = 0,$$

$$\bar{w}^{(B1)} = 0 \quad \text{at} \quad Y = 0,$$

and therefore the solution in these boundary layers is

$$\bar{w}^{(B1)} = \text{constant}; \quad \text{free surface},$$

$$\bar{w}^{(B1)} = 0; \quad \text{bottom}.$$

Consequently, the matching conditions with the core at the surface and bottom are, respectively,

$$\frac{\partial \bar{w}^*}{\partial y} = 0 \quad \text{at} \quad y = 0$$

$$\bar{w}^* = 0 \quad \text{at} \quad y = -h$$

Due to the decoupling of the governing equations, the matching conditions for the velocity components in the x and y directions follow from the results of Longuet-Higgins [2], and therefore their derivation will not be repeated. Thus,

$$\bar{v}^* = 0 \quad \text{at} \quad y = 0, \quad -h,$$

$$\frac{\partial \bar{u}^*}{\partial y} = \tau = 8\pi^2 \coth 2\pi h \quad \text{at} \quad y = 0, \tag{b}$$

$$\bar{u}^* = U = \frac{3}{2} \frac{\pi}{\sinh^2 2\pi h} \quad \text{at} \quad y = -h. \tag{c}$$

Recall that here we are using the Eulerian velocities and therefore some manipulation is required if these expressions are to be obtained from the Lagrangian form of the results given by Longuet-Higgins [2].

A further comment is in order. Note that the matching or boundary conditions on the core velocity $\bar{\mathbf{u}}^*$ are discontinuous at the corners of the channel cross section. The velocity in reality will vary smoothly but rapidly near the corners and a more complete analysis requires the introduction of sublayers in each corner which matches the two intersecting boundary layers. However, these sublayers or corner solutions are passive as far as the leading-order interior motion is concerned, i.e., they do not influence the core motion considered here. One should be aware, however, that the present solution is not uniformly valid as you approach the corners.

(b) Viscous Dissipation in the Sidewall Layers

From the boundary layer solution we can determine the rate of energy dissipation due to the sidewalls, and compare it to the other dissipative mechanisms present. The average rate of energy dissipation per unit length due to the two sidewalls of a wave tank is,

$$\dot{E}_{\text{sides}} \approx 2\mu(\omega a)^2 \mathrm{Re}^{1/2} \int_{-h}^{0} \int_{0}^{\infty} \overline{\left[\left(\frac{\partial u^{(B0)}}{\partial Z} \right)^2 + \left(\frac{\partial v^{(B0)}}{\partial Z} \right)^2 \right]} dZ\, dy$$

$$= \mu(\omega a)^2 \mathrm{Re}^{1/2} \frac{1}{2\sqrt{2}\pi} \coth k\hat{h},$$

where

$$\mathrm{Re}^{1/2} = \sqrt{\frac{\omega}{\nu}}\, \lambda.$$

For a channel of width $2\hat{l}$ the average rate of energy dissipation from the potential flow in the core and the viscous boundary layer at the bottom is

$$\dot{E}_{\text{core}} = 4\pi\mu(\omega a)^2 \frac{2\hat{l}}{\lambda} \coth k\hat{h},$$

$$\dot{E}_{\text{bottom}} = \frac{1}{2\sqrt{2}} \mu(\omega a)^2 \frac{2\hat{l}}{\lambda} \mathrm{Re}^{1/2} \operatorname{csch}^2 k\hat{h},$$

see Phillips [15]. The boundary layer at the surface makes a negligible contribution to the overall energy dissipation, since the velocity gradients are of the same magnitude as those in the potential flow and the layer is thin. Consequently, the sidewall boundary layers are the dominant dissipative mechanism when the channel is sufficiently narrow and deep so that $\hat{l}/\lambda << \mathrm{Re}^{1/2}$ and $\hat{l}/\lambda << \sinh 2\, k\hat{h}$. In this case, following Phillips [15], we determine the attenuation coefficient of the wave motion as

$$\gamma = \frac{\dot{E}_{\text{sides}}}{2E} = \frac{\omega}{2\sqrt{2}} \mathrm{Re}_l^{-1/2},$$

where

$$\mathrm{Re}_l^{1/2} = \sqrt{\frac{\omega}{\nu}}\, \hat{l}.$$

$E = k^{-1}\hat{l}\rho(\omega a)^2 \coth k\hat{h}$ is the total mean energy per unit length, potential plus kinetic energy, due to the wave motion. The energy density of the wave motion decreases as $\exp(-2\gamma\hat{t})$ and the amplitude as $\exp(-\gamma\hat{t})$. Note that γ is independent of depth. This result has been found previously by Mei and Liu [7]. They also discuss a possible mechanism by which energy is transferred from the two-dimensional wave train to the sidewall boundary layers. In particular, they find that " . . . the free-surface meniscus is an important passage via which the wave energy is lost from the essentially inviscid interior to the side-wall boundary layer."

APPENDIX 2

The solution for ψ satisfying the governing equation (12) and all but two of the boundary conditions (13) is

$$\psi = \sum_{m=1}^{\infty} b_m \psi_m,$$

$$\psi_m = \sin \beta_m y \left[\frac{z}{l} \tanh \beta_m l \cosh \beta_m z - \sinh \beta_m z \right]$$

$$+ \sum_{n=1}^{\infty} B_{mn} \sin \alpha_n z \left[\frac{y}{h} \tanh \alpha_n h \cosh \alpha_n y - \sinh \alpha_n y \right],$$

$$\beta_m = \frac{m\pi}{h}, \quad \alpha_n = \frac{n\pi}{l},$$

Downloaded 02 May 2010 to 171.66.16.246. Redistribution subject to ASME license or copyright; see http://www.asme.org/terms/Terms_Use.cfm

The remaining two boundary conditions that determine b_m and B_{mn} are

$$\frac{\partial \psi}{\partial y}(-h, z)=0, \quad \frac{\partial \psi}{\partial z}(y,l)=V(y).$$

Applying the first condition and defining $\sigma = h/l$ we find

$$B_{mn} = -\frac{2}{l} H_n^{-1} \int_0^l G_m(z) \sin \alpha_n z dz$$

$$= -\frac{4}{H_n} \frac{m^2 n}{\sigma\pi\left(\left(\frac{m}{\sigma}\right)^2 + n^2\right)^2} \cos m\pi \cos n\pi \sinh \frac{m\pi}{\sigma} \tanh \frac{m\pi}{\sigma}$$

where

$$H_n = (h^{-1} \tanh \alpha_n h - \alpha_n) \cosh \alpha_n h + \alpha_n \tanh \alpha_n h \sinh \alpha_n h$$

$$G_m(z) = \beta_m \cos \beta_m h \left(\frac{z}{l} \tanh \beta_m l \cosh \beta_m z - \sinh \beta_m z \right)$$

Finally, applying the last condition gives

$$\sum_{m=1}^{\infty} b_m \left[L_m \sin \beta_m y + \sum_{n=1}^{\infty} B_{mn} F_n(y) \right] = V(y)$$

where

$$L_m = (l^{-1} \tanh \beta_m l - \beta_m) \cosh \beta_m l + \beta_m \tanh \beta_m l \sinh \beta_m l$$

$$F_n(y) = \alpha_n \cos \alpha_n l \left(\frac{y}{h} \tanh \alpha_n h \cosh \alpha_n y - \sinh \alpha_n y \right)$$

Consequently the coefficients b_m are determined from the following system of an infinite number of linear equations

$$b_r L_r + \sum_{m=1}^{\infty} b_m A_{mr} = q_r, \quad 1, 2, 3, \ldots ,$$

where

$$A_{mr} = \sum_{n=1}^{\infty} B_{mn} p_{nr},$$

$$p_{nr} = \frac{2}{h} \int_{-h}^{0} F_n(y) \sin \beta_r y \, dy$$

$$= \frac{4}{l} \frac{n^2 r \sigma}{\pi((n\sigma)^2 + r^2)^2} \cos r\pi \cos n\pi \tanh n\pi\sigma \sinh n\pi\sigma,$$

$$q_r = \frac{2}{h} \int_{-h}^{0} V(y) \sin \beta_r y dy = \frac{2r}{(4h)^2 + r^2} \coth 2\pi h.$$

The coefficients b_r were determined numerically retaining 20 terms in the summations over m and n. Results found by retaining a greater number of terms (e.g., 40 and 50) showed almost no difference from those found using 20 terms.

Downloaded 02 May 2010 to 171.66.16.246. Redistribution subject to ASME license or copyright; see http://www.asme.org/terms/Terms_Use.cfm

Boundary Layers on Characteristic Surfaces for Time-Dependent Rotating Flows

R. F. Gans
Associate Professor,
Department of Mechanical Engineering,
University of Rochester,
Rochester, N.Y. 14627
Mem. ASME

Time-dependent motion of a fluid in a container rotating at Ω is characterized by boundary layers on the container surfaces if ν/Ω, where ν denotes kinematic viscosity, is small compared to the square of a typical length of the container. Let the frequency of the motion, measured in a corotating coordinate system, be $\omega\Omega$. If $\omega \sim 1$, then the length scale of the boundary layer is $(\nu/\Omega)^{1/2}$, unless $|\omega|$ is equal to twice the normal component of the unit rotation vector. If $|\omega|$ does equal twice the normal component of the unit rotation vector, scales of $(\nu/\Omega L^2)^{1/3} L$ and $(\nu/\Omega L^2)^{1/4} L$ are possible. If the normal vector and rotation vectors are parallel, the former scale vanishes.

Introduction

The study of flow in rotating systems almost always deals with situations for which the viscosity is small and boundary layers appear on bounding surfaces. In many circumstances free shear layers appear, emanating from discontinuities on the bounding surfaces.

The earliest work is that of Ekman [1]. References [2] and [3] contain recent review articles. Greenspan's monograph [4] contains a unified presentation. Much of his notation will be adopted in the following.

The typical boundary layer is the Ekman layer, within which the dominant balance is between the viscous and coriolis forces. The associated length scale is $(\nu/\Omega)^{1/2}$, where ν and Ω denote kinematic viscosity and rotation rate. Time dependence modifies this balance, usually benignly. At frequencies much greater than the rotation rate, the Ekman layers go smoothly over to Stokes layers. In the inertial range, where the absolute value of the frequency is bounded by twice the rotation frequency, the Ekman layers remain Ekman layers unless the frequency equals plus or minus twice the normal projection of the rotation vector. What happens in this circumstance is the subject of this paper.

Let $\mathbf{k}$ and $\mathbf{n}$ denote unit vectors parallel to the rotation axis and normal to the bounding surface (See Fig. 1). Then $\Omega\mathbf{k}\cdot\mathbf{n} = \Omega\sin\theta$ is the normal projection. If the flow is proportional to $\exp i(\Omega\omega t)$, then the exceptional case is one for which $\omega = \pm 2\sin\theta$. (The classical examples of this are the Stewartson layers [5] (see also [4]), for which $\theta = \pi/2$ and $\omega = 0$.) The inviscid equations of motion are hyperbolic in space when $0 < |\omega| < 2$.

The boundary layers described in the following would form within a fluid-filled spinning container were the container to oscillate at an exceptional frequency, defined by its basic rotation rate and geometry. A direct analytic demonstration of the role of these boundary layers in a global problem is difficult, primarily because the inviscid equations of motion are separable only in Cartesian and cylindrical coordinates. One example is given in [6]. A general linear problem would need to be dealt with numerically. However, the choice of numerical scheme will be better assisted by an understanding of the basic boundary layer structure to be expected.

This paper discusses boundary layers on characteristic surfaces of finite area. (Stewartson layers are a special case.) The plan of the paper is:

(1) to formulate the linear boundary layer problem in general;

(2) to discuss the special cases $\sin\theta = 0$ (Stewartson layers) and $\cos\theta = 0$; and

(3) to examine a case for $\sin\theta$ and $\cos\theta$ of order unity.

Formulation

The general differential equations for boundary layer flow in a rotating system can be obtained by following and extending the procedure outlined in Greenspan's book [4].

Let an incompressible fluid with kinematic viscosity ν be contained in a volume with a characteristic dimension L. Let the volume rotate about an axis $\mathbf{k}$ at Ω, and imagine the fluid to be corotating. Suppose that some small perturbation, either boundary motions or a body force, causes the fluid to have some small additional motion. Then the velocity field in the fluid, $\mathbf{v}$, can be written

$$\mathbf{v} = \Omega L(\mathbf{k}\times\mathbf{r} + \epsilon\mathbf{q}), \tag{1}$$

where ϵ is a small parameter measuring departure from solid rotation. It is convenient to work in a rotating coordinate system and to measure length, time, and velocity in units of L, Ω^{-1}, and ΩL. The governing equations become the familiar

Contributed by the Applied Mechanics Division for publication in the JOURNAL OF APPLIED MECHANICS.

Discussion on this paper should be addressed to the Editorial Department, ASME, United-Engineering Center, 345 East 47th Street, New York, N.Y. 10017, and will be accepted until two months after final publication of the paper itself in the JOURNAL OF APPLIED MECHANICS. Manuscript received by ASME Applied Mechanics Division, June, 1982; final revision, June, 1982.

Copyright © 1983 by ASME
Downloaded 02 May 2010 to 171.66.16.246. Redistribution subject to ASME license or copyright; see http://www.asme.org/terms/Terms_Use.cfm

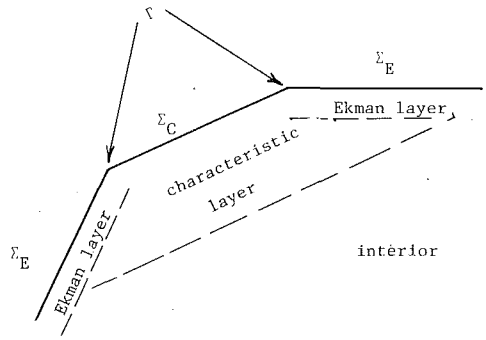

Fig. 1 Sketch of a characteristic layer bounded by Ekman layers (see text)

$$\frac{\partial \mathbf{q}}{\partial t} + 2\mathbf{k}\times\mathbf{q} + \nabla p = E\nabla^2\mathbf{q}; \quad \nabla\cdot\mathbf{q} = 0, \tag{2}$$

where p denotes the reduced pressure and $E = \nu/\Omega L^2$ is the Ekman number. When $E << 1$ a boundary layer formulation is appropriate. That assumption is made, as is the assumption that $\epsilon = o(E)$, so that the problem is strictly linear.

Time dependence is incorporated by assuming a simple exponential variation, letting $\mathbf{q}(\mathbf{x},t) = \mathbf{u}(\mathbf{x})e^{i\omega t}$. It is not necessary to restrict the magnitude of ω, but the interesting cases are those for which $|\omega| \leq 2$. The inviscid equations, (2) with E set equal to zero, are hyperbolic in space when $0 < |\omega| < 2$. This is also the range for which free oscillations of an inviscid rotating fluid are possible.

The boundary layer analysis is based on dividing $\mathbf{u}$ into $\hat{\mathbf{u}}(\mathbf{x})$ and $\tilde{\mathbf{u}}(\mathbf{x})$, an interior and boundary layer component. The boundary layer component $\tilde{\mathbf{u}}$ is distinguished by a rapid variation normal to the boundary and an exponential decay away from the boundary. It is most easily analyzed in terms of an orthogonal curvilinear coordinate system x_1, x_2, x_3 in which the velocity components are u, v, w, the boundary of the container is $x_1 = 0$, and the normal vector $\mathbf{n} = \hat{\mathbf{x}}_1$. The most general such system can be defined in terms of its differential line element as

$$ds^2 = h_1^2dx_1^2 + h_2^2dx_2^2 + h_3^2dx_3^2, \tag{3}$$

and the boundary layer hypothesis can be expressed as

$$\left|\frac{\partial\tilde{\mathbf{u}}}{\partial x_1}\right| >> \left|\frac{\partial\tilde{\mathbf{u}}}{\partial x_2}\right|, \left|\frac{\partial\tilde{\mathbf{u}}}{\partial x_3}\right|. \tag{4}$$

It is also necessary that the boundary shape vary slowly enough that the spatial derivatives of the unit vectors and scale factors be at most 0(1).

The general boundary layer equations are derived from (2) as follows. Let

$$\tilde{\mathbf{u}} = \tilde{u}\cdot\mathbf{n} - \mathbf{n}\times(\mathbf{n}\times\tilde{\mathbf{u}}) \tag{5}$$

(and drop the tilde as unnecessary in the sequel). The divergence condition serves to eliminate $\mathbf{n}\cdot\mathbf{u} = u$:

$$(\mathbf{n}\cdot\nabla + \nabla\cdot\mathbf{n})u = -\mathbf{n}\cdot\nabla\times(\mathbf{n}\times\mathbf{u}) + \nabla(\log h_1)\cdot\mathbf{n}\times(\mathbf{n}\times\mathbf{u}) \tag{6}$$

The second term on the left will be negligible.

The normal component of the momentum equation serves to eliminate the reduced pressure:

$$\mathbf{n}\cdot\nabla p = 2\mathbf{k}\cdot(\mathbf{n}\times\mathbf{u}) + [E(\mathbf{n}\cdot\nabla)^2 - i\omega]u$$
$$-E\nabla(\log h_1)\cdot(\mathbf{n}\cdot\nabla)\mathbf{n}\times(\mathbf{n}\times\mathbf{u}) + 0(E) + 0(E\mathbf{n}\cdot\nabla u) \tag{7}$$

The first term on the right-hand side dominates the pressure unless $\mathbf{k}\times\mathbf{n} = 0$. In all cases for which the pressure is important, the term proportional to $\nabla(\log h_1)$ is negligible compared to $[E(\mathbf{n}\cdot\nabla)^2 - i\omega]u$.

The governing equations for the tangential components of the velocity are obtained by adding and subtracting $\mathbf{n}x$ and $i\mathbf{n}\times(\mathbf{n}\times)$ the momentum equation. The identity

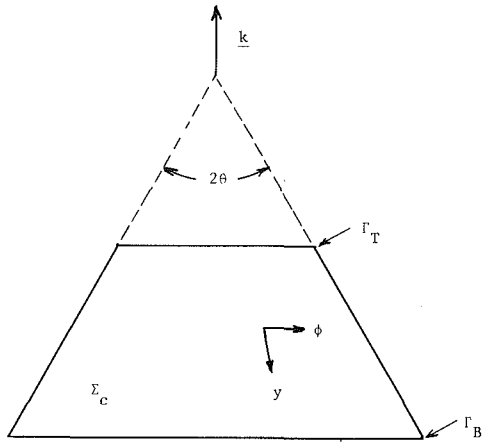

Fig. 2 The conical surface

$$\mathbf{n}\times\mathbf{u} \pm i\mathbf{n}\times(\mathbf{n}\times\mathbf{u}) = (v \mp iw)(\pm i\hat{\mathbf{x}}_2 + \hat{\mathbf{x}}_3) \tag{8}$$

allows the equations to be converted to scalar equations:

$$[i(\omega - 2\mathbf{n}\cdot\mathbf{k}) - E(\mathbf{n}\cdot\nabla)^2][v - iw]$$
$$= -\left(\frac{1}{h_2}\frac{\partial}{\partial x_2} - \frac{1}{h_3}\frac{\partial}{\partial x_3}\right)p - 2i[\hat{\mathbf{x}}_2\cdot\mathbf{k} - i\hat{\mathbf{x}}_3\cdot\mathbf{k}]u$$
$$[i(\omega + 2\mathbf{n}\cdot\mathbf{k}) - E(\mathbf{n}\cdot\nabla)^2][v + iw]$$
$$= -\left(\frac{1}{h_2}\frac{\partial}{\partial x_2} + \frac{1}{h_3}\frac{\partial}{\partial x_3}\right)p + 2i[\hat{\mathbf{x}}_2\cdot\mathbf{k} + i\hat{\mathbf{x}}_3\cdot\mathbf{k}]u \tag{9}$$

These equations are of constant coefficient form in the coordinate x_1. Thus they admit solutions of the form $\exp\mu x_1$, and the boundary layer hypothesis requires $|\mu| >> 1$ and Re $\mu > 0$. If $\omega \pm 2\mathbf{n}\cdot\mathbf{k}$ is not zero, then the right-hand sides of these equations are negligible, and one obtains

$$E\mu^2 = i(\omega \pm 2\mathbf{n}\cdot\mathbf{k}). \tag{10}$$

These are essentially time-dependent Ekman layers.

If $\omega = \pm 2\mathbf{k}\cdot\mathbf{n}$, a more subtle analysis is called for. The two extreme special cases, $\mathbf{k}\cdot\mathbf{n} = 0$ and $|\mathbf{k}\cdot\mathbf{n}| = 1$, have been examined, the former by Stewartson [4, 5] and the latter by Gans [6]. These two cases, as well as a relatively general case, can be derived from a specialization of the coordinate system.

Surfaces for which $\omega \neq \pm 2\mathbf{k}\cdot\mathbf{n}$ will be termed Ekman surfaces, and surfaces for which the $\omega = \pm 2\mathbf{k}\cdot\mathbf{n}$ will be called characteristic surfaces. The outward normal to Ekman surfaces will be denoted by $\mathbf{n}_E$. The transition between characteristic and Ekman surfaces will be supposed to be abrupt, and marked by curves Γ. Figure 1 shows a general case. Σ_C and Σ_E denote the characteristic and Ekman surfaces. The characteristic layer is shown schematically, anticipating the result that it is always thicker than the Ekman layer.

If ζ,η denote the characteristic coordinates of the inviscid equations, then Σ_C is just ζ = constant. The conjugate characteristics shown are η = constant. Free shear layers may occur on such surfaces.

Characteristic Boundary Layers on a Conical Surface

This section examines the surface formed by making two horizontal slices through a vertical cone. Figure 2 shows the surface. An x, y, ϕ coordinate system is defined. In this system $x = 0$ defines the surface, the differential line element is $ds^2 = dx^2 + dy^2 + r^2d\phi^2$, so that $h_1 = 1 = h_2$, and

$$h_3 = r = R + x\cos\theta + y\sin\theta \sim R + y\sin\theta. \tag{11}$$

The length scale is chosen so that the curves Γ are given by $y = \mp 1$; $\mathbf{n}\cdot\mathbf{k} = \sin\theta$. The reader will note that the bounding

Downloaded 02 May 2010 to 171.66.16.246. Redistribution subject to ASME license or copyright; see http://www.asme.org/terms/Terms_Use.cfm

surfaces of a right circular cylinder can be obtained in the limits $\sin\theta \to 0$, R fixed (for the curved outer wall) and $\cos\theta \to 0$, R fixed (for the end plates). This will allow one to use this system to explore those two special cases.

Let $\omega = 2\sin\theta$. (The analysis for $\omega = -2\sin\theta$ is the same.) Define $Q^{\pm} = v \pm iw$, and suppose these to be proportional to $e^{\mu x}$, where $|\mu| >> 1$ and $\mathrm{Re}\,\mu > 0$. The governing equations (9) may then be rewritten as

$$-E\mu^2 Q^- = 2i\cos\theta u - \left(\frac{dp}{dy} + \frac{m}{r}p\right)$$

$$(4i\sin\theta - E\mu^2)Q^+ = -2i\cos\theta u - \left(\frac{dp}{dy} - \frac{m}{r}p\right) \tag{12}$$

where solutions proportional to $e^{im\phi}$ have been assumed. Equations (6) and (7) can be used to eliminate u and p in favor of v and w, and hence Q^+ and Q^-. When those expressions are substituted into equation (12) the result is a general formulation for characteristic boundary layers on the conical surface:

$$-E\mu^2 Q^- + \frac{i\cos\theta}{\mu}\left[2\frac{dQ^-}{dy} + \frac{1}{r}\sin\theta Q^- + \frac{1}{r}\sin\theta Q^+\right]$$
$$= i\frac{2i\sin\theta - E\mu^2}{2\mu^2}\left\{\left[\frac{d^2}{dy^2} + \frac{1}{r}(2m+\sin\theta)\frac{d}{dy}\right.\right.$$
$$\left. + \frac{1}{r^2}(m^2 - \sin\theta)\right]Q^+$$
$$\left. - \left[\frac{d^2}{dy^2} + \frac{1}{r}\sin\theta\frac{d}{dy} - \frac{1}{r^2}(m-\sin\theta)^2\right]Q^-\right\} \tag{13}$$

$$(4i\sin\theta - E\mu^2)Q^+ - \frac{i\cos\theta}{\mu}\left[2\frac{dQ^+}{dy} + \frac{1}{r}\sin\theta Q^+\right.$$
$$\left. + \frac{1}{r}\sin\theta Q^-\right] = i\frac{2i\sin\theta - E\mu^2}{2\mu^2}\left\{\left[\frac{d}{dy} + \frac{1}{r}\sin\theta\frac{d}{dy}\right.\right.$$
$$\left. - \frac{1}{r^2}(m+\sin\theta)^2\right]Q^+ - \left[\frac{d^2}{dy^2} - \frac{1}{r}(2m-\sin\theta)\frac{d}{dy}\right.$$
$$\left.\left. + \frac{1}{r^2}(m^2 - \sin^2\theta)\right]Q^-\right\}. \tag{14}$$

The right-hand side of equation (14) is always negligible. The right-hand side of (13) is negligible unless $\cos\theta = 0$. $E\mu^2$ can equal $4i\sin\theta$ and an $o(1)$ value. If $\sin\theta = 0$, both $E\mu^2$ are 0(1). The two special cases, $\sin\theta = 0$ and $\cos\theta = 0$, will be considered first.

The Case, $\sin\theta = 0$. Let $\sin\theta = 0$. $E\mu^3$ will be 0(1) and the right-hand side of each equation is negligible. By inspection $Q^- \propto \exp iE\mu^3/2\, y$ and $Q^+ \propto \exp - iE\mu^3/2\, y$; the boundary layers are Stewartson layers. Since the scale is large compared to the Ekman scale, the boundary conditions (in y) are those of Ekman compatibility, which can be written [4]

$$\mathbf{n}_E \cdot \mathbf{u} = -\frac{1}{2}E^{1/3}\mathbf{n}_E \cdot \nabla \times \left\{\left[\mathbf{n}_E \times \mathbf{u} + \frac{\mathbf{n}_E \cdot \mathbf{k}}{|\mathbf{n}_E \cdot \mathbf{k}|}\mathbf{u}\right]\frac{1}{|\mathbf{n}_E \cdot k|^{1/2}}\right\} \tag{15}$$

where $\mathbf{n}_E$ denotes the normal to the Ekman surfaces bounding the characteristic surface. In the case that the Ekman surfaces are the flat ends of a cylinder $\mathbf{n}_E = \pm\mathbf{k}$ and this approach will yield exactly the result originally found by Stewartson [4, 5].

The Case, $\cos\theta = 0$. When $\cos\theta = 0$ the solution to equation (14) is

$$Q^+ = Q_0^+(y)\exp 2\frac{1+i}{(2E)^{1/2}}x. \tag{16}$$

Equation (13) becomes a second-order equation in y:

$$\frac{d^2Q^-}{dy^2} + \frac{1}{r}\frac{dQ^-}{dy} - \frac{1}{r^2}(m-1)^2 Q^- + E\mu^4 Q^- = 0. \tag{17}$$

This is recognizable as Bessel's equation of order $m-1$ (after the variable change to $r = R+y$). The boundary conditions are those derivable from (15), remembering that only Q^- participates because Q^+ varies on the Ekman scale and is negligible. The result, to lowest order, is that Q^- must vanish at $r = R \pm 1$. Thus

$$Q^- = \sum_{n=1}^{\infty} A_n\left\{\frac{J_{m-1}(k_n r)}{J_{m-1}[k_n(R+1)]} - \frac{Y_{m-1}(k_n r)}{Y_{m-1}[k_n(R+1)]}\right\}e^{\mu_n x} \tag{18}$$

where $E\mu_n^4 = k_n$ and k_n satisfies the eigenvalue relation

$$J_{m-1}[k_n(R-1)]\,Y_{m-1}[k_n(R+1)]$$
$$- Y_{m-1}[k_n(R-1)]J_{m-1}[k_n(R+1)] = 0. \tag{19}$$

(If $\mathbf{n}_E \cdot \mathbf{k} = 0$, equation (15) fails. An alternative formulation leaves the conclusions unchanged.)

The coefficients a_n are found by expanding the boundary conditions in the given eigenfunctions. If v_0, w_0 are the values v and w are required to take on the wall, then

$$Q_0^+(y) = v_0 + iw_0$$

and

$$a_n = \frac{\int_{R-1}^{R+1}(u_0 - iw_0)r\Phi_n(r)\,dr}{\int_{R-1}^{R+1} r\Phi_n(r)\,dr} \tag{20}$$

where Φ_n denotes the function in braces in equation (18).

The General Case. When $\sin\theta$ and $\cos\theta$ are both 0(1), equation (14) has the solution

$$Q^+ = Q_0^+(y)\exp^2\frac{1+i}{(2E\csc\theta)^{1/2}}x.$$

Equation (13) reduces to

$$\frac{dQ^-}{dr} + \frac{1}{2r}Q^- + \frac{iE\mu^3}{\sin 2\theta}Q^- = 0, \tag{21}$$

which has the solution

$$Q^- \propto \frac{1}{\sqrt{r}}\exp -\frac{iE\mu^3}{2\cos\theta}y. \tag{22}$$

The boundary condition (15) can be written, in this case, as

$$\mp v = -\tfrac{1}{2}\mu E^{1/2} w,$$

to leading order. The upper sign applies at Γ_T, $y = -1$, and the lower at $y = 1$. Let $Q^- \propto \exp -i[My + \psi]$, where $M = E\mu^3/2\cos\theta$. Identification of v and $-w$ with the real and imaginary parts of the exponential leads to the eigenvalue relation

$$\mp\cos(\psi \mp M) = -\tfrac{1}{2}\mu E^{1/2}\sin(\psi \mp M),$$

from which $\psi = \pi/2$ and $M = n\pi, \mu E^{1/2}/2$. In the former case the analog of the $E^{1/3}$ layers arise and in the latter one obtains $E^{1/4}$ layers.

(Alternatively one can let $\sqrt{r}v = A\sin ky$ and $\sqrt{r}w = B\cos ky$. Then $Q^- = A\sin ky - iB\cos ky$. The differential equation gives $k = E\mu^3/2\cos\theta$ and $B = -A$. The matching condition gives the same result as that cited in the foregoing.)

When $M = n\pi$ there is a single root with $\mathrm{Re}(\mu) > 0$ when $n > 0$, and two when $n < 0$. When $M = \mu E^{1/2}/2$ there is one admissible μ. Denote that by $\mu_0 = (\cos\theta/E^{1/2})^{1/2}$.

Let $2\mu_n = (2\,|\cos\theta n|\,\pi/E)^{1/3}$. Then the roots for $M = n\pi$ are given by $2\mu_n$ for $n > 0$ and $\mu_n(1 \pm i\sqrt{3})$ for $n < 0$. Thus Q^- can be represented as a complex Fourier series:

Downloaded 02 May 2010 to 171.66.16.246. Redistribution subject to ASME license or copyright; see http://www.asme.org/terms/Terms_Use.cfm

$$\sqrt{r}Q^{-} = A_0 e^{\mu_0 x} + \sum_{n=-\infty}^{-1} e^{in\pi y} e^{\mu_n x}[a_n e^{i\sqrt{3}x} + b_n e^{-i\sqrt{3}x}] + \sum_{n=1}^{\infty} e^{-in\pi y} C_n e^{2\mu_n x}, \quad (23)$$

which can be rewritten in the more useful form

$$\sqrt{r}Q^{-} = A_0 e^{\mu_0 x} + \sum_{n=1}^{\infty} \sin n\pi y e^{\mu_n x}[A_n \cos\sqrt{3}\mu_n x + B_n \sin\sqrt{3}\mu_n x + C_n e^{\mu_n x}] - i \sum_{n=1}^{\infty} \cos n\pi y e^{\mu_n x}[A_n \cos\sqrt{3}\mu_n x + B_n \sin\sqrt{3}\mu_n x - C_n e^{\mu_n x}], \quad (24)$$

where the boundary conditions determine A_0, A_n, and C_n.

The leading term of the normal velocity u must also vanish. In solving for u one needs to differentiate the series (24), and there is no guarantee that the result will converge. An alternative boundary condition is that the flux being transported through the layer be independent of y at any given instant. Imposing this condition on the integral of (24) leads to $B_n = (A_n - 2C_n)/\sqrt{3}$.

Discussion

Boundary layers (and free shear layers) have been shown to have scales of variation of $E^{1/3}$ and $E^{1/4}$ when the surface is a characteristic surface for the associated inviscid problem. The formulation given can be adapted to specific problems, although such an adaptation may not be practical in cases where an inviscid solution is not available. In such cases knowledge of the scale of variation can be used to design an efficient numerical scheme.

In the usual Ekman layer problem the balance is between the viscous force and a combination of the leading terms of the coriolis force and the inertial force. For the characteristic layers the primary balance is between the coriolis and inertial forces, leaving the viscous force unbalanced. In that case the viscous force is balanced by a combination of horizontal pressure gradients and the weak coriolis force associated with local normal velocities. When $\cos\theta = 0$ this weak coriolis force vanishes and the horizontal pressure gradient is also weakened in consequence. This explains the dissappearance of the $E^{1/3}$ layer in that case.

Acknowledgments

This work has been supported by the National Science Foundation under grant MCS-8019566.

References

1 Ekman, V. W., "Om Jordrotationens Inverkan pa Vindströmmer i Hafvet," Ph.D. Dissertation, Upsala, 1902.

2 Roberts, P. H., and Soward, A. M., eds., *Rotating Fluids in Geophysics*, Academic Press, London, 1978.

3 Fein, J. S., ed., *Boundary Layers in Homogeneous and Stratified Rotating Fluids*, U. of Florida Press, Gainesville, 1978.

4 Greenspan, H. P., *The Theory of Rotating Fluids*, Cambridge U. Press, 1968.

5 Stewartson, K., "On Almost Rigid Rotations," *Journal of Fluid Mechanics*, Vol. 3, No. 1, 1957, pp. 17-26.

6 Gans, R. F., "Steady Flow in a Partially Filled Rotating Horizontal Cylinder, III. The Viscoelastic Interface," in preparation.

Downloaded 02 May 2010 to 171.66.16.246. Redistribution subject to ASME license or copyright; see http://www.asme.org/terms/Terms_Use.cfm

Flow Inside a Pneumatic Tire: A Peristaltic-Pumping Analysis for the Thin-Tire Limit at Very Low Forward Speed[1,2]

W. J. Rae
Aerodynamic Research Department,
Calspan Corporation,
Advanced Technology Center,
P.O. Box 400,
Buffalo, N.Y. 14225

The flow inside a pneumatic tire is analyzed in the limit where the cross-sectional diameter of the tire is small in comparison to the wheel diameter, and where the forward speed is sufficiently low that centrifugal pressure gradients can be neglected. The movement of the contact point around the circumference of the tire produces an internal flow by a mechanism analogous to peristaltic pumping in long flexible ducts. Analytic expressions for the flow velocities and pressures predicted by this model are derived, and are related to tire velocity and load.

Introduction

The air inside a pneumatic tire is set in motion, relative to the tire, by the movement of the ground-contact region around the periphery. Hot-wire-anemometer measurements [1] have shown that the internal velocities can reach 20–30 percent of the forward speed, for a typical range of loads. Speeds of this magnitude affect the heat transfer from the tire wall to the air inside, to a degree that is comparable with the heat transfer from the tire wall to the air outside. Thus, an understanding of the flow and heat-transfer characteristics of the internal flow is a necessary step in quantifying rolling resistance and the temperature buildup of the contained air.

The present study was undertaken in an attempt to provide some understanding of the problem, by treating a limiting case for which an analytic solution is possible. The limit chosen is that of a thin tire, (i.e., one whose cross-sectional diameter is small compared with the wheel diameter) which moves at a forward speed low enough to permit the centrifugal pressure gradients to be neglected. In this limit, the flow is equivalent to that in a thin, flexible-walled tube, along which a constriction moves at a constant speed. The motion resulting from the movement of the constriction is called peristaltic pumping (see, for example, [2]) and can be analyzed very simply in the limit of small values of the Reynolds number (where the Reynolds number is based on the speed of the constriction, the cross-sectional diameter, and the kinematic viscosity of the contained air). The following sections contain a review of this analysis, and an extension to the present case, where the tube is not infinitely long, but rather is periodic. The case analyzed is that of an adiabatic flow, i.e., no heat transfer is allowed between the air and the tire wall. The rate of temperature buildup of the contained air due to viscous dissipation is calculated. Results for a sample case are given in the next section, and the final section contains remarks on the nature of the approximations made and the extensions required to treat the case where centrifugal pressure gradients cannot be neglected, the Reynolds number is larger, and the cross-sectional diameter is a significant fraction of the wheel diameter.

Analysis

Jaffrin and Shapiro [2] present a description of the mechanism of peristaltic pumping, by considering the case of a long flexible tube of diameter d, along which a restriction slides from left to right at speed c (see Fig. 1). If the ends at 1 and 2 are closed, the pressure at 1 will rise above that at 2, to the level required to force the required mass flow through the restriction. The required mass flow, in turn, is given by the cross-sectional areas of the tube and restriction, and by the speed at which the restriction moves. The flow pattern described in the foregoing becomes steady if it is viewed in a coordinate system fixed to the restriction (see Fig. 2): the flow and the wall then move from right to left. The wall speed is equal to c if longitudinal extensions of the wall material are neglected, which is the case assumed here.

If now the ends of the tube are opened partially, and if the pressures imposed at the two ends differ from those that were developed in the closed-end case, the result will be that a certain amount of mass flows into and out of the tube at Stations 1 and 2, and the mass flow through the restriction is altered (see Fig. 3). This flow pattern has the appearance shown in Fig. 4, in the coordinate system attached to the restriction.

[1] This research was supported by the United States Department of Energy.

[2] This paper is dedicated to William R. Sears on the occasion of his 70th birthday, in deep gratitude for all he has done for me and for many others, as teacher, researcher, mentor, and friend.

Contributed by the Applied Mechanics Division for publication in the JOURNAL OF APPLIED MECHANICS.

Discussion on this paper should be addressed to the Editorial Department, ASME, United Engineering Center, 345 East 47th Street, New York, N.Y. 10017, and will be accepted until two months after final publication of the paper itself in the JOURNAL OF APPLIED MECHANICS. Manuscript received by ASME Applied Mechanics Division, July, 1981; final revision, January, 1983.

Copyright © 1983 by ASME
Downloaded 02 May 2010 to 171.66.16.246. Redistribution subject to ASME license or copyright; see http://www.asme.org/terms/Terms_Use.cfm

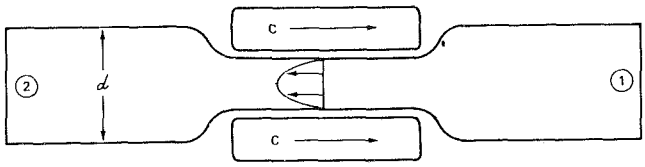

Fig. 1 Peristaltic pumping, tube-fixed coordinates

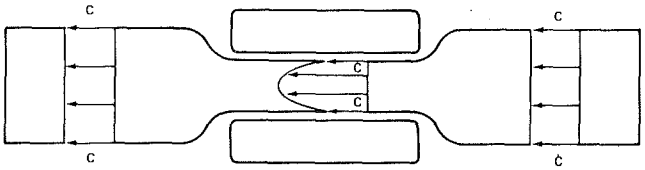

Fig. 2 Peristaltic pumping, restriction-fixed coordinates

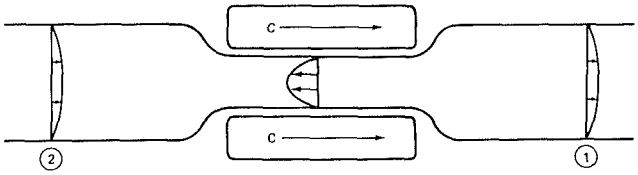

Fig. 3 Open-ended case, tube-fixed coordinates

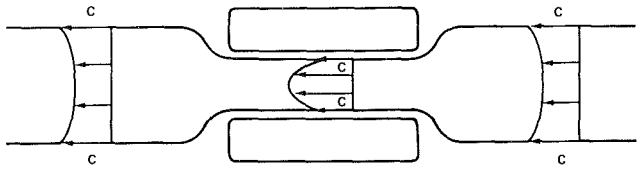

Fig. 4 Open-ended case, restriction-fixed coordinates

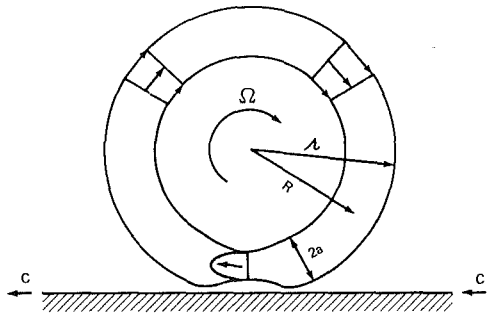

Fig. 5 Tire-flow model

The flow inside a tire is now modeled by taking a finite length of this tube, and joining the free ends (see Fig. 5). Note that this configuration is viewed in a coordinate system which translates with the axle: the roadway moves from right to left at speed c, the tire surface moves with a constant angular velocity Ω, and the internal flow is steady. The radius R locates the centroid of the undeformed cross section, $\mathcal{R}$ is a cylindrical coordinate, and a denotes the radius of the local tire cross section, which is taken to be circular in the present work.

The key to solving for the flow pattern is to find an expression for the mass flow being transported past any station, in terms of the local pressure and tube geometry. For steady flow, the mass flow is the same at all positions around the circumference, and is equal to the value that will make the pressures equal at the two ends of the tube length shown in Fig. 4, i.e., periodic in the angular coordinate of Fig. 5.

In the low Reynolds-number, thin-tire limit, the relation between mass flow, pressure gradient, and tube geometry can be written very simply: the vorticity introduced by shear stresses at the walls diffuses toward the center of the cross section at a rate that is large compared to the rate at which it is convected along the tube. Thus, there are no distinct regions of boundary layer and core flow; rather, the entire cross section is filled with a viscous flow, whose properties adjust immediately to the wall conditions imposed at that station. This is the limit described by the Hagen-Poiseuille flow in a tube (see, for example, [3], Section 5.2) where the inertial terms in the momentum equation are neglected, and the pressure gradient and shear stress gradient are equal at each station. The Poiseuille-flow behavior can also be derived formally from the equations of motion as the Reynolds number ca/ν and radius ratio a/R both approach zero (where ν is the kinematic viscosity).

The momentum equation is (see Fig. 6 for definition of the coordinates):

$$\frac{dp}{dx} = \frac{\mu}{r}\frac{\partial}{\partial r}\left(r\frac{\partial w'}{\partial r}\right) \tag{1}$$

where p is the pressure, μ the dynamic viscosity, $x = \mathcal{R}\phi \approx R\phi$, and w' is the increment in the ϕ-component of velocity that is added to the solid-body motion, i.e., $v_\phi = \Omega\mathcal{R} + w' \approx \Omega R + w'$. The gradients of pressure in the r and ψ - directions are proportional to higher powers of the Reynolds number and radius ratio. The solution is the parabolic profile:

$$w' = \frac{dp/dx}{4\mu}(r^2 - a^2) \tag{2}$$

This solution is now applied in the same manner as in lubrication theory, i.e., both the pressure gradient and the local radius are allowed to vary with x. The mass flow $\dot{m}$ is given by (here ρ denotes the density):

$$\frac{\dot{m}}{\rho} = \int_0^a w' 2\pi r dr = \frac{\pi a^4 dp/dx}{8\mu} \tag{3}$$

The moving wall transports an additional mass flow ρcA, where $A = \pi a^2$ is the local cross-sectional area and $c = \Omega R$ in the thin-tire limit. Thus, the total mass flow is

$$\dot{m} = \pi a^2 \rho c + \frac{\pi a^4 \rho dp/dx}{8\mu} \tag{4}$$

This can be solved for the local pressure gradient:

$$\frac{dp}{dx} = \frac{8\mu}{\pi a^4 \rho}(\dot{m} - \pi a^2 \rho c) \tag{5}$$

The variation of cross-sectional area around the tire leads to positive and negative values of the pressure gradient; the value of mass flow is determined by the condition that the pressure be periodic, i.e.:

$$\int_{-l}^{+l} \frac{dp}{dx}\, dx = 0 \tag{6}$$

where $l = \pi R$. This condition can be written entirely in terms of the distribution of cross-sectional area A/A_∞, which is assumed given (A_∞ is the cross-sectional area of the undeformed tire). Substituting equation (5) into (6) gives:

$$\frac{\dot{m}}{\rho c A_\infty} = \int_{-l}^{+l} \frac{dx}{A/A_\infty} \Big/ \int_{-l}^{+l} \frac{dx}{(A/A_\infty)^2} \tag{7}$$

The pressure distribution is then found from:

$$\frac{A_\infty \dfrac{dp}{dx}}{8\pi\mu c} = \frac{\dfrac{\dot{m}}{\rho c A_\infty} - \dfrac{A}{A_\infty}}{(A/A_\infty)^2} \tag{8}$$

At each station x, the local centerline velocity w_c' and cross-sectional-average velocity $\bar{w}'$ are given by:

Downloaded 02 May 2010 to 171.66.16.246. Redistribution subject to ASME license or copyright; see http://www.asme.org/terms/Terms_Use.cfm

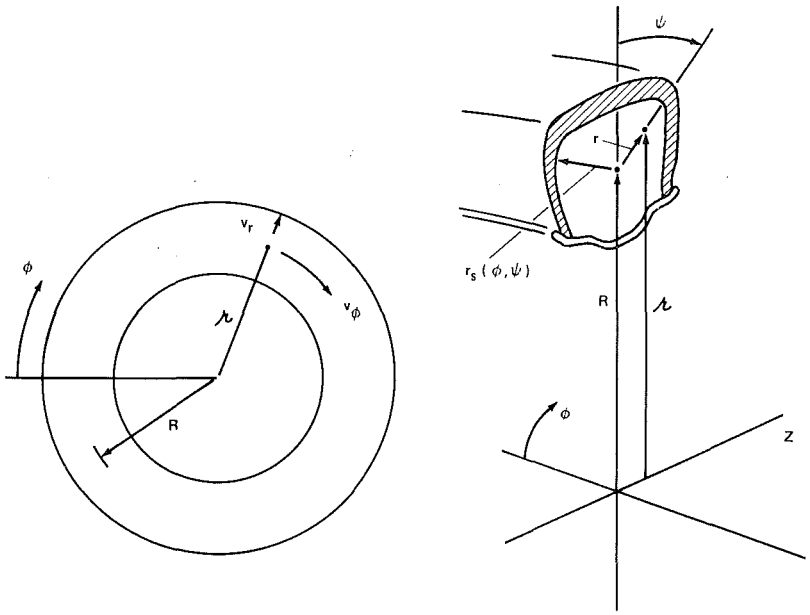

Fig. 6 Cylindrical coordinates (r, ϕ, Z) and toroidal coordinates (r, ϕ, ψ)

$$\frac{w_c'}{c} = \frac{2\bar{w}'}{c} = 2\frac{A}{A_\infty}\frac{A_\infty \dfrac{dp}{dx}}{8\pi\mu c} \tag{9}$$

Finally, the increments in rolling resistance ΔF and power consumption ΔP caused by viscous dissipation can be found by integrating the local rate:

$$\Delta P = \Delta F \cdot c = \int_{-l}^{+l}\int_0^a \mu\left(\frac{\partial w'}{\partial r}\right)^2 2\pi r dr dx \tag{10}$$

The integration over the radius can be done analytically, giving:

$$\frac{\Delta P}{8\pi\mu c^2 \cdot 2l} = \int_{-l}^{+l}\left(\frac{A}{A_\infty}\right)^2\left(\frac{A_\infty \dfrac{dp}{dx}}{8\pi\mu c}\right)^2 dx \tag{11}$$

The expressions in the foregoing display the scaling laws and functional dependences that apply at low Reynolds number. It should be noted that the right-hand sides of these equations depend only on the area distribution (and, thus, on the load or tire deflection), while the left-hand sides give the scaling parameters: c for the air velocity and $\mu c/A_\infty$ for the pressure gradient. The dependence of pressure gradient on the first powers of viscosity and velocity is typical of flow at very low Reynolds number.

Results for a Sample Case

The relations derived in the preceding section are next applied to a specific example, in which the (circular) cross-sectional area of the tire is reduced, over a portion of the circumference, according to a cosine law:

$$\frac{A}{A_\infty} = 1, \quad |x| > L$$

$$= 1 - \frac{\Delta A}{A_\infty}\frac{1+\cos\dfrac{\pi x}{L}}{2}, \quad |x| < L \tag{12}$$

Note that the angular extent of the area change is $2L/R$.

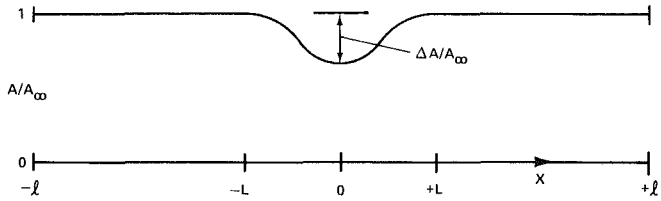

Fig. 7 Distribution of cross-sectional area

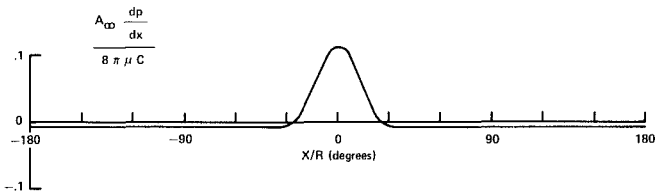

Fig. 8 Pressure-gradient distribution

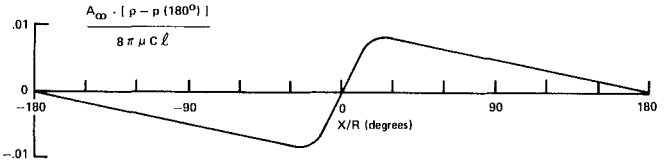

Fig. 9 Pressure distribution

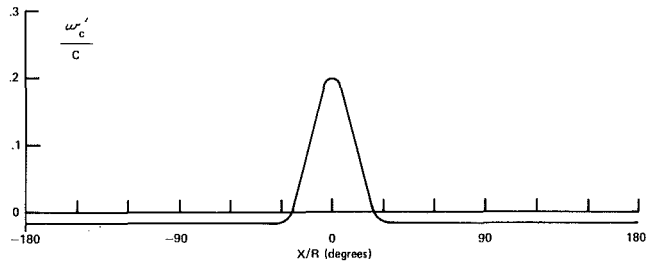

Fig. 10 Distribution of peak velocities

For this case, the integrals required for the mass flow determination can be found in closed form:

Downloaded 02 May 2010 to 171.66.16.246. Redistribution subject to ASME license or copyright; see http://www.asme.org/terms/Terms_Use.cfm

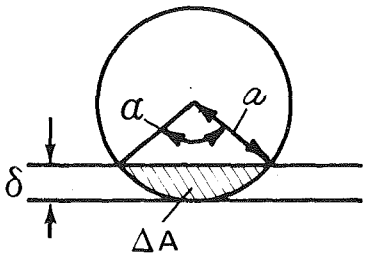

Fig. 11 Tire deflection model

$$\frac{\dot{m}}{\rho c A_\infty} = \frac{2\pi - 2\frac{L}{R} + \frac{L}{R}\int_{-1}^{1} \frac{d(x/L)}{A/A_\infty}}{2\pi - 2\frac{L}{R} + \frac{L}{R}\int_{-1}^{1} \frac{(dx/L)}{(A/A_\infty)^2}} \tag{13}$$

where

$$\int_{-1}^{1} \frac{d(x/L)}{A/A_\infty} = 2/(1-\Delta A/A_\infty)^{1/2};$$

$$\int_{-1}^{1} \frac{d(x/L)}{(A/A_\infty)^2} = \frac{2-\frac{\Delta A}{A_\infty}}{\left(1-\frac{\Delta A}{A_\infty}\right)^{3/2}} \tag{14}$$

Figures 8-10 show the distributions of pressure gradient, pressure, and centerline velocity for $\Delta A/A_\infty = 0.1$ and $2L/R = \pi/3$. These distributions are symmetric with respect to $x=0$ because the assumed area distribution was symmetric. They show uniform values of the pressure gradient and velocity in the undeformed portions of the tire.

The velocity variation displays the same scaling law noted in the experiments cited earlier [1]: for small changes in area, the general formula can be approximated as follows:

$$\frac{\dot{m}}{\rho c A_\infty} = 1 - \frac{L}{2\pi R}\frac{\Delta A}{A_\infty} + O\left(\frac{\Delta A}{A_\infty}\right)^2$$

$$\left.\frac{A_\infty \frac{dp}{dx}}{8\pi\mu C}\right)_{\max} = \left.\frac{1}{2}\frac{w_c'}{c}\right)_{\max}$$

$$= \left(1-\frac{L}{2\pi R}\right)\frac{\Delta A}{A_\infty} + O\left(\frac{\Delta A}{A_\infty}\right)^2 \tag{16}$$

where the subscript denotes the maximum value, which occurs at the point of minimum cross section. The area change, in turn, can be related to tire deflection in several ways [1, 4]; the formula used by Schuring et al. [1] considers the deflection as due to the removal of a sector from an initially circular cross section (see Fig. 11).

$$\frac{\Delta A}{\pi a^2} = \frac{1}{2\pi}(\alpha - \sin\alpha);$$

$$\alpha = 2\arcsin\left[2\frac{\delta}{a} - \left(\frac{\delta}{a}\right)^2\right]^{1/2} \tag{17}$$

For small deflections, these reduce to:

$$\frac{\Delta A}{A_\infty} = \frac{\alpha^3}{12\pi} = \frac{4\sqrt{2}}{3\pi}\left(\frac{\delta}{a}\right)^{3/2} \tag{18}$$

If this relationship is used, the peak velocity scales with tire deflection according to:

$$w_c')_{\max} = 2c\left(1-\frac{L}{2\pi R}\right)\frac{4\sqrt{2}}{3\pi}\left(\frac{\delta}{a}\right)^{3/2} \tag{19}$$

This is essentially the same result as that of reference [1], except that it contains a further dependence on deflection, implied by the L/R term, since the length of the footprint region will change with load.

The dependence of peak velocity on tire deflection involves only the continuity equation, and thus is independent of Reynolds number. The other scaling laws derived in the foregoing apply only for the low-Reynolds-number limit, and were not observed in the experiments of reference [1]. For example, the measured distribution of peak velocities (see Fig. 6 of [1]) does not have the symmetry shown in Fig. 9 for the present limiting case.

Concluding Remarks

The model used in the foregoing illustrates some of the fluid-mechanical features that are present in the flow of air inside a tire: the motion of the footprint region around the periphery causes a mass flow, relative to the tire wall. The particular value of the mass flow that will occur is that value whose associated pressure drop will meet the periodicity condition.

In the low Reynolds-number limit studied here, the pressure drop and viscous shear stresses are in complete equilibrium at every station, and so the flow experiences negligible accelerations. In the case of automobile and truck tires, however, the flow takes place at much higher Reynolds numbers, where the effects of viscosity are confined to boundary layers that do not respond immediately to the local changes in the cross-sectional area. Moreover, these boundary layers are probably turbulent. In addition, the centrifugal pressure gradients that are present in the auto and truck-tire case are not negligible, and undoubtedly produce substantial secondary flows. Thus, in the next level of approximation, the effects, on peristaltic pumping, of turbulence, boundary-layer development, and radial pressure gradients must be considered. The present model, which applies to laminar, fully viscous, zero radial-pressure-gradient flows, will provide a useful starting point for the addition of these more complex features.

Although the predictions of the present model are restricted to very low Reynolds numbers (for example the rolling resistance and the rate of temperature rise), nevertheless the scaling law for the center line velocity is not so restricted, because it is based on the continuity equation, which is not affected directly by viscosity. The peak velocity will be proportional to the first power of the cross-sectional area change for any model of the flow, although the magnitude of the peak and its variation through the footprint region will be sensitive to the details of how the boundary layers are represented. Thus, the ability to correlate center line velocity data is not a valid test of whether a particular analysis accurately models the boundary-layer behavior of the flow (and thus also the heat-transfer properties of the flow).

References

1 Schuring, D. J., Skinner, G. T., and Rae, W. J., "Contained Air Flow in a Radial Tire," SAE Technical Paper 810165 (Feb. 1981); *SAE Transactions*, Vol. 90, 1982, pp. 705-712.

2 Jaffrin, M. Y., and Shapiro, A. H., "Peristaltic Pumping," of *Annual Review of Fluid Mechanics*, Vol .3, by Van Dyke, M. D., et al., eds., Annual Reviews, Inc., Palo Alto, Calif., 1971, pp. 13-36.

3 Streeter, V. L., and Wylie, E. S., *Fluid Mechanics*, 7th Ed., McGraw-Hill, New York, 1979.

4 Koutny, F., "A Method for Computing the Radial Deformation Characteristics of Belted Tires," *Tire Science and Technology*, Vol. 4, Aug. 1976, pp. 190-212.

Downloaded 02 May 2010 to 171.66.16.246. Redistribution subject to ASME license or copyright; see http://www.asme.org/terms/Terms_Use.cfm

Superpotential Solution for Jet-Engine External Potential and Internal Rotational Flow Interaction

W. C. Chin
7703 Meadowbriar Lane,
Houston, Texas 77063

For flows with prescribed parallel shear far upstream, the vorticity generation term in the disturbance stream-function (ψ) equation and the Bernoulli "constant," both of which vary from stream surface to stream surface, are explicitly evaluated as power series in ψ with curvature-dependent coefficients, for axisymmetric flows using some invariant properties of vorticity. By casting the linearized stream-function equation in conservation form, extended Cauchy-Reimann conditions are obtained, implying a "superpotential" ϕ^* satisfying a "Laplace-like" equation useful for solving flows past prescribed shapes; the corresponding tangency and Kutta conditions, interestingly, take a "potential form," so that simple changes to existing potential flow algorithms extend their applicability to strong oncoming shears with arbitrary curvature. The theory, which applies to duct flows behind actuator disks generating shear, is sketched for both "analysis" and "design" formulations; here, we address the interaction between external potential and internal rotational jet-engine flows occurring through both an assumed actuator disk and a trailing edge slipstream, and provide representative numerical calculations.

1 Introduction

In many aerodynamic problems, the important effects of oncoming shear usually require a direct attack on Euler's equations or on a very complicated stream-function equation useful in only the simplest applications. The shear, for example, might result from radially varying work imparted by turbomachinery blade rows, or, from the effects of nonuniform winds. This paper, using the "superpotential" approach outlined in the Abstract, shows how small disturbances to strong shears with arbitrary curvature can be solved, making only simple changes to existing potential flow algorithms. Both the "analysis" problem, solving for pressures induced by prescribed geometries, and the "design" problem, solving for shapes inducing prescribed pressures, are easily handled within the theoretical framework. A particularly challenging problem not yet tackled by existing computational methods is the jet-engine external potential and internal rotational flow interaction occurring through an actuator disk and a trailing edge slipstream. The power, flexibility, and simplicity of the superpotential is applied to this very important engineering problem and numerical results are obtained; however, lack of experimental data precludes comparisons.

The basic ideas derive from an invariant property of vorticity: for axisymmetric flow, the vorticity convected along a stream surface changes only in proportion to its length. If a parallel shear flow is prescribed in some part of the flow domain (not necessarily upstream infinity), then the nonlinear vorticity generation term in the disturbance stream-function (ψ) equation governing the remaining perturbed flow and the Bernoulli "constant," both of which vary from stream surface to stream surface, in principle can be evaluated explicitly as functionals of the base flow; here, they are expanded in powers of ψ with variable shear-dependent coefficients. The linearized stream-function equation, put in conservation form, implies the existence of a "superpotential" ϕ^* satisfying extended Cauchy-Riemann conditions: the ϕ^* equation is potential-like, and the corresponding tangency and Kutta conditions, interestingly, take the usual potential form, indicating only minor required changes to existing potential flow algorithms! For our jet-engine problem, the only difference with irrotational formulations turns out to be an additional but discontinuous coefficient in the governing equation; this interfacial discontinuity, handled carefully, is stably implemented. The approach taken is quite general and obvious applications to other applications will be seen by the reader.

Our superpotential results, actually, appeared quite fortuitously in the course of extending the stream-function approach of references [1, 2] for aerodynamic "design" or "inverse" problems to flows with oncoming shear (these formulations solve for shapes inducing prescribed pressures subject to geometric constraints). The design formulation for rotational flow is presented in this paper, but calculations and engineering applications are deferred to future papers; here, we concentrate instead on "analysis" problems solving for

Contributed by the Applied Mechanics Division for publication in the JOURNAL OF APPLIED MECHANICS.
Discussion on this paper should be addressed to the Editorial Department, ASME, United Engineering Center, 345 East 47th Street, New York, N.Y. 10017, and will be accepted until two months after final publication of the paper itself in the JOURNAL OF APPLIED MECHANICS. Manuscript received by ASME Applied Mechanics Division, April, 1982; final revision, October, 1982.

Copyright © 1983 by ASME
Downloaded 02 May 2010 to 171.66.16.246. Redistribution subject to ASME license or copyright; see http://www.asme.org/terms/Terms_Use.cfm

pressures induced by prescribed shapes satisfying Kutta-type conditions that are more conveniently handled by potential-like formulations (analysis problems prefer auxiliary conditions described by potential jumps that control vortex strength and lift, whereas design problems prefer shape constraints described by stream-function discontinuities that control source strength or mass efflux). In particular, we have selected a very difficult analysis problem involving the interaction of an external potential flow and an internal rotational flow, a problem of significant interest in jet-engine nacelle design not previously considered. Although our numerical results are preliminary and, of course, subject to improvement, what is demonstrated is the power, simplicity, and flexibility of the superpotential approach. In the following, the general theory, the required linearizations, application, and numerical results are presented.

2 The Rotational Flow Equations

Let U and V be the full velocities in the streamwise (x) and radial (r) directions, P be the static pressure, and ρ be the fluid density. The governing momentum and continuity equations for a steady axisymmetric flow without swirl are $UU_x + VU_r = -P_x/\rho$, $UV_x + VV_r = -P_r/\rho$, and $U_x + V_r + V/r = 0$. A stream-function Ψ can be defined satisfying $\Psi_r = rU$, $\Psi_x = -rV$, and $\Psi_{xx} + \Psi_{rr} - \Psi_r/r = r\zeta$ where $\zeta = U_r - V_x$ is the vorticity. To obtain more specific information, we note the dependence of ζ/r on Ψ alone, that is, $\zeta/r = f(\Psi)$ where the function f, fixed for the entire stream surface, can be explicitly written once the flow is known in any particular region of space. Thus,

$$\Psi_{xx} + \Psi_{rr} - \frac{1}{r}\Psi_r = r^2 f(\Psi) \tag{1}$$

For simplicity we assume a parallel shear flow far upstream with prescribed $U = U_m(r)$ and $V = 0$. The stream function for this mean flow $\psi_m(r)$ satisfies $r^2 f(\psi_m) = \psi_{m_{rr}} - \psi_{m_r}/r$. From this, the derivatives $d^n f(\psi_m)/d\psi_m^n$ are easily written in terms of r and $U_m(r)$. Now if our mean flow is slightly perturbed, a disturbance stream-function ψ satisying $\Psi = \Psi_m + \psi$ can be introduced which satisfies

$$\psi_{xx} + \psi_{rr} - \frac{1}{r}\psi_r = r^2 \psi \frac{f(\psi_m + \psi) - f(\psi_m)}{\psi}$$

$$\cong r^2 \psi \left\{ \frac{df(\psi_m)}{d\psi_m} + \frac{1}{2}\psi \frac{d^2 f(\psi_m)}{d\psi_m^2} + \frac{1}{6}\psi^2 \frac{d^3 f(\psi_m)}{d\psi_m^3} + \ldots \right\}$$

or, more explicitly,

$$\psi_{xx} + \psi_{rr} - \frac{1}{r}\psi_r = \left(\frac{U_m''}{U_m} - \frac{U_m'}{U_m r} \right)\psi$$

$$+ \frac{1}{2}\left(\frac{U_m'''}{U_m^2 r} - \frac{U_m'' U_m'}{U_m^3 r} - \frac{3U_m''}{U_m^2 r^2} + \frac{U_m'^2}{U_m^3 r^2} + \frac{3U_m'}{U_m^2 r^3} \right)\psi^2$$

$$+ \frac{1}{6}\left(\frac{U_m''''}{U_m^3 r^2} - \frac{3U_m''' U_m'}{U_m^4 r^2} - \frac{6U_m'''}{U_m^3 r^3} - \frac{U_m''^2}{U_m^4 r^2} + \frac{3U_m'' U_m'^2}{U_m^5 r^2} \right.$$

$$\left. + \frac{11U_m'' U_m'}{U_m^4 r^3} + \frac{15U_m''}{U_m^3 r^4} - \frac{3U_m'^3}{U_m^5 r^3} - \frac{10U_m'^2}{U_m^4 r^4} - \frac{15U_m'}{U_m^3 r^5} \right)\psi^3$$

$$+ \ldots \tag{2}$$

Equation (2) explicitly evaluates the vorticity generation term by expanding f in powers of ψ with curvature-dependent coefficients (small disturbance assumptions are implicit in the use of Taylor series).

A similar analysis applies to the Bernoulli "constant" in the usual pressure integral, which varies from streamline to streamline. It is convenient to define a function J within a "true constant" by $J'(\Psi) = f(\Psi)$. Then, the streamwise and radial momentum equations and the definition of vorticity lead to the Bernoulli equation

$$P/\rho + \frac{1}{2}(U^2 + V^2) - J(\Psi) = C \tag{3}$$

where the constant C, fixed throughout space, does not change from stream surface to stream surface (the "variable constant" appears through $J(\Psi)$). J is easily determined in any particular example. Suppose that $U_m(r)$, and hence $\psi_m(r)$, are given analytically upstream (this is not required in our later work). This functional relation can be inverted to yield $r = g(\psi_m)$, which is substituted in $f(\psi_m) = U_m'(r)/r$ to provide the required integrand in $J = \int^{\Psi} f(\Psi)\, d\Psi$. If we now write equation (3) using conditions at infinity, we have

$$\frac{P}{\rho} + \frac{1}{2r^2}(\Psi_r^2 + \Psi_x^2) - J(\Psi) = \frac{P_m(r)}{\rho} + \frac{1}{2r^2}\psi_{m_r}^2 - J(\psi_m)$$

or,

$$C_p = \frac{P - P_m(r)}{\frac{1}{2}\rho U_{\text{ref}}^2} =$$

$$- \frac{2\psi_{m_r}\psi_r + \psi_r^2 + \psi_x^2}{U_{\text{ref}}^2 r^2} + \frac{2\psi}{U_{\text{ref}}^2}\frac{J(\psi_m + \psi) - J(\psi_m)}{\psi} \tag{4}$$

where C_p is a nondimensional pressure normalized by a dynamic head based on the reference velocity U_{ref}. Then, replacing the derivative-like J term in equation (4) by its Taylor series approximation lead to

$$C_p = \frac{P - P_m(r)}{\frac{1}{2}\rho U_{\text{ref}}^2} = -\frac{2\psi_{m_r}\psi_r + \psi_r^2 + \psi_x^2}{U_{\text{ref}}^2 r^2} + \frac{2U_m'}{U_{\text{ref}}^2 r}\psi$$

$$+ \left(\frac{U_m''}{U_m r^2} - \frac{U_m'}{U_m r^3} \right)\frac{\psi^2}{U_{\text{ref}}^2} + \ldots \tag{5}$$

In summary, equations (2) and (5) provide explicit working equations with coefficients expressed in terms of known upstream conditions; they were obtained using some invariant properties of the stream function and the vorticity in axisymmetric flow. The linearized equations and their consequences are discussed next.

3 The Linearized Problem

In many engineering applications, simplifications are introduced by applying boundary conditions along slits. For these small-disturbance flows, the foregoing equations can be linearized; then, it turns out, that the notion of the velocity potential can be extended without difficulty (we will show how existing potential flow algorithms can be simply modified to handle strong shears). Let us now drop the nonlinear terms in equation (2). It is almost remarkable that the linearized equation can be cast in the conservation form

$$\frac{\partial}{\partial x}\left(\frac{U_m \psi_x}{rU_{\text{ref}}} \right) + \frac{\partial}{\partial r}\left(\frac{U_m \psi_r}{rU_{\text{ref}}} - \frac{U_m' \psi}{rU_{\text{ref}}} \right) = 0 \tag{6}$$

This implies the "extended Cauchy-Riemann conditions"

$$\phi_x^* = \frac{U_m}{U_{\text{ref}}}\frac{\psi_r}{r} - \frac{U_m'}{U_{\text{ref}}}\frac{\psi}{r} \tag{7}$$

$$\phi_r^* = -\frac{U_m}{U_{\text{ref}}}\frac{\psi_x}{r} \tag{8}$$

where $\phi^*(x,r)$ is our "superpotential" (ϕ^* derivatives are not velocities unless $U_m' = 0$). Equations (7) and (8) in turn show that ϕ^* satisfies the "potential-like" equation

Downloaded 02 May 2010 to 171.66.16.246. Redistribution subject to ASME license or copyright; see http://www.asme.org/terms/Terms_Use.cfm

$$\phi^*_{xx} + \phi^*_{rr} + \left(\frac{1}{r} - \frac{2U'_m}{U_m}\right)\phi^*_r = 0 \tag{9}$$

Thus only minor changes to existing potential flow finite-difference or finite-element algorithms are needed. The ϕ^*_r/r term in irrotational flow, incidentially, couples the effects of thickness and camber; here, we see that mean vorticity introduces additional coupling. The corresponding tangency conditions obtained from equation (8) are

$$\phi^*_r(x,R\pm) \cong \frac{U^2_m(R\pm)}{U_{\text{ref}}} F'_\pm(x) \tag{10}$$

where $r = R$ is a suitable mean radius and $F'_\pm$ (x) are streamwise surface slopes. For bodies with trailing edges, Kutta's conditions is required and a formula for C_p must be obtained. The linearized expression for C_p simplifies as follows:

$$C_p \cong -2\frac{\phi^*_x}{U_{\text{ref}}} \tag{11}$$

In summary, the Laplace-like equation (9) is solved together with the potential-like tangency condition in equation (10) and a trailing edge "potential jump" specified through a branch cut as inferred from equation (11). The strong resemblance to potential flow formulations allows us to "think irrotationally" in algorithm development.

Flows in ducts, for example, can be trivially solved. In contrast, flows through engine nacelles have constant U_m externally and nonzero $U'_m(r)$ behind assumed actuator disks; here, a specific $U'_m(r)$ is inferred from the radial blade loading, and Kutta's condition is handled "irrotationally," with the "potential jump" $[\phi^*]$ through the trailing edge slipstream specified but as a functional of x and ϕ^* (the discontinuous coefficients in the differential equation will be addressed more completely later). This "analysis" formulation solves for the surface pressure induced by a prescribed shape subject to Kutta's condition. In "design" or "inverse" problems, the shape that induces a prescribed chordwise pressure subject to auxiliary shape constraints is required. For nacelle flows, one might specify trailing edge closure or edges with opened cusps to model displacement thickness effects; a convenient dependent variable is the stream-function, because the jump $[\psi]$ controls gap and mass efflux directly, while $[\psi_x]$ automatically controls the included angle. These "Kutta-like" edge constraints would be solved with the linearized stream-function equation and the mixed Dirichlet and Newmann boundary condition

$$-2\frac{U_m(R\pm)}{U^2_{\text{ref}}R}\psi_r(x,R\pm) + \frac{2U'_m(R\pm)}{U^2_{\text{ref}}R}\psi(x,R\pm) = C^\pm_p(x) \tag{12}$$

The requried surface coordinates are then obtained from

$$dF_\pm/dx = -\Psi_x/\Psi_r \cong -\psi_x(x,R\pm)/RU_m(R\pm) \tag{13a}$$

$$F_\pm(x) = -\psi(x,R\pm)/RU_m(R\pm) + \text{constant} \tag{13b}$$

Similar remarks apply to design problems in annular or coannular ducts and pipes (for a more complete discussion on stream-function methods in aerodynamic design, the reader is referred to the references previously cited). Applications to these geometries are the subject of current research.

4 Application to Jet-Engine External Potential and Internal Rotational Flow Interaction

We will examine the flow through a finite-length axisymmetric nacelle immersed in a uniform freestream. Without power addition, the flow field is easily modeled by potential methods; here, the internal flow is irrotational up to an assumed actuator disk, beyond which the flow is rotational due to radially varying work imparted by the turbomachinery (Fig. 1). Thus, the flow field is potential externally and "superpotential internally" and in the downstream plume; matching conditions at the disk and plume interfaces connect both dependent variables.

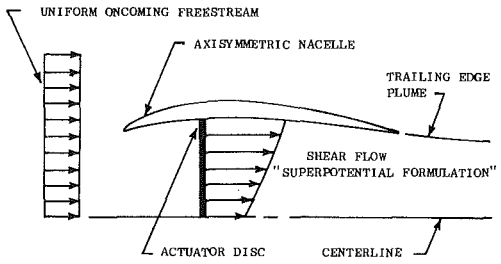

Fig. 1 Jet-engine external potential and internal rotational flow interaction

For the external irrotational flow, subscripted "e," the superpotential is a true potential, and the oncoming freestream is constant with $U_m(r) = U_\infty$. We introduce the nondimensional variables $\bar{x} = x/c$, $\bar{r} = r/c$, and $\bar{\phi}_e$ $(\bar{x},\bar{r}) = \phi^*_e(x,r)/U_\infty c$ where c is the semichord and take $U_{\text{ref}} = U_\infty$. Then the governing equations become

$$\bar{\phi}_{e_{\bar{x}\bar{x}}} + \bar{\phi}_{e_{\bar{r}\bar{r}}} + \frac{1}{r}\bar{\phi}_{e_{\bar{r}}} = 0 \tag{14a}$$

$$\bar{\phi}_{e_{\bar{r}}}(\bar{x},\bar{R}+) = F'_e(\bar{x}) \tag{14b}$$

$$C_{Pe} = (P_e - P_\infty)/\frac{1}{2}\rho U^2_\infty = -2\bar{\phi}e_{\bar{x}} \tag{14c}$$

Now consider the internal flow. So that our previous linearizations are physically meaningful, U_{ref} is chosen as a suitable "maximum speed." Here we assume a prescribed internal parallel shear flow originating at the actuator disk ("upstream infinity" in the context of Sections 2 and 3) with a horizontal speed that increases monotonically outward, resulting in a maximum speed $\tilde{U}$ found at the blade tips. With $U_{\text{ref}} = U_m(R\text{-}) = \tilde{U}$ and a different normalization, namely, $\bar{\phi}_i(x,r) = \phi^*_i(x,r)/\tilde{U}c$ and $U_m(r) = \tilde{U}\,\bar{U}(\bar{r})$, the internal elliptic equations (subscripted "i") becomes

$$\bar{\phi}_{i_{\bar{x}\bar{x}}} + \bar{\phi}_{i_{\bar{r}\bar{r}}} + \left(\frac{1}{\bar{r}} - 2\frac{\bar{U}_{\bar{r}}}{\bar{U}}\right)\bar{\phi}_{i_{\bar{r}}} = 0 \tag{15a}$$

$$\bar{\phi}_{i_{\bar{r}}}(\bar{x},\bar{R}-) = F'_i(\bar{x}) \tag{15b}$$

$$C_{p_i} = (P_i - P_m(\bar{r}))/\frac{1}{2}\rho\tilde{U}^2 = -2\bar{\phi}_{i_{\bar{x}}} \tag{15c}$$

F'_e and F'_i being actual geometric slopes; also, we note that other normalizations are possible, for example, U_∞ internally, but the quadratic terms in C_p would then be retained.

Next, pressure continuity through the trailing edge plume or slipstream is computationally applied along a mean radius R for simplicity. Because C_{p_e} and C_{p_i} are normalized differently, pressure continuity does not imply C_p continuity. Setting $P_e = P_i$ along $r = R$ and using equations (14c) and (15c) lead to

$$(\bar{\phi}_e - \bar{\phi}_i)_{\bar{x}} = \frac{P_\infty - P_m(R)}{\rho U^2_\infty} + \delta\bar{\phi}_{i\bar{x}} \tag{16}$$

where $(\tilde{U}/U_\infty)^2 = 1 + \delta$. If we now denote $[\bar{\phi}] = \bar{\phi}_e - \bar{\phi}_i$ and $\bar{\phi}_{\text{avg}} = 1/2(\bar{\phi}_e + \bar{\phi}_i)$, we obtain

$$[\bar{\phi}]_{\bar{x}} = \frac{P_\infty - P_m(R)}{\rho U^2_\infty(1 + \frac{1}{2}\delta)} + \frac{\delta}{1 + \frac{1}{2}\delta}\bar{\phi}_{\text{avg}\bar{x}} \tag{17}$$

Downloaded 02 May 2010 to 171.66.16.246. Redistribution subject to ASME license or copyright; see http://www.asme.org/terms/Terms_Use.cfm

Integrating with respect to x from the trailing edge $\bar{x}_{te}$ to $\bar{x}$, the wake matching condition

$$[\bar{\phi}]_{(\bar{x})} = [\bar{\phi}]_{(\bar{x}_{TE})} + \frac{P_\infty - P_m(R)}{\rho U_\infty^2 \left(1 + \frac{1}{2}\delta\right)} (\bar{x} - \bar{x}_{TE}) + \frac{\delta}{1 + \frac{1}{2}\delta} \{\bar{\phi}_{\text{avg}}(\bar{x},R) - \bar{\phi}_{\text{avg}}(\bar{x}_{TE},R)\} \quad (18)$$

is obtained for a "potential jump" with two "power corrections" to the irrotational $[\bar{\phi}]_{(x_{te})}$ term. This is not a true jump, of course, since the superpotentials are normalized differently, equation (18) merely describing a difference between two variables to be enforced numerically; our normalizations were in part motivated by the desire to keep the computer algorithm as "irrotational" and original as possible. For reference, specialized forms of equation (7) are given; in the external flow, with $U_m(r) = U_{\text{ref}} = U_\infty$, we set $\psi_e = c^2 U_\infty \bar{\psi}_e(\bar{x},\bar{r})$ so that

$$\frac{\bar{\psi}_{e_{\bar{r}}}}{\bar{r}} = \bar{\phi}_{e_{\bar{x}}} \quad (19)$$

Internally, we reference ψ to $\tilde{U}$; then $\psi_i = c^2 \tilde{U} \bar{\psi}_i(\bar{x},\bar{r})$ leads to

$$\frac{\bar{U}(\bar{r})}{\bar{r}} \bar{\psi}_{i_{\bar{r}}} = \bar{\phi}_{i_{\bar{x}}} + \bar{U}_{\bar{r}} \frac{\bar{\psi}_i}{\bar{r}} \quad (20)$$

Finally, we discuss actuator disk matching conditions. Actuator disks mathematically idealize changes to flow properties imparted by turbomachinery; for our purposes, the particular model is arbitrary and unimportant, because we are interested more in the effects of power addition arising from slipstream interaction. First, continuity of disturbance stream function through the disk requires that $\bar{\psi}_i = \bar{\psi}_e/(1+\delta)^{1/2}$; then continuity of the horizontal speed ψ_r/r (see equation (7)) leads to the matching condition

$$\frac{\bar{U}\bar{\phi}_{e_{\bar{x}}} - \frac{\bar{U}_{\bar{r}}}{\bar{r}} \bar{\psi}_e}{(1+\delta)^{1/2}} = \bar{\phi}_{i_{\bar{x}}} \quad (21)$$

used numerically, where a $\bar{\psi}_i$ was rewritten in terms of $\bar{\psi}_e$. Equation (21) was motivated by a finite-difference column relaxation solution method where lines of constant $\bar{x}$ are swept from upstream to downstream. Knowing the external flow left side, and hence the gradient $\bar{\phi}_{i_{\bar{x}}}$, allows us to march into the rotational flow ($\bar{\psi}_e$ is obtained by integrating equation (19) with respect to $\bar{r}$, from the centerline $\bar{r} = 0$ where $\bar{\psi}_e = 0$). This completes the analytical formulation; next, we review some numerical issues connected with the discontinuity of actual physical quantities through contact surfaces.

Because the ϕ_r^* coefficient in the governing field equation changes discontinuously through the disk and the slipstream, the usual potential-flow difference formulas must be reexamined since certain smoothness properties are implicitly assumed. A continuous function $f(r)$ with continuous first and second derivatives at $r = r_j$ can be described using $f_j' = (f_{j+1} - f_{j-1})/(r_{j+1} - r_{j-1})$ and $f_j'' = 4(f_{j+1} - 2f_j + f_{j-1})/(r_{j+1} - r_{j-1})^2$. If f is discontinuous at r_j, we cannot define a first derivative unless it is continuous; then, $f_j' = (f_{j+1} - f_{j-1} - [f])/(r_{j+1} - r_{j-1})$ where the discontinuity $[f]$ is subtracted out.

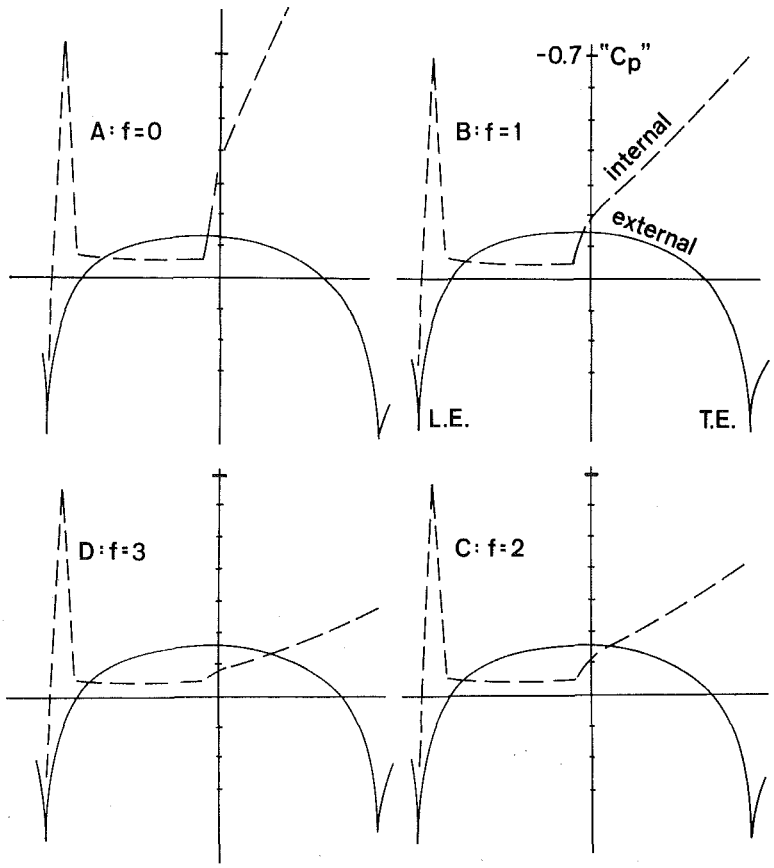

Fig. 2 $\lambda = 2$ rotational flow solutions

Downloaded 02 May 2010 to 171.66.16.246. Redistribution subject to ASME license or copyright; see http://www.asme.org/terms/Terms_Use.cfm

If, in addition, f_j'' is continuous, we can write $f_j'' = ((f_{j+1} - f_j)/(r_{j+1} - r_j) - (f_j - f_{j-1})/(r_j - r_{j-1}))/(1/2(r_{j+1} - r_{j-1}))$. These extended formulas allow discontinuities in f, provided f' and f'' are continuous; they are commonly used to difference through aerodynamic wakes. In wing flows the velocity normal to the wake is always continuous, but "ϕ_z" and "ϕ_{zz}" through an assumed flat wake is not—these formulas are used only with the restriction to the weak discontinuities allowed in small disturbance theory. For our jet-engine problem we must be certain that the usual difference formulas used through the slipstream are not physically unrealistic; f should be precisely defined and the assumed continuities in f' and f'' checked. Let us define $f = (\bar{\phi}_e$, externally; $\bar{\phi}_i$, internally) noting again that $\bar{\phi}_e$ and $\bar{\phi}_i$ are normalized differently. In the slipstream $\phi^*_{e_r}/U_\infty$ and $\phi^*_{i_r}/\tilde{U}$ both equal the streamwise plume slope; thus the nondimensional variables so defined allow for f' continuity, as required (f'' continuity, related to smooth curvature, is also assumed). When the customary "mean difference equation" is used in the wake for $f_m = 1/2(\bar{\phi}_e + \bar{\phi}_i)$, the difference approximations for the differential equation appear exactly as they would in potential flow formulations, except that the jump in f satisfies equation (18), more complicated, but easily implemented.

5 Calculated Resutls and Closing Discussion

Our new approach for inviscid rotational flow allows a simple "potential-like" solution to those problems where velocity shear is important. The ideas were developed for cylindrical axisymmetric flows without swirl; but the same approach, with similar results, extends to "mathematically axisymmetric" flows for arbitrary, say body-fitted, three-dimensional coordinate systems, using properties of vorticity special to these systems. Our particular jet-engine problem, because of the obvious complications, has not been examined in the literature; thus, we insist on a simple streamwise nacelle section, so that physical intuition can check anticipated and unanticipated results. We will use an external profile corresponding to the upper half of a symmetric unpitched 10 percent thick parabolic arc airfoil and assume a perfect circular cylinder internally, with a chord-to-diameter ratio of two. Thus we qualitatively expect an "airfoil-like" external surface C_p with stagnation peaks near both edges, and internal flow which, being energized by power, continues straight more or less. The modified wake condition in equation (18) shows that two nondimensional parameters are needed to characterize the shear, namely, $\delta = (\tilde{U}/U_\infty)^2 - 1$ and $\lambda = (P_m(R) - P_\infty)/1/2\rho U_\infty^2$ (the second is related to a total pressure increase). For simplicity we assume that U_m is proportional to $1 + fr$ (only the ratio U_m'/U appears in the governing equation), so that f, the strength, equivalently measures δ; computationally, we take $f = 0$, 1, 2, and 3 with $\lambda = +2$ (i.e., the static pressure $P_m(R)$ equals the external total pressure plus one dynamic head). Our first set of results, shown in Figs. 2(*a-d*) imply the streamline pattern in Fig. 3. As f increases, the external flow expands more, with C_p becoming more negative near midchord; at the same time, the internal leading edge lip flow expands less, indicating a movement of the external lip stagnation point toward the left as shown. Since the internal surface is flat, ψ is constant; in this case only, from equation (11), the C_p is proportional to the streamwise disturbance speed as in potential theory. As f increases, this speed decreases consistently, since the total pressure along the body streamline is fixed and the transverse velocity is zero. The same computer code was run irrotationally using $f = 0$ and $\lambda = 0$, with and without actuator disk logic; calculated internal results showed minor discrepancies since disk matching conditions occupied two course meshes. Figure 4 shows two solutions for $f = 0$, the

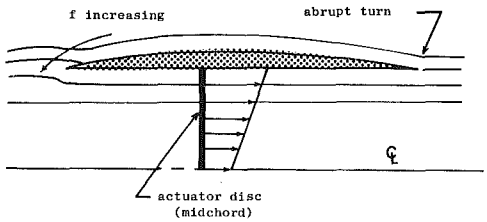

Fig. 3 Implied streamline pattern

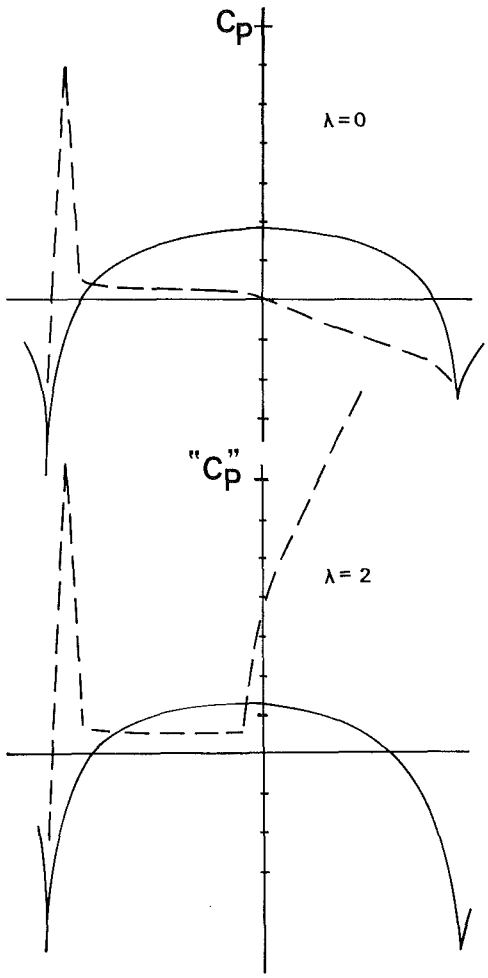

Fig. 4 Irrotational flow solutions with $f = 0$. Top: "flow-through nacelle without power. Bottom: Constant radial energy addition

first with $\lambda = 2$, the second with $\lambda = 0$ (in the former case C_p uses a different normalization downstream of the disk). A velocity slip is clearly seen in the powered flow. These finite difference calculations were implemented using a modified potential flow code on a coarse 60 × 60 mesh, with 20 over the chord, and carried to convergence.

In closing we emphasize that the superpotential approach requires only simple modifications to available potential flow algorithms; yet, it is rigorous and founded on the exact fluid-dynamic equations. The superpotential, we note, is a consequence of linearization but without restriction to shear strength; it is not the Clebsch potential often used to represent rotationality, nor is it related to Lighthill's "similar" pressure function (e.g., see reference [3]), which is restricted to weak shears. Its existence, incidentally, was motivated by some mathematical constructions used in inviscid hydrodynamic

Downloaded 02 May 2010 to 171.66.16.246. Redistribution subject to ASME license or copyright; see http://www.asme.org/terms/Terms_Use.cfm

stability theory. The particular application to jet-engine external potential and internal rotational flow interaction, of course, is not final; many code refinements are due before the code becomes a working tool. Direct and inverse applications to pipes and coannular ducts are currently in progress and the general coordinate approach mentioned earlier is nearing completion. Finally, general theoretical consequences to the planar limit of our shear flow equations have been obtained for thin airfoils, in both analysis and design problems (references [4]), and are available from the author.

References

1 Chin, W. C., "Direct Approach to Aerodynamic Design Problems," ASME JOURNAL OF APPLIED MECHANICS, Vol. 48, Dec. 1981, pp. 721–726.

2 Chin, W. C., and Rizzetta, D. P., "Airfoil Design in Subcritical and Supercritical Flows," ASME JOURNAL OF APPLIED MECHANICS, Vol. 46, Dec. 1979, pp. 761–766.

3 Lighthill, M. J., "The Flow Behind a Stationary Shock," *Phil, Mag.*, Vol. 40, 1949, pp. 214–220.

4 Chin, W. C., "Thin Airfoil Theory for Planar Inviscid Shear Flow," submitted for publication.

Downloaded 02 May 2010 to 171.66.16.246. Redistribution subject to ASME license or copyright; see http://www.asme.org/terms/Terms_Use.cfm

Perturbation Procedures for Nonlinear Viscous Flows

D. Nixon
Nielsen Engineering and Research, Inc.,
510 Clyde Avenue,
Mountain View, Calif. 94043

The perturbation theory for transonic flow is further developed for solutions of the Navier-Stokes equations in two dimensions or for experimental results. The strained coordinate technique is used to treat changes in location of any shock waves or large gradients.

1 Introduction

A series of papers recently published [1, 2] concern the development of a perturbation method for transonic flow problems. A basic problem in transonic flow perturbations is the treatment of possible movement of discontinuities (shock waves) that can make the perturbation invalid. A means of solving this problem, using a strained coordinate method, has been derived [1] in which the location of the discontinuities in the strained coordinate system remain the same throughout the perturbation, leading to a final linear perturbation equation for the perturbed unknowns. The final solution is not linear because of the transformation from the strained coordinate system to the physical coordinate system. However, since the perturbation equation is linear, the principle of superposition can be used, and the effect of several different types of perturbations can be easily, and inexpensively, estimated.

The most common application [2] of the method has been concerned with extrapolating transonic flow solutions. For example, given two transonic flow solutions for the same airfoil and Mach number, but at two different angles of attack, then the pressure distribution for any other angle of attack can be found by simple proportion and the use of the strained coordinate transformation. Applications of this technique to two-dimensional, multiparameter flow solutions and to three-dimensional, multishock problems are reported in [1] and [2]. These examples are concerned with the physical perturbation quantities, such as angle of attack, profile geometry changes, etc.

For the present work the perturbation theory is concerned with solutions of the Navier-Stokes equations. In particular, the application of the perturbation theory to solutions of the Navier-Stokes equations and to experimental data is investigated. In all cases the strained coordinate technique [1] is employed to treat shock waves or large gradients in the solutions.

First consider the perturbations of the Navier-Stokes equations. The first step in deriving a perturbation equation is to write the governing equations and their associated boundary conditions in such a form that only the basic equations or only the boundary conditions contain the perturbation parameter, otherwise the correct parameter to use may not be obvious. In the previous work for the TSD equation [2] the perturbation parameter is contained only in the boundary conditions. For the Navier-Stokes equations the perturbation parameter appears only in the set of equations, if these are written in a general body conforming curvilinear coordinate system and the variables nondimensionalized with respect to free-stream quantities. Both attached flows and flows with shock-induced separation are considered.

The basic principle behind the perturbation theory is that, relative to certain physical features of the problems, for example, the geometric confines of the airfoil and the shock location, the physical processes throughout the perturbation are in some sense similar. For instance, if two solutions are known (the base and calibration solutions) and have shock-induced separation, then an interpolated solution will also have shock-induced separation. Examples with attached flow and with separated flow are calculated with satisfactory results. However, in contrast to the earlier potential equation work [1, 2], it is found in the present case that the base and calibration solutions should not be too close, otherwise numerical inaccuracies in the Navier-Stokes solution can dominate the perturbation quantities.

2 Basic Principles of the Perturbation Theory

2.1 General Concepts. It is usually assumed in perturbation theory that the form of the perturbation parameter characterizing the disturbance is known or can be easily found. For example, in the earlier work [1, 2] on the perturbation theory, the transonic small-disturbance equation was written in an invariant form and the "natural" perturbation parameters were easily discernible from a study of the boundary conditions. In the present work, the strained coordinate perturbation theory is to be extended to treat the Navier-Stokes equations. It is unlikely that these equations can be written in a form independent of the free-stream conditions and consequently, the choice of the "natural" perturbation parameter for a perturbation in free-stream quantities may not be obvious. Accordingly, it is proposed to write the Navier-Stokes equations in a form where the boundary conditions are invariant, and then examine the

Contributed by the Applied Mechanics Division for publication in the JOURNAL OF APPLIED MECHANICS.
Discussion on this paper should be addressed to the Editorial Department, ASME, United Engineering Center, 345 East 47th Street, New York, N.Y. 10017, and will be accepted until two months after final publication of the paper itself in the JOURNAL OF APPLIED MECHANICS. Manuscript received by ASME Applied Mechanics Division, February, 1982; final revision, January, 1983.

Copyright © 1983 by ASME
Downloaded 02 May 2010 to 171.66.16.246. Redistribution subject to ASME license or copyright; see http://www.asme.org/terms/Terms_Use.cfm

transformed equations to determine the correct choice of perturbation parameters. A further simplification is to use the thin layer [3] approximation to the Navier-Stokes equations. This latter assumption is consistent, since these are the equivalent equations solved in most computer codes, whether explicitly coded or not.

If the reference values are free-stream quantities the steady thin-layer Navier-Stokes equations for two dimensions can be written [4] in a general curvilinear coordinate system as

$$\frac{\partial E}{\partial \xi} + \frac{\partial F}{\partial \eta} = R_e^{-1} \frac{\partial S}{\partial \eta} \tag{1}$$

where R_e is the Reynolds number, and (ξ, η) are the computational coordinates which are functions of Cartesian coordinates (x, y) with a transformation Jacobian J, given by

$$J = \xi_x \eta_y - \xi_y \eta_x = 1/(x_\xi y_\eta - x_\eta y_\xi) \tag{2}$$

The transformation metrics are given by

$$\begin{aligned} \xi_x &= J y_\eta \quad \eta_x = -J y_\xi \\ \xi_y &= -J x_\eta \quad \eta_y = J x_\xi \end{aligned} \tag{3}$$

and the contravariant velocities (U, V) are related to the Cartesian velocities u, v by

$$\begin{aligned} U &= \xi_x u + \xi_y v \\ V &= \eta_x u + \eta_y v \end{aligned} \tag{4}$$

The vectors E, F, and S are given by

$$E = J^{-1} \begin{bmatrix} \rho U \\ \rho u U + \xi_x p \quad \dfrac{1}{\gamma M_\infty^2} \\ \rho v U + \xi_y p \quad \dfrac{1}{\gamma M_\infty^2} \\ [\rho e + p(\gamma - 1)] U \end{bmatrix} \tag{5a}$$

$$F = \begin{bmatrix} \rho V \\ \rho u V + \eta_x p \quad \dfrac{1}{\gamma M_\infty^2} \\ \rho v V + \eta_y p \quad \dfrac{1}{\gamma M_\infty^2} \\ [\rho e + p(\gamma - 1)] V \end{bmatrix} \tag{5b}$$

$$S = J^{-1} \begin{bmatrix} 0 \\ \mu(\eta_x^2 + \eta_y^2) u_\eta + \dfrac{\mu}{3} \eta_x (\eta_x u_\eta + \eta_y v_\eta) \\ \mu(\eta_x^2 + \eta_y^2) v_\eta + \dfrac{\mu}{3} \eta_y (\eta_x u_\eta + \eta_y v_\eta) \\ \kappa Pr^{-1} \gamma (\eta_x^2 + \eta_y^2) \dfrac{\partial a^2}{\partial \eta} + \dfrac{\mu}{2} \gamma(\gamma - 1) M_\infty^2 (\eta_x^2 + \eta_y^2)(u^2 + v^2)_\eta \\ + \dfrac{\mu}{3} \gamma(\gamma - 1) M_\infty^2 (\eta_x u + \eta_y v)(\eta_x u_\eta + \eta_y v_\eta) \end{bmatrix} \tag{5c}$$

ρ, p, e are the density, pressure, and internal energy, respectively. Pr is the Prandtl number, κ is the conductivity, and a is the speed of sound of the gas. The pressure is related to e, ρ, u, v by

$$p = (\gamma - 1)\rho e - \frac{1}{2}\rho(u^2 + v^2) \tag{6}$$

where γ is the ratio of specific heats. M_∞ is the free-stream Mach number.

The computational coordinates (ξ, η) are chosen such that the surface $\eta\ (x, y) = 0$ represents the body surface. The boundary conditions are the tangency and no-slip conditions and therefore, on $\eta = 0$,

$$\begin{aligned} V &= 0 \\ U &= 0 \end{aligned} \tag{7}$$

The far-field boundary conditions are that free-stream conditions, prevail.
Thus, at infinity

$$\rho = p = e = u = v = 1 \tag{8}$$

It can be seen then, that, with the exception of changes in M_∞, the basic equation set and its boundary conditions are independent of the free-stream conditions. Changes in geometry are transmitted through the changes in the matrices ξ_x, ξ_y, η_x, η_y and the Jacobian J.

The system of equations (1), (5), and (6) can be written in the form

$$L(\rho, p, e, u, v, M_\infty^2, m) = 0 \tag{9}$$

where $L(\ )$ is a vector differential operator and m denotes the metric terms. Now consider a perturbation about some state or geometry denoted by a subscript o, and that the perturbation quantities, denoted by the subscript 1, are characterized by the parameter ϵ. First consider changes in geometry. An expansion of (9) for m then gives

$$\Delta m \frac{\partial L[\rho_o, p_o, e_o, u_o, v_o, M_\infty^2, m_o]}{\partial m} + \epsilon \bar{L}[\rho_1, p_1, e_1, u_1, v_1, M_\infty^2, m_1] = 0 \tag{10}$$

where $\bar{L}[\ ]$ is a linear operator, related to $L[\ ]$ and which depends on the zeroth-order quantities. In general, the metrics are functions of the geometry of the airfoil and hence for the small perturbations that are considered, Δm is given by

$$\Delta m = \left(\frac{\partial m}{\partial \theta}\right)_{\theta_o} \Delta\theta \tag{11}$$

where θ is some geometry parameter such as angle of attack. It can be seen from equation (10) that if $(\partial m/\partial\theta) \sim 0(1)$ then the natural choice of perturbation parameter, ϵ, is $\Delta\theta$, i.e., the change in the geometry characteristics. Hence, if two solutions are known for two cases that differ by a one-parameter variation then the solution for any other value of this parameter can be found by simple proportion.

A similar analysis to the foregoing but for Mach number variations indicates that the correct parameter to use for Mach number changes is ΔM_∞^2.

Downloaded 02 May 2010 to 171.66.16.246. Redistribution subject to ASME license or copyright; see http://www.asme.org/terms/Terms_Use.cfm

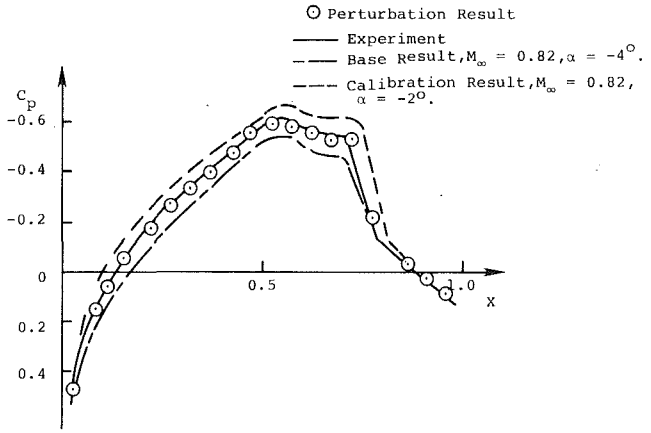

Fig. 1 Pressure distribution on the upper surface of a NACA 64A410 airfoil; $M_\infty = 0.82$; $\alpha = -3$ deg

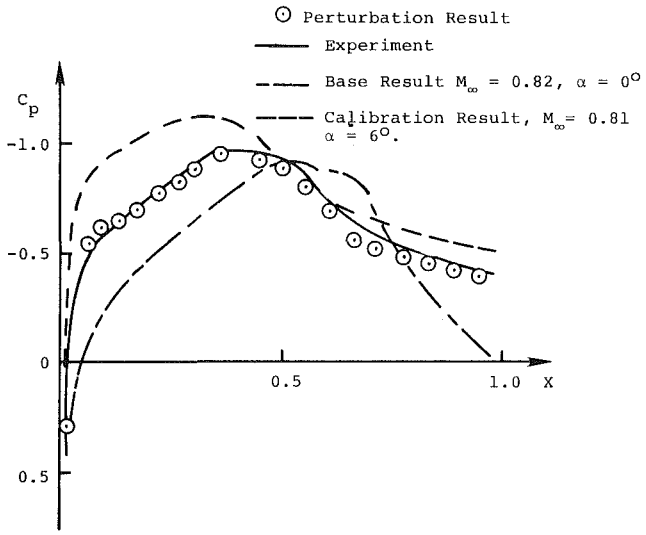

Fig. 2 Pressure distribution on the upper surface of a NACA 64A410 airfoil; $M_\infty = 0.82$; $\alpha = 4$ deg

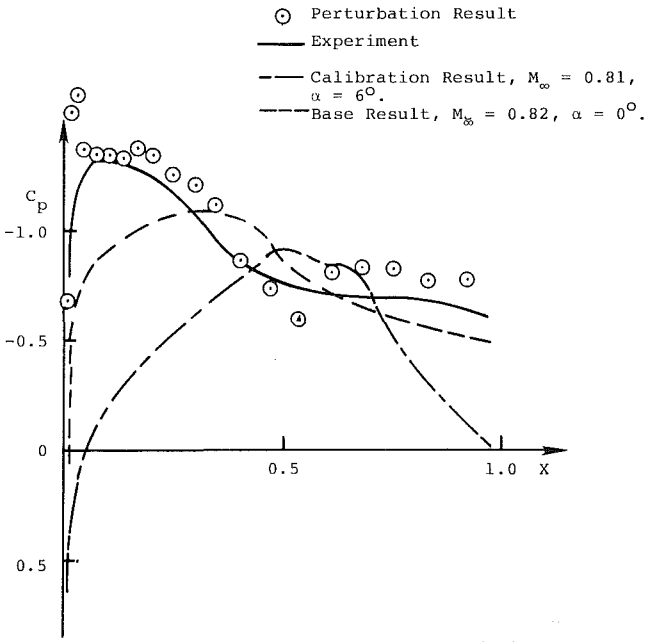

Fig. 3 Pressure distribution on the upper surface of a NACA 64A410 airfoil; $M_\infty = 0.79$; $\alpha = 10$ deg

The perturbation equation, (10), will also model separated flow since the physics of such flows are contained in the basic equations. However, since separation (or reattachment) is a discontinuous phenomenon, the derivatives in equation (10) are valid only when the flow does not change type. A separated flow cannot be determined from an attached flow from equation (10). The perturbation parameter for separated flow is an unknown function of M_∞ and the geometry θ. The perturbation parameter can, however, be approximated for small perturbations by the relation of equation (11) if the metric terms m reflect the separated flow zone. Since it may be assumed that the Navier-Stokes equations describe the physical flow, it follows that experimental data can be used in the interpolation theory instead of numerical results.

2.2 The Strained Coordinate Method. The interpolation procedure outlined in the preceding section is only valid for smooth functions. A device for treating discontinuous functions using a strained coordinate system has been derived in previous papers (e.g., [1]), and the reader is referred to this paper for further details.

3 Application of the Strained Coordinate System to the Navier-Stokes Equations

3.1 Theory for the Navier-Stokes Equations. Consider the set of equations, (1):

$$\frac{\partial E(\xi,\eta)}{\partial \xi} + \frac{\partial F(\xi,\eta)}{\partial \eta} = Re^{-1}\frac{\partial S(\xi,\eta)}{\partial \eta}$$

Let both the independent variables (ξ,η) be strained such that the location of one or more discontinuities or rapid gradients are held invariant. The new coordinates are denoted by (ξ', η') where

$$\xi = \xi' + \epsilon\delta\xi\,\xi_1(\xi',\eta') + \ldots$$
$$\eta = \eta' + \epsilon\delta\eta\,\eta_1(\xi',\eta') + \ldots \qquad (12)$$

where ϵ is the perturbation parameter, $\delta\xi$, $\delta\eta$ are measures of the movement of the straining points, and ξ_1 (ξ',η'), η_1 (ξ',η') are (fairly arbitrary) straining functions.

Now let the dependent variables be expanded in a series in ϵ. Thus

$$E(\xi,\eta) = E_o(\xi',\eta') + \epsilon E_1(\xi',\eta') + \ldots$$
$$F(\xi,\eta) = F_o(\xi',\eta') + \epsilon F_1(\xi',\eta') + \ldots \qquad (13)$$
$$S(\xi,\eta) = S_o(\xi',\eta') + \epsilon S_o(\xi',\eta') + \ldots$$

Using equations (12) and (13), the perturbation equation for (1) (the coefficient of ϵ) is

$$\frac{\partial E_1}{\partial \xi'} - \delta\xi\left(\frac{\partial E_o}{\partial \xi'}\xi_{1_{\xi'}} + \frac{\partial F_o}{\partial \eta'}\eta_{1_{\xi'}}\right) + \frac{\partial F_1}{\partial \eta'} - \delta\eta\left(\frac{\partial F_o}{\partial \eta'}\eta_{1_{\eta'}} + \frac{\partial E_o}{\partial \xi'}\xi_{1_{\eta'}}\right) = R_e^{-1}\left(\frac{\partial S_1}{\partial \eta'} - \delta\eta\frac{\partial S_o}{\partial \eta'}u_{1_{\eta'}} - \delta\xi\frac{\partial S_o}{\partial \xi'}\eta_{1_{\xi'}}\right) \qquad (14)$$

Now since ϵ is not contained in (14), it follows that a solution to this equation can be applied to any value of ϵ. As in the previous work [2], the perturbation equation is not solved; instead, the solution of the perturbation equation is assumed to be the difference between two complete solutions, differing only by a perturbation characterized by the parameter ϵ_o. Hence, for example, if

$$\bar{\xi} = \xi' + \epsilon_o\delta\xi\ \xi_1(\xi',\eta')$$
$$\bar{\eta} = \eta' + \epsilon_o\delta\eta\ \eta_1(\xi',\eta') \qquad (15)$$

Downloaded 02 May 2010 to 171.66.16.246. Redistribution subject to ASME license or copyright; see http://www.asme.org/terms/Terms_Use.cfm

and, if for the velocity component, $u(\xi, \eta)$, the two solutions are denoted by u_o (ξ, η) (base solution) and u_1 (ξ, η) (calibration solution, $\epsilon = \epsilon_o$), then, following the previous work [5],

$$u(\xi,\eta) = u_o(\xi',\eta') + \frac{\epsilon}{\epsilon_o}[u_1(\bar{\xi},\bar{\eta}) - u_o(\xi',\eta')] \tag{16}$$

and

$$\xi = \xi' + \epsilon\ \delta\xi\ \ \xi_1(\xi',\eta') = \xi' + \frac{\epsilon}{\epsilon_o}(\bar{\xi} - \xi')$$

$$\eta = \eta' + \epsilon\ \delta\eta\ \ \eta_1(\xi',\eta') = \eta' + \frac{\epsilon}{\epsilon_o}(\bar{\eta} - \eta') \tag{17}$$

The coordinates $\bar{\xi}$, $\bar{\eta}$ are found from (15) by making the straining points coincide. A similar relation to (16) applies for all the dependent variables, the most useful of which is the pressure coefficient C_p (ξ, η). Thus

$$C_p(\xi,\eta) = C_{p_o}(\xi',\eta') + \frac{\epsilon}{\epsilon_o}[C_{p_1}(\bar{\xi},\bar{\eta}) - C_{p_0}(\xi',\eta')] \tag{18}$$

In the present work, only values on the airfoil surface ($\eta = 0$) are considered and only the ξ coordinate is strained. The coordinate straining function ξ_1 $(\xi', 0)$ is given by the following equation or by a piecewise application of the following equation, depending on the number of straining points required.

$$\xi_1(\xi,0) = \sum_{i=1}^{N}\left\{\delta\xi'_{A_{i-1}} + \frac{(\delta\xi'_{A_i} - \delta\xi'_{A_{i-1}})}{(\xi_{A_i} - \xi'_{A_{i-1}})}(\xi' - \xi'_{A_{i-1}})\right\}H(\xi' - \xi'_{A_{i-1}}) \times H(\xi'_{A_i} - \xi') \quad 0 \le \xi' \le 1$$

where $\delta\xi_{A_i}$ denote the straining of the point ξ_{A_i} during the perturbation and $H(\ )$ is the step function. Note that ξ'_{A_o}, $\delta\xi'_{A_N}$, and $\delta\xi'_{A_o}$ are zero and $\xi'_{A_N} = 1$.

A further result can be obtained from equation (18) for the lift and pitching moment coefficients C_L, C_m. Consider the lift coefficient C_L, where

$$C_L = \int_o^1 \Delta C_p(\xi,0)d\xi \tag{19}$$

where $\Delta C_p(\xi, 0)$ denotes the pressure jump between upper and lower surfaces. Using equations (15), (17), and (18) the lift coefficient is then given by

$$C_L = \int_o^1 \left\{\Delta C_{p_o}(\xi',0') + \frac{\epsilon}{\epsilon_o}[\Delta C_{p_1}(\bar{\xi},\bar{0}) - \Delta C_{p_o}(\xi',0')]\right\} \times \left\{d\xi' + \frac{\epsilon}{\epsilon_o}[d\bar{\xi} - d\xi']\right\} \tag{20}$$

Now the basis of the perturbation theory implies that

$$[C_{p_1}(\bar{\xi},\bar{\eta}) - C_{p_o}(\xi',\eta')] \sim \underline{0}(\epsilon)$$
$$[d\bar{\xi} - d\xi'] \sim \underline{0}(\epsilon)$$

and also that $d\bar{\xi} = d\xi' + \underline{0}(\epsilon)$. Using these results in (24), it can be shown that

$$C_L = \int_o^1 \left[\Delta C_{p_o}(\xi',0)d\xi' + \frac{\epsilon}{\epsilon_o}\Delta C_{p_1}(\bar{\xi},0)d\bar{\xi} - \frac{\epsilon}{\epsilon_o}\Delta C_{p_o}(\xi',0)d\xi'\right] \tag{21}$$

or

$$C_L = C_{L_o} + \frac{\epsilon}{\epsilon_o}[C_{L_1} - C_{L_o}] \tag{22}$$

where C_{L_o}, C_{L_1} are the lift coefficients for the base and calibration solutions, respectively. A similar result applies for the pitching moment C_m, namely

$$C_m = C_{m_o} + \frac{\epsilon}{\epsilon_o}[C_{m_1} - C_{m_o}] \tag{23}$$

3.2 Some Comments on Applications to Separated Flow. If the strength of the shock wave is too strong, the flow behind the shock will separate and the shock structure will probably change from a single shock to a bifurcated shock. The separated flow may or may not reattach on the airfoil. If separated flows are to be considered in the perturbation theory, it is helpful to note the following features.

It is a basic premise of the perturbation theory that the topology of the flow does not change during a perturbation, for example, shock waves may not be generated or destroyed during the perturbation. Since the appearance of a separated flow region is a change in topology, a unified perturbation theory that goes from attached to separated flow cannot be constructed. However, a piecewise theory can be constructed. Hence the emphasis here is on using the perturbation theory separately for attached and separated flow regimes. The Navier-Stokes equations are sufficient to model separated flows, and the theory outlined in the previous section is applicable.

The appearance of separated flow can be regarded as an additional perturbation to a perturbation due to viscous effects for attached flow. It is of some interest to consider how the flow behaves with, say, increasing angle of attack, as the flow moves from attached to separated.

It is difficult to conduct an experiment just at the point where shock-induced separation occurs. A simplified analysis [7] indicates that the transition from attached to separated occurs smoothly if the intersection of two C_L-curves, one for attached flow and one for separated flow, occurs at a point that is demonstrably not attached or separated from other evidence. If the transition is smooth then this intersection point gives the separation point. A study of Stivers' [6] results seems to indicate that the transition is smooth.

3.3 Discussion of Results. A series of results of the perturbation theory are shown in Figs. 1-3 where the base and calibration data are taken from the experimental results of Stivers [6]. The theory has been applied to data with an increasing angle of attack. Since Stivers' data do not give a constant Mach number for each test, the data have been corrected for Mach number effects using a second application of the perturbation theory.

In Fig. 1 the pressure distribution around the upper surface of a NACA 64A410 airfoil at $M_\infty = 0.82$, $\alpha = -3$ deg is shown. This is an attached flow; the base data is at $\alpha = -4$ deg and the calibration solution is at $\alpha = -2$ deg. The agreement of the present results with the data is excellent. In Fig. 2 the pressure distribution at $\alpha = 4$ deg is shown compared to the data. The base data is at $\alpha = 0$ deg and the calibration solution is at 6 deg. This result is for a shock-induced separated flow, and the agreement with the experimental data is again excellent. A further result for $\alpha = 10$ deg using the same base and calibration data is shown in Fig. 3. The agreement with the data is fair; this result is probably getting toward the limit of application of the theory. At $\alpha = 12$ deg the experimental data indicate that the flow is separated at the leading edge.

It was found that to obtain sufficient accuracy the base and calibration solutions had to be further apart than is the case

Downloaded 02 May 2010 to 171.66.16.246. Redistribution subject to ASME license or copyright; see http://www.asme.org/terms/Terms_Use.cfm

for the earlier potential flow applications. This is attributed to the larger relative errors in the experimental data.

4 Concluding Remarks

The main object of the present work is to extend some recent developments in perturbation theories of transonic flow to treat solutions of the Navier-Stokes equations or to be applicable to experimental data. The extension of the perturbation theory to solutions of the Navier-Stokes equations is straightforward; the only additional fact to appear is that the necessary base and calibration solutions should not be too close together, otherwise the perturbation quantities can be seriously degraded by the experimental error. The results obtained by the present method compare favorably with experimental data. Both separated and attached flows are considered.

Acknowledgment

Research sponsored by the Air Force Office of Scientific Research (AFSC), under Contract F49620-79-C-0054. The United States Government is authorized to reproduce and distribute reprints for governmental purposes notwithstanding any copyright notation herein.

References

1 Nixon, D., "Perturbation of a Discontinuous Transonic Flow," *AIAA Journal*, Vol. 16, No. 1, 1978.

2 Nixon, D., "Perturbations in Two and Three-Dimensional Transonic Flow," *AIAA Journal*, Vol. 16, No. 7, 1978.

3 Baldwin, B. S., and Lomax, H., "Thin Layer Approximation and Algebraic Model for Separated Turbulent Flows," AIAA Paper 78-257, 1978.

4 Steger, J. L., "Implicit Finite Difference Simulation of Flow about Arbitrary Geometries with Application to Airfoils," AIAA Paper 77-665, 1977.

5 Nixon, D., "Design of Transonic Airfoils Using a Similarity Theory," AIAA Paper 79-0076, 1979.

6 Stivers, L. S., "Effects of Subsonic Mach Numbers on the Forces and Pressure Distributions on Four NACA64A-Series Airfoil Sections at Angles of Attack as High as 28°," NACA TN 3162, 1954.

7 Nixon, D., "Perturbation Procedures for Nonlinear Viscous Flows," Nielsen Engineering & Research, Inc. Paper No. 154, 1982.

Downloaded 02 May 2010 to 171.66.16.246. Redistribution subject to ASME license or copyright; see http://www.asme.org/terms/Terms_Use.cfm

D. Nixon

G. H. Klopfer

Nielsen Engineering & Research, Inc.,
510 Clyde Avenue,
Mountain View, Calif. 94043

Some Remarks on Transonic Potential Flow Theory

The validity of the commonly used transonic potential equation for flows with shock waves is examined. It is concluded that in such cases the potential formulation is inconsistent with the basis assumptions of the theory because of the nonconservation of momentum across a shock. The relationship of this momentum source to wave drag is also discussed. Another topic examined is the rationalization of means to make solutions of the transonic potential equation agree better with solutions of the Euler equations.

1 Introduction

At present, the main means of predicting transonic flow characteristics is by numerically solving either the full potential equation [1, 2] or its approximate form, the transonic small disturbance equation [3, 4]. To justify the use of a potential equation to describe transonic flows with shock waves it is usual to assume that entropy changes through a weak shock are negligible and hence, from Crocco's theorem [5] the flow can be considered irrotational. However, the derivation of Crocco's results requires that mass, momentum, and energy be conserved, and since in the present transonic potential, computer-codes axial momentum is not conserved if there are shock waves in the flow, it is obvious that there is an inconsistency in the model. This momentum error is often used to define a wave drag of the airfoil. The present study is concerned with examining the origin and effect of the inconsistency of potential flow theory when shock waves are present in the flow and also the relationship of the momentum error to wave drag.

In Section 2, a perturbation analysis of the potential theory through a normal shock is conducted and it is shown that the momentum error produced by the potential formulation leads to a "wave drag" proportional to the shock strength, whereas the correct result is the cube of the shock strength. Also, a possible theoretical basis for modifying potential theory to give more realistic shock jumps is described. In Section 3, the effect of not conserving momentum on the irrotationality assumption is examined and it is concluded that the potential formulation is only valid for a free-stream Mach number close to unity. An analysis is given which derives a consistent potential theory but it is concluded that this theory would give worse results than the conventional theory.

2 Comments on Isentropic Shock Waves

In this section the behavior of the flow through a one-dimensional isentropic shock wave is examined.

The isentropic density relation is

$$\frac{\rho}{\rho_\infty} = \left[1 + \left(\frac{\gamma-1}{2}\right) M_\infty^2 (1-q^2)\right]^{\frac{1}{\gamma-1}} \tag{1}$$

where $q = U/U_\infty$. The pressure relation is

$$\frac{p}{p_\infty} = \left[1 + \left(\frac{\gamma-1}{2}\right) M_\infty^2 (1-q^2)\right]^{\frac{\gamma}{\gamma-1}} \tag{2}$$

The pressure, density, and velocity are expanded as a series in the perturbation velocity u. Let

$$q = 1 + u \tag{3}$$

and expand the relations of equations (1) and (2) in powers of u. Hence

$$\rho = \rho_\infty \left\{1 - M_\infty^2 u - M_\infty^2 [1 + (\gamma-2)M_\infty^2] \frac{u^2}{2}\right\} \tag{4}$$

$$p = p_\infty \left\{1 - \gamma M_\infty^2 u - \frac{\gamma u^2}{2} M_\infty^2 \beta^2\right\} \tag{5}$$

where

$$\beta^2 = 1 - M_\infty^2 \tag{6}$$

Through a shock wave, mass, momentum, and energy should be conserved. If this is not true then there are errors E_1, E_2, and E_3 in the conservation laws of mass, momentum, and energy, respectively. Hence

$$E_1 = (\rho_1 U_1 - \rho_2 U_2)/\rho_\infty U_\infty = \left\{\beta^2 [u]_-^+ - \frac{k}{2} [u^2]_-^+\right\} \tag{7}$$

$$E_2 = (p_1 + \rho_1 U_1^2 - p_2 - \rho_2 U_2^2)/(p_\infty + \rho_\infty U_\infty^2)$$

$$= \gamma M_\infty^2 \left\{\beta^2 [u]_-^+ - \left(\frac{k-\beta^2}{2}\right) [u^2]_-^+\right\} / (1 + \gamma M_\infty^2) \tag{8}$$

$$E_3 = 0 \tag{9}$$

where subscript 1 denotes a value upstream of the shock, the subscript 2 denotes a value downstream of the shock, and

$$k = M_\infty^2 [3 + (\gamma-2)M_\infty^2] \tag{10}$$

The notation $[\ ]_-^+$ defines the jump across the shock. The energy equation is satisfied because the isentropic density and

Contributed by the Applied Mechanics Division for publication in the JOURNAL OF APPLIED MECHANICS.

Discussion on this paper should be addressed to the Editorial Department, ASME, United Engineering Center, 345 East 47th Street, New York, N.Y. 10017, and will be accepted until two months after final publication of the paper itself in the JOURNAL OF APPLIED MECHANICS. Manuscript received by ASME Applied Mechanics Division, April, 1982; final revision, January, 1983.

Copyright © 1983 by ASME
Downloaded 02 May 2010 to 171.66.16.246. Redistribution subject to ASME license or copyright; see http://www.asme.org/terms/Terms_Use.cfm

pressure relations of equations (1) and (2) are derived by assuming that energy is conserved.

Since $[u]^{+}_{-} = u_1 - u_2$ and $[u^2]^{+}_{-} = u_1^2 - u_2^2$ it can be seen that

$$E_1 = \sigma\left\{\beta^2 - \frac{k}{2}\hat{u}\right\} \tag{11}$$

$$E_2 = \gamma M_\infty^2 \sigma\left\{\beta^2 - \left(\frac{k-\beta^2}{2}\right)\hat{u}\right\}/(1+\gamma M_\infty^2) \tag{12}$$

where

$$\left.\begin{aligned} \sigma &= u_1 - u_2 \\ \hat{u} &= u_1 + u_2 \end{aligned}\right\} \tag{13}$$

Hence if the shock strength σ is zero then there are no errors in the solution. If the transonic small disturbance equation is formulated as

$$(\beta^2 - \hat{k}u)u_x + v_y = 0 \tag{14}$$

where $\hat{k}$ is a function of the free-stream Mach number, then for normal shock waves the jump relation is

$$\hat{u} = 2\beta^2/\hat{k} \tag{15}$$

Hence if $\hat{k} = k$ then the error in mass conservation is zero and there is a momentum error

$$E_2 = \frac{\gamma M_\infty^2}{(1+\gamma M_\infty^2)}\frac{\sigma\beta^4}{k} \tag{16}$$

This is equivalent to an upstream force on the shock wave. If, as is usual in transonic flow calculations, free-stream conditions are enforced at the downstream boundary then a contour integral of momentum around the flow indicates a total conservation of momentum. Hence the momentum error across the shock must be balanced by a pressure force on the airfoil. This is sometimes referred to (erroneously) as the wave drag. It is directly due to an inconsistency of the isentropic equations through a shock wave. This conclusion was obtained by Steger and Baldwin [6]. If the transonic parameter $\hat{k}$ in equation (14) is chosen to be $(k-\beta^2)$ then momentum is conserved but there is a mass error

$$E_1 = -\beta^4\sigma/(k-\beta^2) \tag{17}$$

Note that since transonic small disturbance theory assumes $\beta^4 = 0$ the conservation equations are satisfied to the order of approximation of the theory. However, the foregoing results are also applicable to the full potential equation for which no formal limit on β^2 is required.

It can be inferred from the preceding analysis that since transonic small disturbance theory has traditionally only one flexible parameter, $\hat{k}$, it is impossible to remove both the mass and momentum errors across a shock. However, it may be advantageous to choose the transonic parameter k such that a linear combination of the errors is minimized. Thus, if an error E is defined as

$$E = w_1 E_1 + w_2 E_2 \tag{18}$$

where w_1 and w_2 may be functions of u_1, then E can be minimized for a given u_1. Thus

$$E = \sigma\left\{\beta^2\left[w_1 + \frac{\gamma M_\infty^2}{1+\gamma M_\infty^2}w_2\right] - \left[kw_1 + \frac{\gamma M_\infty^2}{1+\gamma M_\infty^2}w_2(k-\beta^2)\right]\hat{u}\right\} \tag{19}$$

If $w_1 = 1$, $w_2 = 0$, this reduces to the conventional mass conserving result. If

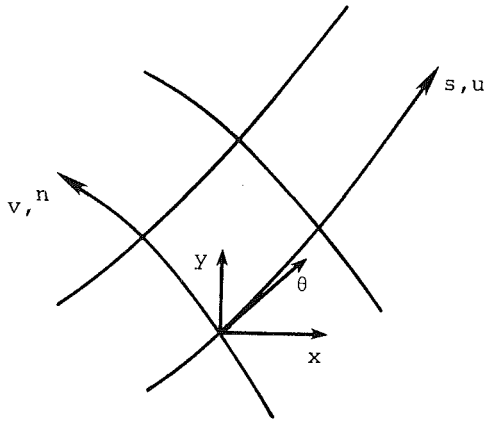

Fig. 1 Sketch of a streamline coordinate system

$$w_1 = \beta^2 - \left(\frac{k-\beta^2}{2}\right)\hat{u}_E; \quad w_2 = -\left(\beta^2 - \frac{k}{2}\hat{u}_E\right)$$

then $E = 0$ if k is chosen such that $u = \hat{u}_E$ where $\hat{u}_E$ is the value of $u_1 + u_2$ given by the Euler equations. To a first approximation

$$\hat{u}_E = u_1\left\{2 - \frac{M_\infty^2(\gamma+1)}{\left(1+\frac{\gamma-1}{2}M_\infty^2\right)^2}\right\} - \frac{M_\infty^2(\gamma+1)}{2\left(1+\frac{\gamma-1}{2}M_\infty^2\right)} \tag{20}$$

Such a modified small disturbance equation is used by Nixon [7].

The existence of the momentum deficit through the shock given by equation (16) is often assumed to be the drag. The drag coefficient, C_D, is given by the relation

$$C_D = \frac{(p_\infty + \rho_\infty U_\infty^2)E_2}{\frac{1}{2}\rho_\infty U_\infty^2} = 2\beta^4\sigma \tag{21}$$

whereas the formal limit of entropy producing drag as given by Murman and Cole [8] is, in the present notation

$$C_D = \frac{(\gamma+1)}{6M_\infty^2}\sigma^3 \tag{22}$$

and which is third order in σ in comparison to the linear dependence on σ of equation (21). Note that to get the complete drag, these drag relations must be integrated along the shock wave.

3 Comments on Momentum Deficit and Irrotationality

In the following analysis it is assumed that mass is conserved, since this allows a simple definition of the stream function coordinate system. It will be assumed that there are possible sources or sinks in momentum and energy. In Fig. 1, s is the streamline direction and n is a coordinate normal to the streamlines. The velocity u is in the stream-wise direction and by definition there is zero flow velocity across the stream tube. The conservation equations for mass, streamwise, and normal momentum and energy are as follows.

$$\frac{\partial \rho U}{\partial s} = 0 \quad \text{(conservation of mass)} \tag{23}$$

Downloaded 02 May 2010 to 171.66.16.246. Redistribution subject to ASME license or copyright; see http://www.asme.org/terms/Terms_Use.cfm

$$\rho U \frac{\partial U}{\partial s} = -\frac{\partial p}{\partial s} + \frac{\partial \epsilon_1}{\partial s} \quad \text{(conservation of streamwise momentum)} \tag{24}$$

$$\rho U^2 \frac{\partial \theta}{\partial s} = -\frac{\partial p}{\partial n} + \frac{\partial \epsilon_2}{\partial n} \quad \text{(conservation of normal momentum)} \tag{25}$$

$$\frac{\partial (h + U^2/2)}{\partial s} = \frac{\partial \epsilon_3}{\partial s} \quad \text{(conservation of energy)} \tag{26}$$

where $\partial \epsilon_1/\partial s$, $\partial \epsilon_2/\partial n$, and $\partial \epsilon_3/\partial s$ are the effects due to sources in streamwise momentum, normal momentum, and energy, respectively.

The entropy gradients in the streamwise and normal directions are defined by

$$T \frac{\partial S}{\partial s} = \frac{\partial h}{\partial s} - \frac{1}{\rho} \frac{\partial p}{\partial s} \tag{27}$$

$$T \frac{\partial S}{\partial n} = \frac{\partial h}{\partial n} - \frac{1}{\rho} \frac{\partial p}{\partial n} \tag{28}$$

Integration of the energy equation, equation (26), gives

$$h + U^2/2 = h_0(n) + \epsilon_3(n) \tag{29}$$

where $h_0(n)$ is the reservoir condition. If the fluid is considered a calorically and thermally perfect gas, then

$$h = C_p T = \frac{\gamma}{\gamma - 1} \cdot \frac{p}{\rho} \tag{30}$$

where C_p is the specific heat at constant pressure. Using equations (25) and (29), equations (28) can be written as

$$T \frac{\partial S}{\partial n} = \frac{\partial h_0}{\partial n} - \left(U \frac{\partial U}{\partial n} - U^2 \frac{\partial \theta}{\partial s} \right) - \frac{1}{\rho} \frac{\partial \epsilon_2}{\partial n} + \frac{\partial \epsilon_3}{\partial n} \tag{31}$$

The quantity $(\partial U/\partial n - U \partial \theta/\partial s)$ is the vorticity, ζ, of the flow and hence equation (31) can be written as

$$T \frac{\partial S}{\partial n} = \frac{\partial h_0}{\partial n} - U\zeta - \left(\frac{1}{\rho} \frac{\partial \epsilon_2}{\partial n} - \frac{\partial \epsilon_3}{\partial n} \right) \tag{32}$$

The entropy gradient in the streamwise direction can be written, using equation (24), as

$$T \frac{\partial S}{\partial s} = \frac{\partial \epsilon_3}{\partial s} - \frac{1}{\rho} \frac{\partial \epsilon_1}{\partial s} \tag{33}$$

Thus there is a streamwise entropy production due to the errors ϵ_1, ϵ_3. It is assumed that any shock waves in the flow are sufficiently weak that the entropy production due to physical phenomena is negligible.

Consider now the case where both normal momentum and the energy are conserved with no source terms. In this case

$$\left.\begin{aligned} \frac{\partial \epsilon_2}{\partial n} &= 0 \\ \frac{\partial \epsilon_3}{\partial n} &= 0 \end{aligned}\right\} \tag{34}$$

and hence if the reservoir condition h_0 is such that

$$\frac{\partial h_0}{\partial n} = 0 \tag{35}$$

(this is usually the case for transonic gas flows) and if the entropy production gradient normal to the streamlines is zero, i.e.,

$$\frac{\partial S}{\partial n} = 0 \tag{36}$$

Then equation (32) gives the irrotational condition

$$\zeta = 0 \tag{37}$$

If ϵ_1, ϵ_3, are expanded as series in terms of a perturbation velocity u, $[U = U_\infty(1+u)]$, such that

$$\epsilon_1 = \epsilon_1{}^{(1)} u + \epsilon_2{}^{(2)} u^2 \ldots$$
$$\epsilon_3 = \epsilon_3{}^{(1)} u + \epsilon_3{}^{(2)} u^2 \ldots$$

and if

$$T = T_\infty (1 + \alpha_T{}^{(1)} u + \alpha_T{}^{(2)} u^2 \ldots)$$
$$p = p_\infty (1 + \alpha_p{}^{(1)} u + \alpha_p{}^{(2)} u^2 \ldots)$$

then

$$\frac{\partial S}{\partial s} = \frac{1}{T_\infty} (\epsilon_3{}^{(1)} + 2\epsilon_2{}^{(2)} u) \times (1 - \alpha_T{}^{(1)} u - (\alpha_T{}^{(2)} - \alpha_T{}^{(1)2}) u^2) \frac{\partial u}{\partial s}$$
$$- \frac{R}{p_\infty} (\epsilon_1{}^{(1)} + 2\epsilon_1{}^{(2)} u) \times (1 - \alpha_p{}^{(1)} u - (\alpha_p{}^{(2)} - \alpha_p{}^{(1)2}) u^2) \frac{\partial u}{\partial s} \tag{38}$$

where the subscript ∞ denotes free-stream conditions and R is the gas constant. Equation (38) can be integrated to give

$$\Delta S = \frac{1}{T_\infty} \left(\epsilon_3{}^{(1)} [u]^{\pm} + \epsilon_3{}^{(2)} [u^2]^{\pm} \right) - \frac{1}{T_\infty} \alpha_T{}^{(1)} [u^2]^{\pm} \epsilon_3{}^{(1)}$$
$$- \frac{R}{p_\infty} \left(\epsilon_1{}^{(1)} [u]^{\pm} + \epsilon_1{}^{(2)} [u^2]^{\pm} \right) + \frac{R}{p_\infty} \alpha_p{}^{(1)} [u^2]^{\pm} \epsilon_1{}^{(1)} + \underline{0}(u)^3 \tag{39}$$

where Δ denotes a difference from some reference condition.

Finally, it should be noted that by using equations (27) and (30),

$$\frac{p}{\rho^\gamma} = K e^{\frac{(\gamma - 1)S}{R}} \tag{40}$$

where K is a constant. If the free-stream conditions are the reference conditions for equation (40) then

$$K = \frac{p_\infty}{\rho_\infty^\gamma} \tag{41}$$

In an inviscid irrotational continuous flow it can be shown [5] that the conservation of mass and energy, together with the isentropic relations for p, ρ ensures conservation of momentum. However, if there is a discontinuity normal to the streamlines in the flow, then it is shown earlier that this set of equations does not conserve momentum through the discontinuity. In many transonic calculations this momentum deficit is erroneously referred to as wave drag. Since the isentropic approximation to transonic flow requires the basic assumption that mass, momentum, and energy be conserved, there is an obvious inconsistency in the overall theory. This momentum error only occurs at a shock wave and from equation (39) this error shows up as an entropy production term. However, it is possible that a self-consistent potential theory can be derived and this possibility is examined in the subsequent analysis.

Consider now the case of a transonic flow that has sufficiently weak shock waves that no entropy production from purely thermodynamic means is significant. Assume also the

Downloaded 02 May 2010 to 171.66.16.246. Redistribution subject to ASME license or copyright; see http://www.asme.org/terms/Terms_Use.cfm

shock wave is normal to the streamlines, thus ensuring conservation of normal momentum. Finally, assume that total enthalpy is conserved throughout the flow; this is consistent with the isentropic model since the necessary density/velocity relation is found by assuming conservation of total enthalpy.

In the remaining analysis the error ϵ_3 is set to zero, implying conservation of total enthalpy and the pressure/density relation, equations (40) and (41) are written as

$$(p/p_\infty)/(\rho/\rho_\infty)^\gamma = 1+\delta \tag{42}$$

where δ is of order $[u]^{\pm}_{\mp}$, the shock strength, from equations (39) and (40). If it is assumed the shock waves are weak, then powers of δ greater than unity can be neglected. Substitution of equation (42) into the energy equation, equation (29) gives

$$\frac{\gamma}{(\gamma-1)}\cdot\frac{p_\infty}{\rho_\infty}\left(\frac{\rho}{\rho_\infty}\right)^{\gamma-1}(1+\delta) = \frac{\gamma}{\gamma-1}\frac{p_\infty}{\rho_\infty}+(U_\infty^2/2)\left(1-\frac{U^2}{U_\infty^2}\right) \tag{43}$$

In terms of the perturbation velocity, this is

$$\frac{\rho}{\rho_\infty} = \left\{1-\frac{\gamma-1}{2}M_\infty^2(2u+u^2)\right\}^{\frac{1}{\gamma-1}}/(1+\delta)^{\frac{1}{\gamma-1}} \tag{44}$$

An expansion to second order in u gives

$$\frac{\rho}{\rho_\infty} = 1-M_\infty^2\,u-\frac{u^2}{2}[1+M_\infty^2(\gamma-2)]M_\infty^2-\frac{\delta}{\gamma-1} \tag{45}$$

The pressure relation is found by taking

$$\frac{p}{P_\infty} = (1+\delta)(\rho/\rho_\infty)^\gamma$$

$$\frac{p}{P_\infty} = 1-\gamma M_\infty^2\,u-\frac{u^2M_\infty^2\beta^2}{2}-\frac{\delta}{\gamma-1} \tag{46}$$

where $\beta^2 = 1-M_\infty^2$.

Across a normal shock wave the errors in the conservation of mass, momentum, and energy are as follows: The error terms ϵ_1,δ only contribute to the values on the downstream side of the shock:

$$E_{\text{mass}} = \rho_1U_1-\rho_2U_2 = \rho_\infty U\left(\beta^2[u]^{\pm}_{\mp}-\frac{k}{2}[u^2]^{\pm}_{\mp}\right)+\frac{\rho_\infty U_\infty\delta}{\gamma-1}. \tag{47}$$

$$E_{\text{momentum}} = p_1+p_1U_1^2-\rho^2-\rho_2U_2^2 =$$

$$\rho_\infty U_\infty^2\left(\beta^2[u]^{\pm}_{\mp}-\frac{(k-\beta^2)}{2}[u^2]^{\pm}_{\mp}\right)+\frac{\rho_\infty U_\infty^2\delta}{\gamma-1}\left(1+\frac{1}{\gamma M_\infty^2}\right) \tag{48}$$

$$E_{\text{energy}} = 0 \tag{49}$$

In the preceding equations, $k=[3+(\gamma-2)M_\infty^2]M_\infty^2$ and $[\ ]^{\pm}_{\mp}$ denotes a jump across the shock wave. Note that the result of equation (49) confirms the consistency of putting the energy error equal to zero.

Now assume that the solution algorithm conserves mass. Thus the error in equation (47) is zero and then the solution has shock jumps given by

$$u_2 = \frac{1}{k}\left(\beta^2\pm\left[(\beta^2-ku_1)^2-\frac{2k\delta}{\gamma-1}\right]^{1/2}\right) \tag{50}$$

From equations (39)–(42)

$$\delta = \frac{-(\gamma-1)}{p_\infty}\{(\epsilon_1{}^{(1)}[u]^{\pm}_{\mp}+\epsilon_1{}^{(2)}[u^2]^{\pm}_{\mp}) - \alpha_p{}^{(1)}\epsilon_1{}^{(1)}[u^2]^{\pm}_{\mp}\} \tag{51}$$

and since, by definition,

$$E_{\text{momentum}} = -(\epsilon_1{}^{(1)}[u]^{\pm}_{\mp}+\epsilon_1{}^{(2)}[u^2]^{\pm}_{\mp}) \tag{52}$$

equation (48) may be written as

$$-\{\epsilon_1{}^{(1)}[u]^{\pm}_{\mp}+\epsilon_1{}^{(2)}[u^2]^{\pm}_{\mp}\} = \rho_\infty U_\infty^2\left[\beta^2[u]^{\pm}_{\mp}-\frac{k[u^2]^{\pm}_{\mp}}{2}+\frac{\delta}{\gamma+1}\right] + \rho_\infty U_\infty^2\frac{\beta^2}{2}[u^2]^{\pm}_{\mp}-\left[\epsilon_1{}^{(1)}[u]^{\pm}_{\mp} + \epsilon_1{}^{(2)}[u^2]^{\pm}_{\mp}-\alpha_p{}^{(1)}\epsilon_1{}^{(1)}[u^2]^{\pm}_{\mp}\right] \tag{53}$$

Since from conservation of mass the first term in square brackets in equation (50) is zero, equation (53) becomes

$$-\left[\alpha_p{}^{(1)}\epsilon_1{}^{(1)}-\rho_\infty U_\infty^2\frac{\beta^2}{2}\right][u^2]^{\pm}_{\mp} = 0 \tag{54}$$

Hence for a consistent formulation either the flow is continuous,

$$u_1 = u_2 \tag{55}$$

or the flow has a shock wave with the jump relation

$$u_1 = -u_2 \tag{56}$$

or, in terms of the shock strength $\sigma = u_1-u_2$

$$\sigma = 2u_1 \tag{57}$$

To the same order of accuracy the conventional "isentropic" jump relation is

$$\sigma = 2u_1-\frac{2\beta^2}{k} \tag{58}$$

and hence for $\beta^2\neq 0$ the consistent theory gives a stronger shock than the inconsistent conventional theory. Since the conventional shock is already too strong it is probable that a consistent theory is too inaccurate for practical calculations.

From equations (50) and (56) the term δ is given by

$$\delta = -2\beta^2u_1(\gamma-1) \tag{59}$$

for a flow with a discontinuity. The error ϵ_1 is given by a combination of equations (59) and (51); thus

$$\epsilon_1{}^{(1)}[u]^{\pm}_{\mp}+\epsilon_1{}^{(2)}[u^2]^{\pm}_{\mp}-\alpha_p{}^{(1)}[u^2]^{\pm}_{\mp}\epsilon_1{}^{(1)} = 2p_\infty\beta^2u_1 \tag{60}$$

The preceding discussion can be summarized as follows.

(*a*) The conventional potential theory is inconsistent because axial momentum is not conserved.

(*b*) A consistent, irrotational, one-dimensional theory can be derived if the shock wave is normal to the free stream.

(*c*) It is probable that the results of using this consistent theory are more inaccurate than results of the inconsistent conventional theory.

In view of these conclusions, it is suggested that the conventional theory can enhanced by the addition of variables such as modifying the potential equation either by analytic means [9] or nonconservative differencing [10]. Since both conventional and modified theories are inconsistent, it would seem that a modified theory is as valid as the conventional theory.

For the irrotational assumption to hold the quantity $|\delta| << 1$ and hence from equation (59)

Downloaded 02 May 2010 to 171.66.16.246. Redistribution subject to ASME license or copyright; see http://www.asme.org/terms/Terms_Use.cfm

$$\beta^2 u_1 << 1 \tag{61}$$

Now to a first approximation

$$\beta^2 - k u_1 = 1 - M_1^2$$

where M_1 is the Mach number just upstream of the shock. Hence equation (61) can be written as

$$\frac{\beta^2 (M_1^2 - M_\infty^2)}{k} << 1 \tag{62}$$

It can be concluded that apart from its treatment of the tangency boundary conditions, the full potential equation is formally no more accurate than the small disturbance equation since both require $\beta^2 u_1 << 1$.

In equations (11) and (12) it can be seen that if mass is conserved then momentum is conserved only if

$$[u^2]^{+}_{-} = 0$$

which, in the case of conventional potential theory, is not possible since $[u^2]^{+}_{-}$ is solely determined by the mass conservation equation. In the consistent theory, although the same requirement of $[u^2]^{+}_{-}$ is needed, there is an additional parameter in the mass conservation equation, the "δ" term that allows this requirement to be satisfied. It should be noted that even for very weak shock waves, the consistent theory does not approach the conventional theory; this only occurs for continuous flow.

Finally, it should be noted that since $\delta < 0$ for equation (59) the entropy due to the momentum change through the shock wave decreases, which contravenes the second law of thermodynamics. Thus the consistent potential theory is not physically plausible.

Concluding Remarks

Several aspects of the transonic potential theory have been examined and it is concluded that there are several inconsistencies in the theory. It is also suggested that there are some commonly held misunderstandings in the interpretation of the results of potential theory calculations.

Acknowledgment

The work was sponsored by the Air Force Office of Scientific Research under Contract F49260-79-C-0054. The United States Government is authorized to reproduce and distribute reprints for governmental purposes notwithstanding any copyright notation hereon.

References

1 Jameson, A., "Iterative Solution of Transonic Flows Over Airfoil and Wings, Including Flows of Mach 1," *Comm. P. & App. Maths*, Vol. XXVII, 1974, pp. 283–209.

2 Holst, T. L., "Fast Conservative Algorithm for Solving the Transonic Full Potential Equation," *AIAA J.*, Vol. 18, No. 12, 1980, p. 1431.

3 Murman, E. M., and Cole, J. D., "Calculation of the Plane Steady Transonic Flows," *AIAA Journal*, Vol. 9, No. 1, 1971, p. 114.

4 Murman, E. M., "Analysis of Embedded Shock Waves Calculated by Relaxation Methods," *AIAA J.*, Vol. 12, No. 5, 1971, p. 626.

5 Liepmann, H. W., and Roshko, A., *Elements of Gas Dynamics*, Wiley, New York, 1957.

6 Steger, J. L., and Baldwin, B. S., "Shock Waves and Drag in the Numerical Calculation of Isentropic Transonic Flow," NASA TN-D-6997, 1971.

7 Nixon, D., "Transonic Small Disturbance Theory With Strong Shock Waves," *AIAA J.*, Vol. 18, No. 6, 1980, p. 717.

8 Murman, E. M., and Cole, J. D., "Inviscid Drag at Transonic Speeds," AIAA paper 74-540, 1974.

9 Klopfer, G. H., and Nixon, D., "Non-Isentropic Potential Formulation for Transonic Flows," AIAA paper 83-0375, 1983.

10 Gregg, R. D., and Henne, P. A., "An Assessment of Mass Conservation for Potential Flow Shock Simulation," AIAA Paper 82-0158, 1982.

Downloaded 02 May 2010 to 171.66.16.246. Redistribution subject to ASME license or copyright; see http://www.asme.org/terms/Terms_Use.cfm

The Effect of a Normal Shock on the Aeroelastic Stability of a Panel[1]

M. H. Williams[2]
School of Aeronautics and Astronautics,
Purdue University,
West Lafayette, Ind. 47907

The effect of a standing shock wave on the static and dynamic aeroelastic stability of a flexible panel is investigated using a linear structural and aerodynamic theoretical model. It is found that the shock is generally stabilizing. The lowest critical dynamic pressures are associated with shock positions downstream from the panel, where the panel is uninfluenced by the shock.

Panel Flutter, Introduction

The aeroelastic response of a flexible panel is known to depend strongly on the flow Mach number. For most practical edge support conditions, the plate diverges (buckles) at subsonic speeds and flutters at supersonic speeds [1]. Moreover, the critical speed, at which instability first occurs, is generally smallest at transonic Mach numbers. According to linear theory, in fact, the critical speed drops to zero at Mach 1 for a two-dimensional panel, since any static deformation induces an infinite aerodynamic reaction (by the Prandtl-Glauert rule).

In reality, of course, the panels aeroelastic response in the transonic regime is also influenced by aerodynamic and/or structural nonlinearities, boundary layers, and nonuniformities in the flow field. This paper deals with one such effect: the influence on stability of a plane shock standing on or near the plate (see Fig. 1). This configuration can be viewed as an idealization of a skin panel on a transonic wing, the shock location and strength being determined (on a larger scale) by the wing geometry and Mach number. We assume that the surface curvature and mean flow nonuniformities (other than the shock discontinuity) are negligible on the scale of the panel.

If the shock stands far upstream, the panel will clearly respond to a uniform subsonic stream (divergence). Conversely, if the shock lies downstream, the panel sees a uniform supersonic stream and, accordingly, must flutter [1]. The object of this investigation is to describe the transition from divergence to flutter as the shock "moves" downstream, and to deduce from this whether the shock degrades or enhances the stability of the plate.

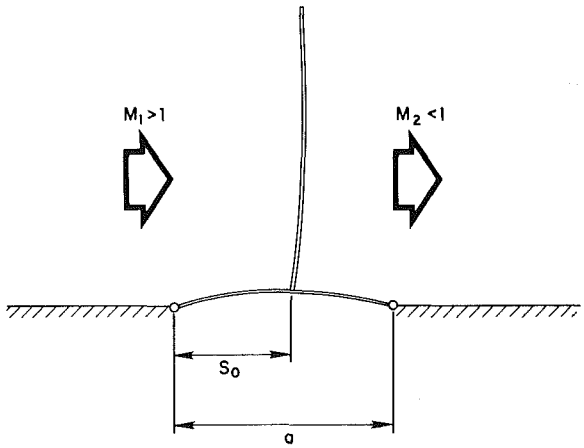

Fig. 1 Schematic of panel geometry

Equations of Motion of the Panel

The elastic deformation of the panel is governed by simple beam theory,

$$Df'''' + m\ \ddot{f} = -\Delta p \tag{1}$$

where

$f(x,t)$ = vertical displacement of the plate
D = plate bending stiffness
m = plate mass/unit area
Δp = $p_{\text{upper}} - p_{\text{lower}}$ = pressure difference across plate

$$\dot{f} = \frac{\partial f}{\partial t}, \quad f' = \frac{\partial f}{\partial x}$$

We consider the plate to be simply supported at both ends, $x=0$, a, so that the displacement satisfies the homogeneous boundary conditions:

$$f(0,t) = f(a,t) = f''(0,t) = f''(a,t) = 0 \tag{2}$$

This choice is made primarily because of the simplicity of the corresponding structural modes (sine functions). Other types of fixed end support (e.g., clamped-clamped) should yield qualitatively similar stability characteristics.

The aerodynamic load, Δp, consists of two parts: the static load existing without deformation and the aeroelastic load induced by the deformation,

[1]This research was sponsored by NASA Ames Research Center, under NASA Grant NSG 2194.

[2]This paper was written while the author was at Princeton University.

Contributed by the Applied Mechanics Division for presentation at the 1983 ASME Applied Mechanics, Bioengineering, and Fluids Engineering Conference, Houston, Texas, June 20-22, 1983 of THE AMERICAN SOCIETY OF MECHANICAL ENGINEERS.

Discussion on this paper should be addressed to the Editorial Department, ASME, United Engineering Center, 340 East 47th Street, New York, N.Y. 10017, and will be accepted until two months after final publication of the paper itself in the JOURNAL OF APPLIED MECHANICS. Manuscript received by ASME Applied Mechanics Division, September 1980; final revision, March, 1982. Paper No. 83-APM-28.

Copies will be available until February, 1984.

Copyright © 1983 by ASME
Downloaded 02 May 2010 to 171.66.16.246. Redistribution subject to ASME license or copyright; see http://www.asme.org/terms/Terms_Use.cfm

$$\Delta p = \Delta p_0 + q_1 A[f], \tag{3}$$

where

$\Delta p_0(x)$ = given static load (uniform on either side but discontinuous across the shock)
q_1 = $1/2\,\rho_1 U_1^2$ = upstream dynamic pressure
$A[\ ]$ = aerodynamic operator, to be determined.

If the operator A is linear then equations (1)–(3) have solutions of the form:

$$f(x,t) = f_0(x) + Re\{f_1(x)e^{i\omega t}\} \tag{4}$$

where the static deformation, f_0, and the complex dynamic amplitude, f_1, satisfy the independent equations:

$$Df_0'''' = -\Delta p_0 - q_1 A_0[f_0] \tag{5}$$

$$Df_1'''' - m\,\omega^2 f_1 = -q_1 A_\omega[f_1], \tag{6}$$

and

$$A_\omega[f_1] \equiv e^{-i\omega t} A[f_1 e^{i\omega t}]. \tag{7}$$

Each component, i.e., f_0 and f_1, must satisfy the boundary conditions, equation (2).

Equation (5) determines the static aeroelastic deformation under the shock load. Equation (6) determines the stability of the panel. Under the present assumptions of both structural and aerodynamic linearity, the two problems are not coupled. In practice, nonlinearities (of either type) can play an important role in the plate dynamics, in which case the two problems are coupled. This point will be discussed in a subsequent section.

Equation (6), with the boundary conditions (2), is an eigenvalue problem determining the possible natural frequencies and plate mode shapes of the combined fluid-structure system. In general (since the system is nonconservative) these eigenfrequencies will be complex, representing either damped or divergent motion, depending on the parameters of the problem (plate length, stiffness and mass, fluid density, pressure, and velocity and shock location). We will be concerned here only with those parameter combinations that lead to neutrally stable oscillations ($I_m\{\omega\} = 0$), where flutter first occurs, or to the onset of static instability ($\omega = 0$) termed divergence.

Flutter Boundaries

The in vacuo normal modes and eigenfrequencies of the plate are defined by,

$$D\,\psi_n'''' - m\,\omega_{0n}\,\psi_n = 0, \quad \frac{2}{a}\int_0^a dx\ \psi_n(x)\,\psi_m(x) = \delta_{nm}. \tag{8}$$

For the simply supported case these quantities are,

$$\psi_n(x) = \sin(n\pi x/a), \quad \omega_{0n} = \sqrt{\frac{D}{ma^4}}\,n^2\pi^2. \tag{9}$$

The deformation of the plate under the aerodynamic load can clearly be expressed in terms of these normal modes,

$$f_1(x) = \sum_{n=1} a_n\,\psi_n(x), \tag{10}$$

where the coefficients satisfy (using (8), (10), and (6)),

$$a\,m\,a_n(\omega_{0n}^2 - \omega^2) = -q_1 \sum_{m=1} a_m\,Q_{nm}, \quad n = 1,2\ldots \tag{11}$$

and where

$$Q_{nm} \equiv 2\int_0^a dx\ \psi_n(x)\,A_\omega[\psi_m], \tag{12}$$

are the "generalized forces."

The system of equation (11) has nontrivial solutions only if its determinant vanishes,

$$D(\omega) \equiv \| am\ (\omega_{0n}^2 - \omega^2)\delta_{nm} + q_1 Q_{nm} \| = 0 \tag{13}$$

which is a complex transcendental equation for the eigenfrequencies of the combined system.

The generalized forces are nondimensional functions of the upstream Mach number, reduced frequency, and shock location,

$$Q_{nm} = Q_{nm}\left(M_1, \frac{\omega a}{U_1}, s_0/a\right), \tag{14}$$

where s_0 is the distance between the leading edge and shock. Consequently the roots of the characteristic equation (13) can be expressed, formally, as

$$\frac{\omega}{\omega_{01}} = F_n\left(M_1, s_0/a, \frac{m}{\rho_1 a}, \frac{q_1 a^3}{D}\right). \tag{15}$$

The condition $Im(\omega) = Im(F_n) = 0$ defines a stability boundary for each mode, expressed as,

$$\frac{q_1 a^3}{D} = \lambda_n^*\left(M_1, s_0/a, \frac{m}{\rho_1 a}\right), \quad \frac{\omega}{\omega_{01}} = F_n^*\left(M_1, s_0/a, \frac{m}{\rho_1 a}\right). \tag{16}$$

Normally only the smallest such $q_1 a^3/D$ is of interest.

Divergence Boundary

The divergence or static stability boundary of the plate is determined by the condition $D(0) = 0$. The corresponding roots, from equations (13) and (14), are clearly of the form,

$$\frac{q_1 a^3}{D} = \lambda_n^D(M_1, s_0/a), \tag{17}$$

which, unlike the flutter boundaries, do not depend on the mass ratio.

Aerodynamic Analysis

We require the relation between the induced pressure and the deformation of an infinite plane wall for the initial flow sketched in Fig. 1. To simplify the analysis we shall suppose that the perturbed flow is isentropic and irrotational, although, in fact, the shock does generate entropy and vorticity in the subsonic region downstream. This "potential approximation" is widely used for transonic flows, where the shocks are weak and nearly isentropic [2].

It will be assumed, moreover, that the flow is an infinitesimal perturbation of the piecework uniform initial (or "mean") flow shown in Fig. 1. Mean flow quantities will be designated by a subscript "0," with the convention "0 = 1" upstream and "0 = 2" downstream from the shock. The perturbation velocity potential ϕ (the full potential being $u_0\,x + \phi$), then satisfies the linear wave equation,

$$\frac{D_0^2\,\phi}{Dt^2} = C_0^2\nabla^2\phi, \quad \frac{D_0}{Dt} = \frac{\partial}{\partial t} + U_0\frac{\partial}{\partial x}, \tag{18}$$

where C_0 is the undisturbed speed of sound, which must be solved subject to the outgoing wave condition at infinity and the linearized flow tangency condition on the surface,

$$\phi_y = \frac{D_0 f}{Dt} \ \text{ on } \ y = 0, \tag{19}$$

where $f(x,t)$ is the displacement of the surface from $y = 0$.

The density and pressure are related to the potential by the linearized Bernoulli equation and isentropic relation

$$P - P_0 = C_0^2(\rho - \rho_0) = -\rho_0\frac{D_0\phi}{Dt}. \tag{20}$$

To complete the formulation we must specify how the solutions of equation (18) in the supersonic and subsonic regions are connected across the shock. The usual shock jump conditions, conservation of mass, momentum, and energy provide four relations between the flow variables and shock

Downloaded 02 May 2010 to 171.66.16.246. Redistribution subject to ASME license or copyright; see http://www.asme.org/terms/Terms_Use.cfm

geometry. Within the linear approximation the conservation of energy is automatically satisfied by the Bernoulli equation (20). Conservation of transverse momentum implies continuity of the velocity component tangent to the shock, which is satisfied in the potential approximation by taking the full potential to be continuous. To maintain this condition in the linearized theory, the perturbation potential must be discontinuous across the mean shock with a jump proportional to the shock displacement.

$$s - s_0 = = \Delta_0\phi/\Delta_0 U_0 \tag{21}$$

where $x = s(y,t)$ is the instantaneous shock location and Δ_0 is the difference across the mean shock.

The final two conservation laws, mass and normal momentum, take on the following forms after linearization and use of equations (20) and (21),

$$\text{(mass)}\ \ \Delta_0\left[\frac{1}{U_0}(1-M_0^2)\phi_x - \left(\frac{1}{C_0{}^2} + \frac{1}{U_1U_2}\right)\phi_t\right] = 0 \tag{22}$$

$$\text{Normal (momentum)}\quad \Delta_0\left[(1-M_0^2)\phi_x - \frac{1}{U_0}(1+M_0^2)\phi_t\right] = 0, \tag{23}$$

where $M_0 = U_0/C_0$ is the mean flow Mach number.

Each of these equations is a compatibility condition relating the potentials on the subsonic and supersonic side of the mean shock. However, only one such condition can be imposed on the solution: either mass or momentum, but not both, can be conserved across the shock in the potential approximation. It is conventional to impose mass conservation (see, for example, Jameson [2]), although the other choice is equally consistent and both yield asymptotically equivalent results for weak shocks. Formally the difference between solutions obtained using the two conditions should be indicative of the error introduced by the potential approximation itself. However it will be shown that there is good reason for the conventional choice (mass conservation) in the present problem: the solution obtained using momentum conservation becomes unbounded in the steady limit.

We shall obtain the solution for the case of simple harmonic motion $f \sim \phi \sim e^{i\omega t}$ (now using $f(x)$ and $\phi(x,y)$ to denote the complex harmonic amplitudes). The analysis is similar to that of reference [3], with two main differences: (1) we consider the nonlifting problem here (as opposed to the lifting problem in reference [3]); and (2) we deal with the linearized full potential equation here (as opposed to the linearized transonic small disturbance equation in reference [3]).

For brevity we introduce the following notation,

$$\beta_0 = \sqrt{|M_0^2 - 1|}, \quad \lambda_0 = \frac{\omega}{U_0}\frac{M_0^2}{1-M_0^2}, \quad \nu_0 = \frac{\omega}{C_0\beta_0^2}$$

$$\Omega(x) = \left(\frac{d}{dx} + \frac{i\omega}{U_0}\right) f(x). \tag{24}$$

Upstream Solution. In the region $x < s_0$ the flow is supersonic and therefore uninfluenced by the shock. The potential field, therefore, is given by classical supersonic linear theory (equations (18) and (19) and the radiation condition),

$$\phi(x,y) = -\frac{U_1}{\beta_1}\int_{-\infty}^{x-\beta_1 y} dx_1\ \Omega(x_1)\ e^{i\lambda_1(x-x_1)}$$

$$J_0(\nu_1\sqrt{(x-x_1)^2 - \beta_1^2 y^2}), \tag{25}$$

$$x < s_0, \quad y > 0$$

where J_0 is the zeroth-order Bessel function.

Downstream Solution. The flow in $x > s_0$ is subsonic and therefore determined by the shock compatibility condition, as well as the radiation and surface tangency conditions. The shock relation (either (22) or (23)) can be written in the form,

$$\phi_x - 2\,i\sigma_2\phi = q(y)/\beta_2^2 \ \text{ on } \ x = s_0^+, \quad y > 0 \tag{26}$$

where, using the upstream solution (25),

$$q(y) = -\beta_1^2\ \bar{\delta}\ U_2/U_1[\phi_x - 2i\sigma_1\phi]_{x=s_0^-} \tag{27}$$

$$= \frac{U_2}{U_1}\bar{\delta}\int_{-\infty}^{s_0-\beta_1 y} dx\ e^{i\lambda_1(s_0-x)} J_0$$

$$(\nu_1\sqrt{(s_0-x)^2 - \beta_1^2 y^2})\left(\frac{d}{dx} - 2i\sigma_1\right)\Omega(x)$$

the coefficients $\sigma_0, \bar{\delta}$ depend on the choice of mass or momentum conservation,

(mass, equation (22))

$$2\sigma_0 = \frac{\omega U_0}{1-M_0^2}(1/C_0^2 + 1/U_1U_2), \quad \bar{\delta} = 1$$

(momentum, equation (23))

$$2\sigma_0 = \frac{\omega}{U_0}\frac{1+M_0^2}{1-M_0^2}, \quad \bar{\delta} = U_1/U_2 \tag{28}$$

As in reference [3], the potential that satisfies the surface and shock boundary conditions is constructed by distributing singularities along the axes of an image plane ($-\infty < x_1 < \infty, -\infty < y_1 < \infty$),

$$\phi(x,y) = \frac{iU_2}{2\beta_2}\int_{-\infty}^{\infty} dx_1\ w(x_1)$$

$$e^{i\lambda_2(x-x_1)} H_0^{(2)}(\nu_2\sqrt{(x-x_1)^2 + \beta_2^2\ y^2})$$

$$+ \frac{i}{2\beta_2}\int_{-\infty}^{\infty} dy_1\ q(|y_1|)\ G_1(x-s_0,\ y-y_1), \quad x > s_0,\ y > 0, \tag{29}$$

where $H_0^{(2)}$ is the zeroth-order Hankel function and

$$G_1(\xi,\eta) \equiv \int_{\infty}^{\xi} d\xi\ e^{2i\sigma_2(\xi-\xi_1)+i\lambda_2\xi_1}$$

$$\frac{\partial}{\partial\xi_1}\ H_0^{(2)}\ (\nu_2\sqrt{\xi_1^2 + \beta_2^2\ \eta^2}). \tag{30}$$

This potential satisfies the wave equation (18) and the radiation condition for arbitrary source distributions w and q. Since the second term in (29) is symmetric in y, the surface tangency condition (19) is satisfied if we take

$$w(x) = \Omega(x), \ x > s_0. \tag{31}$$

Finally the shock boundary condition (27) is satisfied identically if we take the quantity $[w'(x_1) - 2i\sigma_2 w(x_1)]e^{i\lambda_2(s_0-x_1)}$ to be antisymmetric about $x_1 = s_0$, which provides the required definition of w for $x_1 < s_0$,

$$w(x) = e^{i\lambda_2(x-s_0)}\ \Omega(2s_0 - x) + 2i(\lambda_2 - 2\sigma_2)\ e^{2i\sigma_2(x-s_0)}$$

$$\int_x^{s_0} dx_1\ e^{2i(\lambda_2-2\sigma_2)(x_1-s_0)}\ \Omega(2s_0 - x_1),$$

$$x < s_0 \tag{32}$$

Surface Potentials. The potential on the surface $y = 0$ will be split into three parts,

$$\phi(x,0) = H(s_0 - x)\ \phi^{(1)}(x)$$

$$+ H(x - s_0)\ [\bar{\phi}^{(2)}(x) + \phi^{(3)}(x)]. \tag{33}$$

The first part is the disturbance upstream from the shock, from equation (25),

Downloaded 02 May 2010 to 171.66.16.246. Redistribution subject to ASME license or copyright; see http://www.asme.org/terms/Terms_Use.cfm

$$\phi^{(1)}(x) = -\frac{U_1}{\beta_1}\int_0^\infty dx_1\ \Omega(x-x_1)\ e^{i\lambda_1 x_1}\ J_0(\nu,x_1). \quad (34)$$

The second part is the downstream disturbance generated by downstream motion, from the first term in equation (29),

$$\phi^{(2)}(x) = \frac{iU_2}{2\beta_2}\int_{-\infty}^{\infty} dx_1\ e^{i\lambda_2 x_1}\ H_0^{(2)}\ (\nu_2|x_1|)\ w(x-x_1) \quad (35)$$

(where w is defined by (31) and (32)).

The third part is the downstream disturbance generated by upstream motion, from the second term in equation (29). Using equation (27) to eliminate the source strength, q, we find that

$$\phi^{(3)}(x) = i\ U_2\ \beta/k\ \bar{\delta}/\beta^2\int_{-\infty}^{s_0} dx_1\ \Omega(x_1)\ G\left(\frac{s_0-x_1}{\beta_1}, \frac{x-s_0}{\beta^2}\right), \quad (36)$$

where the kernel G is defined by,

$$G(\xi_1,\xi_2) = e^{i(\lambda_1\beta_1\xi_1+\lambda_2\beta_2\xi_2)}\left[\frac{\partial}{\partial\xi} + i\beta_1(\lambda_1-2\sigma_1)\right]\int_{-\infty}^{0} dt\ e^{2i\sigma_2\beta_2 t}\ \frac{\partial}{\partial t}\ X(\xi_1,\xi_2-t) \quad (37)$$

$$X(\xi_1,\xi_2) = \int_0^{\xi_1} dz\ H_0^{(2)}(\nu_2\beta_2\sqrt{\xi_2^2+z^2})J_0(\nu_1\beta_1\sqrt{\xi_1^2-z^2}). \quad (38)$$

In practice the evaluation of each of these expressions is considerably simplified if the Bessel functions are replaced by their corresponding integral representations,

$$J_0(x) = \frac{1}{\pi}\int_{-1}^{1} dt\frac{e^{ixt}}{\sqrt{1-t^2}},$$

$$H_0^{(2)}(x) = \frac{2}{i\pi}\int_{-i}^{-\infty} dt\frac{e^{xt}}{\sqrt{1+t^2}}. \quad (39)$$

Thus equation (34) becomes,

$$\phi^{(1)}(x) = -\frac{U_1}{\pi\beta_1}\int_{-1}^{1} dt\frac{1}{\sqrt{1-t^2}}L_1(t,x) \quad (40)$$

where

$$L_1(t,x) = -\int_0^\infty d\,x_1\ \Omega(x-x_1)\ e^{i(\lambda_1+\nu_1 t)x_1}. \quad (41)$$

Similarly equation (35) becomes (using equations (31) and (32) for w),

$$\phi^{(3)}(x) = \frac{U_2}{\pi\beta_2}\int_{-i}^{-\infty} dt\frac{1}{\sqrt{1+t^2}}\ L_2(t,x), \quad (42)$$

where

$$L_2(t,x) = 2\int_{s_0}^{x} dx_1\ \Omega(x_1)e^{i\lambda_2(x-x_1)}\sinh\ \nu_2 t(x-x_1) + \left[\frac{i(\lambda_2-2\sigma_2)-\nu_2 t}{i(2\sigma_2-\lambda_2)-\nu_2 t}e^{(\nu_2 t+i\lambda_2)(x-s_0)} + e^{(i\lambda_2-\nu_2 t)(x-s_0)}\right] \quad (43)$$

$$\int_0^\infty dx_1\ \Omega(s_0+x_1)e^{(\nu_2 t-i\lambda_2)x_1}$$

Simplification of the third potential requires a preliminary result, an integral representation of the function X defined in (38). It is easily shown that this function satisfies the Helmholtz equation

$$\left(\frac{\partial^2}{\partial\xi_1^2}+\frac{\partial^2}{\partial\xi_2^2}+\nu_1^2\beta_1^2+\nu_2^2\beta_2^2\right)X(\xi_1,\xi_2)=0 \quad (44)$$

and boundary conditions

$$X(0,\xi)=0,\quad \frac{\partial X}{\partial\xi_1}(0,\xi_2)=H_0^{(2)}(\nu_2\beta_2\xi_2). \quad (45)$$

Thus an alternative definition of X is (using equation (39)),

$$X(\xi_1,\xi_2) = \frac{2}{i\pi}\int_{-i}^{-\infty} dt\ \frac{e^{\nu_2\beta_2\xi_2 t}}{\sqrt{1+t^2}}\frac{\sin\Gamma\xi_1}{\Gamma} \quad (46)$$

$$\Gamma \equiv \sqrt{\nu_1^2\beta_1^2+\nu_2^2\beta_2^2(1+t^2)}.$$

When this representation is substituted into equations (37) and (36), we find that

$$\phi^{(3)}(x) = \frac{U_2}{\pi\beta_2}\int_{-i}^{\infty} dt\ \frac{1}{\sqrt{1+t^2}}e^{(i\lambda_2+\nu_2 t)(x-s_0)}L_3(t) \quad (47)$$

where

$$L_3(t) = (2\ \bar{\delta})\frac{t}{t-2i\sigma_2/\nu_2}\int_0^\infty dx_1\ \Omega(s_0-x_1)e^{i\lambda_1 x_1}\left[\cos\frac{\Gamma x_1}{\beta_1}+\frac{i\beta_1}{\Gamma}(\lambda_1-2\sigma_1)\sin\frac{\Gamma x_1}{\beta_1}\right]. \quad (48)$$

The formulas (40)–(48) involve only elementary functions and are, therefore, relatively easy to evaluate. In fact, for sufficiently simple displacements (i.e., $\Omega(x)$) the integrals L_j can be evaluated explicitly, leaving a single quadrature (for each potential) to be performed numerically.

These forms are not, however, useful in the steady limit ($\omega=0$), because the corresponding integrals are then poorly converged. We shall, therefore, consider the steady solution separately.

Steady Limit. We consider the behavior of the solution in the limit $\omega\to 0$. Upstream from the shock we obtain from equation (25) the simple relation

$$\phi(x,y) = -\frac{U_1}{\beta_1}f(x-\beta_1 y)+0(\omega),\quad x<s_0. \quad (49)$$

Downstream from the shock we find from equation (29) and (30), using the asymptotic behavior of the Hankel function,

$$\phi(x,y) = \frac{U_2}{\pi\beta_2}\int_{-\infty}^{\infty} dx_1\ w(x_1)\ ln\ (\nu_2\sqrt{(x-x_1)^2+\beta_2^2(y-y_1)^2} + \frac{1}{\pi\beta_2}\int_{-\infty}^{\infty} dy_1\ q(|y_1|)\ ln\ (\nu_2\sqrt{(x-s_0)^2+\beta_2^2(y-y_1)^2},\quad x>s_0 \quad (50)$$

where, to lowest order in frequency,

$$w(x) = w(2s_0-x)=f'(x),\ x>s_0$$
$$q(y) = \beta_1 U_2\bar{\delta}\,f'(s_0-\beta_1 y). \quad (51)$$

Thus the potential on the subsonic side has a bounded steady limit only if the net source strength vanishes:

$$\int_{-\infty}^{\infty} dx_1\ w(x_1)+\int_{-\infty}^{\infty} dy_1\ q(|y|)=2U_2(\bar{\delta}-1)\,f(s_0)=0. \quad (52)$$

Downloaded 02 May 2010 to 171.66.16.246. Redistribution subject to ASME license or copyright; see http://www.asme.org/terms/Terms_Use.cfm

This condition is met (cf equation (28)) if conservation of mass is imposed, but not with conservation of momentum.

It will be noted that the divergent term $(1n\nu_2)$ in equation (50) is a constant and therefore has no effect on the velocities or pressures (whether or not condition) (52) holds). However the shock displacement, as given by equation (11), is proportional to the potential and so has a bounded limit only if we impose conservation of mass.

If we impose condition (52) the steady-state surface potential may be written in the final form,

$$\phi(x,0)=\begin{cases} -U_1/\beta_1\, f(x) & x<s_0 \\ \dfrac{U_2}{\pi\beta_2}\displaystyle\int_{-\infty}^{\infty} dx_1\, f'(x_1)\, \ln\,|(x-s_0)^2 & \\ +(x_1-s_0)^2\,\epsilon(x_1-s_0)|, & x>s_0 \end{cases} \tag{53}$$

where

$$\epsilon(\xi)=\begin{cases} -1, \xi>0 \\ \beta_2^2/\beta_1^2, \ \xi<0 \end{cases}$$

Generalized Forces. In computing any integrated load (such as a generalized force) the shock displacement must be taken into account. The additional load due to the shock displacement appears in the linear approximation as a concentrated force. To show this we consider the Bernoulli equation (20) in the form,

$$P=P_1+H(x-s)(P_2-P_1)-\rho_0\frac{D_0\phi}{Dt} \tag{54}$$

with the mean pressure jump occurring at the instantaneous shock location s. Taylor expanding H about the mean shock position s_0 and eliminating the shock displacement by equation (21) gives,

$$H(x-s)=H(x-s_0)+\frac{\Delta_0\phi}{\Delta_0 U_0}\delta(x-s_0)+\ \ldots\ . \tag{55}$$

Using this result and the Hugoniot relation $\Delta_0 P_0 / \Delta_0 U_0 = -\rho_0 U_0$ in equation (54) gives the required result,

$$P=P_0-\rho_0\frac{D_0\phi}{Dt}\rho_0 U_0\ \Delta_0\ \phi\ \delta(x-s_0). \tag{56}$$

We now consider the displacement amplitude $f(x)=\psi_n(x)$ corresponding to the nth structural mode of vibration, and denote the induced surface potential by $\phi(x,0)=1/2U_1\phi_n(x)$. It follows from equations (3), (7), and (52) that

$$A_\omega[\psi_n]=-2\left(\frac{d}{dx}+\frac{i\omega}{U_0}\right)\phi_n(x)-2\Delta_0\phi_n\ \delta(x-s_0), \tag{57}$$

and thus that the generalized forces as defined in equation (12) are given, after an integration by parts, by

$$Q_{nm}=4\int_0^a dx\ \phi_m(x)\ \Omega_n^*(x) \tag{58}$$

where (cf equation (24)) $\Omega_n(x)=\psi_n'+i\omega/U_0\ \psi_n$ and Ω_n^* is its complex conjugate. We observe that the shock point load does not appear explicitly in the generalized forces when expressed in terms of the potential.

The evaluation of the generalized forces is further simplified if we make use of the potential splitting introduced in equation (33) and the integral representation, equations (40), (42), and (47). For nonzero frequencies, then the generalized forces can be evaluated from,

$$Q_{nm}=Q_{nm}^{(1)}+Q_{nm}^{(2)}+Q_{nm}^{(3)} \tag{59}$$

where

$$Q_{nm}^{(1)}=\frac{4}{\pi\beta_1}\int_{-1}^{1} dt\frac{1}{\sqrt{1-t^2}}\ Z_{nm}^{(1)}\ (t),\ Q_{nm}^{(j)}$$

$$=\frac{4}{\pi\beta_2}\int_{-i}^{-\infty} dt\frac{1}{\sqrt{1+t^2}}\ Z_{nm}^{(j)}\ (t) \tag{60}$$

$$j=2,3,$$

and

$$Z_{nm}^{(1)}(t)=-\int_0^{S_0} dx\int_0^x$$

$$dx_1\ \Omega_n^*(x)\ \Omega_m(x_1)\ e^{i(\lambda_1+\nu_1 t)(x-x_1)} \tag{61}$$

$$Z_{nm}^{(2)}=2\frac{U_2}{U_1}\int_{s_0}^a dx\int_{s_0}^x$$

$$dx_1\,\Omega_n^*(x)\ \Omega_m(x_1)\ e^{i\lambda_2(x-x_1)}\ \sinh\ \nu_2 t(x-x_1) \tag{62}$$

$$+\frac{U_2}{U_1}K_m(t)\left[\frac{t-i(\lambda_2-2\sigma_2)/\nu_2}{t+i(\lambda_2-2\sigma_2)/\nu_2}K_n^*(t)+K_n^*(-t)\right]$$

$$Z_{nm}^{(3)}(t)=\frac{U_2}{U_1}\delta\frac{2t}{t-2i\sigma_2/\nu_2}K_n^*(t)\ I_m(t) \tag{63}$$

$$K_n(t)=\int_{s_0}^a dx\ \Omega_n(x)e^{(\nu_2 t-i\lambda_2)(x-s_0)} \tag{64}$$

$$I_n(t)=\int_0^{s_0} dx\ \Omega_n(x)\ e^{i\lambda_1(s_0-x)}$$

$$\left[\cos\frac{\Gamma(s_0-x)}{\beta_1}+i\frac{\beta_1}{\Gamma}(\lambda_1-2\sigma_1)\ \sin\ \frac{\Gamma(s_0-x)}{\beta_1}\right. \tag{65}$$

The zero frequency case, required for divergence calculations, is best treated from equations (53) and (58), from which we find that,

$$Q_{nm}^{(1)}=-\frac{4}{\beta_1}\int_0^{s_0} dx\ \psi_m(x)\psi_n'(x) \tag{66}$$

$$Q_{nm}^{(2)}=\frac{4U_2}{\pi U_1}\frac{1}{\beta_2}\int_{s_0}^a dx\int_{s_0}^a$$

$$dx_1\ \psi_n'(x)\ \psi_m'(x_1)\ 1n|(x-s_0)^2-(x_1-s_0)^2| \tag{67}$$

$$Q_{nm}^{(3)}=\frac{4}{\pi}\ \frac{U_2}{U_1}\ \frac{1}{\beta_2}\int_{s_0}^a dx\int_0^{s_0}$$

$$dx_1\ \psi_n'(x)\psi_m'(x_1)\ 1n|(x-s_0)^2+\beta_2^2/\beta_1^2(x_1-s_0)^2| \tag{68}$$

As in the unsteady case, these can be reduced, for the simply supported plate, to single quadratures.

If the shock is downstream from the plate, $s_0>a$, then $Q_{nm}^{(2)}=Q_{nm}^{(3)}=0$ and $Q_{nm}=Q_{nm}^{(1)}$ is given by equations (60) and (61) with $s_0=a$, i.e., the "classical" supersonic result is recovered. If the shock is upstream from the plate, $s_0<0$, then $Q_{nm}^{(1)}=Q_{nm}^{(3)}=0$ (since there is no disturbance in the supersonic zone) and $Q_{nm}=Q_{nm}^{(2)}$ is given by equations (60), (62), and (64) with $s_0=0$ in the integration limits. The generalized force, in this case, does depend on the shock location (through the

Downloaded 02 May 2010 to 171.66.16.246. Redistribution subject to ASME license or copyright; see http://www.asme.org/terms/Terms_Use.cfm

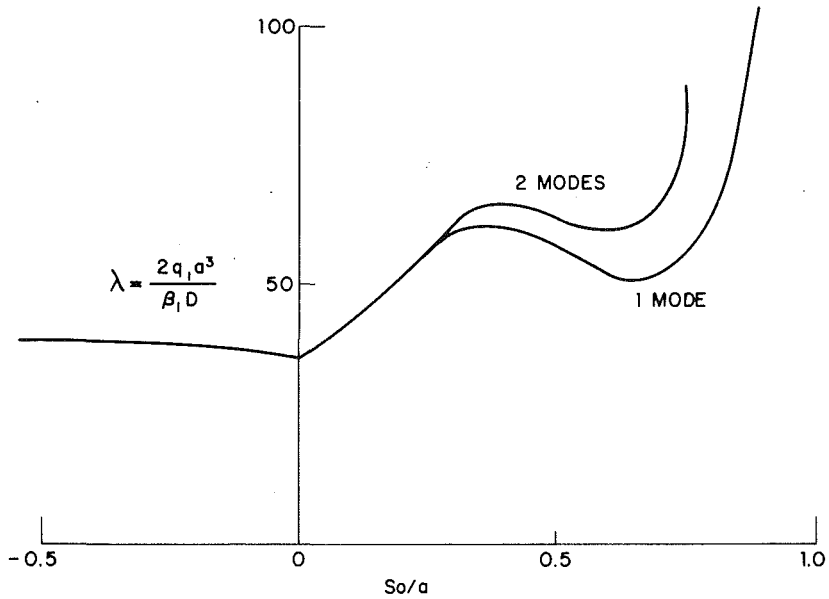

Fig. 2 Variation of divergence dynamic pressure with shock location, $M_1 = 1.1$

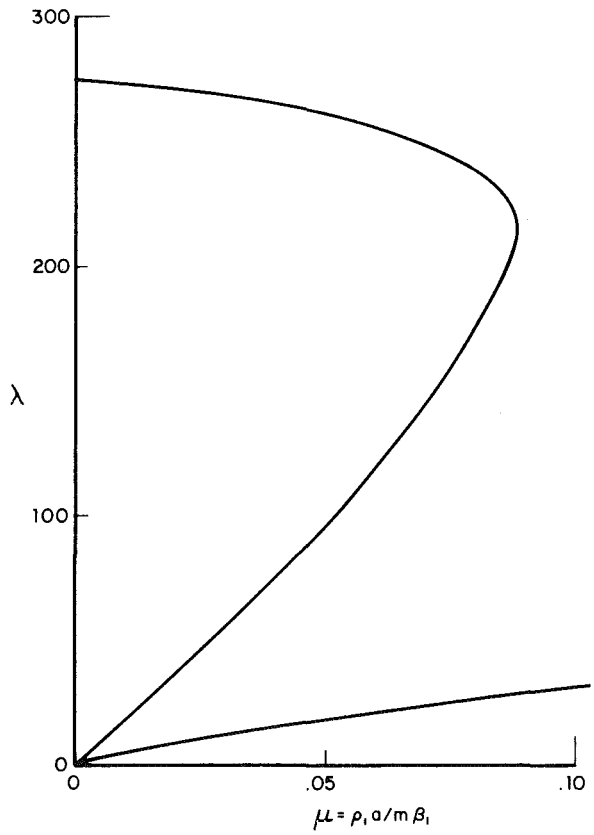

Fig. 3 Flutter dynamic pressure versus mass ratio $S_0/a = 1.0$, $M_1 = 1.1$

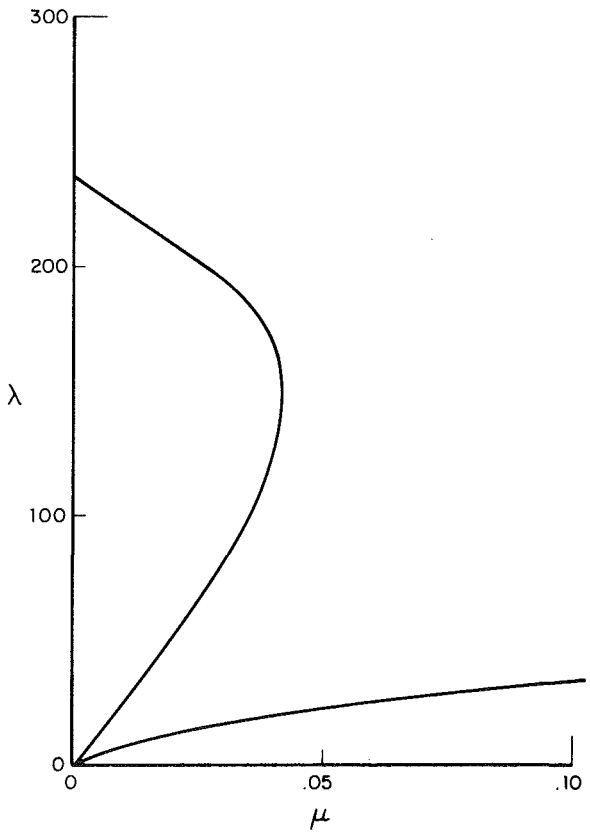

Fig. 4 Flutter dynamic pressure versus mass ratio $S_0/a = 0.95$, $M_1 = 1.1$

exponential factor in equation (64)) because acoustic waves can reflect off the shock back onto the plate. The contribution of these reflected waves (given by the term proportional to $K_m(t)$ in equation (62) decays rapidly as $s_0 \to -\infty$, leaving the "classical" subsonic result.

Results

Calculations have been performed for an upstream Mach number $M_1 = 1.1$. For simplicity only the first two terms have been retained in the modal expansion, equation (10). When the shock is upstream or downstream from the plate it is known that the first instability occurs predominately in the first structural mode [1]. It is expected, then, that two modes should be adequate to describe, at least qualitatively, the variation of the stability boundary with shock location.

Figure 2 shows the variation of divergence dynamic pressure with shock location according to the one and two-mode truncations. It is apparent that the divergence occurs

Downloaded 02 May 2010 to 171.66.16.246. Redistribution subject to ASME license or copyright; see http://www.asme.org/terms/Terms_Use.cfm

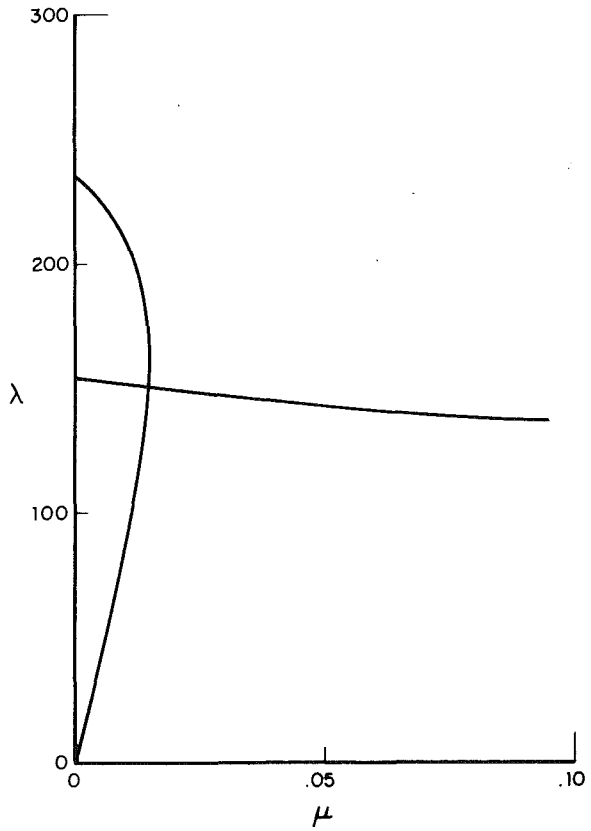

Fig. 5 Flutter dynamic pressure versus mass ratio $S_0/a = 0.85$, $M_1 = 1.1$

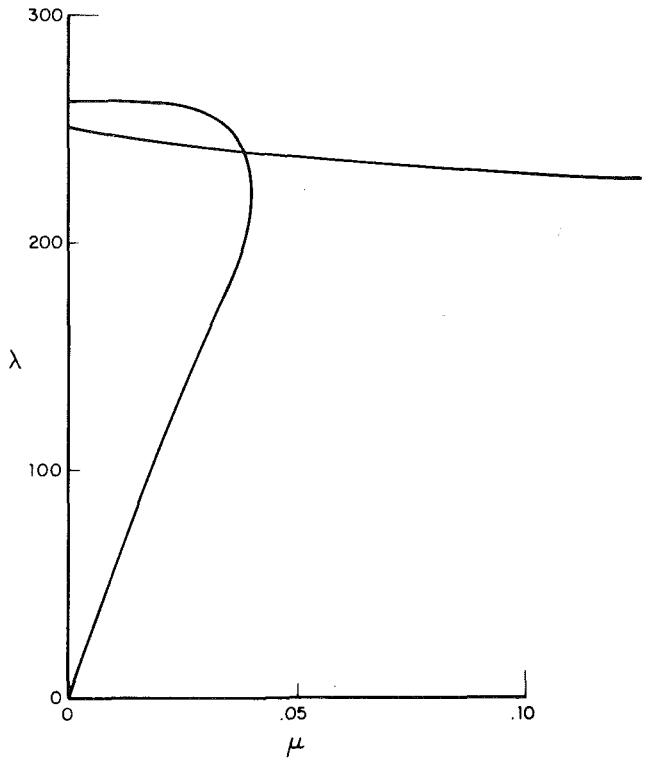

Fig. 6 Flutter dynamic pressure versus mass ratio $S_0/a = 0.75$, $M_1 = 1.1$

almost entirely in the first mode for shock locations upstream of the panel quarter-chord, but that the second mode content becomes increasingly important as the shock moves downstream. The shock is slightly destabilizing for positions upstream from the panel but generally stabilizing when the shock sits on the panel. In the two-mode approximation the plate is statically stable for shock positions downstream from the 80 percent chord point. With only one mode, divergence can occur (but only at increasingly larger dynamic pressures) for any shock position forward of the trailing edge.

In fact, though, the panel stability for these downstream shock locations is controlled by flutter, not divergence. Two mode flutter dynamic pressure variations with mass ratio and shock position are illustrated in Figs. 3–7. These boundaries generally consist of two distinct branches corresponding to the two possible flutter modes. When the shocks are at or very near the trailing edge (Figs. 3 and 4) both the first and second structural modes (individually) are unstable at low mass ratios (heavy plates), although the second mode becomes stable at higher mass ratios. In fact, though, the second mode is unimportant: the panel flutters in the first structural mode at all mass ratios. When the shock sits further upstream, however, (Figs. 5 and 6), the single-degree-of-freedom, first-mode flutter is lost. In this case the panel experiences single-degree-of-freedom, second-mode flutter at low mass ratios and coupled mode flutter at high mass ratios. The coupled mode instabilty (characterized by insensitivity to mass ratio), occurs at relatively high dynamic pressures. Shock positions yet further upstream (Fig. 7) the flutter boundaries remain much the same, buat the stability at high mass ratios becomes dominated by divergence. Only at very low mass ratios is flutter (in the second mode) of any importance.

The foregoing results are summarized in Figs. 8 and 9, which show the stability boundary (dynamic pressure and

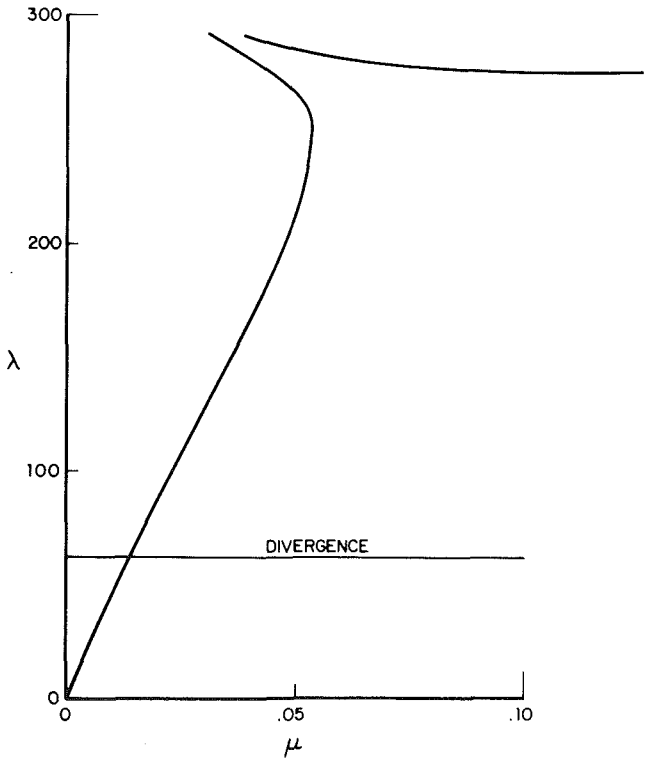

Fig. 7 Flutter dynamic pressure versus mass ratio $S_0/a = 0.65$, $M_1 = 1.1$

frequency) as a function of shock position at fixed mass ratio. It is apparent from Fig. 8, that by far the lowest critical dynamic pressures occur when the shock is downstream from the trailing edge and so has no effect whatsoever on the panel.

Downloaded 02 May 2010 to 171.66.16.246. Redistribution subject to ASME license or copyright; see http://www.asme.org/terms/Terms_Use.cfm

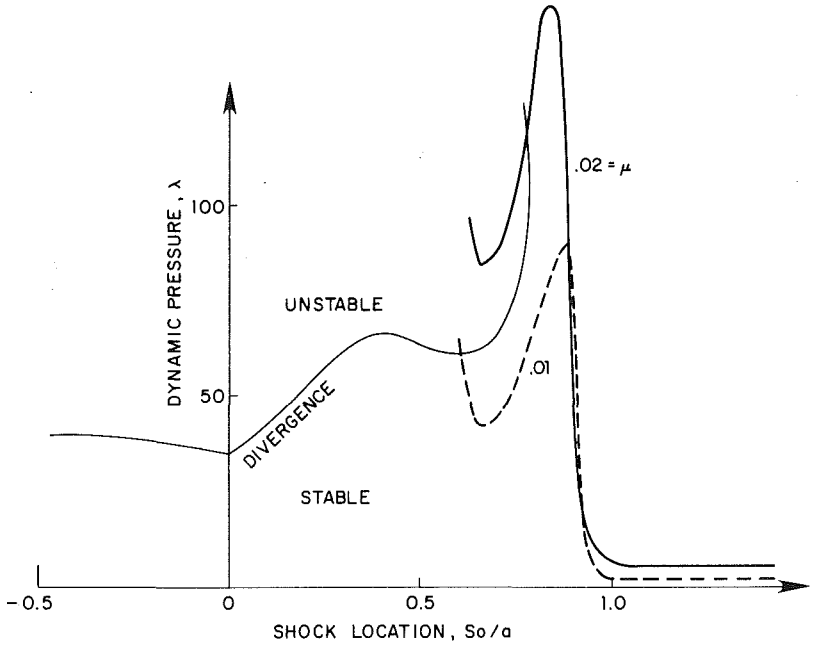

Fig. 8 Dependence of stability boundaries on shock location, $M_1 = 1.1$

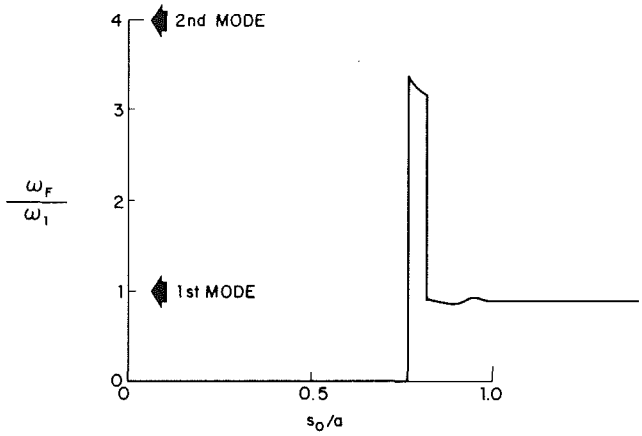

Fig. 9 Flutter frequency versus shock location, $\mu = 0.02$, $M_1 = 1.1$

Conclusions

The results obtained from the present simple model clearly demonstrate that the presence of a normal shock (and its associated mixed supersonic-subsonic flow regimes) does not have a deleterious effect on the aeroelastic stability of a flat panel. The shock does strongly influence the mode of instability in a manner depending primarily on the shock location relative to the panel. However, the critical dynamic pressure in all cases was higher than it would have been in a uniform supersonic flow at the preshock Mach number.

The numerical results are, of course, limited by the use of only two structural modes to represent the actual aeroelastic deformations. This truncation is probably not adequate in those cases (associated with moderately aft shock locations) in which second-mode or strongly coupled mode flutter occurred. However, the analysis shows a dramatic increase in critical dynamic pressure in these cases, which is undoubtedly correct qualitatively, if not quantitatively.

It should be noted, furthermore, that the present analysis neglects structural damping, which can have a significant effect (generally stabilizing at Mach numbers considered here). For example, the second-mode single-degree-of-freedom flutter observed here in some cases at low mass ratio may be eliminated entirely by a small amount of structural damping [4]. It would be surprising, though, if the addition of damping were to alter the general conclusions of the study regarding the influence of the shock on stability.

A final word of caution is in order. It is well known that the stability of a panel in uniform flow is strongly influenced (generally in a beneficial way) by preloading, as occurs, for example, where there is a finite static pressure differential across the plate. (This effect is important, for rigid supports, whenever the static deformation is larger than or comparable to the panel thickness.) For the shocked flow considered here, the plate is *necessarily* preloaded since the (uniform) undersurface pressure cannot simultaneously balance both the preshock and postshock upper-surface pressures. If the plate is pinned at either end to rigid supports, the nonuniform static load will generally induce large tensile stresses in the plate, which in turn will alter the plates apparent rigidity and, hence, its stability. This effect (which is clearly stabilizing) should, strictly speaking, be included in the analysis. Neglecting the effect, as we have done, is justifiable if we imagine the plate to be pinned to elastic supports with sufficient play to eliminate the induced tensile stresses.

References

1 Dowell, E. H., *Aeroelasticity of Plates and Shells*, Noordhoff, Leyden, 1975.

2 Jameson, A., "Iterative Solution of Transonic Flows Over Airfoils and Wings, Including Flows at Mach 1," *Comm. of Pure and App. Math.*, Vol. 27, May 1974, pp. 283–309.

3 Williams, M. H., "Unsteady Thin Airfoil Theory for Transonic Flow With Embedded Shocks," *AIAA Journal*, Vol. 18, No. 6, June 1980, pp. 615–624.

4 Dowell, E. H., and Voss, H. M., "Theoretical and Experimental Panel Flutter Studies in the Mach Number Range 1.0 to 5.0," *AIAA Journal*, Vol. 3, No. 12, 1965, pp. 2292–2304.

Downloaded 02 May 2010 to 171.66.16.246. Redistribution subject to ASME license or copyright; see http://www.asme.org/terms/Terms_Use.cfm

Magnetoelastic Plane Waves in Infinite Rotating Media

S. K. Roy Choudhuri
Department of Mathematics,
Burdwan University,
Burdwan, West Bengal, India

L. Debnath
Department of Mathematics,
East Carolina University,
Greenville, N.C. 27834

A study is made of the propagation of magnetoelastic plane waves in an electrically conducting, infinite elastic solid permeated by a primary uniform magnetic field when the entire medium rotates with a constant angular velocity. A more general dispersion relation is obtained to investigate the effects of rotation and the external magnetic field on the phase velocity of the waves. This analysis reveals that when the applied magnetic field has both longitudinal and transverse components, the coupled magnetoelastic waves are dispersive and damped in an infinitely conducting medium in contrast to the nonrotating medium where the coupled waves are dispersive, but undamped. In the case of finite conductivity, the waves are dispersive and undamped in the absence of the applied magnetic field. At low frequency ω, the phase velocity of the waves varies as $\omega^{1/2}$ for finite conductivity, and is independent of the external magnetic field and rotation; while in the nonrotating case with low frequency (when the applied magnetic field has either longitudinal or transverse components) the phase speed is less than that in the rotating medium and is found to depend on the applied magnetic field. Also in both rotating and nonrotating cases, the phase velocity becomes very small for finitely conducting material with a very high magnetic permeability.

1 Introduction

The study of the propagation of elastic waves in a nonrotating electrically conducting medium under the action of a magnetic field was made by several authors including Knopoff [1], Kaliski and Petykiewics [2], and Dunkin and Eringen [3]. In his recent books Parkus [4, 5] has given all of the major general information and recent developments of magnetoelasticity and magnetothermoelasticity in nonrotating elastic media. Schoenberg and Censor [6] have investigated the propagation of elastic plane waves in a uniformly rotating medium and obtained interesting results concerning energy flux, slowness surfaces, reflected waves, and the generalized Rayleigh waves. They have shown that the rotation causes the elastic waves to be dispersive and anisotropic. Their study also included some discussion on the free-surface phenomenon in a rotating half space.

It seems from the preceding discussion that little attention has been given to the propagation of magnetoelastic plane waves in a rotating medium in the presence of the external magnetic field. In view of the fact that most large bodies like the earth, the moon, and other planets have an angular velocity, it is important to consider the propagation of magnetoelastic plane waves in an electrically conducting, rotating elastic medium under the action of the external magnetic field. It is very likely that rotation will have some important effects on the propagation of the magnetoelastic waves.

The main objective of the present study is to investigate magnetoelastic plane waves in an electrically conducting, infinite elastic solid permeated by a primary magnetic field when the entire medium rotates with a uniform angular velocity. Special attention is given to the interaction between the electromagnetic field and rotation and their effects on the principal features of the elastic waves.

2 Formulation of the Problem and the Basic Equations

We consider an infinite, isotropic, electrically conducting, elastic solid permeated by a primary magnetic field $\mathbf{B}_0 = (B_1, B_2, B_3)$. The elastic solid is characterized by the density ρ, Lamé's constants λ, μ, and is uniformly rotating with an angular velocity $\Omega = \Omega\mathbf{w}$, where $\mathbf{w}$ is the unit vector representing the direction of the axis of rotation.

The displacement equation of motion in the rotating frame of reference is

$$\rho[\ddot{\mathbf{u}} + \Omega \times (\Omega \times \mathbf{u}) + 2\Omega \times \dot{\mathbf{u}}] = (\lambda + \mu)\nabla(\nabla \cdot \mathbf{u}) + \mu\nabla^2\mathbf{u} + \mathbf{J} \times \mathbf{B}, \tag{2.1}$$

where the dot denotes differentiation with respect to time t, $\mathbf{u}$ is the displacement vector, $\mathbf{J}$ is the current density, and $\mathbf{B}$ is the total magnetic field so that $\mathbf{B} = \mathbf{B}_0 + \mathbf{b}$, $\mathbf{b} \equiv (b_x, b_y, b_z)$ is the perturbed magnetic field.

The equation of motion (2.1) has two additional terms: centripetal acceleration, $\Omega \times (\Omega \times \mathbf{r})$ due to time-varying motions only and the Coriolis acceleration, $2\Omega \times \dot{\mathbf{u}}$ where $\mathbf{u}$ is the dynamic displacement vector measured from a steady-

Contributed by the Applied Mechanics Division for publication in the JOURNAL OF APPLIED MECHANICS.

Discussion on this paper should be addressed to the Editorial Department, ASME, United Engineering Center, 345 East 47th Street, New York, N.Y. 10017, and will be accepted until two months after final publication of the paper itself in the JOURNAL OF APPLIED MECHANICS. Manuscript received by ASME Applied Mechanics Division, September, 1982; final revision, December, 1982.

Copyright © 1983 by ASME
Downloaded 02 May 2010 to 171.66.16.246. Redistribution subject to ASME license or copyright; see http://www.asme.org/terms/Terms_Use.cfm

state deformed position and the deformation is assumed to be small. These two terms do not appear in the equation of motion for the nonrotating media. In addition, the Lorentz force term $\mathbf{J} \times \mathbf{B}$ is included in the displacement equation of motion to incorporate the electromagnetic field effects. As we look for the time-varying dynamic solutions, the time-independent part of the centripetal acceleration $\boldsymbol{\Omega} \times (\boldsymbol{\Omega} \times \mathbf{u})$ as well as all body forces will be neglected. The effect of time-independent centripetal acceleration should in effect make the elastic medium anisotropic. We shall take into account the time-independent part of the electromagnetic body force. Finally, the study of magnetoelastic plane waves will be made within the scope of the linearized theory. We assume that $\mathbf{u}$, $\mathbf{b}$, the second-order terms on the right-hand side of (2.1) involving $\mathbf{u}$, $\mathbf{b}$ and their derivatives are small in order to justify linearization.

In view of the fact that frequencies associated with the vibrations and mechanical waves are much smaller than the frequency of the electromagnetic waves with the same wavelength, the electromagnetic fields may be regarded as quasi-steady. The electromagnetic fields are governed by the Maxwell equations with the displacement current and charge density neglected [10]:

$$\operatorname{curl} \mathbf{H} = \mathbf{J}, \quad \operatorname{curl} \mathbf{E} = -\frac{\partial \mathbf{B}}{\partial t}, \quad \operatorname{div} \mathbf{B} = 0, \tag{2.2a,b,c}$$

where $\mathbf{B} = \mu_e \mathbf{H}$, μ_e is the magnetic permeability and $\mathbf{E}$ is the electric field.

The generalized Ohm's law is

$$\mathbf{J} = \sigma\left[\mathbf{E} + \left(\frac{\partial \mathbf{u}}{\partial t} + \boldsymbol{\Omega} \times \mathbf{u}\right) \times \mathbf{B}\right], \tag{2.3}$$

where the time-independent part of $\boldsymbol{\Omega} \times \mathbf{u}$ is neglected, σ is the electrical conductivity, and $\partial \mathbf{u}/\partial t$ is the particle velocity of the medium.

3 Plane Wave Solutions and Dispersion Relation

We consider the propagation of plane waves in the conducting rotating elastic medium in the x-direction so that all field quantities $\mathbf{u}$, $\mathbf{J}$, $\mathbf{b}$, are proportional to $\exp[i(kx - \omega t)]$ where k is the complex wave number and ω is the real wave frequency so that $\omega/Re(k)$ represents the phase velocity of the waves. Thus we can write all field quantities in the form

$$\mathbf{u} = (p,q,r) = (p_0,q_0,r_0)\exp[i(kx-\omega t)], \tag{3.1}$$

$$\mathbf{J} = (J_x,J_y,J_z) = (J_1,J_2,J_3)\exp[i(kx-\omega t)], \tag{3.2}$$

$$\mathbf{b} = (b_x,b_y,b_z) = (b_1,b_2,b_3)\exp[i(kx-\omega t)], \tag{3.3}$$

$$\mathbf{E} = (E_x,E_y,E_z) \quad \text{and} \quad \boldsymbol{\Omega} = (\Omega_1,\Omega_2,\Omega_3), \tag{3.4a,b}$$

where p_0, q_0, r_0; J_1, J_2, J_3; and Ω_1, Ω_2, Ω_3 are all constants.

It follows from (2.2c) that div $\mathbf{b} = 0$ which implies that $b_x = 0$, since initially $\mathbf{b} = 0$. Also, it follows from (2.2a) that $\mu_e \mathbf{J} = \operatorname{curl} \mathbf{b}$ so that

$$\mathbf{J} = \left(0, -\frac{ik}{\mu_e} b_z, \frac{ik}{\mu_e} b_y\right) \tag{3.5}$$

and

$$\mathbf{J} \times \mathbf{B} \simeq \mathbf{J} \times \mathbf{B}_0 = \left[-\frac{ik}{\mu_e}(b_z B_3 + b_y B_2), \frac{ik}{\mu_e} b_y B_1, \frac{ik}{\mu_e} b_z B_1\right]. \tag{3.6}$$

The term $\mathbf{J} \times \mathbf{B}$ in (2.1) will be replaced with $\mathbf{J} \times \mathbf{B}_0$ given by (3.6).

The equation $\operatorname{curl} \mathbf{E} = -\dfrac{\partial \mathbf{b}}{\partial t}$ implies that

$$\mathbf{E} = \left(E_x, \frac{\omega}{k} b_z, -\frac{\omega}{k} b_y\right). \tag{3.7}$$

Making use of (3.1) and (3.7), and neglecting the product terms, the generalized Ohm's law with $\mathbf{B}_0$ in place of $\mathbf{B}$ gives

$$J_x = \sigma[E_x - i\omega(qB_3 - rB_2) + B_3(p\Omega_3 - r\Omega_1) - B_2(q\Omega_1 - p\Omega_2)], \tag{3.8}$$

$$J_y = \sigma\left[\frac{\omega}{k} b_z - i\omega(rB_1 - pB_3)\right], \tag{3.9}$$

$$J_z = \sigma\left[-\frac{\omega}{k} b_y - i\omega(pB_2 - qB_1) + B_2(\Omega_2 r - q\Omega_3) - B_1(p\Omega_3 - r\Omega_1)\right]. \tag{3.10}$$

Elimination of $\mathbf{J}$ from (3.5) and (3.8)-(3.10) gives

$$\sigma[E_x - i\omega(qB_3 - rB_2) + B_3(p\Omega_3 - r\Omega_1) - B_2(q\Omega_1 - p\Omega_2)] = 0 \tag{3.11}$$

$$\sigma\left[\frac{\omega}{k} b_z - i\omega(rB_1 - pB_3) + B_1(q\Omega_1 - p\Omega_2) - B_2(\Omega_2 r - q\Omega_3)\right] = -\frac{ik}{\mu_e} b_z \tag{3.12}$$

$$\sigma\left[-\frac{\omega}{k} b_y - i\omega(pB_2 - qB_1) + B_2(r\Omega_2 - q\Omega_3) - B_1(p\Omega_3 - r\Omega_1)\right] = \frac{ik}{\mu_e} b_y. \tag{3.13}$$

The equation (3.11), in turn, determines E_x.

We next substitute for p, q, r from (3.1) into the basic equation (2.1) with $\mathbf{J} \times \mathbf{B}$ given by (3.6) to obtain the following equations for p_0, q_0 and r_0

$$p_0[\rho(\Omega_1{}^2 - \Omega^2 - \omega^2) + (\lambda + 2\mu)k^2] + q_0[\rho(2i\,\omega\Omega_3 + \Omega_1\Omega_2)] + r_0[\rho(\Omega_1\Omega_3 - 2i\,\omega\Omega_2)] + \frac{ik}{\mu_e}(B_3 b_3 + B_2 b_2) = 0, \tag{3.14}$$

$$p_0[\rho(\Omega_1\Omega_2 - 2i\,\omega\Omega_3)] + q_0[\rho(\Omega_2{}^2 - \Omega^2 - \omega^2) + \mu k^2] + r_0[\rho(\Omega_2\Omega_3 + 2i\,\omega\Omega_1)] - \frac{ik}{\mu_e} b_2 B_1 = 0, \tag{3.15}$$

$$p_0[\rho(\Omega_1\Omega_3 + 2i\,\omega\Omega_2)] + q_0[\rho(\Omega_2\Omega_3 - 2i\,\omega\Omega_1)] + r_0[\rho(\Omega_3{}^2 - \Omega^2 - \omega^2) + \mu k^2] - \frac{ik}{\mu_e} B_1 b_3 = 0. \tag{3.16}$$

We also rewrite (3.12) and (3.13) in order to express them in terms of p_0, q_0, and r_0 as

$$p_0[\rho(i\omega B_3 - B_1\Omega_2)] + q_0[\sigma(B_1\Omega_1 + B_3\Omega_3)] + r_0[-\sigma(i\omega B_1 + B_3\Omega_2)] + b_3\left[\frac{ik}{\mu_e} + \frac{\sigma\omega}{k}\right] = 0, \tag{3.17}$$

$$p_0[-\sigma(i\omega B_2 + B_1\Omega_3)] + q_0[\sigma(i\omega B_1 - B_2\Omega_3)] + r_0[\sigma(B_2\Omega_2 + B_1\Omega_1)] - b_2\left[\frac{ik}{\mu_e} + \frac{\sigma\omega}{k}\right] = 0. \tag{3.18}$$

Equations (3.14)-(3.18) constitute a system of five equations with five unknowns p_0, q_0, r_0, and the perturbed quantities b_2 and b_3.

Since $\mathbf{b} = (0, b_y, b_z)$ and $\mathbf{b}$-field is normal to the x-axis, we then choose the y-axis and the z-axis such that $\mathbf{b}$-field is along the y-axis. Thus $b_1 = b_3 = 0$ and $b_2 \neq 0$. Also, invoking an additional assumption, $\Omega_1 = \Omega_2 = 0$ and $\Omega_3 = \Omega \neq 0$, equations (3.14)-(3.18) take the form

$$p_0[-\rho(\omega^2 + \Omega^2) + (\lambda + 2\mu)k^2] + 2i\omega\rho\Omega q_0 + \frac{ik}{\mu_e} B_2 b_2 = 0, \tag{3.19}$$

Downloaded 02 May 2010 to 171.66.16.246. Redistribution subject to ASME license or copyright; see http://www.asme.org/terms/Terms_Use.cfm

$$p_0[-2i\omega\rho\Omega]+q_0[-\rho(\Omega^2+\omega^2)+\mu k^2]-\frac{ik}{\mu_e}B_1 b_2=0, \tag{3.20}$$

$$r_0(-\rho\omega^2+\mu k^2)=0, \tag{3.21}$$

$$p_0 i\omega\sigma B_3+q_0\sigma\Omega B_3-r_0\sigma i\omega B_1=0, \tag{3.22}$$

$$p_0[-\sigma(i\omega B_2+B_1\Omega)]+q_0[\sigma(i\omega B_1-B_2\Omega)]-b_2\left[\frac{ik}{\mu_e}+\frac{\sigma\omega}{k}\right]=0. \tag{3.23}$$

In view of the inherent rotation of the earth, the additional assumption has important geophysical implications. It follows from (3.21) that $r_0 \equiv 0$ provided $\mu k^2 - \rho\omega^2 \neq 0$ and then (3.22) implies that $B_3 \equiv 0$. Thus, if the applied magnetic field $\mathbf{B}_0 = (B_1, B_2, 0)$ and the perturbed magnetic field $\mathbf{b} = (0, b_2, 0)$, then equations (3.21) and (3.22) are satisfied.

This leads to three homogeneous equations (3.19), (3.20), and (3.23) with three quantities p_0, q_0 and b_2. Eliminating these quantities, we obtain a dispersion equation in the following form involving a determinant:

$$\begin{vmatrix} -\rho(\omega^2+\Omega^2)+(\lambda+2\mu)k^2 & 2i\omega\rho\Omega & \frac{ik\,B_2}{\mu_e} \\ -2i\omega\rho\Omega & \mu k^2-\rho(\omega^2+\Omega^2) & -\frac{ik\,B_1}{\mu_e} \\ \sigma(\Omega B_1+i\omega B_2 & \sigma(\Omega B_2-i\omega B_1) & \left(\frac{ik}{\mu_e}+\frac{\sigma\omega}{k}\right) \end{vmatrix}=0. \tag{3.24}$$

It follows from the dispersion equation that the significant effects of the rotation on the phase velocity, $Re\ (\omega/k)$ are reflected through the terms involving Ω.

In a nonrotating medium ($\Omega=0$) without thermal effects, the dispersion equation (3.24) reduces to that of Wilson [7]. Also, Paria's [8] results follow from the present analysis when $\Omega = 0$, $B_1 = 0$. Purushothama [9] investigated the propagation of magnetothermoelastic plane waves in the presence of uniform thermal and magnetic field. Although he extended the works of both Wilson and Paria, the results of the present study are consistent with his results in a nonrotating case with special choices of the angle of orientation of the magnetic field and the thermal effects neglected. However, the dispersion relation (3.24) gives a fairly general result in the theory of magnetoelastic plane waves.

Introducing a new quantity $\sigma_i = \omega/c_i$, $i = 1, 2$; the dispersion equation (3.24) can be expressed in the following form

$$\begin{vmatrix} k^2-\sigma_1{}^2-\frac{\Omega^2}{c_1{}^2} & \frac{2i\omega\Omega}{c_1{}^2} & \frac{ik\,R_H}{B_2} \\ -\frac{2i\omega\Omega}{c_2{}^2} & k^2-\sigma_2{}^2-\frac{\Omega^2}{c_2{}^2} & -\frac{ik\,R_L}{B_1} \\ k\left(iB_2+\frac{B_1\Omega}{\omega}\right) & k\left(-iB_1+\frac{B_2\Omega}{\omega}\right) & 1+i\nu k^2 \end{vmatrix}=0, \tag{3.25}$$

where the nondimensional pressure numbers R_H and R_L are defined [10] by

$$(R_H, R_L)=\frac{1}{\rho\mu_e}\left(\frac{B_2{}^2}{c_1{}^2}, \frac{B_1{}^2}{c_2{}^2}\right), \tag{3.26a,b}$$

$c_1=\sqrt{\dfrac{\lambda+2\mu}{\rho}}$ is the dilational wave velocity,

$c_2=\sqrt{\dfrac{\mu}{\rho}}$ is the shear wave velocity,

$\nu=(\mu_e\sigma\omega)^{-1}=\dfrac{\nu_H}{\omega}$, and $\nu_H=(\sigma\mu_e)^{-1}$ is the magnetic viscosity.

Expanding the determinant, we obtain the equation of degree three in k^2 as

$$\begin{aligned}(1+i\nu k^2)&\left[\left(k^2-\sigma_1{}^2-\frac{\Omega^2}{c_1{}^2}\right)\left(k^2-\sigma_2{}^2-\frac{\Omega^2}{c_2{}^2}\right)-\frac{4\omega^2\Omega^2}{c_1{}^2c_2{}^2}\right]\\ &+k^2\left(k^2-\sigma_1{}^2-\frac{\Omega^2}{c_1{}^2}\right)\left(R_L+\frac{i\,R_L\,B_2}{B_1}\,\frac{\Omega}{\omega}\right)\\ &+\frac{2\omega\Omega}{c_1{}^2}\left(\frac{R_L\,B_2\,i}{B_1}+\frac{\Omega\,R_L}{\omega}\right)-\frac{2k^2R_H\omega\Omega}{B_2c_2{}^2}\left(iB_1-\frac{B_2\Omega}{\omega}\right)\\ &-\frac{ik^2R_H}{B_2}\left(k^2-\sigma_2{}^2-\frac{\Omega^2}{c_2{}^2}\right)\left(iB_2+\frac{\Omega B_1}{\omega}\right)=0.\end{aligned} \tag{3.27}$$

This represents a general dispersion relation, and shows that if the primary magnetic field has both longitudinal and transverse components, then the displacement fields p, q, and the perturbed magnetic field b_2 are linked together. It also follows from (3.27) that the significant effects of rotation on the phase velocity of the waves are reflected through the terms involving Ω. The coupled magnetoelastic waves characterized by the dispersion relation are damped and dispersive.

4 Infinite Conductivity

In this case, $\sigma\to\infty$ so that ν_H and ν tend to zero. The corresponding dispersion relation can be obtained from (3.27) and has the form

$$\begin{aligned}k^4&\left[1+R_L+R_H+\frac{i\Omega}{\omega}\left(\frac{R_LB_2}{B_1}-\frac{R_HB_1}{B_2}\right)\right]\\ &-k^2\left[\left(\sigma_1{}^2+\frac{\Omega^2}{c_1{}^2}\right)\left(1+R_L+\frac{i\,R_LB_2}{B_1}\cdot\frac{\Omega}{\omega}\right)\right.\\ &+\left(\sigma_2{}^2+\frac{\Omega^2}{c_2{}^2}\right)\left\{1-\frac{i\,R_H}{B_2}\left(iB_2+\frac{B_1\Omega}{\omega}\right)\right\}\\ &-\frac{2\omega\Omega}{c_1{}^2}\left(\frac{i\,R_LB_2}{B_1}+\frac{\Omega\,R_L}{\omega}\right)\\ &\left.+\frac{2\omega\Omega}{c_2{}^2}\left(\frac{i\,B_1R_H}{B_2}-\frac{\Omega\,R_H}{\omega}\right)\right]+\left(\sigma_1{}^2+\frac{\Omega^2}{c_1{}^2}\right)\left(\sigma_2{}^2+\frac{\Omega^2}{c_2{}^2}\right)\\ &-\frac{4\omega^2\Omega^2}{c_1{}^2c_2{}^2}=0.\end{aligned} \tag{4.1}$$

Downloaded 02 May 2010 to 171.66.16.246. Redistribution subject to ASME license or copyright; see http://www.asme.org/terms/Terms_Use.cfm

Thus, if the applied primary magnetic field has both longitudinal and transverse components, then the longitudinal and transverse components of the displacement field are coupled, and modified by both rotation and electromagnetic field. Both the waves are dispersive and damped. In the case of nonrotating medium ($\Omega=0$), result (4.1) reduces to that of Nowacki [5], and all conclusions of Nowacki can readily be obtained from our analysis.

If the primary magnetic field is absent, that is, if $B_1 \equiv B_2 \equiv 0$ so that $R_L \equiv R_H \equiv 0$, the dispersion relation (3.27) simplifies to

$$k^4 - k^2\left[\left(\sigma_1^2 + \frac{\Omega^2}{c_1^2}\right) + \left(\sigma_2^2 + \frac{\Omega^2}{c_2^2}\right)\right] + \left(\sigma_1^2 + \frac{\Omega^2}{c_1^2}\right)\left(\sigma_2^2 + \frac{\Omega^2}{c_2^2}\right) - \frac{4\omega^2\Omega^2}{c_1^2 c_2^2} = 0. \quad (4.2)$$

The roots of this equation are

$$2k_{1,2}^2 = \sigma_1^2 + \sigma_2^2 + \Omega^2\left(\frac{1}{c_1^2} + \frac{1}{c_2^2}\right) \pm \sqrt{D}, \quad (4.3a,b)$$

$$D = \left[\left(\sigma_1^2 + \frac{\Omega^2}{c_1^2}\right) - \left(\sigma_2^2 + \frac{\Omega^2}{c_2^2}\right)\right]^2 + \frac{16\omega^2\Omega^2}{c_1^2 c_2^2} > 0. \quad (4.4)$$

Also, since $\sigma_1^2 + \sigma_2^2 + \Omega^2\left(\frac{1}{c_1^2} + \frac{1}{c_2^2}\right) > \sqrt{D}$,

the roots are real and so the waves are dispersive, but undamped.

In the nonrotating medium, the equation (4.2) factorizes into two parts:

$$(k^2 - \sigma_1^2)(k^2 - \sigma_2^2) = 0. \quad (4.5)$$

This corresponds to both the dilatational and the transverse elastic waves. However, for the rotating medium ($\Omega \neq 0$), the roots of (4.2) correspond to the dilatational and transverse elastic waves modified by rotation.

If, on the other hand, the primary magnetic field has a nonzero transverse component ($R_H \neq 0$, $R_L = 0$), then the dispersion relation (4.1) simplifies into

$$k^4(1+R_H) - k^2\left[\sigma_1^2 + (1+R_H)\sigma_2^2 + \frac{\Omega^2}{c_1^2} + (1-R_H)\frac{\Omega^2}{c_2^2}\right] + \frac{(\omega^2-\Omega^2)^2}{c_1^2 c_2^2} = 0. \quad (4.6)$$

For the case of weak electromagnetic field ($0 < R_H << 1$), the quadratic in k^2 has either two positive roots or two complex roots. This means that the magnetoelastic waves are dispersive, but may or may not be damped depending on the rotation and the applied magnetic field.

Again, in the nonrotating case, the dispersion equation has the form

$$(k^2 - \sigma_2^2)[(1+R_H)k^2 - \sigma_1^2] = 0. \quad (4.7)$$

This corresponds to a transverse elastic wave propagating with the phase velocity c_2 independent of the electromagnetic field, and a longitudinal magnetoelastic wave traveling with the phase speed $c_1\sqrt{1+R_H}$. Since $R_H > 0$, this phase speed increases with increasing R_H which implies an increase in solidity of the elastic material.

If the applied magnetic field has a longitudinal component only, then $R_H = 0$ and $R_L \neq 0$. The dispersion equation (4.1) in this case reduces to

$$k^4(1+R_L) - k^2\left[\sigma_2^2 + \frac{\Omega^2}{c_2^2} + (1+R_L)\sigma_1^2 + (1-R_L)\frac{\Omega^2}{c_1^2}\right] + \frac{(\omega^2-\Omega^2)^2}{c_1^2 c_2^2} = 0. \quad (4.8)$$

For weak electromagnetic field, $0 < R_L << 1$ and so conclusion similar to that of the foregoing case, $0 < R_H << 1$, can be drawn.

In the nonrotating situation, the equation (4.8) becomes

$$(k^2 - \sigma_1^2)\{(1+R_L)k^2 - \sigma_2^2\} = 0. \quad (4.9)$$

This leads to the longitudinal elastic wave propagating with the phase velocity c_1 and to the transverse magnetoelastic wave traveling with the phase speed $c_2\sqrt{1+R_L}$.

If the initially applied magnetic field has both longitudinal and transverse components ($R_H \neq 0$ and $R_L \neq 0$), then the longitudinal and the transverse waves are coupled. These waves are modified by the electromagnetic field and rotation. Since the roots k_1^2 and k_2^2 of (4.1) are complex, the waves are dispersive and damped. The dispersion equation (4.1) for the nonrotating case has the form

$$k^4(1+R_H+R_L) - k^2\{\sigma_1^2(1+R_L) + \sigma_2^2(1+R_H)\} + k_1^2 k_2^2 = 0, \quad (4.10)$$

with the roots

$$2k_{1,2}^2 = (1+R_L+R_H)^{-1}[\sigma_1^2(1+R_L) + \sigma_2^2(1+R_H)] \pm \sqrt{D}], \quad (4.11a,b)$$

where

$$D = \{\sigma_1^2(1+R_L) - \sigma_2^2(1+R_H)\}^2 + 4\sigma_1^2\sigma_2^2(R_L+R_H) > 0.$$

Since $\sigma_1^2(1+R_L) + \sigma_2^2(1+R_H) > \sqrt{D}$, the roots k_1 and k_2 are real, and therefore, the longitudinal and the transverse waves are dispersive, but undamped. This shows a striking contrast between the nature of the waves in the rotating and the nonrotating media.

5 Finite Conductivity

The dispersion relation for the case of finite conductivity is given by (3.27) and corresponds to the coupled waves. In the absence of the magnetic field ($R_L = R_H = 0$), the equation (3.27) assumes the form

$$(1+i\nu k^2)\left[\left(k^2 - \sigma_1^2 - \frac{\Omega^2}{c_1^2}\right)\left(k^2 - \sigma_2^2 - \frac{\Omega^2}{c_2^2}\right) - \frac{4\omega^2\Omega^2}{c_1^2 c_2^2}\right] = 0. \quad (5.1)$$

The first factor of (5.1) represents quasi-static oscillations of the electromagnetic field, but it is not coupled with the displacement field. The second factor leads to coupled longitudinal and transverse waves with the phase velocities modified by the rotation of the medium. Since the roots of (5.1) corresponding to the second factor are real, the waves are dispersive and undamped.

In the nonrotating case, equation (3.27) reduces to

$$(1+i\nu k^2)(k^2 - \sigma_1^2)(k^2 - \sigma_2^2) + k^2 R_L(k^2 - \sigma_1^2) + k^2 R_H(k^2 - \sigma_2^2) = 0. \quad (5.2)$$

This corresponds to three coupled waves that are dispersive and damped in nature.

If the applied magnetic field has a transverse component ($R_H \neq 0$ and $R_L = 0$), then (5.2) takes the form

$$(k^2 - \sigma_2^2)[\nu k^4 - k^2\{\nu\sigma_1^2 + i(1+R_H)\} + i\sigma_1^2] = 0. \quad (5.3)$$

The first factor corresponds to the elastic transverse wave, while the second factor leads to the coupled waves with an interaction between the longitudinal displacement field and the induced magnetic field. Thus the coupled waves are dispersive and damped.

To discuss the waves with small frequency, we replace ν with ν_H/ω in the second factor of (5.3) to obtain

Downloaded 02 May 2010 to 171.66.16.246. Redistribution subject to ASME license or copyright; see http://www.asme.org/terms/Terms_Use.cfm

$$\nu_H k^4 - k^2\left\{\omega^2 \cdot \frac{\nu_H}{c_1^{\,2}} + i\omega(1+R_H)\right\} + \frac{i\omega^3}{c_1^{\,2}} = 0, \qquad (5.4)$$

and set $k^2 = i\,a\omega + 0(\omega^2)$ where a is an unknown constant, and $k = 0$ when $\omega = 0$.

To determine a, we next substitute the value of k^2 into (5.4) and ignore the terms of $0(\omega^3)$. This leads to the value of $a = (1+R_H)\,\nu_H^{-1}$,

$$k \simeq \left\{\frac{(1+R_H)\,\mu_e\sigma\omega}{2}\right\}^{\frac{1}{2}}(1+i), \qquad (5.5)$$

and the phase velocity c_{p1} as

$$c_{p1} = \left\{\frac{2\omega}{(1+R_H)\,\sigma\mu_e}\right\}^{\frac{1}{2}}. \qquad (5.6)$$

This implies that the phase speed varies as $\omega^{1/2}$ and $\mu_e^{-1/2}$ so that c_{p1} becomes very small in a material with high magnetic permeability. For a weak electromagnetic field, the phase speed becomes

$$c_{p1} = \left(\frac{2\omega}{\sigma\mu_e}\right)^{\frac{1}{2}}\left(1 - \frac{1}{2}R_H\right). \qquad (5.7)$$

On the other hand, if the applied magnetic field has only a longitudinal component ($R_L \neq 0$, $R_H = 0$) then the dispersion equation is

$$(k^2 - \sigma_1^{\,2})[\nu k^4 - k^2\{\nu\sigma_2^{\,2} + i(1+R_L)\} + i\sigma_2^{\,2}] = 0, \qquad (5.8)$$

leading to pure longitudinal elastic wave, and the interaction of the transverse displacement field and the induced magnetic field produces coupled waves. The phase velocity of the coupled waves is

$$c_{p2} \simeq \left(\frac{2\omega}{\sigma\mu_e}\right)^{\frac{1}{2}}\left(1 - \frac{1}{2}R_L\right) \qquad (5.9)$$

for the case of a low frequency and weak electromagnetic field.

Finally, in the rotating medium with finite electrical conductivity, the dispersion equation (3.27) can be written as

$$\begin{aligned} &i\,\nu_H k^6 + k^4\left[(1+R_L+R_H)\,\omega - i\,\nu_H(\omega^2+\Omega^2)\left(\frac{1}{c_1^{\,2}} + \frac{1}{c_2^{\,2}}\right)\right. \\ &\quad \left. + i\,R_L\Omega\left(\frac{B_2}{B_1}\right) - i\,R_H\Omega\left(\frac{B_1}{B_2}\right)\right] \\ &\quad + k^2\left[-\omega(\omega^2+\Omega^2)\left(\frac{1}{c_1^{\,2}} + \frac{1}{c_2^{\,2}}\right)\right. \\ &\quad + \frac{i\,\nu_H}{c_1^{\,2}c_2^{\,2}}(\omega^4 + \Omega^4 - 2\omega^2\Omega^2) \\ &\quad - \frac{R_L}{c_1^{\,2}}(\omega^2+\Omega^2)\left(\omega + i\Omega\frac{B_2}{B_1}\right) \\ &\quad + \frac{2\omega\Omega\,R_L}{c_1^{\,2}}\left(\frac{i\omega\,B_2}{B_1} + \Omega\right) - \frac{2\omega\,R_H\Omega}{B_2c_2^{\,2}}(i\omega\,B_1 - B_2\Omega) \\ &\quad \left. + \frac{i\,R_H}{B_2c_2^{\,2}}(\omega^2+\Omega^2)(iB_2\omega + B_1\Omega)\right] \\ &\quad + \frac{\omega}{c_1^{\,2}c_2^{\,2}}(\omega^4 - 2\omega^2\Omega^2 + \Omega^4) = 0. \end{aligned} \qquad (5.10)$$

This shows the interaction between the displacement and the induced magnetic fields, and corresponds to coupled magnetoelastic waves which are dispersive and damped.

For the case of small frequency, we set $k^2 = ib\omega + 0(\omega^2)$ where b is a constant to be determined by replacing k^2 with $ib\omega$ in (5.10). This leads to the values for b and k as

$$b \simeq \frac{1}{\nu_H} \quad \text{and} \quad k \simeq (1+i)\left(\frac{\sigma\omega\mu_e}{2}\right)^{\frac{1}{2}}, \qquad (5.11a,b)$$

so that the phase velocity is

$$c_{p3} \simeq \left(\frac{2\omega}{\sigma\mu_e}\right)^{\frac{1}{2}}. \qquad (5.12)$$

This means that the phase speed is independent of both rotation and the initial magnetic field, and becomes very small for high magnetic permeability. It is interesting to note $c_{pr} < c_{p3}$ where $r = 1, 2$.

6 Conclusions

A general dispersion equation for the magnetoelastic plane waves is derived to explain the important effects of rotation and external magnetic field on the waves. Special attention has been given to special cases of the dispersion equation in various problems of physical interest. The phase velocities of the waves are obtained in explicit form with physical significance. The nature of the waves is investigated in Sections 4–6.

When the applied magnetic field has longitudinal and transverse components, the coupled waves are found to be dispersive and damped in an infinitely conductive medium. This is in contrast to the result in a nonrotating medium where the waves are coupled, dispersive, and undamped. For the case of finite conductivity, the waves are dispersive and undamped in the absence of a magnetic field. At low frequency ω, the phase velocity of the waves varies as $\omega^{1/2}$ for finite conductivity, and is independent of the external magnetic field and rotation; whereas in the nonrotating medium with low frequency (when the applied magnetic field has either longitudinal or transverse components) the phase speed of the waves is less than that in the rotating medium, and is seen to depend on the applied magnetic field. Also, in rotating and nonrotating cases, the wave velocity becomes very small for finitely conducting medium with a very high magnetic permeability.

Finally, it has also been shown that results of the present analysis are in excellent agreement with those obtained by several authors [1, 7–9] in a nonrotating conducting or nonconducting elastic medium.

Acknowledgment

This work was partially supported by a research grant from East Carolina University. The authors express their grateful thanks to the referees for suggesting some improvements in the paper.

References

1 Knopoff, L., "The Interaction Between Elastic Wave Motions and a Magnetic Field in Electrical Conductors," *J. Geophys. Res.*, Vol. 60, 1955, pp. 441–453.

2 Kaliski, S., and Petykiewics, T., "Dynamical Equations of Motions Coupled With the Field of Temperature and Resolving Functions For Elastic and Viscoelastic Anisotropic Bodies in the Magnetic Field," *Proc. Vibration Problems*, Vol. 1, 1960, pp. 3–15.

3 Dunkin, J. W., and Eringen, A. C., "On the Propagation of Waves in an Electromagnetic Elastic Solid," *Int. J. Eng. Sci.*, Vol. 1, 1963, pp. 461–473.

4 Parkus, H., *Magneto-Thermo-Elasticity*, Springer-Verlag, 1972.

5 Parkus, H., "Electromagnetic Interactions in Elastic Solids," Springer-Verlag, 1979 (W, Nowacki, On Magneto-Elasticity, p. 179).

6 Schoenberg, M., and Censor, D., "Elastic Waves in Rotating Media," *Quart. Appl. Math.*, Vol. 31, 1973, pp. 115–125.

7 Wilson, A. J., "The Propagation of Magneto-Thermo-Elastic Plane Waves," *Proc. Camb. Phil. Soc.*, Vol. 59, 1963, pp. 483–488.

8 Paria, G., "On Magneto-Thermo-Elastic Plane Waves," *Proc. Camb. Phil. Soc.*, Vol. 58, 1962, pp. 527–531.

9 Purushothama, C. M., "Magneto-Thermo-Elastic Plane Waves," *Proc. Camb. Phil. Soc.*, Vol. 61, 1965, pp. 939–944.

10 Pai, S. I., "Some Consideration on the Fundamental Equations of Electro-Magneto-Gasdynamics," *Golden Jubilee Commemoration Volume of the Calcutta Mathematical Society*, Vol. 1, Part 1, 1958–1959, pp. 235–248.

Downloaded 02 May 2010 to 171.66.16.246. Redistribution subject to ASME license or copyright; see http://www.asme.org/terms/Terms_Use.cfm

Use of Coefficients of Influence to Solve Some Inverse Problems in Plane Elasticity

A. J. Durelli
Professor,
Department of Mechanical Engineering,
University of Maryland,
College Park, Md. 20742
Mem. ASME

D. Wu
Graduate Student,
Department of Mechanical Engineering,
University of Mexico

The principle of superposition of the order of isochromatic fringes and the concept of the coefficient of influence of the order of those fringes are introduced. The method is proposed to solve some inverse problems in elasticity and is applied to the determination of the forces that act at the points of contact between disks loaded in their plane. For this purpose Michell equations are used to determine the stresses at selected points of a disk and the coefficients of influence are computed numerically. The method can be generalized to other plane bodies loaded in the plane and if no theoretical solution is available the problem could be solved completely experimentally. The application presented in the paper is related to a study of discrete, or granular, media.

Introduction

In the mechanics of soils and rocks the analyzed media are frequently considered as discontinuous, or granular. It is possible to use then physical models made of spheres, or of disks loaded in the plane, to better understand the distribution of loads between grains. The models can be observed photoelastically. For the analysis of such a system a numerical method is proposed here which simplifies in many cases the determination of the forces applied at the points of contact between disks.

R. Marsal [1, 2], J. Alberro [3] and M. Mendoza [4] have contributed several theoretical and experimental papers to the study of this subject. An attempt is made in these investigations at the determination of the distribution of stresses in each of the disks of a system of loaded disks. This knowledge would permit the determination of the loads applied to each disk at the points of contact with the other disks. An independent contribution to the three-dimensional simulation of the granular medium using spheres can be found in [5].

The isochromatics corresponding to a system of disks are shown in Fig. 1. It can be seen that the distribution of stresses at the contact between disks is complicated. It can also be seen that since the size and the order of the disks are more or less arbitrary, the position of the points of contact between disks also is arbitrary. It is also difficult to know beforehand the number of points of contact in each disk. If it were possible to determine the intensity and the direction of each of the loads acting on each disk, the analysis of the system of the disks that simulates the medium would be feasible.

It is possible to determine the loads applied to the disks from photoelastic isochromatics using Hertz' equations. This would require the measurement of the width of the surface of contact, or of the position of the maximum shear stress, or of the value of this stress, etc. This method, however, has limitations and one of them is requirement of a high resolution in the photographic recordings. Frequently, the method described here will give more precise results. It is planned to publish the results obtained using Hertz' approach in another paper.

The method to be presented requires: (1) the knowledge of the maximum shear stress τ_{max} at points in the field of a typical disk when unit loads are applied at arbitrary points along its border. This relation between the stress and the load is what will be called a coefficient of influence, and in the specific case of the circular disk, it is known from theory from Michell's equations [6]. In the general case of bodies of arbitrary geometry this relation could be obtained experimentally if no theoretical solution is available. (2) A photoelastic test of the system of disks and the determination of τ_{max} at a sufficient number of points in the field of each disk to compute the intensity and the direction of the desired loads.

For convenience the expression, isochromatic fringes, or more simply isochromatics, will be used to identify the loci of points that have the same value of τ_{max}, whether these loci have been determined photoelastically or mathematically. Isoclinics are those fringes that give the direction of the planes on which the principal stresses act. The word isobar will be used to identify the loci of points that have the same value of normal stress, σ.

Contributed by the Applied Mechanics Division for presentation at the 1983 ASME Applied Mechanics, Bioengineering, and Fluids Engineering Conference, Houston, Texas, June 20–22, 1983 of THE AMERICAN SOCIETY OF MECHANICAL ENGINEERS.

Discussion on this paper should be addressed to the Editorial Department, ASME, United Engineering Center, 345 East 47th Street, New York, N.Y. 10017, and will be accepted until two months after final publication of the paper itself in the JOURNAL OF APPLIED MECHANICS. Manuscript received by ASME Applied Mechanics Division, June, 1982; final revision, November, 1982. Paper No. 83-APM-23.

Copies will be available until February, 1984.

Copyright © 1983 by ASME
Downloaded 02 May 2010 to 171.66.16.246. Redistribution subject to ASME license or copyright; see http://www.asme.org/terms/Terms_Use.cfm

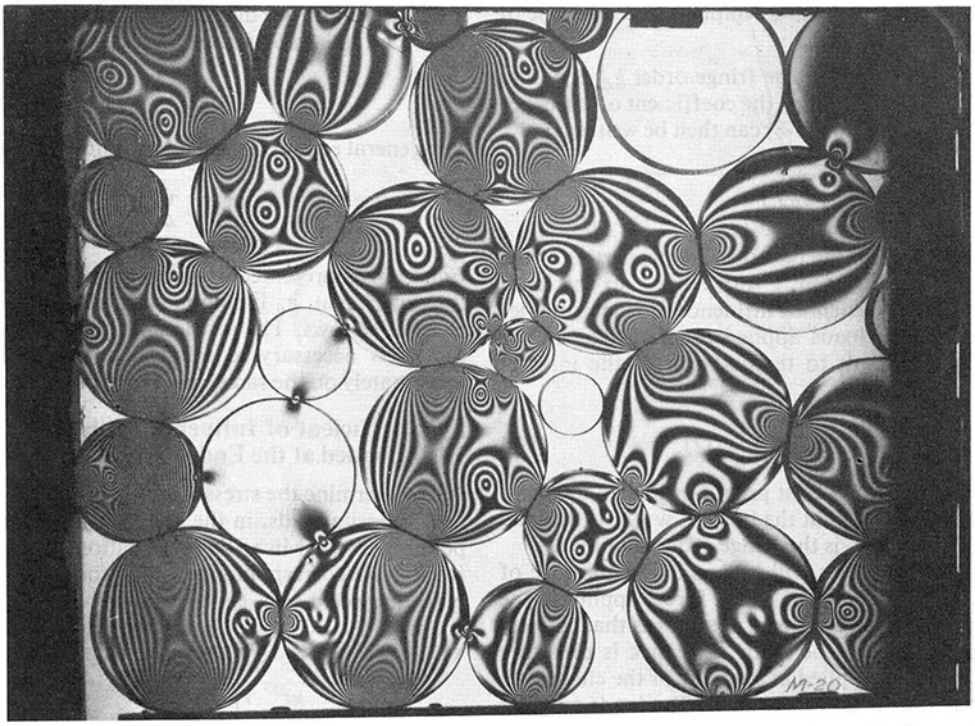

Fig. 1 Simulation of a loaded granular medium using a system of contacting disks

1 The Principle of Superposition of Isochromatics and the Coefficient of Influence

1.1 Superposition of Isochromatics. The basic law of photoelasticity can be expressed as [7]:

$$\tau_{\max} = \frac{f}{t} n \tag{1-1}$$

where t is the thickness of the model, n the isochromatic order, and f the fringe value expressed in terms of stresses. The fringe value is a constant depending on the material of the model and independent of the length of the path of light in the model. The units are psi-in.-fringe or lbs/in.-fringe or kg/cm fringe, or in the S.I. system N/m-fringe.

In these equations there is a linear relationship between the isochromatic orders and the maximum shear stresses. But, in general, the maximum shear stresses at a point and the loads applied to the boundaries are not related in a linear manner because for a load F_j

$$\tau_{\max j} = \sqrt{\left(\frac{\sigma_{x_j} - \sigma_{y_j}}{2}\right)^2 + \tau_{xy_j}^2}$$

$$= \frac{\sigma_{x_j} - \sigma_{y_j}}{2} \sqrt{1 + \left(\frac{2\tau_{xy_j}}{\sigma_{x_j} - \sigma_{y_j}}\right)^2} \tag{1-2}$$

When subjected to several simultaneous loads, the maximum shear stress is

$$\tau_{\max} = \Sigma \tau_{\max j} = \frac{\Sigma \sigma_{xj} - \Sigma \sigma_{yj}}{2} \tag{1-3}$$

provided:

$$\tau_{xy1} = \tau_{xy2} = \ldots = \tau_{xyn} = 0 \tag{1-4}$$

This means that at every point the principal planes should be the same for the stresses produced by all the loads that will be superimposed. Then the principle of superposition of isochromatics can be expressed as follows: If the applied loads are smaller than the ones that may produce plastic strains and

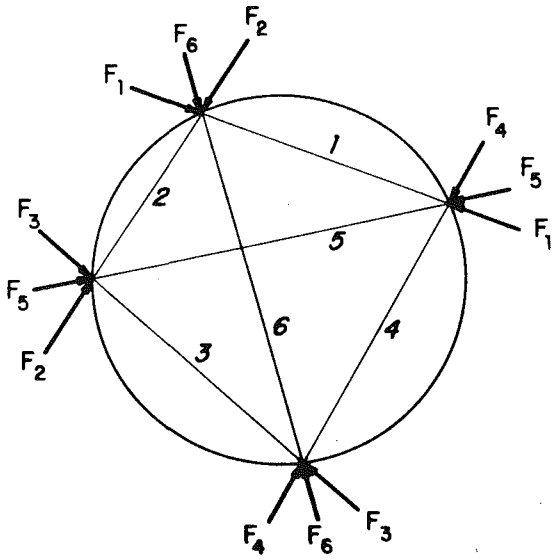

Fig. 2 Disk loaded on its boundary by four concentrated forces. The forces are split in six pairs following the direction of the chords.

provided that the planes on which the maximum shear stresses act are the same for all the loads, or approximately the same, the fringe order at a point of the model is given by the sum of the fringe orders corresponding to each of the applied loads, i.e., the fringe order in a generic point is

$$n_i = \sum_{j=1}^{n} n_{ij} \tag{1-5}$$

where n_i = fringe order at point i; n_{ij} = fringe order at point i, produced by the load F_j only.

It will be seen later that although it is not common that maximum shear stresses act on the same planes when they are associated with different boundary conditions, in the particular case that will be studied, this does occur and it also

Downloaded 02 May 2010 to 171.66.16.246. Redistribution subject to ASME license or copyright; see http://www.asme.org/terms/Terms_Use.cfm

occurs that the problem gets further simplified because one of the principal stresses is constant.

1.2 Coefficient of Influence. The fringe order g_{ij} at point i when the load $F_j = 1$ will be called the coefficient of influence of the isochromatics. Equation (1-8) can then be written:

$$n_i = \sum_{j=1}^{n} g_{ij} F_j \tag{1-6}$$

The coefficient is related to the photoelastic properties of the model and the position of point i with respect to the load. Using the concept of coefficient of influence of isochromatics the determination of the loads applied to the border in the plane problem is equivalent to the solution of the integral linear equation:

$$n_i = \int w(Q) g(i,Q) dx(Q) \tag{1-7}$$

where $g(i,Q)$ is the fringe order at point i produced by a unit load applied at the position Q at the border, $w(Q)$ is the load applied at the border, and n_i is the fringe order at point i.

The previous considerations will be applied to the case of the disk shown in Fig. 2. Each one of the forces applied at the border will be split in the directions of the chords that connect the points of application of the loads. The disk is therefore loaded by pairs of forces applied at the ends of the chords. In Fig. 2 the disk has four points of contact. The loads are split in six pairs of forces. Then the isochromatic order at point i in the disk is:

$$n_i = \sum_{j=1}^{6} g_{ij} F_j \tag{1-8}$$

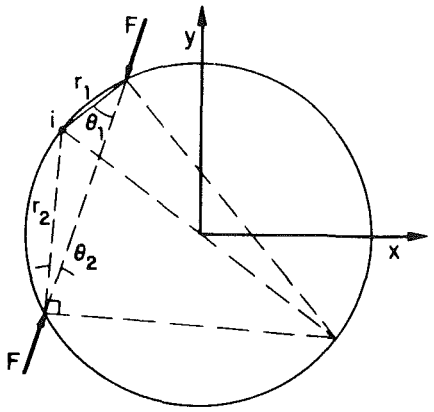

Fig. 3 Polar coordinates of a point on the boundary of a disk

In general if the disk has r points of contact the applied forces are split in S pairs of forces

$$S = \frac{r(r-1)}{2} \tag{1-9}$$

The general equation therefore would be

$$n_i = \sum_{j=1}^{S} g_{ij} F_j \tag{1-10}$$

Equations represented by (1-10) are linear. n_i is determined by the experiment. g_{ij} is computed theoretically as will be shown in what follows. The restrictions already mentioned indicate that it is necessary to select points i so that τ_{max} act approximately on the same plane for all the loads considered.

2 Coefficient of Influence of the Isochromatics in the Disk Loaded at the Ends of a Chord

To determine the stresses taking place in a disk subjected to two opposite loads, in the direction of a chord (Fig. 3), it is possible to use Michell's [6] equation which can be obtained from those corresponding to the problem of the semi-infinite plate subjected to a concentrated load (Fig. 4). The stresses are given by:

$$\sigma_{r_1} = -\frac{2F}{\pi t}\frac{\cos\theta_1}{r_1} + A; \quad \sigma_{\theta_1} = 0; \quad \tau_{r_1\theta_1} = 0$$

$$\sigma_{r_2} = -\frac{2F}{\pi t}\frac{\cos\theta_2}{r_2} + A; \quad \sigma_{\theta_2} = 0; \quad \tau_{r_2\theta_2} = 0 \tag{2-1}$$

where

$$A = \frac{2F}{\pi D\, t}\sin(\theta_1 + \theta_2) \tag{2-2}$$

It is important to observe that the direction of the chord is a principal direction of stress. In local polar coordinates when r is the distance from the point considered to the point of contact of the force on the disk and θ is the angle between the radius going through the point and the direction of the force, Michell's equation can be expressed as:

$$\sigma_\theta = \sigma_1 = 0; \quad \sigma_r = \sigma_2 = -\frac{2F}{\pi t}\frac{\cos\theta}{r}$$

$$\tau_{r\theta} = \tau_{12} = 0; \quad \tau_{max} = \frac{\sigma_1 - \sigma_2}{2} = \frac{F}{\pi t}\frac{\cos\theta}{r} \tag{2-3}$$

This means: (1) that the isostatics are radial lines and circumferences, as shown in Fig. 4, and (2) that the normal stress, σ_θ, which has the direction of the tangent to the circumference and is σ_1, is zero everywhere.

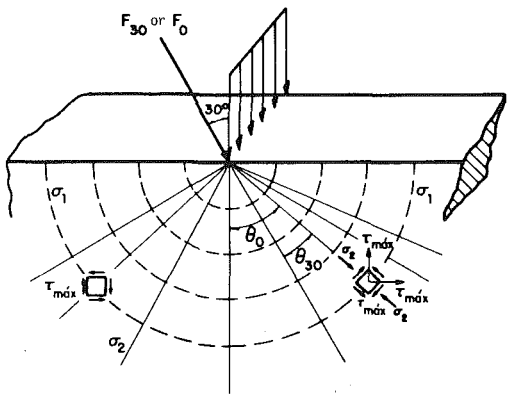

(ANGLE ϑ MUST BE MEASURED FROM THE DIRECTION OF THE FORCE)

$$\sigma_\theta = \sigma_1 = 0$$

$$\sigma_r = \sigma_2 = -\frac{2F}{\pi}\frac{\cos\theta}{r}$$

$$\tau_{máx} = \tau_{1\text{-}2} = 0$$

$$\tau_{r\theta} = \frac{\sigma_1 - \sigma_2}{2} = \frac{F}{\pi}\frac{\cos\theta}{r}$$

ISOSTATICS:

FOR F_0 OR F_{30} LOADS

Fig. 4 Semi-infinite plate to a concentrated force on its boundary. The isotatics are circles concentric for any direction of the force.

Downloaded 02 May 2010 to 171.66.16.246. Redistribution subject to ASME license or copyright; see http://www.asme.org/terms/Terms_Use.cfm

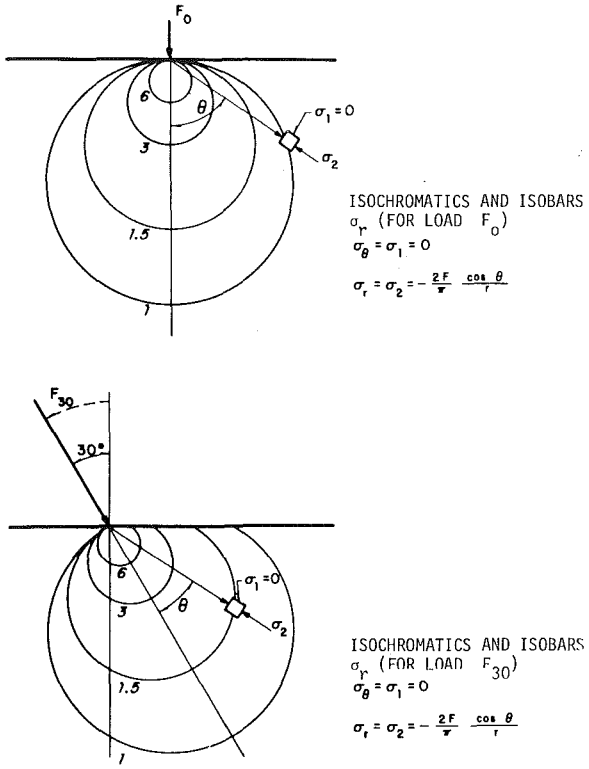

Fig. 5 Semi-infinite plate subjected to a concentrated force on its boundary. (a) Perpendicular to the boundary; (b) making 30 deg with a normal to the boundary. Isochromatics and isobars σ_r are the same in the two cases, when referred to the direction of the force as axis.

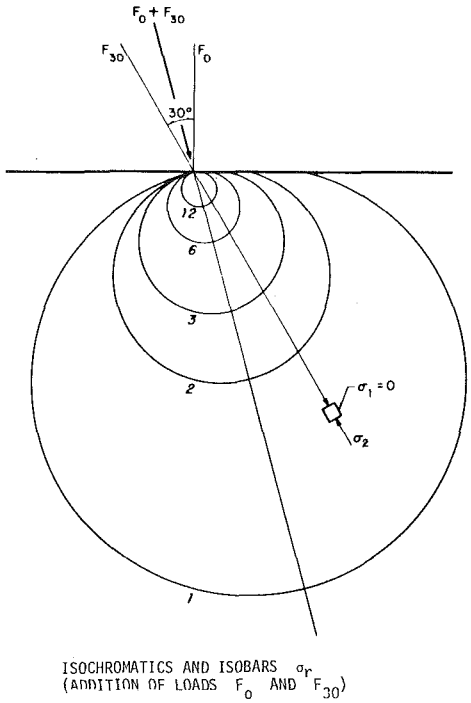

Fig. 6 Semi-infinite plate subjected to a concentrated resultant force on its boundary. The stress σ_2 acts on the same plane for the two components. They can be added algebraically.

Isochromatics for the case of the load perpendicular to the tangent at the point of contact are shown in Fig. 5. All are circumferences tangent at the point of contact, with centers on the line of action of the load. Isochromatics corresponding to the case of the inclined load are also shown in Fig. 5. They are represented by the same equations (2-3) provided the direction of the force is taken as origin of the angles. Therefore (1) the isostatics in Fig. 4 are applicable to forces of any direction; (2) the isochromatics for forces of any direction are also isobars σ_2; and (3) it is possible to add arithmetically the stresses corresponding to forces of different directions applied to the same point of the border. This is shown graphically in Fig. 6.

This idea can be applied to the case of the disk. It is convenient then to express equation (2-1) using x coordinates and Fig. 3.

$$\sigma_x = -\frac{2F}{\pi t}\left(\frac{\cos\theta_1}{r_1}\sin^2\theta_1 + \frac{\cos\theta_2}{r_2}\sin^2\theta_2\right) + A$$

$$\sigma_y = -\frac{2F}{\pi t}\left(\frac{\cos\theta_1}{r_1}\cos^2\theta_1 + \frac{\cos\theta_2}{r_2}\cos^2\theta_2\right) + A$$

$$\tau_{xy} = -\frac{2F}{\pi t}\left(\frac{\cos^2\theta_1 \sin\theta_1}{r_1} - \frac{\cos^2\theta_2 \sin\theta_2}{r_2}\right) \tag{2-4}$$

From this equation it is possible to obtain the expression giving τ_{max} at any point:

$$\tau_{max}^2 = \left(\frac{F}{\pi t}\right)^2\left(\frac{\cos^2\theta_1}{r_1^2} + \frac{\cos^2\theta_2}{r_2^2} + \frac{2\cos\theta_1\cos\theta_2\cos 2(\theta_1+\theta_2)}{r_1 r_2}\right) \tag{2-5}$$

Replacing τ_{max} from equation (1-1) into equation (2-5), and if $F = 1$ then the coefficient of influence at the point i is:

$$g_{ij} = \frac{1}{\pi f}\sqrt{\frac{\cos^2\theta_1}{r_1^2} + \frac{\cos^2\theta_2}{r_2^2} + \frac{2\cos\theta_1\cos\theta_2\cos 2(\theta_1+\theta_2)}{r_1 r_2}} \tag{2-6}$$

Calling D the diameter of the disk, d the length of the chord, corresponding to the force j and:

$$l = \frac{d}{D}; \quad m = \frac{D}{r_1} \tag{2-7}$$

and recalling that

$$r_1\cos\theta_1 + r_2\cos\theta_2 = d; \quad r_1\sin\theta_1 - r_1\sin\theta_2 = 0 \tag{2-8}$$

the following equation is obtained to compute the coefficient of influence:

$$g_{ij} = \frac{1}{\pi D f}k_{ij} \tag{2-9}$$

where

$$k_{ij} = m\sqrt{1 + \frac{2lm-1}{(lm-1)^2}} \quad \text{for} \quad \theta_1 = \theta_2 = 0 \tag{2-10}$$

$$k_{ij} = \frac{m^2 l}{1+(ml)^2} \quad \text{for} \quad \theta_1 = 90 \text{ deg} \tag{2-11}$$

$$k_{ij} = m\cos\theta_1\sqrt{1 + \left(\frac{\sin 2\theta_2}{\sin 2\theta_1}\right)^2 + 2\left(\frac{\sin 2\theta_2}{\sin 2\theta_1}\right)\cos 2(\theta_1+\theta_2)} \quad \text{for} \quad 0 < \theta_1 < 90 \text{ deg} \tag{2-12}$$

$$\theta_2 = \tan^{-1}\left(\frac{\sin\theta_1}{lm - \cos\theta_1}\right) \tag{2-13}$$

It can be seen that g_{ij} is a function of the constants D and f of the model and of the local coordinates (l, m, θ_1). When parameters l, m, θ_1 are known the value of k_{ij} can be determined using tables like Table 1 prepared for $m = 10$.

Downloaded 02 May 2010 to 171.66.16.246. Redistribution subject to ASME license or copyright; see http://www.asme.org/terms/Terms_Use.cfm

Table 1 Coefficients of influence k_{ij}, for points located at $m = 10$, and for different angles θ_1

θ_1 \ l	0.40	0.55	0.60	0.70	0.80	0.85	1.00
0	13.333	12.222	12.000	11.667	11.429	11.333	11.111
5	13.221	12.140	11.923	11.598	11.365	11.272	11.054
10	12.889	11.897	11.696	11.393	11.175	11.087	10.883
15	12.353	11.500	11.324	11.056	10.863	10.784	10.601
20	11.637	10.962	10.818	10.597	10.435	10.369	10.214
25	10.771	10.298	10.193	10.026	9.902	9.851	9.729
30	9.786	9.527	9.462	9.356	9.273	9.238	9.154
35	8.717	8.669	8.645	8.600	8.561	8.543	8.499
40	7.595	7.743	7.760	7.775	7.779	7.778	7.774
45	6.448	6.770	6.823	6.895	6.939	6.956	6.990
50	5.300	5.767	5.853	5.975	6.057	6.088	6.158
55	4.171	4.752	4.864	5.029	5.143	5.188	5.290
60	3.077	3.738	3.871	4.070	4.211	4.266	4.396
65	2.028	2.738	2.886	3.110	3.271	3.335	3.486
70	1.032	1.763	1.919	2.159	2.333	2.404	2.570
75	0.094	0.820	0.979	1.225	1.407	1.481	1.657
80	0.782	0.084	0.072	0.317	0.500	0.576	0.755
85	1.598	0.945	0.796	0.560	0.381	0.307	0.129
90	2.353	1.760	1.622	1.400	1.231	1.160	–

$l = d/D$; $m = D/r_1$

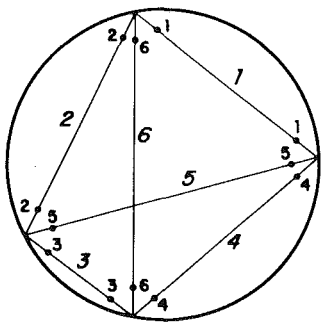

Fig. 7 Every chord is subjected to two opposite forces applied at its ends, in the direction of the chord. The isochromatic orders have to be determined at as many pairs of points as there are chords.

3 Examples

To determine the value of S components of loads applied to a disk all that is necessary according to equation (1-9) is to select S points in the field of isochromatics, at which the principal directions do not change or change little with the loads to be considered, and to determine for each one of those points the coordinate and the fringe order. To make the computation easier it is convenient to select the points on the lines of application of the forces at a distance $D/10$ from the points of contact ($m = 10$).

The following rules make the interpretation easier: (1) on each chord only a pair of opposite forces act (Fig. 7) and their direction is the direction of the chord; (2) on each chord two points are selected to which the same number is assigned and this number is the same as the one of the component of the force which acts in the direction of the chord. When the fringe order is not sufficiently high and it is possible to observe the model in the polariscope it is possible to increase the precision using a method of compensation. The coefficient of influence at a point is the result of the addition of the influence of a particular force on the two points that have the same number.

The fringe value of the material used can be determined from a disk diametrically loaded. At the center of a disk

$$f = \frac{4F}{\pi D n_c} \tag{3-1}$$

where n_c is the isochromatic order. Using "Homalite 100," $f = 7.82$ kg/cm-fringe.

If the examples that follow the applied loads are known by statics which permits a verification of the computation and an estimate of the precision. Different details of the procedure will be used in each of the examples to be shown.

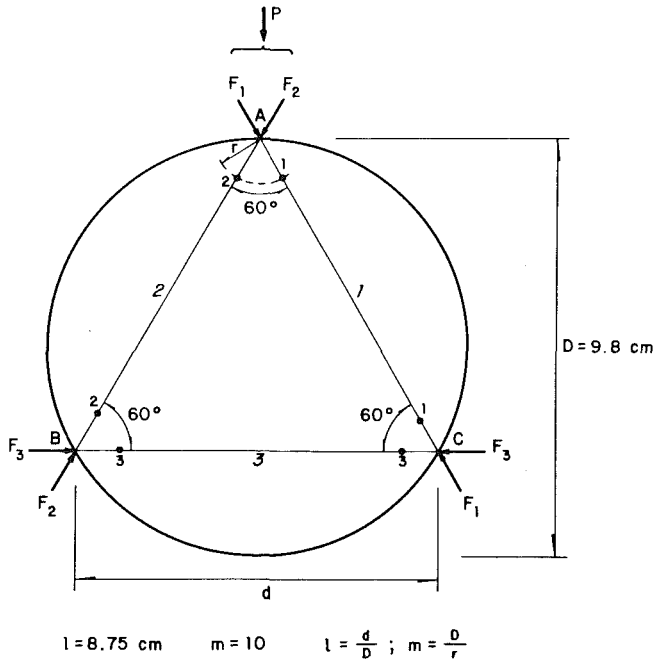

Fig. 8 Disk loaded at three points on the boundary at the same distance from each other

3.1 Disk With Three Symmetric Points of Contact.

3.1.1 Making an Equilateral Triangle (and Using Birefringence Compensation). The length of the three chords are the same (Fig. 8). Following equation (1-10), the regular equations are

$$\begin{aligned} n_1 &= g_{11}F_1 + g_{12}F_2 + g_{13}F_3 \\ n_2 &= g_{21}F_1 + g_{22}F_2 + g_{23}F_3 \\ n_3 &= g_{31}F_1 + g_{32}F_2 + g_{33}F_3 \end{aligned} \tag{3-2}$$

and from equation (2-9): $k_{ij} = g_{ij}\,\pi D f$.

Equation (3-2) can be written as a matrix:

$$\{k\}\,\{F\} = \pi D f \{n\} \tag{3-3}$$

The forces are then:

Downloaded 02 May 2010 to 171.66.16.246. Redistribution subject to ASME license or copyright; see http://www.asme.org/terms/Terms_Use.cfm

Table 2 Computation of the loads applied to a disk with three symmetric points of contact (neglecting the far-away load)

No. of Load Order	Experiment (Tardy's Compensation)				Computation				Relative Error
	P(kg)	n_1	n_2	n_3	F_1	F_2	F_3	P_{ca}	$(P-P_{ca})/P$(percent)
2	28.85	1.85	2.08	1.14	15.16	18.18	5.84	28.87	+ 0.00
3	43.35	2.96	2.75	2.07	24.86	22.10	13.17	40.69	− 6.14
4	57.85	3.76	4.15	2.37	30.86	35.98	12.61	57.88	+ 0.00
5	72.35	4.63	5.05	3.13	37.73	43.25	8.04	70.13	− 3.07
6	86.84	6.00	6.05	3.99	49.90	50.56	23.52	87.00	+ 0.00

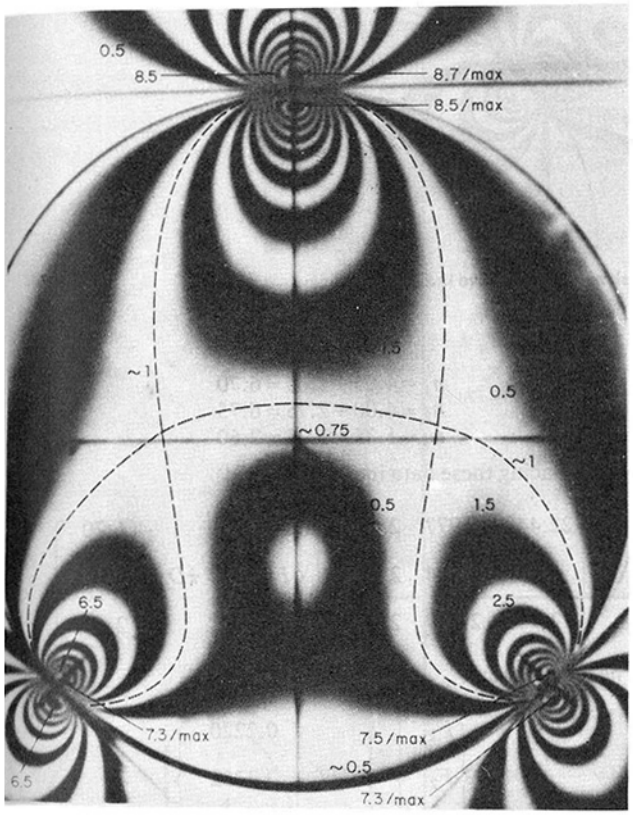

Fig. 9 Isochromatics in a disk subjected to one vertical load and two loads inclined at 30 deg

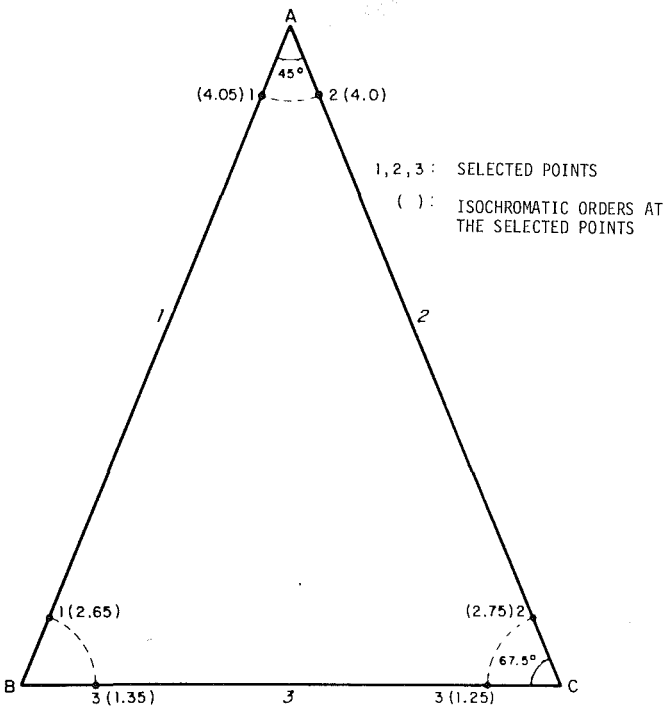

Fig. 10 Sketch to determine the forces applied to a disk with three points of contact (isosceles triangle distribution)

$$\{F\} = \pi D f \{k\}^{-1} \{n\} \tag{3-4}$$

When the influence of the forces located far away from the point considered is neglected, for instance the influence of force F_3 on the points A_1 and A_2 and of the force F_1 on the points B_2 and B_3, etc., then the principal planes at the points under consideration are the same for each of the loads considered.

For the disk with three symmetric points of contact according to equation (2-7) $l_1 = l_2 = l_3 = 0.866\, D/D = 0.866$. Coefficients k_{ij} are obtained from Table 1. Every coefficient depends on three parameters m, l, θ. Parameter m has been fixed and is equal to 10. It is only necessary then to consider l and θ

Point 1: Component 1: $l_1 = 0.866$

$$\theta_1 = 0 \quad k_{11} = 2 \times 11.305$$

Component 2: $l_2 = 0.866$

$$\theta_1 = 60 \text{ deg} \quad k_{12} = 1 \times 4.283$$

Component 3: $l_3 = 0.866$

$$\theta_1 = 60 \text{ deg} \quad k_{13} = 1 \times 4.283$$

and for points 2 and 3:

$$k_{21} = 4.283 \quad k_{23} = 4.283 \quad k_{22} = 22.61$$

$$k_{31} = 4.283 \quad k_{32} = 4.283 \quad k_{33} = 22.61$$

Therefore, the matrix for coefficient of influence is:

$$\{k\} = \begin{bmatrix} 22.61 & 4.283 & 4.283 \\ 4.283 & 22.61 & 4.283 \\ 4.283 & 4.283 & 22.61 \end{bmatrix}$$

The inverse of $\{k\}$ is:

$$\{k\}^{-1} = \begin{bmatrix} 0.04707 & -0.007496 & -0.007496 \\ -0.007496 & 0.04707 & -0.007496 \\ -0.007496 & -0.007496 & 0.04707 \end{bmatrix}$$

Replacing $\{k\}^{-1}$ in (3-4):

Downloaded 02 May 2010 to 171.66.16.246. Redistribution subject to ASME license or copyright; see http://www.asme.org/terms/Terms_Use.cfm

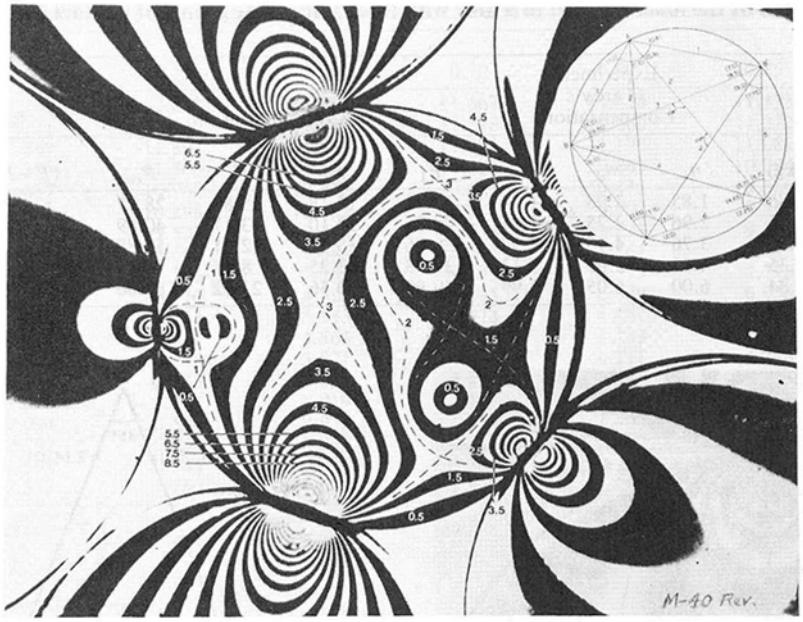

Fig. 11 Isochromatics in a disk subjected to five loads

$$\{F\} = \pi D f \begin{bmatrix} 0.04707 & -0.007496 & -0.007496 \\ -0.007496 & 0.04707 & -0.007496 \\ -0.007496 & -0.007496 & -0.04707 \end{bmatrix} \begin{Bmatrix} n_1 \\ n_2 \\ n_3 \end{Bmatrix} \quad (3\text{-}5)$$

Since the matrix $\{k\}$ depends only on the coordinates of the point of contact equation (3-5) can be used for any disk with three symmetric points of contact.

The results are shown in Table 2 where P is the vertical load applied at point A (Fig. 8) and P_{ca} is the load computed from $\{n\}$ which was obtained for several load levels using Tardy's compensation.

For a disk with $D = 9.8$ cm and $f = 7.82$ the solution for $\{F\}$ and P_{ca} is the following

$$\begin{Bmatrix} F_1 \\ F_2 \\ F_3 \end{Bmatrix} = \begin{bmatrix} 11.33 & -1.80 & -1.80 \\ -1.80 & -11.33 & -1.80 \\ -1.80 & -1.80 & 11.33 \end{bmatrix} \begin{Bmatrix} n_1 \\ n_2 \\ n_3 \end{Bmatrix} \quad (3\text{-}6)$$

and

$$P_{ca} = (F_1 + F_2) \cos 30 \text{ deg}$$

3.1.2. Making Isosceles Triangle (and Interpolating Isochromatics). In this case the values of n have been obtained by interpolation between the fringes of a photograph (Fig. 9) and are shown in (Fig. 10). The parameters are $D = 6.0$ cm, $l_1 = l_2 = 0.924$, and $l_3 = 0.707$. Using Table 1 it is possible to obtain the elements of the matrix $\{k\}$:

at point 1: $k_{11} = 2 \times 11.22$; $k_{12} = 6.977$; $k_{13} = 2.634$
at point 2: $k_{21} = k_{12} = 6.977$; $k_{22} = k_{11} = 22.44$; $k_{23} = 2.634$
at point 3: $k_{31} = 2.949$; $k_{32} = 2.949$; $k_{33} = 23.32$

Using the photographs and interpolating between isochromatics it is found that

$$n_1 = 4.05 + 2.65 = 6.70$$
$$n_2 = 4.00 + 2.75 = 6.75$$
$$n_3 = 1.35 + 1.25 = 2.60$$

and replacing these data in equation (3-4)

$$\begin{bmatrix} 22.44 & 6.977 & 2.634 \\ 6.977 & 2.244 & 2.634 \\ 2.949 & 2.949 & 2.332 \end{bmatrix} \begin{Bmatrix} F_1 \\ F_2 \\ F_3 \end{Bmatrix} = \pi D f \begin{Bmatrix} 6.70 \\ 6.75 \\ 2.60 \end{Bmatrix}$$

The results are:

$$\begin{Bmatrix} F_1 \\ F_2 \\ F_3 \end{Bmatrix} = \pi D f \begin{Bmatrix} 0.2220 \\ 0.2252 \\ 0.05521 \end{Bmatrix}$$

Giving to the parameters the values: $D = 6.0$ cm, $f = 7.82$

$$\begin{Bmatrix} F_1 \\ F_2 \\ F_3 \end{Bmatrix} = \begin{Bmatrix} 32.72 \\ 33.20 \\ 8.14 \end{Bmatrix} \text{kg}$$

The computed vertical load at the point of contact A is

$$P_{ca} = (F_1 + F_2) \cos 22.5 \text{ deg} = 60.90 \text{ kg}$$

The applied load was $P = 63.24$ kg, then $P - P_{ca}/P = -3.79$ percent. Then the normal and tangential forces at each point of contact are:

Point of contact	Normal load (kg)	Tangential load (kg)
A	60.90	0.18
B	35.98	6.77
C	36.43	6.95

3.2 Disk With Five Points of Contact (One Axis of Symmetry). The distribution of the isochromatics is ap-

Downloaded 02 May 2010 to 171.66.16.246. Redistribution subject to ASME license or copyright; see http://www.asme.org/terms/Terms_Use.cfm

proximately symmetric and the forces to be determined are only those identified in Fig. 11. The applied loads in this case are not known and therefore no verification is possible.

The geometric parameters are:

$$l_1 = \frac{2\,D/2 \text{ sub } 36 \text{ deg}}{D} = 0.588;$$

$$l_2 = \frac{2\,D/2 \sin 72 \text{ deg}}{D} = 0.951$$

$$l_3 = 0.951; \quad l_4 = 0.951; \quad l_5 = 0.588; \quad l_6 = 0.588$$

(*a*) Some of the k_{ij} will be computed using equation (2-6) and (2-9) because the values given in the table are good only for θ_2 smaller than 90 deg. For $k_{15} = k_{51} = k_{56} = k_{65}$ the parameters are: $l = 0.6$; $m = 1.6$; $\theta_1 = 8.74$ deg and $\theta_2 = 1.08$ deg. The results are: $k_{15} = k_{51} = k_{56} = k_{65} = 5.894$. The other coefficients of influence can be obtained from Table 1.

Particular Cases of Application of Michell's Equations

	Coefficients of influence at particular points k_i	Formula for the loads n_i = order of isochromatic
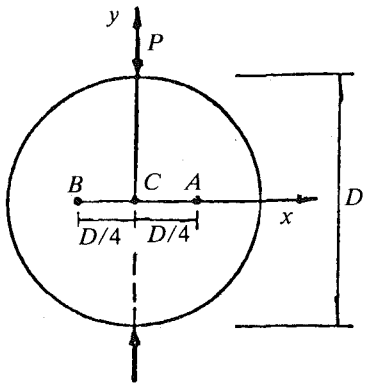	$k_A = k_B = 1.92$ $k_c = 4.0$	$p = \frac{\pi D f}{k_i} n_i$ $i = A,B,C$
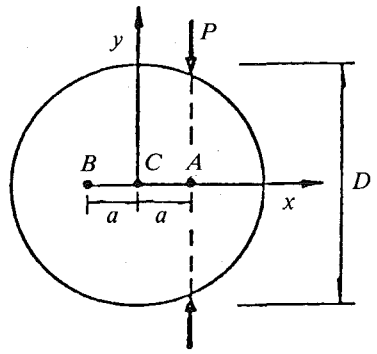	$k_A = \frac{4D}{d}$ $k_c = \frac{2\sqrt{2}\,d}{D}\sqrt{1+\cos 4\theta}$ $k_B = \frac{2\sqrt{2}\cos\theta_B}{\sqrt{1+12\,a^2/D^2}}\sqrt{1+\cos 4\,\theta_B}$ $\tan\theta_c = \frac{2a}{d}, \quad \tan\theta_B = \frac{a}{d}$	$p = \frac{\pi D f}{k_i} n_i$ $i = A,B,C$
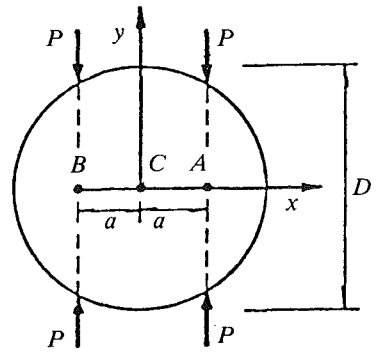	$k_A = k_B = \frac{4D}{d} + \frac{2\sqrt{2}\cos\theta_B}{\sqrt{1+12\,a^2/D^2}}\sqrt{1+\cos 4\,\theta_B}$ $k_c = \frac{4\sqrt{2}\,d}{D}\sqrt{1+\cos 4\,\theta_c}$ $\tan\theta_c = \frac{2a}{d}$ $\tan\theta_B = \frac{a}{d}$	$p = \frac{\pi D f}{k_i} n_i$ $i = A,B,C$

Downloaded 02 May 2010 to 171.66.16.246. Redistribution subject to ASME license or copyright; see http://www.asme.org/terms/Terms_Use.cfm

$$k = \begin{array}{c} \\ 1 \\ 2 \\ 3 \\ 4 \\ 5 \\ 6 \end{array} \begin{array}{c} \begin{array}{cccccc} 1 & 2 & 3 & 4 & 5 & 6 \end{array} \\ \begin{bmatrix} 26.10 & 8.362 & 8.362 & 2.205 & 5.894 & 0 \\ 8.468 & 22.37 & 0 & 8.362 & 8.468 & 1.419 \\ 8.468 & 0 & 11.195 & 8.362 & 1.419 & 0 \\ 1.419 & 8.362 & 8.362 & 22.37 & 1.419 & 8.468 \\ 5.894 & 8.362 & 2.205 & 10.567 & 24.00 & 5.894 \\ 0 & 2.205 & 0 & 8.362 & 5.894 & 12.05 \end{bmatrix} \end{array}$$

(*b*) The matrix $\{n\}$ can be obtained from the isochromatics and the sketch shown in Fig. 11.

$$\{n\} = \frac{1}{2} \begin{Bmatrix} (7.0+0.8+1.0+6.0) \\ (5.7+0.9+3.15+1.10) \\ (8.5+9.5) \\ (9.0+3.0+4.65+9.0) \\ (7.75+5.7+6.0+2.65) \\ (2.25+2.0) \end{Bmatrix} = \begin{Bmatrix} 7.4 \\ 5.425 \\ 9.00 \\ 8.64 \\ 11.05 \\ 2.125 \end{Bmatrix}$$

(*c*) Using the equation giving the forces $[K]\{F\} = \pi Df\{n\}$ the six components are:

$$\begin{Bmatrix} F_1 \\ F_2 \\ F_3 \\ F_4 \\ F_5 \\ F_6 \end{Bmatrix} = \Pi Df \begin{Bmatrix} -0.129196 \\ 0.150270 \\ 0.845580 \\ 0.016028 \\ 0.365688 \\ -0.039747 \end{Bmatrix}$$

(*d*) Therefore the normal and tangential forces are:

Point of contact	Normal loads	Tangential loads
A	$0.134\ \pi Df$	~ 0
B	$0.957\ \pi Df$	$-0.143\ \pi Df$
B^1	$0.957\ \pi Df$	$0.143\ \pi Df$
C	$0.348\ \pi Df$	$0.370\ \pi Df$
C^1	$0.348\ \pi Df$	$-0.370\ \pi Df$

4 Particular Cases

The equations of Michell can be expressed in simple form for certain special cases of distribution of loads. It is not necessary then to follow the procedure explained in the foregoing. Loads can be determined directly from the fringe order at a selected point of the disk. Some of these cases and the corresponding equations have been tabulated.

The general equation (2-6), where $r_1 = r_2$ and $\theta_1 = \theta_2$ becomes:

$$k = \sqrt{2\, m^2 \cos^2\theta}\quad \sqrt{1+\cos 4\,\theta} \tag{4-1}$$

and the applied load is given by:

$$P = \frac{\pi Df}{k} n \tag{4-2}$$

5 Conclusion

A method has been presented that permits the determination of any system of forces applied to the boundary of a disk, when the isochromatics are known at some selected points of the field. The method is approximate in the sense that it neglects the influence of forces applied to points located far away from the points under consideration.

Acknowledgments

The manuscript of this paper was prepared at the Instituto de Ingenieria of the Universidad Nacional de Mexico (UNAM) when A. Durelli had the Nabor Carrrillo chair at that university, and Delun Wu was conducting studies for his master's degree in civil engineering. The research work was partially supported by the Office of Naval Research at the University of Maryland, in College Park. The authors would like to express their appreciation to the monitors Drs. N. Perrone and N. Basdekas for their continuous support, and to Professors J. Alberro, R. J. Sanford, and D. Barker for reading the manuscript and making very valuable suggestions. The photograph of Fig. 1 was provided by Professor Mendoza. Thelma C. Miller was in charge of the reproduction of the manuscript.

References

1 Marsal, R. J., "Contact Forces in Soils and Rockfill Materials," *Proc. II Panamerican Conf. Soil Mechanics, Found. Engr.*, Vol. 2, pp. 67-98.

2 Marsal, R. J., *Mechanical Properties of Rockfill Embankment Dam*, Engrg. Casagrande Volume, Wiley, New York, 1973, pp. 109-200.

3 Alberro, J., "Estructura Discontinua y Propiedades Mecanicas de los Suelos Granulares," Informe del Instituto de Ingenieria, UNAM, Proyecto 811.

4 Mendoza, M., "Measurement of Contact Forces in Photoelastic Models," *Proc. Panam. Conf. Soil Mechanics and Found. Eng.*, Vol. I, Buenos Aires, 1975, pp. 1-10.

5 Thurston, C. W., and Dersiewicz, H., "Analysis of a Compression Test of a Model of a Granular Medium," ASME JOURNAL OF APPLIED MECHANICS, June 1959, pp. 251-258.

6 Timoshenko, S., *Theory of Elasticity*, McGraw-Hill, New York, 1934, p. 106. The problem had been solved originally by J. S. Michell, *Proc. London Math. Soc.*, Vol. 32, 1900, p. 44, and Vol. 34, 1901, p. 134.

7 See for instance: Durelli, A. J., and Riley, W. F., *Introduction to Photomechanics*, Prentice-Hall, 1965, p. 54.

Downloaded 02 May 2010 to 171.66.16.246. Redistribution subject to ASME license or copyright; see http://www.asme.org/terms/Terms_Use.cfm

A Free Boundary Value Problem in Plate Theory

P. Villaggio
Istituto di Scienza delle Costruzioni
dell' Università di Pisa,
56100 Pisa, Italy

In this paper the equilibrium configuration of a thin rectangular plate, supported on an elastic foundation that reacts in compression only, is studied. It is assumed that the foundation is described by the Winkler model in the contact region. The plate is supposed to be weightless and subjected to a concentrated load in its midpoint. The shape of the free boundary, where the plate loses contact with the foundation, is determined.

1 Introduction

In 1884 Hertz [1] gave a closed solution to the problem of a infinite thin elastic plate resting on an elastic foundation, subjected to a concentrated load. Hertz himself realized that his assumption that the surface of the plate experienced a reaction proportional to the displacement was in contrast with the effective behavior of the foundation, which reacts only with compressive pressures where the plate penetrates into the foundation. Hertz's solution is more appropriate to describe the deformation of an infinite plate floating inside of (or on the surface of) a fluid, in which case(s) the fluid exerts on the plate an increment in hydrostatic pressure proportional to the displacement of the plate (Föppl [2, § 20]).

Weitsman [3] considered a version of Hertz's problem and was able to describe the realistic behavior of an infinite plate on an elastic foundation. If the plate is loaded by a concentrated force P, it is plausible to expect that it makes contact with the foundation only along a bounded circular region surrounding the point of application of P. Outside this region the plate remains above the elastic foundation and does not interact with it. The radius of the contact circle is not known in advance, but must be determined by suitable conditions of continuity of the solution across the circumference at which the plate leaves the elastic foundation.

Once the radius of the contact circle is determined, the entire solution is also determined, both inside and outside of the contact circle. An unexpected property of the solution is that the radius of the contact circle does not depend on the magnitude of P, but only on the flexural rigidity of the plate and the elastic modulus of the foundation (Weitsman [3, §3]).

In this paper I consider the case of a rectangular weightless plate supported on an elastic foundation that reacts in compression only. The plate is subjected to a point load P at its midpoint. Under the assumption that the sides of the rectangle are not too different, and both are sufficiently large with respect to the fourth root of the ratio between the flexural rigidity of the plate and the stiffness of the foundation, the contact region is very small compared to the size of the plate and the shape of the boundary of the contact region can be determined by first-order perturbation of Weitsman's solution. Also in this situation the shape and the extent of the free boundary is independent of P.

2 Basic Equations

Let us consider a plane rectangular plate supported on an elastic foundation and loaded transversally by a point load P at its center (Fig. 1). Let us denote the transversal displacement of the plate by w, the lengths of the sides ($a \geq b$) by $2a$ and $2b$, and the flexural rigidity of the plate by D. The foundation is represented by the Winkler model; that is, it offers a reaction kw, where k is a constant called *modulus of the foundation*. This reaction, however, is only compressive and occurs only where w is positive. Let us denote the unknown curve by L, separating the contact and the non-contact regions of the plate.

Let us introduce a system of plane polar coordinates (r,θ) in such a way that the origin coincides with the point of application of P (Fig. 2). The deflection w is thus a function of the type $w = w(r,\theta)$, and this function must be periodic of period π in θ, since the deflection is symmetric with respect the axes of the rectangle.

Let us assume that, in terms of (r,θ), L has the equation $r = \hat{r}(\theta)$, where $\hat{r}(\theta)$ is a continuously differentiable function, periodic with period π.

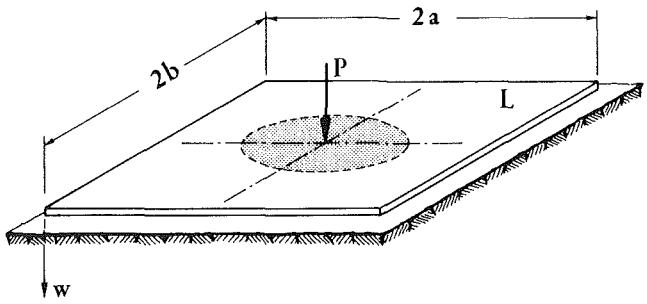

Fig. 1

Contributed by the Applied Mechanics Division for publication in the JOURNAL OF APPLIED MECHANICS.

Discussion on this paper should be addressed to the Editorial Department, ASME, United Engineering Center, 345 East 47th Street, New York, N.Y. 10017, and will be accepted until two months after final publication of the paper itself in the JOURNAL OF APPLIED MECHANICS. Manuscript received by the ASME Applied Mechanics Division, March, 1981; final revision, August, 1982.

Copyright © 1983 by ASME
Downloaded 02 May 2010 to 171.66.16.246. Redistribution subject to ASME license or copyright; see http://www.asme.org/terms/Terms_Use.cfm

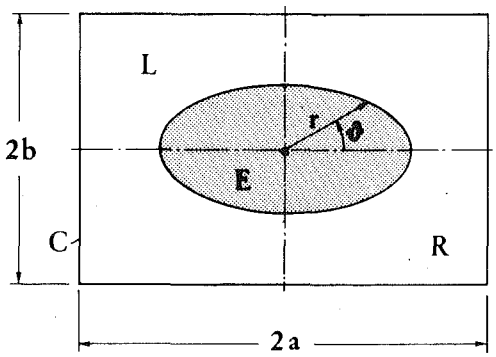

Fig. 2

The function $w(r,\theta)$ is the solution to the following pair of differential equations

$$D\left(\frac{\partial^2}{\partial r^2}+\frac{1}{r}\frac{\partial}{\partial r}+\frac{1}{r^2}\frac{\partial^2}{\partial\theta^2}\right)\left(\frac{\partial^2 w}{\partial r^2}+\frac{1}{r}\frac{\partial w}{\partial r}+\frac{1}{r^2}\frac{\partial^2 w}{\partial\theta^2}\right)+kw=0 \quad \text{in} \quad E,$$

$$D\left(\frac{\partial^2}{\partial r^2}+\frac{1}{r}\frac{\partial}{\partial r}+\frac{1}{r^2}\frac{\partial^2}{\partial\theta^2}\right)\left(\frac{\partial^2 w}{\partial r^2}+\frac{1}{r}\frac{\partial w}{\partial r}+\frac{1}{r^2}\frac{\partial^2 w}{\partial\theta^2}\right)=0 \quad \text{in} \quad E_1, \tag{2.1}$$

where E and E_1 are, respectively, the contact and the non-contact set.

The boundary conditions associated with equations (2.1) are the following. At the origin, that is, for $r=0$, $w(0)$ and its derivative $\partial w/\partial r(0)$ must remain bounded. Moreover, if Γ_ϵ is a circle of radius r_ϵ around the origin, we must have

$$\lim_{r\epsilon\to 0}\int_{\Gamma\epsilon} V_n ds+P=\lim_{r\epsilon\to 0}\int_{\Gamma\epsilon}\left(Q_n+\frac{\partial}{\partial s}M_{nt}\right)ds+P=0, \tag{2.2}$$

where Q_n is the normal shear force, M_{nt} is the twisting moment, and $\partial/\partial s$ denotes the partial tangential derivative.

The exterior boundary C of the rectangle is free. Therefore V_n and the normal bending moment M_n must vanish along it:

$$V_n=Q_n+\frac{\partial}{\partial s}M_{nt}=0, \quad M_n=0 \quad \text{on} \quad C. \tag{2.3}$$

In addition, certain conditions of continuity must be satisfied across the free boundary L. These conditions require that w, evaluated as limit from inside and outside L along the normal derivative to L, vanish:

$$w(L^-)=w(L^+)=0, \tag{2.4}$$

and that normal derivatives, and the exterior characteristics M_n, V_n be continuous:

$$\frac{\partial w}{\partial n}(L^-)=\frac{\partial w}{\partial n}(L^+), \tag{2.5}$$

$$M_n(L^-)=M_n(L^+), \tag{2.6}$$

$$V_n(L^-)=V_n(L^+). \tag{2.7}$$

It is important to remark that the free boundary L, the locus separating E and E_1, is unknown.

3 An Asymptotic Solution of the Problem

In order to construct an explicit solution for the problem formulated in the foregoing, it is useful to introduce the notation (see Timoshenko and Woinowski-Krieger [4,§57])

$$\frac{k}{D}=\frac{1}{l^4}, \tag{3.1}$$

and define the nondimensional quantities

$$\frac{w}{l}=v, \quad \frac{r}{l}=\rho. \tag{3.2}$$

Let us introduce the ratios $\alpha=a/l$, $\beta=b/l$ and make the following assumptions:

(1) The number $\lambda=(\alpha-\beta)/(\alpha+\beta)$ is small compared to unity and its square can be disregarded;

(2) The number $R_0=(\alpha+\beta)/2$ is much greater than 1 so that powers on the ratio $1/R_0$ of order higher than 1 can be neglected.

Assumption (1) means that the plate must not be too different from a square plate. Assumption (2), as it will be seen later, implies that the contact set E is small compared to R. It is not strictly necessary, but simplifies subsequent calculations.

In the following, the boundary C of the rectangle will be *approximated* by the curve of equation

$$R(\theta)=R_0(1+\lambda\cos 2\theta) \quad 0\le\theta<2\pi, \tag{3.3}$$

while it is *assumed* that L has the equation

$$\rho(\theta)=\rho_0+\lambda\rho_1\cos 2\theta \tag{3.4}$$

where ρ_0 and ρ_1 are two unknown constants, which must be determined by the conditions of the problem. Equation (3.4) contains the implicit assumption that L is a simple closed continuously differentiable curve; the solution will confirm that this conjecture is correct.

In terms of v and (ρ,θ) equations (2.1) become

$$\left(\frac{\partial^2}{\partial\rho^2}+\frac{1}{\rho}\frac{\partial}{\partial\rho}+\frac{1}{\rho^2}\frac{\partial^2}{\partial\theta^2}\right)\left(\frac{\partial^2 v}{\partial\rho^2}+\frac{1}{\rho}\frac{\partial v}{\partial\rho}+\frac{1}{\rho^2}\frac{\partial^2 v}{\partial\theta}\right)+v=0 \quad 0<\rho<\rho(\theta), \tag{3.5}$$

$$\left(\frac{\partial^2}{\partial\rho^2}+\frac{1}{\rho}\frac{\partial}{\partial\rho}+\frac{1}{\rho^2}\frac{\partial^2}{\partial\theta^2}\right)\left(\frac{\partial^2 v}{\partial\rho^2}+\frac{1}{\rho}\frac{\partial v}{\partial\rho}+\frac{1}{\rho^2}\frac{\partial^2 v}{\partial\theta}\right)=0 \quad \rho(\theta)<\rho<R(\theta). \tag{3.6}$$

It is easy to find particular solutions to equations (3.5) and (3.6). For instance, the function

$$v(\rho,\theta)=C_1 ber\rho+C_2 bei\rho+C_3 ker\rho+C_4 kei\rho+\lambda(D_1 ber_2\rho+D_2 bei_2\rho+D_3 ker_2\rho+D_4 kei_2\rho)\cos 2\theta, \tag{3.7}$$

where $C_1,\ldots,C_4$ and $D_1,\ldots,D_4$ are constants, and $ber\rho,\ldots,kei\rho$, $ber_2\rho,\ldots,kei_2\rho$ are the Kelvin functions of grade zero and two, is a solution to (3.5). Similarly, the function

Nomenclature

a,b = lengths of the sides of the plate
D = flexural rigidity of the plate
k = modulus of the foundation
w = displacement in the direction of the normal
$1/l^4=K/D$ = ratio between the moduli
$v=w/l$ = dimensionless normal displacement
$r/l=\rho$ = dimensionless length
$\alpha=a/l$ = dimensionless length
$\beta=b/l$ = dimensionless length
$\lambda=(\alpha-\beta)/(\alpha+\beta)$ = eccentricity of the plate
$R_0=(\alpha+\beta)/2$ = mean length of the dimensionless sides
$R=R(\theta)$ = equation of the boundary in polar coordinates
$\rho=\rho(\theta)$ = equation of the contact line in polar coordinates

Downloaded 02 May 2010 to 171.66.16.246. Redistribution subject to ASME license or copyright; see http://www.asme.org/terms/Terms_Use.cfm

$$v(\rho,\theta)=a+b\rho^2+c\ln\rho+d\rho^2\ln\rho+\lambda(a_1\rho^2+b_1\rho^{-2}+c_1\rho^4+d_1)\cos2\theta, \tag{3.8}$$

where $a, \ldots, d, a_1, \ldots, d_1$ are constants, is a solution for (3.6).

The arbitrary constants in (3.7) and (3.8) must be determined by using the boundary conditions and the continuity conditions across L. These conditions will be satisfied by neglecting the terms of order higher than one in λ.

From the Taylor expansion of the Kelvin function in the neighborhood of $\rho=0$[1], it is seen that $ker\rho$, $ker_2\rho$, $kei_2\rho$, and their first derivatives are unbounded as $\rho\to0$. Therefore, the conditions that v and $\partial v/\partial\rho$ remain bounded at the origin imply that

$$C_3=D_3=D_4=0. \tag{3.9}$$

Consider now a circle of radius ρ_ϵ around the origin. Using again the Taylor expansions of the Kelvin functions, one has from (2.2)

$$\lim_{\rho_\epsilon\to0}\int_{\Gamma_\epsilon}V_n ds+P=\lim_{\rho_\epsilon\to0}\int_{\Gamma_\epsilon}Q_r ds+P$$

$$=-\frac{D}{l^2}\lim_{\rho_\epsilon\to0}\int_0^{2\pi}\frac{\partial}{\partial\rho}\left(\frac{\partial^2 v}{\partial\rho^2}+\frac{1}{\rho}\frac{\partial v}{\partial\rho}+\frac{1}{\rho^2}\frac{\partial^2 v}{\partial\theta^2}\right)\rho d\theta+P=0, \tag{3.10}$$

where

$$v(\rho,\theta)=-C_4\left(\frac{1}{2}\rho^2\ln\rho+\frac{\pi}{4}+\ldots\right)$$

correct to terms of higher order in ρ.

Condition (3.10) thus yields

$$\frac{D}{l^4}C_4 2\pi+P=0,$$

and, consequently,

$$C_4=-\frac{Pl^4}{2\pi D}. \tag{3.11}$$

The boundedness conditions at $\rho=0$ impose restrictions on the constants in (3.7). Other restrictions on the constants in (3.8) can be found from the boundary conditions on C. If the original boundary is replaced by the curve (3.3), the components of the unit normal vector in the ρ and θ directions are

$$(N_\rho,N_\theta)=\frac{1}{\sqrt{1+\dfrac{4\lambda^2R_0^2}{\rho^2}\cos^2 2\theta}}\left(1,\frac{2\lambda R_0}{\rho}\cos2\theta\right), \tag{3.12}$$

and, this expression, disregarding the terms of order higher than 1 in λ, can be simplified to

$$(N_\rho,N_\theta)\simeq(1,2\lambda\cos2\theta). \tag{3.13}$$

On introducing the stress-resultants M_ρ, M_θ, $M_{\rho\theta}$, Q_ρ, Q_θ in the ρ,θ-system it is possible to write

$$M_n=M_\rho N_\rho^2+M_\theta N_\theta^2+2M_{\rho\theta}N_\rho N_\theta, \tag{3.14}$$

$$M_{nt}=-(M_\rho-M_\theta)N_\rho N_\theta+M_{\rho\theta}(N_\rho^2-N_\theta^2), \tag{3.15}$$

$$V_n=Q_\rho N_\rho+Q_\theta N_\theta+\frac{\partial M_{nt}}{\partial s}$$

$$=Q_\rho N_\rho+Q_\theta N_\theta-\frac{\partial M_{nt}}{\partial\rho}N_\theta+\frac{\partial M_{nt}}{\partial\theta}\frac{N_\rho}{\rho}. \tag{3.16}$$

Neglecting terms of order higher than 1 in λ yields

$$M_n\simeq M_\rho+2M_{\rho\theta}N_\theta, \tag{3.17}$$

$$V_n\simeq Q_\rho+\frac{\partial M_{nt}}{\partial\theta}\frac{1}{\rho}$$

$$\simeq Q_\rho-\frac{1}{\rho}(M_\rho-M_\theta)\frac{\partial N_\theta}{\partial\theta}+\frac{1}{\rho}\frac{\partial M_{\rho\theta}}{\partial\theta}. \tag{3.18}$$

But, on using the constitutive relations

$$M_\rho=-D\left[\frac{\partial^2 v}{\partial\rho^2}+\nu\left(\frac{1}{\rho}\frac{\partial v}{\partial\rho}+\frac{1}{\rho^2}\frac{\partial^2 v}{\partial\theta^2}\right)\right],$$

$$M_{\rho\theta}=-(1-\nu)D\left[\frac{\partial}{\partial\rho}\left(\frac{1}{\rho}\frac{\partial v}{\partial\theta}\right)\right],$$

$$Q_\rho=-D\frac{\partial}{\partial\rho}\left[\frac{\partial^2 v}{\partial\rho^2}+\frac{1}{\rho}\frac{\partial v}{\partial\rho}+\frac{1}{\rho^2}\frac{\partial^2 v}{\partial\theta^2}\right],$$

where D is the flexural rigidity and ν Poisson's ratio, and neglecting again the terms of higher order in λ, M_n, and V_n become

$$M_n\simeq-D\left[\frac{\partial^2 v}{\partial\rho^2}+\nu\left(\frac{1}{\rho}\frac{\partial v}{\partial\rho}+\frac{1}{\rho^2}\frac{\partial^2 v}{\partial\theta^2}\right)\right]_{\rho=R(\theta)}, \tag{3.19}$$

$$V_n\simeq-D\left[\frac{\partial}{\partial\rho}\left(\frac{\partial^2 v}{\partial\rho^2}+\frac{1}{\rho}\frac{\partial v}{\partial\rho}\right)+\frac{\partial}{\partial\rho}\left(\frac{1}{\rho^2}\frac{\partial^2 v}{\partial\theta^2}\right)-\frac{1}{\rho}(1-\nu)\left(\frac{\partial^2 v}{\partial\rho^2}-\frac{1}{\rho}\frac{\partial v}{\partial\rho}\right)\frac{4\lambda R_0}{\rho}\cos2\theta+(1-\nu)\frac{1}{\rho}\frac{\partial}{\partial\rho}\left(\frac{1}{\rho}\frac{\partial^2 v}{\partial\theta^2}\right]_{\rho=R(\theta)} \tag{3.20}$$

The introduction of (3.8) into (3.19) and (3.20) permits us to write the boundary conditions on C in the following form:

$$\left[2b-\frac{c}{\rho^2}+d(2\ln\rho+3)+\lambda\left(2a_1+6\frac{b_1}{\rho^4}+12c_1\rho^2\right)\cos2\theta\right.$$

$$+\frac{\nu}{\rho}\left(2b\rho+\frac{c}{\rho}+d(2\rho\ln\rho+\rho)\right)+\frac{\nu}{\rho}\lambda\left(2a_1\rho-\frac{2b_1}{\rho^3}+4c_1\rho^3\right)$$

$$\left.-\frac{4\nu\lambda}{\rho^2}\left(a_1\rho^2+\frac{b_1}{\rho^2}+c_1\rho^4+d_1\right)\cos2\theta\right]_{\rho=R(\theta)}=0,$$

$$\left[4\frac{d}{\rho}+\lambda\left(-16\frac{b_1}{\rho^5}+32c_1\rho\right)\cos_2\theta-4\lambda\left(-4\frac{b_1}{\rho^5}+2C_1\rho\right.\right.$$

$$\left.-2\frac{d_1}{\rho^3}\right)\cos2\theta-\frac{1}{\rho}(1-\nu)\left(-2\frac{c}{\rho^2}+2d\right)4\lambda\frac{R_0}{\rho}\cos2\theta$$

$$\left.-4(1-\nu)\frac{\lambda}{\rho}\left(a_1-3\frac{b_1}{\rho^4}+3c_1\rho^2-\frac{d_1}{\rho^2}\right)\right]_{\rho=R(\theta)}=0.$$

In these equations $R(\theta)$ is given by (3.3). This expression for $R(\theta)$ is substituted into the equations in the foregoing and the expansions in λ up to the first order are considered. By comparing the coefficients for equal powers of λ, a system of linear equations in b, c, d and a_1, b_1, c_1, d_1 is derived, from which:

$$b=\frac{1-\nu}{1+\nu}\frac{c}{2R_0^2},\quad d=0, \tag{3.21}_1$$

[1] Cf Jahnke-Emde-Lösch [5, IX, B3].

Downloaded 02 May 2010 to 171.66.16.246. Redistribution subject to ASME license or copyright; see http://www.asme.org/terms/Terms_Use.cfm

$$a_1 = \frac{1}{3+\nu}\left[(3-\nu)\frac{c}{R_0^2} + 3(1-\nu)\frac{b_1}{R_0^4} + 2\frac{3+\nu^2}{1-\nu}\frac{d_1}{R_0^2}\right], \quad (3.21)_2$$

$$c_1 = -\frac{1-\nu}{3+\nu}\left[\frac{c}{R_0^4} + 2\frac{b_1}{R_0^6} + \frac{d_1}{R_0^4}\right]. \quad (3.21)_3$$

The remaining constants are determined by the continuity conditions on the free boundary L. If the equations of L in the ρ,θ-coordinates is (3.4) and λ is much smaller than 1, the components of the exterior unit normal vector to L are

$$(n_\rho, n_\theta) = \frac{1}{\sqrt{1+\frac{4\lambda^2}{\rho^2}\rho_1^2\sin^2_{2\theta}}}\left(1, 2\lambda\frac{\rho_1}{\rho}\sin 2\theta\right)$$

$$\simeq \left(1, 2\lambda\frac{\rho_1}{\rho_0}\sin 2\theta\right).$$

Then, up to the terms linear in λ, one obtains

$$\frac{\partial v}{\partial n} = \left[\frac{\partial v}{\partial \rho}n_\rho + \frac{n_\theta}{\rho}\frac{\partial v}{\partial \theta}\right]_{\rho=\rho(\theta)} \simeq \frac{\partial v}{\partial \rho},$$

$$M_n \simeq -D\left[\frac{\partial^2 v}{\partial \rho^2} + \nu\left(\frac{1}{\rho}\frac{\partial v}{\partial \rho} + \frac{1}{\rho^2}\frac{\partial^2 v}{\partial \theta^2}\right)\right]_{\rho=\rho(\theta)},$$

$$V_n \simeq -D\left[\frac{\partial}{\partial \rho}\left(\frac{\partial^2 v}{\partial \rho^2} + \frac{1}{\rho}\frac{\partial v}{\partial \rho} + \frac{1}{\rho^2}\frac{\partial^2 v}{\partial \theta^2}\right) - \frac{1}{\rho}(1-\nu)\left(\frac{\partial^2 v}{\partial \rho^2} - \frac{1}{\rho}\frac{\partial v}{\partial \rho}\right)4\lambda\frac{\rho_1}{\rho_0}\cos 2\theta + (1-\nu)\frac{1}{\rho}\left[\frac{\partial}{\partial \rho}\left(\frac{1}{\rho}\frac{\partial^2 v}{\partial \theta^2}\right)\right]_{\rho=\rho(\theta)}.$$

Once successively replacing (3.7) and (3.8) into these expressions, it is easily verified that the conditions of continuity across L are maintained when

$$v(L^-) = v(L^+) = 0,$$

$$\frac{\partial v}{\partial \rho}(L^-) = \frac{\partial v}{\partial \rho}(L^+),$$

$$\frac{\partial^2 v}{\partial \rho^2}(L^-) = \frac{\partial^2 v}{\partial \rho^2}(L^+),$$

$$\frac{\partial^3 v}{\partial \rho^3}(L^-) = \frac{\partial^3 v}{\partial \rho^3}(L^+),$$

or, in explicit form,

$$\left[C_1 ber\rho + C_2 bei\rho - \frac{Pl^2}{2\pi D}kei\rho + \lambda(D_1 ber_2\rho + D_2 bei_2\rho)\cos 2\theta\right]_{\rho=\rho(\theta)} = 0,$$

$$\left[a + b\rho^2 + cln\rho + \lambda\left(a_1\rho^2 + \frac{b_1}{\rho^2} + c_1\rho^4 + d_1\right)\cos 2\theta\right]_{\rho=\rho(\theta)} = 0,$$

$$\left[C_1 ber'\rho + C_2 bei'\rho - \frac{Pl^2}{2\pi D}kei'\rho + \lambda(D_1 ber_2'\rho + D_2 bei_2'\rho)\cos 2\theta\right]_{\rho=\rho(\theta)} = \left[2b\rho + \frac{c}{\rho} + \lambda\left(2a_1\rho - 2\frac{b_1}{\rho^3} + 4C_1\rho^3\right)\cos 2\theta\right]_{\rho=\rho(\theta)},$$

$$\left[C_1 ber''\rho + C_2 bei''\rho - \frac{Pl^2}{2\pi D}kei''\rho + \lambda(D_1 ber_2''\rho + D_2 bei_2''\rho)\cos 2\theta\right]_{\rho=\rho(\theta)} = \left[2b - \frac{c}{\rho^2} + \lambda\left(2a_1 + 6\frac{b_1}{\rho^4} + 12c_1\rho^2\right)\cos 2\theta\right]_{\rho=\rho(\theta)},$$

$$\left[C_1 ber_\rho''' + C_2 bei''' \rho - \frac{Pl^2}{2\pi D}kei'''\rho + \lambda(D_1 ber_2''' \rho + D_2 bei_2'''\rho)\cos 2\theta\right]_{\rho=\rho(\theta)} = \left[2\frac{c}{\rho^3} + \lambda\left(-24\frac{b_1}{\rho^5} + 24c_1\rho\right)\right]_{\rho=\rho(\theta)},$$

where $\rho(\theta)$ is given by (3.4), and b, a_1, and c_1 by (3.21).

The expansion of the terms of the equations in the foregoing up to the first order in λ and the comparison of the coefficients of equal order in λ, yields the following system

$$C_1 ber\rho_0 + C_2 bei\rho_0 - \frac{Pl^2}{2\pi D}kei\rho_0 = 0, \quad (3.22)_1$$

$$a + b\rho_0^2 + cln\rho_0 = 0, \quad (3.22)_2$$

$$C_1 ber'\rho_0 + C_2 bei'\rho_0 - \frac{Pl^2}{2\pi D}kei'\rho_0 = 2b\rho_0 + \frac{c}{\rho_0}, \quad (3.22)_3$$

$$C_1 ber''\rho_0 + C_2 bei''\rho_0 - \frac{Pl^2}{2\pi D}kei''\rho_0 = 2b - \frac{c}{\rho_0^2}, \quad (3.22)_4$$

$$C_1 ber'''\rho_0 + C_2 bei'''\rho_0 - \frac{Pl^2}{2\pi D}kei'''\rho_0 = 2\frac{c}{\rho_0^3}, \quad (3.22)_5$$

$$\rho_1\left(C_1 ber'\rho_0 + C_2 bei'\rho_0 - \frac{Pl^2}{2\pi D}kei'\rho_0\right) + D_1 ber_2\rho_0 + D_2 bei_2\rho_0 = 0 \quad (3.22)_6$$

$$2b\rho_0\rho_1 + \frac{c}{\rho_0}\rho_1 + a_1\rho_0^2 + \frac{b_1}{\rho_0^2} + c_1\rho_0^4 + d_1 = 0, \quad (3.22)_7$$

$$\rho_1\left(C_1 ber''\rho_0 + C_2 bei''\rho_0 - \frac{Pl^2}{2\pi D}kei''\rho_0\right) + D_1 ber_2'\rho_0 + D_2 bei_2'\rho_0 = 2b\rho_1 - \frac{c}{\rho_0^2}\rho_1 + 2a_1\rho_0 - 2\frac{b_1}{\rho_0^3} + 4c_1\rho_0^3, \quad (3.22)_8$$

$$\rho_1\left(C_1 ber'''\rho_0 + C_2 bei'''\rho_0 - \frac{Pl^2}{2\pi D}kei'''\rho_0\right) + D_1 ber_2''\rho_0 + D_2 bei_2''\rho_0 = 2\frac{c}{\rho_0^3}\rho_1 + 2a_1 + 6\frac{b_1}{\rho_0^4} + 12c_1\rho_0^2, \quad (3.22)_9$$

$$\rho_1\left(C_1 ber^{iv}\rho_0 + C_2 bei^{iv}\rho_0 - \frac{Pl^2}{2\pi D}kei^{iv}\rho_0\right) + D_1 ber_2'''\rho_0 + D_2 bei_2'''\rho_0 = -6\frac{c}{\rho_0^4}\rho_1 - 24\frac{b_1}{\rho^5} + 24C_1\rho_0. \quad (3.22)_{10}$$

These equations can be further simplified by substitution of $(3.22)_3$ into $(3.22)_6$, $(3.22)_4$ into $(3.22)_8$, $(3.22)_5$ into $(3.22)_9$, and the use of relations between the Kelvin functions (see Jahnke-Emde-Lösch [5,IX,B3]). The system thus becomes

$$a + b\rho_0^2 + cln\rho_0 = 0, \quad (3.23)_1$$

$$C_1 ber\rho_0 + C_2 bei\rho_0 = \frac{Pl^2}{2\pi D}kei\rho_0, \quad (3.23)_2$$

Downloaded 02 May 2010 to 171.66.16.246. Redistribution subject to ASME license or copyright; see http://www.asme.org/terms/Terms_Use.cfm

$$C_1 ber'\rho_0 + C_2 bei'\rho_0 = \frac{Pl^2}{2\pi D} kei'\rho_0 + 2b\rho_0 + \frac{c}{\rho_0}, \quad (3.23)_3$$

$$C_1 bei\rho_0 - C_2 ber\rho_0 = -\frac{Pl^2}{2\pi D} ker\rho_0 - 4b, \quad (3.23)_4$$

$$C_1 bei'\rho_0 - C_2 ber'\rho_0 = -\frac{Pl^2}{2\pi D} ker'\rho_0, \quad (3.23)_5$$

$$2b\rho_0\rho_1 + \frac{c}{\rho_0}\rho_1 + a_1\rho_0^2 + \frac{b}{\rho_0^2} + c_1\rho_0{}^4 + d_1 = 0, \quad (3.23)_6$$

$$D_1 ber_2\rho_0 + D_2 bei_2\rho_0 = -2b\rho_1\rho_0 - c\frac{\rho_1}{\rho_0}, \quad (3.23)_7$$

$$D_1 ber_2'\rho_0 + D_2 bei_2'\rho_0 = 2a_1\rho_0 - 2\frac{b_1}{\rho_0{}^3} + 4c_1\rho_0{}^3, \quad (3.23)_8$$

$$D_1 bei_2\rho_0 - D_2 ber_2\rho_0 = -\frac{4}{\rho_0}\left(a_1\rho_0 + \frac{b_1}{\rho_0{}^3} + 4c_1\rho_0^3\right) + 4\rho_1\left(2b\rho_0 + \frac{c}{\rho_0}\right), \quad (3.23)_9$$

$$D_1 bei_2'\rho_0 - D_2 ber_2'\rho_0 = 8a_1\rho_0 - \frac{8}{\rho_0{}^3}\left(1 - \frac{2}{\rho_0^2}\right)b_1 + 16\rho_0^3\left(1 - \frac{2}{\rho_0^2}\right)c_1. \quad (3.23)_{10}$$

By solving equations (3.21) and (3.23) it is possible to determine the constants defining the expressions (3.7), (3.8) together with the radii ρ_0, ρ_1.

4 The Approximate Solution of (3.21) and (3.23)

A rather simple solution to (3.23) can be obtained by making use of the assumption (2) in Section 3. If $1/R_0$ is much smaller than 1, its powers of order greater than 1 can be disregarded. Consequences of this assumption – confirmed by the explicit solution – are that $1 < \rho_0 < < R_0$ and $\rho_1 < < \rho_0$.

Under these conditions, equations (3.21) can be replaced by

$$b = \frac{1-\nu}{1+\nu}\frac{c}{2R_0^2}, \quad d = 0, \quad (4.1)$$

$$a_1 \simeq \frac{3-\nu}{3+\nu}\frac{c}{R_0^2}, \quad c_1 \simeq -\frac{1-\nu}{3+\nu}\frac{c}{R_0^4}, \quad (4.1)_2$$

equations $(3.23)_1$ and $(3.23)_6$ can be simplified into

$$a + c\ln\rho_0 = 0, \quad c\frac{\rho_1}{\rho_0} + d_1 = 0, \quad (4.1)_3$$

and the remaining equations can be replaced by

$$\left.\begin{aligned} &C_1 ber\rho_0 + C_2 bei\rho_0 = \frac{Pl^2}{2\pi D} kei\rho_0, \\ &C_1 ber'\rho_0 + C_2 bei'\rho_o = \frac{Pl^2}{2\pi D} kei'\rho_0 + \frac{c}{\rho_0}, \\ &C_1 bei\rho_0 - C_2 ber\rho_0 = -\frac{Pl^2}{2\pi D} kei\rho_0, \\ &C_1 bei'\rho_0 - C_2 ber'\rho_0 = -\frac{Pl^2}{2\pi D} ker'\rho_0; \end{aligned}\right\} \quad (4.1)_4$$

and

$$\left.\begin{aligned} &D_1 ber_2\rho_0 + D_2 bei_2\rho_0 \simeq -c\frac{\rho_1}{\rho_0}, \\ &D_1 ber_2'\rho_0 + D_2 bei_2'\rho_0 \simeq 2\frac{3-\nu}{3+\nu}\frac{c}{R_0^2}\rho_0 - 2\frac{b_1}{\rho_o{}^3}, \\ &D_1 bei_2\rho_0 - D_2 ber_2\rho_0 \simeq -4\frac{3-\nu}{3+\nu}\frac{c}{R_0^2} - 4\frac{b_1}{\rho_o{}^4} + 4c\frac{\rho_1}{\rho_0}, \\ &D_1 bei_2'\rho_0 - D_2 ber_2'\rho_0 \simeq -8\frac{3-\nu}{3+\nu}\frac{c}{R_0^2}\rho_0 - 8\frac{b_1}{\rho_0^3}\left(1 - \frac{2}{\rho_0^2}\right). \end{aligned}\right\} \quad (4.1)_5$$

Substituting the asymptotic expansions of the Kelvin function into $(4.1)_4$ (cf. Jahnke-Ende-Lösch [5, IX, B3]) and eliminating c, C_1, C_2 one obtains the transcendental equation

$$\mathrm{tg}\left(\frac{\rho_0}{\sqrt{2}} + \frac{\pi}{8}\right) = -\mathrm{cotg}(\sqrt{2}\rho_0),$$

the first positive root of which is

$$\rho_0 = \frac{5\sqrt{2}\pi}{8} \simeq 2.78. \quad (4.2)$$

Once ρ_0 is known, it is easy to find the other unknowns:

$$C_1 = \frac{Pl^2}{2\pi D} e^{-\sqrt{2}\rho_0}\pi(\sqrt{2} + \cos\sqrt{2}\rho_0), \quad (4.3)_1$$

$$C_2 = -\frac{Pl^2}{2\pi D} e^{-\sqrt{2}\rho_0}\pi\sin\sqrt{2}\rho_0, \quad (4.3)_2$$

$$c = -\frac{Pl^2}{2\pi D}\frac{\sqrt{2\pi\rho_0}e^{-\rho_0/2}}{\sin\left(\frac{\rho_0}{\sqrt{2}} - \frac{\pi}{8}\right)}, \quad (4.3)_3$$

$$a = \frac{Pl^2}{2\pi D}\frac{\sqrt{2\pi\rho_0}e^{-\rho_0/2}}{\sin\left(\frac{\rho_0}{\sqrt{2}} - \frac{\pi}{8}\right)} \ln\rho_0. \quad (4.3)_4$$

Using again the asymptotic expansion of the Kelvin functions of order two in $(4.1)_5$ and solving with respect to ρ_1, b_1, D_1, and D_2 one obtains

$$\rho_1 = \frac{3-\nu}{3+\nu}\frac{\rho_0}{R_0^2}\frac{24\sqrt{2} - 4\rho_0 - \left(16\rho_0 - \frac{32}{\sqrt{2}}\right)\left(1 - \frac{2}{\rho_0^2}\right)}{20\sqrt{2}\left(1 - \frac{2}{\rho_0^2}\right) + 3\sqrt{2} - \frac{4}{\rho_0}}, \quad (4.4)_1$$

$$b_1 = \frac{3-\nu}{3+\nu}\frac{c}{R_0^2}\rho_0^3\frac{23\sqrt{2}\rho_0 + 4}{20\sqrt{2}\left(1 - \frac{2}{\rho_0^2}\right) + 3\sqrt{2} - \frac{4}{\rho_0}}, \quad (4.4)_2$$

$$D_1 = -\frac{4}{bei_2\rho_0}\left[\frac{3-\nu}{3+\nu}\frac{c}{R_0^2} + \frac{b_1}{\rho_0^4} - c\frac{\rho_1}{\rho_0}\right], \quad (4.4)_3$$

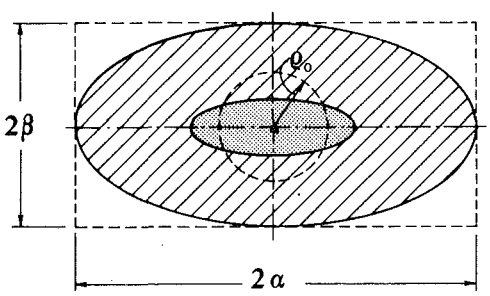

Fig. 3

Downloaded 02 May 2010 to 171.66.16.246. Redistribution subject to ASME license or copyright; see http://www.asme.org/terms/Terms_Use.cfm

$$D_2 = -\frac{c}{bei_2\rho_0}\frac{\rho_1}{\rho_0}. \qquad (4.4)_4$$

It is clear that this result confirms the correctness of the initial conjecture $\rho_1 << \rho_0$. Since ρ_1 is positive the contact set E has the major axis parallel to the larger side of the rectangle (Fig. 3). In the figure, the original boundary of the rectangle is replaced by the curvilinear contour, which, in the present approximate analysis, is assumed as the boundary of the plate.

It may be worthwhile to remark that ρ_0 and ρ_1 do not depend on the magnitude of P. In addition, the deflection at the origin (given by setting $\rho = 0$ in (3.7)) depends only on the terms of first order since

$$ber_2(0) = bei_2(0) = 0,$$

and

$$D_3 = D_4 = 0.$$

Both of these properties seem somewhat unexpected.

Remark. As α tends to infinity and β remains fixed, the plate tends to assume the shape of an infinite strip pressed against an elastic foundation by a force P concentrated at the origin. The results of the present analysis no longer apply, since λ tends to one as α tends to infinity, and, consequently, the procedure of asymptotic expansion of solutions in λ fails. Nevertheless it is interesting to note that R_0 tends to infinity as α tends to infinity, and therefore ρ_1, given by $(4.4)_1$, tends to zero. It follows that the major axis of the contact region is $\rho_0 \simeq 2.78$.

The calculation (performed by Weitsman [3]) of the half-amplitude of the contact interval of an infinite beam on an elastic foundation that reacts in compression only is $\rho'_0 = \pi/\sqrt{2} \simeq 2.22$. On considering the unilateral contact between a layer and a half space Keer, Dundurs, and Tsai [6] showed that Weitsman's results can be recovered as limit of the three-dimensional case when the layer is rather stiff in comparison to the foundation.

References

1 Hertz, H., "Über das Gleichgewicht Schwimmender Elastischer Platten," *Gesammelte Werke*, Vol. 1, 1895, p. 228.

2 Föppl, A., *Vorlesungen über Technische Mechanik*, Teubner, Leipzig/Berlin, 1920.

3 Weitsman, Y., "On Foundations That React in Compression Only," ASME JOURNAL OF APPLIED MECHANICS, Vol. 37, 1970, pp. 1019–1030.

4 Timoshenko, S., and Woinowski-Krieger, S., *Theory of Plates and Shells*, McGraw-Hill, New York/London, 1959.

5 Jahnke, E., Emde, F., and Lösch, F., *Tafeln Höherer Funktionen*, Tuebner, Stuttgart, 1966.

6 Keer, L. M., Dundurs, J., and Tsai, K. C., "Problems Involving a Receding Contact Between a Layer and a Half Space," ASME JOURNAL OF APPLIED MECHANICS, Vol. 39, 1972, pp. 1115–1120.

Downloaded 02 May 2010 to 171.66.16.246. Redistribution subject to ASME license or copyright; see http://www.asme.org/terms/Terms_Use.cfm

F. T. Geyling

K. L. Walker

R. Csencsits

Bell Laboratories,
600 Mountain Avenue,
Murray Hill, N.J. 07974

The Viscous Collapse of Thick-Walled Tubes

The collapse of glass tubes, as used in the manufacture of optical fiber preforms, constitutes a problem involving Stokes flow, driven by surface tension and applied pressure. Undesirable, noncircular modes of deformation may grow or decay, depending on initial tube dimensions, radial viscosity variations, and the pressure differential across the tube wall. A two-dimensional model of the collapse process has been developed. Numerical results show trends that agree with experimental observations and are useful in the control of actual, three-dimensional collapse.

1 Introduction

The manufacture of high-precision optical components, such as lenses and prisms, has been traditionally accomplished in the glass industry by grinding and polishing solid pieces of material. This state of the art is changing somewhat with the advent of optical fiber technology, where dimensional control in the liquid state is often the preferred, if not the only feasible approach. Thus an interest in slow, essentially Newtonian, flows with carefully controlled free surfaces has been generated. One example of this trend is the manufacture and processing of so-called preform tubes. In this paper we address the process by which such tubes are collapsed to solid rods the preforms from which optical fibers can be drawn.

The preform collapse process involves slow viscous flow of the glass, driven by surface tension and differential pressures on the inner and outer tube surfaces, rather than contact forces from dies and tools, as used in other forming processes. By and large, physical contact with preform tubes must be avoided to minimize contamination.[1]

During collapse, departures from the nominally circular shape may occur and are of primary interest in process control. The time evolution of these perturbations is a gradual departure from axisymmetry, rather than a distinct bifurcation as encountered with typical buckling phenomena. Nevertheless, we shall loosely refer to such deformations as "instabilities" if they grow in magnitude.

The standard collapse process for preform tubes is commonly executed on a glass lathe. While the tube rotates to preserve axisymmetry, a torch traverses along its length, producing a local hot zone where the glass softens sufficiently to permit viscous flow of the tube walls. Several passes of the torch are usually needed to collapse the tube to a solid rod. As the heated portion of tubing necks down, it is partially supported by adjacent sections of tubing at lower temperatures. The collapse process is therefore truly a three-dimensional one. One may argue, however, that for long hot zones the three-dimensional end effects lose significance and a two-dimensional representation of collapse, neglecting variations with the axial coordinate, z, can be quite acceptable. Further refinements of this qualitatively correct model of tube collapse cannot be justified at the present, since glass viscosities are subject to uncertainties resulting from inaccurate measurements of local temperatures and glass compositions in typical preform tubes.

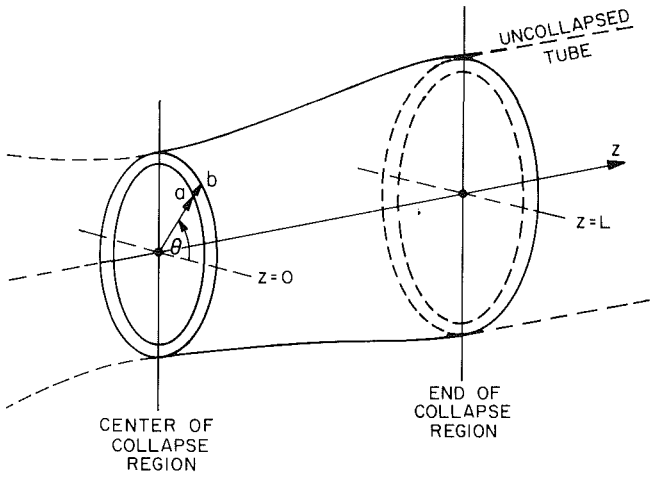

Fig. 1 Schematic of collapse zone

Section 2 defines the physical problem in detail and presents the approach to modeling viscous collapse, adopted in this paper. Results for uniform viscosity, i.e., homogeneous tubes, are summarized in Section 3. Numerical solutions of the differential equations for the more relevant, and more difficult, case of nonuniform viscosity are discussed in

[1] Both, the Newtonian characteristics and the absence of surface loads distinguish the hot forming of glasses and ceramics from that of metals and plastics. The latter material processes have been modeled extensively as flow problems involving elastic-plastic and non-Newtonian media. Unfortunately, none of this literature is of much help in dealing with the viscous collapse of preform tubes.

Contributed by the Applied Mechanics Division for presentation at the 1983 Applied Mechanics, Bioengineering, and Fluids Engineering Conference, Houston, Texas, June 20–22, 1983 of THE AMERICAN SOCIETY OF MECHANICAL ENGINEERS.

Discussion on this paper should be addressed to the Editorial Department, ASME, United Engineering Center, 345 East 47th Street, New York, N.Y. 10017, and will be accepted until two months after final publication of the paper itself in the JOURNAL OF APPLIED MECHANICS. Manuscript received by ASME Applied Mechanics Division, March 1982; final revision, January, 1983. Paper No. 83-APM-27.

Copies will be available until February, 1984.

Copyright © 1983 by ASME
Downloaded 02 May 2010 to 171.66.16.246. Redistribution subject to ASME license or copyright; see http://www.asme.org/terms/Terms_Use.cfm

Section 4. Section 5 presents results for tubes of nonuniform viscosity. Some comparisons with experimental observations and conclusions are also given.

2 Problem Statement and Analytic Formulation

Figure 1 illustrates the geometry of a typical collapse zone in preform tubes. The neckdown region is centered at $z=0$ and tapers off toward $z=\pm L$, in both directions along the tube axis. Our two-dimensional model addresses deformations at $z=0$ as if this section were part of an infinite cylinder, shrinking uniformly, without end effects. In short, a plane-strain assumption is made for the deformations of such a cross section throughout its collapse history.

The cross-sectional geometry is described by polar coordinates r, θ, with inner and outer radii a and b. The relevant material property is viscosity $\mu(r)$, which may be nonuniform throughout the cross section. Fluid density does not enter into our model because of the very low accelerations involved. Surface loadings are given by inner and outer pressures $P_a(\theta)$ and $P_b(\theta)$, as well as surface tension σ. The purpose of this model is to simulate the time history of tube deformations which are produced by initial noncircularities of the tube, various surface loadings, and viscosity variations in the tube wall, due to variations in glass temperature and composition.[2]

The viscous flow problem for the tube walls is formulated in terms of primitive variables, i.e., the velocity components and pressure. These were chosen in preference to a stream function/vorticity formulation for the sake of physical insight. The Stokes equations in polar coordinates r, θ read [2] as follows:

Radial equilibrium

$$ru_{rr}+\left(3+\frac{2r\,\mu_r}{\mu}\right)u_r+\frac{u}{r}+\frac{u_{\theta\theta}}{r}-\frac{rp_r}{\mu}=0 \qquad (2\text{-}1)$$

Azimuthal equilibrium

$$(r^3V_r)_r+\frac{r^3\mu_rV_r}{\mu}+\left(1+\frac{r\,\mu_r}{\mu}\right)u_\theta-ru_{r\theta}-\frac{rp_\theta}{\mu}=0 \qquad (2\text{-}2)$$

Continuity

$$\frac{u}{r}+u_r+V_\theta=0 \qquad (2\text{-}3)$$

where

u = radial velocity
v = azimuthal velocity
V = v/r
p = hydrostatic pressure
μ = viscosity

and subscripts r, θ denote partial derivatives. The two stress boundary conditions at the inner and outer free surfaces $r=R_a(\theta)$ and $r=R_b(\theta)$ can be written as

$$4u_rR_\theta+(R^2V_r+u_\theta)\left[1-\left(\frac{R_\theta}{R}\right)^2\right]=0 \qquad (2\text{-}4)$$

and

$$-p+2\mu(u_r-R_\theta V_r-R_\theta u_\theta/R^2)=-P\pm K\sigma \qquad (2\text{-}5)$$

where R = R_a and R_b as appropriate, corresponding to $-$ and $+$ signs of the last term in (2-5)
K = $K_a(\theta)$ or $K_b(\theta)$ the free surface curvatures
σ = surface tension
P = $P_a(\theta)$ or $P_b(\theta)$ the applied pressures.

It remains to express the free-surface deformation rates in terms of velocity components u, v.

One finds

$$R_t=[u]-[v]\frac{R_\theta}{R} \qquad (2\text{-}6)$$

where $R=R_a$ or R_b and u, v are evaluated along $R_{a,b}(\theta)$, representing the current deformed boundary configuration, and the subscripts t, θ indicate differentiation.[3]

The space-time solution of (2-1)–(2-6) is $u(r,\theta,t)$, $V(r,\theta,t)$, $p(r,\theta,t)$, and $R_{a,b}(\theta,t)$. Analytic procedures seem out of the question for $\mu \neq const.$ To begin with, it is expedient to separate the spatial and time integrations. The latter is executed as a sequence of finite steps Δt, once a method has been determined for calculating the velocity field for any instantaneous boundary geometry and surface loading of the cross section. Thus, if solution of (2-1)–(2-5) for the nth time step, using $R^{n-1}_{a,b}$ for the tube geometry from the preceding time step, yields u^n, v^n, this leads to R^n_{a,b_t} by means of (2-6) and then permits updating the tube deformation according to

$$R^n_{a,b}=R^{n-1}_{a,b}+\Delta t\,R^n_{a,b_t}. \qquad (2\text{-}7)$$

The main effort of this study had to concern itself with the spatial solution of (2-1)–(2-5), especially for cases where the viscosity varies drastically through the tube wall. For $\mu \equiv const.$ the viscous flow problem defined by (2-1)–(2-5) has an exact dual in the two-dimensional theory of elasticity, where complex variable techniques can be used to develop elegant, analytic solutions in polar coordinates [3]. However, this formalism breaks down if μ becomes variable and numerical techniques have to be used.

Direct numerical solution of the partial differential equations in r and θ by finite differences or by finite element methods was considered. However, geometric distortions of the cross section can only be extracted from such computations by further processing of the results, viz. a Fourier analysis of boundary displacements. Alternatively, the most direct and computationally efficient approach to tube deformations consists of formulating (2-1)–(2-5) in terms of Fourier components to begin with.

[2] The axially symmetric version of this problem has been treated previously by J. A. Lewis [1].

[3] Equations (2-1)–(2-6) can be nondimensionalized with the following factors (see Nomenclature and Section 4 for quantities relating to composite tubes): lengths: $1/c$, where c = initial interface radius; stress or pressure: c/σ; velocity: μ_b/σ; time: $\sigma/(c\mu_b)$. Consequently, (2-1,3) will be multiplied by $c\mu_b/\sigma$ and (2-2,6) by μ_b/σ. We assume that this has been done, without change of notation.

Nomenclature

a = inner radius
b = outer radius
c = interface radius
μ_b = viscosity of outer layer (silica tube)
μ_a = viscosity of inner layer (low viscosity deposit)
R = general symbol for free surface radii
K = general symbol for free surface curvatures
P = general symbol for applied pressures
r,θ = polar coordinates
u,v = radial and azimuthal velocities
V = v/r
p = hydrostatic pressure
σ = surface tension
$(\,)'$ = $\partial(\,)/\partial r$
W = V'
subscript 0 = 0(1) quantities
subscript 2 = $0(\epsilon)$ quantities

Downloaded 02 May 2010 to 171.66.16.246. Redistribution subject to ASME license or copyright; see http://www.asme.org/terms/Terms_Use.cfm

We assume that the solution can be described by a regular expansion of the form

$$F=f_0+\sum_{n=1}^{\infty}\epsilon^n\sum_{m=1}^{\infty}(f_{nm}\cos m\,\theta+g_{nm}\sin m\,\theta) \tag{2-8}$$

where f_0 represents the unperturbed axisymmetric tube collapse and f_{nm}, g_{nm} represent departures from circularity. From a practical point of view, we are primarily interested in small departures from circularity ($\epsilon<0.15$) and can therefore restrict the expansion (2-8) to $O(\epsilon)$. It can be argued physically that the collapse will be most sensitive to deformations of the form $\cos 2\theta$, $\sin 2\theta$ and we therefore truncate the Fourier expansion at $m=2$. These terms represent flattening of the tube and ellipticity of the resulting preform core.

The ansatz used for individual variables is:

$$\begin{aligned}
u(r,\theta) &= u_o(r)+u_2(r)\cos 2\theta\\
v(r,\theta) &= v_2(r)\sin 2\theta\\
V(r,\theta) &= V_2(r)\sin 2\theta\\
p(r,\theta) &= p_0(r)+p_2(r)\cos 2\theta\\
P(\theta) &= P_0+P_2\cos 2\theta\\
R(\theta) &= R_0+R_2\cos 2\theta\\
K(\theta) &= K_0+K_2\cos 2\theta,
\end{aligned} \tag{2-9}$$

the latter three expressions holding at both surfaces, i.e., $R\to R_{a,b}$, $P\to P_{a,b}$ and $K\to K_{a,b}$. Quantities with subscript zero are 0(1) and with subscript 2 are $0(\epsilon)$.

Using the notation $d(\ )/dr=(\ )'$, equation (2-1) yields to 0(1)

$$ru_0''+\left(3+\frac{2r\,\mu'}{\mu}\right)u_0'+\frac{1}{r}u_0-\frac{r}{\mu}p_0'=0 \tag{2-10}$$

and to $0(\epsilon)$

$$ru_2''+\left(3+\frac{2r\,\mu'}{\mu}\right)u_2'-\frac{3}{r}u_2-\frac{rp_2'}{\mu}=0. \tag{2-11}$$

Similarly, equation (2-2) yields to $0(\epsilon)$

$$r^3V_2''+\frac{r^3\mu'}{\mu}V_2'-2\left(1+\frac{r\,\mu'}{\mu}\right)u_2+2ru_2'+\frac{2rp_2}{\mu}=0 \tag{2-12}$$

Finally, from (2-3) to 0(1)

$$(ru_0)'=0 \tag{2-13}$$

and to $0(\epsilon)$

$$\frac{u_2}{r}+u_2'+2V_2=0. \tag{2-14}$$

In an analogous fashion, the b.c's (2-4) and (2-5), may be separated into 0(1) and $0(\epsilon)$ terms. To $0(\epsilon)$ equation (2-4) yields

$$-8R_2u_0'+R_0^2V_2'-2u_2=0 \tag{2-15a,b}$$

while (2-5) yields to 0(1)

$$-p_0+2\mu\,u_0'=-P_0\pm K_0\sigma \tag{2-16a,b}$$

and to $0(\epsilon)$

$$-p_2+2\mu u_2'+(2\mu'u_0'+2\mu u_0''-p_0')R_2=-P_2\pm K_2\sigma, \tag{2-17a,b}$$

where the last term on the left results from the $0(\epsilon)$ extrapolation of 0(1) quantities to the deformed boundary, viz.

$$[u,v,p,\mu]_R=[u,v,p,\mu]_{R_0}+[u',v',p',\mu']_{R_0}R_2\cos 2\theta. \tag{2-18a,b}$$

Note that the Fourier expansion permits separation of variables, where the factors $\cos 2\theta$, $\sin 2\theta$ cancel out of all equations, leaving a set of ordinary differential equations in r to be solved numerically at each time step. The results of this integration are used to update the inner and outer mean radii a, b, and their $0(\epsilon)$ perturbations a_2, b_2 by a predictor-corrector algorithm.

The 0(1) problem (2-10), (2-13), and (2-16) simplifies as follows. From (2-13)

$$u_0=\frac{U}{r} \tag{2-19}$$

where U is an integration constant and, from (2-10), the integration of the following differential equation

$$p_0'=\frac{-2U\,\mu'}{r^2} \tag{2-20}$$

involves another constant. These two constants follow from the b.c.'s

$$\overline{p_0}+\frac{2\bar{\mu}U}{R_0^2}=P_0\pm\frac{\sigma}{R_0} \tag{2-21a,b}$$

which are obtained from (2-16) with $K_0=1/R_0$. Barred quantities designate the values of variables at $r=R_0\equiv a,b=$ current values of inner and outer mean radii.

Using (2-14), (2-19), (2-21), and $K_2=3R_2/R_0^2\cos 2\theta$ to simplify (2-11), (2-12), (2-15), and (2-17), the $0(\epsilon)$ system becomes

$$u_2'=-\frac{u_2}{r}-2V_2 \tag{2-22}$$

$$p_2'=-2\left(\frac{2\mu}{r}+\mu'\right)\frac{u_2}{r}-4\left(\frac{\mu}{r}+\mu'\right)V_2-2\mu W_2 \tag{2-23}$$

$$W_2'=-\left(\frac{3}{r}+\frac{\mu'}{\mu}\right)W_2+\frac{2}{r^2}\left(\frac{2}{r}+\frac{\mu'}{\mu}\right)u_2+\frac{4}{r^2}V_2-\frac{2p_2}{r^2\mu} \tag{2-24}$$

where

$$V_2'=W_2 \tag{2-25}$$

with the b.c.'s

$$R_0^2\bar{W}_2-2\bar{u}_2=\frac{8R_2U}{R_0^2} \tag{2-26a,b}$$

$$\bar{p}_2+\frac{2\bar{\mu}\bar{u}_2}{R_0}+4\bar{\mu}\bar{V}_2=\frac{4UR_2\bar{\mu}}{R_0^3}+P_2\pm\frac{3\sigma R_2}{R_0^2}. \tag{2-27a,b}$$

The fact that barred quantities are evaluated at the limits of integration a, b does *not* mean that the solution of (2-20), (2-22)–(2-25) is confined to these radii. The solution is actually carried to the deformed boundaries by including extrapolations such as (2-18) in the b.c.'s.

The computational algorithm is now completed by writing explicitly for each time step

$$\begin{aligned}
a^{n+1} &= a^n+[u_0^n]_{r=a}\Delta t\\
b^{n+1} &= b^n+[u_0^n]_{r=b}\Delta t\\
a_2^{n+1} &= a_2^n\left\{1+[u_0'^n]_{r=a}\Delta t\right\}+[u_2^n]_{r=a}\Delta t\\
b_2^{n+1} &= b_2^n\left\{1+[u_0'^n]_{r=b}\Delta t\right\}+[u_2^n]_{r=b}\Delta t
\end{aligned} \tag{2-28}$$

where superscripts designate indices in the time sequence.

Finally, one notes that a preform tube whose viscosity varies through the wall thickness due to compositional and thermal gradients, can be modeled either by letting μ be a continuous function of r or by defining discrete layers with different but constant viscosities. Either way, some account must be given of distortions in the viscosity profile across the wall thickness, due to internal mass transport during the deformation process. The viscosity profile in typical preform

Downloaded 02 May 2010 to 171.66.16.246. Redistribution subject to ASME license or copyright; see http://www.asme.org/terms/Terms_Use.cfm

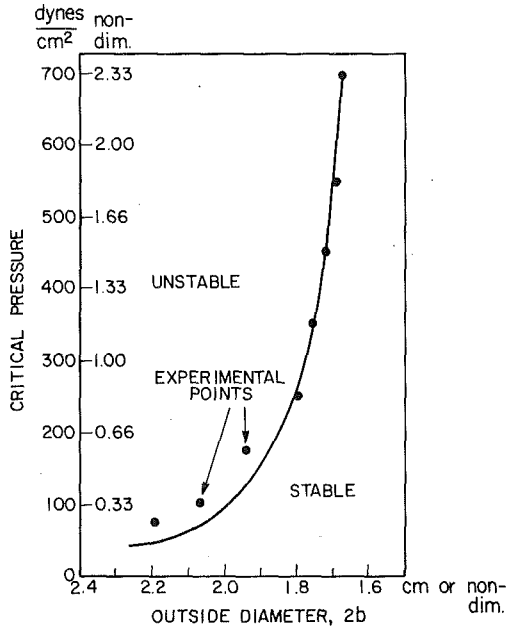

Fig. 2 Critical pressure versus outer diameter, 2*b*

tubes is roughly a step change between the high viscosity silica tube and the lower viscosity deposit. The layer interfaces in the discrete-layer model are treated as internal boundaries, requiring continuity of stresses and velocities. Diplacements of these interfaces are indicative of distortions in the viscosity profile.

3 Results for Uniform Viscosity

We begin by discussing the viscous flow of homogeneous silica tubes, based on our two-dimensional numerical simulations. This initial study elucidates some basic features of viscous tube collapse and serves for later comparison with more complicated models involving nonuniform viscosity. Recall that the tube dimensions can be expressed as

$$a = a_0 + a_2 \cos 2\theta$$

and

$$b = b_0 + b_2 \cos 2\theta$$

where a and b are the inner and outer surfaces, respectively.

One defines a critical pressure as the value of $\Delta P = (P_b - P_a)$ at which the ellipticity neither grows nor decays. The ellipticity grows if the pressure difference is larger than this value and decays if it is smaller. The critical ΔP rises as a silica tube collapses because stability increases as the walls become thicker.

The critical pressure difference was experimentally determined during the collapse of silica tubes. The ellipticity was first measured along the entire length of a tube using an optical line scan camera with 2000 diodes. The camera measures the tube diameter as a function of time. The ellipticity causes the diameter to vary through two periods per revolution of the tube. The diameter variation data from the line scan camera is fitted by a computer to a function of the form

$$b(t) = b_0 + b_2 \cos(2\omega t + \phi)$$

where ω is the rotational frequency of the tube and ϕ is a phase shift angle. This procedure allows the determination of b_0 and b_2 as a function of position. The torch was then traversed the length of the tube, resulting in a shrinkage of about 5 percent. The internal pressure was varied linearly during this collapse pass. The ellipticity was measured a second time and compared with the previous measurement. It was found there were two distinct regions; in one section of the tube the ellipticity grew and in the other it decayed. At the point separating these two regions the ellipticity remained constant, corresponding to the critical pressure.

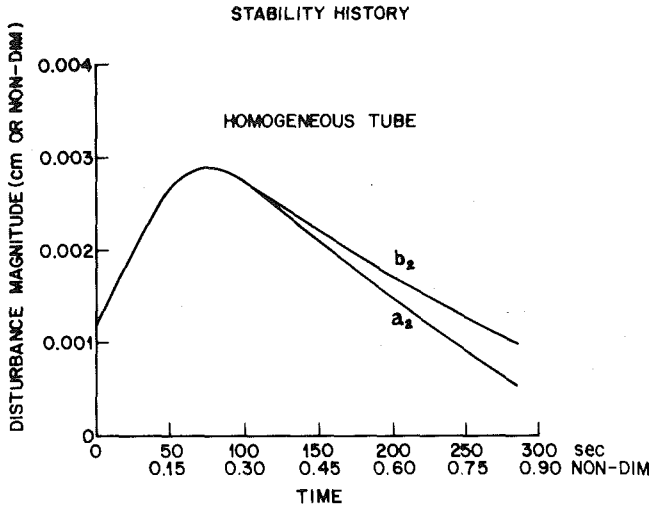

Fig. 3 *Deformation history of homogeneous tube*

Figure 2 compares the theoretical and the experimentally measured critical pressures as a 19×25 mm tube collapses. The excellent quantitative agreement verifies the accuracy of the theoretical model.

Also of interest is the time behavior of the perturbation quantities a_2 and b_2 which specify the magnitude of the tube flattening. Typical initial perturbations in the starting tube[4] are assumed to be $\bar{a}_2 = \bar{b}_2 = 0.001$ cm and we use a value for the surface tension of $\sigma = 300$ dynes/cm.

The history of tube deformation during collapse is shown in Fig. 3 for a pressure difference $\Delta P = 100$ dynes/cm^2 (0.04 in. of water) between outer and inner surface and initial radii $a_0 = 1.0$ cm and $b_0 = 1.3$ cm.[5] It can be seen that a_2 and b_2 develop nonmonotonically in time, increasing initially, but as the tube radius decreases, the disturbance eventually decays in magnitude. The pressure difference ΔP acts to destabilize the tube deformation, whereas surface tension forces σ/R have a stabilizing effect. As the tube shrinks in size, the stabilizing force increases in magnitude and eventually causes the disturbances to decay.

The geometry of the preform rod, which is the result of complete collapse, is of physical interest. The final deformation of the homogeneous tube is presented in terms of $\epsilon_b = b_2/b_0$, i.e., a fractional distortion of the outer surface. Figure 4 shows the dependence of ϵ_b on the pressure difference ΔP for the case of $\bar{a} = 1.0$ cm and $\bar{b} = 1.3$ cm.[6] It can be seen that ϵ_b is very sensitive to ΔP, varying from $\epsilon_b = 0.0014$ at $\Delta P = 100$ dynes/cm^2 (~ 0.04 in. of water) to $\epsilon_b = 0.013$ at $\Delta P = 250$ dynes/cm^2 (0.1 in. of water). The dependence of ϵ_b on the initial tube wall thickness $d = \bar{b} - \bar{a}$ is shown in Fig. 5 for $\bar{a} = 1.0$ cm and $\Delta P = 100$ dynes/cm^2. As one might expect, thinner-walled tubes are more susceptible to flattening than thicker-walled tubes. The foregoing results also illustrate that the fundamental flattening mode develops gradually in time, i.e., as a divergence from the axisymmetric condition rather than a sudden departure from circularity.

[4] Note that the response of disturbances in the linear model, expressed by (2-1)–(2-5), will scale directly with the magnitude of initial perturbations.

[5] While the numerical results of Sections 3–5 are discussed in dimensional terms, for the benefit of those involved with lightguide technology, numerical values on the plots are also supplied in nondimensional form to facilitate their application to entirely different physical situations.

[6] In this context, barred quantities represent initial values of the tube radii.

Downloaded 02 May 2010 to 171.66.16.246. Redistribution subject to ASME license or copyright; see http://www.asme.org/terms/Terms_Use.cfm

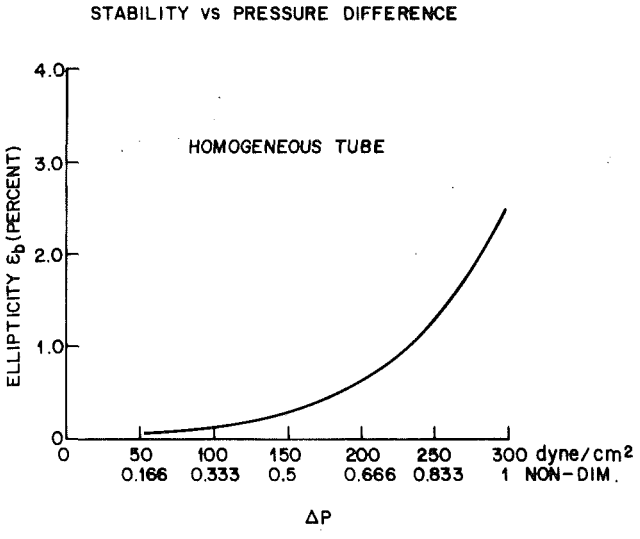

Fig. 4 Stability versus ΔP; homogeneous tube

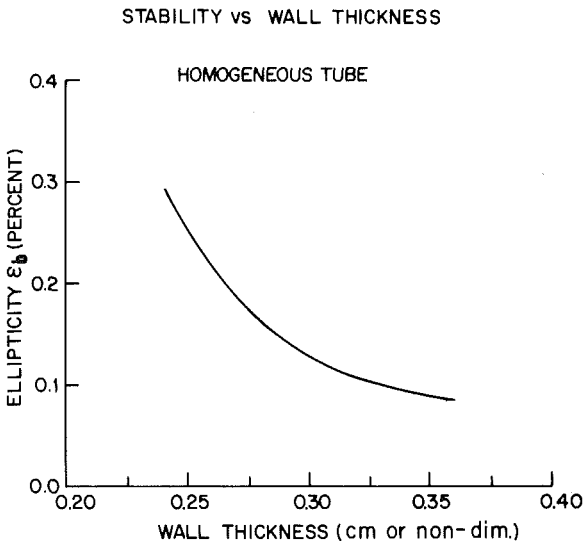

Fig. 5 Stability versus wall thickness; homogeneous tube

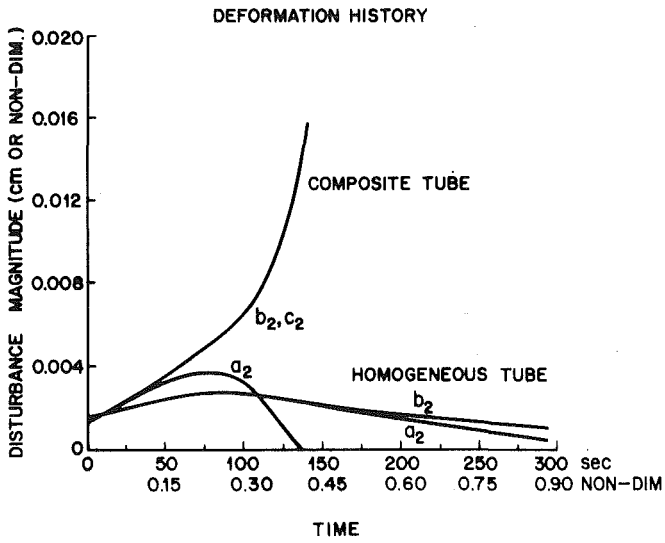

Fig. 6 Deformation history of composite tube

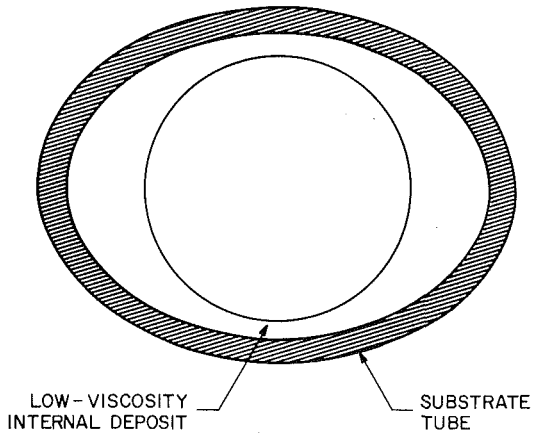

Fig. 7 Deformed composite cross section

4 Numerical Solutions for Nonuniform Viscosity

The remaining discussion of this paper will concern the more relevant case of a high-viscosity tube, the silica "substrate," containing a low-viscosity internal layer, a doped glass deposit that constitutes the waveguide core. Let the interface radius between the low and high-viscosity layers be designated c. The formulation of Section 2 must now be generalized in terms of two boundary value problems, one for each layer, with continuity conditions imposed on the stresses and velocity components at the interface. Whereas a straightforward shooting procedure and linear combination of independent solutions (with individual, normalized b.c.'s) sufficed in dealing with the single-layer case, the two-layer model requires careful planning of the numerical procedure. This is true especially for cases involving large viscosity ratios between the substrate and the deposit, where "boundary layer" effects occur near the interface in the $0(\epsilon)$ solution. If the numerical results fail to capture this feature of the spatial velocity profile, the time evolution of deformations will also be adversely affected.

The necessary continuity conditions at the layer interface give rise to the following equations at $r=c$. Letting quantities in the inner layer ($a \le r \le c$) be denoted by subscript $-$ and in the outer layer ($c \le r \le b$) by subscript $+$, the continuity of velocity components yields at $r=c$:

$$u_0 = u_{0_+} \quad \text{hence} \quad U_- = U_+; \quad u_2 = u_{2_+}; \quad V_{2_-} = V_{2_+}. \tag{4-1}$$

From (2-23), one observes that

$$\left[\frac{p_2'}{2\mu} + V_2'\right]_- = \left[\frac{p_2'}{2\mu} + V_2'\right]_+, \tag{4-2}$$

to be used in the following. Continuity of the radial stress yields

$$p_{0_+} - p_{0_-} = \frac{2U}{c^2}(\mu_- - \mu_+) \tag{4-3}$$

and

$$p_{2_+} - p_{2_-} = 2(\mu_+ - \mu_-)\left[\frac{2c_2}{c^3}U - V_2 + \frac{cV_2'}{2} + \frac{cp_2'}{4\mu}\right], \tag{4-4}$$

where $c_2 = 0(\epsilon)$ radial deformation at $r=c$. Note that, in view of (4-2), it is immaterial from which of the two layers the last two terms in the square brackets are computed. Continuity of the shear stress yields

$$\mu_+ V_{2_+}' - \mu_- V_{2_-}' = 2(\mu_- - \mu_+)\left[\frac{4c_2}{c^4}U + \frac{V_2}{c} + \frac{p_2'}{4\mu} + \frac{V_2'}{2}\right]. \tag{4-5}$$

Downloaded 02 May 2010 to 171.66.16.246. Redistribution subject to ASME license or copyright; see http://www.asme.org/terms/Terms_Use.cfm

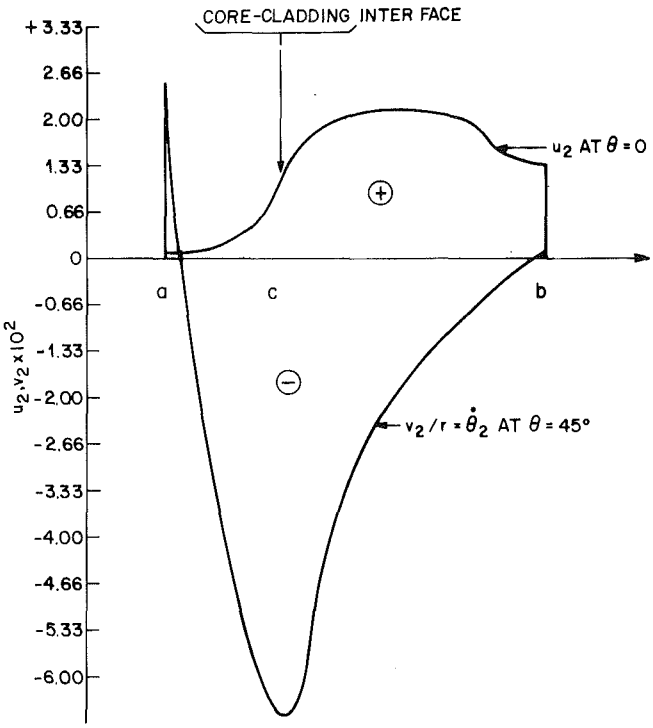

Fig. 8 Velocity plots across wall thickness

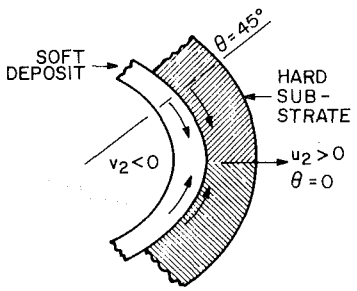

NOTE = $v_2 < 0$ IMPLIES TRANSPORT OF MATERIAL TOWARD BULGE IN TUBE WALL AT $\theta = 0$.

Fig. 9 Schematic of flow in tube wall

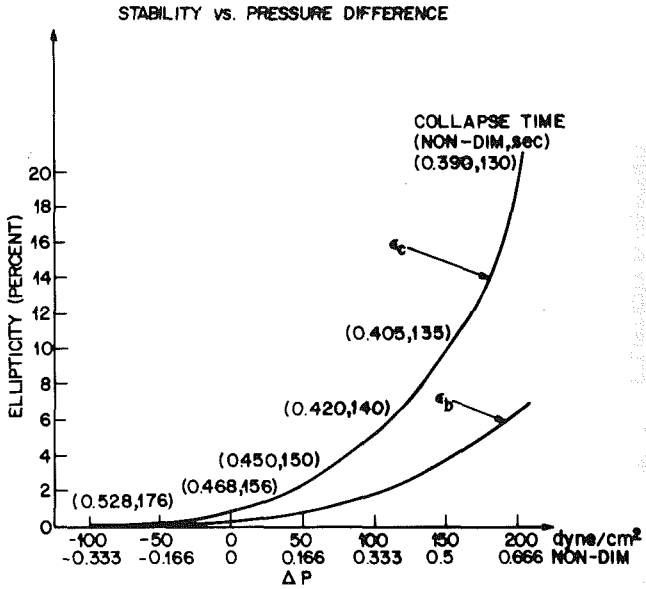

Fig. 10 Stability versus ΔP

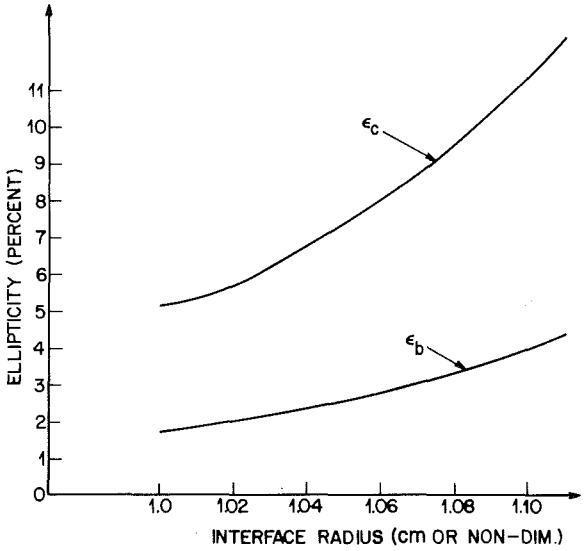

Fig. 11 Stability versus interface radius

Equations (4-3)–(4-5) represent jump conditions in p_0, p_2, and V_2', to be satisfied at the interface.

The 0(1) solutions for the two layers are found from (2-19)–(2-21) and (4-3) in simple analytic form.

The most straightforward numerical approach to the $0(\epsilon)$ problem consists of integrating across the wall thickness, taking care of conditions at c along the way. Since four b.c.'s are imposed by (2-26), (2-27), one may generate four independent solutions by integrating, say, from a to b; each of these solutions being normalized to $[u_2]_{r=a} = 1$, $[p_2]_{r=a} = 1$, $[V_2]_{r=a} = 1$, $[W_2]_{r=a} = 1$, in turn with the remaining i.c.'s zero. Each integration proceeds continuously across $r=c$. A "particular" solution is then generated with homogeneous i.c.'s at $r=a$ and accommodating the jump conditions (4-4)–(4-5) in p_2 and V_2' at $r=c$. A linear combination of these five solutions satisfies the b.c.'s. Numerical integration for this approach was effected with an extrapolative integration algorithm, using spline functions (4). This procedure yielded reasonable results for modest viscosity ratios ($0(10^2)$) between inner and outer layer, which we describe in the following.

Let a "standard" tube geometry be specified by

interior radius	$a = 0.95$ cm
interface radius	$c = 1.00$ cm
exterior radius	$b = 1.30$ cm
viscosity of "soft" interior deposit	$\mu_a = 2 \times 10^3$ poise
viscosity of "hard" outer shell	$\mu_b = 10^5$ poise
applied pressure difference	$\Delta P = 100$ dynes/cm^2

This set of parameters will henceforth be used as a reference case.

The time history of a composite tube for the preceding conditions is compared with the corresponding homogeneous tube in Fig. 6. As mentioned before, the substrate by itself behaves nonmonotonically, with a_{2H} and b_{2H} reaching a maximum and thereafter decaying gradually as surface tension overcomes the initial growth of perturbations. By comparison, the composite tube behaves quite differently. It collapses in less than half the time required for the homogeneous tube and all three perturbations a_{2c}, c_{2c}, b_{2c} rise above their counterparts for the homogeneous tube a_{2H}, b_{2H} early in the collapse history. The disturbance a_{2c} reaches a maximum and then rapidly decays to zero. The other two

Downloaded 02 May 2010 to 171.66.16.246. Redistribution subject to ASME license or copyright; see http://www.asme.org/terms/Terms_Use.cfm

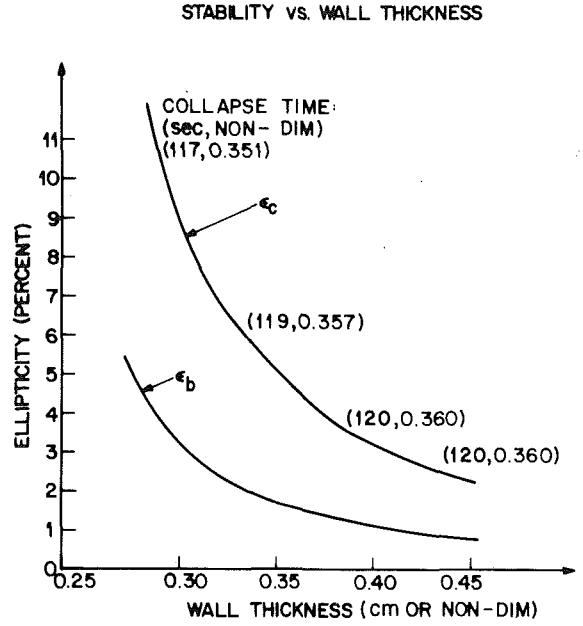

Fig. 12 Stability versus wall thickness

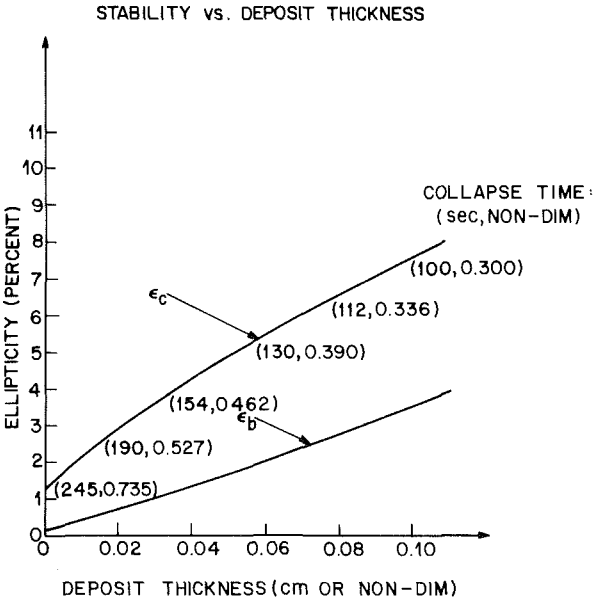

Fig. 13 Stability versus deposit thickness

perturbations b_{2c} and c_{2c} grow monotonically, to become an order of magnitude larger than the final deformation in a homogeneous preform. Note that c_{2c} actually exceeds b_{2c} by a slight amount. This behavior of the three perturbations suggest that the interior surface rapidly recovers its circular shape, due to the fluidity of the low-viscosity deposit, while the core-cladding interface and the outer surface continue to flatten, as far as linear perturbation theory goes. In the regions of maximum flattening the interior deposit increases in thickness (due to circumferential flow into these parts of the tube), i.e., it "fills the bulges" in the flattened substrate, while the latter slightly reduces its wall thickness in these areas (Fig. 7). The fluid dynamic implications of this behavior can be seen from Figs. 8 and 9, where velocity profiles have been plotted for u_2 and v_2 across the wall thickness and interpreted schematically.

The rapid return to circularity of the inner tube surface, as illustrated by the behavior of a_2 in Fig. 6, should become more pronounced as the viscosity of the inner layer is decreased. At the same time, the velocity derivatives and strain rates in the low-viscosity layer, near the interface, should intensify and lead to a more abrupt boundary layer behavior in that region. For large viscosity ratios, the "shooting" procedure described in the foregoing will continue to generate solutions that formally satisfy all boundary and interface conditions but yield meaningless results in the interior of the layers. Replacement of the integration package with one designed for "stiff" differential equations does not remove this difficulty.

Fundamentally different approaches to the numerical analysis had to be explored, and three different procedures were tried: (1) Gram-Schmidt orthonormalization (for example, see [5]), (2) interface matching, and (3) a finite-difference boundary value problem solver that avoids shooting methods altogether. Results from the second and third algorithms agreed reasonably well up to viscosity ratios of 10^4.

5 Results for Composite Tubes

We now summarize typical results for two-layer tubes in terms of physical parameters of practical interest.

Out-of-roundness of the two-layer interface is of particular importance and can be expressed as $\epsilon_c = c_2/c_0$ for the collapsed preform. The dependence of the final geometric distortions ϵ_c and ϵ_b or ΔP, the mean tube diameter, the total wall thidkness, and the thickness of the low viscosity deposit was studied. Figure 10 shows the effect of varying ΔP on ϵ_c and ϵ_b. The computed collapse time required for each case is shown in parentheses in Fig. 10 beside each data point. The collapse time t is proportional to the viscosity. It is not possible to estimate the actual time required for collapse because of insufficient information on the temperature and pressure profiles in the hot zone and on the dependence of viscosity on dopant level and temperature. Therefore, these collapse times are only intended to provide a qualitative comparison. It can be seen that the final tube deformations are very sensitive, increasing by two orders of magnitude as ΔP is increased from -100 to 200 dynes/cm^2. However, the time required for collapse decreases only by 15 percent because, at these pressures, surface tension is the dominant force in driving collapse. Thus, in theory, one should minimize the overpressure during collapse in order to optimize preform quality. In practice, one finds that significant benefits can be realized by using a small, constant, excess back pressure throughout the entire process.

Figures 11 and 12 predict the sensitivities of percentage distortions ϵ_c and ϵ_b to changes in the initial interface radius, c(a and b being scaled appropriately), and total wall thickness, $d = b - a$. For c varying between 1.0 and 1.1, out-of-roundness ϵ_c increases by a factor of 2 and the collapse time increases by 20 percent. For $0.25 \rightarrow d \rightarrow 0.45$ with a constant ratio of deposit to substrate thickness, out-of-roundness decreases by an order of magnitude, with negligible penalty in the collapse time. With regard to collapse, this clearly suggests a preference for heavy-walled substrates and proportionately heavier deposits. The process should not be scaled up by going to larger tube diameters but either by depositing more glass with subsequent rod-in-tube overcladding or by using thicker walled tubes with proportionately heavier deposits. Thicker-walled tubes may necessitate the use of different (hotter) torches in order to adequately heat them.

We now turn to the case of variable deposit thickness inside a substrate of constant initial wall thickness, i.e. $\bar{c} \equiv 1.00$, $\bar{b} \equiv 1.30$, and $0.90 \leq \bar{a} \leq 0.99$. Figure 13 displays resulting ellipticities for this case and one notes that ϵ_c and ϵ_b tend monotonically toward the appropriate values for the

Downloaded 02 May 2010 to 171.66.16.246. Redistribution subject to ASME license or copyright; see http://www.asme.org/terms/Terms_Use.cfm

homogeneous tube as $\bar{a} \rightarrow 1.00$ (viz. $\epsilon_b = 0.0012$ on Fig. 3 for $P_b = 100$ dynes/cm^2). Collapse times are also found to increase dramatically with increasing a (decreasing thickness of deposit), tending to the much longer collapse times characteristic of homogeneous tubes. This result is consistent with the experimental observation that more time is required to collapse the preform tube in the entry region where there is less deposit. These results are extremely interesting. They imply that, if one can deposit a low viscosity but rather thick cladding at a substantial rate (1-2 gm/min) then the longer deposit time for the thicker cladding can be largely offset by a shorter collapse time, while minimizing terminal values of ϵ_c, and ϵ_b with suitable control of ΔP.

6 Conclusions

A theoretical model of the collapse process has been developed and verified by experimental measurements. The dominant driving force for collapse is surface tension. The stability depends strongly on the pressure difference, the deposit viscosity relative to silica, and the deposit thickness. The decreased stability and shorter collapse times of multimode preforms is due to the fluid deposit. The insights gained from the two-dimensional model in this study have permitted control and optimization of the actual (three-dimensional) collapse process.

References

1 Lewis, J. A., JFM, "The Collapse of a Viscous Tube," Vol. 81, 1977, pp. 129–135.

2 Bird, R. B., Stewart, W. E., and Lightfoot, E. N., *Transport Phenomena*, Wiley, New York, 1960.

3 Lewis, J. A., unpublished work.

4 Schryer, N. L., "A User's Guide to DODES," Comp. Sci. Tech. Rep. No. 33, Bell Laboratories, Aug. 1975.

5 Davey, A., and Nguyen, H. P. F., "Finite Amplitude Stability of Pipe Flow," *J. Fluid Mech.*, Vol. 45, No. 4, 1971, p. 701.

Downloaded 02 May 2010 to 171.66.16.246. Redistribution subject to ASME license or copyright; see http://www.asme.org/terms/Terms_Use.cfm

Buckling and Postbuckling of a Long-Hanging Elastic Column Due to a Bottom Load

C. Y. Wang
Departments of Mathematics and Mechanical Engineering, Michigan State University, East Lansing, Mich. 48824

A long heavy elastic column is supported at the top end. The bottom end is subjected to a compressive force. The critical buckling loads, related to zeroes of Airy functions, are quite different from the Euler buckling loads. Postbuckling shapes are integrated numerically.

1 Introduction

The stability of a weightless column under compressive loads was studied by Euler [1]. If the column is pinned at both ends, the buckling loads are $n^2\pi^2 EI/L^2$ where n is an integer, EI is the rigidity, and L is the length of the column. The problem of a heavy vertical column, bottom end fixed and top end free, was studied by Greenhill [2] who found the critical density or height of a uniformly weighted column. The combined effect of column density and end load was considered by Grishcoff [3] and extended recently by Wang and Drachman [4] to cases where a finite column is hanging from a foundation.

In this paper we shall study the long-hanging column. The column is secured at the top which supports all of its weight. We are interested at the response of the column when a compressive load is added to the bottom (free) end.

We assume the column length L is much greater than the "bending length" $(EI/\rho)^{1/3}$, where ρ is the weight per length. In fact, we assume

$$L/(EI/\rho)^{1/3} \to \infty \tag{1}$$

There are three characteristics of this *long*-hanging column:

1. Conditions at the top end (forces and moments applied at the top end) does not effect the bottom region.
2. There exists a long stretch of midregion which is almost vertical.
3. The bottom region can move freely as a whole laterally, i.e., it does not admit horizontal forces.

Figure 1(*a*) shows the three regions, which may be considered independent of each other when the column is long enough. To simplify the present work, we shall consider a pinned top end such that the column differs from the vertical only in the bottom region, where buckling may occur. In this particular case the top region would be absent.

The present work may be applied to deep sea drilling from a platform and also to heavy curtains or drapes. In these cases the assumption equation (1) is well satisfied.

2 Formulation

Figure 1(*b*) shows the origin of a cartesian coordinate system (x', y') is situated at the bottom end. A local balance of moment (Fig. 1(*c*)) gives

$$(F' - \rho s')\sin\theta = \frac{dm}{ds'} = -EI\frac{d^2\theta}{ds'^2} \tag{2}$$

Here F' is the force applied at the bottom end, s' is the arc length from that end, θ is the local angle of inclination, and m is the local moment. Using the following normalizations

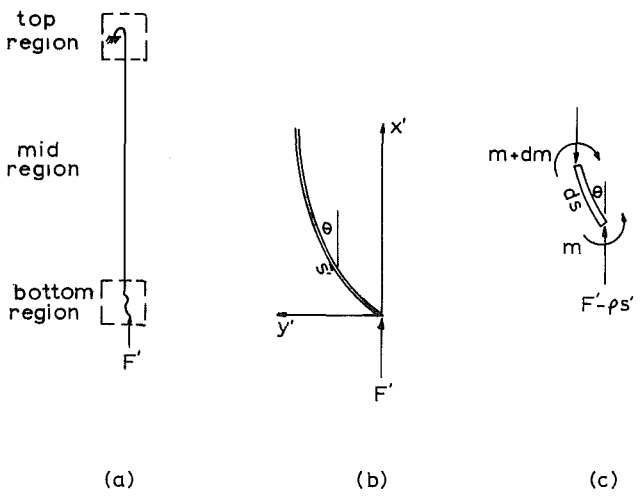

Fig. 1 *(a) The three independent regions of a long-hanging column; (b) the coordinate system situated at the bottom end; and (c) local moment balance of an arbitrary small segment*

Contributed by the Applied Mechanics Division for presentation at the 1983 ASME Applied Mechanics, Bioengineering, and Fluids Engineering Conference, Houston, Texas, June 20-22, 1983 of THE AMERICAN SOCIETY OF MECHANICAL ENGINEERS.

Discussion on this paper should be addressed to the Editorial Department, ASME, United Engineering Center, 345 East 47th Street, New York, N.Y. 10017, and will be accepted until two months after final publication of the paper itself in the JOURNAL OF APPLIED MECHANICS. Manuscript received by ASME Applied Mechanics Division, June 1982; final revision, October, 1982. Paper No. 83-APM-22.

Copies will be available until February, 1984.

Copyright © 1983 by ASME
Downloaded 02 May 2010 to 171.66.16.246. Redistribution subject to ASME license or copyright; see http://www.asme.org/terms/Terms_Use.cfm

$$F=F'(EI)^{-1/3}\rho^{-2/3},\quad s=s'(\rho/EI)^{1/3},\quad x=x'(\rho/EI)^{1/3},$$
$$y=y'(\rho/EI)^{1/3} \tag{3}$$

Equation (2) becomes

$$\frac{d^2\theta}{ds^2}+(F-s)\sin\theta=0 \tag{4}$$

The boundary conditions are that the bottom end is free to rotate.

$$\frac{d\theta}{ds}(0)=0 \tag{5}$$

and that the column becomes vertical at large distances

$$\theta(\infty)\to 0 \tag{6}$$

The actual configuration of the column can be found by

$$\frac{dx}{ds}=\cos\theta,\quad \frac{dy}{ds}=\sin\theta,\quad x(0)=y(0)=0 \tag{7}$$

3 Stability

The buckling loads are found by linearizing equation (4)

$$\frac{d^2\theta}{ds^2}+(F-s)\theta=0 \tag{8}$$

Let $s-F=r$. The problem becomes

$$\frac{d^2\theta}{dr^2}-r\theta=0 \tag{9}$$

$$\frac{d\theta}{dr}(-F)=0,\quad \theta(\infty)=0 \tag{10}$$

The general solution to equation (9) is composed of the Airy functions

$$\theta=C_1A_i(r)+C_2B_i(r) \tag{11}$$

The boundary conditions dictate $C_2 = 0$ and for a nontrivial solution

$$\frac{dA_i}{dr}(-F)=0 \tag{12}$$

The roots of equation (12) are $F = 1.018793$, 3.248198, 4.820099, 6.163307, 7.372177, etc. [5]. Thus the smallest (critical) buckling load below which the column is stable, is

$$F'=1.018793\,(EI)^{1/3}\rho^{2/3} \tag{13}$$

The other roots correspond to higher modes of buckling. These buckling loads are entirely different from the Euler loads $n^2\pi^2EI/L^2$. The linear buckling of a long heavy column was first considered by Willers [6] who, using infinite series, obtained the value of $F = 1.0188$ for the lowest mode.

4 Numerical Integration of Postbuckling Shapes

For finite deflections, equations (3)–(6) do not admit analytic solutions. Numerical integration is required to obtain the postbuckling characteristics. Such a two-point boundary value problem may be obtained in principle, for given F, by guessing $\theta(0)$, integrate to large values of s, and see if θ decays to zero. This scheme, however, is highly inaccurate due to the oscillatory nature of θ for $s < F$. We find the following modified method is much better.

Rewrite equation (4) as

$$\frac{d^2\theta}{dr^2}=r\sin\theta \tag{14}$$

pick any $\theta|_{r=0}$, guess $d\theta/dr|_{r=0}$ and integrate equation (14) as an initial value problem to large r ($r = 5$ was found to be sufficient), and see if θ decays to zero. This one parameter shooting is much more accurate since equation (14) is nonoscillatory for $r > 0$. Then using the correct values θ and $d\theta/dr$ at $r = 0$, we integrate equation (14) *backward* until $d\theta/dr$ first becomes zero, say at $r = r^*$. Then

$$F=-r^*>0,\quad \theta|_{s=0}=\theta|_{r=r^*} \tag{15}$$

Using equations (4), (5), (7), and (15) the postbuckling configurations for the primary mode can be found. For the higher buckling modes one can integrate to the second or

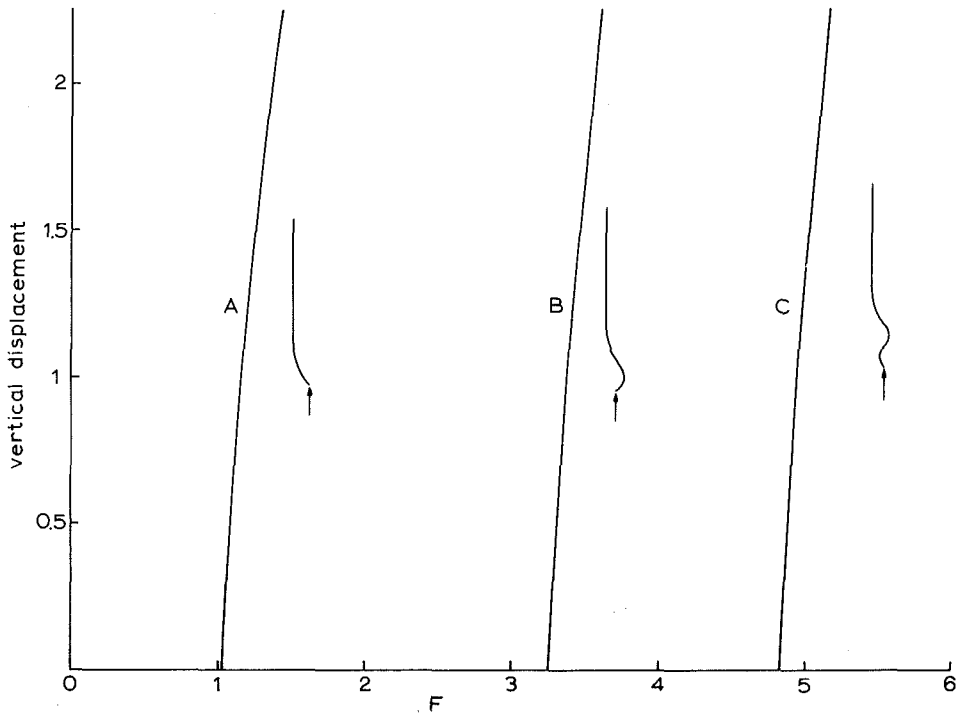

Fig. 2 Bifurcation of the force-vertical displacement curve. The curves *A,B,C* represent the primary, secondary, and tertiary modes.

Downloaded 02 May 2010 to 171.66.16.246. Redistribution subject to ASME license or copyright; see http://www.asme.org/terms/Terms_Use.cfm

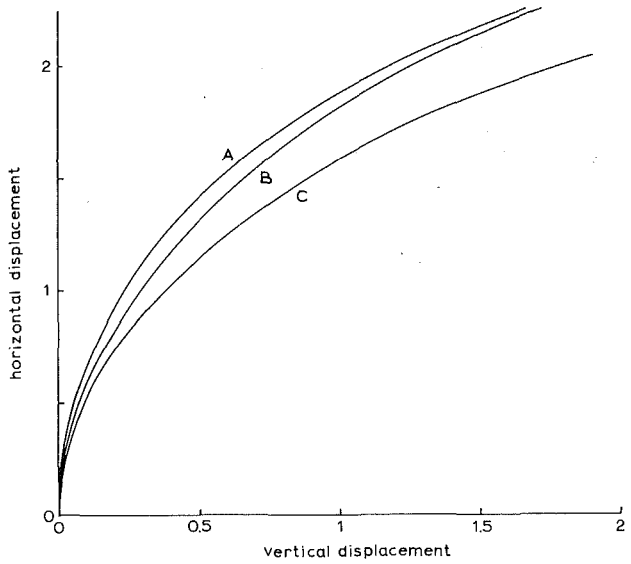

Fig. 3 The displacements of the bottom end showing the first three modes

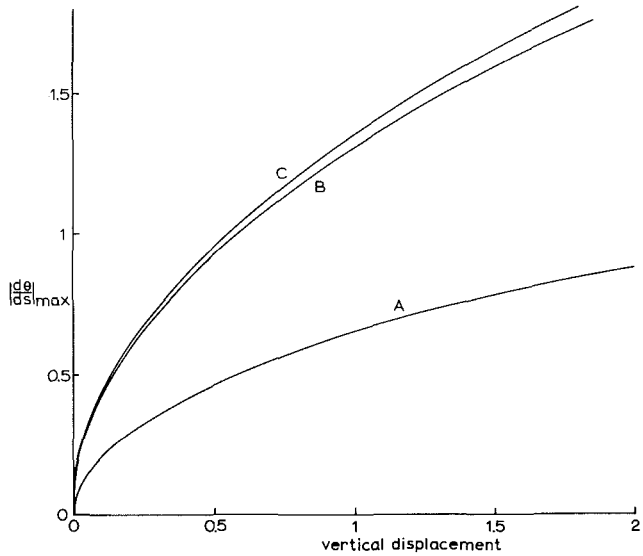

Fig. 4 The maximum normalized moment represented by $|d\theta/ds|$ max for the first three modes

higher zeros of $d\theta/dr$. The integration was done by the fourth-order Runge-Kutta algorithm. The error was adjusted by varying the step size.

Results and Discussion

Figure 2 shows the force-vertical displacement curve for the long-hanging column. The vertical displacement is obtained by the difference between s and x at large s. We see that the curves bifurcate from the trivial solution at 1.018793, 3.248198, 4.820099, etc. These branches are the stability boundaries for the primary, secondary, and tertiary modes, respectively.

Figure 3 shows the lateral displacement of the bottom end versus the vertical displacement. The displacements are normalized with respect to the bending length $(EI/\rho)^{1/3}$.

The maximum local moment is an important design criterium. Since the moment is proportional to $d\theta/ds$, equation (14) shows the maximum moment occurs at either $s = F$ or $\theta = 0$. Since θ is never zero for the primary mode, the maximum moment is at $s = F$. For the higher modes the

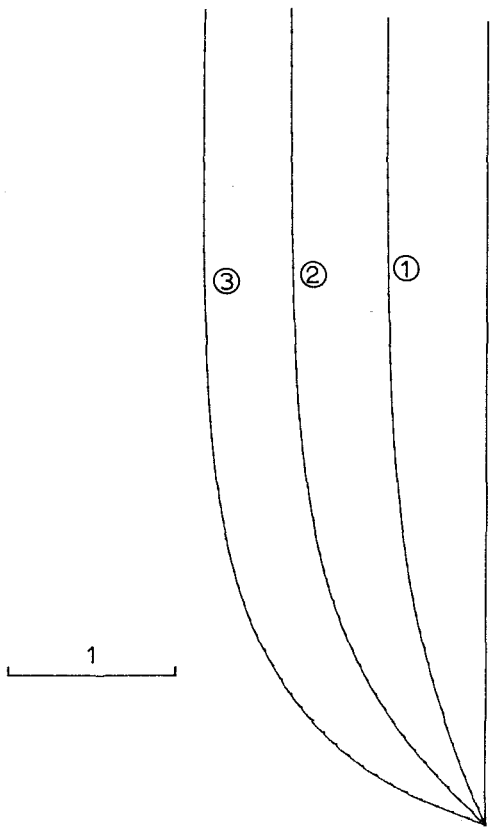

Fig. 5 Postbuckling configurations for the primary mode. ① $F = 1.029$, ② $F = 1.061$, ③ $F = 1.122$.

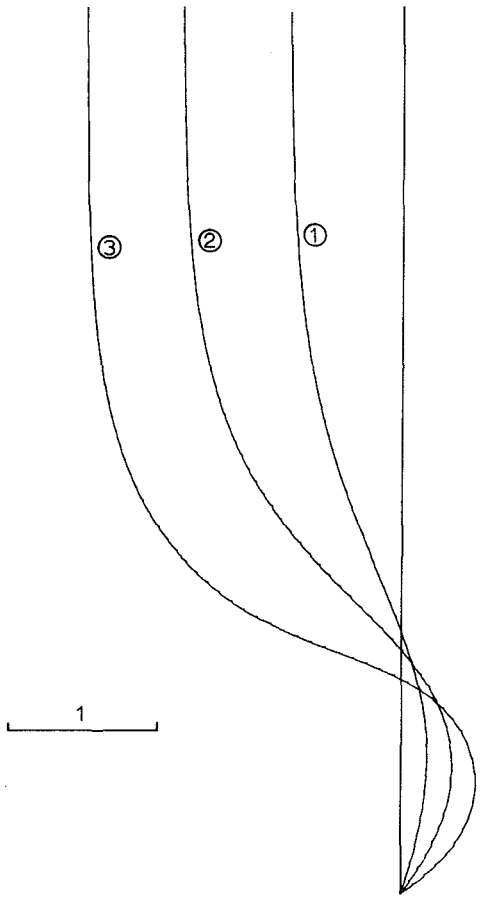

Fig. 6 Postbuckling configurations for the secondary mode. ① $F = 3.268$, ② $F = 3.330$, ③ $F = 3.445$.

Downloaded 02 May 2010 to 171.66.16.246. Redistribution subject to ASME license or copyright; see http://www.asme.org/terms/Terms_Use.cfm

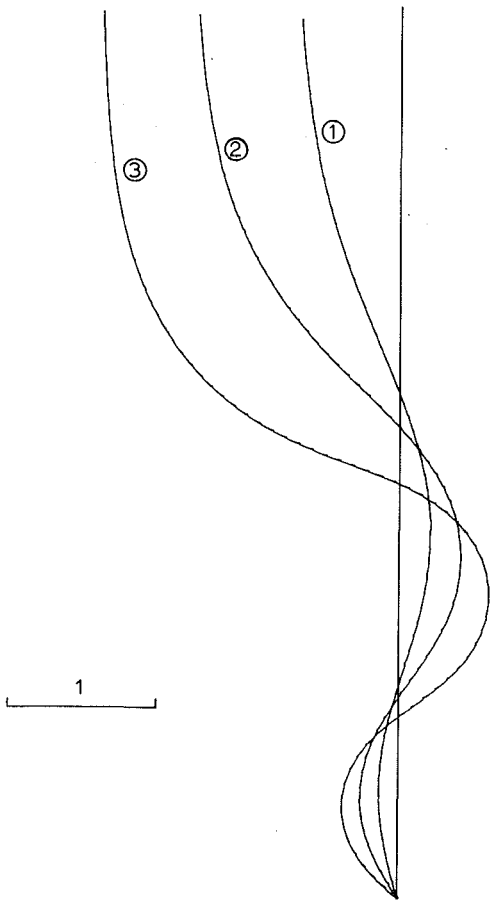

Fig. 7 Postbuckling configurations for the tertiary mode. ① $F = 4.844$, ② $F = 4.919$, ③ $F = 5.058$.

maximum moment is at the first $\theta = 0$. Figure 4 shows the maximum moment for the primary mode is considerably lower than those of the higher modes due to the difference in the location of maximum $|d\theta/ds|$.

The postbuckling configurations for the primary mode are shown in Fig. 5. The decrease in θ is monotonic. Figure 6 shows the secondary mode where θ changes sign once, while Fig. 7 depicts the tertiary mode. Elastic columns that buckle in higher modes have higher potential energy and therefore thay are less stable than those in the primary mode. However, similar to the higher modes of the Euler column, they do occur in laterally restrained cases.

One may mention that it is possible to do a similar analysis for a clamped bottom end. The normalized buckling loads are 2.338107, 4.087949, 5.520560, etc. Unlike the Euler column, the higher buckling loads in both pinned and clamped cases are not simple multiples of the lowest buckling load.

Our present results also differ substantially from the short-hanging column [4] which is essentially dominated by the stiffness. For the short column the buckling is highly sensitive to conditions at the top end while in the present case the two end regions are independent. Our numerical results show disturbances at the bottom end are limited to a region of less than 10 bending lengths from the bottom.

References

1 Euler, L., *De Curvis Elastics*, 1744.

2 Greenhill, A. G., "Determination of the Greatest Height Consistent With Stability That a Vertical Pole or Mast Can be Made, and of the Greatest Height to Which a Tree of Given Proportions Can Grow," *Camb. Phil. Soc. Proc.*, Vol. 4, 1881, pp. 65–73.

3 Grishcoff, N., in *Theory of Elastic Stability*, Timoshenko, S. P., and Gere, J. M., eds., McGraw-Hill, New York, 1961, p. 104.

4 Wang, C. Y., and Drachman, B., "Stability of a Heavy Column With an End Load," ASME JOURNAL OF APPLIED MECHANICS, Vol. 48, 1981, pp. 668–669.

5 Abramowitz, M., and Stegun, I. A., eds., *Handbook of Mathematical Functions*, Dover, New York, 1965, p. 478.

6 Willers, F. A., "Das Knicken Schwerer Gestänge," *Z. angew Math. Mech.*, Vol. 21, 1941, pp. 43–51.

Downloaded 02 May 2010 to 171.66.16.246. Redistribution subject to ASME license or copyright; see http://www.asme.org/terms/Terms_Use.cfm

T. Q. Ye[1]
Northwestern Polytechnical University,
Xi'an, Shaanxi, China

R. H. Gallagher
Dean,
College of Engineering,
University of Arizona,
Tucson, Ariz. 85721
Fellow ASME

Instability Analysis of Pressure-Loaded Thin Arches of Arbitrary Shape

The governing differential equations and the virtual work expressions for the large displacement analysis of thin arches of arbitrary shape, subjected to pressure loads, are derived. The virtual work expressions are employed as the basis for formulation of finite element stiffness equations. Classical solutions are obtained, from the differential equations, for the buckling of circular rings under uniform "follower" (hydrostatic) and "dead" (constant direction) pressure loadings. Finite element solutions are calculated for elliptical rings for a wide range of axis ratios.

Introduction

Although basic theoretical principles for the inclusion of pressure-load effects in finite element, elastic instability analysis have been established for some time now [1], there is considerable interest in and need for relationships for specific cases of interest and for the study of the basic properties of these relationships. Thus, Hibbitt [2], Loganathan, et al. [3], and Mang [4] have examined the algebraic form and permissible approximations for finite element stiffness relationships that arise when the effects of follower forces are taken into account. Batoz [5, 6] has studied the formulation of such relationships for the particular case of circular arch finite elements.

Because the finite element method owes its significance to its potentiality for the treatment of structures of rather arbitrary geometry, it is desirable to have available the theoretical basis for formulation of arch elements of any shape. Thus, the purpose of this paper is to derive geometrically nonlinear formulations for arches of arbitrary shape acted on by pressure loads. Both the governing differential equations and the associated virtual work expressions are presented. Generalized stress vectors are defined which are consistent with the definitions of the strains. The interaction of membrane and bending deformations is taken into account.

The governing differential equations derived herein are more general than those that have appeared previously. Frisch-Fay [7] gives basic nonlinear equations for arches of arbitrary shape, but neglects the interaction of bending and membrane deformations. Wang [8] presents a linear static analysis for a class of ring segments. The equilibrium equations, however, are established for the undeformed configuration. The theory can only be used for cycloidal, circular, catenary, and parabolic rings. If the radius of ring segments cannot be expressed by $R = a \sec^n \phi$, it is inapplicable.

In this paper, following the derivation of the equations for general shapes, various aspects of circular arches are studied. Using the hypothesis of small middle-surface strain and moderately small rotation, the governing differential equations for circular rings are obtained from the more general equations. These equations are solved for the eigenvalues for the cases of "follower" (hydrostatic) and "dead" (constant direction) pressures, yielding solutions in accordance with previously derived results. Certain aspects of Batoz's formulations for circular arches are also verified. Finally, the finite element method is used to calculate the critical loads for the elliptical rings of different geometric parameters under two kinds of pressures. In case of "follower" load, symmetrized load stiffness matrices are employed.

Strain-Displacement Relations

The middle surface of an undeformed thin arch of arbitrary shape can be expressed by the parametric equations (see Fig. 1)

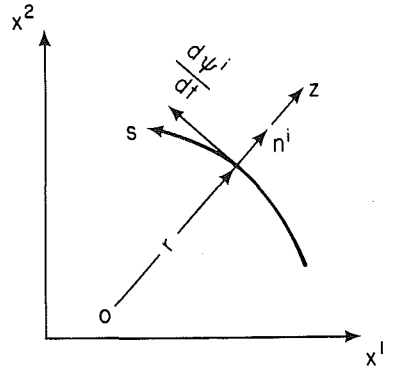

Fig. 1

[1] Visting Associate Professor, University of Arizona, Tucson, Ariz. 85721.

Contributed by the Applied Mechanics Division for publication in the JOURNAL OF APPLIED MECHANICS.

Discussion on this paper should be addressed to the Editorial Department, ASME, United Engineering Center, 345 East 47th Street, New York, N.Y. 10017, and will be accepted until two months after final publication of the paper itself in the JOURNAL OF APPLIED MECHANICS. Manuscript received by ASME Applied Mechanics Division, January, 1982; final revision, December 1982.

Copyright © 1983 by ASME
Downloaded 02 May 2010 to 171.66.16.246. Redistribution subject to ASME license or copyright; see http://www.asme.org/terms/Terms_Use.cfm

$$x^i = \psi^i(t), \quad i=1,2 \tag{1}$$

The displacement of a point on the middle surface, referred to the undeformed shape, is

$$u^i = \frac{d\psi^i}{dt} v^0 + n^i w, \quad i=1,2 \tag{2}$$

where v^0 is the tangent component of displacement, w is the normal component, and n^i is the unit normal to the undeformed middle surface. Lowercase letters are used here to denote the displacements measured from the undeformed state. Subsequently, we will use capital letters to denote displacements referred to the deformed state.

For the deformed middle surface, the expressions for the metric A and the coefficient of the second fundamental form F can be written as follows

$$A = a[(1+e)^2 + \phi^2] \tag{3}$$

and

$$F = \sqrt{\frac{a}{A}}\left\{(1+e)\left[f(1+e) + \frac{d}{dt}(\sqrt{a}\,\phi)\right] - \sqrt{a}\,\phi\left(\frac{de}{dt} - \frac{f}{\sqrt{a}}\phi\right)\right\} \tag{4}$$

where

$$a = \left(\frac{d\psi^1}{dt}\right)^2 + \left(\frac{d\psi^2}{dt}\right)^2 \tag{5}$$

is the metric of the undeformed middle surface, and

$$f = n^1 \frac{d^2\psi^1}{dt^2} + n^2 \frac{d^2\psi^2}{dt^2} \tag{6}$$

is the coefficient of the second fundamental form.
Also, in equations (3) and (4), e represents the membrane deformation and ϕ is the rotation of a normal to the middle surface of the arch. These are, in terms of the displacements

$$e = \frac{dv^0}{dt} - \frac{f}{a} w \tag{7}$$

$$\phi = \frac{1}{\sqrt{a}}\left(fv^0 + \frac{dw}{dt}\right) \tag{8}$$

The strain of the middle surface of the arch is defined as

$$E_m = \frac{1}{2}\frac{(d\hat{s})^2 - (ds)^2}{(ds)^2} = e + \frac{1}{2}e^2 + \frac{1}{2}\phi^2 \tag{9}$$

where ds and $d\hat{s}$ are the length of the element of the undeformed and deformed middle surface, respectively.

The strain at a point with coordinate z is

$$E_z = \frac{1}{2}\frac{(d\hat{s}_z)^2 - (ds_z)^2}{(ds_z)^2} = \frac{1}{2\left(1 - \frac{f}{a}z\right)^2}\left[\frac{(A-a)}{a} - 2(F-f)z + \left(\frac{F^2}{A} - \frac{f^2}{a}\right)z^2\right] \tag{10}$$

where ds_z and $d\hat{s}_z$ are the length of the element of a fiber that is parallel to and at a distance z from the middle surface.

Virtual Work Equations

In the following, the virtual work equations are derived from which the nonlinear finite element analysis of arches of arbitrary shape under hydrostatic and constant direction pressure can be established on the basis of a consistent theory.

First, the equilibrium equations of the deformed arch (see for example, reference [9]) are

$$\left.\begin{aligned} &\frac{d}{dt}\left(\frac{N_0}{\sqrt{A}}\right) - \frac{Q}{R} + q_0 = 0 \\ &\frac{N_0}{R} + \frac{1}{\sqrt{A}}\frac{dQ}{dt} + p = 0 \\ &\frac{1}{\sqrt{A}}\frac{dM}{dt} + Q = 0 \end{aligned}\right\} \tag{11}$$

where N_0 is the axial force, Q is the shear force, q_0 is the frictional drag, p is the pressure, and R is the radius of curvature. From (A.8), $R = A/F$. According to the principle of virtual work, we can construct the following integral

$$\int_L \left\{\left[\frac{d}{dt}\left(\frac{N_0}{\sqrt{A}}\right) - \frac{Q}{R} + q_0\right]\delta V_0 + \left(\frac{N_0}{R} + \frac{1}{\sqrt{A}}\frac{dQ}{dt} + p\right)\delta W + \left(\frac{1}{\sqrt{A}}\frac{dM}{dt} + Q\right)\delta\theta\right\} ds = 0 \tag{12}$$

δV_0 and δW are the tangent and normal virtual displacements, respectively, referred to the deformed configuration, $\delta\theta$ is the virtual rotation, and $ds = \sqrt{a}\,dt$. L is the length of the middle surface of the arch with boundaries l_1 and l_2.

Integration by parts of equation (12) yields

$$\left[\frac{1}{\sqrt{A}}(N_0\,\delta V_0 + Q\,\delta W + M\,\delta\theta)\right]\Big|_{l_1}^{l_2} + \int_L (q_0\,\delta V_0 + p\,\delta)\,ds = \int_L \left[\left(\frac{1}{\sqrt{A}}\delta\left(\frac{dV_0}{dt}\right) - \frac{1}{R}\delta W\right)N_0 + \left(\frac{1}{R}\delta V_0 + \frac{1}{\sqrt{A}}\delta\left(\frac{dW}{dt}\right) - \delta\theta\right)Q + \frac{1}{\sqrt{A}}\delta\left(\frac{d\theta}{dt}\right)M\right] ds \tag{13}$$

After deformation of the arch, a point on the undeformed middle surface wtih coordinates x^i moves to a new position

$$\hat{x}^i = x^i + u^i \tag{14}$$

where u^i is given by equation (2). Let $\hat{n}^i$ be the unit normal to the deformed middle surface. The virtual displacements can be expressed as follows

$$\delta u^i = \frac{d\hat{x}^i}{dt}\delta V^0 + \hat{n}^i\,\delta W = \frac{d\psi^i}{dt}\,\delta v^0 + n^i\,\delta w \tag{15}$$

where

$$V^0 = \frac{V_0}{\sqrt{A}} \quad \text{and} \quad v^0 = \frac{v_0}{\sqrt{a}}.$$

Differentiating (15) and using (A2), (A3), (A6), (A7), (7), and (8), we obtain

$$\left[\delta\left(\frac{dV^0}{dt}\right) - \frac{F}{A}\delta W\right]\frac{d\hat{x}^i}{dt} + \left[F\,\delta V^0 + \delta\left(\frac{dW}{dt}\right)\right]\hat{n}^i = \frac{dx^i}{dt}\delta e + n^i\sqrt{a}\,\delta\phi \tag{16}$$

Multiplying both sides of (16) by $d\hat{x}^i/dt$ and $\hat{n}^i$, respectively, and taking account of expressions (9), (A9), and (A5), the following equations are obtained

$$\delta\left(\frac{dV^0}{dt}\right) - \frac{F}{A}\delta W = \frac{1}{2A}\delta A \tag{17}$$

$$\frac{1}{R}\delta V_0 + \frac{1}{\sqrt{A}}\delta\left(\frac{dW}{dt}\right) = -\frac{a}{A}[\phi\,\delta e - (1+e)\,\delta\phi] \tag{18}$$

In (13) the coefficient of Q is the virtual shear deformation for the arch. This effect is small and setting it equal to zero we have

Downloaded 02 May 2010 to 171.66.16.246. Redistribution subject to ASME license or copyright; see http://www.asme.org/terms/Terms_Use.cfm

$$\frac{1}{R}\delta V_0 + \frac{1}{\sqrt{A}}\delta\left(\frac{dW}{dt}\right) - \delta\theta = 0 \tag{19}$$

By using (18), (19), and (A.6)–(A.9), it can be shown that

$$\frac{1}{\sqrt{A}}\delta\left(\frac{d\theta}{dt}\right) = \frac{1}{A}\left[\delta F - \frac{1}{2R}\delta A + \frac{d}{dt}\left(\frac{1}{\sqrt{A}}\right) A\,\delta\theta\right] \tag{20}$$

In (13) the coefficient of M is $1/\sqrt{A}\ \delta(d\theta/dt)$, which is the variation of the bending curvature. In expression (20) the last term in the square brackets therefore represents the influence of the shear strain on the bending curvature, and can be neglected according to the Love-Kirchoff hypothesis. Thus, equation (20) can be written as

$$\frac{1}{\sqrt{A}}\delta\left(\frac{d\theta}{dt}\right) \approx \frac{1}{A}\left(\delta F - \frac{1}{2R}\,\delta A\right) \tag{21}$$

By using (17), (19), and (21), the internal virtual work in expression (13) can be reduced to

$$\delta I_i = \int_L \left[\frac{N_0}{2A}\,\delta A + \frac{M}{A}\left(\delta F - \frac{1}{2R}\,\delta A\right)\right] ds$$

$$= \int_L (\tilde{N}\,\delta\tilde{E} + \tilde{M}\,\delta\tilde{K})\, ds \tag{22}$$

where E and K are defined as the generalized normal and bending strains, respectively. In consideration of (9) and (10)

$$\tilde{E} = \frac{1}{2}(A - a) = aE_m \tag{23a}$$

$$\tilde{K} = F - f \tag{23b}$$

and $\tilde{N}$ and $\tilde{M}$ are the corresponding generalized normal stress vector and bending moment:

$$\tilde{N} = \frac{1}{A}\left(N_0 - \frac{M}{R}\right) \tag{24a}$$

$$\tilde{M} = \frac{M}{A} \tag{24b}$$

The stress-strain relations can be written in the form

$$\tilde{N} = (E\,\Omega/A^2)\,\tilde{E} \tag{25a}$$

$$\tilde{M} = (EI/A^2)\,\tilde{K} \tag{25b}$$

where $E\,\Omega$ is membrane rigidity and EI is bending rigidity.

Thus, in view of (25a,b) equation (22) can be written as

$$\delta I_i = \int\left[\left(\frac{E\,\Omega}{A^2}\right)\tilde{E}\,\delta\tilde{E} + \left(\frac{EI}{A^2}\right)\tilde{K}\,\delta\tilde{K}\right] ds \tag{26}$$

Substituting equations (3), (4), (7), and (8) into (23a) and (23b), we obtain

$$\tilde{E} = a\left[\frac{dv^0}{dt} - \frac{f}{a}w + \frac{1}{2}\left(\frac{dv^0}{dt} - \frac{f}{a}w\right)^2 + \frac{1}{2a}\left(fv^0 + \frac{dw}{dt}\right)^2\right] \tag{27a}$$

$$\tilde{K} = \sqrt{\frac{a}{A}}\left\{f\left(1 + \frac{dv^0}{dt} - \frac{f}{a}w\right)^2 + \left(1 + \frac{dv^0}{dt} - \frac{f}{a}w\right)\left[\frac{d}{dt}(fv^0) + \frac{d^2w}{dt^2}\right] - \left(fv^0 + \frac{dw}{dt}\right)\left[\frac{d^2v^0}{dt^2} - \frac{d}{dt}\left(\frac{f}{a}w\right) - \frac{f^2}{a}v^0 - \frac{f}{a}\frac{dw}{dt}\right] - \sqrt{\frac{A}{a}}f\right\} \tag{27b}$$

Substitution of (27a) and (27b) into equation (26) gives the virtual work in terms of the displacements v^0, w, and the metric a, and the coefficient of the second fundamental form f.

The external virtual work is

$$\delta I_h = \int_L p\sqrt{\frac{a}{A}}\left[-\left(fv^0 + \frac{dw}{dt}\right)\delta v^0 + \left(1 + \frac{dv^0}{dt} - \frac{f}{a}w\right)\delta w\right] ds, \tag{28}$$

for the hydrostatic pressure, and

$$\delta I_c = \int_L p\,\delta w\, ds, \tag{29}$$

for the constant direction pressure.

The principle of virtual work then can be expressed as

$$\delta(I_i - I_e) = 0 \tag{30}$$

where δI_e is the external virtual work, for the hydrostatic pressure $\delta I_e \equiv \delta I_h$ and, for the constant direction pressure $\delta I_e \equiv \delta I_c$.

In accordance with the small middle-surface strain and moderately small rotation hypothesis, i.e.,

$$e << 1,\ \phi^2 << 1 \quad \text{and} \quad Z\frac{d\phi}{ds} << 1$$

the virtual work expressions (26) and (28) become

$$\delta I_i = \delta\int_L \frac{E\Omega}{2a^2}\left[\sqrt{a}\frac{dv}{dt} - \frac{1}{2\sqrt{a}}\frac{da}{dt}v - fw + \frac{1}{2}\left(\frac{f}{\sqrt{a}}v + \frac{dw}{dt}\right)^2\right]^2 ds + \delta\int_L \frac{EI}{2a^3}\left[f\frac{dv}{dt} + \left(\frac{df}{dt} - \frac{f}{2a}\frac{da}{dt}\right)v + \sqrt{a}\frac{d^2w}{dt^2}\right]^2 ds \tag{31}$$

and

$$\delta I_h = \int_L p\left[-\frac{1}{\sqrt{a}}\left(\frac{f}{\sqrt{a}}v + \frac{dw}{dt}\right)\delta v + \delta w\right] ds \tag{32}$$

where

$$v = \sqrt{a}\,v^0$$

Formulation of Governing Differential Equations

The internal virtual work of (26) can be written in the alternative form

$$\delta I_i = \int_L \left\{\tilde{N}A\left[\delta\left(\frac{dV^0}{dt}\right) - \frac{F}{A}\delta W\right] + \tilde{M}\sqrt{A}\left[\frac{d}{dt}\left(\frac{\sqrt{A}}{R}\delta V^0\right) + \frac{d}{dt}\left(\frac{1}{\sqrt{A}}\delta\left(\frac{dW}{dt}\right)\right)\right] + \tilde{M}\left[\frac{A}{R}\delta\left(\frac{dV^0}{dt}\right) - \frac{F}{R}\delta W\right]\right\} ds \tag{33}$$

For the hydrostatic pressure, the external virtual work is

$$\delta I_h = \int_L p\,\delta W\, ds \tag{34}$$

and, for the constant direction pressure

$$\delta I_c = \int_L p\left[\sqrt{a}\,\phi\,\delta V^0 + \sqrt{\frac{a}{A}}(1+e)\,\delta W\right] ds \tag{35}$$

The external virtual work for the frictional drag q_0 is

$$\delta I_d = \int_L q_0\sqrt{A}\,\delta V^0\, ds \tag{36}$$

Integrating (33) by parts and then combining with (34) and (36) we obtain the following form of the equilibrium equations

Downloaded 02 May 2010 to 171.66.16.246. Redistribution subject to ASME license or copyright; see http://www.asme.org/terms/Terms_Use.cfm

$$\frac{d}{dt}(\tilde{N}A)+\frac{F}{\sqrt{A}}\frac{d}{dt}(\tilde{M}\sqrt{A})+\frac{d}{dt}(\tilde{M}F)+q_0\sqrt{A}=0 \quad (37a)$$

$$\tilde{N}F-\frac{d}{dt}\left[\frac{1}{\sqrt{A}}\frac{d}{dt}(\tilde{M}\sqrt{A})\right]+\tilde{M}\frac{F}{R}+p=0 \quad (37b)$$

Elimination of $\tilde{N}$ from these two equations gives a single general nonlinear equation for arches of arbitrary form under hydrostatic pressure and frictional drag, with force parameters as unknowns:

$$\frac{d^3\tilde{M}}{dt^3}+c_2\frac{d^2\tilde{M}}{dt^2}+c_1\frac{d\tilde{M}}{dt}+c_0\tilde{M}+D_2\frac{dp}{dt}+D_1p+D_0q_0=0 \quad (38)$$

where

$$c_2=\frac{3}{2}\frac{1}{A}\frac{dA}{dt}-\frac{1}{F}\frac{dF}{dt},\ c_1=\frac{1}{A}\frac{d^2A}{dt^2}-\frac{1}{2A}\frac{dA}{dt}\left(\frac{1}{A}\frac{dA}{dt}+\frac{1}{F}\frac{dF}{dt}\right)+\frac{F}{R}$$

$$c_0=\frac{1}{2A}\frac{d^3A}{dt^3}-\frac{1}{A}\frac{dA}{dt}\left[\frac{1}{A}\frac{d^2A}{dt^2}-\frac{1}{2A^2}\left(\frac{dA}{dt}\right)^2\right]-\frac{1}{2FA}\frac{dF}{dt}\left[\frac{d^2A}{dt^2}-\frac{1}{A}\left(\frac{dA}{dt}\right)^2\right]+\frac{1}{R}\frac{dF}{dt}+\frac{F}{R^2}\frac{dR}{dt}-\frac{1}{2R^2}\frac{dA}{dt},\ D_2=-1,\ D_1=\frac{1}{F}\frac{dF}{dt}-\frac{1}{A}\frac{dA}{dt},\ D_0=\frac{F}{\sqrt{A}}.$$

Substituting (25*b*) into (38) gives the general nonlinear equation with displacement parameters as unknowns, for hydrostatic pressure and frictional drag

$$\frac{d^3}{dt^3}\left(\frac{EI}{A^2}\tilde{K}\right)+c_2\frac{d^2}{dt^2}\left(\frac{EI}{A^2}\tilde{K}\right)+c_1\frac{d}{dt}\left(\frac{EI}{A^2}\tilde{K}\right)+c_0\frac{EI}{A^2}\tilde{K}+D_2\frac{dp}{dt}+D_1p+D_0q_0=0 \quad (39)$$

Similar expressions can also be obtained for constant direction pressure.

Circular Arch

To confirm the foregoing, we derive the equations of thin circular arches as a special case. The parametric equations of the middle surface of circular arches are

$$x^1=\rho\cos t,\ x^2=\rho\sin t$$

The metric and the coefficient of the second fundamental form are therefore $a=\rho^2, f=-\rho$. Consider a circular ring under hydrostatic pressure and constant direction pressure. For the case of uniformly distributed pressure without frictional drag, $q_0=0$, $dp/dt=0$, and $p=-p_{cr}$, in accordance with the small middle-surface strain and moderately small rotation hypotheses. From equation (39) the following differential equation for the hydrostatic pressure case can be derived.

$$\frac{d^5w}{ds^5}+\frac{2}{\rho^2}\frac{d^3w}{ds^3}+\frac{1}{\rho^4}\frac{dw}{ds}+\frac{p_{cr}\rho}{EI}\left(\frac{d^3w}{ds^3}+\frac{1}{\rho^2}\frac{dw}{ds}\right)=0 \quad (40)$$

Similarly for constant direction pressure the equation is

$$\frac{d^6w}{ds^6}+\frac{2}{\rho^2}\frac{d^4w}{ds^4}+\frac{1}{\rho^4}\frac{d^2w}{ds^2}+\frac{p_{cr}\rho}{EI}\left(\frac{d^4w}{ds^4}+\frac{2}{\rho^2}\frac{d^2w}{ds^2}+\frac{w}{\rho^4}\right)=0 \quad (41)$$

where $ds=\rho\,dt$.

The buckling mode is assumed as $w=w_0\sin ns/\rho$, where n is the number of waves.

When $n=2$, we obtain the well-known critical pressure (for example see [10]), for the hydrostatic pressure

$$p_{cr}=3\frac{EI}{\rho^3}$$

and for the constant direction pressure

$$p_{cr}=4\frac{EI}{\rho^3}$$

Finite Element Formulations

The buckling of rings of different dimensions and shapes under both hydrostatic and constant direction pressures can be investigated by the finite element method. For this we use expressions for the virtual work written in terms of displacements, i.e., equations (29), (31), and (32).

To transform the preceding expressions into algebraic form, we first choose approximations for the displacements and virtual displacements as follows:

$$v=\lfloor N_1\rfloor\{\Delta\} \qquad \delta v=\lfloor N_1\rfloor\{\delta\Delta\}$$

$$w=\lfloor N_2\rfloor\{\Delta\} \qquad \delta w=\lfloor N_2\rfloor\{\delta\Delta\}$$

where $\lfloor N_i\rfloor$ is row vector of expressions that approximate the shape of the displaced state (i.e., "shape functions") and $\{\Delta\}$ is a column vector of displacements (including rotations, as appropriate) of specified points on the element, and $\{\delta\Delta\}$ is the column vector of joint virtual displacements. After differentiation of v, w, δv, and δw and insertion of the foregoing into the left-hand side of the virtual work expression (30), for an element, we obtain,

$$\delta(I_i-I_e)=\lfloor\delta\Delta\rfloor[[K^e]+p_{cr}([K^e_G]-[K^e_L])]\{\Delta\} \quad (42)$$

where $[K^e]$ is the elastic stiffness matrix which includes the membrane stiffness matrix $[K^e_m]$ and the bending stiffness matrix $[K^e_b]$,

$$[K^e_m]=\int_L(\lfloor d_m\rfloor[N])^T E\Omega(\lfloor d_m\rfloor[N])a^{-2}\,ds$$

and

$$[K^e_b]=\int_L(\lfloor d_b\rfloor[N])^T EI(\lfloor d_b\rfloor[N])a^{-2}\,ds$$

where

$$\lfloor d_m\rfloor=\left\lfloor\left(\sqrt{a}\frac{d}{dt}-\frac{1}{2\sqrt{a}}\frac{da}{dt}\right)\right|-f\rfloor$$

and

$$\lfloor d_b\rfloor=\left\lfloor\left(\frac{f}{\sqrt{a}}\frac{d}{dt}+\frac{1}{\sqrt{a}}\left(\frac{df}{dt}-\frac{f}{2a}\frac{da}{dt}\right)\right)\right|\frac{d^2}{dt^2}\rfloor$$

$[K^e_G]$ is the "geometric stiffness matrix"

$$[K^e_G]=\int_L\frac{1}{f}(\lfloor d_g\rfloor[N])^T(\lfloor d_g\rfloor[N])\,ds$$

where

$$\lfloor d_g\rfloor=\frac{f}{\sqrt{a}}\quad\frac{d}{dt}J$$

The load stiffness matrix is

Downloaded 02 May 2010 to 171.66.16.246. Redistribution subject to ASME license or copyright; see http://www.asme.org/terms/Terms_Use.cfm

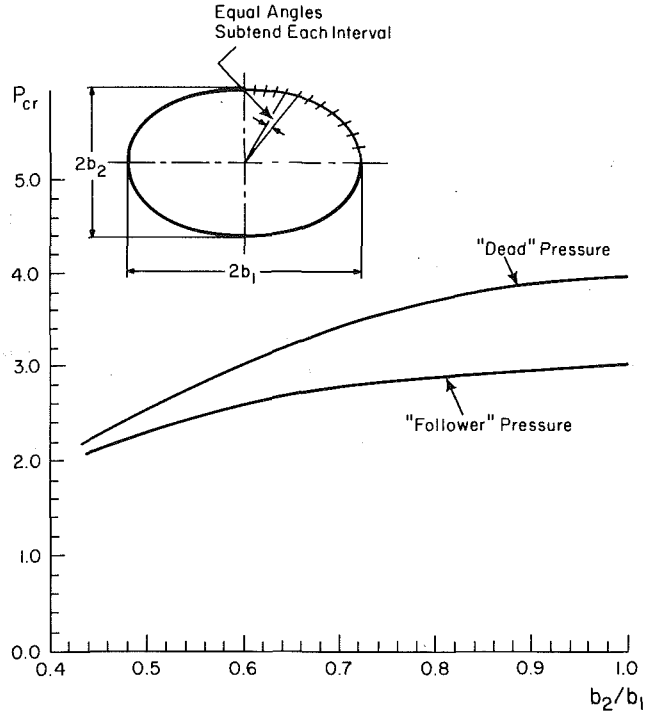

Fig. 2

$$[K_L^e] = \int_L (\lfloor d_{l1} \rfloor [N])^T (\lfloor d_{l2} \rfloor [N])\, ds$$

where

$$\lfloor d_{l1} \rfloor = \lfloor 1\ 0 \rfloor, \quad \lfloor d_{l2} \rfloor = \left\lfloor \frac{f}{a} \frac{1}{\sqrt{a}} \frac{d}{dt} \right\rfloor$$

It should be noted that $[K_L^e]$, in general, is an unsymmetric matrix.

Summation of the element virtual work of all elements gives the global virtual work. In accordance with the principle of virtual work, equation (30), from equation (42), we have for the structural system

$$[[K] + P_{cr}([K_G] - [K_L])]\{\Delta\} = 0 \tag{43}$$

The critical pressures are obtained by solving the algebraic eigenvalue equation stemming from the foregoing.

Finite Element Solution for Elliptical Rings

The buckling of elliptical rings of different dimensions under both "follower" and "dead" pressures is now investigated by use of the finite element method. For elliptical arches the middle-surface equations are

$$x^1 = b_1 \cos t, \quad x^2 = b_2 \sin t$$

According to (4) and (5), we have

$$a = b_1^2 \sin^2 t + b_2^2 \cos^2 t$$

and

$$f = \frac{-b_1 b_2}{(b_1^2 \sin^2 t + b_2^2 \cos^2 t)^{1/2}}$$

The hypotheses of small middle-surface strain and moderate rotation are used in the formulation. Both displacement functions, v and w, are approximated by cubic polynomials. The finite element mesh of a quarter of the ring (see inset, Fig. 2) consists of 12 elements with a total of 52 degrees of freedom. For the "follower" pressure the load stiffness matrix is symmetrized.

Table 1

	P_{cr}			
Load	$*b_1 = b_2 = 100$	$b_1 = 110$ $b_2 = 90$	$b_1 = 120$ $b_2 = 80$	$b_1 = 140$ $b_2 = 60$
"dead"	4.0000	3.7724	3.3128	2.1617
"follower"	3.0232	2.8140	2.7352	2.0333

$*2b_1$ – long diameter of the ellipse
$2b_2$ – short diameter of the ellipse

$$[K_L^{(s)}] = \frac{1}{2}([K_L] + [K_L]^T)$$

where $[K_L]$ is the unsymmetric load stiffness matrix. The thickness of the arch is taken to be $t = 1.0$, the width $b = 12.0$, and elastic modulus $E = 10^6$. The results of the computation are summarized in Table 1 and Fig. 2.

The results show that the 1.33 ratio between "dead" and "follower" instability pressures for circular rings approaches 1.0 as the axis ratio decreases. Comparison of the finite element and classical solutions for the circular ring discloses a high degree of accuracy for the former. However, there appears to be no available comparison solutions for elliptical rings for the phenomena studied.

Concluding Remarks

The purpose of this paper has been to present the basic relationships, in the form of both differential equations and the virtual work expression for pressure-loaded thin arches of arbitrary shape. Using the virtual work expression and displacement approximations often employed in the finite element representation of circular arches, finite element stiffness equations are constructed for an elliptic arch element. These are employed in analyses of pressure-loaded elliptic arches for the full range of axis ratios.

References

1 Hibbitt, H. D., Marcal, P. V., Rice, J. R., "A Finite Element Formulation for Problems of Large Strain and Large Displacement," *Int. J. Solids Struct.*, Vol. 6, 1970, pp. 1069–1086.

2 Hibbitt, H. D., "Some Follower Forces and Load Stiffness," *Int. J. Num. Meth. Eng.*, Vol. 14, 1979, pp. 937–941.

3 Loganathan, K., Chang, S. C., Gallagher, R. H., and Abel, J. F., "Finite Element Representation and Pressure Stiffness in Shell Stability Analysis," *Int. J. Num. Meth. Eng.*, Vol. 14, 1979, pp. 1413–1429.

4 Mang, H. A., "Symmetricability of Pressure Stiffness Matrices for Shell With loaded Free Edges," *Int. J. Num. Meth. Eng.*, Vol. 15, 1980, pp. 981–990.

5 Batoz, J. L., "Curved Finite Element and Shell Theories With Particular Reference to Buckling of a Circular Arch," *Int. J. Num. Meth. Eng.*, Vol. 14, 1979, pp. 774–779.

6 Batoz, J. L., "Importance de la Theorie Nonlineaire et du Type de Pression sur le Flambement D'Arcs et D'Anneaux Circularies (to appear).

7 Frisch-Fay, R., *Flexible Bars*, Butterworths, London, 1962.

8 Wang. J. T.-S., "Exact Analysis of Class of Ring Segments," *Journal of the Engineering Mechanics Division*, ASCE, Vol. 104, 1978, pp. 871–880.

9 Wempner, G. A., *Mechanics of Solids, With Applications to Thin Bodies*, McGraw-Hill, New York, 1973.

10 Bodner, S. R., "On the Conservativeness of Various Distributed Forces System," *J. Aeronaut. Sci.*, Vol. 25, 1958, pp. 132–133.

APPENDIX

Basic Geometric Relations

For the undeformed middle surface, the relations between the geometric characteristics are

Downloaded 02 May 2010 to 171.66.16.246. Redistribution subject to ASME license or copyright; see http://www.asme.org/terms/Terms_Use.cfm

$$n^i = \frac{1}{\sqrt{a}} e_{ij} \frac{d\psi^j}{dt} \tag{A1}$$

$$\frac{dn^i}{dt} = -\frac{f}{a} \frac{d\psi^i}{dt} \tag{A2}$$

$$\frac{d^2\psi^i}{dt^2} = fn^i \tag{A3}$$

$$r = \frac{a}{f} \tag{A4}$$

where e_{ij} is the permutation symbol and r is the radius of curvature of the undeformed middle surface.

Similarly, for the deformed middle surface we have

$$\hat{n}^i = \frac{1}{\sqrt{A}} e_{ij} \frac{d\hat{x}^j}{dt} \tag{A5}$$

$$\frac{d\hat{n}^i}{dt} = -\frac{F}{A} \frac{d\hat{x}^i}{dt} \tag{A6}$$

$$\frac{d^2\hat{x}^i}{dt^2} = F\hat{n}^i \tag{A7}$$

$$R = \frac{A}{F} \tag{A8}$$

where R is the radius of curvature of the deformed middle surface.

According to expressions (2), (7), (8), and (14) the tangent to the middle surface of deformed arches can be written as

$$\frac{d\hat{x}^i}{dt} = \frac{d\psi^i}{dt}(1+e) + n^i \sqrt{a}\, \phi \tag{A9}$$

Downloaded 02 May 2010 to 171.66.16.246. Redistribution subject to ASME license or copyright; see http://www.asme.org/terms/Terms_Use.cfm

Theoretical and Experimental Investigation of the Nonlinear Torsion and Extension of Initially Twisted Bars

A. Rosen
Senior Lecturer,
Department of Aeronautical Engineering,
Technion-Israel Institute of Technology,
Haifa, Israel

A set of nonlinear equations that describe the nonlinear deformation of initially twisted bars under the influence of torsional moment and tension force, which act simultaneously, are derived. Special attention is devoted to the case of thin symmetrical cross sections and the equations appropriate to this case are shown. The linear terms of the equations, in the case of thin rectangular cross sections, are compared to solutions of the same problem, obtained by other researchers, who investigated the torsion and extension of helicoidal shells. It is shown that even for thin cross sections having large values of initial twist, the deviations between the two linear solutions are very small. To check the applicability of the theory to nonlinear regions, the theoretical results are compared to experimental results obtained during the course of the present research. The experiments include the torsion and extension of thin steel strips having rectangular cross sections. The agreement between both is very good, which proves the validity of the theory.

1 Introduction

The influence of initial twist on the torsional rigidity of thin prismatical bars was pointed out by Chu [1] who investigated the problem theoretically and experimentally. Recently it was pointed out [2] that the mathematical treatment of the problem, presented by Chu suffered from certain kinds of inaccuracies. These inaccuracies resulted mainly from the fact that a nonorthogonal system of coordinates was used without using the appropriate theory for such a system. These inaccuracies have continued to appear in the vast literature dealing with the structural behavior of initially twisted blades of marine and aircraft propellers, helicopter rotors, different kinds of turbines, and other cases. It was also pointed out [2] that the influence of initial twist on the behavior of bars may be explained by the influence of the initial twist on the contributions of warping. Following this indication, a new theory that decribes the influence of initial twist on the torsional rigidity of the bars was developed [3, 4]. It was shown that in certain cases the results, according to the new theory, were identical to those of Chu [1] and matched experimental results very well. In other cases they succeeded in overcoming the weak points on the previous theory. Following the results of [2] the torsion of initially twisted bars due to extension was also explained by the influence of initial twist on the warping of the bar [5].

In the present paper the investigation presented in the foregoing is extended as follows: while in the previous cases, application of torsional moment alone or tension alone were considered here, the behavior of the bar under the simultaneous action of the two is considered. Moreover, the derivation is consistent and the region of the applicability of the theory is defined. To prove the validity of the theory the linear terms are compared to the linear solution to the problem of extension and torsion of thin strips with rectangular cross sections obtained by other investigators using shell theory. In addition, theoretical results are also compared to experimental results that were obtained during the present research, so the ability of the theory to describe the nonlinear behavior is also assessed.

2 Theoretical Derivation

An initially twisted bar is shown in Fig. 1. The length of the bar is l and all the cross sections are identical. The initial twist is presented by a rotation β of the cross section about the x axis. The initial twist k, is given by:

$$k = \frac{d\beta}{dx} \tag{1}$$

The present derivation will be restricted to the case of constant initial twist. It is also limited to twisted bars with cross sections having two-fold symmetry. Otherwise the torsion and axial extension are coupled with bending, which is not included in the present analysis.

Contributed by the Applied Mechanics Division for publication in the JOURNAL OF APLLIED MECHANICS.

Discussion on this paper should be addressed to the Editorial Department, ASME, United Engineering Center, 345 East 47th Street, New York, N.Y. 10017, and will be accepted until two months after final publication of the paper itself in the JOURNAL OF APPLIED MECHANICS. Manuscript received by ASME Applied Mechanics Division July, 1980; final revision, July, 1982.

Copyright © 1983 by ASME
Downloaded 02 May 2010 to 171.66.16.246. Redistribution subject to ASME license or copyright; see http://www.asme.org/terms/Terms_Use.cfm

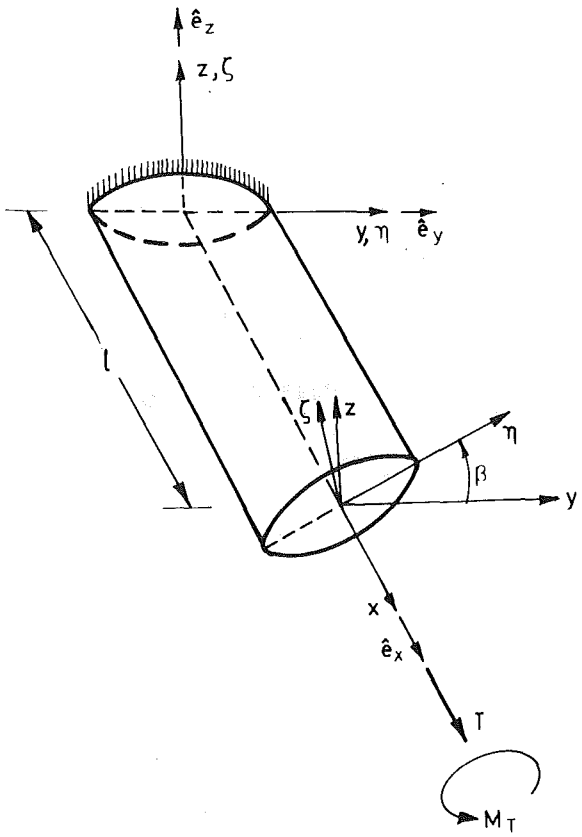

Fig. 1 General description of the loaded initially twisted bar

In Fig. 1 two different systems of coordinates are presented. The first system is the x, y, z system which is a fixed-in-space system. The axes y and z are orthogonal to x and to each other, which yields an orthogonal system of coordinates. The second system is the x, η, ζ system where η and ζ are the principal axes of the cross section of the bar, perpendicular to each other, and rotate with the cross section along x. The angle between the axes η and y equals β.

A torque M_t and an axial force T are applied at the end of the bar. As a result, the bar deforms and the displacement vector of each point of the bar, $\bar{W}$, is given by

$$\bar{W} = u\,\hat{e}_x + v\,\hat{e}_y + w\,\hat{e}_z \tag{2}$$

where $\hat{e}_x$, $\hat{e}_y$, and $\hat{e}_z$ are unit vectors in the directions of x, y, and z, respectively. It is assumed, as was done previously [3, 4], that the deformation is a superposition of a Saint-Venant torsion together with some axial motion u_1 of each cross section, unknown at this stage. The displacement components will then be:

$$u = u_1 + \theta\psi \tag{3a}$$

$$v = y(\cos\varphi - 1) - z\sin\varphi \tag{3b}$$

$$w = y\sin\varphi + z(\cos\varphi - 1) \tag{3c}$$

where ψ is the Saint-Venant warping function, φ is the angle of rotation of the cross section, and θ is the change in φ per unit length, given by:

$$\theta = \frac{d\varphi}{dx} \tag{4}$$

Equations (3a–c) differ from equations (10a–c) of [3] or equations (3a–c) of [4] by the fact that finite values of φ are allowed. Equations (3a–c) converge to the other equations assuming φ to be small enough so that cos φ equals unity and sin φ equals φ. To simplify the derivation it will be assumed that the bar is free to warp at the ends. This assumption results in uniform torsion along the bar, which mathematically means that θ is constant and not a function of x. If necessary, the equations for the case where warping at the ends is restrained may be obtained in the same way that is presented here, but the derivation is a little more tedious.

By differentiation of equations (3a–c) the nonlinear strain components are obtained as:

$$\epsilon_{xx} = \frac{\partial u}{\partial x} + \frac{1}{2}\left[\left(\frac{\partial u}{\partial x}\right)^2 + \left(\frac{\partial u}{\partial x}\right)^2 + \left(\frac{\partial w}{\partial x}\right)^2\right] =$$

$$= \epsilon_1 + \theta\frac{\partial\psi}{\partial x} + \frac{1}{2}\left[\left(\epsilon_1 + \theta\frac{\partial\psi}{\partial x}\right)^2 + \theta^2(y^2+z^2)\right] \tag{5a}$$

Nomenclature

A = cross-sectional area of the bar
a = the length of a rectangular cross section
b = the thickness of a rectangular cross section
D = cross-sectional constant defined by equation (10a)
E = Young's modulus of elasticity
$\hat{e}_x, \hat{e}_y, \hat{e}_z$ = unit vectors in the directions x, y, and z, respectively
F = cross-sectional constant defined by equation (10b)
G = shear modulus of elasticity
I_p = polar moment of inertia of the cross section
J_s = the Saint-Venant linear torsional stiffness of a bar without an initial twist
K = cross-sectional constant defined by equation (10e)
k = the initial twist of the bar defined by equation (1)
l = length of the bar
M_t = the torsional moment that is applied to the bar
N,Q = constants of a thin symmetrical cross section defined by equations (16a,b), respectively
S = cross-sectional constant defined by equation (10f)
T = the tension force that is applied to the bar
t_1,t_2,t_3,t_4 = correction factors in equations (18a,b)
u,v,w = displacement components, in the directions x,y, and z, respectively
u_1 = the axial motion of the cross section
V = the total potential of the deformed bar
$\bar{W}$ = the displacement vector of each point of the bar
x,y,z = orthogonal fixed-in-space system of coordinates
β = the angle of initial twist of each cross section of the bar
$\epsilon_{xx}, \epsilon_{xy}, \epsilon_{xz}$ = the strain components
ϵ = ordering measure
ϵ_1 = defined by equation (6)
η,ζ = the principal axes of each cross section of the bar
θ = elastic twist
ν = Poisson's ratio
φ = angle of elastic torsional rotation
ψ = the warping function

Downloaded 02 May 2010 to 171.66.16.246. Redistribution subject to ASME license or copyright; see http://www.asme.org/terms/Terms_Use.cfm

$$\epsilon_{xy} = \frac{1}{2}\left(\frac{\partial u}{\partial y} + \frac{\partial v}{\partial x}\right) + \frac{1}{2}\left(\frac{\partial u}{\partial x}\frac{\partial u}{\partial y} + \frac{\partial v}{\partial x}\frac{\partial v}{\partial y} + \frac{\partial w}{\partial x}\frac{\partial w}{\partial y}\right) =$$

$$= \frac{1}{2}\theta\left[\frac{\partial \psi}{\partial y} - z + \underline{\frac{\partial \psi}{\partial y}\left(\epsilon_1 + \theta\frac{\partial \psi}{\partial x}\right)}\right] \tag{5b}$$

$$\epsilon_{xz} = \frac{1}{2}\left(\frac{\partial u}{\partial z} + \frac{\partial w}{\partial x}\right) + \frac{1}{2}\left(\frac{\partial u}{\partial x}\frac{\partial u}{\partial z} + \frac{\partial v}{\partial x}\frac{\partial v}{\partial z} + \frac{\partial w}{\partial x}\frac{\partial w}{\partial z}\right) =$$

$$= \frac{1}{2}\theta\left[\frac{\partial \psi}{\partial z} + y + \underline{\frac{\partial \psi}{\partial z}\left(\epsilon_1 + \theta\frac{\partial \psi}{\partial x}\right)}\right] \tag{5c}$$

where

$$\epsilon_1 = \frac{\partial u_1}{\partial x} \tag{6}$$

As a result of our assumptions ϵ_1 is constant along the bar. The derivation will now be restricted to the case of small strains and finite rotations. This means that the terms $(\partial u_1/\partial x + \theta\,\partial\psi/\partial x)$, $1/2\,\theta\,(\partial\psi/\partial y - z)$, and $1/2\,\theta\,(\partial\psi/\partial z + y)$ are of order ϵ, which is the order of strain. Since the derivation is restricted to the elastic region it means that for metals ϵ equals 0.005, at the most. Mathematically the finite rotations mean that the terms θy, θz, $\theta\,\partial\psi/\partial z$ and $\theta\,\partial\psi/\partial y$ are of lower order than the strains. The derivation will be restricted to cases where these terms are of order $\sqrt{\epsilon}$. For metals this means that these terms are, at the most, of order 0.07. Since $\sqrt{\epsilon}$ is still small, it will be neglected compared to unity. Therefore the underlined terms in equations (5*a*,*c*) will be neglected.

If at the edge $x = 0$, rotation and axial motion are restricted such that:

$$\varphi = u_1 = 0 \quad \text{for} \quad x = 0 \tag{7}$$

Then the potential of all the internal and external forces that act on the bar is given according to bar theory, and based on our assumptions, by:

$$V = \int_0^l \int_A \int \left[\frac{\mathrm{E}}{2}\epsilon_{xx}^2 + 2G(\epsilon_{xy}^2 + \epsilon_{xz}^2)\right] dx\,dy\,dz$$

$$- T\,u_{1(z=l)} - M_{t(z=l)} =$$

$$= \int_0^l \left\{\int_A \int \left[\frac{\mathrm{E}}{2}\epsilon_{xx}^2 + 2G(\epsilon_{xy}^2 + \epsilon_{xz}^2)\right] dx\,dy - T\epsilon_1 - M_t\theta\right\} dz \tag{8}$$

Substitution of equations (5*a*–*c*) into equation (8) implies:

$$V = \int_0^l \left\{\frac{\mathrm{E}}{2}\left(A\epsilon_1^2 + 2S\epsilon_1\theta + K\theta^2 + I_p\epsilon_1\theta^2 + D\theta^3 + \frac{1}{4}F\theta^4\right) + \frac{G}{2}J_s\theta^2 - T\epsilon_1 - M_t\theta\right\} dx \tag{9}$$

where

$$D = \int_A \int \left(\frac{\partial \psi}{\partial x}\right)(y^2 + z^2)\,dy\,dz \tag{10a}$$

$$F = \int_A \int (y^2 + z^2)^2\,dy\,dz \tag{10b}$$

$$I_p = \int_A \int (y^2 + z^2)\,dy\,dz \tag{10c}$$

$$J_s = \int_A \int \left[\left(-z + \frac{\partial \psi}{\partial y}\right)^2 + \left(y + \frac{\partial \psi}{\partial z}\right)^2\right] dy\,dz \tag{10d}$$

$$K = \int_A \int \left(\frac{\partial \psi}{\partial x}\right)^2 dy\,dz \tag{10e}$$

$$S = \int_A \int \left(\frac{\partial \psi}{\partial x}\right) dy\,dz \tag{10f}$$

J_s is the well-known Saint-Venant torsional stiffness of the same uniform bar without initial twist; I_p is the cross-sectional moment of inertia, while F is the fourth-order area moment of the cross section. All the other terms D, K, and S involve integration of terms containing $\partial\psi/\partial x$ over the cross section. In the present case of uniform cross section the only contribution to $(\partial\psi/\partial x)$ is due to the initial twist.

Since the bar is in equilibrium, V should obtain a stationary value. This means that the first variation of V with respect to ϵ_1 and θ should vanish, which implies that:

$$\mathrm{E}A\epsilon_1 + \mathrm{E}S\theta + \underline{\frac{1}{2}\mathrm{E}I_p\theta^2} = T \tag{11a}$$

$$\mathrm{E}S\epsilon_1 + (GJ_s + \mathrm{E}K)\theta + \mathrm{E}I_p\epsilon_1\theta + \underline{\frac{3}{2}\mathrm{E}D\theta^2 + \frac{1}{2}\mathrm{E}F\theta^3} = M_t \tag{11b}$$

The underlined terms in equations (11*a*,*b*) are the nonlinear contributions. Substitution of the expression for ϵ_1, as obtained from equation (11*a*) into equation (11*b*), yields:

$$\left\{GJ_s + \mathrm{E}\left[K - \frac{S^2}{A} + \underline{\frac{3}{2}\left(D - \frac{I_pS}{A}\right)\theta + \frac{1}{2}\left(F - \frac{I_p^2}{A}\right)\theta^2}\right] + \underline{\frac{I_p}{A}T}\right\}\theta =$$

$$= M_t - \frac{S}{A}T \tag{12}$$

The first term in the curly brackets on the left side of equation (12) presents the usual Saint-Venant torsional rigidity of the bar without initial twist. The terms in the square brackets present the change in the torsional rigidity due to the initial twist and nonlinear terms associated with the elastic twist. The last term in the braces presents the increase in the torsional rigidity due to axial force in the bar [6, 7]. This term is known to be important in the case of open, thin cross sections. The first term on the right side of equation (12) is the applied torsional moment while the second term represents the contribution of the axial force to the torsional moment due to the presence of initial twist. The underlined terms in equation (12) are again the nonlinear contributions.

3 The Case of Thin Symmetrical Cross Sections

It was shown [3, 4] that in the case of thin symmetrical cross sections, as shown in Fig. 2:

$$\frac{\partial \psi}{\partial x} = \frac{\partial \psi}{\partial \eta}\frac{\partial \eta}{\partial x} + \frac{\partial \psi}{\partial \zeta}\frac{\partial \zeta}{\partial x} = k\left(\zeta\frac{\partial \psi}{\partial \eta} - \eta\frac{\partial \psi}{\partial \zeta}\right) \cong k(\eta^2 - \zeta^2) \tag{13}$$

Substitution of equation (13) into equations (10*a*–*f*) implies:

Downloaded 02 May 2010 to 171.66.16.246. Redistribution subject to ASME license or copyright; see http://www.asme.org/terms/Terms_Use.cfm

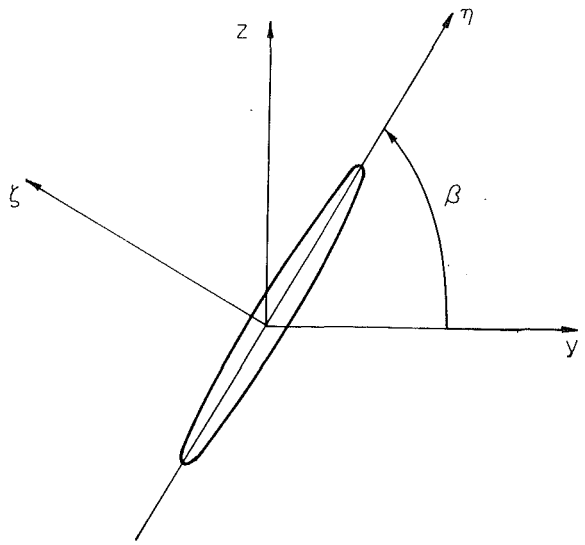

Fig. 2 Cross section of a thin-walled prismatical bar with initial twist

$$D = k\int_A\int \eta^4\left(1-\underline{\frac{\zeta^4}{\eta^4}}\right)d\eta\,d\zeta \tag{14a}$$

$$F = \int_A\int \eta^4\left(1+\underline{\frac{\zeta^2}{\eta^2}}\right)^2 d\eta\,d\zeta \tag{14b}$$

$$I_p = \int_A\int \eta^2\left(1+\underline{\frac{\zeta^2}{\eta^2}}\right)d\eta\,d\zeta \tag{14c}$$

$$K = k^2\int_A\int \eta^4\left(1-\underline{\frac{\zeta^2}{\eta^2}}\right)^2 d\eta\,d\zeta \tag{14d}$$

$$S = k\int_A\int \eta^2\left(1-\underline{\frac{\zeta^2}{\eta^2}}\right)d\eta\,d\zeta \tag{14e}$$

The underlined terms in equations (14*a–e*) are negligible in the case of thin cross sections which results in:

$$D \cong k\,N \tag{15a}$$

$$F \cong N \tag{15b}$$

$$I_p \cong Q \tag{15c}$$

$$K \cong k^2 N \tag{15d}$$

$$S \cong k\,Q \tag{15e}$$

where

$$N = \int_A\int \eta^4\,d\eta d\zeta \tag{16a}$$

$$Q = \int_A\int \eta^2\,d\eta d\zeta \tag{16b}$$

In the case of thin rectangular cross sections where the length of the cross section is a and the thickness b, one obtains:

$$N = \frac{a^5 b}{80} \tag{17a}$$

$$Q = \frac{a^3 b}{12} \tag{17b}$$

$$A = a\,b \tag{17c}$$

$$J_s = \frac{1}{3}\,a\,b^3 \tag{17d}$$

Equation (17*d*) may be found in any elementary book on the theory of elasticity (for example [8] page 273, equation (155)).

If equations (15*a–e*) and equations (17*a–d*) are substituted into equations (11*a–b*) and the nonlinear terms are neglected, the linear equations for the case of thin rectangular cross sections are obtained. These linear equations enable one to obtain an assessment of the accuracy of the present theory. This is done by comparing these linear equations to the linear solution of the same problem which was obtained by Knowles and Reissner [9] who investigated the torsion and extension of helicoidal shells. The linear solution may be described as:

$$\mathrm{E}ab(1+t_1)\epsilon_1 + \frac{1}{12}\mathrm{E}ka^3b(1+t_2)\theta = T \tag{18a}$$

$$\frac{1}{12}Eka^3b(1+t_2)\epsilon_1 + \left[\frac{1}{3}\,Gab^3(1+t_3) + \frac{1}{80}\mathrm{E}k^2a^5b(1+t_4)\right]\theta = M_t \tag{18b}$$

According to the results of the theory presented in this paper t_1, t_2, t_3, and t_4 are zero while according to equations (7.5), (7.6), and (8.4) of [9] they obtain the following values:

$$t_1 = -\frac{3+4\nu}{24}(ka)^2 + \frac{29+88\nu+56\nu^2}{1920}(ka)^4 + 0[(ka)^6] \tag{19a}$$

$$t_2 = -\frac{9+8\nu}{40}(ka)^2 + \frac{161+304\nu+152\nu^2}{4480}(ka)^4 + 0[(ka)^6] \tag{19b}$$

$$t_3 = -\frac{7}{24}(ka)^2 + \frac{63}{640}(ka)^4 + 0[(ka)^6] \tag{19c}$$

$$t_4 = -\frac{45+20\nu}{168}(ka)^2 + \frac{531+504\nu+232\nu^2}{10368}(ka)^4 + 0[(ka)^6] \tag{19d}$$

From equations (18*a–b*) and (19*a–d*) it is clear that in the cases where (ka) is smaller then 0.5 the difference between the results of the two theories will not exceed 8 percent. For value of (ka) smaller than 0.25 the difference is less than 2 percent.

Additional theoretical confirmation of the present nonlinear theory, beyond the support offered by the *linear* theory of helicoidal shell [9], may be found in an unpublished work of E. Reissner. In that work, a solution on the finite axial torsion and extension of a slightly pretwisted strip is obtained by using Marguerr's shallow shell formulation. The nonlinear results of that work agree with equations (11*a–b*) when the case of thin rectangular cross sections is considered.

Substitution of equations (15*a–e*) and equations (17*a–d*) into equation (12) yields the nonlinear equation:

$$\left\{1+\frac{1}{60}\frac{\mathrm{E}}{G}\left(\frac{a}{b}\right)^2\left[(ka)^2+\frac{3}{2}(ka)(\theta a) + \frac{1}{2}(\theta a)^2 + 15\frac{T}{\mathrm{E}ab}\right]\right\}(\theta a) = \frac{3M_t}{Gb^3} - \frac{1}{4}\frac{\mathrm{E}}{G}\left(\frac{a}{b}\right)^2(ka)\frac{T}{\mathrm{E}ab} \tag{20}$$

The terms in the square brackets on the left side of equation (20) present the relative increase in the torsional rigidity due to initial twist and nonlinear contributions. The first term on the right side presents the linear value of (θa) due to the applied torsional moment for the same untwisted beam, while the second term presents the linear contribution to (θa) of externally applied tension. In the next section the validity of equation (20) is checked by comparison to experimental results.

Downloaded 02 May 2010 to 171.66.16.246. Redistribution subject to ASME license or copyright; see http://www.asme.org/terms/Terms_Use.cfm

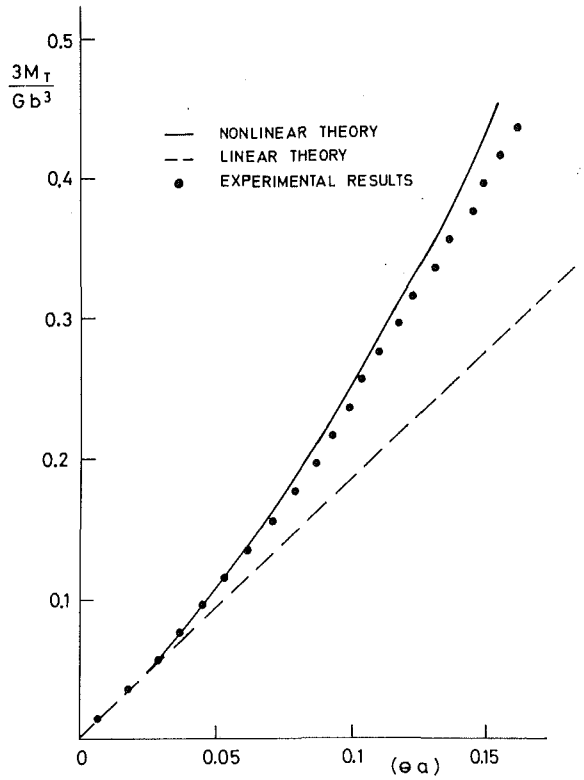

Fig. 3 The behavior of initially twisted steel strip under the action of end torisonal moment

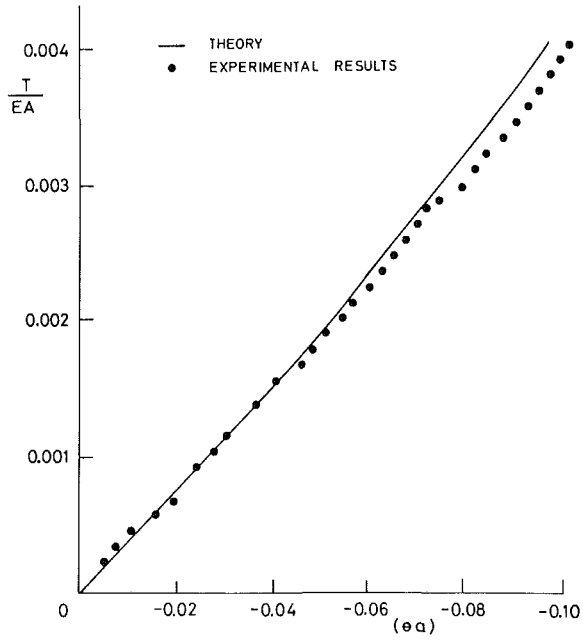

Fig. 4 The behavior of initially twisted steel strip under the action of end tension force

4 Experimental Results

The experiments included measurements of the elastic torsion of initially twisted, thin rectangular steel strips under the action of external tension force and torsional moment. The material properties were $E = 1.92 \cdot 10^5$ N/mm^2 and $G = 7.45 \cdot 10^4$ N/mm^2.

The dimensions of the first specimen's cross section were: a = 10mm and b = 0.5mm. The length of the strip was 600mm, long enough to allow the neglect of any influence of the boundary conditions. The initial twist was $ka = 0.224$. The purpose of this experiment was to investigate the behavior of the strip under increasing end torsional moment. The strip was held fixed at one end and the other free end was loaded by a tension force of 28.6 N. Then increasing values of torsional moments, M_t, were applied at the same free end while at each moment the elastic twist was measured. In Fig. 3 the elastic twist (θa) as a function of the nondimensionalized torsional moment $3M_t/Gb^3$, relative to the case $M_t = 0$ $T = 28.6$ N, is given. The solid dots present the experimental results while the solid line is the theoretical results obtained by using equation (20). It is shown that up to values of $(\theta a) = 0.12$ the agreement between theoretical and experimental results is excellent. As the applied torque is increased the deviation between theory and experiment is increased, while theory predicts a slightly lower elastic torsion. This deviation is expected since the values of (θz) and (θy) slightly exceeds the previously mentioned limit of 0.07. Even then one can conclude that the agreement between theoretical and experimental results is still very good. The dotted line in Fig. 3 represents the linear theory. It is clearly seen that at values of (θa) as low as $(\theta a) = 0.05$, nonlinear effects should be included to accurately enough predict the behavior of the strip.

The dimensions of the second specimen were: a = 4.45mm, b = 0.2mm, and length of 710mm. The initial twist was ka = 0.203. The purpose of this experiment was to investigate the elastic untwist of the strip due to the action of tensile force. During initial tests it was found that the compressive stresses that are developed in the edges of the strip, while untwisting, tend to cause edge buckling of the thin strip. As a result of this buckling the torsional rigidity of the strip is reduced and the present mathematical model is no longer appropriate. To avoid this problem, a concentrated torsional moment of 57.5N•mm was initially applied to the free edge of the strip which caused a substantial elastic twist. Increasing values of the tension force were then applied at the same edge which caused elastic untwist. This caused a reduction of the tensile stresses due to the initial torsional moment, but since they did not prove to be negative, buckling of the edges was eliminated.

Figure 4 presents the elastic untwist of the bar relative to the state of $M_t = 57.5$N•mm and $T = 3.92$N. In Fig. 4 the experimental results are compared with the theoretical predictions according to equation (20). Throughout all the regions the agreement between the two is very good. Part of the deviation may be explained by experimental errors which are also noticed if one examines the smoothness of the experimental curve.

The almost linear behavior of (θa) as a function of (T/EA) may lead to the wrong conclusion that the phenomenon is mainly linear. The reason for the linear appearance is the fact that while the term 3/2 (ka) (θa) in equation (20) presents a reduction of the torsional rigidity, the terms 1/2 $(\theta a)^2$ + 15 T/Eab present an increase of this rigidity. These two opposite influences, although noticeable by themselves (the increase in the torsional rigidity due to the term $15T/Eab$) exceeds 47 percent) tend to cancel each other and results in a "linear-looking" behavior.

5 Conclusions

A nonlinear theory that describes the nonlinear behavior of initially twisted bars under the simultaneous action of axial tension and torsional moment has been derived. The theory includes the influence of the initial twist on the torsional rigidity and torsional moment through its influence on the warping of the bar. Nonlinear effects include the influence of elastic twist and tension on the torsional rigidity. Special

Downloaded 02 May 2010 to 171.66.16.246. Redistribution subject to ASME license or copyright; see http://www.asme.org/terms/Terms_Use.cfm

attention has been devoted to the case of thin symmetrical cross sections. The validity of the derivation for the case of thin cross sections was proved in two ways. At first the linear set of equations for the case of thin rectangular cross sections was compared to the equations of other researchers who solved the same problem from another point of view, by considering it as torsion and extension of helicoidal shells. It was shown that up to values of $(ka) = 0.5$ the difference between the beam theory and the shell theory did not exceed 8 percent. This difference is proportional to $(ka)^2$ and decreases very rapidly with a decrease of (ka). The second way to check the accuracy of the derivation included a comparison of theoretical predictions to experimental results. The experiments included the extension and torsion of thin rectangular strips. In all cases the agreement between the two was very good, a fact that proves the validity. The experiments and theoretical calculations covered large regions of nonlinear behavior. It was shown that to obtain valuable theoretical results it is important to take all the nonlinear effects into consideration.

Acknowledgment

The author would like to acknowledge the reviewers of the paper whose comments helped to improve it.

References

1 Chen, C., "The Effect of Initial Twist on the Torsional Rigidity of Thin Prismatical Bars and Tubular Members," *Proceedings of the 1st U.S. National Congress of Applied Mechanics*, June 11-16, 1951, pp. 265-269.

2 Rosen, A., and Friedman, P., "Nonlinear Equations of Equilibrium for Elastic Helicopter or Wind Turbine Blades Undergoing Moderate Deformation," Univ. of Calif., L.A., School of Engineering and Applied Science Report UCLA-ENG-7718 (revised ed.), June, 1977.

3 Rosen, A., "The Effect of Initial Twist on the Torsional Rigidity of Beams—Another Point of View," Technion-Israel Inst. of Tech., Dept. of Aeronautical Eng., TAE Report No. 360, Apr., 1978.

4 Rosen, A., "The Effect of Initial Twist on the Torsional Rigidity of Beams—Another Point of View," ASME JOURNAL OF APPLIED MECHANICS, Vol. 47, 1980, pp. 389-392.

5 Hodges, D. H., "Torsion of Pretwisted Beams Due to Axial Loading," ASME JOURNAL OF APPLIED MECHANICS, Vol. 47, 1980, pp. 393-397.

6 Biot, M. A., "Increase of Torsional Stiffness of a Prismatic Bar Due to Axial Tension," *Journal of Applied Physics*, Vol. 10, 1939, pp. 860-864.

7 Goodier, J. N., "Elastic Torsion in the Presence of Initial Axial Stress," ASME JOURNAL OF APPLIED MECHANICS, Vol. 17, No. 4, 1950, pp. 383-387.

8 Timoshenko, S., and Goodier, J. N., *Theory of Elasticity*, 2nd ed., McGraw-Hill, New York, 1951.

9 Knowles, J. K., and Reissner, E., "Torsion and Extension of Helicoidal Shells," *Quarterly of Applied Mathematics*, Vol. 27, No. 4, 1960, pp. 409-422.

Downloaded 02 May 2010 to 171.66.16.246. Redistribution subject to ASME license or copyright; see http://www.asme.org/terms/Terms_Use.cfm

Penetration of Targets Described by a Mohr-Coulomb Failure Criterion With a Tension Cutoff[1]

D. B. Longcope

M. J. Forrestal

Sandia National Laboratories,
Albuquerque, N. Mex. 87185
Mems. ASME

A model is developed to estimate the force on a conical-nosed penetrator for normal entry into geological targets that have linear hydrostats and fail according to a Mohr-Coulomb criterion with a tension cutoff. The model is applicable to targets with shear strength which either increases with pressure (dry rocks) or is constant (sea ice, concrete, saturated rocks). For high enough penetrator velocity the target response is elastic-plastic, but at lower velocities stresses exceed the target tensile strength and the response includes an additional cracked region. Parametric results are obtained via a similarity transformation and solution to a nonlinear wave propagation problem. Predicted and measured penetrator decelerations are compared for a field test into a dry rock target and reasonable agreement is shown.

Introduction

Projectile penetration has been studied extensively for both metal and geological targets [1]. Investigations have focused on depth of penetration, deceleration history, loads, and structural response. Various approaches have been taken including the development of empirical relations such as those of [2] to predict penetration depth, the use of cylindrical or spherical cavity expansion approximations of target response for metals [3] and rocks [4], and the detailed modeling and numerical solution of rock target responses with two-dimensional wave codes [5].

The present study is concerned with predicting the resistive force on a rigid conical-nosed penetrator during normal entry into a geological target and uses a cylindrical cavity expansion approximation. As in [4], a linear hydrostat represents the target pressure-volume strain behavior in contrast with the locking hydrostat model which has been employed in other cavity expansion analyses, such as [6]. The target shear strength is modeled by a Mohr-Coulomb failure criterion with a tension cutoff [7] and includes unconfined compressive strength which was neglected in [4]. This model is used to represent pressure-dependent triaxial failure data of antelope tuff [8], a dry porous rock from the Sandia Tonopah Test Range, Nevada, and can also represent materials with constant shear strength such as sea ice, concrete, and saturated rock.

[1] This work was supported by the U. S. Department of Energy and the U. S. Army, Pershing II Project Manager's Office.

Contributed by the Applied Mechanics Division for presentation at the 1983 Applied Mechanics, Bioengineering, and Fluids Engineering Conference, Houston, Texas, June 20–22, 1983 of THE AMERICAN SOCIETY OF MECHANICAL ENGINEERS.

Discussion on this paper should be addressed to the Editorial Department, ASME, United Engineering Center, 345 East 47th Street, New York, N.Y. 10017, and will be accepted until two months after final publication of the paper itself in the JOURNAL OF APPLIED MECHANICS. Manuscript received by ASME Applied Mechanics Division, August, 1982; final revision, February, 1983. Paper No. 83-APM-31.

Copies will be available until February, 1984.

At high enough penetration speeds the target response is elastic-plastic, but at lower speeds when the circumferential stress σ_θ exceeds the target tensile strength, an additional cracked region with $\sigma_\theta = 0$ is included in the response. The extent of the cracked region may be significant when the target tensile strength is much less than its compressive strength, which is typical of geological materials [7].

The target response is calculated by solving a nonlinear, radial wave propagation problem via a similarity transformation and numerical integration. Graphical results include stress wave profiles in the target, stress on the nose versus penetrator velocity, and the effect of uncertainty in tensile strength on the stress on the penetrator nose. For quasi-static penetration, a closed-form expression is developed for the stress on the conical nose. Predicted and measured penetrator deceleration histories are compared for a field test into a layer of antelope tuff and reasonable agreement is shown. Velocity-dependent interface friction is considered as an explanation of a significant increase in the measured deceleration just prior to the penetrator stopping.

Governing Equations

A rigid projectile with a conical nose penetrates a uniform target medium with normal incidence in the z direction; see Fig. 1. The axisymmetric target response is reduced to a one-dimensional response by making the cylindrical cavity expansion approximation. This approximation allows only radial target motion, which is reasonable for penetrators with sharply pointed, slender noses, and enforces plane strain, $\epsilon_z = 0$, a condition that may be approached at depths greater than a few penetrator aft-body diameters. Penetration of a given elemental layer of thickness dz produces wave motion in the radial direction only and the layer responds independently of other layers. Lagrangian and Eulerian radial coordinates, denoted R and r, respectively, are employed in the analysis and are related by

Copyright © 1983 by ASME
Downloaded 02 May 2010 to 171.66.16.246. Redistribution subject to ASME license or copyright; see http://www.asme.org/terms/Terms_Use.cfm

$$r = R + u \tag{1}$$

where u is the displacement in the radial direction. Target response regions are separated by two radially propagating wave fronts located at Eulerian coordinates $c_1 t$ and $c_2 t$ at a particular time t after the nose has begun to penetrate a given layer.

The equations of momentum and mass conservation in terms of the Lagrangian coordinate R are, respectively,

$$\rho_0 R \frac{\partial^2 u}{\partial t^2} = -(R+u)\frac{\partial \sigma_r}{\partial R} - (\sigma_r - \sigma_\theta)\left(1 + \frac{\partial u}{\partial R}\right) \tag{2}$$

$$\rho_0 R = \rho(R+u)\left(1 + \frac{\partial u}{\partial R}\right) \tag{3}$$

where ρ_0, ρ are the initial and current densities and σ_r, σ_θ are the radial and circumferential components of Cauchy stress taken positive in compression.

Material compressibility is modeled by a linear pressure-volume change relation (hydrostat)

$$P = K\eta; \quad P = \frac{1}{3}(\sigma_r + \sigma_\theta + \sigma_z); \quad \eta = 1 - \rho_0/\rho \tag{4a, b, c}$$

where K is a constant, P is the pressure, and η is the volumetric strain. A pressure-dependent yield or failure condition is assumed in the form

$$\sigma_r - \sigma_\theta = \mu P + \tau_0; \quad \tau_0 = (1 - \mu/3)Q \tag{5}$$

where μ and τ_0 are constants and Q is the unconfined compressive strength. An additional requirement is that the tensile strength Y of the material may not be exceeded,

$$\sigma_\theta \geq -Y \tag{6}$$

Together, equations (5) and (6) have been called a Mohr-Coulomb failure criterion with a tension cutoff [7]. It is assumed that (5) and (6) hold for large strains. In fact, ϵ_θ, according to the elementary strain definition is infinite along the conical nose, $R = 0$. At stress states below failure, the response is elastic and is governed by the isotropic Hooke's laws expressed in terms of Poisson's ratio ν and the bulk modulus K, taken to be the same as in (4a). Equation (4a) with $K = 2.0$ GPa and (5) with $\sigma_z = \sigma_\theta$ (discussed later), $\mu = 1$ and $\tau_0 = 10$ MPa are compared with triaxial test data of antelope tuff [8] in Figs. 2 and 3. Antelope tuff is a partially welded ash-flow tuff with 30 percent porosity. The data are from field cores taken over a depth of 7.5 m at the Sandia Tonopah Test Range, Nevada. The data of Fig. 2 suggest some nonlinearity in the hydrostat; however, the linear fit is within 10 percent of the mean data over the range shown. This range is sufficient for typical geologic penetration calculations (including those of this paper), as verified a posteriori. In addition, the total force on the penetrator is an integration of the stresses on the nose which is not as sensitive to small errors in the target model as other results might be, such as stress waves in the target. In Fig. 3 each data point represents the failure of a sample at a particular confining pressure which corresponds to σ_θ in a penetration application. Since the

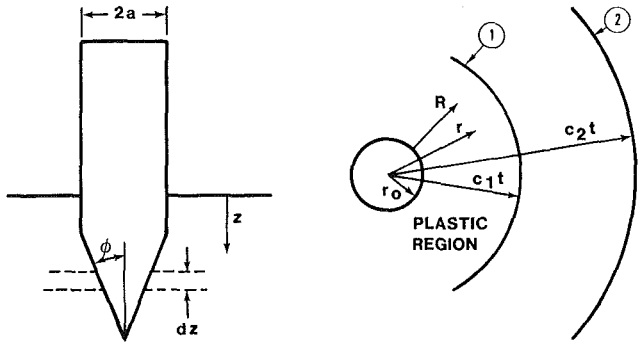

Fig. 1 Geometry of the problem and target response regions

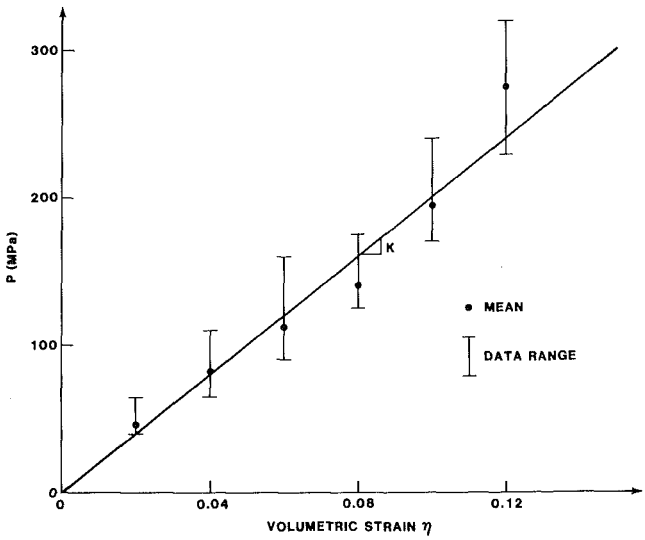

Fig. 2 Pressure-volume strain data for antelope tuff and linear hydrostat

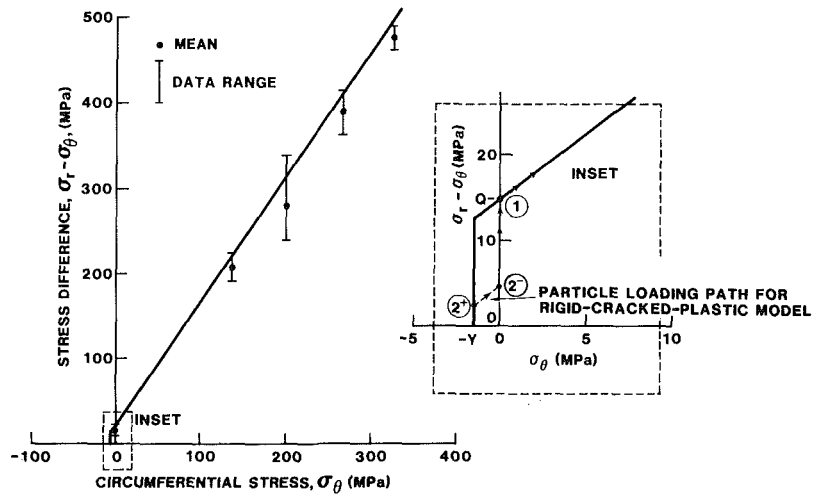

Fig. 3 Triaxial strength data for antelope tuff and the Mohr-Coulomb failure criterion with a tension cutoff

Downloaded 02 May 2010 to 171.66.16.246. Redistribution subject to ASME license or copyright; see http://www.asme.org/terms/Terms_Use.cfm

difference in axial and lateral stress, $\sigma_r - \sigma_\theta$, increased moderately with increasing axial strain to sample failure, equation (5) fitted to the data will overestimate the material resistance to deformation. The tensile strength of antelope tuff was not measured but the ratio $Q/Y = 11$ is estimated from data in [7] for a similar rock, Nevada Test Site tuff, described as welded volcanic ash with a porosity of 20 percent.

To simplify the solution procedure we assume

$$\sigma_z = \sigma_\theta \tag{7}$$

except where the response is elastic, which eliminates use of the Prandtl-Reuss equations [9]. The calculated σ_r at the conical nose is not sensitive to the assumption (7) as shown later by a comparison with results from $\sigma_z = (\sigma_r + \sigma_\theta)/2$ which has frequently been assumed in plasticity calculations [9].

The equations of conservation of momentum and mass across a cylindrical wavefront propagating in the radial direction with speed c are

$$\sigma_r^- + \rho^- v^- (v^- - c) = \sigma_r^+ + \rho^+ v^+ (v^+ - c) \tag{8}$$

$$\rho^- (v^- - c) = \rho^+ (v^+ - c) \tag{9}$$

in which $v = \partial u/\partial t$ is the particle velocity and + and − refer to particles on the radially outer and inner sides of the wave front, respectively.

The boundary condition is that the cavity radius in a given layer dz conforms to the conical nose

$$u(0, t) = (V\tan\phi)t \tag{10}$$

where V is the vertical velocity of the penetrator, assumed constant during passage through a layer, and $t = 0$ is the time at which the conical nose first contacts the layer.

Elastic-Plastic Response

For high enough radial expansion velocity, tensile stresses in the target do not exceed the tensile strength of the rock and an elastic-plastic solution is valid. In Fig. 1 the response region between interfaces 1 and 2 is elastic with wave front speed c_2 while the inner region is plastic with interface speed c_1.

Elastic Response. Equation (2) is linearized and written in terms of u using Hooke's law (with K, ν) and $\epsilon_r = \partial u/\partial R$, $\epsilon_\theta = u/R$, and $\epsilon_z = 0$. The resulting equation is reduced to a first-order ordinary differential equation in $dq/d\xi$ by the transformations

$$\xi = \frac{R}{c_1 t}; \quad \bar{u} = \frac{u}{c_1 t}; \quad \bar{u} = \xi q \tag{11}$$

where ξ is a similarity variable and c_1 is the unknown velocity of the elastic-plastic interface. Integrating, satisfying $u = 0$ at the elastic wave front ($\xi = 1/\gamma$, $\gamma = c_1/c_2$, $c_2^2 = [3((1-\nu)/(1+\nu)]K/\rho_0$), and satisfying the condition of incipient plasticity (5) at the elastic-plastic interface ($\xi = 1$) gives the results

$$\bar{u} = (1+\nu)D[f(x) - xg(x)]/(3\gamma);$$

$$\bar{v} = 2(1+\nu)Df(x)/(3\gamma) \tag{12a, b}$$

$$\bar{\sigma}_r = D[(1-2\nu)f(x)/x + g(x)]; \quad \bar{\sigma}_\theta = 2Dg(x) - \bar{\sigma}_r \tag{12c, d}$$

$$f(x) = (1-x^2)^{1/2}/x; \quad g(x) = ln[f(x) + 1/x]; \quad x = \gamma\xi$$

$$D = 3\gamma\bar{\tau}_0/[6(1-2\nu)\gamma f(\gamma) - 2\mu(1+\nu)\gamma g(\gamma)]$$

where

$$1 < \xi < 1/\gamma, \ \bar{\tau}_0 = \tau_0/K, \ \bar{v} = v/c_1, \ \bar{\sigma}_r = \bar{\sigma}_r/K, \ \bar{\sigma}_\theta = \sigma_\theta/K.$$

Elastic-Plastic Interface Speed. Equations (4), (5), and (7) are combined in the form

$$\sigma_r = (1 + 2\mu/3)K(1 - \rho_0/\rho) + 2\tau_0/3 \tag{13}$$

which applies on either side of the interface at $\xi = 1$. Then (9), and (13) are used to express (8) across $\xi = \xi_1 = 1$ in terms of v_1^-, c_1, v_1^+, σ_{r1}^+ with the result

$$\bar{v}_1^- = \bar{v}_1^+ + \frac{(\bar{\sigma}_{r1}^+ - 2\bar{\tau}_0/3)(1 - \bar{v}_1^+)}{1 + 2\mu/3 - \alpha^2(1 - \bar{v}_1^+)^2} \tag{14}$$

where $\alpha = c_1/c_P$ and $c_P = (K/\rho_0)^{1/2}$. In (14), $\bar{v}_1^+$ and $\bar{\sigma}_{r1}^+$ are known through (12b, c), but α^2 and $\bar{v}_1^-$ are unknown. c_P is often called the "plastic" wave speed and is the elastic-plastic interface speed for one-dimensional strain elastic-perfectly plastic problems. For spherical waves this interface speed is not always c_P and is unknown a priori; e.g., see Hopkins [10].

Plastic Response. Using (3)–(5) and (13) to substitute into (2) along with the transformations (11) gives the equation of motion in the plastic region

$$\left[\alpha^2\xi^4 - \left(1 + \frac{2}{3}\mu\right)(\xi + \bar{u})^2\right]\frac{d^2\bar{u}}{d\xi^2} + \left[\left(1 + \frac{2}{3}\mu\right)(\xi + \bar{u})\left(\frac{\bar{u}}{\xi} - \frac{d\bar{u}}{d\xi}\right) + -\mu\left(\xi\frac{d\bar{u}}{d\xi} + \bar{u} + \bar{u}\frac{d\bar{u}}{d\xi}\right) + \bar{\tau}_0\xi\right]\left(1 + \frac{d\bar{u}}{d\xi}\right) = 0 \tag{15}$$

Equation (15) reflects both finite strains and density changes. The solution procedure in the plastic region is an inverse numerical integration beginning at the interface $\xi = 1$ and proceeding to the cavity surface $\xi = 0$. Dependent variables

$$U = \bar{u} + \xi, \qquad N = (dU/d\xi)/\xi \tag{16a, b}$$

are used to convert (15) into a pair of first-order nonlinear differential equations which are solved by a Runge-Kutta integrating subroutine [11]. A value for the unknown constant α is assumed. With the restriction $\alpha^2 < 1 + 2\mu/3$, the coefficient of $d^2\bar{u}/d\xi^2$ in (15) will always be negative and no singularity will occur during the integration. Continuity of $\bar{u}$ at $\xi = 1$ gives a starting value, $U(\xi = 1)$, while (14) with the assumed value of α gives v_1 from which $N(\xi = 1)$ is determined. The integration progresses with ξ decreasing until $\xi = 0$ is reached and $U(\xi = 0)$ is calculated. Then the cavity expansion velocity $V\tan\phi$ corresponding to the assumed value of α is determined

$$V\tan\phi = c_1 U(0) = \alpha c_P U(0) \tag{17}$$

The stresses σ_r and σ_θ in the plastic region are related to the displacement through (13), (3), and (5). Graphical results are produced conveniently by assuming a range of values of α and calculating directly σ_r/K over a range of values of V. Results of the calculations show σ_r is always positive and $\sigma_\theta > -Y$ for high enough values of the expansion velocity V. Then the assumed elastic-plastic response is valid. At low values of V, the tensile limit is exceeded, $\sigma_\theta < -Y$, and radial cracking should be modeled.

Quasi-Static Penetration

When the penetration speed is low enough, a quasi-static analysis of the target response is valid and leads to a closed-form result for the penetration resistance. Solutions of this type with application to metal punching have been developed in [9]. The target response consists of three regions denoted plastic ($r_0 < r < r_1$), cracked ($r_1 < r < r_2$) and rigid ($r_2 < r$) where 1 and 2 refer to the interfaces in Fig. 1 and r is the Eulerian coordinate. The rigid region approximates an elastic region in which (6) is satisfied. If $\sigma_r = Y$ at $r = r_2$, the maximum tensile stress in an elastic region is $\sigma_\theta = -Y$ at $r = r_2$. The elastic region is approximated by a rigid region by requiring

Downloaded 02 May 2010 to 171.66.16.246. Redistribution subject to ASME license or copyright; see http://www.asme.org/terms/Terms_Use.cfm

$$u(r_2)=0; \quad \sigma_r(r_2)=Y \tag{18a, b}$$

In the cracked region we require $\sigma_\theta = 0$ to represent radial cracking of the material when its tensile strength is exceeded, $\sigma_\theta < -Y$. This region is significant if Y is much less than the compressive strength Q, as for rocks [7].

Stress Solution. Rewriting (2) in terms of r and omitting the interia term gives the equation of static equilibrium. This is integrated in the cracked region by using $\sigma_\theta = \sigma_z = 0$ and in the plastic region by using (4), (5), and (7). After satisfying (18*b*), incipient plasticity (5) at $r = r_1^+$, and continuity of σ_r at r_1, the stresses are determined in terms of the unknown r_1. Particular results are

$$r_2/r_1 = (\tau_0/Y)/(1-\mu/3) \tag{19}$$

$$\sigma_{r0} = \frac{\tau_0}{\mu}\left[\frac{(1+2\mu/3)}{(1-\mu/3)}\left(\frac{r_1}{r_0}\right)^{\mu/(1+2\mu/3)} - 1\right] \tag{20}$$

where σ_{r0} is the radial stress at the known cavity surface r_0.

Displacement Solution. The compressibility equation (3) is now used to determine the displacement field u and the ratio r_1/r_0. In (3) ρ_0/ρ is written in terms of P through (4) and, following Chadwick [12], the substitution $u = r - R$ is made to give

$$RdR = \frac{rdr}{(1-P/K)} \tag{21}$$

After substitution for the previously determined stresses in P, equation (21) is integrated. The result that satisfies $R = b$ at $r = r_0$, equation (18*a*), and continuity of displacements at r_1 is

$$b^2 + 2\int_{r_0}^{r_1} \frac{xdx}{1+\frac{\bar\tau_0}{\mu} - \frac{\bar\tau_0}{\mu(1-\mu/3)}(r_1/x)^{\mu/(1+2\mu/3)}} = r_2{}^2 - 2\int_{r_1}^{r_2} \frac{xdx}{1-\frac{\bar\tau_0 r_1}{(3-\mu)x}} \tag{22}$$

where b is the initial hole radius. $\bar\tau_0$ is a small parameter, $\bar\tau_0 << 1$, and the integrand on the right side of (22) is approximated by

$$\frac{x}{1-\frac{\bar\tau_0 r_1}{(3-\mu)x}} = x + \frac{\bar\tau_0 r_1}{(3-\mu)} + \ldots$$

while the terms involving $\bar\tau_0$ in the integrand on the left side of (22) are neglected. Then setting $b = 0$, and using (19) gives

$$\frac{r_1}{r_0} = \frac{(3-\mu)}{\bar\tau_0}\left(\frac{\bar Y}{6}\right)^{1/2} + \ldots \tag{23}$$

where $\bar Y = Y/K$. The error in the approximation (23) is less than 1 percent for the antelope tuff parameter values given in the following. The stress σ_{r0} required to expand a hole from zero initial radius to finite radius r_0 is given by (20) with r_1/r_0 given by (23) and estimates the stress on a penetrator at low speed.

In the limit as $\mu \to 0$, equation (23) and the use of L'Hospital's rule with equation (20) gives

$$\sigma_{r0} = \tau_0\left(1 + \ln\frac{r_1}{r_0}\right), \quad \mu = 0 \tag{24}$$

Equation (24) has application to quasi-static penetration in materials such as concrete and sea ice which have approximately constant shear strength over a substantial range of pressure.

Rigid-Cracked-Plastic Response

Results (given later) of the elastic-plastic solution for antelope tuff parameters show σ_θ exceeds the target tensile strength $\sigma_\theta < -Y$ at low enough penetration speeds. A model is introduced in which the dynamic target response consists of three regions as for the quasi-static response, a plastic region for $0 < R < R_1$, a cracked region ($\sigma_\theta = 0$) for $R_1 < R < R_2$, and a rigid region for $R > R_2$, where R is the Lagrangian coordinate. The interfaces at R_1 and R_2 are propagating radially outward and $\sigma_\theta > 0$ is required in the plastic region since material enters it from the cracked region. The loading path of a material particle is shown in Fig. 3.

A similarity variable is introduced based on the outer wave speed c_2 and the dependent variables are written in the nondimensional form

$$\xi = \frac{R}{c_2 t}; \quad \bar u = \frac{u}{c_2 t}; \quad \bar v = \frac{v}{c_2} \tag{25a, b, c}$$

which apply throughout this section.

Field Equations. The effect of radial cracking is accounted for by setting $\sigma_\theta = 0$ in the cracked region. Using (3), (4), (7), and (25*a*, *b*) in (2) gives the equation of motion for the cracked region

$$\left[\frac{\alpha^2}{3}\xi^4 - (\xi+\bar u)^2\right]\frac{d^2\bar u}{d\xi^2} + \left(1+\frac{d\bar u}{d\xi}\right)\left[\frac{\bar u^2}{\xi} - 2(\xi+\bar u)\frac{d\bar u}{d\xi}\right] = 0, \ \xi_1 < \xi < 1 \tag{26}$$

$$\alpha = c_2/c_p \tag{27}$$

The equation of motion in the plastic region has the same form as before (15) with ξ, $\bar u$, and α now given by (25*a*, *b*), and (27).

Interface Conditions. As discussed in the quasi-static response section, the rigid region approximates a region of elastic response and is represented by requiring

$$u=0; \quad v=0; \quad \rho=\rho_0; \quad \sigma_r = Y; \quad \sigma_\theta = -Y \tag{28a, b, c, d, e}$$

at $\xi = \xi_2^+$.

Applying the conservation of momentum and mass equations (8) and (9) across the rigid-cracked interface ξ_2, using $\sigma_\theta = 0$ at ξ_2^-, and using (4), (7), and (28*b*–*d*) gives

$$\alpha^2 = 3 - \bar Y/\bar v_2{}^- \tag{29}$$

with α and $\bar v_2{}^-$ given by (27) and (25*c*).

At the cracked-plastic interface ξ_1, a similar procedure shows v, ρ, σ_r, and σ_θ are continuous. An additional condition holds at this location,

$$\sigma_{r1}^+ = \tau_0/(1-\mu/3) \tag{30}$$

as determined from (5) with $\sigma_\theta = \sigma_z = 0$.

Solution Procedure. As in the elastic-plastic calculation, the field equations (26) and (15) are numerically integrated using the variables U, N (16*a*, *b*). One difference is that now both interface speeds c_1 and c_2 are unknown at the beginning of the solution. A value of $\alpha = c_2/c_P$ is assumed which through (29) determines $\bar v_2{}^-$. With this and $\bar u = 0$, equations (16*a*, *b*) determine starting values of U and N for a numerical integration of (26) which continues until a value of σ_r is calculated which satisfies (30). The corresponding value of $\xi = \xi_1$ and the cracked-plastic interface speed is determined from $c_1/c_2 = \xi_1 + \bar u_1$. At ξ_1 the variables are continuous and the plastic field equation (15) is now integrated until $\xi = 0$ is reached and V is determined through (17).

Downloaded 02 May 2010 to 171.66.16.246. Redistribution subject to ASME license or copyright; see http://www.asme.org/terms/Terms_Use.cfm

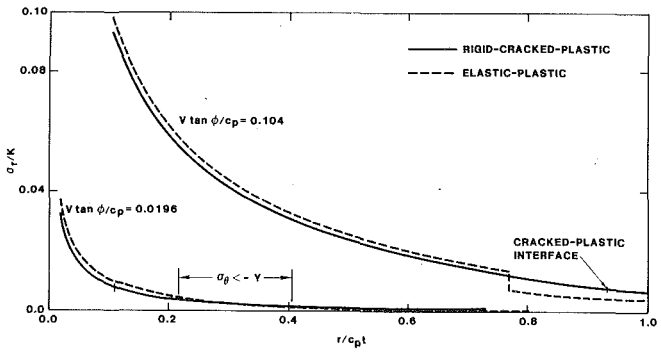

Fig. 4 Radial stress profiles in antelope tuff for two target response models and two penetrator velocities

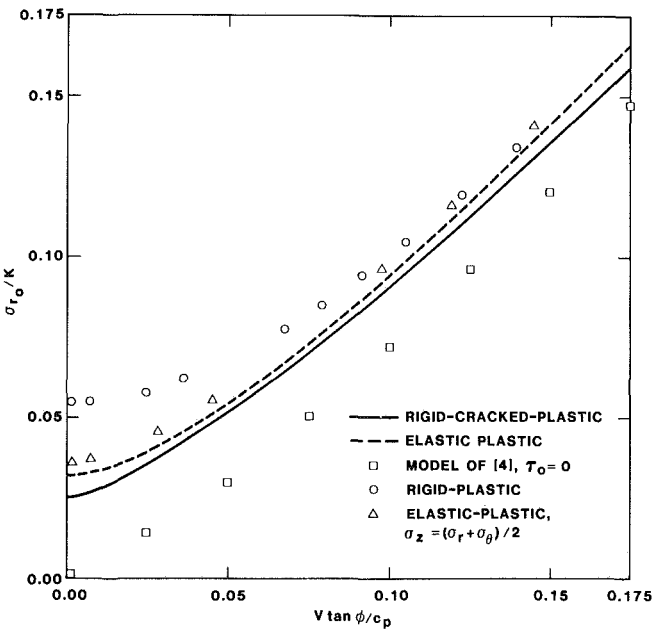

Fig. 5 Radial stress on the conical nose of a penetrator into antelope tuff for various target response models

Results and Comparison of Response Models

Following the numerical procedures discussed previously, results are calculated for the various response models using the antelope tuff target parameters $\mu = 1$, $\bar{\tau}_0 = 0.005$, $\nu = 0.234$, and $\bar{Y} = 0.0007$ from [7, 8]. Stress wave profiles in antelope tuff are shown in Fig. 4 for the elastic-plastic and rigid-cracked-plastic models at two penetrator velocities. $V\tan\phi/c_P = 0.104$ is the minimum speed at which the tensile strength is not exceeded in the elastic-plastic solution and the curves agree closely, except for the small jump at the elastic-plastic interface. At the lower speed the tensile strength Y is exceeded over a region of the elastic-plastic profile which is approximately half the extent of the cracked region. These profiles are representative of quasi-static profiles which depend on the current cavity radius, but not on its history, and, therefore, also represent the response produced by an ogival-nosed penetrator at low speed. They indicate the loading of a material particle increases monotonically and smoothly in contrast with the loading process (initial peak followed by unloading) which has sometimes been assumed in previous penetrator analyses as justification for the locked hydrostat approximation.

Figure 5 shows the radial stress component on the conical nose σ_{r0} over a range of penetration speeds. For $V\tan\phi/c_P > 0.104$, numerical results indicate $\sigma_\theta \geq -Y$ and the elastic-plastic solution is valid. At lower velocities a cracked region should be modeled in the response. The rigid-cracked-plastic solution gives a 20 percent lower value of σ_{r0} than does the elastic-plastic solution as $V \to 0$ and does not differ significantly for $V\tan\phi/c_p > 0.104$. At low penetration speeds the rigid-cracked-plastic stress on the penetrator is higher than that which would be calculated if the rigid region were replaced by an elastic region.

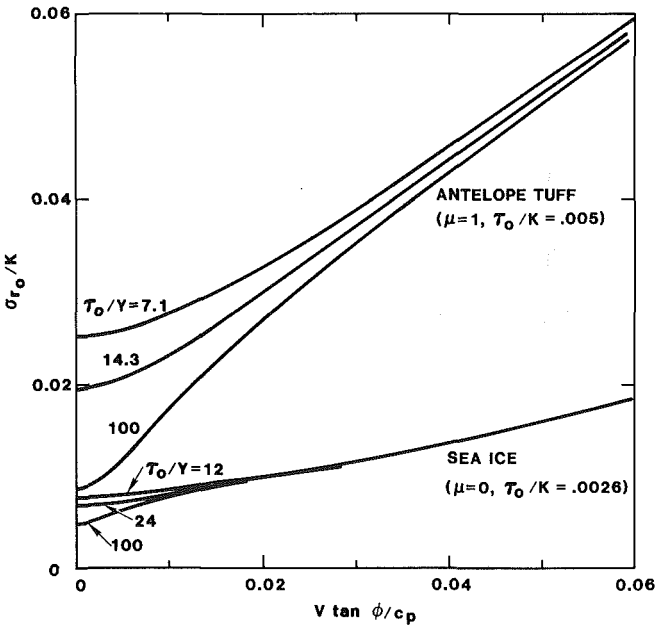

Fig. 6 Radial stress on the conical nose of a penetrator into antelope tuff and sea ice for various values of the tensile strengths

The model of [4] is based on (4) and (5) with $\tau_0 = 0$. It gives $\sigma_{r0} \to 0$ as $V \to 0$, but approaches the other models at high enough velocity.

The "rigid-plastic" model consists of a plastic region governed by (15) and a rigid region represented by setting $\sigma_{r1}^+ = \tau_0 (1 - \mu/3)$, from (30), and $u_1^+ = 0$ at $R = R_1^+$. This model overestimates σ_{r0} by about a factor of two in the quasi-static limit and merges with the more accurate models at higher speeds.

A comparison of elastic-plastic results based on $\sigma_z = (\sigma_r + \sigma_\theta)/2$, as frequently assumed in metal analyses [9], and on $\sigma_z = \sigma_\theta$, as used in the present work, shows a maximum difference of 12 percent in σ_{r0} in the quasi-static limit and a smaller difference at higher speeds.

Tensile strength measurements for rock may vary by a factor of 2 or more as discussed in [7]. Figure 6 shows the effect of uncertainty in Y on the stress versus velocity curves for antelope tuff ($\mu = 1$, $\bar{\tau}_0 = 0.005$) and sea ice ($\mu = 0$, $\bar{\tau}_0 = 0.0026$ from [13]) for the rigid-cracked-plastic model. Differences in Y are significant only at very low speeds for both materials.

Figures 5 and 6 indicate that the rock property detail required to estimate penetration resistance depends on the penetrator speed. At the highest speeds shown, it is sufficient to know ρ_0, K, and μ; as the speed is decreased, τ_0 is also needed; and at still lower speeds into the quasi-static regime, Y becomes important.

Comparison With a Field Test

Results from the rigid-cracked-plastic, cavity-expansion analysis shown in Fig. 5 are used to compute the deceleration, velocity, and depth histories corresponding to a recent field test into a layer of antelope tuff [14]. Target material data are

Downloaded 02 May 2010 to 171.66.16.246. Redistribution subject to ASME license or copyright; see http://www.asme.org/terms/Terms_Use.cfm

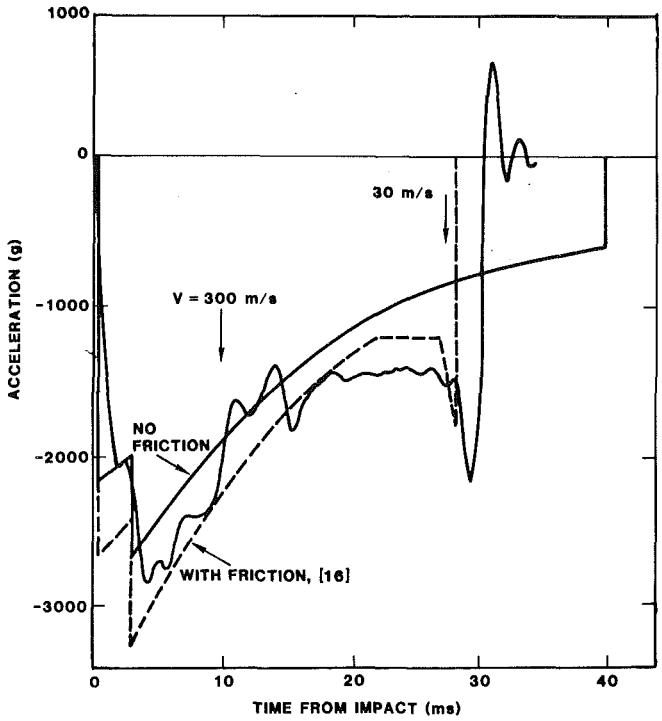

Fig. 7 Acceleration – time measurement and predictions for a field test into antelope tuff

presented in Figs. 2 and 3. Parameters used in the theory are those of Fig. 5 and $K = 2.0$ GPa, $\rho_0 = 1.62$ Mg/m^3.

The penetrator had total length 1.56m, aft-body diameter 0.156m, an ogival nose shape with 6.0 CRH (caliber radius head), and mass 162 kg. For this test, the penetrator was propelled with a Davis Gun [4] and impacted the antelope tuff layer at 520 m/s. A 55.3 kg pusher plate, which fits the internal diameter of the gun barrel, was attached to the end of the penetrator. An onboard accelerometer measured the deceleration history with 2 kHz resolution and this was integrated to give velocity and depth [14]. The deceleration data were filtered to 500 Hz to remove structural vibrations and obtain the rigid body deceleration shown in Fig. 7.

The theory in this study is for a penetrator with a conical nose whereas the test penetrator had an ogival nose. Data from several hundred soil penetration tests [2] indicate that a 6.0 CRH ogival nose and a conical nose with $\tan\phi = 0.30$ are nearly equivalent and this is used for the calculations.

For the theory, it is assumed that no deceleration takes place until the equivalent conical nose is embedded. Post-test observations of dry rock, concrete, and sea ice targets indicate a crater near the target surface, which is usually one to two nose lengths deep, followed by a tunnel, which has nearly the penetrator aft-body diameter. As in [4], sliding frictional forces between the conical nose and the target are neglected and equilibrium in the r and z directions is applied to a target particle at the conical surface to show $\sigma = \sigma_{r0} = \sigma_{z0}$, where σ and σ_{r0} are the normal pressure and the radial stress on the conical nose, respectively. Integrating the normal pressure over the nose gives $F = \pi a^2\ \sigma_{r0}$, where F is the resultant axial force on the penetrator and a is the aft-body radius. The curve of Fig. 5 for the rigid-cracked-plastic model is used to calculate the penetrator rigid body deceleration which is compared with the measurement in Fig. 7. According to the theory, at $t = 0.50$ ms the nose is just embedded, at $t = 3.0$ ms the pusher plate is removed from the penetrator by the rock surface producing a deceleration jump, and at 40 ms the penetrator velocity reduces to zero and is assumed to remain zero which results in the deceleration jumping to zero. The corresponding calculated final penetrator depth is 7.0 m while the measured depth was 7.9 m.

The theory underpredicts deceleration at late time and this could be accounted for by the effect of sliding friction between the penetrator and rock target. Post-test observations [15] of penetrators show surface melting of the nose and some wear on the aft-body. Data for steel on steel [16] indicate a constant coefficient of friction $f = 0.08$ for sliding velocities greater than 300 m/s and that f increases as the sliding velocity decreases; e.g., $f = 0.25$ at 30 m/s. A comparison of the computed and measured responses shows a departure in the velocity regime where the data of [16] would indicate an increased friction resistance. If friction is included on the nose and neglected on the aft-body, the resultant axial force is $F = \pi a^2\ \sigma_{r0}\ (1 + f/\tan\phi)$, where f is the coefficient of sliding friction between the penetrator nose and rock target. In [16] it is suggested that the frictional resistance is controlled by a thin melt layer of the material with the lower melting point, which for the penetrator test would be the steel of the penetrator. Thus, the steel on steel data may approximate the sliding frictional resistance of steel on antelope tuff and these data from [16] are used to obtain the predicted deceleration curve with friction in Fig. 7. This curve shows a significant increase in the deceleration just prior to the penetrator stopping which is in qualitative agreement with the measured deceleration.

Conclusions

At high enough penetration speeds, an elastic-plastic solution for the Mohr-Coulomb target response is valid, while at low speeds an additional response region containing radial cracks is needed in the solution. The present target model gives a nonzero minimum force on the penetrator in the quasi-static limit as compared with a zero force from the model of [4]. Calculated stress wave profiles in antelope tuff show smooth, monotonic loading of a target particle for either conical or ogival-nosed penetrators over a substantial low speed regime. Graphical results indicate that the target description detail required to determine the force on a penetrator depends on the penetrator speed. A comparison of predicted and measured penetrator decelerations for a field test into antelope tuff shows reasonable agreement. A sharp increase in the measured deceleration just before the penetrator stopped could be a result of velocity-dependent frictional forces.

References

1 Backman, M. E., and Goldsmith, W., "The Mechanics of Penetration of Projectiles into Targets," *International Journal of Engineering Science*, Vol. 16, 1978, pp. 1–99.

2 Young, C. W., "Depth Prediction for Earth Penetrating Projectiles," *Journal of Soil Mechanics and Foundation Division of ASCE*, May 1969, pp. 803–817.

3 Hill, R., "Cavitation and the Influence of Headshape in Attack of Thick Targets by Non-Deforming Projectiles," *Journal of the Mechanics and Physics of Solids*, Vol. 28, 1980.

4 Forrestal, M. J., Longcope, D. B., and Norwood, F. R., "A Model to Estimate Forces on Conical Penetrators into Dry Porous Rock," ASME JOURNAL OF APPLIED MECHANICS, Vol. 48, 1981, pp. 25–29.

5 Wagner, M. H., Fulton, C. C., and Kreyenhagen, K. N., "Finite-Difference Code Analyses of Earth Penetrator Dynamics in Rock Media," DNA 4069T, California Research and Technology, Inc., Woodland Hills, Calif., 91367, Nov. 1976.

6 Forrestal, M. J., Norwood, F. R., and Longcope, D. B., "Penetration Into Targets Described by Locked Hydrostats and Shear Strength," *International Journal of Solids and Structures*, Vol. 17, 1981, pp. 915–924.

7 Goodman, R. E., *Introduction to Rock Mechanics*, Wiley, New York, 1980.

8 Cooley, C. H., "Testing Program on TTR Antelope Tuff," Terra Tek, Salt Lake City, Utah, letter reports to Sandia, Aug. 1979, July 1980, and Jan. 1981.

9 Hill, R., *The Mathematical Theory of Plasticity*, Oxford, London, 1950.

10 Hopkins, H. G., "Dynamic Expansion of Spherical Cavities in Metals,"

Downloaded 02 May 2010 to 171.66.16.246. Redistribution subject to ASME license or copyright; see http://www.asme.org/terms/Terms_Use.cfm

Progress in Solid Mechanics, Vol. 1, Chapter 3, Sneddon, I. N., and Hill, R., eds., North Holland, Amsterdam, 1960.

11 Shampine, L. F., and Watts, H. A., "Practical Solution of Ordinary Differential Equations by Runge-Kutta Methods," SAND76-0585, Sandia Laboratories, Albuquerque, NM, Dec. 1976.

12 Chadwick, P., "The Quasi-Static Expansion of a Spherical Cavity in Metals and Ideal Soils," *Quarterly Journal of Mechanics and Applied Mathematics*, Vol. 12, Part 1, 1959, pp. 52–71.

13 Hightower, M. M., Norwood, F. R., and Young, C. W., "An Analytical Model of Ice Penetration," SAND82-0599, Sandia National Laboratories, Albuquerque, N. Mex., Nov. 1982.

14 Wood, W. R., "Instrumentation for Penetrator Test DGU-TP-3," Internal Sandia Letter, Oct. 21, 1980.

15 Forrestal, M. J., and Grady, D. E., "Penetration Experiments for Normal Impact into Geological Targets," *International Journal of Solids and Structures*, Vol. 18, No. 3, 1982, pp. 229–234.

16 Bowden, F. P., and Tabor, D., *The Friction and Lubrication of Solids*, Part 2, Chapter 22, Oxford, London, 1968.

Downloaded 02 May 2010 to 171.66.16.246. Redistribution subject to ASME license or copyright; see http://www.asme.org/terms/Terms_Use.cfm

Inertial Effects in Poroelasticity

R. M. Bowen
Mem. ASME

R. R. Lockett[1]

Department of Mechanical Engineering,
Rice University,
Houston, Texas 77001

The dynamic behavior of a chemically inert, isothermal mixture of an isotropic elastic solid and an elastic fluid is studied. Geometrically, this mixture is assumed to comprise a layer of fixed depth, bounded below by a rigid, impervious surface, and above by a free surface to which loads are applied. The resulting boundary-initial value problem is solved by use of a Green's function. Two different loading conditions are used to demonstrate the effect of including inertia terms in the equations of motion. In the first example of a constant compressive load, our result is found to agree with the inertia-free solution only for a certain long-time approximation. The second example shows that for a harmonically varying compression, resonance displacements occur at certain loading frequencies, whereas the solution obtained by neglecting inertia does not predict this behavior.

1 Introduction

This paper is concerned with the question of whether one can justify neglecting constituent inertia terms in the equations of poroelasticity. The poroelasticity model is a linearized model of a compressible isothermal mixture of an isotropic elastic solid and an elastic fluid. Formulations of this model can be found in many articles on poroelasticity. In this paper, the governing equations are presented in the notation used by Bowen [1, 2].

If one approaches classical diffusion theories from the standpoint of the general theory of mixtures, it becomes apparent that Darcy's law and Fick's law can only be reached after a complicated list of specializing assumptions. This list always contains some assumption regarding the acceleration of the constituents. Within the context of porous media models, Darcy's law simply neglects the acceleration of the fluid. It is frequently the case that the acceleration of the solid is also neglected. For example, the classical article by Biot [3] developed an inertia-free model for the study of consolidation problems. This model has been utilized extensively in the study of fluid-filled porous materials. The article by Rice and Cleary [4] should be consulted by readers interested in the Biot model.

When interia terms are neglected, the resulting partial differential equations are singular perturbations of the original equations. As such, one would not expect the approximate equations to yield acceptable short-time solutions. For example, one could not satisfy the same number of initial conditions with the approximate equations. In spite of the singular nature of the inertia-free approximation, persuasive arguments can be made that suggest that inertia terms are only important for times that are small. Roughly speaking, one argues that diffusion is a slow process whose effects become important for a long time. Therefore, suggests the argument, one might as well neglect at the outset terms in the governing partial differential equations which have no significant efffect on the long-time answers. By the use of a rather simple example, we will show that the preceding argument is not always correct. An example will be given that illustrates a long-time inertial effect that cannot be neglected.

The approach used here is straightforward. We will formulate and solve certain problems with and without the inertia terms. We will then look at approximations sufficient to reduce the solutions with inertia to the solutions without inertia. Next, we will investigate whether these approximations are realistic. In deciding whether a particular approximation is realistic we will frequently use order-of-magnitude arguments based on published material properties of definite porous materials. The material properties adopted here are those summarized by Rice and Cleary [4].

Section 2 contains a summary of the governing equations of poroelasticity. Section 3 represents the solution of a class of one-dimensional initial-boundary value problems in terms of an appropriate Green's function. The initial-boundary value problem for the Green's function is such that it can be represented in a classical form as an eigenfunction expansion. The time-dependent part of the Green's function obeys a system of ordinary differential equations. The inertial effects of interest in this paper are isolated in the form of this system of equations. Section 4 contains the details of how one calculates the Green's function. This calculation involves factoring a certain fourth-order polynomial. It turns out that rather accurate approximations can be derived for the roots of this polynomial. Section 5 contains the derivation of these approximate roots.

Section 6 contains our first example problem. Essentially it is the same one-dimensional problem solved by Biot [3] except that all inertia terms have been restored. This problem attempts to determine the displacement resulting from a compressive load applied to a porous material of specified length. The sufficient conditions required to reduce this solution to Biot's are discussed in detail. Among these conditions is one that characterizes the initial layer, inside of

[1] Currently at M.I.T., Cambridge, Mass. 02139.

Contributed by the Applied Mechanics Division for publication in the JOURNAL OF APPLIED MECHANICS.

Discussion on this paper should be addressed to the Editorial Department, ASME, United Engineering Center, 345 East 47th Street, New York, N.Y. 10017, and will be accepted until two months after final publication of the paper itself in the JOURNAL OF APPLIED MECHANICS. Manuscript received by ASME Applied Mechanics Division, May, 1982; final revision, January, 1983.

Copyright © 1983 by ASME
Downloaded 02 May 2010 to 171.66.16.246. Redistribution subject to ASME license or copyright; see http://www.asme.org/terms/Terms_Use.cfm

which inertial terms cannot be neglected. By use of the example data mentioned in the foregoing, the conclusion for this problem is that inertial effects are essentially unimportant. In other words, the sufficient conditions are reasonable physical assumptions.

Our final section contains a slight modification of the Biot problem. The compressive load is allowed to oscillate with a prescribed frequency. This problem is solved with and without the inertia terms. In this case the approximations sufficient to reduce the solution with inertia to the one without are simply unacceptable. We will show that the prescribed frequency must be unreasonably small so one can utilize the inertia-free solution. This example illustrates the long-time inertia effect essential to the premise of this paper.

In Appendix A we have listed the material constants that have been calculated from the data presented by Rice and Cleary.

2 Governing Equations of Poroelasticity

For a binary isothermal mixture of an isotropic elastic solid with a linear compressible fluid, the governing partial differential equations are:

$$\rho_f \frac{\partial^2 \mathbf{u}_f}{\partial t^2} = \lambda_f \operatorname{grad}(\operatorname{div} \mathbf{u}_f) + \lambda_{fs} \operatorname{grad}(\operatorname{div} \mathbf{u}_s) - \xi\left(\frac{\partial \mathbf{u}_f}{\partial t} - \frac{\partial \mathbf{u}_s}{\partial t}\right) \tag{2.1}$$

and

$$\rho_s \frac{\partial^2 \mathbf{u}_s}{\partial t^2} = (\lambda_s + \mu_s) \operatorname{grad}(\operatorname{div} \mathbf{u}_s) + \mu_s \operatorname{div}(\operatorname{grad} \mathbf{u}_s) + \lambda_{fs} \operatorname{grad}(\operatorname{div} \mathbf{u}_f) + \xi\left(\frac{\partial \mathbf{u}_f}{\partial t} - \frac{\partial \mathbf{u}_s}{\partial t}\right), \tag{2.2}$$

where ρ_f is the reference density of the fluid, $\mathbf{u}_f$ is the fluid displacement, ρ_s is the reference density of the solid, and $\mathbf{u}_s$ is its displacement. The coefficients λ_f, λ_{fs}, λ_s, and μ_s are elastic constants, and ξ is the drag coefficient. A derivation of these field equations from the general theory of mixtures can be found in the articles by Bowen [1, 2]. The material constants in (2.1) and (2.2) are required to obey the following inequalities:

$$\lambda_f > 0, \tag{2.3}$$

$$\lambda_f\left(\lambda_s + \frac{2}{3}\mu_s\right) > \lambda^2_{fs}, \tag{2.4}$$

$$\mu_s > 0, \tag{2.5}$$

and

$$\xi > 0. \tag{2.6}$$

The constitutive equations used to derive (2.1) and (2.2) are

$$\mathbf{T} = (\lambda_f + \lambda_{fs})(\operatorname{div} \mathbf{u}_f)\,\mathbf{I} + (\lambda_s + \lambda_{fs})(tr\,\mathbf{E}_s)\,\mathbf{I} + 2\mu_s \mathbf{E}_s \tag{2.7}$$

and

$$\rho_f \mu_f = -\lambda_f \operatorname{div} \mathbf{u}_f - \lambda_{fs}\, tr\, \mathbf{E}_s, \tag{2.8}$$

where $\mathbf{T}$ is the stress on the porous material and μ_f represents the chemical potential for the fluid. It is customary to replace the chemical potential by the fluid pore pressure P_f. These two quantities are related by

$$\phi P_f = \rho_f \mu_f, \tag{2.9}$$

where ϕ is the porosity of the solid in its reference state. The quantity $\mathbf{E}_s$ appearing in (2.7) and (2.8) is the infinitesimal strain tensor for the solid, defined by

$$\mathbf{E}_s = \frac{1}{2}(\operatorname{grad} \mathbf{u}_s + (\operatorname{grad} \mathbf{u}_s)^T). \tag{2.10}$$

This work is concerned with one-dimensional longitudinal motions of the fluid and solid. For this case, the field equations may be simplified and written in matrix form as

$$\mathbf{M}\frac{\partial^2 \mathbf{u}}{\partial t^2} = \mathbf{Q}\frac{\partial^2 \mathbf{u}}{\partial x^2} - \xi \mathbf{E}\frac{\partial \mathbf{u}}{\partial t}. \tag{2.11}$$

Here, $\mathbf{u}$ is the displacement matrix defined by

$$\mathbf{u} = \begin{bmatrix} u_f(x,t) \\ u_s(x,t) \end{bmatrix}, \tag{2.12}$$

where u_f and u_s are now the one-dimensional fluid and solid displacements, respectively. The matrices $\mathbf{M}$, $\mathbf{Q}$, and $\mathbf{E}$ in (2.11) are symmetric matrices defined by

$$\mathbf{M} = \begin{bmatrix} \rho_f & 0 \\ 0 & \rho_s \end{bmatrix}, \tag{2.13}$$

$$\mathbf{Q} = \begin{bmatrix} \lambda_f & \lambda_{fs} \\ \lambda_{fs} & \lambda_s + 2\mu_s \end{bmatrix}, \tag{2.14}$$

and

$$\mathbf{E} = \begin{bmatrix} 1 & -1 \\ -1 & 1 \end{bmatrix}. \tag{2.15}$$

Here, $\mathbf{M}$ is the bulk density matrix, $\mathbf{Q}$ is the elastic coefficient matrix, and $\xi\mathbf{E}$ is the damping matrix. Because of the inequalities (2.3)–(2.5), the matrix $\mathbf{Q}$ is positive definite. Clearly $\mathbf{M}$ is positive definite and $\mathbf{E}$ is positive semidefinite.

3 Boundary-Initial Value Problem Formulation and the Green's Function

In this paper, we are interested in a class of boundary value problems geometrically similar to one investigated by Biot [3]. Consider a column of fluid-saturated poroelastic material confined laterally by a rigid sheath so that no lateral expansion can occur. At the top, the stress and the pore pressure are prescribed. At the bottom of the column, the fluid and solid displacements are prescribed.

In the mathematical statement of this problem, take x to be positive downward with its origin at the upper surface. Initially we have

$$\mathbf{u}(x,0) = \mathbf{f}(x) \tag{3.1}$$

and

$$\frac{\partial \mathbf{u}}{\partial t}(x,0) = \mathbf{g}(x) \tag{3.2}$$

for $0 < x < h$, where h is the length of the column. At $x = 0$ we require that

$$T(0,t) = -s(t) \tag{3.3}$$

and

$$P_f(0,t) = r(t) \tag{3.4}$$

for $0 < t < \infty$. At $x = h$ we require that

$$\mathbf{u}(h,t) = \mathbf{k}(t) \tag{3.5}$$

for $0 < t < \infty$. The functions $\mathbf{f}$, $\mathbf{g}$, s, r, and $\mathbf{k}$ constitute the data for our class of problems and, of course, are regarded as given. It is convenient to define a column matrix $\mathbf{q}(t)$ by

Downloaded 02 May 2010 to 171.66.16.246. Redistribution subject to ASME license or copyright; see http://www.asme.org/terms/Terms_Use.cfm

$$\mathbf{q}(t) = \begin{bmatrix} -\phi r(t) \\ -s(t) + \phi r(t) \end{bmatrix}. \tag{3.6}$$

With this definition, the boundary conditions (3.3) and (3.4) can be written

$$\mathbf{Q} \frac{\partial \mathbf{u}}{\partial x}(0,t) = \mathbf{q}(t) \tag{3.7}$$

after (2.7)–(2.9) and (2.14) have been used.

By use of standard Green's function arguments, the solution $\mathbf{u}(x,t)$ of our initial-boundary value problem can be expressed in terms of the data and a Green's matrix. The result is as follows:

$$\begin{aligned} \mathbf{u}(x,t) = &\int_0^h \mathbf{G}(x,t,x_0,0)\,\mathbf{M}\,\mathbf{g}(x_0)dx_0 \\ &+ \frac{\partial}{\partial t}\int_0^h \mathbf{G}(x,t,x_0,0)\,\mathbf{M}\,\mathbf{f}(x_0)dx_0 \\ &+ \xi\int_0^h \mathbf{G}(x,t,x_0,0)\,\mathbf{E}\,\mathbf{f}(x_0)dx_0 \\ &- \int_0^t \mathbf{G}(x,t,0,t_0)\,\mathbf{q}(t_0)dt_0 \\ &- \int_0^t \frac{\partial \mathbf{G}}{\partial x_0}(x,t,h,t_0)\,\mathbf{Q}\,\mathbf{k}(t_0)dt_0. \end{aligned} \tag{3.8}$$

The quantity $\mathbf{G}(x,t,x_0,t_0)$ is the Green's matrix defined by

$$\begin{aligned} &\mathbf{M}\frac{\partial^2 \mathbf{G}}{\partial t^2}(x,t,x_0,t_0) + \xi\mathbf{E}\frac{\partial \mathbf{G}}{\partial t}(x,t,x_0,t_0) \\ &\quad - \mathbf{Q}\frac{\partial^2 \mathbf{G}}{\partial x^2}(x,t,x_0,t_0) = \delta(t-t_0)\delta(x-x_0)\mathbf{I}, \end{aligned} \tag{3.9}$$

where

$$\mathbf{G}(x,t,x_0,t_0) = \mathbf{0} \tag{3.10}$$

for $t < t_0$ and $0 < x < h$,

$$\mathbf{G}(h,t,x_0,t_0) = \mathbf{0} \tag{3.11}$$

for $0 < t < \infty$ and

$$\frac{\partial \mathbf{G}}{\partial x}(0,t,x_0,t_0) = \mathbf{0} \tag{3.12}$$

for $0 < t < \infty$. In (3.9) $\mathbf{I}$ is the 2×2 identity matrix, x_0 is an arbitrary point in $(0,h)$, and t_0 is an arbitrary time in $(0,\infty)$. In addition, $\delta(x-x_0)$ and $\delta(t-t_0)$ are the Dirac delta functions with poles at x_0 and t_0, respectively.

4 Solution for the Green's Function

We will use an eigenfunction expansion to determine $\mathbf{G}(x,t,x_0,t_0)$. If one examines the eigenfunctions associated with the space part of our differential operator, it is possible to conclude that $\mathbf{G}(x,t,x_0,t_0)$ has the representation

$$\mathbf{G}(x,t,x_0,t_0) = \sum_{n=1}^{\infty} \mathbf{K}_n(t,t_0)\,\mathrm{Cos}\frac{(2n-1)\pi x}{2h}\,\mathrm{Cos}\frac{(2n-1)\pi x_0}{2h}. \tag{4.1}$$

Note that (4.1) obeys the boundary conditions (3.11) and (3.12). The 2×2 matrices $\mathbf{K}_n$ are determined by substitution of (4.1) into (3.9). The result of this calculation is that each $\mathbf{K}_n(t,t_0)$ must obey

$$\mathbf{M}\ddot{\mathbf{K}}_n(t,t_0) + \xi\mathbf{E}\dot{\mathbf{K}}_n(t,t_0) + \frac{(2n-1)^2\pi^2}{4h^2}\mathbf{Q}\,\mathbf{K}_n(t,t_0) = \frac{2}{h}\delta(t-t_0)\mathbf{I}. \tag{4.2}$$

The initial condition (3.10) implies that

$$\mathbf{K}_n(t,t_0) = \mathbf{0} \tag{4.3}$$

for $t < t_0$. This fact allows us to compute the Laplace transform of (4.2) and obtain

$$\left(s^2\mathbf{M} + \xi s\mathbf{E} + \frac{(2n-1)^2\pi^2}{4h^2}\mathbf{Q}\right)\bar{\mathbf{K}}_n(s,t_0) = \frac{2}{h}e^{-st_0}\mathbf{I}, \tag{4.4}$$

where s denotes the transform parameter and $\bar{\mathbf{K}}_n(s,t_0)$ denotes the Laplace transform of $\mathbf{K}_n(t,t_0)$. The formal solution of (4.4) is

$$\bar{\mathbf{K}}_n(s,t_0) = \frac{2}{h}e^{-st_0}\frac{s^2\,\mathrm{adj}\,\mathbf{M} + \xi s\,\mathrm{adj}\,\mathbf{E} + \frac{(2n-1)^2\pi^2}{4h^2}\mathrm{adj}\,\mathbf{Q}}{\det\left(s^2\mathbf{M} + \xi s\,\mathbf{E} + \frac{(2n-1)^2\pi^2}{4h^2}\mathbf{Q}\right)}, \tag{4.5}$$

where adj denotes the matrix adjoint operation. In other words, adj $\mathbf{Q}$ is the transposed matrix of cofactors of the 2×2 matrix $\mathbf{Q}$. Because $\mathbf{M}$, $\mathbf{Q}$, and $\mathbf{E}$ are 2×2 matrices, the adj operator is linear. It is useful to note in passing that if we neglect inertia in (4.5) by placing $\mathbf{M}$ to zero, the resulting formula is the one obtained by Bowen [5, Sect. 4] in the derivation of the Green's function for classical consolidation problems.

To compute the inverse Laplace transform of $\bar{\mathbf{K}}_n(s,t_0)$ in (4.5), we must calculate the roots β_n of

$$\det\left(\beta_n^2\mathbf{M} + \xi\beta_n\mathbf{E} + \frac{(2n-1)^2\pi^2}{4h^2}\mathbf{Q}\right) = 0. \tag{4.6}$$

The four roots of (4.6) are either all real, two real, and one complex conjugate pair, or two complex conjugate pairs. In each case it is possible to prove that the real part of each root cannot be positive.

Since analytical solutions to fourth-order polynomials are difficult to interpret, it was necessary to solve (4.6) numerically for certain example porous materials. The materials selected and their material properties are discussed in Appendix A. For our immediate purposes, it is sufficient to note that none of the materials considered had four real roots for any nonzero value of n. Roughly speaking, for small n there are two real and one complex conjugate pair of roots, and we will factor (4.6) in the form

$$\begin{aligned} &\det\left(\beta_n^2\mathbf{M} + \xi\beta_n\mathbf{E} + \frac{(2n-1)^2\pi^2}{4h^2}\mathbf{Q}\right) \\ &= \det\mathbf{M}(\beta_n+\alpha_n)(\beta_n+\gamma_n)((\beta_n+\zeta_n)^2+\omega_n^2). \end{aligned} \tag{4.7}$$

As n increases, the numbers α_n and γ_n approach each other until they become equal. For larger values of n these two real roots branch into another complex conjugate pair. In this case, we will factor (4.6) in the form

$$\begin{aligned} &\det\left(\beta_n^2\mathbf{M} + \xi\beta_n\mathbf{E} + \frac{(2n-1)^2\pi^2}{4h^2}\mathbf{Q}\right) \\ &= \det\mathbf{M}((\beta_n+\zeta_n^{(1)})^2+\omega_n^{(1)2})((\beta_n+\zeta_n^{(2)})^2+\omega_n^{(2)2}). \end{aligned} \tag{4.8}$$

In the first case, by use of the factorization (4.7), we can invert (4.5) to obtain

$$\mathbf{K}_n(t,t_0) = \frac{2}{h}H(t-t_0)\left\{e^{-\alpha_n(t-t_0)}\mathbf{A}_n + e^{-\gamma_n(t-t_0)}\mathbf{B}_n\right.$$

Downloaded 02 May 2010 to 171.66.16.246. Redistribution subject to ASME license or copyright; see http://www.asme.org/terms/Terms_Use.cfm

$$-e^{-\zeta_n(t-t_0)}\,\mathrm{Cos}\,\omega_n(t-t_0)(\mathbf{A}_n+\mathbf{B}_n)$$
$$+e^{-\zeta_n(t-t_0)}\,\mathrm{Sin}\,\omega_n(t-t_0)\Big(\frac{\alpha_n-\zeta_n}{\omega_n}\,\mathbf{A}_n+\frac{\gamma_n-\zeta_n}{\omega_n}\,\mathbf{B}_n$$
$$+\frac{1}{\omega_n}\,\mathbf{M}^{-1}\Big)\Big\}, \tag{4.9}$$

where H is the Heaviside step function,

$$\mathbf{A}_n=\frac{1}{(\det\mathbf{M})\,(\gamma_n-\alpha_n)\,((\alpha_n-\zeta_n)^2+\omega_n^2)}\Big\{\alpha_n^2\,\mathrm{adj}\,\mathbf{M}$$
$$-\alpha_n\,\xi\,\mathrm{adj}\,\mathbf{E}+\frac{(2n-1)^2\pi^2}{4h^2}\,\mathrm{adj}\,\mathbf{Q}\Big\}, \tag{4.10}$$

$$\mathbf{B}_n=\frac{1}{(\det\mathbf{M})\,(\alpha_n-\gamma_n)\,((\gamma_n-\zeta_n)^2+\omega_n^2)}\Big\{\gamma_n^2\,\mathrm{adj}\,\mathbf{M}$$
$$-\gamma_n\,\xi\,\mathrm{adj}\,\mathbf{E}+\frac{(2n-1)^2\pi^2}{4h^2}\,\mathrm{adj}\,\mathbf{Q}\Big\}. \tag{4.11}$$

It follows from (4.9) that

$$\mathbf{K}_n(t_0^+,t_0)=\mathbf{0} \tag{4.12}$$

and

$$\mathbf{M}\,\frac{\partial\mathbf{K}_n}{\partial t}\,(t_0^+,t_0)=\frac{2}{h}\,\mathbf{I}. \tag{4.13}$$

These results could have been established directly from (4.2).

In the case of large n, the factorization (4.8) is used and (4.5) inverts to the result

$$\mathbf{K}_n(t,t_0)=\frac{2}{h}\,H(t-t_0)\Big\{e^{-\zeta_n^{(1)}(t-t_0)}(\mathbf{C}_n^{(1)}$$
$$\mathrm{Sin}\,\omega_n^{(1)}(t-t_0)-\mathbf{D}_n^{(1)}\,\mathrm{Cos}\,\omega_n^{(1)}(t-t_0))$$
$$+e^{-\zeta_n^{(2)}(t-t_0)}(\mathbf{C}_n^{(2)}\,\mathrm{Sin}\,\omega_n^{(2)}(t-t_0)$$
$$-\mathbf{D}_n^{(2)}\,\mathrm{Cos}\,\omega_n^{(2)}(t-t_0))\Big\}. \tag{4.14}$$

The matrices $\mathbf{C}_n^{(1)}$, $\mathbf{C}_n^{(2)}$, $\mathbf{D}_n^{(1)}$, and $\mathbf{D}_n^{(2)}$ are defined in terms of $\mathbf{M}$, $\mathbf{Q}$, $\mathbf{E}$, and the roots of (4.8) by lengthy and complicated formulas. It turns out that the number of terms in the expansion (4.1) before one must use (4.14) is extremely large for the example materials discussed in Appendix A. For a height of 100 m, the smallest number of terms arises for Berea sandstone. In this case it takes more than 12,000 terms before one must utilize (4.14) rather than (4.9). Thus, for the sake of brevity, we will not list the formulas that define $\mathbf{C}_n^{(1)}$, $\mathbf{C}_n^{(2)}$, $\mathbf{D}_n^{(1)}$, and $\mathbf{D}_n^{(2)}$.

To make comparisons with the inertia-free case, it is desirable to invert (4.5) in the case where $\mathbf{M}$ is placed to zero. The result in this case turns out to be

$$\mathbf{K}_n(t,t_0)=\frac{2}{h}\,H(t-t_0)\,e^{-\frac{(2n-1)^2\pi^2}{4h^2}c(t-t_0)}\,\mathbf{F}$$
$$+\frac{\mathrm{adj}\,\mathbf{E}}{tr((\mathrm{adj}\,\mathbf{Q})\,\mathbf{E})}\,\frac{8h}{\pi^2(2n-1)^2}\,\delta(t-t_0), \tag{4.15}$$

where c is the compressible consolidation coefficient defined by

$$c=\frac{\det\mathbf{Q}}{\xi tr((\mathrm{adj}\,\mathbf{Q})\,\mathbf{E})} \tag{4.16}$$

and

$$\mathbf{F}=\frac{1}{\xi tr((\mathrm{adj}\,\mathbf{Q})\,\mathbf{E})}\Big(\mathrm{adj}\,\mathbf{Q}-\frac{\det\mathbf{Q}}{tr(\mathrm{adj}\,\mathbf{Q})\,\mathbf{E}}\,\mathrm{adj}\,\mathbf{E}\Big). \tag{4.17}$$

The derivation of (4.15) can be found in the article by Bowen [5, Sec. 4].

Given the representation (4.1) and the preceding forms for $\mathbf{K}_n(t,t_0)$, the solution (3.8) can be written

$$\mathbf{u}(x,t)=\sum_{n=1}^{\infty}\mathrm{Cos}\frac{(2n-1)\pi x}{2h}$$
$$\Big\{\mathbf{K}_n(t,0)\,\mathbf{M}\int_0^h\mathrm{Cos}\,\frac{(2n-1)\pi x_0}{2h}\,\mathbf{g}(x_0)\,dx_0$$
$$+\Big(\frac{\partial\mathbf{K}_n}{\partial t}\,(t,0)\,\mathbf{M}+\xi\mathbf{K}_n(t,0)\,\mathbf{E}\Big)\int_0^h\mathrm{Cos}\,\frac{(2n-1)\pi x_0}{2h}\,\mathbf{f}(x_0)\,dx_0\Big\}$$
$$-\sum_{n=1}^{\infty}\mathrm{Cos}\frac{(2n-1)\pi x}{2h}\Big\{\int_0^t\mathbf{K}_n(t,t_0)\,\mathbf{q}(t_0)\,dt_0$$
$$+(-1)^n\frac{(2n-1)\pi}{2h}\int_0^t\mathbf{K}_n(t,t_0)\,\mathbf{Q}\,\mathbf{k}(t_0)\,dt_0\Big\}. \tag{4.18}$$

In the case where inertia is neglected one simply takes $\mathbf{M}$ to be zero in (4.18) and adopts (4.15) as the expression for $\mathbf{K}_n(t,t_0)$ rather than (4.9) and (4.14).

5 Analytical Approximations

Consider the polynomial (4.6) written in the expanded form

$$(\det\mathbf{M})\,\beta_n^4+\xi\,tr\{(\mathrm{adj}\,\mathbf{M})\,\mathbf{E}\}\,\beta_n^3$$
$$+\frac{(2n-1)^2\pi^2}{4h^2}\,tr\{(\mathrm{adj}\,\mathbf{M})\,\mathbf{Q}\}\,\beta_n^2$$
$$+\frac{(2n-1)^2\pi^2}{4h^2}\,\xi tr\{(\mathrm{adj}\,\mathbf{Q})\,\mathbf{E}\}\,\beta_n$$
$$+\frac{(2n-1)^4\pi^4}{16h^4}\,\det\mathbf{Q}=0. \tag{5.1}$$

It turns out that rather good analytical approximations to the roots of (5.1) can be derived in certain cases. These approximations are useful when we compare our results with results from the inertia-free approximation. First we need to introduce the acceleration wave speeds u_1 and u_2 defined by the roots of

$$\det(\mathbf{Q}-u^2\mathbf{M})=0 \tag{5.2}$$

and the "frozen" wave speed u_0 defined by

$$u_0^2=\frac{tr(\mathrm{adj}\,\mathbf{Q})\,\mathbf{E}}{tr(\mathrm{adj}\,\mathbf{M})\,\mathbf{E}}. \tag{5.3}$$

If by convention we take u_1 to be the largest acceleration wave speed, then it can be shown that

$$u_1^2\geq u_0^2>u_2^2. \tag{5.4}$$

Readers interested in the origins of the squared speeds u_0^2, u_1^2, and u_2^2 within the context of wave propagation problems in poroelasticity should consult Biot [6], Bowen [1, Section 2.10; 2, Section 10], Bowen and Chen [7], and Bowen and Reinicke [8]. Given the definitions (5.2) and (5.3), the polynomial (5.1) can be written

$$\beta_n^4+\omega_0\beta_n^3+\frac{(2n-1)^2\pi^2}{4h^2}\,(u_1^2+u_2^2)\,\beta_n^2$$
$$+\frac{(2n-1)^2\pi^2}{4h^2}\,\omega_0u_0^2\beta_n+\frac{(2n-1)^4\pi^4}{16h^4}\,u_1^2u_2^2=0, \tag{5.5}$$

where

$$\omega_0=\xi\frac{tr\{(\mathrm{adj}\,\mathbf{M})\,\mathbf{E}\}}{\det\mathbf{M}}=\xi\Big(\frac{1}{\rho_f}+\frac{1}{\rho_s}\Big). \tag{5.6}$$

Downloaded 02 May 2010 to 171.66.16.246. Redistribution subject to ASME license or copyright; see http://www.asme.org/terms/Terms_Use.cfm

Numerical values of constants u_0, u_1, u_2, and ω_0 are shown in Table 1 of Appendix A. The quantity ω_0 is defined in terms of the drag coefficient in such a fashion that it has the physical dimension of frequency. Therefore, $1/\omega_0$ is a characteristic time of diffusion. As Table 1 indicates, this time is very small. For this reason we seek approximations to the four roots of (5.5) valid for small ϵ_n, where ϵ_n is a dimensionless quantity defined by

$$\epsilon_n = \frac{(2n-1)\pi}{2h}\,\frac{u_0}{\omega_0}. \tag{5.7}$$

Because ϵ_n increases with n, the approximations given in the following are not valid for all n. However, ϵ_n is small for rather large n for the example materials shown in Table 1 providing the height h is not exceedingly small. For example, with an h of 100 m, the largest value of ϵ_1 arises for Berea sandstone. This value is approximately 5×10^{-5}. One can easily see that it takes approximately 10,000 terms before ϵ_n is near unity. Thus, it is not surprising that approximations based on the assumption of small ϵ_n are often valid. In the notation of the factorization (4.7), the approximate roots of (5.1) are easily shown to be

$$\alpha_n = \frac{u_1^2 u_2^2}{u_0^4}\,\omega_0\epsilon_n^2 + 0(\epsilon_n^3), \tag{5.8}$$

$$\gamma_n = \omega_0 - \frac{u_1^2 + u_2^2 - u_0^2}{u_0^2}\,\omega_0\epsilon_n^2 + 0(\epsilon_n^3), \tag{5.9}$$

$$\zeta_n = \frac{(u_1^2 - u_0^2)(u_0^2 - u_2^2)}{2u_0^4}\,\omega_0\epsilon_n^2 + 0(\epsilon_n^3) \tag{5.10}$$

and

$$\omega_n = \omega_0\epsilon_n + 0(\epsilon_n^3). \tag{5.11}$$

Another form for (5.8) is

$$\alpha_n = \frac{(2n-1)^2\pi^2}{4h^2}\,c + 0(\epsilon_n^3). \tag{5.12}$$

where c is defined by (4.16). If terms $0(\epsilon_n^3)$ are neglected, this root corresponds exactly to the single root which Biot [3] obtained in his inertia-free calculation. There is an interesting special feature of the example materials listed in Table 1. In each case the speed u_1 is very close or equal to the speed u_0. Because of this fact, it follows from (5.10) that the values of the coefficients ζ_n will always be extremely small. One could readily generate approximate roots of (5.1) valid for all n if one were to construct a small dimensionless parameter based on the difference $u_1 - u_0$. Such an approximation might be useful in certain applications, however we prefer not to exploit this approach here.[2]

Given (5.8)–(5.11), it is possible to derive approximations for the matrices $\mathbf{A}_n$ and $\mathbf{B}_n$ defined by (4.10) and (4.11). The results turn out to be

$$\mathbf{A}_n = \mathbf{F} + 0(\epsilon_n) \tag{5.13}$$

and

$$\mathbf{B}_n = \frac{1}{\omega_0}\left\{\frac{\text{adj}\,\mathbf{E}}{tr\{(\text{adj}\,\mathbf{M})\,\mathbf{E}\}} - \mathbf{M}^{-1}\right\} + 0(\epsilon_n{}^2), \tag{5.14}$$

where $\mathbf{F}$ is defined by (4.17). Given (5.13), (5.14), and (4.17), it follows that

$$\mathbf{A}_n + \mathbf{B}_n = \frac{1}{\omega_0}\left\{\frac{\text{adj}\,\mathbf{Q}}{u_0^2\,\det\mathbf{M}} - \mathbf{M}^{-1} + \left(1 - \frac{u_1^2 u_2^2}{u_0^4}\right)\frac{\text{adj}\,\mathbf{E}}{tr\{(\text{adj}\,\mathbf{M})\,\mathbf{E}\}}\right\} + 0(\epsilon_n) \tag{5.15}$$

and

$$\frac{1}{\omega_n}\mathbf{M}^{-1} + \frac{\alpha_n - \zeta_n}{\omega_n}\mathbf{A}_n + \frac{\gamma_n - \zeta_n}{\omega_n}\mathbf{B}_n = \frac{1}{\omega_0}\,\frac{\text{adj}\,\mathbf{E}}{\epsilon_n\,tr\{(\text{adj}\,\mathbf{M})\,\mathbf{E}\}} + 0(\epsilon_n). \tag{5.16}$$

It is possible to see from (5.8)–(5.11) some of the fundamental differences that result when one retains inertia terms. When inertia is omitted, (4.15) shows that there is one exponentially decaying mode for each n. Because of (5.8) and (5.12), we see that this mode decays slowly. This slow diffusion mode is present in (4.9). The root α_n is of the second order in ϵ_n and thus small. Unlike the inertia-free case, equation (4.9) shows a second diffusion mode. Equation (5.9) shows that the root γ_n is quite large. Thus, the second diffusion mode is, in a sense, a fast diffusion mode. In addition to the two exponental modes, (4.9) displays two damped oscillatory modes. It is perhaps clear that in principle one can select boundary conditions that tend to excite any one of these modes. This fact is basic to the fundamental conclusion of this work.

In closing this section, it is interesting to record the large ϵ_n roots of (5.1). In terms of the notation introduced in (4.8), the roots are

$$\zeta_n{}^{(1)}/\epsilon_n\omega_0 = \frac{u_1^2 - u_0^2}{2(u_1^2 - u_2^2)}\,\frac{1}{\epsilon_n} + 0\left(\frac{1}{\epsilon_n^2}\right), \tag{5.17}$$

$$\zeta_n{}^{(2)}/\epsilon_n\omega_0 = \frac{u_0^2 - u_2^2}{2(u_1^2 - u_2^2)}\,\frac{1}{\epsilon_n} + 0\left(\frac{1}{\epsilon_n^2}\right), \tag{5.18}$$

$$\omega_n{}^{(1)}/\epsilon_n\omega_0 = \frac{u_1}{u_0} + 0\left(\frac{1}{\epsilon_n^2}\right), \tag{5.19}$$

and

$$\omega_n{}^{(2)}/\epsilon_n\omega_0 = \frac{u_2}{u_0} + 0\left(\frac{1}{\epsilon_n^2}\right). \tag{5.20}$$

6 Biot Problem

In the inertia-free case, Biot [3] solved a one-dimensional problem that fits our general scheme. His problem corresponds to the following choices for the boundary and initial conditions:

$$s(t) = P_0, \tag{6.1}$$

$$r(t) = 0, \tag{6.2}$$

$$\mathbf{k}(t) = \mathbf{0}, \tag{6.3}$$

and

$$\mathbf{f}(x) = \frac{P_0}{tr\,((\text{adj}\,\mathbf{Q})\,\mathbf{E})}\,(h - x)\begin{bmatrix}1\\1\end{bmatrix}. \tag{6.4}$$

Because Biot neglected inertia, he did not find it necessary to prescribe an initial velocity. In our case we shall take the second initial condition to be:

$$\mathbf{g}(x) = \mathbf{0}. \tag{6.5}$$

The constant P_0 in (6.1) represents a uniform applied stress at $x = 0$. The choice $r(t) = 0$ indicates that $x = 0$ is a surface that is pervious to fluid flow. Equation (6.3) arises from the requirement that the surface $x = h$ is fixed and impervious to

[2] If one equates u_1 to u_0 in (5.1), the resulting polynomial can be shown to have at least two real roots unless the integer n is larger than $1/2\,(1 + \omega_0 h/\pi u_2)$. This result is the basis for our comments in Section 4 regarding the large number of terms in (4.1) before one must utilize (4.14).

Downloaded 02 May 2010 to 171.66.16.246. Redistribution subject to ASME license or copyright; see http://www.asme.org/terms/Terms_Use.cfm

fluid flow. Equation (6.4) results from the assumption that $t = 0$, the fluid content change is zero, and the initial stress equals $-P_0$. The details of this argument can be found in Biot's paper. Because Biot neglected inertia in his model, there is a data compatibility requirement that $T(x,t)$ is, in fact, independent of x for all t. Biot used this fact in deciding on his particular initial condition. In our case such a compatibility requirement does not exist. In any case, equation (6.4) is adopted to make comparisons with Biot's result. Bowen [5] has shown that the displacement that results from (6.1)–(6.4) in the *inertia-free* case is

$$\mathbf{u}_B(x,t) = \frac{8hP_0}{c\pi^2}\,\mathbf{F}\begin{bmatrix}0\\1\end{bmatrix}\sum_{n=1}^{\infty}\frac{1}{(2n-1)^2}\left(1-e^{-\frac{(2n-1)^2\pi^2}{4h^2}\,ct}\right)\operatorname{Cos}\frac{(2n-1)\pi x}{2h} + \frac{P_0}{tr(\operatorname{adj}\mathbf{Q})\,\mathbf{E}}\begin{bmatrix}1\\1\end{bmatrix}(h-x), \tag{6.6}$$

where $\mathbf{F}$ is the square matrix defined by (4.17). Our first example will be shown to be a generalization of the result (6.6).

Given (6.1)–(6.5), the general expression for the displacement, (4.18), reduces to

$$\mathbf{u}(x,t) = \frac{4h^2P_0}{\pi^2}\,\frac{1}{tr\{(\operatorname{adj}\mathbf{Q})\,\mathbf{E}\}}\sum_{n=1}^{\infty}\frac{1}{(2n-1)^2}\,\frac{\partial\mathbf{K}_n}{\partial t}(t,0)\,\mathbf{M}\begin{bmatrix}1\\1\end{bmatrix}\operatorname{Cos}\frac{(2n-1)\pi x}{2h} + P_0\sum_{n=1}^{\infty}\left(\int_0^t\mathbf{K}_n(t,t_0)\,dt_0\right)\begin{bmatrix}0\\1\end{bmatrix}\operatorname{Cos}\frac{(2n-1)\pi x}{2h}, \tag{6.7}$$

where, from (4.9), in the case of small n,

$$\begin{aligned}\frac{h}{2}\,\frac{\partial\mathbf{K}_n}{\partial t}(t,0) &= -\alpha_n e^{-\alpha_n t}\,\mathbf{A}_n - \gamma_n e^{-\gamma_n t}\,\mathbf{B}_n\\ &+\{\zeta_n e^{-\zeta_n t}\operatorname{Cos}\omega_n t + \omega_n e^{-\zeta_n t}\operatorname{Sin}\omega_n t\}(\mathbf{A}_n+\mathbf{B}_n)\\ &+\{-\zeta_n e^{-\zeta_n t}\operatorname{Sin}\omega_n t + \omega_n e^{-\zeta_n t}\operatorname{Cos}\omega_n t\}\left(\frac{\alpha_n-\zeta_n}{\omega_n}\,\mathbf{A}_n + \frac{\gamma_n-\zeta_n}{\omega_n}\,\mathbf{B}_n + \frac{1}{\omega_n}\,\mathbf{M}^{-1}\right)\end{aligned} \tag{6.8}$$

and

$$\begin{aligned}\frac{h}{2}\int_0^t\mathbf{K}_n(t,t_0)\,dt_0 &= \frac{1}{\alpha_n}(1-e^{-\alpha_n t})\,\mathbf{A}_n + \frac{1}{\gamma_n}(1-e^{-\gamma_n t})\,\mathbf{B}_n\\ &-\frac{1}{\omega_n^2+\zeta_n^2}\{\zeta_n(1-e^{-\zeta_n t}\operatorname{Cos}\omega_n t) + \omega_n e^{-\zeta_n t}\operatorname{Sin}\omega_n t\}(\mathbf{A}_n+\mathbf{B}_n)\\ &+\frac{1}{\omega_n^2+\zeta_n^2}\{\omega_n(1-e^{-\zeta_n t}\operatorname{Cos}\omega_n t) - \zeta_n e^{-\zeta_n t}\operatorname{Sin}\omega_n t\}\\ &\left(\frac{\alpha_n-\zeta_n}{\omega_n}\,\mathbf{A}_n + \frac{\gamma_n-\zeta_n}{\omega_n}\,\mathbf{B}_n + \frac{1}{\omega_n}\,\mathbf{M}^{-1}\right).\end{aligned} \tag{6.9}$$

Similar formulas follow from (4.14) for large n.

As explained in Section 1, we are interested in conditions sufficient to reduce (6.7) to (6.6). As a first formal step we will replace the infinite sum in (6.6) and (6.7) by a finite sum of N terms. The integer N is restricted by our next approximation. We will adopt the small ϵ_n approximations derived in Section 5. As explained in Section 5, because of the magnitude of the characteristic frequency ω_0, ϵ_n remains small for rather large n. Immediately we see that we need not concern ourselves with the terms in the solution (6.7) which require the use of (4.14) rather than (4.9). Given our specification of N, equation (6.7) is replaced by

$$\mathbf{u}(x,t) = \frac{4h^2P_0}{\pi^2}\,\frac{1}{tr\{(\operatorname{adj}\mathbf{Q})\,\mathbf{E}\}}\sum_{n=1}^{N}\frac{1}{(2n-1)^2}\,\frac{\partial\mathbf{K}_n}{\partial t}(t,0)\,\mathbf{M}\begin{bmatrix}1\\1\end{bmatrix}\operatorname{Cos}\frac{(2n-1)\pi x}{2h} + P_0\sum_{n=1}^{N}\left(\int_0^t\mathbf{K}_n(t,t_0)\,dt_0\right)\begin{bmatrix}0\\1\end{bmatrix}\operatorname{Cos}\frac{(2n-1)\pi x}{2h}, \tag{6.10}$$

and (6.6) is replaced by

$$\mathbf{u}_B(x,t) = \frac{8hP_0}{c\,\pi^2}\,\mathbf{F}\begin{bmatrix}0\\1\end{bmatrix}\sum_{n=1}^{N}\frac{1}{(2n-1)^2}\left(1-e^{-\frac{(2n-1)^2\pi^2}{4h^2}\,ct}\right)\operatorname{Cos}\frac{(2n-1)\pi x}{2h} + \frac{P_0}{tr\,(\operatorname{adj}\mathbf{Q})\,\mathbf{E}}\begin{bmatrix}1\\1\end{bmatrix}(h-x). \tag{6.11}$$

Next we will approximate (6.8) by

$$\frac{\partial\mathbf{K}_n}{\partial t}(t,0) = -\frac{2}{h}\left\{\left(\frac{\operatorname{adj}\mathbf{E}}{tr\{(\operatorname{adj}\mathbf{M})\,\mathbf{E}\}} - \mathbf{M}^{-1}\right)e^{-\omega_0 t} - \frac{\operatorname{adj}\mathbf{E}}{tr\{(\operatorname{adj}\mathbf{M})\,\mathbf{E}\}}\,e^{-\frac{(u_1^2-u_0^2)(u_0^2-u_2^2)}{2u_0^4}\omega_0\epsilon_n^2 t}\operatorname{Cos}\omega_0\epsilon_n t\right\}. \tag{6.12}$$

Equation (6.12) follows from (6.8) by use of (5.8)–(5.11), (5.13), and (5.14) to approximate each coefficient in (6.8) by the value it takes for small ϵ_n. In addition, the argument of each exponential and trigonometric function is approximated by applying the small ϵ_n approximations (5.9)–(5.11). Since neglecting inertia is a singular perturbation of the equations of motion, we expect (6.11) to agree with (6.10) for times outside of some interval near $t = 0$. Therefore, it is no surprise that the approximations sufficient to reduce (6.10) to (6.11) require some assumption about the time t. The assumption we will make is to restrict t such that

$$\omega_0 t >> 1. \tag{6.13}$$

Because ω_0 is typically quite large, equation (6.13) is satisfied for very small times. This assumption reduces (6.12) to

$$\frac{\partial\mathbf{K}_n}{\partial t}(t,0) = \frac{2}{h}\,\frac{\operatorname{adj}\mathbf{E}}{tr\{(\operatorname{adj}\mathbf{M})\,\mathbf{E}\}}\,e^{-\frac{(u_1^2-u_0^2)(u_0^2-u_2^2)}{2u_0^4}\omega_0\epsilon_n^2 t}\operatorname{Cos}\omega_0\epsilon_n t. \tag{6.14}$$

The same two approximations used to obtain (6.14) can be applied to (6.9). The resulting approximation is

$$\begin{aligned}\frac{h}{2}\int_0^t\mathbf{K}_n(t,t_0)\,dt_0 &= \frac{u_0^4}{u_1^2u_2^2\omega_0\epsilon_n^2}\left\{1-e^{-\frac{u_1^2u_2^2}{u_0^4}\omega_0\epsilon_n^2 t}\right\}\mathbf{F}\\ &+\frac{1}{\omega_0^2}\left\{\frac{\operatorname{adj}\mathbf{E}}{tr\{(\operatorname{adj}\mathbf{M})\,\mathbf{E}\}} - \mathbf{M}^{-1}\right\} - \frac{1}{\omega_0^2\epsilon_n}\left\{\frac{(u_1^2-u_0^2)(u_0^2-u_2^2)}{2u_0^4}\epsilon_n\right.\\ &\left.\left(1-e^{-\frac{(u_1^2-u_0^2)(u_0^2-u_2^2)}{2u_0^4}\omega_0\epsilon_n^2 t}\operatorname{Cos}\omega_0\epsilon_n t\right)\right.\\ &\left.+e^{-\frac{(u_1^2-u_0^2)(u_0^2-u_2^2)}{2u_0^4}\omega_0\epsilon_n^2 t}\operatorname{Sin}\omega_0\epsilon_n t\right\}\left\{\frac{\operatorname{adj}\mathbf{Q}}{u_0^2\det\mathbf{M}}\right.\\ &\left.-\mathbf{M}^{-1}+\left(1-\frac{u_1^2u_2^2}{u_0^4}\right)\frac{\operatorname{adj}\mathbf{E}}{tr\{(\operatorname{adj}\mathbf{M})\,\mathbf{E}\}}\right\}\end{aligned}$$

Downloaded 02 May 2010 to 171.66.16.246. Redistribution subject to ASME license or copyright; see http://www.asme.org/terms/Terms_Use.cfm

$$+\frac{1}{\omega_0^2\epsilon_n^2}\left\{\left(1-e^{-\frac{(u_1^2-u_0^2)(u_0^2-u_2^2)}{2u_0^4}\omega_0\epsilon_n^2 t}\,\mathrm{Cos}\,\omega_0\epsilon_n t\right)\right.$$

$$\left.-\frac{(u_1^2-u_0^2)(u_0^2-u_2^2)}{2u_0^4}\epsilon_n\, e^{-\frac{(u_1^2-u_0^2)(u_0^2-u_2^2)}{2u_0^4}\omega_0\epsilon_n^2 t}\,\mathrm{Sin}\,\omega_0\epsilon_n t\right\}\left\{\frac{\mathrm{adj}\,\mathbf{E}}{tr\,\{(\mathrm{adj}\,\mathbf{M})\,\mathbf{E}\}}\right\}. \tag{6.15}$$

Further approximations to (6.15) seem to be reasonable. We observed in Section 5 and in the foregoing that ω_0 is typically a very large number. Therefore, we will drop from (6.15) terms multiplied by factors $1/\omega_0^2$ and $1/\omega_0^2\epsilon_n$. The term proportional to $1/\omega_0^2\epsilon_n^2$ will be retained because of the small ϵ_n assumption we are utilizing. The same assumption suggests we retain the term proportional to $1/\omega_0\epsilon_n^2$. These assumptions reduce to (6.15) to

$$\frac{h}{2}\int_0^t \mathbf{K}_n(t,t_0)\,dt_0=\frac{u_0^4}{u_1^2u_0^2\omega_0\epsilon_n^2}\left(1-e^{-\frac{u_1^2u_2^2}{u_0^4}\omega_0\epsilon_n^2 t}\right)\mathbf{F}$$

$$+\frac{1}{\omega_0^2\epsilon_n^2}\,\frac{\mathrm{adj}\,\mathbf{E}}{tr\{(\mathrm{adj}\,\mathbf{M})\,\mathbf{E}\}}\left(1-e^{-\frac{(u_1^2-u_0^2)(u_0^2-u_2^2)}{2u_0^4}\omega_0\epsilon_n^2 t}\,\mathrm{Cos}\,\omega_0\epsilon_n t\right). \tag{6.16}$$

Before (6.16) and (6.14) are substituted into (6.10), it is convenient to rewrite (6.16) in the form

$$\int_0^t \mathbf{K}_n(t,t_0)\,dt_0=\frac{8h}{c\pi^2}\,\frac{1}{(2n-1)^2}\left(1-e^{-\frac{(2n-1)^2\pi^2}{4h^2}\mathrm{ct}}\right)\mathbf{F}$$

$$+\frac{8h}{\pi^2}\,\frac{1}{(2n-1)^2}\,\frac{\mathrm{adj}\,\mathbf{E}}{tr(\mathrm{adj}\,\mathbf{Q})\,\mathbf{E}}\left(1-e^{-\frac{(u_1^2-u_0^2)(u_0^2-u_2^2)}{2u_0^4}\omega_0\epsilon_n^2 t}\,\mathrm{Cos}\,\omega_0\epsilon_n t\right). \tag{6.17}$$

In deriving (6.17) from (6.16) we have used (4.16), (5.3), (5.7), and the identity

$$\det\mathbf{Q}=u_1^2u_2^2\det\mathbf{M}. \tag{6.18}$$

Using (6.14) and (6.17) and the identity,

$$\frac{8h}{\pi^2}\sum_{n=1}^{\infty}\frac{1}{(2n-1)^2}\,\mathrm{Cos}\frac{(2n-1)\pi x}{2h}=h-x, \tag{6.19}$$

written in the approximate form

$$\frac{8h}{\pi^2}\sum_{n=1}^{N}\frac{1}{(2n-1)^2}\,\mathrm{Cos}\frac{(2n-1)\pi x}{2h}=h-x, \tag{6.20}$$

we can write (6.10) as

$$\mathbf{u}(x,t)=\mathbf{u}_B(x,t)+\frac{8hP_0}{\pi^2}\,\frac{1}{tr\{(\mathrm{adj}\,\mathbf{Q})\,\mathbf{E}\}}\left\{\frac{(\mathrm{adj}\,\mathbf{E})\,\mathbf{M}}{tr\{(\mathrm{adj}\,\mathbf{M})\,\mathbf{E}\}}\right.$$

$$\left.\begin{bmatrix}1\\1\end{bmatrix}-\mathrm{adj}\,\mathbf{E}\begin{bmatrix}0\\1\end{bmatrix}\right\}\sum_{n=1}^{N}\frac{1}{(2n-1)^2}\,e^{-\frac{(u_1^2-u_0^2)(u_0^2-u_2^2)}{2u_0^4}\omega_0\epsilon_n^2 t}$$

$$\mathrm{Cos}\,\omega_0\epsilon_n t\,\mathrm{Cos}\frac{(2n-1)\pi x}{2h}, \tag{6.21}$$

where, of course, $\mathbf{u}_B$ is given by (6.11). The second term in (6.21) is identically zero because

$$(\mathrm{adj}\,\mathbf{E})\,\mathbf{M}\begin{bmatrix}1\\1\end{bmatrix}=(\mathrm{adj}\,\mathbf{E})\begin{bmatrix}\rho_f\\\rho_s\end{bmatrix}=(\rho_f+\rho_s)\begin{bmatrix}1\\1\end{bmatrix}$$

$$=(tr(\mathrm{adj}\,\mathbf{M})\,\mathbf{E})\begin{bmatrix}1\\1\end{bmatrix} \tag{6.22}$$

and

$$\mathrm{adj}\,\mathbf{E}\begin{bmatrix}0\\1\end{bmatrix}=\begin{bmatrix}1\\1\end{bmatrix}. \tag{6.23}$$

Therefore, we have identified approximations sufficient to reduce the solution (6.10) to the corresponding inertia-free result (6.11). As a summary, the reduction was obtained as a result of the following approximations:

(*i*) Approximate (6.7) by (6.10).

(*ii*) Approximate (6.8) by (6.14) by use of the assumptions that ϵ_n is small and t is such that $\omega_0 t >> 1$.

(*iii*) Approximate (6.9) by (6.16) by use of the assumptions given in (*ii*) and the assumption that ω_0 is sufficiently large to allow terms multiplied by $1/\omega_0^2$ and $1/\omega_0^2\epsilon_n$ to be dropped from (6.15).

As a numerical example, consider Berea sandstone, which has an ω_0 of approximately 10^6 sec^{-1}. The resulting time "boundary layer" defined by $\omega_0 t >> 1$ is extremely thin, with $\omega_0 t = 10$ for t of only 10^{-5} sec. As a result, one would not expect any practical advantage to result from the retention of inertia in the solution of the problem defined by (6.1)-(6.4). However, this expectation is not true for all problems. In the next section, we shall illustrate a problem for which inertia terms have an important effect for all times.

7 Harmonic Loading Problem

In this section, we will make a small modification to the problem considered in Section 6. Instead of the constant loading represented by (6.1), we will consider a harmonically varying pressure:

$$s(t)=P_0\,\mathrm{Cos}\,\omega t, \tag{7.1}$$

where ω is a specified frequency. It we retain the boundary and initial conditions (6.2)-(6.5), our general solution (4.18) reduces to

$$\mathbf{u}(x,t)=\frac{4h^2P_0}{\pi^2}\,\frac{1}{tr\{(\mathrm{adj}\,\mathbf{Q})\,\mathbf{E}\}}\sum_{n=1}^{\infty}\frac{1}{(2n-1)^2}\,\frac{\partial\mathbf{K}_n}{\partial t}(t,0)\mathbf{M}$$

$$\begin{bmatrix}1\\1\end{bmatrix}\mathrm{Cos}\frac{(2n-1)\pi x}{2h}+P_0\sum_{n=1}^{\infty}\left(\int_0^t \mathrm{Cos}\,\omega t_0\,\mathbf{K}_n(t,t_0)\,dt_0\right)$$

$$\begin{bmatrix}0\\1\end{bmatrix}\mathrm{Cos}\frac{(2n-1)\pi x}{2h}, \tag{7.2}$$

where $\partial\mathbf{K}_n(t,0)/\partial t$ is given by (6.8) and, from (4.9),

$$\frac{h}{2}\int_0^t \mathrm{Cos}\,\omega t_0\,\mathbf{K}_n(t,t_0)\,dt_0=\frac{1}{\alpha_n^2+\omega^2}\{\alpha_n(\mathrm{Cos}\,\omega t-e^{-\alpha_n t})$$

$$+\omega\,\mathrm{Sin}\,\omega t\}\,\mathbf{A}_n+\frac{1}{\gamma_n^2+\omega^2}\{\gamma_n(\cos\omega t-e^{-\gamma_n t})$$

$$+\omega\,\mathrm{Sin}\,\omega t\}\,\mathbf{B}_n-\frac{1}{\sqrt{(\omega_n^2+\zeta_n^2-\omega^2)^2+(2\omega\zeta_n)^2}}\left\{\sqrt{\zeta_n^2+\omega^2}\right.$$

$$\left.\mathrm{Sin}(\omega t+\psi_n)+\sqrt{\zeta_n^2+\omega_n^2}\,e^{-\zeta_n t}\,\mathrm{Sin}(\omega_n t-\phi_n)\right\}(\mathbf{A}_n+\mathbf{B}_n)$$

Downloaded 02 May 2010 to 171.66.16.246. Redistribution subject to ASME license or copyright; see http://www.asme.org/terms/Terms_Use.cfm

$$+\frac{1}{\sqrt{(\omega_n^2+\zeta_n^2-\omega^2)^2+(2\omega\zeta_n)^2}}\left\{\omega_n \operatorname{Cos}(\omega t-\sigma_n)\right.$$

$$\left.-\sqrt{\zeta_n^2+\omega_n^2}\, e^{-\zeta_n t} \operatorname{Cos}(\omega_n t-\phi_n)\right\}\left\{\left(\frac{\alpha_n-\zeta_n}{\omega_n}\right)\mathbf{A}_n\right.$$

$$\left.+\left(\frac{\gamma_n-\zeta_n}{\omega_n}\right)\mathbf{B}_n+\frac{1}{\omega_n}\mathbf{M}^{-1}\right\}, \tag{7.3}$$

where

$$\operatorname{Sin}\phi_n=\frac{\zeta_n(\zeta_n^2+\omega_n^2+\omega^2)}{\sqrt{\zeta_n^2+\omega_n^2}\sqrt{(\zeta_n^2+\omega_n^2-\omega^2)^2+(2\omega\zeta_n)^2}}, \tag{7.4}$$

$$\operatorname{Cos}\phi_n=\frac{\omega_n(\zeta_n^2+\omega_n^2-\omega^2)}{\sqrt{\zeta_n^2+\omega_n^2}\sqrt{(\zeta_n^2+\omega_n^2-\omega^2)^2+(2\omega\zeta_n)^2}}, \tag{7.5}$$

$$\operatorname{Sin}\psi_n=\frac{\zeta_n(\zeta_n^2+\omega^2+\omega_n^2)}{\sqrt{\zeta_n^2+\omega^2}\sqrt{(\zeta_n^2+\omega_n^2-\omega^2)^2+(2\omega\zeta_n)^2}}, \tag{7.6}$$

$$\operatorname{Cos}\psi_n=\frac{\omega(\zeta_n^2+\omega^2-\omega_n^2)}{\sqrt{\zeta_n^2+\omega^2}\sqrt{(\zeta_n+\omega_n^2-\omega^2)^2+(2\omega\zeta_n)^2}}, \tag{7.7}$$

$$\operatorname{Sin}\sigma_n=\frac{2\omega\zeta_n}{\sqrt{(\zeta_n^2+\omega_n^2-\omega^2)^2+(2\omega\zeta_n)^2}} \tag{7.8}$$

and

$$\operatorname{Cos}\sigma_n=\frac{\zeta_n^2+\omega_n^2-\omega^2}{\sqrt{(\zeta_n^2+\omega_n^2-\omega^2)^2+(2\omega\zeta_n)^2}}. \tag{7.9}$$

A similar formula is obtained if (4.14) is utilized rather than (4.9).

In the inertia-free case, the solution to the boundary value problem (7.1) and (6.2)–(6.4) turns out to be

$$\mathbf{u}_B(x,t)=P_0\sum_{n=1}^{\infty}\left(\int_0^t \operatorname{Cos}\omega t_0\,\mathbf{K}_n(t,t_0)dt_0\right)\begin{bmatrix}0\\1\end{bmatrix}\operatorname{Cos}\frac{(2n-1)\pi x}{2h}, \tag{7.10}$$

where, from (4.15),

$$\frac{h}{2}\int_0^t \operatorname{Cos}\omega t_0\,\mathbf{K}_n(t,t_0)\,dt_0=\frac{1}{\omega^2+\dfrac{(2n-1)^4\pi^4}{16h^4}c^2}$$

$$\left\{\frac{(2n-1)^2\pi^2}{4h^2}c\left(\operatorname{Cos}\omega t-e^{-\frac{(2n-1)^2\pi^2}{4h^2}ct}\right)\right.$$

$$\left.+\omega\operatorname{Sin}\omega t\right\}\mathbf{F}+\frac{4h^2}{\pi^2(2n-1)^2}\frac{\operatorname{adj}\mathbf{E}}{tr\{(\operatorname{adj}\mathbf{Q})\mathbf{E}\}}\operatorname{Cos}\omega t. \tag{7.11}$$

As in Section 6, the solution (7.2) can be shown to reduce to (7.10). The approximations that allow this reduction are those listed at the end of Section 6 *and* the assumption that

$$\omega<<\omega_n \tag{7.12}$$

for $n=1, 2, \ldots$. Without the assumption (7.12), one must adopt the full solution given by (7.2), (6.8), and (7.3).

If one agrees that ϵ_n being small is acceptable, then by use of (5.11) it follows that ω must be small in comparison with the product $\omega_0\epsilon_n$. The worst case arises when $n=1$. For an h of 100 m one can easily calcuate from the data in Table 1 that $\omega_0\epsilon_1$ is of the order of 10 Hz. The largest $\omega_0\epsilon_1$ arises for Tennessee marble where the value is approximately 13 Hz. The smallest value is approximately 8 Hz for Berea sandstone. Therefore, one would not expect (7.12) to be an acceptable approximation for all porous materials. Frequencies ω that violate (7.12) can be regarded as the rule rather than the exception. The important point is that if one adopts (7.12), this assumption contradicts the small ϵ_n assumption.

To stress the point just made, consider the circumstance where

$$\omega=\sqrt{\omega_1^2-\zeta_1^2}. \tag{7.13}$$

This frequency is the one that makes the coefficient

$$\frac{1}{\sqrt{(\omega_n^2+\zeta_n^2-\omega^2)^2+(2\omega\zeta_n)^2}}$$

a maximum for $n=1$. Essentially, the frequency (7.13) corresponds to the lowest resonance frequency for our problem. Given (7.13), it follows that

$$\frac{1}{\sqrt{(\omega_1^2+\zeta_1^2-\omega^2)^2+(2\omega\zeta_1)^2}}=\frac{1}{2\zeta_1\omega_1}, \tag{7.14}$$

$$\operatorname{Sin}\phi_1=\frac{\omega_1}{\sqrt{\omega_1^2+\zeta_1^2}}, \tag{7.15}$$

$$\operatorname{Cos}\phi_1=\frac{\zeta_1}{\sqrt{\omega_1^2+\zeta_1^2}}, \tag{7.16}$$

$$\psi_1=\frac{\pi}{2}, \tag{7.17}$$

$$\operatorname{Sin}\sigma_1=\frac{\sqrt{\omega_1^2-\zeta_1^2}}{\omega_1} \tag{7.18}$$

and

$$\operatorname{Cos}\sigma_1=\frac{\zeta_1}{\omega_1}. \tag{7.19}$$

Because the damping coefficent ζ_1 is small, the coefficient (7.14) is quite large and dominates the expansion (7.2). For example, in the case of 100 m of Ruhr sandstone, numerical values of ζ_1 and ω_1 are such that $1/2\zeta_1\omega_1$ equals approximately 200,000 sec^2. The corresponding coefficients of the higher-order terms are very small. For example, the value for

$$\frac{1}{\sqrt{(\omega_2^2+\zeta_2^2-\omega^2)^2+(2\omega\zeta_2)^2}}$$

turns out to be approximately $(27)(10^{-6})$ sec^2. The small ϵ_n approximations given in Section 5 can be used to show that

$$\frac{1}{2\zeta_1\omega_1}\cong\frac{u_0^4}{(u_1^2-u_0^2)(u_0^2-u_2^2)\omega_0^2\epsilon_1^3}, \tag{7.20}$$

if $u_1\neq u_0$, and

$$\frac{1}{\sqrt{(\omega_n^2+\zeta_n^2-\omega^2)^2+(2\omega\zeta_n)^2}}\cong\frac{1}{\omega_0^2\,\epsilon_1^2(\epsilon_n^2/\epsilon_1^2-1)} \tag{7.21}$$

for $n=2, 3, \ldots$. Because, from (5.7),

$$\frac{\epsilon_n}{\epsilon_1}=2n-1, \tag{7.22}$$

equations (7.20) and (7.21) support the assertion that the $n=1$ term in the solution (7.2) dominates the series and, as a result, the interia term in (2.11) is important for all times t.

One final comment is appropriate at this point. The resonance shown in the solution (7.2) causes a similar effect in the stress $T(x,t)$ and the pore pressure $P_f(x,t)$. These quantities can be calculated from (7.2) by use of the formula

Downloaded 02 May 2010 to 171.66.16.246. Redistribution subject to ASME license or copyright; see http://www.asme.org/terms/Terms_Use.cfm

$$\begin{bmatrix} -\phi P_f(x,t) \\ T(x,t)+\phi P_f(x,t) \end{bmatrix} = \mathbf{Q}\,\frac{\partial \mathbf{u}}{\partial x}\,(x,t) \quad . \qquad (7.23)$$

Acknowledgment

The research reported here was supported in part by a grant from the U. S. National Science Foundation.

References

1 Bowen, R. M., Theory of Mixtures in Continuum Physics, Vol. III, Eringen, A. C., ed., Academic Press, New York, 1976.

2 Bowen, R. M., "Compressible Porous Media Models by Use of the Theory of Mixtures," *Int. J. Eng. Sci.*, Vol. 20, 1982, pp. 697-735.

3 Biot, M. A., "General Theory of Three Dimensional Consolidation," *J. Appl. Phys.*, Vol. 12, 1941, pp. 155-164.

4 Rice, J. R., and Cleary, M. P., "Some Basic Stress Diffusion Solutions for Fluid-Saturated Elastic Porous Media With Compressible Constituents," *Reviews of Geophysics and Space Physics*, Vol. 14, 1976, pp. 227-241.

5 Bowen, R. M., "Green's Functions for Consolidation Problems," *Lett. Appl. Engineering Sci.*, Vol. 19, 1981, pp. 455-466.

6 Biot, M. A., "Theory of Propagation of Elastic Waves in a Fluid-Saturated Porous Solid. I. Low-Frequency Range," *J. Acost. Soc. Amer.* Vol. 28, 1956, pp. 168-178.

7 Bowen, R. M., and Chen, P. J., "Waves in a Binary Mixture of Linear Elastic Materials," *J. de Mecánique*, Vol. 14, 1975, pp. 239-266.

8 Bowen, R. M., and Reinicke, K. M., "Plane Progressive Waves in a Binary Mixture of Linear Elastic Materials," ASME JOURNAL OF APPLIED MECHANICS, Vol. 45, 1978, pp. 493-499.

9 Farmer, I. W., *Engineering Properties of Rocks*, E. and F. N. Spon, Ltd., London, 1968.

APPENDIX A

Material Properties

Equation (5.1) from Section 5 is

$$(\det \mathbf{M})\,\beta_n^4 + \xi tr\,\{(\text{adj}\,\mathbf{M})\,\mathbf{E}\}\,\beta_n^3 + \frac{(2n-1)^2\pi^2}{4h^2}\,tr\,\{(\text{adj}\,\mathbf{M})\,\mathbf{Q}\}\,\beta_n^2 + \frac{(2n-1)^2\pi^2}{4h^2}\,\xi tr\,\{(\text{adj}\,\mathbf{Q})\,\mathbf{E}\}\,\beta_n + \frac{(2n-1)^4\pi^4}{16h^4}\det \mathbf{Q} = 0.$$

A numerical solution for the roots of this polynomial has been carried out. For that solution, numerical values for the material properties ρ_f, ρ_s, ξ, λ_f, λ_{fs}, λ_s, and μ_s were required. The elastic parameters and drag coefficients were derived from the numerical data given in Table 1 of the review article by Rice and Cleary [4]. Presented in the following are the formulas that relate the quantities tabulated by Rice and Cleary to the materials properties used here.

Bowen [2, Sect. 9] shows that Poisson's ratio at constant pore pressure is given by

$$\nu_p = \frac{\lambda_s - \lambda_{fs}^2/\lambda_f}{2\left(\lambda_s - \frac{\lambda_{fs}^2}{\lambda_f} + \mu_s\right)}. \qquad (A.1)$$

Also, the Poisson's ratio at constant m_f (fluid mass per unit of undeformed solid volume) is

$$\nu_m = \frac{\lambda_s + 2\lambda_{fs} + \lambda_f}{2(\lambda_s + 2\lambda_{fs} + \lambda_s + 2\mu_s)}. \qquad (A.2)$$

Likewise, the Skempton coefficient B tabulated by Rice and Cleary [4] is given by

$$B = \frac{(\lambda_f + \lambda_{fs})}{\lambda_s + 2\lambda_{fs} + \lambda_f + \frac{2}{3}\mu_s} \cdot \frac{1}{\phi}, \qquad (A.3)$$

where ϕ is the porosity in the reference configuration. Equations (A.1)-(A.3) can be inverted to obtain λ_s, λ_{fs}, and λ_f in terms of the tabulated values of ν_p, ν_m, B, and μ_s. Of course, the porosity ϕ must be given in to calculate the numerical values of λ_s, λ_{fs} and λ_f.

An expression for the drag coefficient is also requried. It is possible to show that

$$\frac{\phi^2}{\xi} = \frac{k}{\mu_f}, \qquad (A.4)$$

where k is the permeability of the porous material and μ_f is the viscosity of the fluid that saturates the solid.

Numerical values of the elastic parameters and drag coefficient computed from (A.1)-(A.4) are presented in Table 1 for the six materials considered in the Rice and Cleary article. Table 1 also contains numerical valves of the characteristic frequency ω_0 and the characteristic wave speeds u_0, u_1, and u_2. In Table 1 the viscosity of the fluid was taken to be that of water. The reader is cautioned that the data in Table 1 are subject to the same limitations and restrictions as the Rice and Cleary data.

Table 1 Typical rock-fluid mixture properties

Property	Rock types: Ruhr sandstone	Tennessee marble	Charcoal granite	Berea sandstone	Westerly granite	Weber sandstone
ϕ	0.02	0.02	0.02	0.19	0.01	0.06
γ_s, g/cm^2	2.6	2.7	2.7	2.6	2.7	2.6
λ_f, Kbar	0.165	0.468	0.326	4.44	0.0751	1.03
λ_{fs}, Kbar	5.21	4.02	4.13	13.9	3.48	9.91
λ_s, Kbar	206	273	272	84.0	311	147
μ_s, Kbar	133	240	187	60.0	150	122
ξ, Kbar-sec/cm^2	1.9×10^{-3}	3.92	3.92	1.77×10^{-4}	0.245	3.53×10^{-3}
ω_0, sec^{-1}	9.58×10^{7}	1.98×10^{11}	1.98×10^{11}	1.02×10^{6}	2.46×10^{10}	6.03×10^{7}
u_0, m/sec	4335	5344	4955	3208	4800	4056
u_1, m/sec	4338	5345	4955	3208	4802	4056
u_2, m/sec	727	1491	1220	1315	740	1223

True densities for rocks are taken from Farmer [9, p. 15]. The bulk densities are given by $\rho_f = \phi\gamma_f$ and $\rho_s = (1-\phi)\gamma_s$. The fluid density γ_f is taken to be that of water, 1.0 g/cm^3.

Downloaded 02 May 2010 to 171.66.16.246. Redistribution subject to ASME license or copyright; see http://www.asme.org/terms/Terms_Use.cfm

Stability of Steady Frictional Slipping

J. R. Rice
Gordon McKay Professor of Engineering Sciences and Geophysics, Division of Applied Sciences, Harvard University, Cambridge, Mass. 02138
Fellow ASME

A. L. Ruina
Assistant Professor, Department of Theoretical and Applied Mechanics, Cornell University, Ithaca, N.Y. 14850

The shear resistance of slipping surfaces at fixed normal stress is given by $\tau = \tau(V,state)$. Here V = slip velocity, dependence on "state" is equivalent to functional dependence with fading memory on prior $V(t)$, and $\partial\tau(V,state)/\partial V>0$. We establish linear stability conditions for steady slip states ($V(t),\tau(t)$ constant). For single degree-of-freedom elastic or viscoelastic dynamical systems, instability occurs, if at all, by a flutter mode when the spring stiffness (or appropriate viscoelastic generalization) reduces to a critical value. Similar conclusions are reached for slipping continua with spatially periodic perturbations along their interface, and in this case the existence of propagating frictional creep waves is established at critical conditions. Increases in inertia of the slipping systems are found to be destabilizing, in that they increase the critical stiffness level required for stability.

Introduction

For many mechanical systems in sliding contact with an adjoining body, loading by the imposition of a constant relative displacement rate, directed parallel to the contact surface, is observed to lead to nonconstant slip motion at that surface. This unsteady motion is often referred to as "stick slip." It is exemplified by squeaking machinery, oscillating violin strings, and unstable fault slip on the boundaries of the Earth's crustal plates. On the other hand, motion with constant slip rate is often observed in situations that appear very similar. What distinguishes these two cases?

The simplest, although not complete, approach to this problem is to ask: Is steady sliding a possible stable motion? Classically this is analyzed by assuming the friction stress τ (at fixed normal stress σ) to be dependent on slip rate V only, i.e., $\tau = \tau(V)$. Then a one degree-of-freedom elastic system yields the following simple result, attributed to Rayleigh in his study of the violin string-bow interaction (Kosterin and Kragel'skii [1]): If $d\tau(V)/dV>0$, steady sliding is stable; if $d\tau(V)/dV<0$, steady sliding is unstable. If steady sliding is unstable, a nonlinear description, including full description of the function $\tau(V)$, possibly embodying the concept of higher static versus kinetic friction, leads to predictions of oscillations that may be very abrupt (relaxation oscillations) or nearly sinusoidal (Kosterin and Kragel'skii [1], Brockley and Ko [2]).

The simple stability result just mentioned contradicts the common experimental observation of steady slip in an adequately stiff machine even though the frictional stress τ is often less for greater steady sliding rates. The contradiction is resolved, however, by the analysis in this paper, which is based on a recently established constitutive framework for frictional slip, more comprehensive than that mentioned in the foregoing.

We derive conditions within this framework for the stability against small perturbations of steady frictional slipping in some mechanical systems. The analysis generalizes considerably the first results within this constitutive framework, obtained by Ruina [3] for a special class of frictional constitutive relations involving a single evolving state parameter. Implications for nonlinear analysis are mentioned at the end of the paper.

Constitutive Description of Frictional Slip

Recent experiments with rocks (Dieterich [4–8]; Ruina [3]) as well as earlier experiments with metals (Rabinowicz [9, 10]) suggest a constitutive framework, for sliding at fixed normal stress σ, in which the shear stress τ resisting unidirectional slip is regarded as being a function of both the slip rate V and the state of the surface, where the latter evolves with ongoing slip. We summarize this dependence by writing

$$\tau=\tau(V,\text{state}) \quad (\text{for } \sigma \text{ constant}) \tag{1}$$

and regard the dependence on "state" as being equivalent to a functional dependence of τ on prior V. That is, assuming a loss of memory of slips in the distant past,

$$\tau(t)=F[V(t);\quad V(t'),-\infty<t'<t]. \quad (\sigma(t) \text{ constant}) \tag{2}$$

A useful way of studying this functional dependence (Dieterich [6–8]; Ruina [3]), which will be illustrated shortly for a linearized perturbation version of equation (2), is to determine the response $\tau(t)$ to a suddenly imposed step change in $V(t)$. Such experiments as carried out thus far suggest a competition between the instantaneous dependence on rate and the dependence on the evolving state. Namely, τ increases (decreases) simultaneously with the suddenly im-

Contributed by the Applied Mechanics Division for presentation at the 1983 ASME Applied Mechanics, Bioengineering, and Fluids Engineering Conference, Houston, Texas, June 20–22, 1983 of THE AMERICAN SOCIETY OF MECHANICAL ENGINEERS.

Discussion on this paper should be addressed to the Editorial Department, ASME, United Engineering Center, 345 East 47th Street, New York, N.Y. 10017, and will be accepted until two months after final publication of the paper itself in the JOURNAL OF APPLIED MECHANICS. Manuscript received by ASME Applied Mechanics Division, May, 1982; final revision, August, 1982. Paper No. 83-APM-16.

Copies will be available until February, 1984.

Copyright © 1983 by ASME
Downloaded 02 May 2010 to 171.66.16.246. Redistribution subject to ASME license or copyright; see http://www.asme.org/terms/Terms_Use.cfm

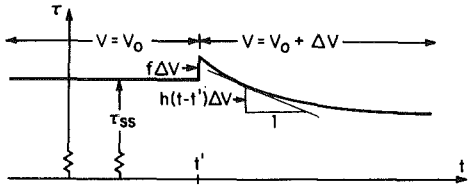

Fig. 1 Resistive shear stress τ in response to a sudden step ΔV in slip rate imposed at time t'

posed increase (decrease) of V. Presuming this instantaneous change to represent response of the surface at its current state, we have therefore that

$$\partial\tau(V,\text{state})/\partial V>0. \tag{3}$$

This may be contrasted with the constitutive framework often considered for straining of inelastic solids, in which the material exhibits an instantaneous elastic response and thus no jump in stress for a jump in deformation rate.

However, the instantaneous increase of τ resulting from an increase of V is not maintained. Rather, as slip progresses with, say, V held constant at its increased value, τ is found to decay in value, and we interpret this as meaning that the "state" of the surface is evolving toward a new one consistent with the increased V. Indeed, it is indicated in the experiments cited that independently of prior slip history, if V is maintained constant, then τ evolves toward a steady state value, τ_{ss}, which is a function only of V. We interpret this as meaning that the state term in equation (1) evolves to one that is dependent only on V, and therefore require that the constitutive relation exhibit the behavior

$$\tau(V,\text{state})\to\tau_{ss}(V), \quad \text{for } V \text{ constant}. \tag{4}$$

Furthermore, in most of the experimental studies cited in the foregoing, it is found that $\tau_{ss}(V)$ is a decreasing function of V,

$$d\tau_{ss}(V)/dV<0, \tag{5}$$

although studies at elevated temperature (Stesky [11, 12]), and on surfaces that have undergone relatively little total slip (Solberg and Byerlee [13]; Dieterich [8]), show that the inequality (5) need not always be met. We show subsequently that under plausible assumptions of the nature of the decay to steady state, inequality (5) is a necessary, but not sufficient, condition for instability (under small perturbations) of steady slip. Regarding the order of magnitude, experimental results [3, 5-8] suggest that the velocity derivatives in (3) and (5) are of order $\pm 0.01\sigma/V$.

The existence of an instantaneous positive viscosity-like property of frictional response as in (3), with a long-term negative viscosity, as in (5), is a recent discovery in the work of Dieterich [5-8] and Ruina [3], although such a competition of effects was postulated by Tolstoi [14]. Classical descriptions of friction seem to recognize only inequality (5), often summarized as saying that "static" friction is greater than "kinetic" friction (e.g., Jenkin and Ewing [15]).

For our present purposes of examining stability within a small-perturbation theory, we linearize the dependence of $\tau(t)$ on $V(t)$ in equation (2). In particular, we perturb (2) about a steady state at slip rate V_0, writing

$$V(t)=V_0+\dot{x}(t) \quad (|\dot{x}(t)|/V_0<<1), \tag{6}$$

and express the result for $\tau(t)$ as

$$\tau(t)=\tau_{ss}+f\dot{x}(t)-\int_0^t h(t-t')\dot{x}(t')\,dt' \tag{7}$$

(assuming that $\dot{x}(t)=0$ for $t<0$ and that conditions at $t=-\infty$ have no effect). Here all of τ_{ss}, f, and $h(t)$ depend on

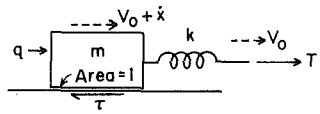

Fig. 2 One degree-of-freedom system represented by sliding block and attached spring. The velocity of the spring end is imposed as V_0 and stability of steady slipping is examined.

V_0. The significance of f and $h(t)$ is illustrated in Fig. 1 for a small step increase in V, from V_0 to $V_0+\Delta V$, at time t'. It is evident that

$$f=\partial\tau(V,\text{state})/\partial V, \quad f-\int_0^\infty h(t)\,dt=d\tau_{ss}(V)/dV \tag{8}$$

where the derivatives of τ are evalated in the steady state with speed V_0. Hence the inequalities (3) and (5) are equivalent, respectively, to

$$f>0, \quad \text{and} \quad \int_0^\infty h(t)\,dt>f \tag{9a,b}$$

where, again, we expect (9*a*) to be a general property and (9*b*) is required for the instabilities to be described. We also assume later that $h(t)\geq 0$, i.e., that the relaxation in Fig. 1 is monotonic.

We close this section with a few further remarks on frictional constitutive relations. First, the discussion thus far is for σ = constant and the same condition is assumed in the subsequent stability analyses. We presume that a suitable generalization for nonconstant $\sigma(t)$ would be to include in F of equation (2) a direct dependence on $\sigma(t)$ and a functional dependence on $\sigma(t')$, $-\infty<t'<t$. A strong, approximately linear dependence of τ on σ is well known but, to our knowledge, experiments have not yet documented whether there are memory effects relating to $\sigma(t)$ analogous to those previously discussed for $V(t)$. Second, characteristic slip distances in the decay process of Fig. 1 are typically small, 0.3 to 200 μm representing the range of surfaces studied so far. Thus, we neglect the fact that points currently mating across the slip surface at time t had slightly different prior slip histories (if the adjoining solids are deformable).

Finally, a special form of the dependence of τ on state, adopted in description of experimental results (Ruina [3], Dieterich [5-8], Kosloff and Liu [16]), is to represent the latter by a set of variables $\theta_1, \theta_2, \ldots, \theta_n$, collectively the column $\{\theta\}$, subject to first-order rate equations. Thus, with σ again constant,

$$\tau=\tau(V,\{\theta\}), \quad \{\dot{\theta}\}=\{\mathbf{g}(V,\{\theta\})\} \tag{10a,b}$$

The equation (7) may be thought of as a linearization of such a state variable description. In this case $h(t)$ would be given as a sum of (possibly complex) exponentially decaying functions. Here we take the form of equation (7), as in Fig. 1, to be the basic constitutive assumption independent of the nonlinear description, such as equation (1), (2), or (10), of which it is a linearization.

Stability of One Degree-of-Freedom Elastic System

Consider a one degree-of-freedom elastic system, represented generically by the rigid block of unit base area in Fig. 2, loaded by a linear spring element whose end is constrained to move at speed V_0, namely, the steady slip speed for which stability is to be examined. Writing the slip speed as $V_0+\dot{x}$, x can be interpreted as the shortening of the spring from its steady state length, and thus the force (or stress, given the unit base area) exerted by the spring is

$$T=\tau_{ss}-kx. \tag{11}$$

The equation of motion is therefore

$$m\ddot{x}=T-\tau+q=\tau_{ss}-kx-\tau+q \tag{12}$$

Downloaded 02 May 2010 to 171.66.16.246. Redistribution subject to ASME license or copyright; see http://www.asme.org/terms/Terms_Use.cfm

where $q(t)$ is an arbitrary perturbing force, switched on at $t = 0$. Hence by equation (7) for τ,

$$kx(t) + m\ddot{x}(t) + f\dot{x}(t) - \int_0^t h(t-t')\dot{x}(t')\,dt' = q(t). \quad (13)$$

The Laplace transform of $x(t)$ is given by

$$\hat{x}(s) \equiv \int_0^\infty x(t)e^{-st}\,dt = \hat{q}(s)/D(s) \quad (14)$$

where

$$D(s) = k + ms^2 + s[f - \hat{h}(s)] \quad (15)$$

A pole in $\hat{x}(s) = \hat{q}(s)/D(s)$ at $s = s_0$ corresponds to a term of the form $\exp(s_0 t)$ in the inverse transform of $\hat{x}(s)$, $x(t)$. Evidently, then, the steady slipping state is stable if the equation $D(s) = 0$ has no solutions s_0 with $Re(s_0) > 0$. If $D(s) = 0$ for some $Re(s) > 0$ then steady sliding is unstable since $\hat{q}(s)$ is arbitrary. (An alternative, less rigorous approach to the stability analysis is to look for solutions of equation (15) of the form $x(t) = \exp(st)$, for large t. This again leads to $D(s) = 0$ and thus the stability condition $Re(s) < 0$ for $D(s) = 0$.)

We consider successively lower values of k and show next that as k reduces from ∞ to 0 one passes through a critical value, k_{cr}, at which two conjugate roots of $D(s) = 0$ cross the $Im(s)$ axis, say, at $\pm i\beta$, into the domain $Re(s) > 0$. Consequently, the steady slip state is stable for sufficiently stiff systems, i.e., if $k > k_{cr}$, and, at least in the vicinity of k_{cr}, the system exhibits flutter oscillations of frequency β whose amplitude grows in time if $k < k_{cr}$ and decays if $k > k_{cr}$.

To demonstrate the result just stated we first observe that due to the presumed integrability of $h(t)$, $\hat{h}(s)$ is bounded and $\hat{h}(\infty) = 0$ in the domain $Re(s) \geq 0$. Thus for $k \to \infty$, the equation $D(s) = 0$ can only possibly be satisfied in $Re(s) \geq 0$ by $s \to \infty$. But $\hat{h}(\infty) = 0$ so that $D(s) = 0$ leads to a quadratic equation for s that has roots with $Re(s) = -f/2m$, a contradiction if $f > 0$ as required by (9*a*). We conclude that in the limit $k \to \infty$, $D(s)$ has no zeros with $Re(s) \geq 0$. Next, for $k = 0$, it can be observed that $D(s) = 0$ has at least one root in $Re(s) \geq 0$, on the positive real s axis. This follows because inequalities (9) and $\hat{h}(\infty) = 0$ show that

$$f - \hat{h}(0) = f - \int_0^\infty h(t)\,dt < 0, \quad f - \hat{h}(\infty) > 0, \quad (16)$$

and therefore that $D(s) < 0$ for small positive real s but $D(s) > 0$ for large positive s. Thus, assuming continuity, a real root or conjugate pair of complex roots must pass into the domain $Re(s) > 0$ as k reduces from ∞ to 0. A root cannot pass through the origin or infinity, because inspection shows that $D(0)$ and $D(\infty) \neq 0$ when $k > 0$ (and $m > 0$ or $f > 0$). By elimination, it is therefore the case that a conjugate pair of complex roots crosses the $Im(s)$ axis at critical conditions since $D(s)$ has real coefficients.

The crossing points $\pm i\beta$ are computed by setting

$$D(\pm i\beta) = k_{cr} - m\beta^2 \pm i\beta[f - \hat{h}(\pm i\beta)] = 0 \quad (17)$$

Separating (17) into real and imaginary parts yields two equations, one determining the critical frequency β by

$$\int_0^\infty \cos(\beta t)\,h(t)\,dt = f \quad (18)$$

and the other giving an expression for the critical spring constant as

$$k_{cr} = m\beta^2 + \beta\int_0^\infty \sin(\beta t)\,h(t)\,dt. \quad (19)$$

Equation (18) shows that the frequency β of the flutter instability is determined solely by properties of the friction law, f and $h(t)$, and not the mass m or stiffness k. Equation (18) also results as an answer to the following question: For what frequency β does the friction force in steady oscillatory motion $x(t) = \cos\beta t$ not absorb any more work than the steady state work $\tau_{ss} V_0$? This is also equivalent to the question: For what frequency β is the oscillatory displacement $x(t) = \cos\beta t$ exactly out of phase with the excess friction force? Both statements follow because in steady oscillatory motion no energy is lost or gained by the spring or mass. Also, in steady sinusoidal motion both the force required to accelerate the mass and to cock the spring are in phase with the position of the mass and spring.

It seems reasonable to assume that $h(t) \geq 0$ because, by reference to Fig. 1, this assumption means that the decay of τ toward its steady state value is monotonic. If we do therefore assume that $h(t) \geq 0$, equation (18) will have a solution if and only if inequality (5), $d\tau_{ss}(V)/dV < 0$, which is equivalent to the second inequality of (9), is met. This is because the cosine transform of a positive function is bounded by the integral of that function,

$$\int_0^\infty h(t)\,dt \geq \int_0^\infty \cos\beta t\; h(t)\,dt, \quad (20)$$

with equality only at $\beta = 0$. Thus a necessary (and sufficient, since the cosine transform vanishes as $\beta \to \infty$) condition for equation (18) to have a solution with $\beta \neq 0$ is that $\int_0^\infty h(t)\,dt > f$, which is the second inequality of (9). Thus, if the decay process is monotonic, $h(t) \geq 0$, then $d\tau_{ss}(V_0)/dV_0 < 0$ is a necessary and sufficient condition for instability to be possible with some (sufficiently reduced) positive spring constant.

We remark further that equation (18) for β can have at most one solution if the cosine transform of $h(t)$ decreases monotonically with increasing β. Such monotonicity would result if $h(t)$ had a decaying exponential representation as would be the case in the state variable description if the equations (10*b*) could be decoupled (at least when linearized). Note that a one-state-variable constitutive law would necessarily generate a $h(t)$ satisfying this monotonicity condition. More generally, however, we cannot rule out the possibility that multisolutions for β may exist in some cases and, in such cases, the solution yielding the highest k_{cr} in (19) is to be taken for the instability criterion.

Equation (19) for k_{cr} shows that mass is always destabilizing, since increasing m increasees the threshold k_{cr} below which instability occurs. Note further that the right side of equation (19) is necessarily positive since the method of derivation has shown that inequalities (9) imply the existence of a k_{cr} between ∞ and 0. The derivation applies for a system with $m = 0$, if $f > 0$, so at β given by equation (18),

$$\beta\int_0^\infty \sin\beta t\; h(t)\,dt > 0. \quad (21)$$

One consequence of the last inequality is that no system is stable when β exceeds its natural vibration frequency $\omega \equiv (k/m)^{1/2}$, because then the result for k_{cr} in equation (19) is plainly in excess of k.

Single Decay Process

To illustrate the preceding formulas, consider the single exponential representation of the decay shown in Fig. 1, namely

$$h(t) = (1 + \lambda) r f e^{-rt}, \quad r > 0. \quad (22)$$

Such an exponential form necessarily results, for example, if the constitutive relation in the form of equations (10) involves only a single state variable as explained in Ruina [3]. Assuming net rate weakening [equations (5), (9*b*)], $\lambda > 0$.

Equations (18) and (19) then give the frequency and stiffness at critical conditions

$$\beta = r\sqrt{\lambda}, \quad k_{cr} = mr^2\lambda + fr\,\lambda. \quad (23)$$

Downloaded 02 May 2010 to 171.66.16.246. Redistribution subject to ASME license or copyright; see http://www.asme.org/terms/Terms_Use.cfm

Alternatively, in terms of the frequency ω of the spring-mass system at critical stiffness ($\omega^2 = k_{cr}/m$)

$$k_{cr} = fr\lambda/(1-\lambda r^2/\omega^2). \tag{24}$$

Since

$$f = \partial\tau(V,\text{state})/\partial V, \quad \lambda f = -d\tau_{ss}(V)/dV,$$

both expressions being evaluated at $V = V_0$, and $1/r$ is the characteristic time of the decay process, the result for k_{cr} may be put into the more inspectable form

$$k_{cr} = -\frac{Vd\tau_{ss}(V)/dV}{d_c}\left[1+\frac{mV}{d_c\partial\tau(V,\text{state})/\partial V}\right] \tag{25}$$

with $V = V_0$. Here we have introduced $d_c \equiv V_0/r$ as the decay parameter expressed in terms of slip distance rather than time, i.e., with the decay in Fig. 1 proportional to $\exp(-V_0 t/d_c)$. Experiments (Dieterich [5-8]; Ruina [3]) suggest that the decay distance d_c is approximately independent of the slip rate V_0, and is thus closer to a material property than is $1/r = d_c/V_0$, which obviously depends on V_0. Ruina [3] derived the quasi-static version of (25), with $m = 0$, by an analysis based on constitutive laws of type (10) with a single state parameter. The dynamical result could have been derived from the static relation since, in steady sinusoidal oscillations $m\ddot{x}$ is in phase with $-kx$, the spring force. Thus any steady sinusoidal oscillation with frequency β found with some k and $m = 0$, as in Ruina [3], could be replaced by a motion with finite m and an increased spring constant $k+\beta^2 m$. This reasoning can lead to (25) directly from the results of Ruina [3]. Similarly the term $m\beta^2$ could have been added to equation (19) by this reasoning after the derivation was done with no inertia ($m = 0$). Note also that, at any fixed V, τ_{ss} is approximately proportional to σ. Hence $\lambda f \propto \sigma$ and thus $k_{cr} \propto \sigma$ (when $m = 0$), as has been emphasized by Dieterich [3, 4] based on a qualitative instability analysis.

Further Discussion

How necessary is inequality (3), i.e., the positive instantaneous viscosity property? We assumed in the analysis leading to equations (18) and (19) that at least one of the instantaneous viscosity f and the mass m is nonzero. Consider the case $m = 0$. The results of our analysis then carry through with $m = 0$ substituted in all equations containing m. Now if the instantaneous viscosity $f \to 0$ equation (18) shows that the frequency of flutter at neutral stability becomes infinite, $\beta \to \infty$, but equation (19) with $m = 0$ shows that k_{cr} tends to a finite value ($\lim \beta\to\infty$ of $\beta\int_0^\infty \sin(\beta t)h(t)\,dt$). On the other hand, if we let $f \to 0$ with *any* finite m, equation (18) shows that $\beta \to \infty$ as in the foregoing, and now equation (19) shows that the critical stiffness becomes infinite, $k_{cr} \to \infty$. Equation (25) for k_{cr}, in the case of a single decay process, clearly shows the result just discussed. If $f \equiv \partial\tau(V,\text{state})/\partial V \to 0$ a quasi-static analysis, i.e., based on setting $m = 0$, gives a finite k_{cr}. But if $m \neq 0$ the limit $f \to 0$ of zero instantaneous viscosity gives an unbounded k_{cr}. Hence, presuming as implicit in the preceding discussion that there is ultimate velocity weakening, steady state slip should not be possible in any elastic system, no matter what its stiffness, if there is no instantaneous viscosity. One might reverse the argument and say that the experimental observation that steady state slip on a given surface is possible, in a system of adequate stiffness, implies a positive instantaneous viscosity (at least on surfaces that exhibit ultimate velocity weakening, inequality (5)).

We now readdress the question of whether instability is possible at all if inequality (5) is *not* satisfied but rather reversed, with $d\tau_{ss}(V)/dV > 0$. This means that the surface exhibits ultimate velocity strengthening; the second of (9) then fails and instead

$$\int_0^\infty h(t)\,dt < f \quad (f>0).$$

We have already shown that no instability is then possible if $h(t) \geq 0$, i.e., if the decay process in Fig. 1 is monotonic. Any case allowing instability must therefore show nonmonotonic decay. A specific mathematical form allowing such instability is that of oscillating exponential decay,

$$h(t) = Re\left[H(a+ib)e^{-(a+ib)t}\right],$$

$a>0$, $b>0$, in which case the foregoing inequality becomes $Re(H) < f$. Equation (18) can still be satisfied, so that instability is possible, if b is sufficiently large compared to a. But experimental observations as made thus far do not lend support to decay with such marked oscillations, that are not likely the result of machine-sample interaction (of the type predicted here for k slightly greater than k_{cr}). We thus propose that the inequality (5), that the steady state friction force is a decreasing function of slip rate, is a necessary condition for the instability of steady sliding.

Viscoelastic Effects

Consider now the same one degree-of-freedom system of Fig. 2 but suppose that the spring element is viscoelastic. Then we may express the force exerted by the spring as

$$T = \tau_{ss} - k\int_0^t \gamma(t-t')\dot{x}(t')\,dt' \tag{26}$$

where $k\gamma(t)$ is the viscoelastic relaxation function; $\gamma(t)$ is normalized so that $\gamma(0) = 1$ and hence k is the instantaneous spring constant and $k\gamma(\infty)$, with $0 < \gamma(\infty) \leq 1$, is the long-time or relaxed spring constant. If one has in mind a viscoelastic element that has an infinite instantaneous spring constant, as for example a spring and dashpot in parallel, the instantaneous viscosity can be subtracted from the viscoelastic element and added to the term f in the friction law. This then leaves the form of equation (26) with k finite. The possibility of instability is then determined by whether inequality (9*b*) is satisfied with this modified f. Writing equations of motion, it is seen that equation (14) applies for $\hat{x}(s)$ with

$$D(s) = k[s\hat{\gamma}(s)] + ms^2 + s[f - \hat{h}(s)]. \tag{27}$$

Observing that $s\hat{\gamma}(s) \to \gamma(\infty)$, 1, respectively, as $s \to 0$, ∞, a similar argument to that outlined earlier can be followed to show that instability occurs by flutter oscillations of frequency β when k is reduced to a critical value, k_{cr}. The critical conditions are again given by $D(\pm i\beta) = 0$ and we find

$$k_{cr}\int_0^\infty \cos(\beta t)[\gamma(t)-\gamma(\infty)]\,dt + f = \int_0^\infty \cos(\beta t)h(t)\,dt,$$

$$k_{cr}\left\{\gamma(\infty) + \beta\int_0^\infty \sin(\beta t)[\gamma(t)-\gamma(\infty)]\,dt\right\} \tag{28}$$

$$= m\beta^2 + \beta\int_0^\infty \sin(\beta t)h(t)\,dt.$$

These equations are difficult to solve and we do not present explicit results. However, we remark that now β is dependent on the viscoelastic properties of the spring and on the mass m, and not merely on characteristics of the friction law, as it is for an elastic system. We can also see from the first of equations (28) that when the cosine transforms of $\gamma(t) - \gamma(\infty)$ and $h(t)$ are monotonic, as in the typical case when both are represented by a sum of decaying exponentials in t with positive coefficients, the effect of viscoelasticity is to reduce β from the value for an elastic system, equation (18). This is as expected, since for steady oscillatory motion the friction surfaces changes from an energy sink to an energy source (once the steady state sink $V_0\tau_{ss}$ is subtracted out) when β decreases through the value given by equation (18). Thus the viscoelastic energy absorbed is accommodated through the decrease in β.

Downloaded 02 May 2010 to 171.66.16.246. Redistribution subject to ASME license or copyright; see http://www.asme.org/terms/Terms_Use.cfm

Slipping Elastic Continua and Creep Waves

In this section we assume that the sliding bodies are identical elastic continua with interface along the ξ_1,ξ_2 plane of a ξ_1,ξ_2,ξ_3 cartesian coordinate system, Fig. 3. For simplicity we neglect inertia here. It is considered in a special version of the problem taken up in the next section. The sliding bodies are assumed to be translationally homogeneous in the ξ_1 direction, and steady relative slip at speed V_0 in either the ξ_1 or ξ_2 direction is enforced by displacement boundary conditions imposed at $\xi_3 = \pm H$. The perturbation from steady slip along the interface is represented by a relative displacement δ, in the same direction as V_0, between $\xi_3 = 0^+$ and 0^- of the form

$$\delta(\xi_1,t) = V_0 t + x(t)\ \cos(\kappa\xi_1 + \phi) \tag{29}$$

where κ is the spatial wave number of the disturbance and ϕ is any constant. More general perturbations may be obtained by Fourier superposition with various κ, ϕ. The relative slip speed at the interface is

$$V(\xi_1,t) = V_0 + \dot{x}(t)\ \cos(\kappa\xi_1 + \phi). \tag{30}$$

Because of the translational homogeneity, the associated variation in resistive shear stress τ along the interface, computed from elasticity theory in terms of the given displacement nonuniformity, must have the same spatial dependence but be exactly out of phase with it. Hence

$$\tau(\xi_1,t) = \tau_{ss}(V_0) - k(\kappa)\ x(t)\ \cos(\kappa\xi_1 + \phi), \tag{31}$$

where the coefficient $k = k(\kappa)$ can evidently be interpreted as an effective spring constant for disturbances with wave number κ (compare equations (6) and (11) with (30) and (31)).

The stiffness $k(\kappa)$ can be found simply for some representative models. For example, if the two elastic bodies are isotropic, homogeneous half spaces of shear modulus G and Poisson ratio ν, then one can derive from elementary elasticity theory that

$$k = G|\kappa|/2(1-\nu), \quad G|\kappa|/2 \tag{32}$$

for the respective cases of plane strain (V in ξ_1 direction) and antiplane strain (V in ξ_2 direction). For finite layers of height H (in the ξ_3 direction) in contact, the preceding formulas remain valid in the short wavelength limit $\kappa H >> 1$, but in the long wavelength limit, $\kappa H << 1$, both expressions for k approach the limiting value

$$k = G/2H, \tag{33}$$

which corresponds to uniform ($\kappa \to 0$) shearing of the layers. In fact, the complete expression for $k(\kappa)$ in the antiplane strain mode (see the next section) is

$$k(\kappa) = G|\kappa|/[2\tanh(|\kappa|H)]. \tag{34}$$

Analogously to the treatment of the sliding block, we assume that a perturbing load distribution, generating shear stress

$$q(t)\cos(\kappa\xi_1 + \phi)$$

along the interface, is switched on at $t = 0$. Precisely, the preceding expression gives the shear stress that the considered load perturbation would cause along the interface if $x(t)$ were constrained to be zero. Hence this term must be added to equation (31) for $\tau(\xi_1,t)$. The resulting τ at each location ξ_1 must satisfy the constitutive relation (7) when $\dot{x}(t)\ \cos(\kappa\xi_1 + \phi)$ is read-in for $\dot{x}(t)$. Hence we find that

$$k(\kappa)x(t) + f\dot{x}(t) - \int_0^t h(t-t')\dot{x}(t')\,dt' = q(t), \tag{35}$$

which is the same as equation (13) for the sliding block without inertia. Thus we may again write $\hat{x}(s) = \hat{q}(s)/D(s)$ as in equation (14), but now with

$$D(s) = k(\kappa) + s[f - \hat{h}(s)]. \tag{36}$$

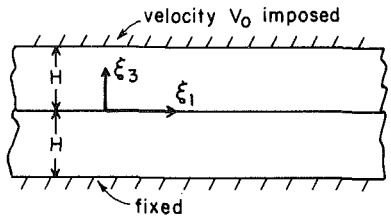

Fig. 3 Elastic continua in slipping contact. Bottom of lower layer is fixed. Top of upper level has imposed velocity V_0 in slip direction.

Hence, following the earlier discussion, instability occurs, if at all, by a flutter mode of frequency β satisfying $D(\pm i\beta) = 0$ and given by equation (18). Disturbances decay or grow in amplitude according to whether (by equation (19) with $m = 0$)

$$k(\kappa) \gtrless k_{cr} \equiv \beta \int_0^\infty \sin(\beta t)\,h(t)\,dt. \tag{37}$$

One expects that k varies monotonically with κ so that one of the following two cases occur: As κ decreases from ∞ to zero, k decreases from ∞ to either: (*i*) a value in excess of k_{cr} (possible when finite H gives a long wavelength cutoff); or, (*ii*) a value smaller than k_{cr} (and equal to 0 when the bodies are unbounded half spaces, $H = \infty$). In case (*i*) all perturbations are stable. In case (*ii*) perturbations with sufficiently high wave number (short wavelength) are stable, but those with lower wave number (long wavelength) are unstable.

The result at critical conditions has an interesting interpretation. Since $x(t)$ then varies as $Re(e^{i\beta t})$ or $Im(e^{i\beta t})$, the combination of space and time dependence as in equation (30) leads to disturbances with

$$V(\xi_1,t) - V_0 \propto \cos(\kappa_{cr}\xi_1 \pm \beta t). \tag{38}$$

This represents propagating quasi-static waves that move along the interface with speed β/κ_{cr}. The existence of such waves was first noted by Ruina [3] in analysis of a simple model of a continuous elastic system with a sliding surface described by a one-state variable form of equations (10).

As an example, for the friction law with a single exponential decay process, equations (22) and (23), $\beta = r\sqrt{\lambda}$ and the speed of the creep waves is

$$\text{speed} \equiv \beta/\kappa_{cr} = r\sqrt{\lambda}/\kappa_{cr} = V\sqrt{\lambda}/(\kappa_{cr}d_c) \tag{39}$$

where d_c is the decay distance, V/r. The critical wave number depends on details of the elastic continua. But for isotropic half spaces under antiplane slip we obtain from (32) that $G\kappa_{cr}/2 = k_{cr}$, where k_{cr} is evaluated from (25) with $m = 0$. Thus the critical wavelength λ_{cr} is

$$\lambda_{cr} \equiv 2\pi/\kappa_{cr} = \pi\, d_c G/[-V d\tau_{ss}(V)/dV] \tag{40}$$

Further, using this κ_{cr} and the interpretation of λ given before, the speed of creep waves is found from equation (39) to be

$$\text{speed} = G/2\sqrt{[-d\tau_{ss}(V)/dV][\partial\tau(V,\text{state})/\partial V]} \tag{41}$$

According to the results presented by Ruina [3] and Dieterich [5–8], the bracketed terms in the last expression are each of order $0.01\ \sigma/V$, where σ is the normal stress. In that case we obtain

$$\lambda_{cr} \approx 300\, d_c G/\sigma, \quad \text{speed} \approx 50\, VG/\sigma. \tag{42}$$

If we choose σ as the overburden pressure in the earth from a 1 to 10 km depth range, one estimates $G/\sigma = 10^3$ to 10^2 for faults under crustal earthquake conditions. Thus the creep wave speed is $5\cdot10^3$ to $5\cdot10^4$ times the nominal steady slip speed V. This is still much slower than seismic shear wave speeds if V is of the order of a cm/sec. or less. The corresponding wavelengths λ_{cr} are then of order $3\cdot10^5$ to $3\cdot10^4$ times d_c, resulting in $\lambda_{cr} \approx 0.1$ to 1 m if d_c is of order 3μm (representative of laboratory studies on polished

Downloaded 02 May 2010 to 171.66.16.246. Redistribution subject to ASME license or copyright; see http://www.asme.org/terms/Terms_Use.cfm

quartzite surfaces, Ruina [3]), but of the order $\lambda_{cr} \approx 30$ to 300 m if, for example, a d_c of the order 1 mm is postulated (which is somewhat larger than the largest results of Dieterich [8] for laboratory fault gauge).

The analysis predicts that disturbances with $\lambda < \lambda_{cr}$ are stable and decay in time but that those with $\lambda > \lambda_{cr}$ exhibit oscillatory growth in amplitude, at least for λ in the vicinity of λ_{cr}.

Inertia Effects in Antiplane Perturbations of Slipping Elastic Continua

Consider isotropic, homogeneous elastic bodies as in Fig. 3, with enforced relative motion in the ξ_2 direction, and let the relative displacement δ along the interface be given as in equation (29) of the preceding section. This loading causes an antiplane strain deformation and, if $u(\xi_1,\xi_3,t)$ is the antiplane displacement field (in the ξ_2 direction) measured relative to the steady sliding state, we have a boundary value problem described by the following equation of motion (43), and antisymmetry and boundary conditions (44):

$$\partial^2 u/\partial \xi_1{}^2 + \partial^2 u/\partial \xi_3{}^2 = (1/c^2)\partial^2 u/\partial t^2; \tag{43}$$

$$u(\xi_1,\xi_3,t) = -u(\xi_1,-\xi_3,t), \quad u(\xi_1,H,t) = 0,$$
$$u(\xi_1,0^+,t) = \frac{1}{2}x(t)\cos(\kappa\xi_1+\phi), \tag{44}$$

where c is the shear wave speed.

The Laplace transform of the solution is (for $\xi_3 > 0$)

$$\hat{u}(\xi_1,\xi_3,s) = \frac{1}{2}\hat{x}(s)\cos(\kappa\xi_1+\phi)\sinh[\sqrt{\kappa^2+s^2/c^2}\,(H-\xi_3)]/$$
$$\sinh(\sqrt{\kappa^2+s^2/c^2}H). \tag{45}$$

The stress $\tau(=\tau_{32})$ along the interface due to this elastodynamic loading can be written as

$$\tau_1(t)\cos(\kappa\xi_1+\phi) = G[\partial u(\xi_1,\xi_3,t)/\partial\xi_3]_{\xi_3=0} \tag{46}$$

The last equation shows that

$$\hat{\tau}_1(s) = -K(s,\kappa)\hat{x}(s), \text{ where}$$
$$K(s,\kappa) \equiv G\sqrt{\kappa^2+s^2/c^2}/[2\tanh(\sqrt{\kappa^2+s^2/c^2}H)]. \tag{47}$$

Now the friction stress τ must equal the steady state stress τ_{ss} in addition to the elastodynamic stress from equation (46) and the perturbation stress:

$$\tau = \tau_{ss}(V_0) + \tau_1(t)\cos(\kappa\xi_1+\phi) + q(t)\cos(\kappa\xi_1+\phi). \tag{48}$$

The perturbation amplitude $q(t)$ is again zero for $t<0$ but otherwise arbitrary.

The expression for τ in equation (48) must equal the value required by the constitutive law of equation (7) with the slip perturbation $x(t)\cos(\kappa\xi_1+\phi)$. The Laplace transform of equation (48) with equation (47) then gives $\hat{x}(s) = \hat{q}(s)/D(s)$, as in equation (14), but now with

$$D(s) = K(s,\kappa) + s[f - \hat{h}(s)] \tag{49}$$

and $K(s,\kappa)$ given by equation (47). Again stability of steady sliding requires no poles in $\hat{x}(s)$ for $Re(s) > 0$ and thus no zeroes of $D(s)$ in $Re(s) > 0$. The subsequent analysis of this case follows the pattern established earlier. As $|\kappa|$ is reduced in value from ∞ to 0, roots of $D(s) = 0$ first pass into $\mathrm{Re}(s) > 0$, if at all, by crossing the $Im(s)$ axis. Hence, setting $D(\pm i\beta) = 0$ we obtain the pair of equations to be met at critical conditions

$$\int_0^\infty \cos(\beta t)h(t)\,dt = f,$$
$$K(i\beta,\kappa_{cr}) = \beta\int_0^\infty \sin(\beta t)h(t)\,dt \tag{50}$$

where

$$K(i\beta,\kappa) = \frac{G\sqrt{\kappa^2-\beta^2/c^2}}{2\tanh(\sqrt{\kappa^2-\beta^2/c^2}H} \quad \text{for} \quad \kappa^2 > \beta^2/c^2$$
$$= \frac{G\sqrt{\beta^2/c^2-\kappa^2}}{2\tan(\sqrt{\beta^2/c^2-\kappa^2}H)} \quad \text{for} \quad \kappa^2 < \beta^2/c^2 \tag{51}$$

The first of the pair of equations (50) is now familiar (see equation (18)) and gives the critical frequency β at flutter instability, if such instability can occur. The second of equation (50) is analogous to equation (19) with $m\beta^2$ moved to the left-hand side.

Instability can occur if the second of equations (50), whose right side is positive by (21), has a solution for some $|\kappa|$ between ∞ and 0. To analyze the second equation, let us observe that the equation $K(i\omega,\kappa) = 0$ implies no traction at $\xi_3 = 0$ and thus gives the natural frequencies of clamped-free vibrations of either layer in Fig. 3, compatible with spatial periodicity of wave number κ. These frequencies are given by

$$\sqrt{\omega_n{}^2/c^2-\kappa^2}H = (2n-1)\pi/2, \quad n = 1,2,3,\ldots,$$
$$\text{or } \omega_n = \sqrt{\kappa^2c^2+(2n-1)^2(\pi c/2H)^2} \tag{52}$$

The lowest frequency of all is ω_1 for $\kappa = 0$; calling this $\omega_1{}^*$, we have $\omega_1{}^* = \pi c/2H$.

We now distinguish two cases: (*i*) $\beta < \omega_1{}^*$, and (*ii*) $\beta > \omega_1{}^*$. For case (*i*) it is possible to show by simple analysis that $K(i\beta,\kappa)$ decreases monotonically with κ as the latter decreases from ∞ to 0; $K(i\beta,\infty) = \infty$ and the least value of K is

$$K(i\beta,0) = \frac{G}{2H}\frac{(\pi\beta/2\omega_1{}^*)}{\tan(\pi\beta/2\omega_1{}^*)}\left(<\frac{G}{2H}\right) \tag{53}$$

If this value of $K(i\beta,0)$ is less than the right side of the second of equations (50), then the equation (50) has a solution and instability occurs by flutter oscillations for wave numbers $|\kappa| < |\kappa_{cr}|$. Again, conditions in the vicinity of neutral stability, $|\kappa| = |\kappa_{cr}|$, can be described as the propagation of frictional creep waves along the interface, which grow in amplitude when $|\kappa| < |\kappa_{cr}|$. On the other hand, if $K(i\beta,0)$ exceeds the right side of the last of equations (50), then no solution exists and slip is stable to perturbations of all wavelengths. This is analogous to the cutoff described in the preceding section with inertia neglected, and the results of that section are approached when the lowest vibration frequency of the layer is much higher than the critical frequency for slip instability, i.e., $\beta/\omega_1{}^* \to 0$. Also, just as for the one degree-of-freedom system, the inclusion of inertia is destabilizing; the critical wave number $|\kappa_{cr}|$ in the analysis with inertia always exceeds that of the quasi-static analysis although, of course, the difference is negligible when $\beta << \omega_1{}^*$.

For case (*ii*), $\beta > \omega_1{}^*$, it is evident from equation (52) that at least one $|\kappa| > 0$ exists such that β coincides with a natural frequency for that κ, and hence that $K(i\beta,\kappa) = 0$. The largest $|\kappa|$ satisfying that condition, say $|\kappa_1|$, is readily seen to be that κ for which β coincides with frequency ω_1. Hence, from (52) with $n = 1$ and $\omega_1 = \beta$ we find

$$|\kappa_1| = \sqrt{\beta^2-\omega_1{}^{*2}}/c. \tag{54}$$

Then from equation (51) one can see that $K(i\beta,\kappa)$ decreases monotonically from ∞ to 0 as $|\kappa|$ decreases from ∞ to $|\kappa_1|$. Thus in this case, for which $\beta > \omega_1{}^*$, there always exists a κ_{cr} satisfying the second of equations (50), and $|\kappa_{cr}|$ is necessarily greater than $|\kappa_1|$. That is, the system is unstable to perturbations of long enough wavelength if β exceeds its lowest vibration frequency.

Since the analysis of this section has relied only on rather general properties to be expected of any function $K(s,\kappa)$ relating nonuniformity of slip to nonuniformity of stress, it seems likely that similar conclusions would be reached for

Downloaded 02 May 2010 to 171.66.16.246. Redistribution subject to ASME license or copyright; see http://www.asme.org/terms/Terms_Use.cfm

other modes of perturbing sliding continua of the general class introduced in the last section.

Concluding Discussion

The systems discussed in our paper exhibit a common general pattern. In particular, if $x(t)$ denotes the displacement perturbation from steady state slip and $q(t)$ the perturbing force, then $\hat{x}(s) = \hat{q}(s)/D(s)$, as in equation (14), where

$$D(s) = Q(s) + s[f - \hat{h}(s)]. \tag{55}$$

Here f and $h(t)$ are defined by the friction law (7) whereas $Q(s)$ is a transfer function. It relates the displacement perturbation to corresponding changes in stress τ induced by the system (e.g., by its elastic or viscoelastic springiness and inertia) on the slip surface; i.e., if $\tau_1(t) = \tau - \tau_{ss}$, then $\hat{\tau}_1(s) = -Q(s)\hat{x}(s)$.

In the various cases that we have examined, subject to (9), the form of the transfer function has assured that instability occurs by the flutter mode when an appropriately defined stiffness is reduced to a critical value. This contrasts with analyses that neglect the memory effects in (7) and thus deduce that rate weakening is a sufficient condition for instability and that oscillations depend on nonlinear effects (e.g., Brockley and Ko [2, 17]).

Indeed, this universality of the flutter instability, meaning that roots of $D(s) = 0$ inevitably pass to $Re(s) > 0$ by traversing the $Im(s)$ axis in conjugate pairs, means that the bifurcation is of the Hopf type (e.g., Howard [18]). We have presented only a linear analysis here, but the generic behavior of the nonlinear solution in the vicinity of critical conditions is understood. In particular, in a one-sided neighborhood of $k = k_{cr}$ (in terms of the spring-block analysis) there exists finite amplitude periodic oscillations of amplitude that increases with $|k - k_{cr}|$. When the neighborhood is that for which $k < k_{cr}$, the growing oscillations of linear instability theory grow into a stable periodic limit cycle, at least close to $k = k_{cr}$. When the neighborhood is that for which $k > k_{cr}$, the periodic oscillation is unstable, and the decaying oscillations of linear stability theory may, in fact, not be realized if the perturbation of the system is of too great an amplitude. Exceptionally, it may occur that the finite amplitude periodic oscillations occur with $k = k_{cr}$. This is precisely what we have found recently (Gu et al. [19]) for the nonlinear stability analysis of a certain one-state variable constitutive law proposed by Ruina [3], namely that for which equation (10) has the form

$$\tau = \tau_1 + A\ ln(V/V_1) - \theta,$$
$$\frac{d\theta}{dt} = -\frac{V}{d_c}[\theta - B\ ln(V/V_1)] \tag{56}$$

where τ_1, d_c, A, and $B(>A)$ are all positive constants. We remark that there is ample experimental evidence for the type of flutter instability that we predict here (Ruina [3], Scholz et al. [20], Teufel [21]). The flutter is of such low frequency in these experiments that inertia is negligible and classical calculations of the Rayleigh type cannot apply. Whether or not our results are appropriate to the type of fast oscillations observed by Brockley and Ko [2, 17] is not clear. Their results do show that τ is not a function of V alone (although they neglect this in their analysis). Also, the experimental results show much richer nonlinear behavior than thus far discussed. For example, signs of period doubling are visible in the experiments of Ruina [3] as k is decreased from k_{cr}.

It is plain that there remains much to be learned about nonlinear stability analysis in the framework of the rate and state-dependent frictional constitutive laws discussed here. The topic is of interest not only as an extension of studies of the type that we have reported, but also as foundation for a more general and realistic fracture mechanics of slip propagation (shear cracking) along fault surfaces.

Acknowledgment

This work was supported by the NSF Geophysics Program and USGS Earthquake Hazards Reduction Program. Pleasant and informative discussion by A. R. with Herbert Hui is appreciated.

References

1 Kosterin, Iu. I., and Kragel'skii, I.V., "Relaxation Oscillations in Elastic Friction Systems," in: *Friction and Wear in Machinery*, Krushchov, M., ed., ASME, N.Y., 1960, pp. 111-134.

2 Brockley, C. A., and Ko, P. L., "Quasi-Harmonic Friction-Induced Vibration," ASME *Journal of Lubrication Technology*, Vol. 92, 1970, pp. 550-556.

3 Ruina, A. L., "Friction Laws and Instabilities: A Quasistatic Analysis of Some Dry Frictional Behavior," Brown University, Providence, R.I., Ph.D. Thesis, 1980; also, "Slip Instability and State Variable Friction Laws," *Journal of Geophysical Research*, in press, 1983.

4 Dieterich, J. H., "Time-Dependent Friction in Rocks," *Journal of Geophysical Research*, Vol. 77, 1972, pp. 3690-3697.

5 Dieterich, J. H., "Time-Dependent Friction and the Mechanics of Stick Slip," *Pure and Applied Geophysics*, Vol. 116, 1978, pp. 790-806.

6 Dieterich, J. H., "Modeling of Rock Friction 1. Experimental Results and Constitutive Equations," *Journal of Geophysical Research*, Vol. 84, 1979, pp. 2161-2168.

7 Dieterich, J. H., "Experimental and Model Study of Fault Constitutive Properties," in: *Solid Earth Geophysics and Geotechnology*, Nemat-Naser, S., ed., ASME, New York, 1980, pp. 21-29.

8 Dieterich, J. H., "Constitutive Properties of Faults With Simulated Gouge," in: *Mechanical Behavior of Crustal Rocks*, AGU Monograph 24, Carter, N. L., Friedman, M., Logan, J. M., and Stearns, D. W., eds., 1981, pp. 21-29.

9 Rabinowicz, E., "The Intrinsic Variables Affecting the Stick Slip Process," *Proceedings of the Physical Society*, Vol. 71, 1958, pp. 665-675.

10 Rabinowicz, E., "A Study of the Stick-Slip Process," in: *Symp. on Friction & Wear*, Detroit, 1957, Davies, R., ed., Elsevier, New York, 1959, pp. 149-161.

11 Stesky, R. M., Brace, W. F., Riley, D. K., and Robin, P.-Y. F., "Friction in Faulted Rock at High Temperature and Pressure," *Tectonophysics*, Vol. 23, 1974, pp. 177-203.

12 Stesky, R. M., "Mechanisms of High Temperature Frictional Sliding in Westerly Granite," *Can. J. Earth Sci.*, Vol. 15, 1978, pp. 361-375.

13 Solberg, P., and Byerlee, J., "Experimental Strain Rate Dependent Frictional Stress and Fault Creep," *J. Geophys. Res.*, in press, 1982.

14 Tolstoi, D. M., "Significance of the Normal Degree of Freedom and Natural Normal Vibrations in Contact Friction," *Wear*, Vol. 10, 1967, pp. 199-213.

15 Jenkin, F., and Ewing, J. A., "On Friction Between Surfaces Moving at Low Speeds," *Phil. Trans. Royal Soc. of London*, Vol. 167, 1877, pp. 508-528.

16 Kosloff, D., and Liu, H.-P., "Reformulation and Discussion of Mechanical Behavior of the Velocity-Dependent Friction Law Proposed by Dieterich," *Geophysical Research Letters*, Vol. 7, 1980, pp. 913-960.

17 Ko, P. L., and Brockley, C. A., "The Measurement of Friction and Friction-Induced Vibration," ASME *Journal of Lubrication Technology*, Vol. 92, 1970, pp. 543-549.

18 Howard, L. N., "Nonlinear Oscillations," in: *Nonlinear Oscillations in Biology*, Vol. 17, Lectures in Applied Mathematics, Hoppensteadt, F. C., ed., American Mathematical Society, Providence, R.I., 1979, pp. 1-67.

19 Gu, J.-c., Rice, J. R., and Ruina, A., "A Non-Linear Analysis of Motion in a Spring and Massless Block Model With a Rate and State Dependent Friction Law," summary paper for 9th U.S. National Congress on Applied Mechanics, Ithaca, N.Y., 1982.

20 Scholz, C., Molnar, P., and Johnson, T., "Detailed Studies of Frictional Sliding of Granite and Implications for the Earthquake Mechanism," *Journal of Geophysical Research*, Vol. 77, 1972, pp. 6392-6406.

21 Teufel, L., private communication, 1981.

Downloaded 02 May 2010 to 171.66.16.246. Redistribution subject to ASME license or copyright; see http://www.asme.org/terms/Terms_Use.cfm

J. Casey
Department of Mechanical Engineering,
University of Houston,
Houston, Texas 77004
Assoc. Mem. ASME

P. M. Naghdi
Department of Mechanical Engineering,
University of California,
Berkeley, Calif. 94720
Fellow ASME

On the Nonequivalence of the Stress Space and Strain Space Formulations of Plasticity Theory

Yoder and Iwan [7] *have recently claimed that the stress space and strain space formulations of plasticity are equivalent. This conflicts with the results of Casey and Naghdi* [6]. *The main objective of the present paper is to demonstrate, with the use of fairly general constitutive equations of the type employed in* [7], *that the stress space and strain space formulations of plasticity theory are not equivalent. It is also shown that if the loading criteria of strain space are adopted as primary, then the main features of* [7] *may be obtained by specializing the results of* [6].

1 Introduction

By way of background, we recall that the traditional formulation of plasticity theory employs yield surfaces in stress space, together with loading criteria that involve the time rate of stress. It was shown by Naghdi and Trapp [1] that this formulation necessarily leads to unreliable results in any region such as that corresponding to the neighborhood of the maximum point of the engineering stress versus engineering strain curve for uniaxial tension of a typical ductile metal. An alternative strain space formulation was therefore proposed in [1] and was found to be free from the shortcomings of the stress space formulation. Furthermore, the strain space formulation was shown [1] to have the additional advantage that the loading criteria for perfectly plastic materials are exactly the same as for work-hardening materials, whereas in the stress space formulation the loading criteria are different for these two classes of materials and a separate treatment is required for perfectly plastic materials.

The strain space formulation is elaborated on further in [2], which also contains a discussion of restrictions imposed on constitutive equations by a work assumption originally introduced in a strain space setting by Naghdi and Trapp [3]. Additional related developments utilizing the strain space formulation, which also include consideration of strain-hardening response, are contained in [4–6].

By way of additional background information, we recall that Naghdi and Trapp [1] also undertook a comparison between the two independently postulated sets of loading criteria in strain space and stress space. They concluded that a correspondence between the two sets of loading criteria could be established for all conditions except that of loading from an elastic-plastic state. However, it was shown by Casey and Naghdi [6] that the two sets of loading criteria cannot be independently postulated because they are connected by the constitutive equations of the theory: If they are independently postulated, then only a limited form of strain-hardening behavior is possible as remarked in the last paragraph of [6, p. 289]. Due to the inadequacies of the stress space formulation, which were discussed in [1], Casey and Naghdi [6] adopted the approach that the loading criteria of the strain space formulation should be regarded as primary and that the constitutive equations of the theory should then be used to deduce associated loading conditions in stress space. The conditions induced in stress space during loading are not identical to those of the strain space formulation, nor do they imply the loading conditions of the strain space formulation.[1]

In a recent paper, Yoder and Iwan [7] have claimed that the stress space and strain space formulations of plasticity theory are equivalent. Although we discussed this issue and related matters previously [8], within the space limitations of the Discussion [8], it was not possible to detail the relationship between the developments of [6] and [7]. The present paper provides the mathematical details that were omitted from [8]. As already noted in [8] the two formulations of plasticity are not equivalent.[2] Moreover, if the loading criteria of strain space are regarded as primary, then as shown in Sections 2 and 3, the main features of the work of Yoder and Iwan [7] may be obtained as a special case of that of Casey and Naghdi [6]. In particular, employing constitutive equations of the type utilized by Yoder and Iwan [7], we show in Section 2 that the loading criteria of their strain space formulation lead, as in [6], to different conditions in stress space. In Section 3, we discuss how the constitutive equations of Section 2 can be obtained as a special case of those employed in [1, 6].

Contributed by the Applied Mechanics Division for publication in the JOURNAL OF APPLIED MECHANICS.

Discussion on this paper should be addressed to the Editorial Department, ASME, United Engineering Center, 345 East 47th Street, New York, N.Y. 10017, and will be accepted until two months after final publication of the paper itself in the JOURNAL OF APPLIED MECHANICS. Manuscript received by ASME Applied Mechanics Division, March, 1982; final revision, October, 1982.

[1] For a summary of the relationship between the conditions in stress space and the loading criteria in strain space, see [6, Table 1].

[2] Although in [7] both single and multiple loading surfaces are employed, it suffices for the present purpose to consider only the case of single loading surfaces.

Copyright © 1983 by ASME
Downloaded 02 May 2010 to 171.66.16.246. Redistribution subject to ASME license or copyright; see http://www.asme.org/terms/Terms_Use.cfm

2 A Special Class of Constitutive Equations

In this section we analyze a special class of constitutive equations of the type introduced by Yoder and Iwan [7]. Confining attention to small deformations only, we denote the components of infinitesimal strain and plastic strain by ϵ_{ij} and ϵ^p_{ij}, respectively, and the components of stress[3] by σ_{ij}. The elastic response is assumed to satisfy generalized Hooke's law so that

$$\sigma_{ij} = c_{ijkl}(\epsilon_{kl} - \epsilon^p_{kl}), \tag{1}$$

where the constant moduli satisfy $c_{ijkl} = c_{jikl} = c_{ijlk} = c_{klij}$. The inverse response may be written as

$$\epsilon_{ij} = \kappa_{ijkl}\sigma_{kl} + \epsilon^p_{ij}, \tag{2}$$

where κ_{ijkl} possess the same symmetries as c_{ijkl}, and

$$c_{ijkl}\kappa_{klmn} = \kappa_{ijkl}c_{klmn} = \tfrac{1}{2}(\delta_{im}\delta_{jn} + \delta_{in}\delta_{jm}), \tag{3}$$

δ_{ij} being the Kronecker symbol. In [7], the material was assumed to be isotropic in its initial reference configuration, so that the material coefficients c_{ijkl} and κ_{ijkl} have a simple isotropic form.[4] However, it is unnecessary to assume isotropy in what follows.

Defining σ^R_{ij} by

$$\sigma^R_{ij} = c_{ijkl}\epsilon^p_{kl}, \tag{4}$$

we note that (1) may be written as

$$\sigma_{ij} = c_{ijkl}\epsilon_{kl} - \sigma^R_{ij}. \tag{5}$$

The tensor $\boldsymbol{\sigma}^R$, called a "stress relaxation" was defined in [7] through the constitutive equation (5) rather than in terms of $\boldsymbol{\epsilon}^p$, as we have done in (4). In view of (3), the relation (4) may be inverted in the form

$$\epsilon^p_{ij} = \kappa_{ijkl}\sigma^R_{kl}. \tag{6}$$

Suppose now, as in [7], that there exists in strain space a "relaxation" function $\hat{F}(\boldsymbol{\epsilon}, \boldsymbol{\sigma}^R, L)$, where the scalar function L is defined by

$$L = \int_0^t \left(\frac{2}{3}\dot{\sigma}^R_{ij}\dot{\sigma}^R_{ij}\right)^{1/2} dt', \tag{7}$$

$0 \le t' \le t$ is an interval of time and a superposed dot signifies material time differentiation. The "relaxation surface" in strain space is defined by $\hat{F} = 0$ at fixed values of $\boldsymbol{\sigma}^R$ and L. In anticipation of later developments, we set

$$\hat{g} = \frac{\partial \hat{F}}{\partial \epsilon_{ij}}\dot{\epsilon}_{ij} \tag{8}$$

and assume that

$$\dot{\sigma}^R_{ij} = \begin{cases} 0 & \text{if } \hat{F} < 0, & (a) \\ 0 & \text{if } \hat{F} = 0 \text{ and } \hat{g} < 0, & (b) \\ 0 & \text{if } \hat{F} = 0 \text{ and } \hat{g} = 0, & (c) \\ \dfrac{1}{D}\hat{g}\dfrac{\partial \hat{F}}{\partial \epsilon_{ij}} & \text{if } \hat{F} = 0 \text{ and } \hat{g} > 0, & (d) \end{cases} \tag{9}$$

where D is a positive scalar-valued function of $(\boldsymbol{\epsilon}, \boldsymbol{\sigma}^R, L)$. It is also assumed that the partial derivative $\partial \hat{F}/\partial \boldsymbol{\epsilon} \neq \mathbf{0}$ on the "relaxation surface."

The consistency condition in strain space implies that $\dot{\hat{F}} = 0$ if $\hat{F} = 0$ and $\hat{g} > 0$. Therefore, in view of (7), (8), and (9d)

$$D = -\frac{\partial \hat{F}}{\partial \sigma^R_{ij}}\frac{\partial \hat{F}}{\partial \epsilon_{ij}} - \frac{\partial \hat{F}}{\partial L}\left(\frac{2}{3}\frac{\partial \hat{F}}{\partial \epsilon_{ij}}\frac{\partial \hat{F}}{\partial \epsilon_{ij}}\right)^{1/2}. \tag{10}$$

Equations (9) and (10) are of the type considered in [7], although the present derivation is slightly different from that given in [7]. If $\hat{F}$ is assumed to be of the special form [7, equation (9)], then D in (10) may be expressed as [7, equation (10)].

The yield or loading function in strain space may be derived from $\hat{F}$ with the use of (4) as follows:

$$\hat{F}(\epsilon_{ij}, \sigma^R_{ij}, L) = \hat{F}(\epsilon_{ij}, c_{ijkl}\epsilon^p_{kl}, L) = g(\epsilon_{ij}, \epsilon^p_{ij}, L). \tag{11}$$

The loading surface in strain space is given by $g = 0$ at fixed values of $\boldsymbol{\epsilon}^p$ and L. Clearly, the "relaxation surface" and the loading surface in strain space coincide.

In view of (8) and (11),

$$\hat{g} = \frac{\partial g}{\partial \epsilon_{ij}}\dot{\epsilon}_{ij}. \tag{12}$$

Further, by (7), (9), and (11),

$$\dot{L} = \frac{1}{D}\hat{g}\left(\frac{2}{3}\frac{\partial g}{\partial \epsilon_{ij}}\frac{\partial g}{\partial \epsilon_{ij}}\right)^{1/2} > 0, \tag{13}$$

if $g = 0$ and $\hat{g} > 0$, and is zero otherwise. Finally, it follows from (4), (9), and (11) that

$$\dot{\epsilon}^p_{ij} = \begin{cases} 0 & \text{if } g < 0, & (a) \\ 0 & \text{if } g = 0 \text{ and } \hat{g} < 0, & (b) \\ 0 & \text{if } g = 0 \text{ and } \hat{g} = 0, & (c) \\ \dfrac{1}{D}\hat{g}\kappa_{ijkl}\dfrac{\partial g}{\partial \epsilon_{kl}} & \text{if } g = 0 \text{ and } \hat{g} > 0, & (d) \end{cases} \tag{14}$$

where the scalar D in (10) can now be expressed as

$$D = -\kappa_{klij}\frac{\partial g}{\partial \epsilon^p_{kl}}\frac{\partial g}{\partial \epsilon_{ij}} - \frac{\partial g}{\partial L}\left(\frac{2}{3}\frac{\partial g}{\partial \epsilon_{ij}}\frac{\partial g}{\partial \epsilon_{ij}}\right)^{1/2}. \tag{15}$$

It is clear that instead of beginning with $\hat{F}$ we could have started out with the loading function g and the flow rules (14), and then we could have derived $\hat{F}$ through (11) as well as the flow rules (9). In this case, we would have written L in terms of $\dot{\boldsymbol{\epsilon}}^p$ by substituting (4) in (7). Thus, the relations (9) and (14) are equivalent statements of the flow rules in strain space.

The conditions involving g and $\hat{g}$ in (14) are the loading criteria of the strain space formulation. These four conditions correspond to (*a*) an elastic state; (*b*) unloading from an elastic-plastic state; (*c*) neutral loading from an elastic-plastic state; and (*d*) loading from an elastic-plastic state.

In their paper, Naghdi and Trapp [1] first discussed the usual stress space formulation of plasticity, in which loading criteria are written in terms of stress rate and the loading function in stress space. They then proposed an alternative strain space formulation, with loading criteria such as appear in (14). Comparing the two independently postulated formulations, they concluded [1, p. 791] that a correspondence existed between the two sets of loading criteria in the case of elastic response, unloading and neutral loading, but *not* during loading.

After observing that the loading criteria of the usual stress space formulation lead to unreliable results,[5] and that the loading criteria of strain space are free from such shortcomings, Naghdi and Trapp [1] proposed that the strain space formulation be adopted as an alternative to the stress space formulation.

For later reference we observe that, during loading, $\dot{L}$ can be written in the form

[3] This may be Cauchy stress or either of the Piola-Kirchhoff stresses, no distinction being made between these tensors in the infinitesimal theory.

[4] Incidentally, the right-hand sides of equations $(4)_{1,2}$ of [7] should be symmetrized with respect to the indices i and j.

[5] See the introductory remarks in Section 1.

Downloaded 02 May 2010 to 171.66.16.246. Redistribution subject to ASME license or copyright; see http://www.asme.org/terms/Terms_Use.cfm

$$\dot{L} = l_{ij}\dot{\epsilon}^p_{ij}, \tag{16}$$

where

$$l_{ij} = \frac{\kappa_{ijkl}\dfrac{\partial g}{\partial \epsilon_{kl}}\left(\dfrac{2}{3}\dfrac{\partial g}{\partial \epsilon_{mn}}\dfrac{\partial g}{\partial \epsilon_{mn}}\right)^{1/2}}{\kappa_{pqrs}\kappa_{pquv}\dfrac{\partial g}{\partial \epsilon_{rs}}\dfrac{\partial g}{\partial \epsilon_{uv}}}. \tag{17}$$

The constitutive equation (2) may be used to derive from g a loading function f in stress space as follows:

$$\begin{aligned} g(\epsilon_{ij},\epsilon^p_{ij},L) &= g(\kappa_{ijkl}\sigma_{kl}+\epsilon^p_{ij},\epsilon^p_{ij},L) \\ &= f(\sigma_{ij},\epsilon^p_{ij},L). \end{aligned} \tag{18}$$

The loading surface in stress space is given by $f=0$ at fixed values of ϵ^p and L.

Once a strain space formulation is adopted, stress appears as a dependent variable and it is conceivable that certain geometrical conditions in stress space might be induced by the conditions assumed in strain space. It was demonstrated by Casey and Naghdi [6] that this is in fact the case.

Proceeding as in [6], in the context of the present discussion we adopt the loading criteria in (14) and the flow rules in (14) as primary. As mentioned before, we could equivalently adopt (9), which are the relations assumed in [7].

In view of (18), (1) and (2)

$$\begin{aligned} &\frac{\partial g}{\partial \epsilon_{ij}} = c_{klij}\frac{\partial f}{\partial \sigma_{kl}}, \quad \frac{\partial f}{\partial \sigma_{ij}} = \kappa_{klij}\frac{\partial g}{\partial \epsilon_{kl}}, \\ &\frac{\partial g}{\partial \epsilon^p_{ij}} = \frac{\partial f}{\partial \epsilon^p_{ij}} - \frac{\partial g}{\partial \epsilon_{ij}}, \quad \frac{\partial g}{\partial L} = \frac{\partial f}{\partial L}. \end{aligned} \tag{19}$$

We adopt the usual notation

$$\hat{f} = \frac{\partial f}{\partial \sigma_{ij}}\dot{\sigma}_{ij}. \tag{20}$$

The relations $(19)_{2,4}$ and the symmetry condition $\kappa_{ijkl}=\kappa_{klij}$ allow (14d), (15), and (17) to be expressed as

$$\dot{\epsilon}^p_{ij} = \frac{1}{D}\hat{g}\frac{\partial f}{\partial \sigma_{ij}},$$

$$D = -\frac{\partial f}{\partial \sigma_{ij}}\frac{\partial g}{\partial \epsilon^p_{ij}} - \frac{\partial f}{\partial L}\left(\frac{2}{3}\frac{\partial g}{\partial \epsilon_{ij}}\frac{\partial g}{\partial \epsilon_{ij}}\right)^{1/2}, \tag{21}$$

$$l_{ij} = \frac{\dfrac{\partial f}{\partial \sigma_{ij}}\left(\dfrac{2}{3}\dfrac{\partial g}{\partial \epsilon_{mn}}\dfrac{\partial g}{\partial \epsilon_{mn}}\right)^{1/2}}{\dfrac{\partial f}{\partial \sigma_{pq}}\dfrac{\partial f}{\partial \sigma_{pq}}}.$$

Taking the time derivative of the identity (18), we find with the use of (12), (20), (14a,b,c), (4), and (7) that $\hat{f}=\hat{g}$ in an elastic state, as well as during unloading and neutral loading. Hence, the strain space criteria (14a,b,c) imply that

$$\begin{aligned} &f<0, && (a) \\ &f=0, \quad \hat{f}<0, && (b) \\ &f=0, \quad \hat{f}=0, && (c) \end{aligned} \tag{22}$$

respectively. This was noted by Naghdi and Trapp [1].

In contrast to the results (22), the strain space criterion in (14d) for loading from an elastic-plastic state does *not* imply that $f=0$ and $\hat{f}>0$. To elaborate, from the condition that $\dot{g}=0$, as well as (18), (12), (20), $(19)_4$, and $(21)_{1,2}$, it follows that during loading

$$\frac{\hat{f}}{\hat{g}} = 1 + \frac{1}{D}\frac{\partial f}{\partial \sigma_{ij}}\left(\frac{\partial g}{\partial \epsilon^p_{ij}} - \frac{\partial f}{\partial \epsilon^p_{ij}}\right)$$

$$= -\frac{1}{D}\left\{\frac{\partial f}{\partial \epsilon^p_{ij}}\frac{\partial f}{\partial \sigma_{ij}} + \frac{\partial f}{\partial L}\left(\frac{2}{3}\frac{\partial g}{\partial \epsilon_{ij}}\frac{\partial g}{\partial \epsilon_{ij}}\right)^{1/2}\right\}. \tag{23a}$$

With the use of $(19)_3$, the first expression in (23a) reduces to

$$\frac{\hat{f}}{\hat{g}} = 1 - \frac{\Xi}{D}, \tag{23b}$$

where[6]

$$\Xi = \frac{\partial f}{\partial \sigma_{ij}}\frac{\partial g}{\partial \epsilon_{ij}}, \tag{24}$$

which may also be deduced from $(19)_3$, $(21)_2$, and the second expression in (23a). Evidently, during loading the sign of $\hat{f}$ is *determined by the constitutive functions* that contribute to the coefficient of $1/D$ in $(23a)_2$. Three distinct types of material behavior are possible during loading, depending on whether $\hat{f}/\hat{g}$ is positive, negative, or zero. In [6], these three responses were called hardening, softening, and perfectly plastic behavior. Thus, during loading ($g=0$, $\hat{g}>0$),

$$\text{if the material exhibits} \begin{cases} \text{hardening}, & (a) \\ \text{softening}, & (b) \\ \text{perfectly plastic}, & (c) \end{cases} \tag{25a}$$

behavior, then

$$\begin{cases} f=0 \text{ and } \hat{f}>0, & (a) \\ f=0 \text{ and } \hat{f}<0, & (b) \\ f=0 \text{ and } \hat{f}=0. & (c) \end{cases} \tag{25b}$$

Thus, the strain space loading criteria do not imply identical conditions in stress space nor do the stress space conditions imply those of strain space. The stress space and strain space formulations are therefore not equivalent. Indeed, the condition $f=0$, $\hat{f}<0$, for example, corresponds both to unloading from an elastic-plastic state—defined by $g=0$, $\hat{g}<0$—and softening behavior during loading.

For purposes of comparison with [7], we set

$$\Delta = -\frac{\partial f}{\partial \epsilon^p_{ij}}\frac{\partial f}{\partial \sigma_{ij}} - \frac{\partial f}{\partial L}\left(\frac{2}{3}\frac{\partial g}{\partial \epsilon_{ij}}\frac{\partial g}{\partial \epsilon_{ij}}\right)^{1/2}. \tag{26}$$

It is then clear from $(23a)_2$ that

$$\frac{\hat{f}}{\hat{g}} = \frac{\Delta}{D} \tag{27}$$

and hence that

$$\Delta = \begin{cases} >0 & \text{if and only if the material is hardening,} \\ <0 & \text{if and only if the material is softening,} \\ =0 & \text{if and only if the material is exhibiting perfectly plastic behavior.} \end{cases}$$

Yoder and Iwan [7, p. 775] also regard strain-hardening, strain-softening and perfectly plastic behavior as corresponding, respectively, to the positivity, negativity, and vanishing of Δ.

From (23b) and (27) we obtain the relations

$$D = \Delta + \Xi, \quad \frac{\hat{f}}{\hat{g}} = \frac{\Delta}{\Delta+\Xi}. \tag{28}$$

[6] This quantity was denoted by Λ in [6], but in order to conform with the notation of [7] we reserve the symbol Λ for later use.

Downloaded 02 May 2010 to 171.66.16.246. Redistribution subject to ASME license or copyright; see http://www.asme.org/terms/Terms_Use.cfm

If a material is exhibiting either hardening or softening behavior, it is possible to express the flow rule $(21)_1$ in stress space form. Thus, in view of $(21)_1$, (25*a*,*b*), and (27)

$$\dot{\epsilon}^p_{ij} = \frac{1}{D}\frac{\partial f}{\partial \sigma_{ij}}\frac{\hat{f}}{\hat{f}/\hat{g}} = \frac{\hat{f}}{\Delta}\frac{\partial f}{\partial \sigma_{ij}}. \tag{29}$$

For hardening, both $\hat{f}$ and Δ are positive, while both are negative for softening. For perfectly plastic behavior $\dot{\epsilon}^p_{ij}$ cannot be written as a product involving $\hat{f}$—which vanishes—and the strain space flow rule $(21)_1$ must be retained.

A geometrical interpretation of the three types of strain-hardening responses was given in [6, Section 3]. While during loading, the yield surface in strain space is always moving outward locally, the corresponding yield surface in stress space may concurrently be moving outward, inward, or may be stationary depending on whether the material is exhibiting hardening, softening, or perfectly plastic behavior. The occurrence of such behavior was illustrated with reference to the response in simple tension of a special class of elastic-plastic materials [6, Section 4] and was also indicated in the discussion [6, Section 1] of the idealized stress-strain diagram for a typical ductile metal.

The quotient $\hat{f}/\hat{g}$, which is rate independent and dimensionless, is related to the ratio of the outward velocities, v_σ and v_ϵ, of the yield surfaces in stress space and strain space during plastic flow, where

$$v_\sigma = \hat{f}\left(\frac{\partial f}{\partial \sigma_{ij}}\frac{\partial f}{\partial \sigma_{ij}}\right)^{-1/2}, \qquad v_\epsilon = \hat{g}\left(\frac{\partial g}{\partial \epsilon_{ij}}\frac{\partial g}{\partial \epsilon_{ij}}\right)^{-1/2} > 0. \tag{30}$$

Thus

$$\frac{\hat{f}}{\hat{g}} = \frac{v_\sigma}{v_\epsilon}\left(\frac{\dfrac{\partial f}{\partial \sigma_{ij}}\dfrac{\partial f}{\partial \sigma_{ij}}}{\dfrac{\partial g}{\partial \epsilon_{kl}}\dfrac{\partial g}{\partial \epsilon_{kl}}}\right)^{1/2}. \tag{31}$$

For the case of uniaxial tension of special elastic-plastic materials, the quotient $\hat{f}/\hat{g}$ is related to the slope of the stress-strain curve [6, equation (65*a*)].

It is worth emphasizing that both stress space and strain space are needed to discuss strain-hardening behavior, as defined in [6]. However, this is the case even in the traditional definitions for one-dimensional loading, where the slope of the stress-strain diagram is taken to be positive for hardening and zero for perfectly plastic behavior.

In order to compare the preceding development further with that of [7], we let

$$\Lambda = \int_0^t \left(\frac{2}{3}\dot{\epsilon}^p_{ij}\dot{\epsilon}^p_{ij}\right)^{1/2} dt'. \tag{32}$$

Then, in view of (14) and $(21)_1$,

$$\dot{\Lambda} = \frac{\hat{g}}{D}\left(\frac{2}{3}\frac{\partial f}{\partial \sigma_{ij}}\frac{\partial f}{\partial \sigma_{ij}}\right)^{1/2} \tag{33}$$

during loading, and is zero otherwise. It is then clear that

$$L = \int_0^t \left(\frac{\dfrac{\partial g}{\partial \epsilon_{ij}}\dfrac{\partial g}{\partial \epsilon_{ij}}}{\dfrac{\partial f}{\partial \sigma_{kl}}\dfrac{\partial f}{\partial \sigma_{kl}}}\right)^{1/2}\dot{\Lambda}\,dt' = \int_0^\Lambda \left(\frac{\dfrac{\partial g}{\partial \epsilon_{ij}}\dfrac{\partial g}{\partial \epsilon_{ij}}}{\dfrac{\partial f}{\partial \sigma_{kl}}\dfrac{\partial f}{\partial \sigma_{kl}}}\right)^{1/2} d\Lambda', \tag{34}$$

where Λ' is the value of Λ at $t = t'$.

Thus, for a given deformation, L is a function $\tilde{L}$, say of Λ (and also Λ is a function of L)[7]. Therefore once the deformation is known, it becomes possible to construct a function $\hat{\Phi}$ as follows[8]:

$$f(\sigma_{ij},\epsilon^p_{ij},L) = f(\sigma_{ij},\epsilon^p_{ij},\tilde{L}(\Lambda)) = \hat{\Phi}(\sigma_{ij},\epsilon^p_{ij},\Lambda). \tag{35}$$

At fixed values of ϵ^p and L the loading surface in stress space coincides with that given by $\hat{\Phi} = 0$ at fixed values of ϵ^p and Λ. Also,

$$\frac{\partial \hat{\Phi}}{\partial \sigma_{ij}} = \frac{\partial f}{\partial \sigma_{ij}}, \quad \frac{\partial \hat{\Phi}}{\partial \sigma_{ij}}\dot{\sigma}_{ij} = \hat{f},$$
$$\frac{\partial \hat{\Phi}}{\partial \epsilon^p_{ij}} = \frac{\partial f}{\partial \epsilon^p_{ij}}, \quad \frac{\partial \hat{\Phi}}{\partial \Lambda} = \frac{\partial f}{\partial L}\left(\frac{\dfrac{\partial g}{\partial \epsilon_{ij}}\dfrac{\partial g}{\partial \epsilon_{ij}}}{\dfrac{\partial f}{\partial \sigma_{kl}}\dfrac{\partial f}{\partial \sigma_{kl}}}\right)^{1/2}, \tag{36}$$
$$\frac{\partial \hat{\Phi}}{\partial \Lambda}\dot{\Lambda} = \frac{\partial f}{\partial L}\dot{L},$$

where (35), (20), and (34) have been used. With the help of $(36)_{1,3,4}$, the expression (26) may be written as

$$\Delta = -\frac{\partial \hat{\Phi}}{\partial \epsilon^p_{ij}}\frac{\partial \hat{\Phi}}{\partial \sigma_{ij}} - \frac{\partial \hat{\Phi}}{\partial \Lambda}\left(\frac{2}{3}\frac{\partial \hat{\Phi}}{\partial \sigma_{ij}}\frac{\partial \hat{\Phi}}{\partial \sigma_{ij}}\right)^{1/2}, \tag{37}$$

which conforms with the definition used in [7].

We also observe that $\dot{\Lambda}$ may be expressed as

$$\dot{\Lambda} = l'_{ij}\dot{\epsilon}^p_{ij} \tag{38}$$

with

$$l'_{ij} = \frac{\dfrac{\partial f}{\partial \sigma_{ij}}}{\left(\dfrac{3}{2}\dfrac{\partial f}{\partial \sigma_{kl}}\dfrac{\partial f}{\partial \sigma_{kl}}\right)^{1/2}}, \tag{39}$$

where $(21)_1$ and (33) have been used. In view of $(21)_3$ and (39)

$$l_{ij} = \left(\frac{\dfrac{\partial g}{\partial \epsilon_{ij}}\dfrac{\partial g}{\partial \epsilon_{ij}}}{\dfrac{\partial f}{\partial \sigma_{kl}}\dfrac{\partial f}{\partial \sigma_{kl}}}\right)^{1/2} l'_{ij}. \tag{40}$$

3 A More General Class of Constitutive Equations

In this section we discuss how the constitutive equations of Section 2 can be obtained as a special case of those employed in [1, 6].[9] It is assumed that the stress response is given by the constitutive equation

$$\sigma_{ij} = \hat{\sigma}_{ij}(\mathfrak{U}), \quad \mathfrak{U} = \{\epsilon_{ij},\epsilon^p_{ij},\kappa\} \tag{41}$$

and that at fixed values of ϵ^p and the work-hardening parameter κ, $(41)_1$ possesses an inverse of the form

$$\epsilon_{ij} = \hat{\epsilon}_{ij}(\mathfrak{V}), \quad \mathfrak{V} = \{\sigma_{ij},\epsilon^p_{ij},\kappa\}. \tag{42}$$

The loading function in strain space is $g(\mathfrak{U})$, with a

[7] For sufficiently special constitutive equations it is possible to express L as a constant multiplied by Λ [7].

[8] It is to be noted that the function f in (18) may be obtained from g *without* a knowledge of the deformation.

[9] The development in [1,6] is valid for finite deformations of elastic-plastic materials. Although we shall continue to use the notation of Section 2 in what follows, σ_{ij} will now stand for the components of the symmetric Piola-Kirchhoff stress tensor, and ϵ_{ij} will denote the components of the Lagrangian finite strain tensor.

Downloaded 02 May 2010 to 171.66.16.246. Redistribution subject to ASME license or copyright; see http://www.asme.org/terms/Terms_Use.cfm

corresponding loading function $f(\mathcal{V})$ in stress space. The constitutive equations for $\dot{\epsilon}^p_{ij}$ are the same as in (14) except that

$$\dot{\epsilon}^p_{ij} = \lambda \hat{g} \rho_{ij} \quad \text{if} \quad g = 0 \quad \text{and} \quad \hat{g} > 0, \tag{43}$$

where λ and $\boldsymbol{\rho}$ are, respectively, a positive scalar-valued function and a nonzero symmetric tensor-valued function of $\mathcal{U}$. The function κ is also assumed to satisfy a rate-type constitutive equation, namely

$$\dot{\kappa} = \mathcal{C}_{ij} \dot{\epsilon}^p_{ij}, \tag{44}$$

where $\mathcal{C}$ is a symmetric tensor-valued function of $\mathcal{U}$. The consistency condition leads to [6, equation (16)]:

$$1 + \lambda \rho_{ij} \left(\frac{\partial g}{\partial \epsilon^p_{ij}} + \frac{\partial g}{\partial \kappa} \mathcal{C}_{ij} \right) = 0 \tag{45}$$

and the quotient $\hat{f}/\hat{g}$ may be written as[10] [6, equations (22) and (24)]:

$$\begin{aligned} \hat{f}/\hat{g} &= 1 + \lambda \rho_{ij} \left\{ \left(\frac{\partial g}{\partial \epsilon^p_{ij}} - \frac{\partial f}{\partial \epsilon^p_{ij}} \right) + \left(\frac{\partial g}{\partial \kappa} - \frac{\partial f}{\partial \kappa} \right) \mathcal{C}_{ij} \right\} \\ &= 1 + \lambda \rho_{ij} \frac{\partial f}{\partial \sigma_{kl}} \left\{ \frac{\partial \hat{\sigma}_{kl}}{\partial \epsilon^p_{ij}} + \frac{\partial \hat{\sigma}_{kl}}{\partial \kappa} \mathcal{C}_{ij} \right\} \\ &= -\lambda \rho_{ij} \left\{ \frac{\partial f}{\partial \epsilon^p_{ij}} + \frac{\partial f}{\partial \kappa} \mathcal{C}_{ij} \right\}. \end{aligned} \tag{46}$$

The work assumption of Naghdi and Trapp [3,4] states that the external work done on an elastic-plastic body in any smooth homogeneous cycle of deformation is non-negative, and implies that

$$\left\{ \frac{\partial \hat{\sigma}_{kl}}{\partial \epsilon^p_{ij}} + \frac{\partial \hat{\sigma}_{kl}}{\partial \kappa} \mathcal{C}_{ij} \right\} \rho_{ij} = -\gamma^* \frac{\partial g}{\partial \epsilon_{kl}}, \tag{47}$$

where γ^* is a non-negative function of $\mathcal{U}$. It then follows from $(46)_2$, (47), and (24) that

$$\frac{\hat{f}}{\hat{g}} = 1 - \lambda \gamma^* \Xi. \tag{48}$$

We now reexamine the constitutive equations of Section 2 in the light of the results listed in the present section. Equation (1) is a special case of $(41)_1$ with[11]

$$\frac{\partial \hat{\sigma}_{ij}}{\partial \epsilon_{kl}} = -\frac{\partial \hat{\sigma}_{ij}}{\partial \epsilon^p_{kl}} = c_{ijkl}, \quad \frac{\partial \hat{\sigma}_{ij}}{\partial \kappa} = 0. \tag{49}$$

Also, equation (2) is a special case of $(42)_1$ and

$$\frac{\partial \hat{\epsilon}_{ij}}{\partial \sigma_{kl}} = \kappa_{ijkl}. \tag{50}$$

Comparing (44) and (16), we may identify[12] κ with L of Section 2 and $\mathcal{C}_{ij}$ with l_{ij}. In addition to the relations $(19)_{1,2,3}$, in view of $(49)_2$ we now also have $\partial g/\partial \kappa = \partial f/\partial \kappa$ or $(19)_4$. Further, from (49), (47), (3), and $(19)_2$, we obtain[13]

$$\rho_{ij} = \gamma^* \frac{\partial f}{\partial \sigma_{ij}}, \tag{51}$$

where the symmetry condition $\kappa_{ijkl} = \kappa_{klij}$ has also been invoked. Since $\boldsymbol{\rho} \neq 0$, γ^* must be positive. The flow rule (43) now becomes

$$\dot{\epsilon}^p_{ij} = \lambda \gamma^* \hat{g} \frac{\partial f}{\partial \sigma_{ij}}, \tag{52}$$

so that the plastic strain rate is normal to the yield surface in stress space. Comparing (52) and $(21)_1$, we find that

$$D = \frac{1}{\lambda \gamma^*}. \tag{53}$$

It is then readily seen that (48) reduces to (23*b*), $(46)_1$ reduces to $(23a)_1$, and $(46)_2$ reduces to (23*b*). Furthermore, with the help of (51), $(21)_3$, (26), and (53), $(46)_3$ reduces to (27) and $(28)_2$.

Finally, it can be shown that for the special stress response (1), the work inequality of Naghdi and Trapp implies that both the yield surface in stress space and the yield surface in strain space are convex [4, Section 4].

Acknowledgment

The work of one of us (J.C.) was supported by Grant RC-A-79-1C from the Engineering Foundation to the University of Houston and that of the other (P.M.N.) was supported by te U.S. Office of Naval Research under Contract N00014-75-C-0148, Project NR 064-436, with the University of California, Berkeley.

References

1 Naghdi, P. M., and Trapp, J. A., "The Significance of Formulating Plasticity Theory With Reference to Loading Surfaces in Strain Space," *Int. J. Eng. Sci.*, Vol. 13, 1975, pp. 785–797.

2 Naghdi, P. M., "Some Constitutive Restrictions in Plasticity," *Proc. Symp. on Constitutive Equations in Viscoplasticity: Computational and Engineering Aspects*, AMD Vol. 20, ASME, 1976, pp. 79–93.

3 Naghdi, P. M., and Trapp, J. A., "Restrictions on Constitutive Equations of Finitely Deformed Elastic-Plastic Materials," *Quart. J. Mech. Appl. Math.*, Vol. 28, 1975, pp. 25–46.

4 Naghdi, P. M., and Trapp, J. A., "On the Nature of Normality of Plastic Strain Rate and Convexity of Yield Surfaces in Plasticity," ASME JOURNAL OF APPLIED MECHANICS, Vol. 42, 1975, pp. 61–66.

5 Caulk, D. A., and Naghdi, P. M., "On the Hardening Response in Small Deformation of Metals," ASME JOURNAL OF APPLIED MECHANICS, Vol. 45, 1978, pp. 755–764.

6 Casey, J., and Naghdi, P. M., "On the Characterization of Strain-Hardening in Plasticity," ASME JOURNAL OF APPLIED MECHANICS, Vol. 48, 1981, pp 285–296.

7 Yoder, P. J., and Iwan, W. D., "On the Formulation of Strain-Space Plasticity With Multiple Loading Surfaces," ASME JOURNAL OF APPLIED MECHANICS, Vol. 48, 1981, pp. 773–778.

8 Casey, J., and Naghdi, P. M., Discussion of ref. [7], ASME JOURNAL OF APPLIED MECHANICS, Vol. 49, 1982, pp. 460–461.

[10] Other forms of $\hat{f}/\hat{g}$ may also be found in [6].

[11] In the constitutive equation $(41)_1$, stress is a function of strain, plastic strain, and a work-hardening parameter. Yoder and Iwan [7, p. 774] remark that Naghdi "did not pursue the possibility of expressing stress as a functional of strain . . . ," an approach that they claim to discuss in [7]. We find no trace of a functional constitutive equation for stress in [7] and indeed, as we have shown, the constitutive equation actually utilized in [7] is a special case of $(41)_1$. We should perhaps point out, however, that once a plasticity problem is solved, the stress may appear as a functional of the strain history.

[12] Alternatively, κ may be identified with Λ and $\mathcal{C}_{ij}$ with l_{ij}. While the latter is perhaps a more natural choice, we shall adopt the other identification because of the appearnace of Lin (11).

[13] We may also obtain (51) from [6, equation (35)], but the present approach is slightly simpler for the constitutive equations being considered. See also [3, Section 5] and [4, Section 4].

Downloaded 02 May 2010 to 171.66.16.246. Redistribution subject to ASME license or copyright; see http://www.asme.org/terms/Terms_Use.cfm

Constitutive Equations for Damaging Materials[1]

D. Krajcinovic
Professor of Structural Engineering,
Department of Civil Engineering,
Mechanics, and Materials,
University of Illinois at Chicago,
Chicago, Ill. 60680
Mem. ASME

The paper focuses on the derivation of the constitutive law for a material containing flat, planar microcracks. The damage law is derived from the dissipation potential in conjunction with the orthogonality principle. The dissipation potential is shown to exist in the space of conjugate thermodynamic forces related to the stress intensity factors. Both brittle and ductile materials are considered within the framework of the small deformation theory and the time-independent processes.

1 Introduction

The energy imparted to a solid by a slowly changing (static) loading in an isothermal process is either stored as an elastic strain energy or dissipated through one of the several mechanisms of microstructural rearrangement. The mode of the energy dissipation has a strong qualitative and quantitative influence on the material response. Various theories of the Continuum Mechanics were established to describe different types of the material behavior governed by a specific dissipation mechanism. The conventional theory of plasticity focuses, for example, on the establishment of a rational macromodel describing the material behavior associated with the propagation of dislocations through the crystalline structure. The nucleation and growth of microvoids and their ultimate coalescence into macrovoids is, however, a distinctly different mechanism through which the imparted energy dissipates. In view of the physical difference existing between the two processes (propagation of dislocations versus the evolution of microdefects), the limited success of the plasticity theory in describing the combined phenomenon is hardly surprising.

The simplifying assumption that the response of the material depends only on the current pattern of structural arrangement allows formulation of reasonably simple analytical models. A rational description of the two distinctly different dissipation mechanisms, i. e., contrasting modes of the microstructural change, obviously requires the introduction of two sets of internal (hidden) variables:

variables reflecting the structural changes associated with the propagation of line defects (typically some functions of the plastic strains), and

variables characterizing the evolution of microdefects or microcracks (damage or material degradation).

This has been first realized by Kachanov [1] who introduced a separate variable defining the integrity of the material locally measured by means of void density in a cross section. The ensuing development of the Continuous Damage Mechanics has been too rapid to allow for a reasonably comprehensive review in this paper. A short summary of some of the proposed models can be found in [2].

In general, the transition from a model describing an event in one of the many sites on the microscale to a typical engineering representation on the macroscale involves some kind of an averaging procedure (see Rice [3]). Such a model has in fact been formulated by Seaman, Shockey, and Curran [4] in the form of a series of powerful computer codes. Yet to quote from Rice [3], "the use of averaging procedures that involve, even with substantial approximations, a direct calculation from microscale models entails substantial complexity, and this would seem overwhelming if required in each increment of deformation of each element of, say, a finite element formulation for some structural problem involving inhomogeneous deformation."

The alternate approach, typical of conventional continuum theories, involves formulation of a phenomenological model based on variables characterizing structural changes in an average sense. For example, as shown by Kroner [5], it is possible to predict the plastic response of a ductile body using a proper set of internal variables describing the dislocation distribution in a statistical sense.

The proposed formulation of the theory presents further development of the model derived in [2]. First, it extends the theory to ductile materials. Second, it introduces considerable improvements into the original formulation for the brittle materials. The derivation of the flow potential directly from the dissipation power density is a major improvement of the model derived in [2] for the following reasons:

it renders unnecessary any assumptions regarding the existence of potentials in spaces of other variables;

it identifies the correct conjugate thermodynamic force which is related to the stress intensity factors from Fracture Mechanics (mindful of the role of the stress intensity factors, this point alone may have a far reaching con-

[1] The work on this paper was sponsored by a grant from the National Science Foundation.

Contributed by the Applied Mechanics Division for presentation at the 1983 ASME Applied Mechanics, Bioengineering, and Fluids Engineering Conference, Houston, Texas, June 20-22, 1983 of THE AMERICAN SOCIETY OF MECHANICAL ENGINEERING.

Discussion on this paper should be addressed to the Editorial Department ASME, United Engineering Center, 345 East 47th Street, New York, N.Y. 10017, and will be accepted until two months after final publication of the paper itself in the JOURNAL OF APPLIED MECHANICS. Manuscript received by ASME Applied Mechanics Division, January, 1982. Paper No. 83-APM-12.

Copies will be available until February, 1984.

Copyright © 1983 by ASME
Downloaded 02 May 2010 to 171.66.16.246. Redistribution subject to ASME license or copyright; see http://www.asme.org/terms/Terms_Use.cfm

sequence in the establishment of proper, experimentally verifiable, damage laws);

it identifies convexity and normality as inherent properties of the flow potential.

It is equally obvious that any other choice of the thermodynamic force would render the extension of the theory to more complex materials highly arbitrary. Therefore, it is felt that the present formulation is both an extension and improvement (in mathematical rigor and essence alike) of the model derived in [2].

2 Damage Variable

From a purely geometrical standpoint, it is possible to classify the microdefects of the crystalline structure into three large groups:

line defects (or dislocations),

sharp, almost planar cracks emanating from triple points or second phase inclusions, and

spheroidal voids (cavities) typically found along the grain boundaries.

The first class of defects characterizes the response of ductile materials and is studied using the methods of the Theory of Plasticity.

The phenomenological models describing the gradual evolution of planar microdefects and the cavitation of spheroidal microvoids belong to a branch of the Continuum Mechanics commonly known as the Continuous Damage Theory. In view of geometrical and metallurgical differences existing between microdefects of the two latter groups, it is unrealistic to expect that they can be described by a single internal (damage) variable. From a purely geometrical standpoint, it makes sense to describe the damage in the form of spheroidal microcavities by a scalar variable (Davison, Stevens, and Kipp [6]) and to use a vector function (Davison and Stevens [7], Kachanov [8], or Krajcinovic and Fonseka [2, 9]) to characterize the damage consisting of multiple planar microcracks.

Another possibility is to ignore the physical nature of the problem and describe the damage indirectly through the effect it has on the strains (Doughill [10], Bazant and Kim [11], or Nicholson [12]). While there is certainly nothing wrong with an artifice of this type, the loss of the physical insight into the phenomenon can hardly be helpful in the process of the material parameter identification.

In an effort to establish a simple and practical analytical model, further discussion will be restricted to the small displacement gradient theory of solids characterized by the material properties that change with the development of line and planar microdefects. The thermodynamics with the internal state variables presents a suitable framework for the development of the constitutive equations for materials depending only on the current pattern of structural arrangement.

To describe the two distinctly different processes of crystalline change, it is necessary to introduce two sets of internal parameters:

- α reflecting the state of plastic deformation, and
- ω characterizing the level of the microvoid evolution locally.

The exhaustive literature dealing with the theory of plastic flow renders unnecessary any further discussion on the relation existing between the set of the internal variable α and the plastic strains (see, for example, [3, 5]).

As originally suggested by Kachanov [1] the area density of voids (and other decohesions) in a given cross section is, by all standards, an intuitively appealing characterization of the damage. Considering the shape of the voids to be of little significance (higher moments of the void distribution [5]), the damage can, therefore, be locally defined by a vector function

$$\omega_J(x_I,t)=\omega(x_I,t)N_J \tag{1}$$

where the scalar ω is the void density in a cross section defined by the normal N_J. Naturally, the orientation of the normal N_J to the void surface must be understood in the sense of an appropriate averaging process over a statistically significant sample.

3 Flow Potential

Concentrating on the derivation of the constitutive equations defining the internal variables in terms of the state variables, it is convenient to start with the Clausius-Duhem inequality which in the case of small deformation gradients reads

$$\sigma_{ij}\dot{\epsilon}_{ij}-\rho(\dot{\psi}+S\dot{T})-\frac{1}{T}\mathbf{q}\cdot\operatorname{grad}T\geq 0 \tag{2}$$

where σ_{ij} and ϵ_{ij} are the stress and strain tensor, ρ, ψ, S, T, and $\mathbf{q}$ the mass density (considered constant in the absence of cavities), Helmholtz free energy, entropy, temperature, and the heat flux vector, respectively.

Assume further that the strain tensor allows decomposition into elastic and plastic component

$$\boldsymbol{\epsilon}=\boldsymbol{\epsilon}^e+\boldsymbol{\epsilon}^p \tag{3}$$

Introduce the stress tensor

$$\boldsymbol{\sigma}=\rho\frac{\partial\psi}{\partial\boldsymbol{\epsilon}^e} \tag{4}$$

and the generalized thermodynamic forces

$$A_j=\rho\frac{\partial\psi}{\partial\alpha_j}\quad\text{and}\quad R_j=\rho\frac{\partial\psi}{\partial\omega_j} \tag{5}$$

The Clausius-Duhem inequality (2) can now be rewritten in the form of a scalar product representing the rate of the entropy production per unit volume

$$\rho\dot{D}\equiv\mathbf{X}\cdot\mathbf{J}\geq 0 \tag{6}$$

where the thermodynamic flux vector $\mathbf{J}$ and the vector of conjugate forces $\mathbf{X}$ are in the present case

$$\mathbf{X}=\rho\left\{\sigma_{ij},-A_j,-R_j,-\frac{1}{T}\operatorname{grad}T\right\} \tag{7}$$

$$\mathbf{J}=\left\{\dot{\epsilon}^p_{ij},\dot{\alpha}_j,\dot{\omega}_j,q_j\right\} \tag{8}$$

A comprehensive discussion of the postulates leading to (6) are available in the excellent "synthesis" paper by Kestin and Bataille [13].

In general, the constitutive equations are given in the form

$$\mathbf{J}=\mathbf{J}(\boldsymbol{\epsilon}^e,\ T,\ \operatorname{grad}T,\ X_I) \tag{9}$$

However, in the neighborhood of the equilibrium state, the general constitutive equations can be linearized (see, for example, Malvern [14]) and cast into a form

$$J_m=L_{mk}X_k \tag{10}$$

or reciprocally

$$X_k=l_{mk}J_m \tag{11}$$

(see again the lucid discussion by Kestin and Bataille [13] or Moreau [15]). In absence of the nondissipative term, the matrices L_{mk} and l_{mk} are symmetric. Hence from (6) and (10)

$$\rho\dot{D}=L_{mk}X_mX_k=l_{mk}J_mJ_k\geq 0 \tag{12}$$

Introducing the dissipative (flow) potential F

Downloaded 02 May 2010 to 171.66.16.246. Redistribution subject to ASME license or copyright; see http://www.asme.org/terms/Terms_Use.cfm

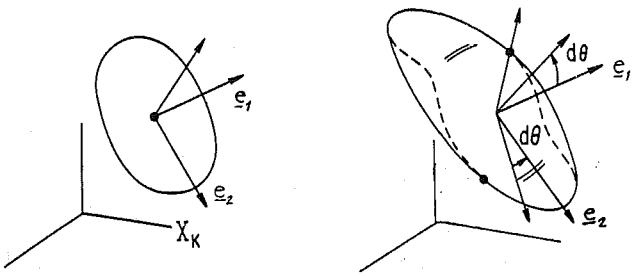

Fig. 1 A planar void at two successive instants of a loading process

$$F = \tfrac{1}{2}\rho\dot{D} = \tfrac{1}{2}L_{mk}X_mX_k \tag{13}$$

the flux vector **J** can be written as

$$J_m = \frac{\partial F}{\partial X_m} \tag{14}$$

A somewhat different discussion of the normality structure (14) of the flow potential is due to Rice [3] who demonstrated that a sufficient condition for the existence of the potential $F(\epsilon^e, \mathbf{X}, T)$ is that the rate of change of each component of the flux vector depends only on its conjugate force, i.e., that

$$J_m = f(X_m, T, H)$$

where H denotes the current state of the microstructural arrangement. The property of the orthogonality of the flux vector **J** (defining the rate of damage and plastic flow change) to the surface of the constant entropy production was also used by Halphen and Son [16], Sidoroff [17], and others.

In certain applications it is convenient to define the dual potential $F^*(\epsilon^e, \mathbf{J}, T)$ such that

$$X_m = \frac{\partial F^*}{\partial J_m} \tag{15}$$

where F^* is a Fenchel transform of F.

The benefits of the proposed procedure are quite obvious. Instead of an attempt to establish a separate damage law for every damage variable it is necessary to define only a single potential F under requirements described by Moreau [15]. In addition, the damage theory established in such a way is at least formally similar to the theory of plasticity.

4 Brittle Materials

The perfectly brittle materials characterized by the total absence of the plastic flow form the simplest class of all damaging materials. While all solids exhibit at least a modicum of ductility, the nonlinear aspects of the response of materials such as ceramics, gray iron, certain rocks, and even some high-strength concrete is dominated by microcracking. The brittleness is also emphasized by low temperature, high strain rates, second phase inclusions, etc.

A comprehensive theory of the mechanical behavior of the brittle solids gradually degraded by the evolution of flat, planar microdefects was formulated by Davison and Stevens [7]. Their model was subsequently modified by Krajcinovic and Fonseka [2] to a form including Kachanov's one-dimensional model as a special case. According to [2] the strain energy can be written in the form

$$\begin{aligned}\rho\psi = {} & \tfrac{1}{2}(\lambda+2\mu)\epsilon_{KK}\epsilon_{LL} - \mu(\epsilon_{KK}\epsilon_{LL} - \epsilon_{KL}\epsilon_{LK}) \\ & + C_1(\omega_P\omega_P)^{-1/2}\epsilon_{KL}\epsilon_{MM}\omega_K\omega_L \\ & + C_2(\omega_P\omega_P)^{-1/2}\epsilon_{KL}\epsilon_{LM}\omega_K\omega_M + C_3(\omega_P\omega_P)^{-3/2}(\omega_K\omega_L\epsilon_{KL})^2\end{aligned} \tag{16}$$

considering for simplicity only terms quadratic in strain and linear in damage variable and only a single damage system. In (16) $\lambda(T)$ and $\mu(T)$ are the Lame constants (which are functions of the damage in case of spheroidal cavities [6]). The two material parameters $\bar{C}_i(\omega, T) = C_i(T)(\omega_P\omega_P)^{-1/2}$ are selected in a form reducing (16) to the original Kachanov's model (obtained for vanishing Poisson's ratio ν).

The damage vector ω is defined locally by the void area density ω_0 in a plane defined by a normal $\mathbf{e}_1$

$$\omega = \omega_0\mathbf{e}_1 \tag{17}$$

where (1, 2, 3,) is the principal damage (void) coordinate system (such that $\mathbf{N} = \mathbf{e}_1$). Selecting the coordinate axes ("rotating" with the void, Fig. 1) such that the resolved shear is directed along $\mathbf{e}_2$, the void "rotates" about the axis $\mathbf{e}_3$. Hence the damage rate is

$$\dot{\omega} = \dot{\omega}_0\mathbf{e}_1 + \omega_0\dot{\mathbf{e}}_1 \tag{18}$$

For an infinitesimal rotation $\dot{\theta} << 1$ (see [2]) about $\mathbf{e}_3$ from (18)

$$\dot{\omega} = \dot{\omega}_0\mathbf{e}_1 + \omega_0\dot{\theta}\mathbf{e}_2 \tag{19}$$

From (4) and (16) the stress can be written in the form

$$\sigma_{IJ} = K_{IJKL}\epsilon_{KL} \tag{20}$$

where

$$\begin{aligned}K_{IJKL} = {} & \lambda\delta_{IJ}\delta_{KL} + 2\mu\delta_{IK}\delta_{JL} \\ & + C_1(\omega_P\omega_P)^{-1/2}(\delta_{IJ}\omega_K\omega_L + \delta_{KL}\omega_I\omega_J) \\ & + C_2(\omega_P\omega_P)^{-1/2}(\delta_{JK}\omega_I\omega_L + \delta_{IL}\omega_J\omega_K) \\ & + 2C_3(\omega_p\omega_p)^{-3/2}\omega_I\omega_J\omega_K\omega_L\end{aligned} \tag{21}$$

The thermodynamic force **R** conjugate to the damage variable ω is from

$$\begin{aligned}R_I = {} & 2C_1(\omega_p\omega_p)^{-1/2}\epsilon_{MM}\epsilon_{KI}\omega_K \\ & + 2C_2(\omega_p\omega_p)^{-1/2}\epsilon_{IL}\epsilon_{LK}\omega_K \\ & - (C_1\epsilon_{MM}\omega_L + C_2\epsilon_{LM}\omega_M)(\omega_p\omega_p)^{-3/2}\omega_I\omega_K\epsilon_{KL} \\ & + 4C_3(\omega_p\omega_p)^{-3/2}\epsilon_{IM}\epsilon_{KL}\omega_M\omega_K\omega_L \\ & - 3C_3(\omega_P\omega_P)^{-5/2}\omega_I(\omega_K\omega_L\epsilon_{KL})^2\end{aligned} \tag{22}$$

The simplest form for **R** and ω is obtained in the damage coordinate system (since $\epsilon_{13} = 0$ and $\omega_2 = \omega_3 = 0$ by definition). Thus from (22)

$$R_1 = C_1e\epsilon_{11} + C_2(\epsilon_{11}^2 + \epsilon_{12}^2) + C_3\epsilon_{11}^2 \tag{23}$$

and

$$R_2 = 2C_1e\epsilon_{12} + 2C_2(\epsilon_{11} + \epsilon_{22})\epsilon_{12} + 4C_3\epsilon_{11}\epsilon_{12} \tag{24}$$

where $e = \epsilon_{MM}$ is the volumetric strain. The dissipation power density is from (6) and (19)

$$\rho\dot{D} = R_1\dot{\omega}_0 + R_2\omega_0\dot{\theta} \geq 0 \tag{25}$$

The final step in establishing the analytical model consists of the formulation of the potential F (13) in terms of the generalized thermodynamic forces $\mathbf{R}$[2]. The dissipation power inequality (12) in conjunction with the linearization (10) requires that J_m (i.e., $\dot{\omega}_m$) is directed along the outward normal to the dissipation potential surface related to the surface of the constant dissipation power. The potential F can be shown to be convex with absolute minimum at $\mathbf{X} = 0$ [13]. Assuming that the function F has a continuous first derivative, equation (14) can be rewritten as

$$\dot{\omega}_I = \Lambda\frac{\partial F}{\partial R_I} \tag{26}$$

where the scalar-valued function $\Lambda \geq 0$ ensures that the damage rate is directed along the outward normal to the surface F.

[2] This is in sharp contrast to the model developed in references [2, 9, 10] where the potential F was arbitrarily defined in terms of strains or stresses.

Downloaded 02 May 2010 to 171.66.16.246. Redistribution subject to ASME license or copyright; see http://www.asme.org/terms/Terms_Use.cfm

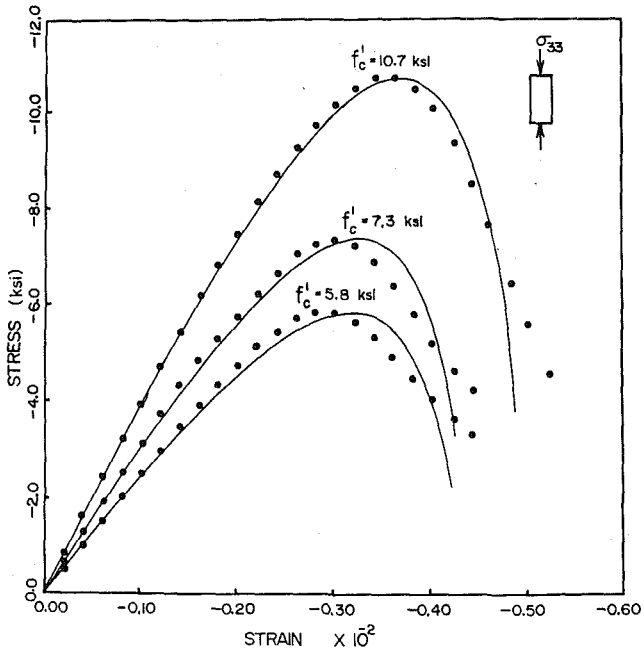

Fig. 2 Stress-strain curves of three concrete samples in uniaxial compression. Dots denote experimental results. The compressive cylinder strength is labeled f_c'.

The scalar-valued dissipation potenetial function $F(\epsilon^e, \mathbf{R}, T)$ should be determined on the basis of specific experimental data satisfying at the same time requirements of convexity and having the form (12). For example, for an isotropic damage surface

$$F = L_{mn} R_m R_n - R_0^2 \tag{27}$$

where $R_0(\omega, T)$ serves as the repository of the recorded history while L_{mn} are some functions of temperature it is trivial to show that

$$\dot{\omega}_m = 2\Lambda L_{mn} R_n \tag{28}$$

leading to

$$\rho \dot{D} = 2\Lambda L_{mn} R_m R_n \geq 0 \tag{29}$$

with

$$\Lambda = \frac{1}{2R_0} \Delta^{-1/2} (L_{22}\dot{\omega}_1^2 + L_{11}\dot{\omega}_2^2 - 2L_{12}\dot{\omega}_1\dot{\omega}_2)^{1/2} \tag{30}$$

where

$$\Delta = L_{11}L_{22} - L_{12}^2 > 0 \tag{31}$$

Thus the form (27) satisfies all necessary requirements. The non-negative value of the specific dissipation power is ensured by the proper selection of material parameters C_i in (21). The parameters L_{mn} and R_0 are determined from experimental results.

Taking the clue from the theory of plasticity (see Martin [18], Chapter 2) an especially convenient form of (26) may be derived assuming that the direction of $\dot{\omega}_m$ depends only on the current state $(\epsilon^e, \mathbf{R}, \omega, T)$ while the magnitude of $\dot{\omega}_m$ can depend on $\dot{R}_n$ as well, when

$$\dot{\omega}_m = G \frac{\partial F}{\partial R_m} \frac{\partial F}{\partial R_n} \dot{R}_n = \kappa f_{mn} \dot{R}_n \tag{32}$$

where $\kappa = 1$ if $F = 0$ and $(\partial F/\partial R_n)\dot{R}_n > 0$ (loading) or $\kappa = 0$ otherwise, while $G(\mathbf{R}, \omega, T)$ is a scalar-valued "softening" function.

An extremely close agreement (Fig. 2) between the experimental data reported in [9] and the numerical results computed on the basis of the developed theory can be obtained for three grades of the high-strength concrete using only three constants. While the absence of a complete set of measured data hinders the determination of the dissipation potential for a specific material, it is important to point out that the developed theory follows the experimentally observed major trends of the material response:

(*a*) In uniaxial tension ($\epsilon_{12} = 0$ and consequently $R_2 = 0$), the damage and ultimate fracture are perpendicular to the maximum tensile (axial) strain (see Dieter [19], Chapter 7).

(*b*) In uniaxial compression ($\epsilon_{12} = R_2 = 0$), the damage and ultimate fracture are again perpendicular to the maximum tensile (lateral) strain (so-called splitting of rocks, Jaeger and Cook [20], Chapter 4.5 and concrete Neville [21], Chapter 5).

(*c*) If a damage field is in pure shear (only $\epsilon_{12} \neq 0$), the microdefects will simultaneously grow ($R_1 \neq 0$, $\dot{\omega}_1 \neq 0$) and "rotate" ($R_2 \neq 0$, $\dot{\omega}_2 \neq 0$, or $\dot{\theta} \neq 0$) (as observed for macrocracks, see Broek [22], Chapter 3 or Jaeger and Cook [20], Chapter 10).

Once the dissipation potential function is determined, it is fairly straightforward to derive the stress-strain law on the basis of (23), (24), and (32). Using the Voight (vector) notation for the strain tensor from equations (23) and (24), it directly follows that

$$\dot{R}_i = g_{ij}\dot{\epsilon}_j \tag{33}$$

where lower case indices denote the damage coordinate system (1, 2, 3,). The strains ϵ_i in the damage coordinate system (1, 2, 3) are related to the strains ϵ_J in the structural coordinates system (x, y, z) through the well-known transformation (capital letters stand for x, y, z axes)

$$\epsilon_i = r_{iJ}\epsilon_J \tag{34}$$

where the components of the matrix r_{iJ} depend on the angle θ subtended by axes x_i and x_J. Since the angle θ changes, in general, during the process of the damage evolution, the strain increments are related through

$$\dot{\epsilon}_i = r_{iJ}\dot{\epsilon}_J + p_{ij}\dot{\omega}_j \tag{35}$$

since in view of (19) $\dot{\omega}_2 = \omega_0\dot{\theta}$. The four preceding formulas with

$$\dot{\omega}_i = n_{iJ}\dot{\omega}_J$$

combine into the damage law

$$\dot{\omega}_M = \kappa Q_{MN}\dot{\epsilon}_N \tag{36}$$

where

$$Q_{MN} = [(\delta_{in} - f_{ij}g_{jk}p_{kn})n_{nM}]^{-1}(f_{ir}g_{rs}r_{sN}) \tag{37}$$

Rewrite further (20) in the Voigt notation as

$$\sigma_I = K_{IJ}\epsilon_J \tag{38}$$

Since the elements of the matrix K_{IJ} depend on ω_I differentiation of (38) leads to

$$\dot{\sigma}_I = K_{IJ}\dot{\epsilon}_J + C_{IJ}\dot{\omega}_J \tag{39}$$

The final incremental stress-strain relationship is obtained combining (36) and (39)

$$\dot{\sigma}_I = D_{IJ}\dot{\epsilon}_J \tag{40}$$

where the "stiffness" of the deteriorating material is given by

$$D_{IJ} = K_{IJ} + \kappa Q_{IM}C_{MJ} \tag{41}$$

It is important to notice that D_{IJ} is not identical for two different unloading paths since K_{IJ} depends on the already accumulated damage. This is, naturally, in sharp contrast to the results of the conventional plasticity theory. This response typical of brittle materials was experimentally measured for rocks [20] and concrete [9, 11].

Downloaded 02 May 2010 to 171.66.16.246. Redistribution subject to ASME license or copyright; see http://www.asme.org/terms/Terms_Use.cfm

5 General Materials

The X-ray diffraction studies of fracture surface provide a conclusive proof that at least some plastic deformation precedes even the "completely brittle" failure mode of metals (Dieter [19], Chapter 7). The microdefects "initially propagate along the slip plane but eventually switch to the plane normal to the tension axis" (Low [23], p. 201). Hence the grain boundary sliding has "a prominent role in promoting the formation and growth of intercrystalline cracks and voids" (Garofalo [24], p. 95). In fact, some authors like Conrad [25] go even further and claim that " . . .no voids (are) *formed* when the (grain) boundary was perpendicular to the stress axis but voids always formed when shear traction was applied parallel to the boundary."

These observations indicate that the gradual degradation of the material occurs as a result of a complex interaction of two dissipative mechanisms (so-called plastic flow and microcracking). The cracking apparently commences in the planes of maximum shears after some plastic deformation takes place. Analytically, the presence of two different dissipative mechanisms and two sets of different internal variables complicates the problem to a significant degree. Two of the most important steps consist of the establishment of the proper forms for the Helmholtz free energy $\psi(\epsilon^e, \alpha, \omega, T)$ and the dissipation potential $F(\mathbf{X}, T)$. Separation of the free energy function is, for example, a popular simplification (see Davison, Steven, Kipp [6], Halphen, Son [16], Chaboche [26], etc.) which is, to a degree, based on a rational argument. Despite numerous attempts, the determination of the free energy function on the basis of the microscale models remains an elusive goal (see Rice [3]). Thus a phenomenological model, based on the present experience and some general speculations (like in Chaboche [26]) offers, at the present time, the best hope for the success.

The dissipation potential is a scalar-valued function of the generalized thermodynamic forces which in two extremal cases of the ideally ductile and perfectly brittle materials reduces to the yield function and the damage function $F(\mathbf{R}, T)$ (given, for example, by equation (27)) correspondingly. The simplest alternative would be a form combining these two extreme cases, i.e.,

$$F = \alpha F^D(A_j, \alpha_j, T) + \beta F^B(X_j, \omega_j, T) \tag{42}$$

For an ideally ductile material $\beta(\dot{\epsilon}, T) = 0$, while for perfectly brittle material $\alpha(\dot{\epsilon}, T) = 0$. Introduction of a brittleness index

$$d = \frac{\alpha + \beta}{\alpha - \beta} \tag{43}$$

offers an attractive way to measure brittleness on the scale $(-1;1)$. For the present purposes, F^B can be taken in any form satisfying the condition (13). The choice of the yield condition F^D is, in view of the existing literature, even wider. The separable form (42) for the dissipation potential is quite obviously the simplest choice available. There is some doubt, though, whether this form would allow for rational analytical modeling of the fatigue process.

Using again the Voigt notation for the stresses and strains, the generalized force and flux vectors are:

$$\mathrm{X}_i = \{\sigma_i, -A_i, -R_i\}^* \tag{44}$$

$$\dot{a}_j^d = \{\dot{\epsilon}_i^p, -\dot{\alpha}_i, -\dot{\omega}_i\}^* = J_i \tag{45}$$

where $\dot{\epsilon}_i^p$ are plastic strain rates while the asterisk denotes transposition.

From the normality property (14)

$$\dot{a}_j^d = \kappa G \frac{\partial F}{\partial X_j} \frac{\partial F}{\partial X_m} \dot{X}_m = \kappa f_{mj} \dot{X}_m \tag{46}$$

where

$$\kappa = 1 \quad \text{if} \quad F = 0 \quad \text{and} \quad \frac{\partial F}{\partial X_m} \dot{X}_m > 0 \quad \text{(loading)}$$

$$\kappa = 0 \quad \text{otherwise} \quad \text{(unloading)}$$

while $G(J_m, \dot{a}_m^d, T)$ is a scalar-valued "hardening/softening" function to be determined from experiments.

The remaining procedure is more cumbersome but formally similar as for the brittle materials. From the Helmholtz free energy function, quadratic in strains and linear in the damage variable, from (4) and (5) it follows (all in structural coordinates system)

$$\dot{X}_i = g_{ij} \dot{a}_j^e = g_{ij}(\dot{e}_j - \dot{a}_j^d) \tag{47}$$

where

$$\dot{a}_j^e = \{\dot{\epsilon}_j^e, \dot{\alpha}_j, \dot{\omega}_j\}^* \tag{48}$$

and

$$\dot{e}_j = \{\dot{\epsilon}_j, 0, 0\}^* \tag{49}$$

A combination of (46) and (47) leads to the damage law for the damaging material

$$\dot{a}_m^d = k_{mn} \dot{\epsilon}_n \tag{50}$$

where

$$k_{ij} = (\delta_{im} - \kappa g_{in} f_{nm})^{-1} g_{mj} \tag{51}$$

From (4)

$$\sigma_m = K_{mn} \epsilon_n^e \tag{52}$$

Differentiating (52) it further follows

$$\dot{\sigma}_m = K_{mn} \dot{\epsilon}_n^e + \bar{K}_{mn} \dot{a}_n^d \tag{53}$$

After some obvious manipulations

$$(\delta_{mr} + \kappa K_{mn} f_{nr}) \dot{\sigma}_r = K_{mn} \dot{\epsilon}_n + \bar{K}_{mn} \dot{a}_n^d \tag{54}$$

where

$$f_{nr} = \frac{\partial F}{\partial \sigma_n} \frac{\partial F}{\partial \sigma_r} \tag{55}$$

The final form of the incremental stress-strain law is derived substituting (50) into (54)

$$\dot{\sigma}_r = (\delta_{mr} + \kappa K_{mn} f_{nr})^{-1} (K_{mn} + \bar{K}_{mp} k_{pn}) \dot{\epsilon}_n \tag{56}$$

or simply

$$\dot{\sigma}_r = D_{rn} \dot{\epsilon}_n \tag{57}$$

6 Summary and Conclusions

The proposed analytical model offers a rational and systematic establishment of constitutive equations for a material undergoing irreversible changes of its crystalline structure under loading. The model is a generalization of the familiar Kachanov's one-dimensional theory which proved to be very successful in many diverse applications.

In contrast to previously developed models (references [2, 7, 8, 10] etc.), the one formulated here has a more rigorous structure avoiding several unnecessary and possibly incorrect assumptions. The "damage law" is derived directly from the "normal dissipative mechanism" [13] in conjunction with the orthogonality property. Consequently, the damage variable is directly related to its conjugate thermodynamic force rather than an arbitrary state variable.

The number of material parameters is reduced to a minimum. Moreover, the intuitively appealing and experimentally verifiable measure of damage along with the rigorous formulation of the kinematics of the damage evolution should be of great help in the process of the identification of these material parameters. Finally, the present formulation establishes a link between the Continuous Damage Theory on one side and the Fracture Mechanics [2, 27] and the Statistical Strength Theories [28] on the other side.

Downloaded 02 May 2010 to 171.66.16.246. Redistribution subject to ASME license or copyright; see http://www.asme.org/terms/Terms_Use.cfm

References

1 Kachanov, L. M., "On the Creep Fracture Time," *Izv. AN SSSR, Ofd. Tekhn. Nauk.*, No. 8, 1958, pp. 26-31 (in Russian).

2 Krajcinovic, D., and Fonseka, G. U., "The Continuous Damage Theory of Brittle Materials—Part I: General Theory," ASME JOURNAL OF APPLIED MECHANICS, Vol. 48, 1981, pp. 809-815.

3 Rice, J. R., "Continuum Mechanics and Thermodynamics of Plasticity in Relation to Microscale Deformation Mechanisms," in *Constitutive Equations in Plasticity*, Argon, A. S., ed., The MIT Press, Cambridge, Mass., 1975.

4 Seaman, L., Curran, D. R., and Shockey, D. A., "Computational Models for Ductile and Brittle Fracture," *J. Appl. Phys.*, Vol. 47, 1976, pp. 4814-4826.

5 Kröner, E., "Dislocation: A New Concept in the Continuum Theory of Plasticity," *J. Math. and Physics*, Vol. 42, 1962, pp. 27-37.

6 Davison, L., Stevens, A. L., and Kipp, M. E., "Theory of Spall Damage Accumulation in Ductile Metals," *J. Mech. Phys. Solids*, Vol. 25, 1977, pp. 11-28.

7 Davison, L., and Stevens, A. L., "Thermomechanical Constitution of Spalling Elastic Bodies," *J. Appl. Phys.*, Vol. 44, 1973, pp. 667-674.

8 Kachanov, L. M., "Creep and Fracture at Complex Loading," *Problem Prochnosti*, 1977, No. 6, pp. 3-5 (in Russian).

9 Fonseka, G. U., and Krajcinovic, D., "The Continuous Damage Theory of Brittle Materials—Part II: Uniaxial and Plane Response Modes," ASME JOURNAL OF APPLIED MECHANICS, Vol. 48, 1981, pp. 816-824.

10 Dougill, J. W., "Some Remarks on the Path Independence in the Small in Plasticity," *Quart. Appl. Math.*, Vol. 33, 1975, pp. 233-243.

11 Bazant, Z. P., and Kim, S. S., "Plastic Fracturing Theory for Concrete," *J. Eng. Mech. Div.*, ASCE, Vol. 105, 1979, pp. 429-446.

12 Nicholson, D. W., "Constitutive Model for Rapidly Damaged Structural Materials," *Acta Mechanics*, Vol. 39, 1981, pp. 195-205.

13 Kestin, J., and Bataille, J., "Irreversible Thermodynamics of Continua and Internal Variables," in *Continuum Models of Discrete Systems*, Provan, J. W., ed., Study No. 12, Univ. of Waterloo Press, 1978.

14 Malvern, L. E., *Introduction to the Mechanics of a Continuous Medium*, Prentice-Hall, Englewood Cliffs, N.J., 1969.

15 Moreau, J. J., "Sur les Lois de Frottement, de Plasticite et de Viscosite," *C. R. Acad. Sc. Paris*, Vol. 271, Ser. *A*, 1970, pp. 608-611.

16 Halphen, B., and Son Nguyen Quoc, "Sur les Materiaux Standards Généralises," *J. de Mécanique*, Vol. 14, 1975, pp. 39-63.

17 Sidoroff, F., "Variables Internes en Viscoelasticite," *J de Mecanique*, Vol. 14, 1975, pp. 545-566.

18 Martin, J. B., *Plasticity: Fundamentals and General Results*, The MIT Press, Cambridge, Mass., 1975.

19 Dieter, G. E., *Mechanical Metallurgy*, 2nd ed., McGraw-Hill, New York 1976.

20 Jaeger, J. C., and Cook, N. G. W., *Fundamentals of Rock Mechanics*, 3rd Ed., Chapman and Hall, 1979.

21 Neville, A. M., *Properties of Concrete*, Wiley, New York, 1963.

22 Broek, D., *Elementary Engineering Fracture Mechanics*, Sijthoff and Noordhoff, 1978.

23 Low, J. R., Jr., "Microstructural Aspects of Fracture," in *Fracture of Solids*, Drucker, D. C., and Gilman, J. J., eds., Metallurgical Soc. Conf., Vol. 20, Interscience, 1963.

24 Garofalo, F., "Ductility in Creep," Chapter 4 in *Ductility*, Amer. Soc. for Metals, Metals Park, Ohio, 1968.

25 Conrad, H., "The Role of Grain Boundaries in Creep and Stress Rupture," in *Mechanical Behavior of Materials at Elevated Temperatures*, Dorn, J. E., ed., McGraw-Hill, New York, 1961.

26 Chaboche, J. L., "Description Thermodynamique et Phenomenologique de la Viscoplasticite Cyclique Avec Endommangement," *ONERA*, No. 1978-3, 1978.

27 Janson, J., and Hult, J., "Fracture Mechanics and Damage Mechanics a Combined Approach," *J. de Mecanique Applique*, Vol. 1, No. 1, 1977, pp. 69-84.

28 Krajcinovic, D., and Silva, M. A. G., "Statistical Aspects of the Continuous Damage Theory," *Int. J. Solids Structures*, Vol. 18, 1982, pp. 551-562.

29 Krajcinovic, D., "A Distributed Damage Theory of Beams in Pure Bending," ASME JOURNAL OF APPLIED MECHANICS, Vol. 46, 1979, pp. 592-596.

APPENDIX

One-Dimensional Model

The derivation of the original Kachanov's model [1] from the developed general theory is in itself a fairly trivial exercise. However, in view of the numerical results presented in references [2, 9, 28, 29], such an exercise proves to be very useful for the determination of the introduced material parameters (at least in terms of the order of magnitude).

From (21) with $\nu = 0$, $\epsilon_{11} = \epsilon$, $\sigma_{11} = \sigma$, and all other ϵ_{ij}, $\sigma_{ij} = 0$ $(i \neq j \neq 1)$, it directly follows that

$$\sigma = E(1 - D\omega)\epsilon \tag{A.1}$$

where

$$D = -2\frac{C_1 + C_2}{E} \tag{A.2}$$

Also from (23) and (24)

$$R_1 = (C_1 + C_2)\epsilon^2 = -\tfrac{1}{2}ED\epsilon^2 < 0, \quad R_2 = 0 \tag{A.3}$$

which satisfies the Clausius-Duhem inequality (2) if $(C_1 + C_2) < 0$. Furthermore, if the dissipation potential is simply

$$F = R_1^2 - R_0^2 \tag{A.4}$$

where $R_0 = R_0(\omega) = k\omega^n$ with n being a positive integer, the consistency equation $dF \equiv 0$ leads to a simple relation

$$\tfrac{1}{2}(ED)^2\epsilon^3 d\epsilon = \alpha k^2 \omega^{2\alpha - 1} d\omega \tag{A.5}$$

The model proposed in [28] for a general case and [29] for concrete is obtained directly by putting

$$D = 1, \quad \alpha = 2 \quad \text{and} \quad k = 8\sigma_F^2/E \tag{A.6}$$

where σ_F is the tensile rupture strength. Since the Poisson's ratio is not actually equal to zero, the values for the material constants as obtained in (A.6) are only approximate.

Downloaded 02 May 2010 to 171.66.16.246. Redistribution subject to ASME license or copyright; see http://www.asme.org/terms/Terms_Use.cfm

Inversion of Creep Response for Retardation Spectra and Dynamic Viscoelastic Functions

L. Thigpen

G. W. Hedstrom

B. P. Bonner

Members of Technical Staff,
Lawrence Livermore National Laboratory,
University of California,
Livermore, Calif. 94550

The basic problem addressed here is that of obtaining the unknown retardation time spectrum from experimental creep response curves. The spectrum may be a set of discrete times or it may be a spectrum characterized by a continuous distribution function. The present work employs a general model which assumes that the observed creep compliance is due to the summed effect of an arbitrary distribution of mechanisms. The analysis requires the solution of Fredholm integral equations of the first kind. It is well known that this problem is ill-conditioned so that any numerical scheme will have to involve some smoothing to obtain accurate solutions. The present work employs Butler's method of constrained regularization which takes advantage of the fact that the solution is positive and uses data-dependent smoothing. This work indicates that the imposition of the positivity constraint makes the computation of the solution much better conditioned. Computations with the method of constrained regularization employing near-optimal smoothing demonstrate its superiority over the method of Schapery for obtaining accurate solutions when the data are very noisy.

Introduction

Creep and stress relaxation data have been used extensively to study the rheological properties of various materials [1–6], and various equations based on phenomenological theories have been proposed to represent experimental or inferred data [7–10]. These phenomenological theories are based on the assumption of linear viscoelasticity and Boltzmann's superposition principle. This makes it possible, in principle, to calculate any other viscoelastic function if one viscoelastic function is known for all values of frequency, or it makes possible the calculation of the distribution function of retardation times of strain when the creep function is given [11, 12].

In the present paper we present a method for the determination of the retardation time spectrum from the creep compliance data. The determination of this spectrum is posed as an inversion problem. Specifically, the spectrum is the solution to a Fredholm integral equation of the first kind. It is well known that the problem is ill-posed [13–15]; large-amplitude, high-frequency oscillations in the solution produce very small change in the data. Conversely, small data variations may produce large variations in the solution. In the literature, many researchers have approximated the kernel in the integral to obtain the spectrum [12]. This is due to the formidable problems in inverting first-kind integral equations with noisy data. Approximation of the kernels requires the computation of various derivatives of the experimental data, and this limits the order of the approximation that may be used, because the effect of noise in the data is magnified in the answer obtained.

Schapery [16] suggested a procedure to invert the integral, but it is difficult to obtain accurate solutions with Schapery's method when the data are noisy. Recently, Swanson [17] used a procedure developed by Bellman [18] to obtain solutions to Laplace transform inversions in dynamic viscoelasticity. The distribution function obtained by both methods could be negative. Furthermore, Swanson's technique was not tested for noisy data or when the solution is made of discrete-impulsive spectra. The method of the present paper is shown to resolve discrete spectra and give accurate solutions from noisy data. This method was developed by Butler [19] for inverse problems in medicine. It uses constrained regularization, in which the solution is constrained to be non-negative and Tihonov [14] regularization is used. A similar constrained regularization was given by Wahba [20].

It should be noted that there are other approaches to the solution of integral equations which could be useful in obtaining the distribution function from the creep response. Sven-Åke Gustafson [21] has introduced a very efficient constrained optimization method. For application to our problem the data would have to be smoothed first because Gustafson's method is not designed for noisy data. Finally,

Contributed by the Applied Mechanics Division for publication in the JOURNAL OF APPLIED MECHANICS.

Discussion on this paper should be addressed to the Editorial Department, ASME, United Engineering Center, 345 East 47th Street, New York, N.Y. 10017, and will be accepted until two months after final publication of the paper itself in the JOURNAL OF APPLIED MECHANICS. Manuscript received by ASME Applied Mechanics Division, May, 1982; final revision, January, 1983.

Copyright © 1983 by ASME
Downloaded 02 May 2010 to 171.66.16.246. Redistribution subject to ASME license or copyright; see http://www.asme.org/terms/Terms_Use.cfm

we mention that the Tihonov regularization could be replaced by other standard regularizations, such as that based on the singular vane decomposition as used by Eckhardt [22].

In the following the method of constrained regularization is briefly reviewed. The method is then applied to the inversion of creep response for quartz monzonite and compared with the method of Schapery. Comparisons with some exact responses are then used to illustrate the applicability of the method.

Determination of Distribution Function

The creep function $J(t)$ is given in terms of the distribution function $X(\tau)$ by [12]

$$J(t) = J_\infty - \int_0^\infty X(\tau) e^{-t/\tau} d\tau; \tag{1}$$

$X(\tau)$ satisfies the condition

$$\int_0^\infty X(\tau)\, d\tau = \Delta J \tag{2}$$

where $\Delta J = J_\infty - J_0$. Here, J_∞ is the relaxed compliance and J_0 is the instantaneous elastic compliance before any appreciable flow or retarded elastic (anelastic) deformations have occurred.

To obtain the distribution function $X(\tau)$, the Laplace integral (1) is written in the more convenient form

$$\phi(t) = \int_0^\infty F(s) e^{-st} ds. \tag{3}$$

The function $F(s)$ introduced in this expression is related to $X(\tau)$ by the equations

$$\phi(t) = J_\infty - J(t), \tag{4}$$

$$X(\tau) = s^2 F(s), \tag{5}$$

and

$$s = 1/\tau. \tag{6}$$

In this paper, F, is referred to as the distribution function. By means of equations (5) and (6), it is always easy to obtain the retardation spectrum $X(\tau)$ from F.

Briefly, the steps involved in Butler's method are as follows. To obtain F from creep data, let us write equation (3) more specificially. Discrete data ϕ_i are taken at various points t_i. It is assumed that these data contain random noise $\{\epsilon_i\}$ associated with the ith measurement. Then, relation (3) may be written

$$y(t_i) = \int_0^\infty k(t_i,s) F(s) ds, \quad i = 1, \ldots, N, \tag{7}$$

where the data vector is $y(t_i) = \phi(t_i) + \epsilon_i(t)$ and $k(t_i,s) = \exp[-st_i]$. In the problems of interest in this paper, physical considerations require the spectrum to be non-negative

$$F(s) \geq 0, \tag{8}$$

and boundedness of the solution and data,

$$\int [F(s)]^2 ds < \infty, \tag{9}$$

$$\int [y(s)]^2 ds < \infty. \tag{10}$$

The technique of Butler solves a minimization problem to approximate the unknown spectrum F by a function f_α which depends on the observed data and a regularization parameter α. The approximate solution f_α is obtained by minimizing the function

$$\psi(f) = \sum_{i=1}^N W_i^2 \left(\int_D k(t_i,s) f(s) ds - y(t_i) \right)^2 + \alpha \|f\|^2, \tag{12}$$

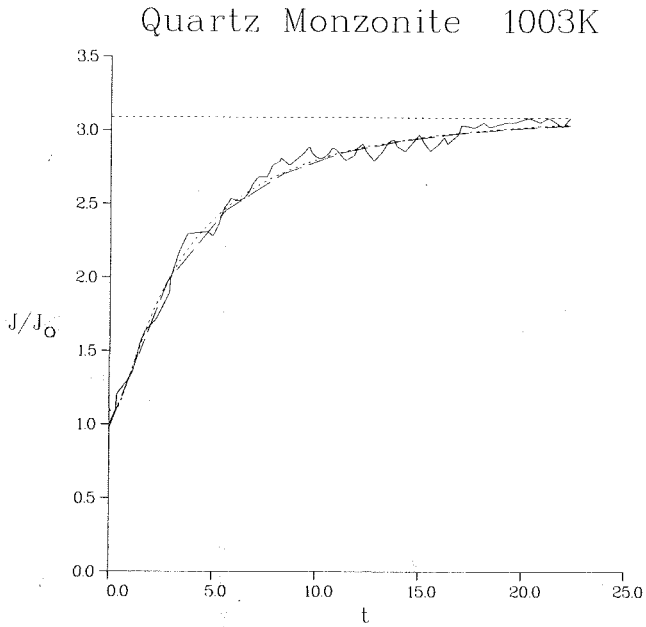

Fig. 1 Creep response for quartz monzonite and comparison with results computed from Schapery's method (dashed curve) and the present work (dash-dot curve)

where the weights W_i^2 are inversely proportional to the measurement error variances. The weights are scaled such that $\Sigma_{i=1}^N W_i^2 = N$. Here D is the domain where the solution f_α is positive, α is a positive regularization or smoothing parameter to be chosen, and $\|\cdot\|$ denotes either the Euclidean R^N vector norm or the L^2-norm as appropriate. Minimization of (12) leads to the system of equations

$$f(s) = \max\ (0, k(s) \cdot c), \tag{13}$$

$$(Kf - y) + \alpha c = 0, \tag{14}$$

where $k(s)$ denotes the vector-valued function whose ith component is $k(t_i,s)$ and the integral operator K is defined by $Kf = \int k(s) f(s) ds$. The desired approximate solution f_α satisfies the preceding system of equations for a given smoothing parameter α. If (13) is substituted into (14), then c satisfies the equation

$$c = T(k \cdot c) y, \tag{15}$$

where $T(k \cdot c) = (M(k \cdot c) + \alpha I)^{-1}$ and $M(k \cdot c)$ is the $N \times N$ matrix whose entries are given by

$$M_{ij}(k \cdot c) = \int_D k(t_i,s) k(t_j,s) ds. \tag{16}$$

Since M is symmetric and positive semidefinite, $(M + \alpha I)$ is nonsingular. Note that c enters nonlinearly in (15), so that we solve it using Newton's method.

The next step in the method of constrained regularization is to determine the optimal smoothing parameter α_{opt}. The parameter α is chosen to minimize a function which is an estimator of the data prediction error less an additive constant $\|F\|^2$ which is independent of α. This auxiliary function is written

$$H(\alpha) = \|f_\alpha - F\|^2 - \|F\|^2$$

$$= y^\dagger TMTy - 2 \int_D f_\alpha(s) F(s) ds, \tag{17}$$

where equation (15) has been used in evaluating f_α. Assuming the noises have mean zero, are uncorrelated, and have known variances, Butler showed that (17) could be written

$$H(\alpha) = y^\dagger TMTy - 2y^\dagger Ty + 2\sigma(N)^{1/2} \|c\|, \tag{18}$$

Downloaded 02 May 2010 to 171.66.16.246. Redistribution subject to ASME license or copyright; see http://www.asme.org/terms/Terms_Use.cfm

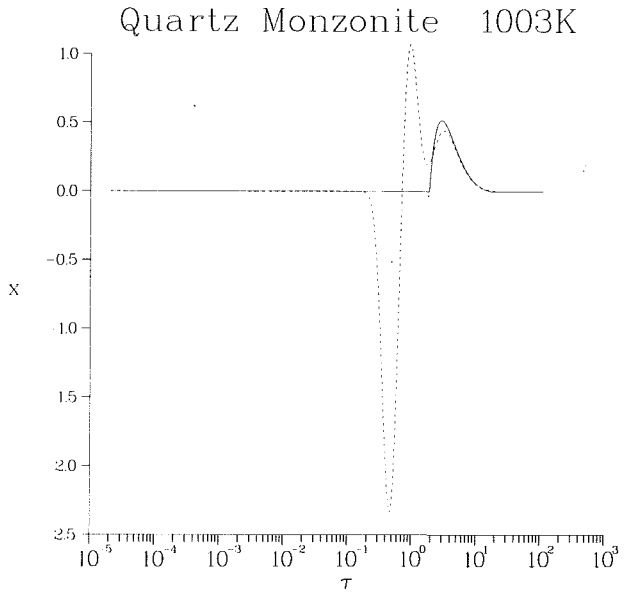

Fig. 2 Comparison of spectra obtained with Schapery's method (dashed curve) and present work (solid curve) for quartz monzonite

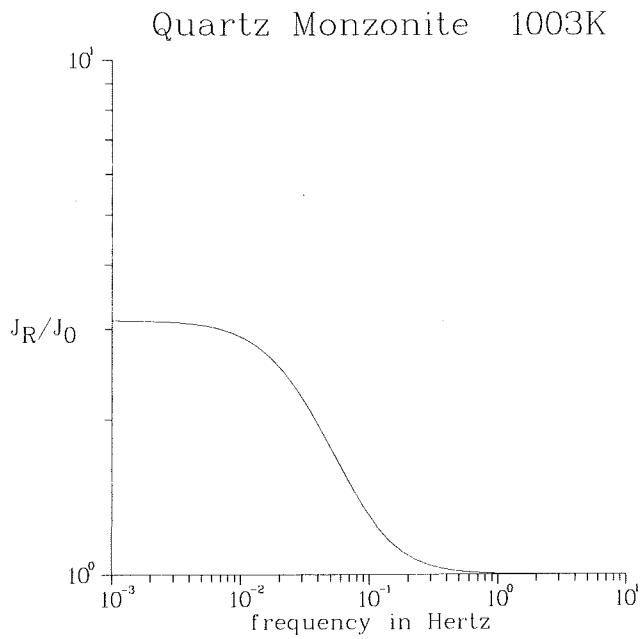

Fig. 3 Normalized storage compliance for quartz monzonite

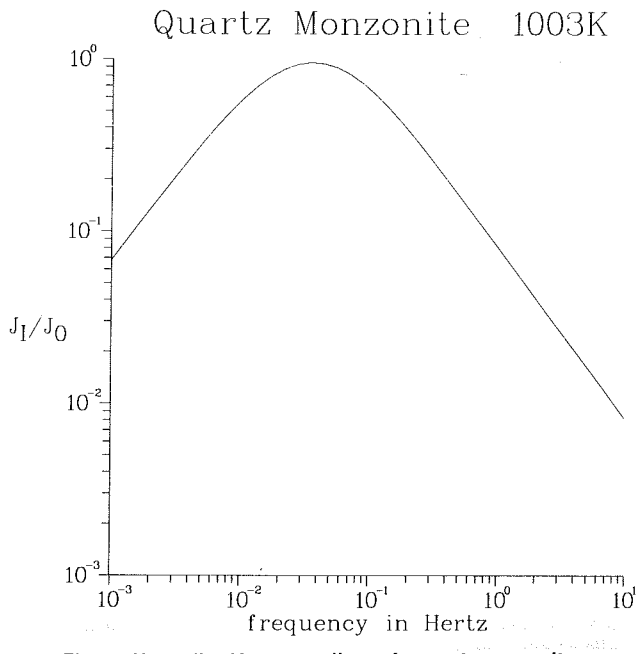

Fig. 4 Normalized loss compliance for quartz monzonite

where all noise variances σ_i^2 are taken equal σ^2. If the noise variances are unequal, simultaneous transformation $k(t_i,s) \rightarrow k(t_i,s)W_i$ and $y(t_i) \rightarrow y(t_i)W_i$ leads to the same formulation. The value of α that minimizes $H(\alpha)$, α_{opt}, is taken as the optimal choice of the amount of smoothing. Three cases of α_{opt} that minimizes $H(\alpha)$ must be distinguished and are discussed in detail by Butler. However, the value of α_{opt} appropriate to the present work is given by

$$\alpha_{opt} = \sigma N^{1/2} / \|c\|. \tag{19}$$

In spite of this theory, we have found in practice that the α_{opt} given by (19) is sometimes too large, leading to excessive smoothing.

Dynamic Viscoelastic Functions

Once the retardation spectra is determined, a Fourier transform of (3) gives the dynamic viscoelastic functions as follows:

$$J_R(\omega) = J_0 + \int_0^\infty \frac{X(\tau)}{1+\omega^2\tau^2}\, d\tau, \tag{20}$$

$$J_I(\omega) = \int_0^\infty X(\tau)\, \frac{\omega\tau}{1+\omega^2\tau^2}\, d\tau, \tag{21}$$

and

$$Q^{-1}(\omega) = J_I(\omega)/J_R(\omega), \tag{22}$$

where $J_R(\omega)$ is defined as the storage compliance and is the ratio of the strain in phase with stress to stress, J_I is the loss compliance and is the ratio of the strain 90 deg out of phase with the stress to the stress, and Q^{-1}, the inverse quality factor, is the tangent of the loss angle. It is associated with dissipation or loss of energy.

The integrals in relations (20) and (21) are evaluated using a modified adaptive Gaussian quadrature (AGM) [23] combined with a Gauss-Laguerre [24] routine.

Examples

To illustrate the potential of the method of constrained regularization to invert retardation spectra from experimental creep data, a selection of problems with time-dependent effects are presented. The first example is that of inverting for viscoelastic properties of quartz monzonite at 1003K and 180 MPa confining pressure from laboratory creep data. The second example is the inversion of two wave-like functions previously studied by Swanson [17]. The final numerical example is that of inverting for spectra that are known to be discrete.

Quartz Monzonite Spectra. This example is considered to show the capability of the method in inverting for retardation spectra of real materials. The creep compliance normalized with respect to the unrelaxed elastic compliance $J_0 = 2.34 \times 10^{-6}$/MPa estimated from the high-frequency modulus in granite at high temperature [25] is shown in Fig. 1 as the solid curve. It must be emphasized that this data set has not been corrected for instrument response and therefore depicts greater energy absorption than is characteristic of this material at the given temperature and frequency. This sample

Downloaded 02 May 2010 to 171.66.16.246. Redistribution subject to ASME license or copyright; see http://www.asme.org/terms/Terms_Use.cfm

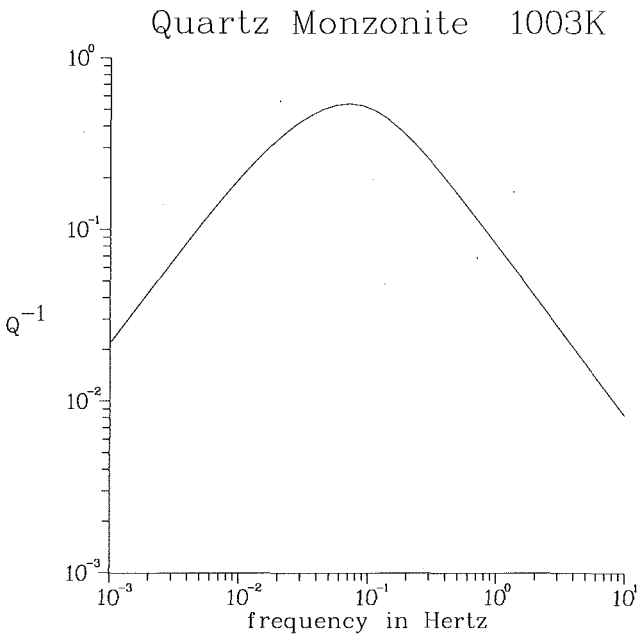

Fig. 5 Inverse quality factor for quartz monzonite

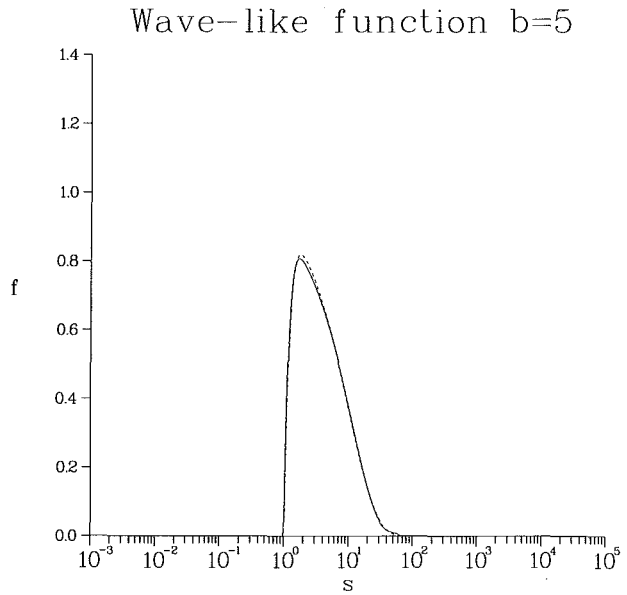

Fig. 6 Comparison of numerical (solid curve) and exact (dashed curve) Laplace transform inversion, $b = 5$

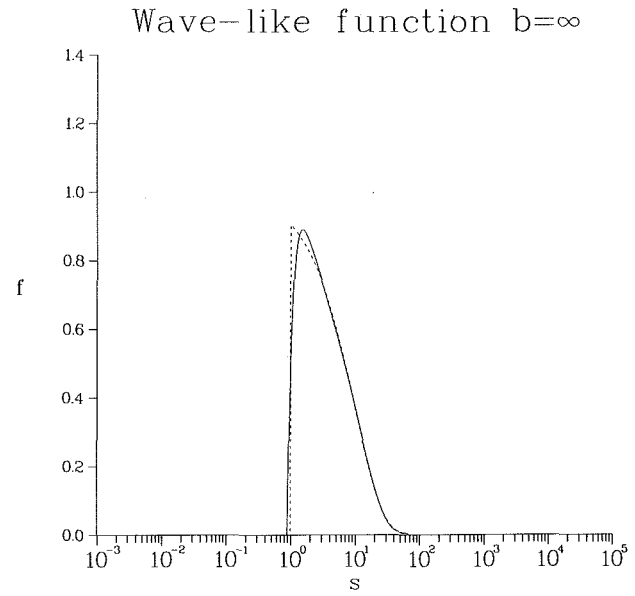

Fig. 7 Comparison of numerical (solid curve) and exact (dashed curve) Laplace transform inversion, $b \to \infty$

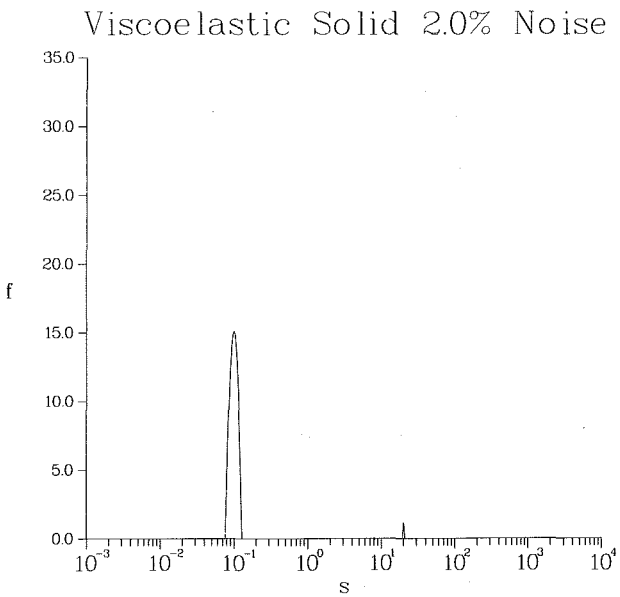

Fig. 8 Spectra for a viscoelastic solid with two relaxation peaks

has been chosen because it shows significant time-dependent strain and is contaminated by noise characteristics of this measurement technique [26]. The mechanisms responsible for this response have not yet been identified. The retardation spectrum is shown by the solid line in Fig. 2. Figures 3–5 depict the normalized dynamic viscoelastic functions and the inverse quality factor obtained by the method discussed in this paper. In Fig. 2, we compare the spectrum obtained from the method of this paper (solid curve) with Schapery's technique (dashed curve). It is clear from this figure that Schapery's technique gives rise to spurious oscillations in the spectrum and is incapable of obtaining a realistic spectrum when the data are noisy although the compliance recomputed from the spectrum clearly represents the data as shown in Fig. 1 where comparisons are made. The oscillations shown in Fig. 2 are characteristic of ill-posed problems.

Although the spectrum depicted in Fig. 2 certainly appears realistic, we have insufficient direct measurements with which to compare our numerical results. It is therefore not possible to assess the accuracy of the method from these results alone. In the following, two examples with known solutions are presented in order to test the accuracy of the method.

Exact Wave-Like Spectra. The following functions were considered by Swanson [17] in his investigation.

$$f(s) = \{1 - \exp[-b(s-1)]\}\{\exp(-0.1s)\}H(s-1), \quad (23)$$

$$y(t) = \exp[-(t+0.1)]\{b/[(t+0.1)(t+b+0.1)]\}, \quad (24)$$

for $b = 5$ and for $b \to \infty$

$$f(s) = \exp(-0.1s)H(s-1), \quad (25)$$

$$y(t) = \exp[-(t+0.1)]/(t+0.1), \quad (26)$$

where $y(t)$ are the data. The functions $f(s)$ have the character of viscoelastic retardation spectra (see Fig. 2 for example). A comparison of the numerical (solid) and exact (dashed) inverse transform $f(s)$ is depicted in Figs. 6 and 7. In these

Downloaded 02 May 2010 to 171.66.16.246. Redistribution subject to ASME license or copyright; see http://www.asme.org/terms/Terms_Use.cfm

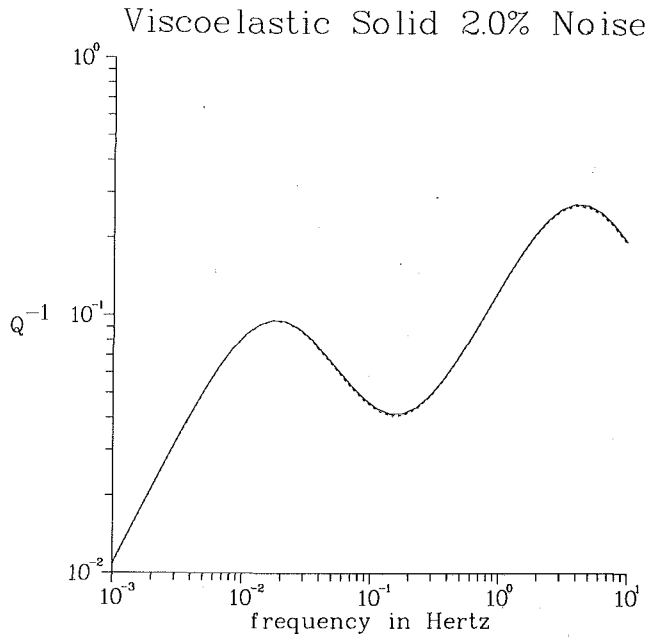

Fig. 9 Comparison of exact (dashed curve) and numerical (solid curve) inverse quality factors (2 percent noise) for a viscoelastic solid with two relaxation peaks

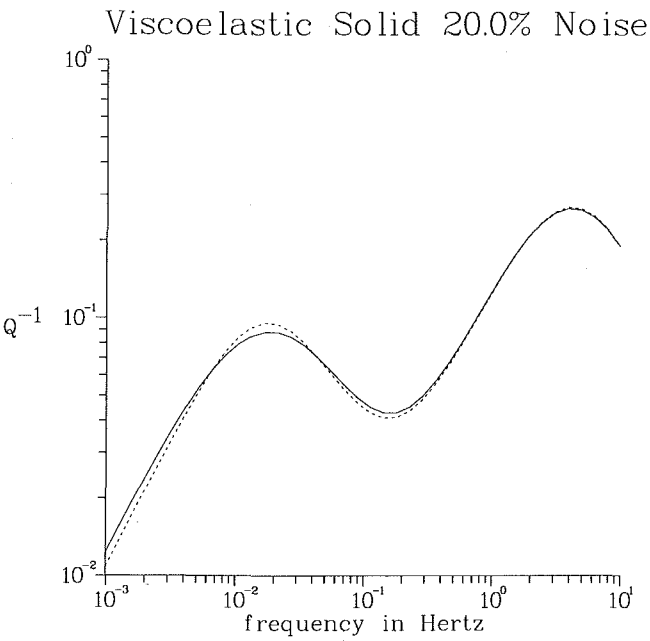

Fig. 10 Comparison of exact (dashed curve) and numerical (solid curve) inverse quality factor (20 percent noise) for a viscoelastic solid with two relaxation peaks

examples, α_{opt} was obtained by using $\sigma = 10^{-5}$ in equation (19). The comparisons of the exact and numerical solutions show the accuracy that can be obtained with the method of constrained optimization. Numerical experiments with $\sigma = 10^{-10}$ gave results similar to those in Figs. 6 and 7. With σ identically zero, the iterations did not converge. Thus it is clear that a very small but necessary amount of smoothing along with a positivity constraint provides acceptable solutions. It is observed that the arrivals are somewhat earlier in the numerical solution and more rounded at the peak for the more step-like solution (large b) than in the exact solution. This is an effect of the regularization. It is also observed that the oscillations observed by Swanson are not seen in the present solutions. In the two cases presented, the numerical solution never deviated far from the exact solution, and the maximum deviation occurred for the more step-like function ($b \to \infty$).

Discrete Spectra. Because materials of practical interest may contain relaxation mechanisms that exhibit discrete spectra or may not be so smooth, it is appropriate to examine the capability of the method to solve first-kind integral equations under more stringent conditions, i.e., impulsive discrete spectra. A numerical creep compliance experiment is performed with the following characteristics.

$$J(t) = J_0 + \Delta J_1(1 - e^{-t}/\tau_1) + \Delta J_2(1 - e^{-t}/\tau_2), \quad (27)$$

where $J_0 = 1.429$/MPa, $\Delta J_1 = 0.5$/MPa, $\tau_1 = 10$ sec, $\Delta J_2 = 1.0$/MPa, and $\tau_2 = 0.05$ sec. The spectrum for this material is clearly represented by Dirac delta functions located at τ_1 and τ_2 of magnitudes ΔJ_1 and ΔJ_2, respectively. A typical numerical solution for spectra containing 2 percent random noise is depicted in Fig. 8. In this analysis, the noise was generated from the equation

$$\epsilon_i(t) = \mu R \phi_i \quad (28)$$

where μ is a fraction representing the percent noise and R is a pseudorandom number distributed between $-1/2$ and $1/2$ having zero mean.

Since the spectra are discrete, it is not appropriate to compare exact and numerical spectra as they are Dirac delta functions. Hence, we make comparisons of the ratio of integrals of the spectra, $J_I/J_R = Q^{-1}$. The exact value of Q^{-1} for this example is obtained from relation (2) using the equations

$$J_R(\omega) = J_0 + \sum_{i=1}^{2} \Delta J_i/[1 + (\omega\tau_i)^2] \quad (29)$$

and

$$J_I(\omega) = \sum_{i=1}^{2} \Delta J_i \omega\tau_i/[1 + (\omega\tau_i)^2]. \quad (30)$$

The comparisons of the exact inverse quality factor Q^{-1} with the numerical solution is shown in Figs. 9 and 10 for 2 percent and 20 percent noise in the data, respectively. Here, the exact Q^{-1} is displayed with dashes and the computed Q^{-1} with solid curves. For those levels, we found noise variances of 3.7×10^{-6} and 3.7×10^{-4}, respectively. For the case of 2 percent noise the computed α_{opt} was adequate. However, the variance of 3.7×10^{-4}, representing 20 percent noise in the data tended to oversmooth the solution using α_{opt} derived from equation (19). In this case we reduced α_{opt} by a factor of 10 and obtained the results shown in Fig. 10. This example does show that we can resolve discrete spectra using the proper amount of smoothing with the method. The selection of α_{opt} by objective criteria is worth further investigation.

Summary and Conclusions

In this paper, a technique to invert creep compliance data for retardation spectra and to determine dynamic viscoelastic functions from the spectra has been shown to give accurate results, even in the presence of noise. This accuracy has been assessed in terms of the comparison of the numerical solutions with exact results. Numerical experiments have shown that to obtain accurate results, it is necessary, but not sufficient that (1) the discretized data be sampled at enough points to reasonably represent the observed behavior, and (2) the difference between the input data and the data function computed from the approximate solution be small, that is,

Downloaded 02 May 2010 to 171.66.16.246. Redistribution subject to ASME license or copyright; see http://www.asme.org/terms/Terms_Use.cfm

small residuals relative to the approximating function $Kf_\alpha - y$. However, our numerical experiments have shown that for decreasing signal to noise ratios, the value of α_{opt} given by equation (19) tends to oversmooth the solution. Excessive smoothing leads to a large residual.

By using the method described in this paper, reliable, accurate solutions can be obtained to problems of inverting relaxation spectra and determining dynamic viscoelastic functions when noisy discrete values of data are given. Certainly, the most surprising aspect of the method is its ability to resolve discrete spectra. This places more stringent demands on this method and overwhelmingly shows its capabilities over previous methods discussed in the literature.

Acknowledgments

This work was performed under the auspices of the U.S. Department of Energy by the Lawrence Livermore National Laboratory under Contract No. W-7405-ENG-48.

References

1 Ke, T. S., "Experimental Evidence of Viscous Behavior of Grain Boundaries in Metals," *Physical Review*, Vol. 71, 1947, pp. 533–546.

2 Nowick, A. S., "Anelastic Effects Arising From Precipitation in Aluminum-Zinc Alloys," *Journal of Applied Physics*, Vol. 22, 1951, pp. 925–933.

3 Tobolsky, A. V., and Catsiff, E., "Elastoviscous Properties of Polyisobutylene (and Other Amorphous Polymers) from Stress-Relaxation Studies. IX. A Summary of Results," *Journal of Polymer Science*, Vol. XIX, 1956, pp. 111–121.

4 Plazek, D. J., and Magill, J. H., "Physical Properties of Aromatic Hydrocarbons. I. Viscous and Viscoelastic Behavior of 1:3:5-Tri-α-Naphthyl Benzene," *The Journal of Chemical Physics*, Vol. 45, 1966, pp. 3038–3050.

5 Pandit, B. I., and Savage, J. C., "An Experimental Test of Lomnitz Theory of Internal Friction in Rocks," *Journal of Geophysical Research*, Vol. 78, 1973, pp. 6097–6099.

6 Ferry, J. D., *Viscoelastic Properties of Polymers*, 2nd Ed., Wiley, New York, 1970.

7 Lomnitz, C., "Linear Dissipation in Solids," *Journal of Applied Physics*, Vol. 28, 1957, pp. 201–205.

8 Anderson, D. L., and Minster, J. B., "The Frequency Dependence of Q in the Earth and Implications for Mantle Rheology and Chandler Wobble," *Geophysical Journal of the Royal Astronomical Society*, Vol. 58, 1979, pp. 430–440.

9 Berckhemer, H., Auer, F., and Drisler, J., "High-Temperature Anelasticity and Elasticity of Mantle Peridotite," *Physics of the Earth and Planetary Interiors*, Vol. 20, 1979, pp. 48–59.

10 Smith, T. L., "Empirical Equations for Representing Viscoelastic Functions and for Deriving Spectra," *Journal of Polymer Science, C*, No. 35, 1971, pp. 39–50.

11 Gross, B., "On Creep and Relaxation," *Journal of Applied Physics*, Vol. 18, 1947, pp. 212–221.

12 Nowick, A. S., and Berry, B. S., *Anelastic Relaxation in Crystalline Solids*, Academic Press, New York, 1972.

13 Franklin, J. N., "Well-Posed Stochastic Extensions of Ill-Posed Linear Problems," *Journal of Mathematical Analysis and Applications*, Vol. 31, 1970, pp. 682–716.

14 Tihonov, A. N., "Solution of Incorrectly Formulated Problems and the Regularization Method," *Soviet Math. Dokl.*, Vol. 4, 1963, pp. 1035–1038.

15 Baker, C. T. H., *The Numerical Treatment of Integral Equations*, Oxford, Clarendon Press, 1977.

16 Schapery, R. A., "Approximate Methods of Transform Inversion for Viscoelastic Stress Analysis," *Proceedings of the 4th U.S. National Congress on Applied Mechanics*, Vol. 2, 1962, pp. 1075–1085.

17 Swanson, S. R., "Approximate Laplace Transform Inversion in Dynamic Viscoelasticity," ASME JOURNAL OF APPLIED MECHANICS, Vol. 47, 1980, pp. 769–774.

18 Bellman, R., Kalaba, R. E., and Lockett, J., *Numerical Inversion of the Laplace Transform*, Elsevier, New York, 1966.

19 Butler, J. P., Reeds, J. A., and Dawson, S. V., "Estimating Solutions of First Kind Integral Equations With Non-negative Constraints and Optimal Smoothing," *SIAM Journal of Numerical Analysis*, Vol. 18, 1981, pp. 381–397.

20 Wahba, G., "Constrained Regularization for Ill-Posed Linear Operator Equations, With Applications in Meteorology and Medicine," University of Wisconsin, Department of Statistics, Technical Report No. 646, 1981.

21 Gustafson, Sven-Åke, "A Computational Scheme for Exponential Approximation," *Z. Angew. Math. Mech.*, Vol. 61, 1981, pp. T284–T287.

22 Eckhardt, U., and Mika, K., "Numerical Treatment of Incorrectly Posed Problems," in *Numerical Treatment of Integral Equations*, Albrecht, J., ed., Birkhäuser Verlag, Basel, 1980, pp. 92–101.

23 Robinson, Ian, "An Algorithm for Automatic Integration Using the Adaptive Gaussian Technique," *Australian Computer Journal*, Vol. 8, 1976, pp. 106–115.

24 Davis, P. J., and Rabinowitz, P., *Methods of Numerical Integration*, Academic Press, New York, 1975.

25 Kern, H., and Richter, A., "Temperature Derivatives of Compressional and Shear Wave Velocities in Crustal and Mantle Rocks at 6 Kbar Confining Pressure," *Journal of Geophysics*, Vol. 49, 1981, pp. 47–56.

26 Bonner, B. P., and Heard, H. C., "Internal Friction and Transient Creep in Granitic Rocks at High Pressure and Temperature," *Int. Union. Geol. Geophys. Gen. Assem., Abstract*, Vol. 17, 1979, p. 119.

Downloaded 02 May 2010 to 171.66.16.246. Redistribution subject to ASME license or copyright; see http://www.asme.org/terms/Terms_Use.cfm

Initial Strain Field and Fatigue Crack Initiation Mechanics

S. R. Lin
Manager,
Thermostructural Analysis Section,
Structures Department,
The Aerospace Corporation,
El Segundo, Calif. 90245

T. H. Lin
Professor,
Mechanics and Structures Department,
School of Engineering and Applied Science,
University of California,
Los Angeles, Calif. 90024
Fellow ASME

On single aluminum crystals under cyclic loadings, fresh slip lines appeared during the reversed loading, lying very close to, but not coincident with the slip lines formed in the forward loading. These slip lines indicate the start of extrusion or intrusion as commonly observed in fatigue specimens. An initial stress field is present in all metals. The initial stress field favorable to the aforementioned sequence of slip is one having a positive shear stress in one thin slice P and a negative one in a closely located thin slice Q. A forward loading causes a positive shear stress, which is of the same sign as the initial shear stress in P, but of opposite sign to that in Q. Hence the shear stress in P will reach the critical value first to cause slip. Due to the ***continuity of the stress field****, slip in P relieves not only the positive shear stress in P but also in Q. This has the same effect as increasing negative shear stress in Q. During the reversed loading, Q has the highest negative shear stress and hence slides. Similarly, this slip causes P to be more ready to slide in the next forward loading. This process is repeated to cause a monotonic alternate sliding in P and Q. In this way, an extrusion or intrusion is nucleated. A crack can be started from an intrusion. The thin slices P and Q are considered to be in a most favorably oriented crystal located at a free surface. An initial stress field giving positive shear stress in P and negative in Q is* ***calculated from an assumed initial inelastic strain field*** *which, in turn, can be caused by distribution of dislocations. The buildup of plastic shear strain in P and Q causing the start of extrusion or intrusion is shown.*

Introduction

Single crystal tests show that slip occurs on certain crystal planes along certain directions. This slip depends on the resolved shear stress and is independent of the normal stress on the sliding plane. The dependence of slip on the resolved shear stress is well known as the Schmid Law. Gough and others [1-3] loaded single crystals under cyclic torsion and found that the slip planes and directions that operated in fatigue were the same as those in unidirectional tests. The active slip systems in each part of the crystal were those subject to the highest resolved shear stress.

Slip lines often were developed in the early stage of fatigue cycling, producing "soft" regions where local deformation tends to concentrate [4-6]. Slip lines generally multiply and grow into persistent slip bands in these regions. They act as preferential sites for the nucleation of microcracks. Material away from these regions is comparatively dislocation-free, showing no apparent plastic deformation.

Tests on single crystals of aluminum under cyclic tension and compression by Charsley and Thompson [7] have shown that a reversal of stress after a prior tensile deformation gives rise to new slip lines. Similar "compressive" slip lines were observed on an aluminum crystal by Buckley and Entwistle [8] to form between "tensile" slip lines. Forsyth [9] found the slip lines produced in forward loading and those produced in the reversed loading to be in the same fatigue band, very close but distinct from each other.

Wood and Bendler [10] have tested copper circular rod specimens under torsion. These specimens were electropolished in phosphoric acid and then scratched as markers with a 0.5 diamond dust. A typical specimen subject to a single twist through a large angle is shown in Fig. 1. The twist has caused the scratches *a*, *b*, and *c* above the slip band *AB* to displace relative to the scratches below *AB*. By contrast, there was no relative displacement for scratches *d*, *e*, and *f* across the fatigue band *CD*, for specimens subject to cyclic torsion, as shown in Fig. 2. Within the fatigue band each scratch displaced equally to the right and left, producing a zigzag. These tests show conclusively that both forward and backward slip have occurred within the fatigue band and the slip that occurs in cyclic loading does not lead to significant deformation in the bulk of the matrix. This explains why there are no dark spots on the X-ray reflection photo of fatigue specimens [11]. Extrusions have been observed in fatigue specimens [12, 13]. The reverse of extrusion (i.e., intrusion) has also been found. Intrusions are often considered an

Contributed by the Applied Mechanics Division for presentation at the 1983 ASME Applied Mechanics, Bioengineering, and Fluids Engineering Conference, Houston, Texas, June 20-22, 1983 of THE AMERICAN SOCIETY OF MECHANICAL ENGINEERS.

Discussion on this paper should be addressed to the Editorial Department, ASME, United Engineering Center, 345 East 47th Street, New, N.Y. 10017, and will be accepted until two months after final publication of the paper itself in the JOURNAL OF APPLIED MECHANICS. Manuscript received by ASME Applied Mechanics Division, July, 1981; final revision, August, 1982. Paper No. 83-APM-20.

Copies will be available until February, 1984.

Copyright © 1983 by ASME
Downloaded 02 May 2010 to 171.66.16.246. Redistribution subject to ASME license or copyright; see http://www.asme.org/terms/Terms_Use.cfm

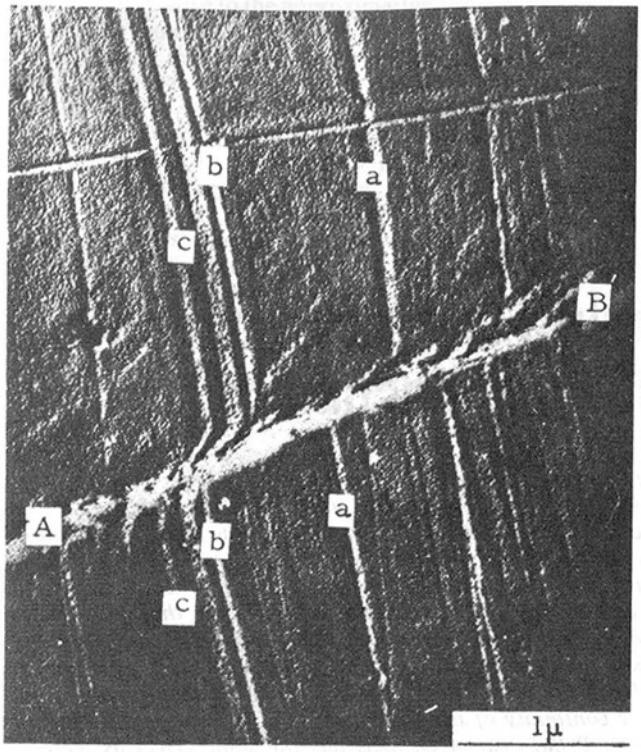

Fig. 1 Initially straight scratches *a*, *b*, *c* are displaced unidirectionally by static band *AB*

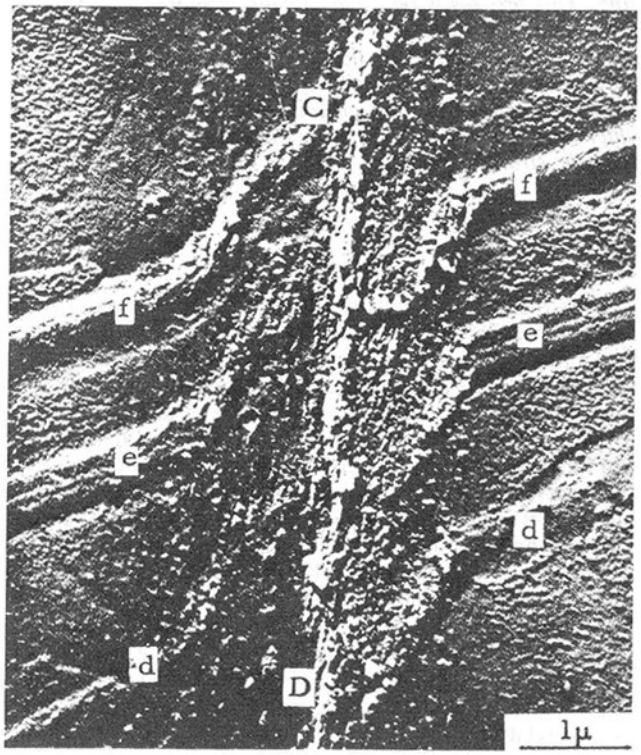

Fig. 2 Cyclic slip band *CD* produces no overall displacement of scratches *d*, *e*, *f*; within the slip band the scratches are displaced equally backward and forward

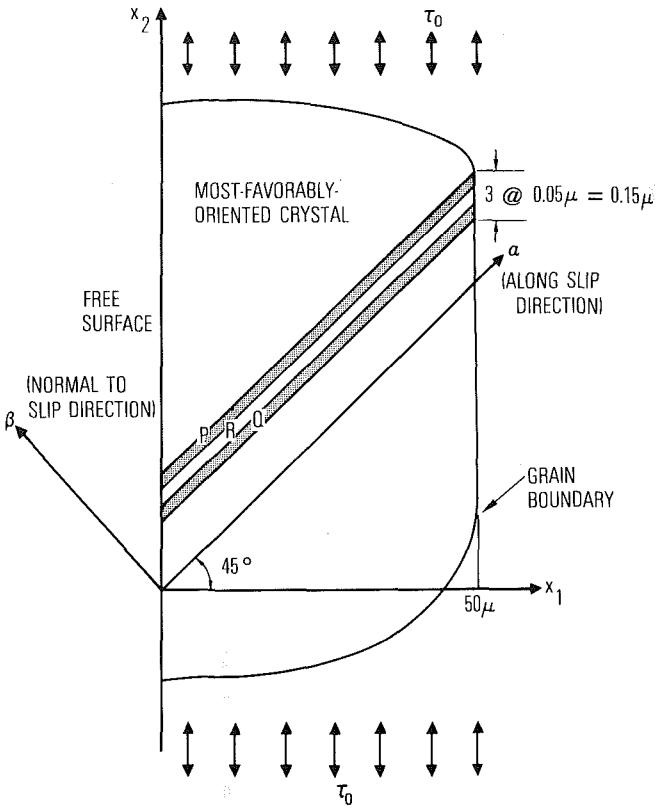

Fig. 3 Most favorably oriented crystal at free surface

embryonic fatigue cracks. Other experimental observations and a number of suggested models for fatigue crack initiation were summarized in two excellent reviews by Grosskreutz [14] and Laird and Duquette [15].

From the previously discussed experimental observations on fatigue slip lines, the slip lines formed in the forward loading and those formed in the reverse loadings are very closely spaced but distinct from each other, and are in the same slip band. It has been shown that to relieve the same amount of resolved shear stress in a thin slice, the amount of slip (i.e., the plastic strain required) near the free surface is much more than that at the interior [16]. Hence the thin slices, alternately sliding in the forward and reversed loading, are taken to be in the most favorably oriented crystal at the free surface of a polycrystal. Under a tensile and compressive loading, the slip plane and slip direction of this crystal make 45 deg with the specimen axis. The initial stress field τ^I favorable for this sequence of slip to initiate an extrusion is one having positive shear stress in one slice P and a negative one in closely located slice Q [17–19], as shown in Fig. 3.

A tensile loading induces a positive resolved shear stress τ^A in the most favorably oriented crystal. In P, the resolved shear stress will be the sum of τ^I and τ^A. This stress will be the first to reach the critical shear stress, τ^C, which is defined as the shear stress necessary to initiate or to cause further slip. Due to the continuity of the stress field, slip in P relieves not only the positive shear stress in P, but also in its neighboring region including Q [17, 18]. This keeps the positive shear stress in the neighboring region from reaching that of P during the forward loading, and also increases the negative resolved shear stress in Q to cause Q to slide more easily in the reverse loading. When the negative resolved shear stress in Q reaches τ^C in the reverse loading, slip occurs in Q and a new residual stress field is produced. The slip in Q causes the relief of negative resolved shear stress not only in Q but also in its neighboring region including P. The relief of negative resolved shear stress has the same effect as increasing the positive resolved shear stress in P, thus making P more ready to slide in the next forward loading. This process is repeated for every cycle, *providing a natural gating mechanism for the monotonic buildup of local slip and plastic shear strain in P and Q*. The plastic strain in P and Q tends to push out the region between them and starts an extrusion. If the signs of

Downloaded 02 May 2010 to 171.66.16.246. Redistribution subject to ASME license or copyright; see http://www.asme.org/terms/Terms_Use.cfm

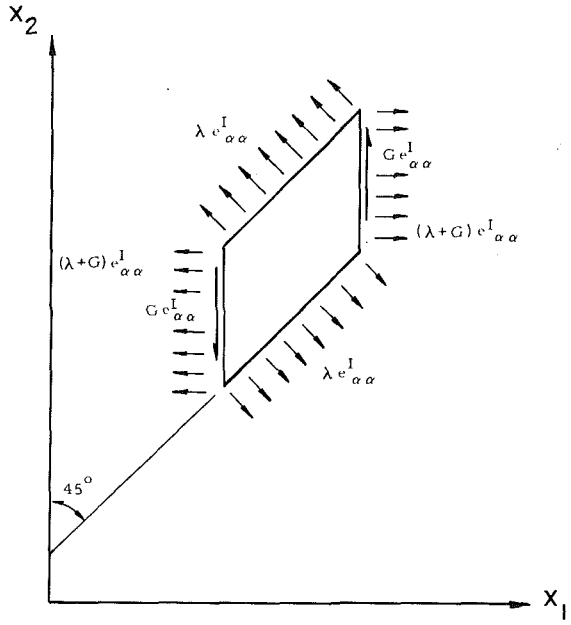

Fig. 4 Equivalent force in a parallelogram grid

initial stress in P and Q are interchanged, an intrusion instead of an extrusion will be initiated. This model explains the observed monotonic raising of extrusions and deepening of intrusions, and also shows the general characteristics of an initial stress field favorable for the initiation of a fatigue crack.

Calculating of Initial Stress From Initial Strain

The stress fields caused by inclusions in an elastic media have been extensively investigated since the publications of Eshelby's papers [20, 21]. The inclusion problem is similar to the problem of finding the initial stress field caused by inelastic strain. The analogy between the externally applied forces, in an elastic body and inelastic strain, which may be composed of plastic, creep, and thermal strains, has been generalized and developed by Lin [22] from Duhamel's analogy for thermal stress. This generalized analogy reduces the analysis of a body with inelastic strain to the analysis of an identical elastic body with an equivalent additional set of applied forces. Referring to a set of rectangular coordinates, the strain is considered to consist of the elastic strain e^E_{ij}, and inelastic strain e^I_{ij}

$$e_{ij} = e^E_{ij} + e^I_{ij} \tag{1}$$

The stress is related to the elastic strain as

$$\tau_{ij} = \delta_{ij}\lambda e^E_{kk} + 2Ge^E_{ij} \tag{2}$$

where δ_{ij} is the Kronecker delta, λ and G are Lame's constants, and the repetition of subscript denotes summation from 1 to 3. The condition of static equilibrium gives

$$\tau_{ij,j} + F_i = 0; \quad \tau_{ij}\nu_j = \overset{\nu}{T}_i \tag{3}$$

where a subscript after a comma denotes differentiation with respect to a coordinate variable, and

F_i = ith component of the body force

$\overset{\nu}{T}_i$ = ith component of the surface traction on the surface with outward unit normal ν.

Substitution of equation (2) into equation (3) yields

$$\lambda e_{kk,i} + 2Ge_{ij,j} + F_i - (\lambda e^I_{kk,i} + 2Ge^I_{ij,j}) = 0 \tag{4}$$

$$\lambda e_{kk}\nu_i + 2Ge_{ij}\nu_j = T^{\nu}_i + (\lambda e^I_{kk}\nu_i + 2Ge^I_{ij}\nu_j) \tag{5}$$

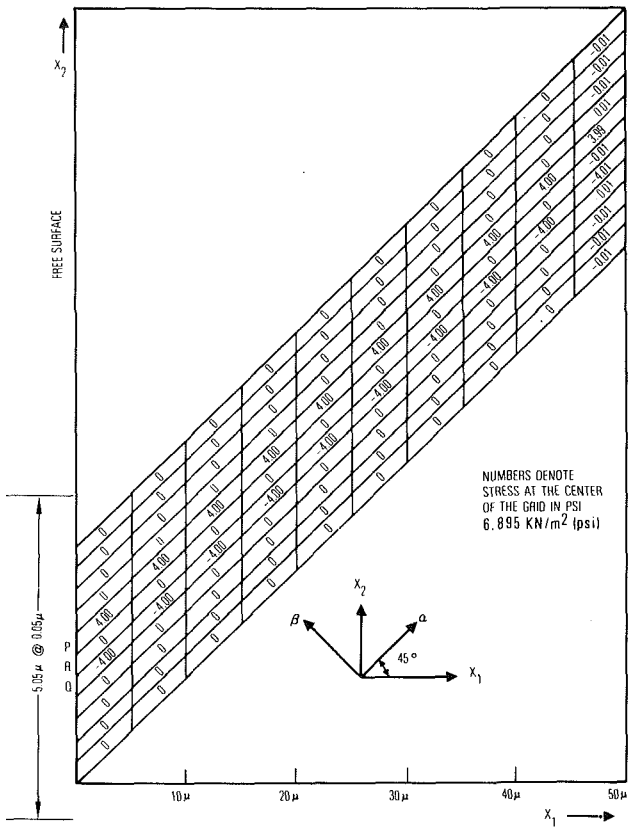

Fig. 5 Initial resolved shear stress field caused by a plastic strain field

It becomes apparent that the term $-(\lambda e^I_{kk,i} + 2Ge^I_{ij,j})$ has an equivalent effect as F_i, and the term $\lambda e^I_{kk}\nu_i + 2Ge^I_{ij}\nu_j$ as $\overset{\nu}{T}_i$ in causing the strain field e_{ij}. Hence, the strain distribution in a body with inelastic strain e^I_{ij} under external load is the same as that in a purely elastic body without any inelastic strain but with the additional equivalent body force and surface traction:

$$\bar{F}_i = -(\lambda e^I_{kk,i} + 2Ge^I_{ij,j}); \quad \overset{\nu}{\bar{T}}_i = \lambda e^I_{kk}\nu_i + 2Ge^I_{ij}\nu_j \tag{6}$$

The residual stress field of the actual body will be given as

$$\tau^I_{ij} = \delta_{ij}\lambda(e_{kk} - e^I_{kk}) + 2G(e_{ij} - e^I_{ij}) \tag{7}$$

where e_{ij} is the strain field caused by $F_i + \bar{F}_i$ and $T_i + \overset{\nu}{\bar{T}}_i$. This inelastic strain such as thermal strain is often discontinuous. When $e^I_{ij,j}$ is discontinuous the equivalent body force per unit volume becomes a surface force $2G\{e^I_{ij}\}\nu_j + \lambda\{e^I_{kk}\}J_i$ where $\{e^I_{ij}\}$ is the jump in e^I_{ij}, similar to the surface force given by equation (5).

The aggregate considered in this study is of fine grain; the grain size is small compared to total volume of the aggregate. The equivalent force caused by inelastic strain in the crystal at the free surface of the metal may be considered acting on a semi-infinite elastic medium. In the later calculation of slip line formation, the thickness of the slices is much less than the length of the slip lines on the surface. Consequently, the inelastic strains and their equivalent forces are taken to be constant along the slip line direction on the surface, and this semi-infinite medium is taken to be under plane deformation. There are four slip planes in a face-centered-cubic crystal. In this paper, sliding in one plane only is considered.

In previous papers [17, 23] an initial stress field was assumed. Since this stress field can be caused by an initial inelastic strain, which can be produced by dislocations, this initial stress field is here explicitly calculated from a given inelastic strain field. The inelastic strain $e^I_{\alpha\alpha}$ is assumed to

Downloaded 02 May 2010 to 171.66.16.246. Redistribution subject to ASME license or copyright; see http://www.asme.org/terms/Terms_Use.cfm

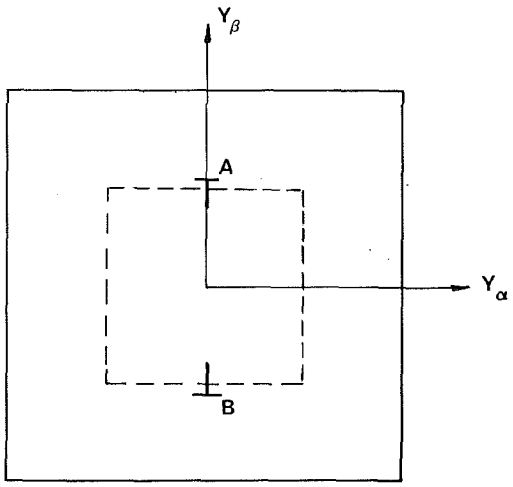

Fig. 6 A dislocation interstitial dipole

exist in three thin slices P, Q, and R (Fig. 3) where α is along the slip direction. This inelastic strain component is taken to vary linearly from zero at the free surface to a maximum at the interior boundary ($x_1 = 50\ \mu$) in P and Q, while in R, it is taken to be twice that of P and Q and of opposite sign. Equation (6) gives the following equivalent body force and surface traction:

$$\bar{F}_\alpha = (\lambda+2\mu)e^I_{\alpha\alpha,\alpha} \tag{7}$$

$$\bar{F}_\beta = 0 \tag{8}$$

$$\overset{\alpha}{\bar{T}}_\alpha = (\lambda+2\mu)e^I_{\alpha\alpha};\quad \overset{\alpha}{\bar{T}}_\beta = 0,\quad \overset{\beta}{\bar{T}}_\alpha = 0 \tag{9}$$

$$\overset{\beta}{\bar{T}}_\beta = \lambda e^I_{\alpha\alpha} \tag{10}$$

where β is normal to the slip plane. Since $e^I_{\alpha\alpha,\alpha}$ is constant, F is uniform within the thin slices. In these equations, the repetition of subscript does not denote summation. These give uniform equivalent body force in the slices balanced by the equivalent surface forces on the right boundaries. These equivalent boundary forces acting on a parallelogram grid is shown in Fig. 4. The thickness of each slice measured along x_2-axis is taken to be 0.05μ. The center distance between P and Q is 0.10μ and the linear dimension of the crystal is taken to be 50μ. The $e^I_{\alpha\alpha}$ at the right boundary of slices P and Q was taken to be 1930KN/m^2 (280 psi)/G and 3860KN/m^2 (560 psi)/G in R. For numerical calculation of initial stress, each slice is divided into 1000 parallelogram grids along their lengths. The inelastic strain is taken to be constant within each grid. From the plane strain solution of a semi-infinite medium, the initial resolved stress field caused by a given equivalent forces $\bar{F}_\alpha$ and $\overset{\alpha}{\bar{T}}_\alpha$ on a parallelogram grid [24] was calculated. Then the resolved shear stresses due to $\bar{F}_\alpha$ and $\overset{\alpha}{\bar{T}}_\alpha$ on all the grids of the three slices were summed to yield the initial resolved shear stress field, which is shown in Fig. 5. It is seen that the initial shear stress $\tau^I_{\alpha\beta}$ in P is positive +27.6 KN/m^2 (4 psi) and in Q negative −27.6 KN/m^2 (−4 psi). The regions outside P and Q as well as the region between P and Q have a negligibly small amount of resolved shear stress. This initial stress field so derived from the initial inelastic strain clearly is favorable to the initiation of extrusion as discussed earlier. This initial stress field satisfies the equilibrium and compatibility conditions. Consider a perfect crystal cube. If we cut a slit through this crystal and force a sheet of material of one atom thick into the slit, a pair of parallel edge dislocations A and B of opposite signs, sometimes called an interstitial dipole, is produced as shown in Fig. 6. If we cut a

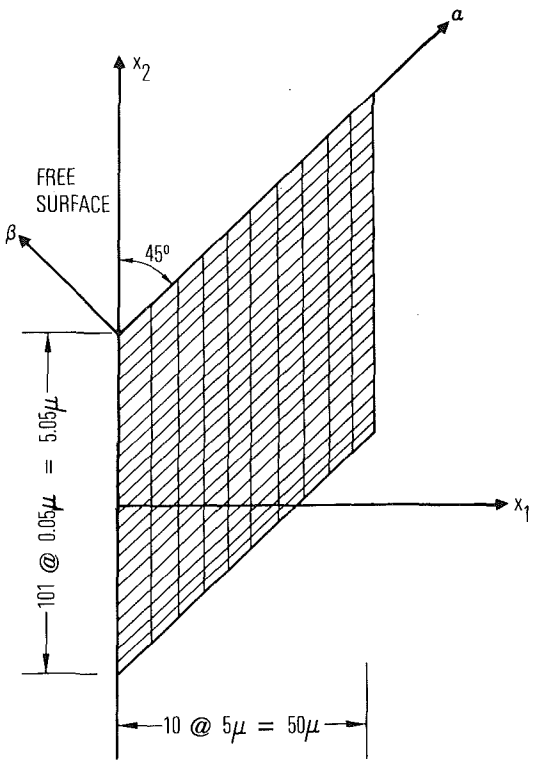

Fig. 7 Grids for numerical calculation

rectangular block shown by the dotted line, the free length of this block will be one atomic spacing more than the corresponding length of the block without this pair of dislocations, due to the presence of this inserted sheet. If there are n such dipoles in a length of N atomic spacings, this gives an inelastic strain $e^I_{\alpha\alpha}$ of n/N. Hence the initial direct inelastic strain can be caused by distributions of dipoles. The effect of dipoles on fatigue crack initiation is also shown by Mura and Tanaka [25].

Initiation of Extrusion and Intrusion

Again from the plane strain solution of a semi-infinite medium, the stress field caused by a given plastic strain $e^P_{\alpha\beta}$ in a parallelogram grid centered at $\mathbf{x}_r$ i.e., (x_{1_r}, x_{2_r}) shown in Fig. 7 was calculated. For numerical calculation, the crystal is divided into 1010 parallelogram grids oriented 45 deg to the free surface (10 grids along the x_1-axis and 101 along the x_2-axis. The relief of the resolved shear stress at $\mathbf{x}$ due to this $e^P_{\alpha\beta}$ is expressed as

$$\tau_{\alpha\beta}(\mathbf{x}) = 2GC(\mathbf{x},\alpha\beta;\ \mathbf{x}_r,\alpha\beta)\quad e^P_{\alpha\beta}(\mathbf{x}_r) \tag{11}$$

where $C(\mathbf{x},\alpha\beta;\mathbf{x}_r;\alpha\beta)$ is the resolved shear stress $\tau_{\alpha\beta}/2G$ at $\mathbf{x}$ due to unit plastic shear strain $e^P_{\alpha\beta}$ at $\mathbf{x}_r$. Here this is called the resolved shear stress influence coefficient. This influence coefficient varies with the dimensions of the grid. For a small thickness-length ratio, this coefficient varies linearly with thickness. These influence coefficients were calculated for the grid dimensions as shown in Fig. 7. The detail calculation of this coefficient is given in reference [26].

The material considered is pure aluminum polycrystal subject to alternate tension and compression applied along the x_2-axis. The resolved shear stress in the most favorably oriented slip system due to the applied cyclic stress τ_0 is the same for all points in the medium.

$$\tau^A_{\alpha\beta}(\mathbf{x}) = \tau_0/2 \tag{12}$$

The plastic strain e^P_{ij} varies from point to point in the slices P

Downloaded 02 May 2010 to 171.66.16.246. Redistribution subject to ASME license or copyright; see http://www.asme.org/terms/Terms_Use.cfm

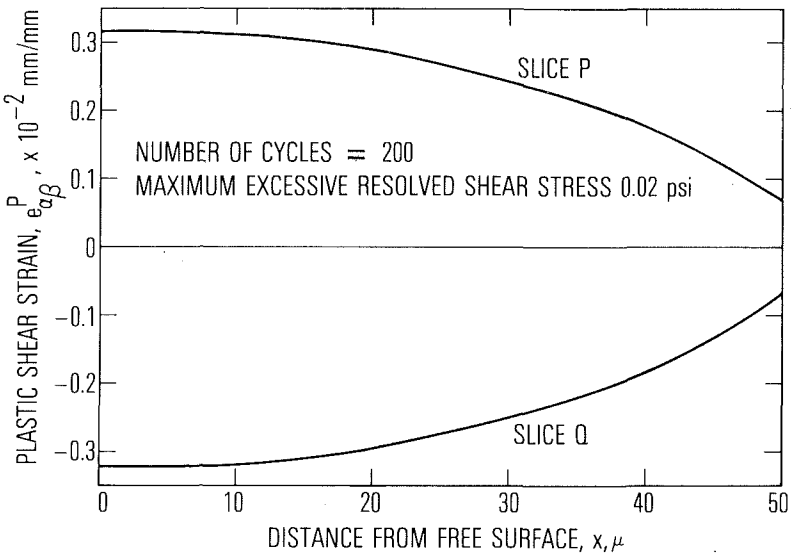

Fig. 8 Plastic shear strain distributions

and Q. After slip occurs, there is a residual shear stress. The total resolved shear stress is the sum of the applied, initial, and residual resolved shear stress, i.e.,

$$\tau_{\alpha\beta}(\mathbf{x}) = \frac{\tau_0}{2} + \tau^I_{\alpha\beta}(\mathbf{x}) - 2G\sum_n C(\mathbf{x},\alpha\beta;\mathbf{x}_n,\alpha\beta)e^P_{\alpha\beta\,n} \tag{13}$$

where $\mathbf{x}_n$ denotes center point and $e^P_{\alpha\beta\,n}$ the plastic strain of the nth grid which slides. It should be noted that the repetition of the subscripts $\alpha\beta$ in the preceding equations does not denote summation. The initial stress field does not change with loading, so that $d\tau^I_{\alpha\beta}(\mathbf{x})/d\tau_0 = 0$. Then

$$\frac{d\tau_{\alpha\beta}(\mathbf{x})}{d\tau_0} = \frac{1}{2} - 2G\sum_n C(\mathbf{x},\alpha\beta;\mathbf{x}_n,\alpha\beta)\frac{de^P_{\alpha\beta\,n}}{d\tau_0} \tag{14}$$

Those grids in which the magnitude of the resolved shear stress is less than the critical shear stress τ^C are referred to as nonactive slip grids. If the sth grid with centroid at $\mathbf{x}_s$ is one of these grids, its increment in plastic strain is zero:

$$|\tau_{\alpha\beta_s}| < \tau^C, \quad \Delta e^P_{\alpha\beta\,s} = 0 \tag{15}$$

In the region currently sliding, the magnitude of the resolved shear stress equals the critical shear stress:

$$|\tau_{\alpha\beta_n}| = \tau^C, \quad |\Delta e^P_{\alpha\beta\,n}| > 0 \tag{16}$$

where x_n denotes the centroid of a sliding grid.

The macroscopic plastic strain of the crystal represents the averge value in the crystal. Since slip is highly concentrated in the thin slices, the macroscopic plastic strain is much less than the local plastic strain. The rate of strain-hardening in terms of the local plastic strain is hence much less than that in terms of macroscopic strain. To simplify the calculation, this local strain-hardening is neglected: $d\tau_{\alpha\beta_n}/d\tau_0 = d\tau_c/d\tau_0 = 0$. Equation (14) then gives the following set of equations for each sliding grid:

$$2G\sum_n C(\mathbf{x}_m,\alpha\beta;\mathbf{x}_n,\alpha\beta)\frac{de^P_{\alpha\beta\,n}}{d\tau_0} = \frac{1}{2} \tag{17}$$

where $(\mathbf{x}_m)$ and $(\mathbf{x}_n)$ represent centroids of sliding grids. There are as many nonzero unknowns $de^P_{\alpha\beta\,n}/d\tau_0$ as there are equations. The plastic strain increment $\Delta e^P_{\alpha\beta\,n}$ in sliding grids for an increment of applied stress $\Delta\tau_0$ can readily be determined from the value of $de^P_{\alpha\beta\,n}/d\tau_0$. Substitution of $de^P_{\alpha\beta\,n}/d\tau_0$ into equation (14) yields the rate of change of the resolved shear stress at all grids. From the known value of $\tau_{\alpha\beta}(\mathbf{x})$ at the nonactive grids and the corresponding values of $d\tau_{\alpha\beta}(\mathbf{x})/d\tau_0$, the increments in τ_0 required to activate each nonactive grid can be calculated and compared. The minimum of these increments in τ_0 is applied, resulting in one additional active slip grid for the next load increment. During the reversed loading, the incremental applied stress τ_0 required for a new grid to slide can similarly be determined.

Since the extrusion thickness has been observed to be about 0.1μ for aluminum crystals, the center distance between slices P and Q measured along the x_2-axis is taken to be 0.1μ. For the present study, the critical shear stress τ^C is taken to be 368.7KN/m^2 (53.5 psi), the shear modulus G to be 26.5KN$\times 10^6$/m^2 (3.85×10^6 psi), and the elastic Poisson ratio to be 0.3. These values correspond approximately to those for pure aluminum [27]. The relief of the resolved shear stress due to plastic strain in the slid grid is taken to be given by that at the centroid of the grid. The buildup of local plastic strain in P and Q is calculated for an applied stress τ_0 of $\pm$689.5KN/m^2($\pm$100 psi) along the x_2-direction. One initial stress field is shown in Fig. 5 which gives a positive resolved shear stress of 27.5KN/m^2(4 psi) in P and a negative resolved shear stress of $-$ 27.5KN/m^2($-$4 psi) in Q. The excessive resolved shear stress, defined as $\Delta\tau \equiv \tau^I_{\alpha\beta} + \tau^A_{\alpha\beta} - \tau^C$, is to be relieved by plastic strains in the slid grids. The maximum excessive resolved shear stress in P for this initial stress field is 3.45KN/m^2(0.5 psi).

Four other initial resolved stress fields with the same distribution and with excessive resolved shear stress in P of 1.38, 0.609, 0.304 and 0.138KN/m^2 (0.2, 0.1, 0.05 and 0.02 psi), respectively, were also computed. The buildup of plastic strain at the free surface for these five initial stress fields at various cycles of loading were calculated. These plastic strains are approximately proportional to the number of cycles and proportional to the excessive resolved shear stresses. The plastic strain distribution in P and Q along the length of the slice is shown in Fig. 8 for the initial stress field with the maximum excessive resolved shear stress of 0.138KN/m^2(0.02 psi) at the end of 200 cycles. The local plastic strain buildup at the free surface is more than three times faster than that at the interior [24]. Hence, in general, fatigue cracks are initiated from the free surface. The amount of the local plastic strain buildup at the free surface is an indication of extrusion and intrusion; hence it is also a measure of crack initiation in the early fatigue damage.

Downloaded 02 May 2010 to 171.66.16.246. Redistribution subject to ASME license or copyright; see http://www.asme.org/terms/Terms_Use.cfm

Conclusion

A micromechanic model for local plastic strain buildup in a slip band of an aluminum polycrystal under cyclic tension-compression loading was described. This model explains the monotonic increase of plastic shear strain in two distinct but adjacent slip lines, leading to the initial formation of extrusion or intrusion observed in many fatigue tests. The existence of a natural gating mechanism in which the residual microstress field inhibits reversal of slip in the same slip line under fatigue loading is fully demonstrated. *An initial stress field causing such a gating mechanism was computed based on an inelastic strain field resulting from material imperfections such as dislocated dipoles.*

The amount of plastic strain buildup at the free surface is an indication of the degree of extrusions or intrusions, and hence is taken as a measure of the fatigue crack initiation. The quantitative calculation shows that the initial buildup of local plastic strains is proportional to the number of loading cycles, and to the initial excessive resolved shear stress. Essentially the same results were obtained when compared to the previous computation based on an assumed simple initial stress [17]. The present initial stress field explicitly satisfies the conditions of compatibility and equilibrium. The slip distribution calculated in this analysis also satisfies these conditions, as well as the dependency of slip on the resolved shear stress throughout the metal at all stages of cyclic loading.

References

1 Gough, H. J., Wright, S. J., and Hanson, D., "Some Further Experiments on the Behavior of Single Crystals of Aluminum Under Reversed Torsional Stresses," *J. Inst. Met.*, Vol. 36, 1926, pp. 173–188.

2 Gough, H. J., and Cox, H. L., "The Mode of Deformation of a Single Crystal of Silver," *J. Inst. Met.*, Vol. 45, 1931, pp. 71–88.

3 Gough, H. J., "Crystalline Structure in Relation to Failure of Metals—Especially by Fatigue," *Proc. Amer. Soc. Test. Mater.*, Vol. 33, 1933, pp. 3–114.

4 Finney, J. M., and Laird, C., "Strain Localization in Cyclic Deformation of Copper Single Crystals," *The Philosphical Magazine*, Vol. 31, 1975, pp. 339–366.

5 Woods, P. J., "Low-Amplitude Fatigue of Copper and Copper-Sat. % Aluminum Single Crystals," *The Philosphical Magazine*, Vol. 28, 1973, pp. 155–191.

6 Winter, A. T., "A Model for the Fatigue of Copper at Low Plastic Strain Amplitudes," *The Philosophical Magazine*, Vol. 30, 1974, pp. 719–738.

7 Charsley, P., and Thompson, N., "The Behavior of Slip Lines on Aluminum Crystals Under Reversed Stresses in Tension and Compression," *The Philosophical Magazine*, Vol. 8, 1963, pp. 77–85.

8 Buckley, S. N., and Entwistle, K. M., "The Bauschinger Effect in Super Pure Aluminum Single Crystals and Polycrystals," *Acta. Metall.*, Vol. 4, 1956, pp. 352–361.

9 Forsyth, P. J. E., "Some Further Observations on the Fatigue Process in Pure Aluminum," *J. Inst. Met.*, Vol. 82, 1954, pp. 449–454.

10 Wood, W. A., and Bendler, A. M., "The Fatigue Process in Copper as Studied by Electron Metallography," *Trans. Metallurgical Society AIME*, Vol. 224, 1962, pp. 180–186.

11 Wood, W. A., "Mechanism of Fatigue," *Fatigue in Aircraft Structures*, Freundenthal, A. F., ed., Academic Press, New York, 1956, pp. 1–19.

12 Forsyth, P. J. E., "Exudation of Material from Slip Bands at the Surface of Fatigued Crystals of an Aluminum-Copper Alloy," *Nature*, Vol. 171, 1953, pp. 172–173.

13 Cottrell, A. H., and Hull, D., "Extrusion and Intrusion by Cyclic Slip in Copper," *Proc. Roy. Soc.*, London, Series *A*, Vol. 242, 1957, pp. 211–213.

14 Grosskreutz, J. C., "The Mechanisms of Metal Fatigue," *Physica Status Solidi (b)*, Vol. 47, 1971, pp. 359–396.

15 Laird, C., and Duquette, D. J., "Mechanisms of Fatigue Crack Nucleation," *Corrosion Fatigue*, Devereux, O. F., McEvily, A. J., and Staehle, R. W., eds., NACE-2, 1972, pp. 88–117.

16 Lin, T. H., and Ito, M., "Slip Distribution in a Thin Slice of a Crystal at a Free Surface," *J. Appl. Phys.*, Vol. 3, 1967, pp. 775–780.

17 Lin, T. H., and Ito, Y. M., "Mechanics of a Fatigue Crack Nucleation Mechanism," *J. Mech. Phys. Solids*, Vol. 17, 1969, pp. 511–523.

18 Lin, T. H., and Lin, S. R., "Fatigue Crack Initiation With Creep," *Proc. Int. Symp. on Defects and Fracture*, Tuscno, Poland, 1980.

19 Lin, T. H., "Micromechanics of Deformation of Slip Bands Under Monotonic and Cyclic Loading," *Reviews on the Deformation Behavior of Materials*, Feltham, P., ed., Vol. II, 1977, pp. 263–316.

20 Eshelby, J. D., "The Determination of the Elastic Field on an Ellipsoidal Inclusion and Related Problems," *Proc. Roy. Soc.*, London, Series *A*, Vol. 241, 1957, pp. 376–396.

21 Eshelby, J. D., "The Elastic Field Outside an Ellipsoidal Inclusion," *Proc. Roy. Soc.*, London, Series *A*, Vol. 252, 1959, pp. 561–569.

22 Lin, T. H., *Theory of Inelastic Structures*, Wiley, New York, 1968.

23 Lin, T. H., and Lin, S. R., "Micromechanics Theory of Fatigue Crack Initiation Applied to Time Dependent Fatigue," *ASTM STP675*, American Society for Testing and Materials, 1979, pp. 707–728.

24 Lin, T. H., and Ito, Y. M., "Slip Distribution in a Thin Slice of a Crystal at a Free Surface," *J. Appl. Phys.*, Vol. 3, 1967, pp. 775–780.

25 Mura, T., and K. Tanaka, "Dislocation Dipole Models for Fatigue Crack Initiation," *Proc. Mechanics of Fatigue*, Applied Mech. Div., Vol. 47, ASME, 1981.

26 Lin, S. R., "Effect of Secondary Slip Systems on Early Fatigue Damage," Ph.D. Dissertation, University of California, Los Angeles, 1971, also published in *J. Mech. Phys. Solids*, Vol. 22, 1974, pp. 177–191.

27 Wu, T. T., "A Note on the Early Deformation of Aluminum Crystals in Simple Tension," ASME JOURNAL OF APPLIED MECHANICS, Vol. 31, 1964, pp. 711–713.

Downloaded 02 May 2010 to 171.66.16.246. Redistribution subject to ASME license or copyright; see http://www.asme.org/terms/Terms_Use.cfm

J. W. Nicholson
Assistant Professor,
Department of Theoretical
and Applied Mechanics,
University of Illinois at Urbana-Champaign,
Urbana, Ill. 61801
Assoc. Mem. ASME

S. T. Weidman
Graduate Student.

J. G. Simmonds
Professor.
Assoc. Mem. ASME

Department of Applied Mathematics
and Computer Science,
University of Virginia,
Charlottesville, Va. 22901

Sanders' Energy-Release Rate Integral for a Circumferentially Cracked Cylindrical Shell

Analytical and numerical values for Sanders' path-independent energy-release rate integral I and the combined stress-intensity factor are obtained for a circumferentially through-cracked cylindrical shell. Two types of loadings are considered. First, the shell is subject to axial tension and, second, the shell is subject to edge moments. New procedures for evaluating I from the governing integral equations are presented. In particular, for a very thin shell subject to edge moments, a method of evaluating I by circumventing the solution of the integral equations is shown.

Introduction

Recently, Sanders' path-independent energy-release rate integral I [1] has been specialized to an arbitrarily loaded shallow shell containing a stress-free void and has been used to define and compute a "combined" stress-intensity factor for a bent cylindrical shell with an *axial* through-crack [2]. Also, the combined stress-intensity factor for a closed cylindrical shell with an axial through-crack subject to internal pressure has been computed [3, 4]. Furthermore, I has been shown to be a generalization of the more familiar path-independent integrals for plates J, L, and M [5].

In this paper we calculate I for two companion problems to those considered in [2] and [3]. We will compute the combined stress-intensity factors for a linearly elastic, isotropic, cylindrical shell with a circumferential through-crack subject to two different types of loading. The length of the crack $2c$ is assumed to be small compared to the radius of the shell R so that shallow shell theory is valid. For a cracked shell, I depends on Poisson's ratio ν and the dimensionless crack length

$$\lambda=\left[\frac{3}{4}(1-\nu^2)\right]^{1/4} c/\sqrt{Rh} \tag{1}$$

where h is the shell thickness. All positive values of λ are of interest. For c fixed, $\lambda<<1$ implies the shell is nearly flat while $\lambda>>1$ implies the shell is very thin. I can also be shown to be related to the so-called stretching stress-intensity factor S and bending stress-intensity factor B through the relation

$$\frac{I(\lambda,\nu)}{2\pi}=C^2(\lambda,\nu)=S^2(\lambda,\nu)+\frac{B^2(\lambda,\nu)}{(3+\nu)(1-\nu)}. \tag{2}$$

$C(\lambda, \nu)$ is the combined stress-intensity factor and exhibits the coupling between stretching and bending in a shell.

One problem considered consists of a long closed cylindrical shell, with a circumferential crack, under internal pressure p. The internal pressure produces axial tension that acts to open the crack. We will refer to this problem as the "stretching problem." The second problem under consideration consists of an open cylindrical shell, with a circumferential crack, subject to uniform moments along its edges. If the axis of the cylinder is in the x_1 direction and the crack lies along the x_2 axis then the moments applied along edges of the shell parallel to the x_1-x_2 axes are $M_{11}=M_0$, $M_{22}=\nu M_0$ where M_0 is some reference moment. The boundary conditions allow an uncracked shell to maintain a uniform cross section parallel to the x_2 axis. We will refer to this problem as the "bending problem."

The stretching problem has been considered previously by Folias [6], Erdogan and Ratwani [7], Duncan-Fama and Sanders [8], Murthy, Rao, and Rao [9], and Lakshminarayana and Murthy [10] for relatively small λ. Here we consider the full range of λ. In addition, a concurrent analysis of the circumferentially cracked general cylindrical shell under axial tension has been performed by Sanders [11]. We thank Professor Sanders for allowing us to see his analysis prior to publication. This is the first consideration of a bent cylindrical shell with a circumferential crack.

For both the stretching problem and bending problem our analysis is split into three parts. For $\lambda<<1$, a standard perturbation expansion in λ is obtained for $C(\lambda, \nu)$. For

Contributed by the Applied Mechanics Division for presentation at the 1983 ASME Applied Mechanics, Bioengineering, and Fluids Engineering Conference, Houston, Texas, June 20-22, 1983 of THE AMERICAN SOCIETY OF MECHANICAL ENGINEERS.

Discussion on this paper should be addressed to the Editorial Department, ASME, United Engineering Center, 345 East 47th Street, New York, N.Y. 10017, and will be accepted until two months after final publication of the paper itself in the JOURNAL OF APPLIED MECHANICS. Manuscript received by ASME Applied Mechanics Division, July, 1982; final revision, January, 1983. Paper No. 83-APM-32.

Copies will be available until July, 1984.

Copyright © 1983 by ASME
Downloaded 02 May 2010 to 171.66.16.246. Redistribution subject to ASME license or copyright; see http://www.asme.org/terms/Terms_Use.cfm

$\lambda = O(1)$ numerical results are reported. Lastly, for $\lambda >> 1$ asymptotic solutions are obtained. Graphs for $C(\lambda, 0.3)$ are displayed.

The analysis of the cylindrically cracked shell is sufficiently different from that of the axially cracked cylindrical shell to provide a nontrivial application of the methods reported in [2] and [3]. In particular, the asymptotic form of the governing equations and computation of $C(\lambda, \nu)$ for $\lambda >> 1$ demonstrate new procedures. For the stretching problem the asymptotic form of the governing integral equations are solved with the use of delta functions and the I integral is subsequently evaluated. For the bending problem we are able to *directly* evaluate the I integral for the asymptotic form of the governing equations without actually solving them.

We consider only the nondimensionalized form of these problems as defined in [2]. To dimensionalize I for the stretching problem use

$$\bar{I} = \frac{4Eh}{cp^2R^2} I.$$

To dimensionalize I for the bending problem use

$$\bar{I} = \frac{D}{cM_0^2} I$$

where $D = Eh^3/[12(1-\nu^2)]$ is the bending stiffness of the shell.

Sanders' Energy-Release Rate Integral

We begin with the nondimensionalized governing equations for a linearly elastic, isotropic, shallow shell [2]. For a cylindrical shell of radius R under internal pressure p these are:

$$N_{\alpha\beta,\beta} = 0, \tag{3a}$$

$$M_{\alpha\beta,\alpha\beta} + 4\lambda^2 (z_{,\alpha\beta} N_{\alpha\beta} + p) = 0, \tag{3b}$$

$$\frac{1}{2}(u_{\alpha,\beta} + u_{\beta,\alpha}) - 4\lambda^2 z_{,\alpha\beta} w = (1+\nu) N_{\alpha\beta} - \nu\delta_{\alpha\beta} N_{\gamma\gamma}, \tag{3c}$$

$$M_{\alpha\beta} = -(1-\nu) w_{,\alpha\beta} - \nu\delta_{\alpha\beta} w_{,\gamma\gamma} \tag{3d}$$

where

$$z_{,11} = z_{,12} = 0, \quad z_{,22} = 1. \tag{4}$$

Linearity of the governing equations and a stress-free crack allows the analysis of the cracked shell to be split into the consideration of the uncracked shell and the residual problem. The residual problem consists of the analysis of the shell with a crack subject to stresses equal and opposite to those in the uncracked shell.

For the stretching problem the nonzero stress resultants and displacements for the uncracked shell found by solving equations (3) and appropriate boundary conditions are

$$N_{11}^o = 1, \quad u_1^o = x_1, \quad w^o = \nu\lambda^{-2}, \tag{5}$$

where the superscript "o" indicates the uncracked shell. For the bending problem we find that

$$M_{11}^o = 1, M_{22}^o = \nu, w^o = -\frac{1}{2}x_2^2, u_2^o = -\frac{2}{3}\lambda^2 x_2^3. \tag{6}$$

In [2] Sanders' path-independent, energy release rate integral was derived for an arbitrarily loaded shallow shell containing a stress-free void. Two forms of I exist for the cracked shell. One is an integral along the crack. The other is an integral over circles of vanishing radius centered at the crack tips.

Starting with equation (29) of [2] and noting that the void is a crack running from -1 to 1 along the x_2 axis we obtain the first form of I as

$$I(\lambda,\nu) = \frac{1}{2}\int_{-1}^{1} \{N_{11}^o[2u_1 + \lambda\dot{u}_1] + N_{12}^o[2u_2 + \lambda\dot{u}_2] + (Q_1^o + M_{12,2}^o)[3w + \lambda\dot{w}] - M_{11}^o[2w_{,1} + \lambda\dot{w}_{,1}]\} dx_2 \tag{7}$$

where a dot denotes differentiation with respect to λ and the brackets denote the jump across the crack of the enclosed quantity, i.e.,

$$[f](x) = \lim\{f(x,\epsilon) - f(x,-\epsilon)\} \quad \text{as} \quad \epsilon \to 0.$$

Using equations (5) and (6) we see that I reduces to

$$I^s(\lambda,\nu) = \int_{-1}^{1} \left[u_1 + \frac{1}{2}\lambda\dot{u}_1\right] dx_2 \tag{8}$$

for the stretching problem and

$$I^b(\lambda,\nu) = -\frac{1}{2}\int_{-1}^{1} [2w_{,1} + \lambda\dot{w}_{,1}] dx_2 \tag{9}$$

for the bending problem. Where necessary the superscripts "s" and "b" will be used to denote, respectively, a stretching problem quantity or a bending problem quantity.

The second form of I is used to relate I to the stress-intensity factors. Start with equation (45) of [2] and integrate around a contour that consists of two straight lines $|x_2| \le 1 - \delta$, $x_1 = \pm 0$ and two circles of radius δ centered at the crack tips. It can be shown that the crack-tip stresses and displacements are given by the usual asymptotic square root expressions for a plate (see Chapter 4 of [12]). Letting $\delta \to 0$ we obtain equation (2) which is the same relationship between the energy release rate and stress-intensity factors as for an axially cracked shell.

The Residual Problem

For the two problems considered here the residual boundary value problems are given by equations (3) and (4) and boundary conditions

$$N_{11}(\pm 0, x_2) = A, \tag{10a}$$

$$N_{12}(\pm 0, x_2) = 0, \tag{10b}$$

$$w_{,11}(\pm 0, x_2) + \nu w_{,22}(\pm 0, x_2) = B, \tag{10c}$$

$$(2-\nu) w_{,221}(\pm 0, x_2) + w_{,111}(\pm 0, x_2) = 0, \quad |x_2| < 1, \tag{10d}$$

where $A = -1$, $B = 0$ for the stretching problem and $A = 0$, $B = -1$ for the bending problem. Also, all stresses must vanish as $r \to \infty$.

The governing equations and boundary conditions can be reduced to two coupled singular integral equations by using double Fourier transforms (see, for example, references [13] and [2]). Specializing the results of [13] to the problems at hand we have

$$\int_{-1}^{1} K_{21}(y-t) F_1(t;\lambda,\nu)\, dt + \int_{-1}^{1} \{K_{22}(y-t) + 4\lambda^2 L_2^+(y-t)\} F_2(t;\lambda,\nu)\, dt = A, \tag{11}$$

$$\int_{-1}^{1} K_{31}(y-t) F_1(t;\lambda,\nu)\, dt + \int_{-1}^{1} \{K_{32}(y-t) + 4\lambda^2 L_3^+(y-t)\} F_2(t;\lambda,\nu)\, dt = B, \quad |y| < 1, \tag{12}$$

where

$$L_2^+(y) = -\frac{1}{2}\Re\{g_{,yy}(0,y-1) + g_{,yy}(0,y+1)\}, \tag{13a}$$

$$L_3^+(y) = \frac{(1+\nu)}{2}\Im\{g_{,yy}(0,y-1) + g_{,yy}(0,y+1)\}, \tag{13b}$$

$$K_{21}(y) = \Re\{g_{,yyy}(0,y)\}, \tag{13c}$$

$$K_{22}(y) = (1+\nu)\Im\{g_{,yyy}(0,y)\} - 4\lambda^2\Re\{g_{,y}(0,y)\}. \tag{13d}$$

$$K_{31}(y) = -(1+\nu)\Im\{g_{,yyy}(0,y)\}, \tag{13e}$$

Downloaded 02 May 2010 to 171.66.16.246. Redistribution subject to ASME license or copyright; see http://www.asme.org/terms/Terms_Use.cfm

$$K_{32}(y) = -(3+\nu)(1-\nu)\,\Re\{g_{,yyy}(0,y)\} + 4\lambda^2\nu\,\Im\{g_{,y}(0,y)\}. \quad (13f)$$

As usual, $\Re$ and $\Im$ denote, respectively, the "real part of" and the "imaginary part of" and $\dot{+}$ denotes the Cauchy principal value of the integral. The unknowns in the integral equations are related to stress resultants and displacements through

$$F_1(x_2;\lambda,\nu) = \int_0^{x_2} [N_{22,1}](t)\,dt, \quad (14)$$

$$F_2(x_2;\lambda,\nu) = -[w_{,21}](x_2). \quad (15)$$

Occasionally, for compactness, we will omit some or all of the arguments of F_1, F_2 and other quantities. The quantity g is the fundamental solution for a shallow cylindrical shell satisfying

$$\Delta\Delta g - 4i\lambda^2 g_{,11} = \delta(x_1)\delta(x_2). \quad (16)$$

Explicit representations for the needed derivatives of g can be obtained from Sanders and Simmonds [14]. They are:

$$4\pi\, g_{,y}(0,y) = (\text{sgny}) i^{1/2}\left\{\frac{\pi}{2} - \int_\rho^\infty K_0(z)\,dz\right\}, \quad (17a)$$

$$4\pi\, g_{,yy}(0,y) = -K_0(\rho), \quad (17b)$$

$$4\pi\, g_{,yyy}(0,y) = i^{1/2}\lambda(\text{sgny}) K_1(\rho) \quad (17c)$$

where $\rho = i^{1/2}\lambda|y|$, K_0 and K_1 are modified Bessel functions, and $i^{1/2}$ is short for $e^{i\pi/4}$. Asymptotic expansions and series expansions for $g_{,y}$, $g_{,yy}$, and $g_{,yyy}$ are needed for the approximate solution of (11) and (12). These are readily obtainable for K_0 and K_1 [15]. Asymptotic expressions for the integral of $K_0(z)$ in $g_{,y}(0,y)$ are obtainable by integrating asymptotic expansions for $K_0(z)$ ([16] or [17]).

The solution of the integral equations have the form

$$F_\alpha(t;\lambda,\nu) = (1-t^2)^{-1/2} G_\alpha(t;\lambda,\nu), \quad |t|<1, \quad \alpha = 1,2, \quad (18)$$

where the G_α are continuous [2]. This representation is used in analytic and numeric work.

I in Terms of F_1 and F_2

The equations for a cylindrical shell can be used to show that

$$u_{2,21} - 4\lambda^2 w_{,1} = N_{22,1} + \nu N_{12,2}, \quad (19)$$

$$(1+\nu)N_{12} = \frac{1}{2}(u_{1,2} + u_{2,1}). \quad (20)$$

Evaluating the jump of each side of these equations across the crack and using the boundary conditions (10) for the stretching problem reveals that

$$[u_{2,21}] - 4\lambda^2[w_{,1}] = [N_{22,1}], \quad (21)$$

$$[u_{1,2}] + [u_{2,1}] = 0. \quad (22)$$

Thus

$$[u_{1,22}] + 4\lambda^2[w_{,1}] = -[N_{22,1}]. \quad (23)$$

Integration with respect to x_2 and noting that $[u_{1,2}] = 0$ at $x_2 = 0$ yields

$$[u_{1,2}] + 4\lambda^2 \int_0^{x_2} [w_{,1}]\,(t)\,dt = -F_1. \quad (24)$$

Integrate by parts to obtain

$$F_1 = -[u_{1,2}] - 4\lambda^2 x_2 [w_{,1}] - 4\lambda^2 \int_0^{x_2} tF_2\,(t)\,dt. \quad (25)$$

Now, integration by parts and continuity of the shell at $x_2 = \pm 1$ implies

$$\int_{-1}^{1} [u_1]dx_2 = -\int_{-1}^{1} x_2 [u_{1,2}]dx_2. \quad (26)$$

So, using (25),

$$\int_{-1}^{1} [u_1]dt = \int_{-1}^{1} \{t\,F_1 + 4\lambda^2 t^2 [w_{,1}]\}dt + 4\lambda^2 \int_{-1}^{1} t\left(\int_0^t \xi\,F_2 d\xi\right)dt. \quad (27)$$

Integration by parts results in

$$\int_{-1}^{1} [u_1]dt = \int_{-1}^{1} tF_1\,dt + 2\lambda^2 \int_{-1}^{1} \left(t - \frac{t^3}{3}\right)F_2\,dt. \quad (28)$$

Finally, differentiating (28) with respect to λ and collecting results we have Sanders' energy-release rate for the stretching problem in terms of the unknowns F_1 and F_2;

$$I^s(\lambda,\nu) = \int_{-1}^{1} t\left(F_1 + \frac{1}{2}\lambda\dot{F}_1\right)dt + 2\lambda^2 \int_{-1}^{1} \left(t - \frac{t^3}{3}\right)\left(2F_2 + \frac{1}{2}\lambda\dot{F}_2\right)dt. \quad (29)$$

For the bending problem, integration by parts and continuity of the shell at $x_2 = \pm 1$ implies

$$\int_{-1}^{1} [w_{,1}]dx_2 = -\int_{-1}^{1} x_2 [w_{,12}]dx_2 = \int_{-1}^{1} t\,F_2\,dt. \quad (30)$$

Differentiating (30) with respect to λ and collecting results we obtain

$$I^b(\lambda,\nu) = \int_{-1}^{1} t\left(F_2 + \frac{1}{2}\lambda\dot{F}_2\right)dt. \quad (31)$$

Perturbation and Numerical Solutions of the I.E.'s

For $\lambda << 1$ a perturbation solution in λ of the integral equations (11) and (12) may be obtained by the same procedures used previously in [18] or [13]. For the stretching problem we find that

$$F_1^s(x_2;\lambda,\nu) = \frac{4x_2}{(1-x_2^2)^{1/2}}\left(1 + \frac{\pi}{4}\lambda^2 + \ldots\right), \quad (32)$$

$$F_1^s(x_2;\lambda,\nu) = \frac{4x_2}{(1-x_2^2)^{1/2}}\left(\frac{\pi}{16}\lambda^2 + \ldots\right). \quad (33)$$

Thus, using (29) and (2) we see that

$$C^s(\lambda,\nu) = 1 + \frac{\pi}{16}\lambda^2 + \ldots \quad \text{for} \quad \lambda << 1. \quad (34)$$

For the bending problem we find that

$$F_2^b(x_2;\lambda,\nu) = \frac{-4x_2}{(3+\nu)(1-\nu)(1-x_2^2)^{1/2}}\left(1 - \frac{\pi(5+2\nu+\nu^2)}{16}\lambda^2 + \ldots\right) \quad (35)$$

(only F_2^b is needed in I^b). Thus, using (31) and (2)

$$C^b(\lambda,\nu) = \frac{1}{(3+\nu)(1-\nu)}\left(1 - \frac{(5+2\nu+\nu^2)\pi}{8(3+\nu)(1-\nu)}\lambda^2 + \ldots\right). \quad (36)$$

For $\nu = 0.3$.

$$C^b(\lambda,0.3) \cong 0.6580(1 - (0.4836)\lambda^2 + \ldots) \quad \text{for} \quad \lambda << 1. \quad (37)$$

For $\lambda = O(1)$ we have obtained numerical solutions of (11) and (12) for the stretching and bending problems by using the Lobatto-Chebyshev method used in the solution of other crack problems [19, 2, 3]. The only new aspect of this part of the work involves determining the asymptotic series for $g_{,y}(0,y)$. Accurate results for C^b and C^s up to $\lambda = 12$ were obtained. These are shown (for $\nu = 0.3$) as the solid lines in the figures.

Downloaded 02 May 2010 to 171.66.16.246. Redistribution subject to ASME license or copyright; see http://www.asme.org/terms/Terms_Use.cfm

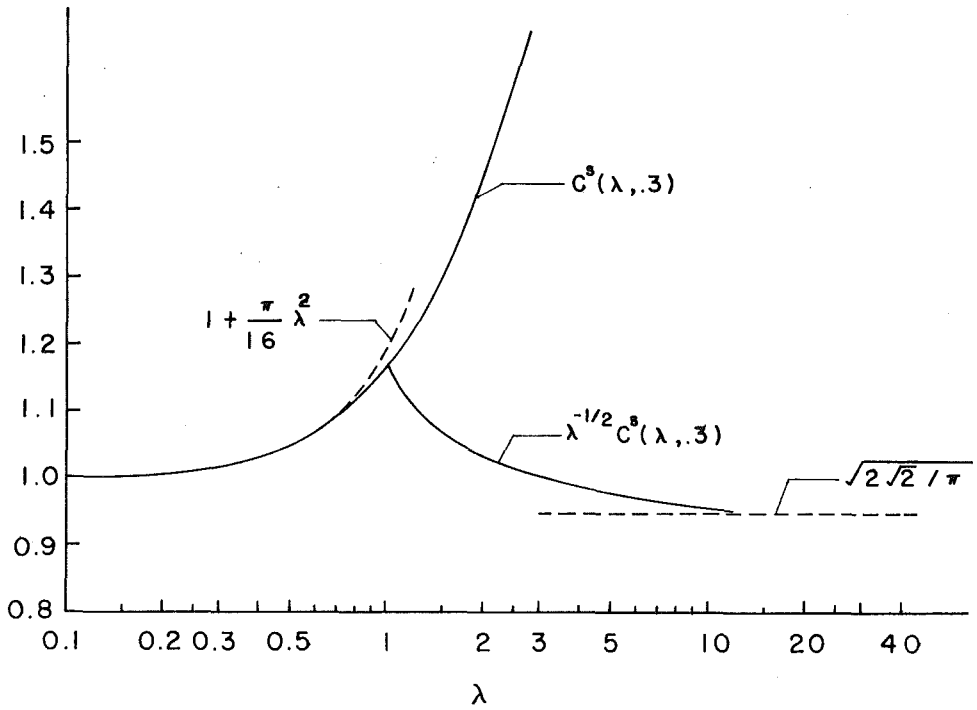

Fig. 1 Combined stress-intensity factor for stretching problem

Asymptotic Solutions for Large λ

To obtain asymptotic expressions for C^s and C^b as $\lambda\to\infty$ we modify the integral equations (11) and (12) to avoid singularities in the kernels as λ becomes large. Express the unknown F_1 in terms of displacements by substituting (25) into (11) and (12). Simplifying, we find alternate integral equations

$$-\int_{-1}^{1} \Re\{g_{,\eta\eta\eta}(0,\eta)\}\, f(t)\,dt + (1+\nu)\int_{-1}^{1} \Im\{g_{,\eta\eta\eta}(0,\eta)\}\, F_2(t)dt = A, \tag{38}$$

$$(1+\nu)\int_{-1}^{1} \Im\{g_{,\eta\eta\eta}(0,\eta)\}\, f(t)\,dt - (3+\nu)(1-\nu)\int_{-1}^{1} \Re\{g_{,\eta\eta\eta}(0,\eta)\}\, F_2(t)\,dt - 4\lambda^2\int_{-1}^{1} \Im\{g_{,\eta}(0,\eta)\}\, F_2(t)\,dt = B \tag{39}$$

where $\eta=y-t$, $f(t)=[u_{1,2}](t)$ and $|y|<1$. Note that for the stretching problem these are the integral equations of Duncan-Fama and Sanders [8]. To determine expressions for $f(t)$ for the stretching problem (which is sufficient to evaluate the leading term in the large-λ asymptotic expansion of C^s) we first integrate (38) and (39) with respect to y to obtain a more convenient form of the integral equations. Thus, noting that $K_0'(z)=-K_1(z)$ and that

$$K_0(i^{1/2}x)=ker(x)+i\,kei(x)$$

where *ker x* and *kei x* are Kelvin functions, we find that (38) and (39) become

$$-\frac{1}{4\pi}\int_{-1}^{1} ker\ |\lambda\eta|\, f(t)\,dt + \frac{(1+\nu)}{4\pi}\int_{-1}^{1} kei\ |\lambda\eta|\, F_2(t)\,dt = Ay + c_1(\lambda), \tag{40}$$

$$\frac{(1+\nu)}{4\pi}\int_{-1}^{1} kei\ |\lambda\eta|\, f(t)\,dt + \frac{(3+\nu)(1-\nu)}{4\pi}\int_{-1}^{1} ker\ |\lambda\eta|\, F_2(t)\,dt + 4\nu\int_{-1}^{1} \Im\{g(0,\lambda\eta)\}F_2(t)\,dt = By + c_2(\lambda). \tag{41}$$

Both of the Kelvin functions form delta sequences as $\lambda\to\infty$. To see this, consider

$$I_1 \equiv \frac{\lambda}{4\pi}\int_{-1}^{1} ker\ |\lambda y-\lambda t|\,dt. \tag{42}$$

Let $\sigma=\lambda y-\lambda t$ so that

$$I_1 = -\frac{1}{4\pi}\int_{\lambda(y-1)}^{\lambda(y+1)} ker\ |\sigma|\,d\sigma \to \frac{1}{4\pi}\int_{-\infty}^{\infty} ker\ |\sigma|\,d\sigma \tag{43}$$

as $\lambda\to\infty$, $|y|<1$. Now $\int_0^\infty ker\ \sigma\,d\sigma=\pi/2\sqrt{2}$, [13], and we see that

$$\frac{1}{4\pi}\int_{-1}^{1} ker\ |\lambda y-\lambda t|\,dt \to \frac{1}{4\sqrt{2}\lambda} \quad \text{as} \quad \lambda\to\infty. \tag{44}$$

Numerical evaluation of $ker\,|\lambda y-\lambda t|$ for increasing λ suggests that the function is tending to a spike about $y-t=0$ and that the area under the curve approaches $1/4\sqrt{2}\lambda$. Thus, we propose that

$$\frac{1}{4\pi}ker\ |\lambda y-\lambda t| \sim \frac{\delta(y-t)}{4\sqrt{2}\lambda} \quad \text{as} \quad \lambda\to\infty. \tag{45}$$

Similarly

$$\frac{1}{4\pi}kei\ |\lambda y-\lambda t| \sim -\frac{\delta(y-t)}{4\sqrt{2}\lambda} \quad \text{as} \quad \lambda\to\infty. \tag{46}$$

Substituting (45) and (46) into (40) we have (for the stretching problem)

Downloaded 02 May 2010 to 171.66.16.246. Redistribution subject to ASME license or copyright; see http://www.asme.org/terms/Terms_Use.cfm

$$-\int_{-1}^{1}\frac{\delta(y-t)}{4\sqrt{2}\lambda}f(t)\,dt$$

$$-(1+\nu)\int_{-1}^{1}\frac{\delta(y-t)}{4\sqrt{2}\lambda}F_2(t)\,dt\sim y+c_2(\lambda) \tag{47}$$

as $\lambda\to\infty$. Our numerical results for $\lambda=O(1)$ for the stretching problem suggest that as λ becomes large F_2 approaches an odd linear combination of delta functions. Following a suggestion made by J. L. Sanders [20] we let

$$F_2(t)=K(\lambda,\nu)[\delta(t-1)-\delta(t+1)] \tag{48}$$

in (47). Thus (since $y\neq\pm1$)

$$-\frac{f(y)}{4\sqrt{2}\lambda}\sim y+c_2(\lambda)\quad\text{as}\quad\lambda\to\infty. \tag{49}$$

By symmetry, $f_2(y)$ is an odd function of y so $c_2(\lambda)\equiv0$ and

$$[u_{1,2}](y)\sim-4\sqrt{2}\lambda y\quad\text{as}\quad\lambda\to\infty. \tag{50}$$

Using (8), (26), and (50) we find that

$$I^s(\lambda,\nu)\sim6\sqrt{2}\lambda\int_{-1}^{1}t^2dt=4\sqrt{2}\lambda\quad\text{as}\quad\lambda\to\infty. \tag{51}$$

So

$$C^s(\lambda,\nu)\sim\sqrt{2\sqrt{2}/\pi}\,\lambda^{1/2}\quad\text{as}\quad\lambda\to\infty. \tag{52}$$

Next, note that according to Sanders and Simmonds [14]

$$g(0,y)\sim\frac{i^{3/2}\,|y|}{8}\quad\text{as}\quad y\to\infty.$$

Thus, the asymptotic form of the integral equations (40) and (41) are

$$-\int_{-1}^{1}\frac{\delta(y-t)}{4\sqrt{2}\lambda}f(t)\,dt$$

$$-(1+\nu)\int_{-1}^{1}\frac{\delta(y-t)}{4\sqrt{2}\lambda}F_2(t)\,dt\sim c_1(\lambda), \tag{53}$$

$$-(1+\nu)\int_{-1}^{1}\frac{\delta(y-t)}{4\sqrt{2}\lambda}f(t)\,dt$$

$$+(3+\nu)(1-\nu)\int_{-1}^{1}\frac{\delta(y-t)}{4\sqrt{2}\lambda}F_2(t)\,dt$$

$$-\int_{-1}^{1}\frac{\lambda|y-t|}{2\sqrt{2}}F_2(t)\,dt\sim-y+c_2(\lambda) \tag{54}$$

as $\lambda\to\infty$. By assuming continuity of $f(t)$ and $F_2(t)$ equation (53) implies that

$$\frac{f(y)}{4\sqrt{2}\lambda}+\frac{(1+\nu)}{4\sqrt{2}\lambda}F_2(y)\sim-c_1(y)\quad\text{as}\quad\lambda\to\infty,\quad|y|<1. \tag{55}$$

Both $f(y)$ and $F_2(y)$ are odd so $c_1(y)\equiv0$ and

$$f(y)\sim-(1+\nu)F_2(y)\quad\text{as}\quad\lambda\to\infty. \tag{56}$$

Substituting (56) into (54) we obtain

$$\frac{(1+\nu)^2}{4\sqrt{2}\lambda}\int_{-1}^{1}\delta(y-t)F_2(t)\,dt$$

$$+\frac{(3+\nu)(1-\nu)}{4\sqrt{2}\lambda}\int_{-1}^{1}\delta(y-t)F_2(t)\,dt$$

$$-\frac{\lambda}{2\sqrt{2}}\int_{-1}^{1}|y-t|\,F_2(t)\,dt=-y+c_2(\lambda). \tag{57}$$

The last term on the left-hand side of (57) dominates as $\lambda\to\infty$ which implies that

$$\frac{\lambda}{2\sqrt{2}}\int_{-1}^{1}|y-t|\,F_2(t)\,dt\sim y-c_2(\lambda). \tag{58}$$

If $y=0$ then

$$\frac{\lambda}{2\sqrt{2}}\int_{-1}^{1}|t|\,F_2(t)\,dt\sim-c_2(\lambda) \tag{59}$$

which implies that $c_2(\lambda)\equiv0$. So

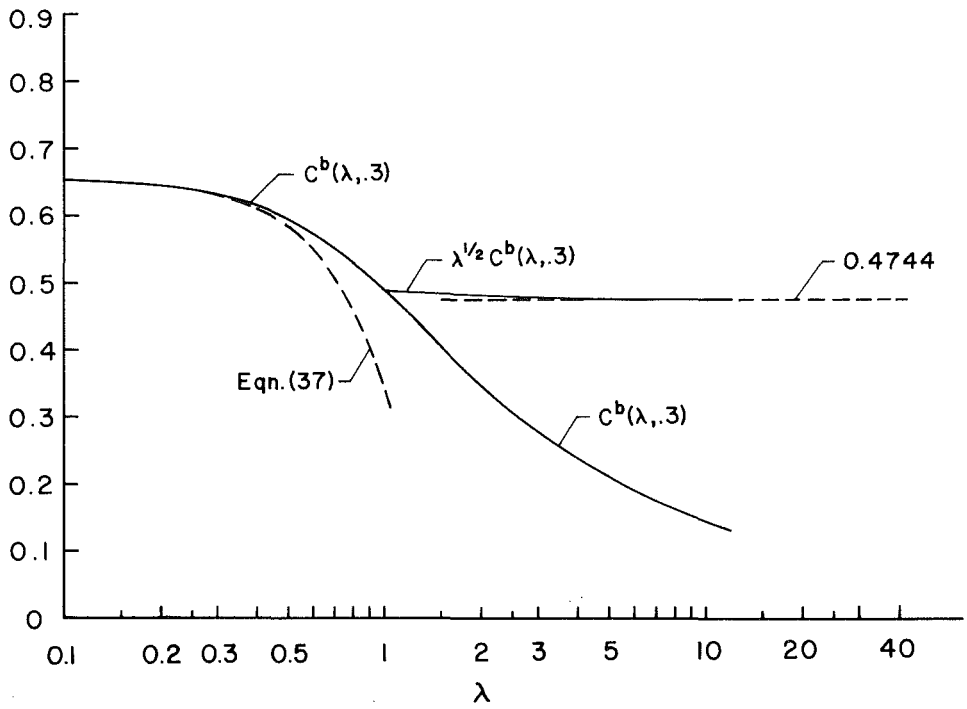

Fig. 2 Combined stress-intensity factor for bending problem

Downloaded 02 May 2010 to 171.66.16.246. Redistribution subject to ASME license or copyright; see http://www.asme.org/terms/Terms_Use.cfm

$$\frac{\lambda}{2\sqrt{2}}\int_{-1}^{1} |y-t|\,F_2(t)\,dt \sim y \quad \text{as} \quad \lambda\to\infty, \quad |y|<1. \tag{60}$$

Note that (60) implies that $F_2(t)$ must be of the form

$$F_2(t,\lambda,\nu) \sim \frac{g(t)}{\lambda} \quad \text{as} \quad \lambda\to\infty. \tag{61}$$

So we have

$$\frac{1}{2\sqrt{2}}\int_{-1}^{1} |y-t|\,g(t)\,dt = y, \quad |y|<1. \tag{62}$$

This is a Fredholm integral equation of the first kind for $g(y)$ with a displacement kernel. Formal solution of (62) by the use of Hilbert-Schmidt theory [21] results in a nonconvergent infinite series of trigonometric eigenfunctions for $g(y)$. Even so, proceeding to evaluate I^b using this divergent series results in

$$C^b(\lambda,\nu) \sim \frac{1}{2^{1/4}\sqrt{\pi}\lambda^{1/2}} = (0.4744\ldots)\lambda^{-1/2} \quad \text{as} \quad \lambda\to\infty, \tag{63}$$

which matches the numerical results (see Fig. 2).

An alternate method for evaluating I^b (which avoids solution of (62)) is now presented. Recalling (31), (61), and (62) and that $g(y)$ is an odd function we see that

$$I^b = \frac{1}{2\lambda}\int_{-1}^{1} t\,g(t)\,dt. \tag{64}$$

Now

$$I_2 \equiv \int_{-1}^{1} t\,g(t)\,dt = -\int_{-1}^{1} (1-t)g(t)\,dt \tag{65}$$

since $g(t)$ is odd. Let $y=1-\epsilon$ $(0<\epsilon<<1)$ in (62) so that

$$\int_{-1}^{1} |1-\epsilon-t|\,g(t)\,dt = 2\sqrt{2}\,(1-\epsilon) \tag{66}$$

or

$$\int_{-1}^{1-\epsilon} (1-\epsilon-t)\,g(t)\,dt + \int_{1-\epsilon}^{1} (t+\epsilon-1)\,g(t)\,dt = 2\sqrt{2}\,(1-\epsilon). \tag{67}$$

Let $\epsilon\to 0$ so that

$$\int_{-1}^{1} (1-t)\,g(t)\,dt = 2\sqrt{2} = 2\lambda I^b \tag{68}$$

which implies that

$$I^b(\lambda,\nu) = 2\pi(C^b(\lambda,\nu))^2 = \frac{\sqrt{2}}{\lambda}. \tag{69}$$

Again, we see that

$$C^b(\lambda,\nu) \sim \frac{1}{2^{1/4}\sqrt{\pi}\lambda^{1/2}} \quad \text{as} \quad \lambda\to\infty. \tag{70}$$

Conclusion and Remarks

We have used Sanders' energy-release rate integral I for a shallow shell to compute the behavior of the combined stress-intensity factor for a cylindrical shell with a circumferential crack subject to, alternately, axial tension and edge moments. These results and those of [2] and [3] may be able to provide upper and lower bounds on the combined stress-intensity factor for a cylindrical shell with a crack at an arbitrary angle. In this respect the results of [10] and [13] may be useful. Furthermore, for the very thin, bent shell we were able to arrive at an expression for the energy-release rate integral by directly applying the governing integral equations; that is, without actually solving the integral equations. This raises the interesting question whether the value of energy-release rate integrals (including I, J, L, and M) can be obtained directly (either analytically or numerically) without the pain of solving difficult integral equations.

References

1 Sanders, J. L., Jr., "On the Griffith-Irwin Fracture Theory," ASME JOURNAL OF APPLIED MECHANICS, Vol. 27, 1960, pp. 352-353.

2 Nicholson, J. W., and Simmonds, J. G., "Sanders' Energy-Release Rate Integral for Arbitrarily Loaded Shallow Shells and Its Asymptotic Evaluation for a Cracked Cylinder," ASME JOURNAL OF APPLIED MECHANICS, Vol. 47, 1980, pp. 363-369.

3 Nicholson, J. W., Bradley, M. R., and Carrington, C. K., "Asymptotic Evaluation of a Combined Stress-Intensity Factor for a Pressurized Cylindrical Shell Containing a Longitudinal Crack," ASME JOURNAL OF APPLIED MECHANICS, Vol. 47, 1980, pp. 583-585.

4 Copley, L. G., and Sanders, J. L., Jr., "Longitudinal Crack in a Cylindrical Shell Under Internal Pressure," *International Journal of Fracture Mechanics*, Vol. 5, 1969, pp. 117-131.

5 Simmonds, J. G., and Nicholson, J. W., "On Sanders' Energy-Release Rate Integral and Conservation Laws in Finite Elastostatics," *Archive for Rational Mechanics and Analysis*, Vol. 76, 1981, pp. 1-8.

6 Folias, E. S., "A Circumferential Crack in a Pressurized Cylindrical Shell," *International Journal of Fracture Mechanics*, Vol. 3, 1967, pp. 1-11.

7 Erdogan, F., and Ratwani, M., "Fatigue and Fracture of Cylindrical Shells Containing a Circumferential Crack," *International Journal of Fracture Mechanics*, Vol. 6, 1970, pp. 379-392.

8 Duncan-Fama, M. E., and Sanders, J. L., Jr., "A Circumferential Crack in a Cylindrical Shell Under Tension," *International Journal of Fracture Mechanics*, Vol. 8, 1972, pp. 15-20.

9 Murthy, M. V. V., Rao, K. P., and Rao, A. K., "On the Stress Problem of Large Elliptical Cutouts and Cracks in Circular Cylindrical Shells," *International Journal of Solids and Structures*, Vol. 10, 1974, pp. 1243-1269.

10 Lakshminarayana, H. V., and Murthy, M. V. V., "On Stresses Around an Arbitrarily Oriented Crack in a Cylindrical Shell," *International Journal of Fracture*, Vol. 12, 1976, pp. 547-566.

11 Sanders, J. L., Jr., "Circumferential Through-Cracks in Cylindrical Shells Under Tension," ASME JOURNAL OF APPLIED MECHANICS, Vol. 49, 1982, pp. 103-107.

12 Weidman, S. T., "Sanders' Energy-Release Rate Integral for a Circumferentially Cracked Cylindrical Shell," Master's Thesis, University of Virginia, Charlottesville, 1981.

13 Simmonds, J. G., Bradley, M. R., and Nicholson, J. W., "Stress-Intensity Factors for Arbitrarily Oriented Cracks in Shallow Shells," ASME JOURNAL OF APPLIED MECHANICS, Vol. 45, 1978, pp. 135-141.

14 Sanders, J. L., Jr., and Simmonds, J. G., "Concentrated Forces on Shallow Cylindrical Shells," ASME JOURNAL OF APPLIED MECHANICS, Vol. 37, 1970, pp. 367-373.

15 Abramowitz, M., and Stegan, I. A., *Handbook of Mathematical Functions*, U.S. Government Printing Office, 1964.

16 Luke, Y. L., *Mathematical Functions and Their Approximations*, Academic Press, New York, 1975.

17 Nicholson, J. W., and Weidman, S. T., "Accurate Polynomial Approximations for $\int_0^{i^{1/2}r} K_o(s)\,ds$," DAMACS report No. 80-13, University of Virginia, Charlottesville, 1980.

18 Simmonds, J. G., and Bradley, M. R., "Stress-Intensity Factors for Very Short Cracks in Arbitrary Pressurized Shells," ASME JOURNAL OF APPLIED MECHANICS, Vol. 43, 1976, pp. 657-662.

19 Theocaris, P. S., and Ioakimidis, N. I., "Numerical Integration Methods for the Solution of Singular Integral Equations," *Quarterly Journal of Applied Mathematics*, Vol. 35, 1977, pp. 173-183.

20 Sanders, J. L., Jr., private communication, July, 1980.

21 Hildebrand, F. B., *Methods of Applied Mathematics*, Prentice-Hall, Englewood Cliffs, N.J., 1965.

Downloaded 02 May 2010 to 171.66.16.246. Redistribution subject to ASME license or copyright; see http://www.asme.org/terms/Terms_Use.cfm

R. B. King

G. Herrmann
Fellow ASME

Division of Applied Mechanics,
Stanford University,
Stanford, Calif. 94305

Acoustoelastic Determination of Forces on a Crack in Mixed-Mode Loading

A technique previously presented [1] for the nondestructive evaluation of the J integral in cracked samples from ultrasonic measurements of stress, and successfully tested on specimens under mode I loading, is extended here to mixed-mode loading. Experimental results are presented for both the J and L integrals in a specimen with a slanted central crack loaded in tension, which agree well with theoretical values.

Introduction

In reference [1] a method was proposed for evaluating the J integral nondestructively using ultrasonic measurements with longitudinal waves. The method was based on a semianalytic technique called "rescaling." Results were presented for two mode I, linear elastic fracture mechanics (LEFM) experiments, for which the measured value of J compared well with theoretical values.

In this paper an experiment which was conducted to explore the applicability of this procedure to more complicated loading is described. The experiment involved a specimen with a slanted central crack. For this case of mixed-mode loading both the J and L integrals were evaluated. Before discussing this experiment, the experimental procedure for applying acoustic stress analysis, and the "rescaling" method, both of which are described in detail in [1], are summarized here for completeness.

Acoustic Stress Analysis

Stress measurements with acoustic waves in the ultrasonic range are based on the dependence of acoustic velocity in a solid on the state of stress. The relation between velocity and stress is predicted by the theory of acoustoelasticity. For longitudinal waves in plane specimens,

$$\frac{V-V_0}{V_0} \equiv \frac{\Delta V}{V_0} = B(\sigma_{11}+\sigma_{22}) \tag{1}$$

where V is the velocity of a normally incident wave in the stressed state, V_0 is the velocity in the unstressed state, B is a material property depending on the elastic constants (including the third-order (Murnaghan) constants) of the material, and σ_{11} and σ_{22} are in-plane stress components. To apply (1) to stress analysis, an apparatus has been developed that permits scanning measurements with longitudinal waves on a plane specimen mounted in a liquid bath (Fig. 1). The electronic system needed to measure the relative velocity change is discussed in [1].

Evaluation of Path-Independent Integrals

The experiment to be described involved evaluation of the J and L integrals in a plane cracked specimen using acoustic stress measurements. This evaluation is motivated by the utility of J and L in fracture mechanics. The importance of J as a fracture parameter is well known [2]. The meaning of L

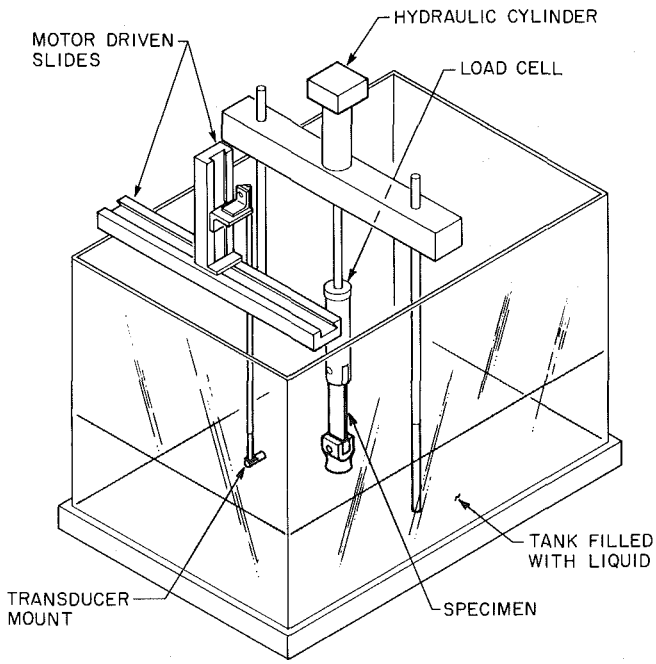

Fig. 1 Acoustoelastic apparatus

Contributed by the Applied Mechanics Division for publication in the JOURNAL OF APPLIED MECHANICS.

Discussion on this paper should be addressed to the Editorial Department, ASME, United Engineering Center, 345 East 47th Street, New York, N.Y. 10017, and will be accepted until two months after final publication of the paper itself in the JOURNAL OF APPLIED MECHANICS. Manuscript received by ASME Applied Mechanics Division, June, 1981; final revision, January, 1983.

Copyright © 1983 by ASME
Downloaded 02 May 2010 to 171.66.16.246. Redistribution subject to ASME license or copyright; see http://www.asme.org/terms/Terms_Use.cfm

for plane bodies containing cracks has only recently been discussed [3]. The following relation is derived there for the case of a crack in an infinite body subject to far field loading σ_{11}^A, σ_{22}^A, and σ_{12}^A:

$$L = \frac{-2aK_{II}}{E}(K_I + \sigma_{11}^A\sqrt{\pi a}) \tag{2}$$

where $K_{II} = \sigma_{12}^A\sqrt{\pi a}$, $K_I = \sigma_{22}^A\sqrt{\pi a}$ for the infinite plate. Using this expression and the mixed-mode Irwin relation

$$J = \frac{1}{E}(K_I^2 + K_{II}^2) \tag{3}$$

would permit evaluation of K_I and K_{II} from J and L if an appropriate value for σ_{11}^A were known. It should be noted, however, that (2) holds only for homogeneous loading on a crack in an infinite body, and must be generalized for other types of loading.

The approach used to nondestructively evaluate J or L is to determine the integrand at various points along a contour and then perform numerical integration. The J integral is given by

$$J = \int_c (Wn_x - t_k u_{k,x})\,ds \tag{4}$$

where c is a contour enclosing the tip of a crack, W is the strain energy density, n_x is the outer normal to c, t_k is the traction vector, and u_k is the displacement vector.

L is given by

$$L = \int_C e_{3ij}(Wx_j n_i - T_i u_j - T_k u_{k,i} x_j)\,dl \tag{5}$$

where C completely encloses the crack.

Determination of the integrand of either J or L involves knowledge of all components of stress, and also the rotation w_{xy}. To obtain an estimate for all of these quantities from the limited information given by (1), the semianalytic "rescaling" technique was proposed in [1]: Acoustic data are taken in a specimen in the vicinity of the crack and sufficiently far from the boundaries of the specimen. In this region it is assumed the stress (and rotation) components in the finite specimen vary with position in the same manner as those in an analogously loaded infinite cracked panel, the only effect of the finiteness of the specimen being the altering of a multiplicative constant. The value of this constant is determined such that it will fit best the stress sum $(\sigma_{11} + \sigma_{22})$ from the infinite plate solution to $(\sigma_{11} + \sigma_{22})$ in the specimen (determined acoustically using (1)) and the adjusted infinite plate solution is then used to evaluate J or L.

In a more complicated loading situation the infinite plate solution might involve several multiplicative constants that must be adjusted simultaneously using a procedure such as least squares fitting.

Experimental Procedure and Results

To test the performance of the rescaling method under more complicated loading conditions, an experiment was conducted in which a specimen was subjected to both biaxial tension and shear deformation. The specimen used was a panel containing a crack tilted at 45 deg to the axis of the panel (Fig.2) to which far-field uniaxial tension was applied. The specimen was made of Aluminum 6061 T6, for which the constant B in (1) had previously been calibrated to be 10.5×10^{-6}/MPa. Expressed in coordinates normal and tangential to the crack, this leads to the biaxial tension and shear tractions shown in Fig. 3. To simulate a nonlaboratory situation where the far-field tractions would be unknown, it was assumed the parameters σ_1, σ_2, and τ are not known in advance and should be determined from the ultrasonic measurements. Two regions were scanned in the first and fourth quadrants of the X-Y coordinates system as shown in

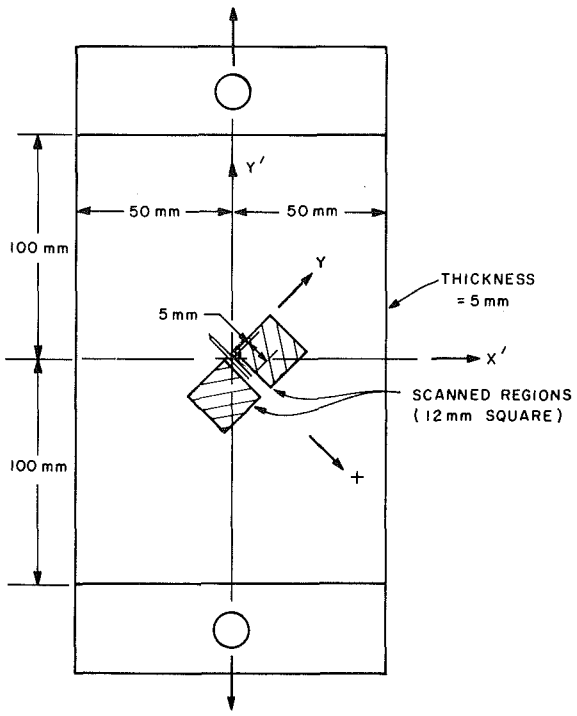

Fig. 2 Slanted center-cracked panel specimen

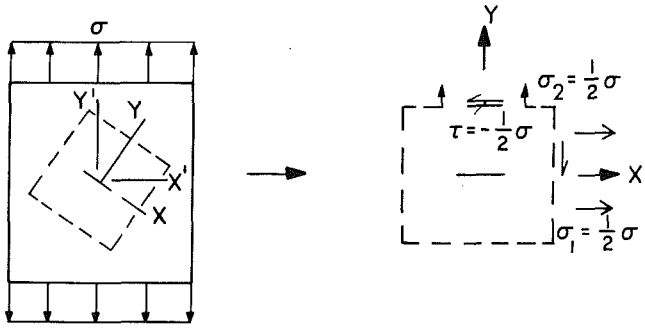

Fig. 3 Tractions on slanted crack

Fig. 2. To apply the rescaling method to this case, the values of the parameters σ_1, σ_2, and τ must first be determined, which will make the infinite plate solution "best fit" the measured data in the finite specimen. This was done using least squares fitting, as follows. Denote the measured value of the first stress invariant as $(\sigma_{11} + \sigma_{22})^M$ and the value of the infinite plate as $(\sigma_{11} + \sigma_{22})^0$. It is desired to minimize

$$E = \sum_{i=1}^{n}[(\sigma_{11} + \sigma_{22})_i^M - (\sigma_{11} + \sigma_{22})_i^0]^2 \tag{6}$$

where n is the number of points at which data are taken.

$$(\sigma_{11} + \sigma_{22})_i^0 = \sigma_1 f(f(x_i, y_i) + \sigma_2 + \tau h(x_i, y_i)$$

where f and h come from the infinite plate solutions for far-field tension and shear [4]. Equating the three derivatives $\partial E/\partial\sigma_1$, $\partial E/\partial\sigma_2$, and $\partial E/\partial\tau$ to zero leads to three equations that may be solved for σ_1, σ_2, τ:

$$\sigma_1\sum_{i=1}^{n} f_i h_i + \sigma_2\sum_{i=1}^{n} h_i + \tau\sum_{i=1}^{n} h_i^2 = \sum_{i=1}^{n} h_i(\sigma_{11} + \sigma_{22})_i^M$$

$$\sigma_1\sum_{i=1}^{n} f_i^2 + \sigma_2\sum_{i=1}^{n} f_i + \tau\sum_{i=1}^{n} h_i = \sum_{i=1}^{n}(\sigma_{11} + \sigma_{22})_i^M$$

$$\sigma_1\sum_{i=1}^{n} f_i + \sigma_2 n + \tau\sum_{i=1}^{n} h_i = \sum_{i=1}^{n}(\sigma_{11} + \sigma_{22})_i^M \tag{7}$$

Downloaded 02 May 2010 to 171.66.16.246. Redistribution subject to ASME license or copyright; see http://www.asme.org/terms/Terms_Use.cfm

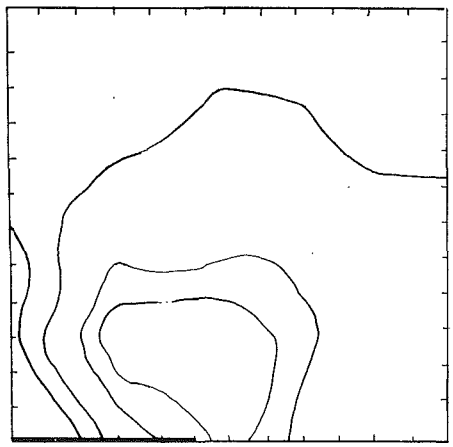

(a)

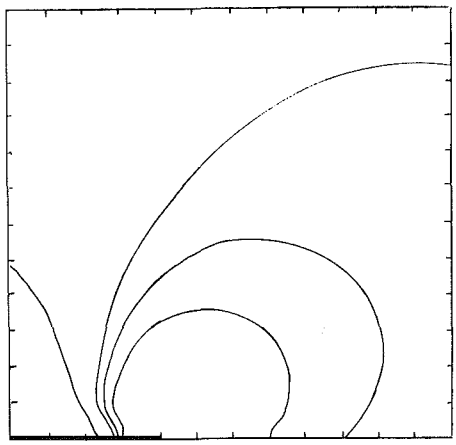

(b)

Fig. 4 $(\sigma_{11} + \sigma_{22})$ **contours in the first quadrant of the x-y coordinate system in Fig. 2; (*a*) measured, and (*b*) infinite plate solution**

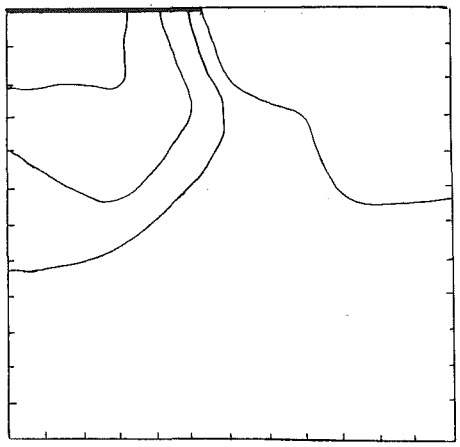

(a)

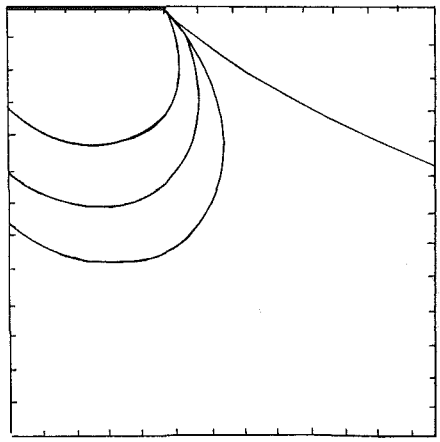

(b)

Fig. 5 $(\sigma_{11} + \sigma_{22})$ **contours in the fourth quadrant; (*a*) measured, and (*b*) infinite plate solution**

where $f_i = f(x_1^i, x_2^i)$ and $h_i = h(x_1^i, x_2^i)$. Frequency measurements were made in the regions shown in Fig. 2 with the specimen unloaded and loaded to 90kN. Contour plots of the measured value of $(\sigma_{11} + \sigma_{22})$ in the first quadrant of the xy coordinate system in Fig. 2 are shown in Fig. 4(*a*), and for comparison the values of $(\sigma_{11} + \sigma_{22})$ in the same region of the infinite plate are shown in Fig. 4(*b*). The comparison for the fourth quadrant is shown in Fig. 5. The measured contours are similar in shape to the theoretical contours (with allowance for experimental noise). The discrepancy between the experimental and theoretical contours is most pronounced in the vicinity of the crack tip. This is due to the acoustic transducer size (approximately 3 mm in diameter) which causes averaging over a finite area which is noticeable in regions of high stress gradients. A computer program employing the least squares fitting method described in the foregoing was used on the experimental data, and the result was $\sigma_2 = 99.25$ MPa, $\sigma_1 = 114.7$ MPa, and $\tau = -93$ MPa. The 90kN load on the specimen produced an applied stress of 180 MPa. If this value of stress is remotely applied to an infinite plate with a slanted crack, the following theoretical values are obtained: $\sigma_2 = \sigma_1 = -\tau = 90$ MPa. The specimen dimensions are sufficiently large in comparison with the crack length so that the infinite plate values can serve as a theoretical check. The measured and theoretical values agree within 10, 27, and 3 percent, respectively. It is interesting (and fortunate) that the largest discrepancy is in σ_1, but this error is unimportant because it does not affect the singular stresses at the crack tip and hence does not alter J.

For this linear-elastic case the estimated value of σ_2 and τ can be used directly to determine the stress intensity factors

$$K_I = \sigma_2\sqrt{\pi a}, \quad K_{II} = \tau\sqrt{\pi a}$$

resulting in $K_I = 393.03$ MPa $(\text{mm})^{1/2}$ $K_{II} = -366.28$ MPa (mm). The theoretical values are $K_I = -356.4$ and $K_{II} = -356.4$. The value of the J integral can be determined directly from the stress intensity factors using relation (3). This leads to the measured value $J = 4.14$ MPa-mm and the theoretical value $J = 3.63$, which agree with 14 percent. To this point the rescaling method as described previously has not yet been employed. It can be used to obtain a refined estimate of J. As discussed in [1], the value of the multiplicative constant adjusted during rescaling varies with position because of noise. The process of integration can be used to smooth out this noise if, while integrating along a contour to obtain J, the local value of this constant is used to evaluate the integrand at each point. The J integral thus obtained will be somewhat path-dependent due to the noise, and the values of J from several contours should be averaged. Following this procedure, the average value of J obtained along eight dif-

Downloaded 02 May 2010 to 171.66.16.246. Redistribution subject to ASME license or copyright; see http://www.asme.org/terms/Terms_Use.cfm

ferent contours was 3.86 MPa-mm, which agrees with the theoretical value of J within 7 percent, so it is seen that this rescaling procedure refined the estimate of J considerably.

As discussed in the foregoing, it is in mixed-mode loading that the usefulness of the L integral may arise. Consequently the L integral was also evaluated from the "rescaled" infinite plate solution, with the result $L = 44.35$ N. The theoretical value for L using the correct values of σ_1, σ_2, and τ for this specimen and relation (2) is 36.34 N. The discrepancy is 22 percent. The higher discrepancy with theory for L was apparently caused by the error in σ_1, which had no effect on J but did affect the L integral.

Conclusions

The experimental results presented here and in [1] have demonstrated the possibility of nondestructively evaluating the J integral in several plane laboratory specimens containing cracks subjected to both mode I and combined mode I and mode II loadings. For the mixed-mode experiment described in this paper, the L integral was successfully evaluated and the values of the stress intensity factors K_I and K_{II} were determined.

The technique presented leads to accurate results in each of the experiments reported which were confined to the LEFM regime. In a subsequent paper the application of this procedure to the evaluation of the J integral in the presence of elastoplastic deformation will be described.

Acknowledgment

This research was supported in part by AFOSR F49620-79-C-0217 to Stanford University.

References

1 King, R. B., Herrmann, G., and Kino, G. S., "Use of Stress Measurements With Ultrasonics for Nondestructive Evaluation of the J Integral," *Engineering Fracture Mechanics*, in print.

2 Begley, J. A., and Landes, J. D., "The J Integral as a Fracture Criterion," *Fracture Toughness*, Proceedings of 1971 Symposium on Fracture Mechanics, ASTM S.T.P. 514, 1972, pp. 1–20.

3 Herrmann, A. G., and Herrmann, G., "On Energy-Release Rates for a Plane Crack," ASME JOURNAL OF APPLIED MECHANICS, Vol. 48, 1981, pp. 525–528.

4 Tada, H., et al., *The Stress Analysis of Cracks Handbook*, Del Research Corp., 1973.

Downloaded 02 May 2010 to 171.66.16.246. Redistribution subject to ASME license or copyright; see http://www.asme.org/terms/Terms_Use.cfm

The Dynamic Stress Intensity Factor Due to Arbitrary Screw Dislocation Motion

L. M. Brock
Department of Engineering Mechanics,
University of Kentucky,
Lexington, Ky. 40506
Mem. ASME

The dynamic stress intensity factor for a stationary semi-infinite crack due to the motion of a screw dislocation is obtained analytically. The dislocation position, orientation, and speed are largely arbitrary. However, a dislocation traveling toward the crack surface is assumed to arrest upon arrival. It is found that discontinuities in speed and a nonsmooth path may cause discontinuities in the intensity factor and that dislocation arrest at any point causes the intensity factor to instantaneously assume a static value. Morever, explicit dependence on speed and orientation vanish when the dislocation moves directly toward or away from the crack edge. The results are applied to antiplane shear wave diffraction at the crack edge. For an incident step-stress plane wave, a stationary dislocation near the crack tip can either accelerate or delay attainment of a critical level of stress intensity, depending on the relative orientation of the crack, the dislocation, and the plane wave. However, if the incident wave also triggers dislocation motion, then the delaying effect is diminished and the acceleration is accentuated.

Introduction

Bilby and Eshelby [1] have noted the possible role of dislocations in fracture. Simlarly, Rice and Thomson [2], Tirosh and McClintock [3], Burns and Majumdar [4], and Thomson and Sinclair [5] have related fracture initiation to dislocation nucleation and assembly near an existing crack.

In elasticity theory, the stress intensity factor is a key parameter in characterizing fracture initiation. Moreover, if the fracture process is dynamic, the motion of the dislocations should be considered in applying mechanisms such as those in [2–5]. This paper, therefore, attempts to gain insight into the role of dislocations in dynamic fracture by (1) studying the effects of a moving screw dislocation on the dynamic stress intensity factor generated for a stationary crack and (2) applying the information gained to the problem of stress wave diffraction at the crack edge.

Because engineering and geological materials are often assemblies of crystalline grains that may contain local distortions, dislocation paths in a small region such as around a crack edge may not be rectilinear. Therefore, the study considers a screw dislocation that moves from equilibrium along a continuous, piecewise-smooth path. Its speed is subsonic and nonuniform, although the Johnston-Gilman [6] observations that inpath acceleration effects may be negligible should be noted. The dislocation is of unit strength, the crack is semi-infinite, and, as a first step, the cracked material is isotropic, homogeneous, linearly elastic, and unbounded. The dislocation is allowed to travel to the crack surface, but is assumed to arrest upon arrival. The dynamic stress intensity factor is derived and examined for dependence on dislocation position, orientation, and speed.

The study results are then applied to the problem of a screw dislocation near a crack edge at which antiplane shear wave diffraction occurs. The diffraction-dislocation interaction in the crack edge stress field is examined for its fracture initiation implications. Both the stationary dislocation and a dislocation which, triggered by the wave pattern, moves to the crack edge are considered.

The basic problem is analyzed beginning in the next section. The dislocation is represented by an equivalent body force distribution, following [7]. The existence of a characteristic length implies a Wiener-Hopf problem of a nonstandard type. It is advantageous, therefore, to obtain the exact solution by means of the superposition scheme outlined in the following section. This scheme was also used in [8] for the calculation of the dislocation motion-induced portion of the intensity factor when the path is strictly rectilinear.

Basic Problem Formulation

Consider the unbounded elastic plane containing the crack and screw dislocation shown in Fig. 1(*a*). In terms of the Cartesian coordinates (x,y) the crack surface is defined by $y=0$, $x<0$. It is convenient to define the dislocation as the cut

Contributed by the Applied Mechanics Division for presentation at the 1983 ASME Applied Mechanics, Bioengineering, and Fluids Engineering Conference, Houston, Texas, June 20–22, 1983 of THE AMERICAN SOCIETY OF MECHANICAL ENGINEERS.

Discussion on this paper should be addressed to the Editorial Department, ASME, United Engineering Center, 345 East 47th Street, New York, N.Y. 10017, and will be accepted until two months after final publication of the paper itself in the JOURNAL OF APPLIED MECHANICS. Manuscript received by ASME Applied Mechanics Division, April, 1982; final revision, October, 1982. Paper No. 83-APM-21.

Copies will be available until February, 1984.

Copyright © 1983 by ASME
Downloaded 02 May 2010 to 171.66.16.246. Redistribution subject to ASME license or copyright; see http://www.asme.org/terms/Terms_Use.cfm

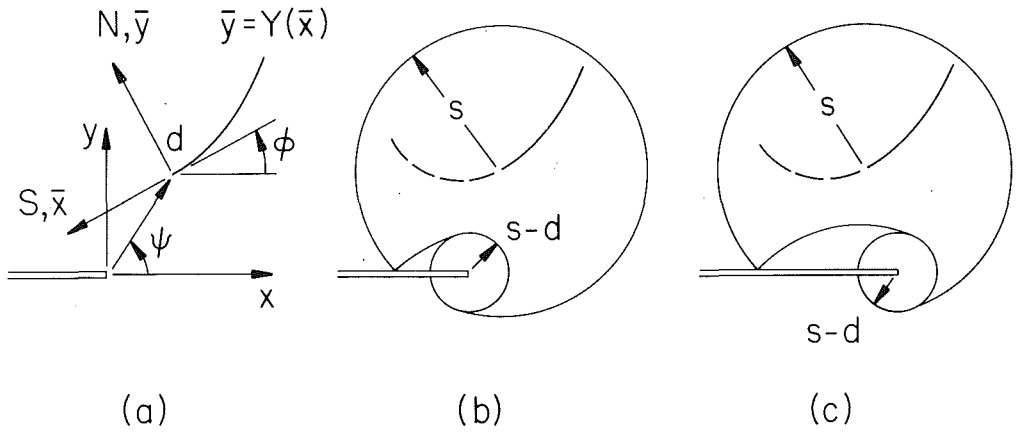

Fig. 1 *(a)* **Initial crack-screw dislocation configuration; *(b)* wave pattern for $|\psi|<\pi/2$; and (c) wave pattern for $|\psi|>\pi/2$**

$N=0$, $S<0$ where (S, N) are tangential and normal coordinates along the dislocation path $\bar{y}=Y(\bar{x})$. As seen in Fig. 1(*a*), the Cartesian coordinates $(\bar{x},\bar{y})$ are centered at the dislocation edge so that the $(\bar{x},S)$ and $(\bar{y},N)$-directions, respectively, coincide there. If ϕ is the path slope at the dislocation edge w.r.t. the crack plane and (d,ψ) are the plane polar coordinates of the dislocation edge w.r.t. the crack edge then

$$\bar{x}=d\cos\Omega-x\cos\phi-y\sin\phi, \quad \bar{y}=d\sin\Omega-x\sin\phi+y\cos\phi,$$
$$\Omega=\phi-\psi \tag{1}$$

We first examine continuous, piecewise-smooth, single-valued path functions Y. Therefore, $|Y'|$ is finite, where $(\,)'$ denotes argument differentiation, while the path-length

$$S=\int_0^{\bar{x}}\sqrt{[1+(Y')^2]}du \tag{2}$$

has a single-valued inverse $\bar{x}=X(S)$. The single-valuedness restriction will eventually be relaxed. For $s<0$, where $s=cx$(time) and c is the shear wave speed, the dislocation and crack are in equilibrium. For $s>0$ the dislocation moves along the path $\bar{y}=Y(\bar{x})$ and is located at $N=0$, $S=D(s)$. Here $D(s)$ is continuous, where $D(0)=0$, $0\le\dot{D}<1$, $(\dot{})\equiv\partial(\,)/\partial s$, and the last inequality assures a subsonic speed. If the dislocation reaches the crack surface at some $s=t_0>0$, we require that $\dot{D}(s)=0$, $D(s)=D(t_0)$ for all $s>t_0$. This motion generates a cylindrical shear wave. As seen in Fig. 1(*b*), if $|\psi|<\pi/2$ this wave will first reach the crack edge and there generate a diffracted shear wave. As seen in Fig. 1(*c*), if $|\psi|>\pi/2$ the wave is first reflected by the crack surface itself.

The equations governing the motion are

$$\nabla^2 w+\frac{b}{\mu}=\ddot{w}, \quad \tau_y=0 \quad (y=0, \quad x<0), \quad w\equiv w_0\,(s\le 0) \tag{3}$$

$$\tau_y=w_{,y}, \quad b=\mu H[D(s)-S]\delta'(N) \tag{4}$$

where $w(x,y,s)$ is the antiplane displacement, w_0 is its equilibrium value, μ is the shear modulus, ∇^2 is the Laplacian operator, and $(\,)_{,u}\equiv\partial(\,)/\partial u$. The quantity b is the body force equivalent of the screw dislocation of unit strength while H and δ are the Heaviside and Dirac functions. It is convenient to introduce the superposition

$$w=w_b+w_c+w_0 \tag{5}$$

$$\nabla^2 w_b+\frac{1}{\mu}(b-b_0)=\ddot{w}_b, \quad b_0=\mu H(-S)\delta'(N),$$
$$w_b\equiv 0\,(s\le 0) \tag{6}$$

where b_0 is the initial dislocation equivalent. In view of (3)–(6), then, w_c must satisfy the equations

$$\nabla^2 w_c=\ddot{w}_c, \quad \tau_{yc}=-\tau_{yb}\,(y=0,x<0), \quad w_c\equiv 0 \quad (s\le 0) \tag{7}$$

Equations (6) are the relations governing the displacement w_b due to a body force $b-b_0$ applied in an unbounded, uncracked elastic plane while (7) are those for a displacement w_c generated by the sudden imposition of tractions $-\tau_{yb}$ along a crack $y=0$, $x<0$. This latter field will contain the information about the dynamic stress intensity factor. The general solution for w_b is given in the next section.

General Solution for Dislocation

In view of the dependence of $b-b_0$ and the invariance of ∇^2, it is convenient to seek the function $w_b(\bar{x},\bar{y},s)$. The Laplace transform over s, the Fourier transform over $\bar{x}$ and its inverse are given by, see Sneddon [9]

$$g_L=\int_0^\infty g(s)e^{-ps}ds; \quad g_B=\int_{-\infty}^{\infty} g(\bar{x})e^{-ipq\bar{x}}d\bar{x},$$
$$g(\bar{x})=\frac{p}{2\pi}\int_\Gamma g_B e^{ipq\bar{x}}dq \tag{8a-c}$$

respectively, where p is real, positive, and large enough to insure convergence of (8*a*), q is, in general, complex, and Γ is the inversion integral path. Application of (8*a*,*b*) to (6) in view of appropriate radiation conditions yields

$$\hat{w}_{b,\bar{y}\bar{y}}-p^2a^2\hat{w}_b=\frac{1}{\mu}(\hat{b}_0-\hat{b}), \quad a=\sqrt{(1+q^2)} \tag{9}$$

where $\hat{(\,)}\equiv(\,)_{BL}$ and a is defined in the q-plane cut along $Re(q)=0$, $|Im(q)|>1$, such that $Re(a)\ge 0$. It can be shown that the solution to (9) which is bounded for $|\bar{y}|\to\infty$ is, in view of (4) and (6),

$$2p\hat{w}_b=-\int_0^\infty \dot{D}\frac{dX}{dS}\left[\operatorname{sgn}(Y-\bar{y})-i\frac{q}{a}Y'\right]$$
$$\backslash e^{-p(t+iqX+a|Y-\bar{y}|)}dt, \quad \frac{dX}{dS}=\frac{1}{\sqrt{[1+(Y')^2]}} \tag{10a,b}$$

where it is understood that $Y=Y(X)$, $X=X(D)$, and $D=D(t)$. Substitution of (10) in (8*c*) gives

$$4\pi w_{bL}=-\int_0^\infty \dot{D}\frac{dX}{dS}e^{-pt}\int_\Gamma\left[\operatorname{sgn}(Y-\bar{y})-i\frac{q}{a}Y'\right]$$
$$e^{p[iq(\bar{x}-X)-a|Y-\bar{y}|]}dqdt \tag{11}$$

where Γ can be taken along the $Re(q)$-axis. By following the work of deHoop [10], the Cauchy theorem is used to alter the integration path to the q-plane contour along which the

Downloaded 02 May 2010 to 171.66.16.246. Redistribution subject to ASME license or copyright; see http://www.asme.org/terms/Terms_Use.cfm

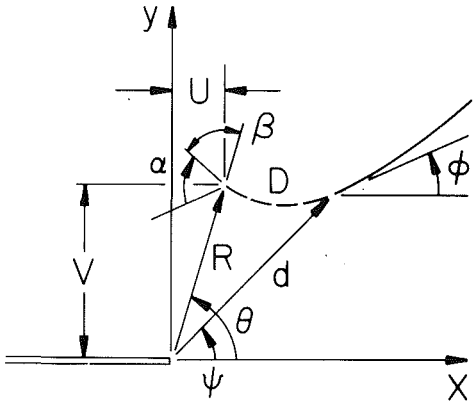

Fig. 2 Instantaneous crack-screw dislocation configuration

imaginary part of the p-factor vanishes while the real part is negative. Then, it is readily shown that (11) becomes

$$2\pi w_{bL} = \int_0^\infty \dot{D} e^{-pt} \int_r^\infty \frac{ne^{-pn}}{\sqrt{(n^2-r^2)}} \frac{1}{r} \frac{dr}{dN} dn dt \tag{12}$$

$$r = \sqrt{[(\bar{x}-X)^2 + (\bar{y}-Y)^2]},$$

$$\frac{dr}{dN} = \frac{1}{r} \frac{dX}{dS} [\bar{y} - Y + Y'(\bar{x}-X)] \tag{13}$$

where dr/dN is the normal derivative of the distance r along the dislocation edge path. The inverse Laplace transform follows by inspection as

$$2\pi w_b = \int_0^\infty \frac{\dot{D}H(\tau-r)}{\sqrt{(\tau^2-r^2)}} \frac{\tau}{r} \frac{dr}{dN} dt, \quad \tau = s-t \tag{14}$$

By recognizing a first integral w.r.t. s, equation (14) can be rewritten as

$$w_b = \dot{W}, \quad 2\pi W = \int_0^\infty \dot{D}H(\tau-r)\sqrt{(\tau^2-r^2)} \frac{1}{r} \frac{dr}{dN} dt \tag{15}$$

so that, from (4)

$$\tau_{yb} = \mu \dot{G}, \quad G = W_{,y} \tag{16}$$

In light of (1), W can be viewed as a function of (ϕ,Ω) and it can be shown that along $y=0$

$$G(x,s) = -\frac{1}{x} \frac{\partial W}{\partial \phi}(\phi,\Omega) \tag{17}$$

The relationships (13) and (15)–(17) prove convenient in the next section.

Diffracted Stress Ahead of Crack

The problem (7) was also considered by Brock [8]. By following schemes by Kostrov [11] and Achenbach [12], the stress τ_{yc} for $y=0, x>0, s>d$ was found to be

$$\tau_{yc}(\xi,\eta) = \frac{1}{\pi\sqrt{(\eta-\xi)}} \int_{L(\xi)}^{\xi} \tau_{yb}(\xi,u) \frac{\sqrt{(\xi-u)}}{\eta-u} du \tag{18}$$

$$L(\xi) = \frac{d}{\sqrt{2}} \left(\frac{d+\sqrt{2}\xi\cos\psi}{\sqrt{2}\xi + d\cos\psi} \right), \quad \sqrt{2}\xi = s-x, \quad \sqrt{2}\eta = s+x \tag{19}$$

where $\sqrt{2}\xi > d$, $\eta > \xi$. Here (ξ,η) are characteristic coordinates, u is an integration variable representing η-dependence, and $\eta = L(\xi)$ defines in the $\xi\eta$-plane the shear wave front radiating from the equilibrium dislocation edge position. In view of (16), (17), (19), and the fact that G vanishes along the wave front, equation (18) can be rewritten as

$$\frac{1}{\mu}\tau_{yc}(\xi,\eta) = \frac{1}{\pi\sqrt{(\eta-\xi)}} \frac{\partial}{\partial s} \int_{L(\xi)}^{\xi} G\left[\frac{1}{\sqrt{2}}(u-\xi), \frac{1}{\sqrt{2}}(u+\xi)\right] \frac{\sqrt{(\xi-u)}}{\eta-u} du \quad (x>0, s\geq d) \tag{20}$$

Dynamic Stress Intensity Factor

By introducing (1), (13), (15), and (17) with $y=0$ and the variable change $\sqrt{2}z = \xi - u$ while noting that the integration order in the zt-plane can be interchanged, equation (20) can be rewritten as

$$\frac{2\pi^2}{\mu}\tau_{yc}(x,s) = \frac{-1}{\sqrt{x}} \frac{\partial}{\partial s} \int_0^{t^*} \dot{D} \frac{dX}{dS} \sqrt{2} \frac{\partial}{\partial \phi} \sqrt{(\tau+U)} \int_0^Z \frac{\sqrt{(Z-z)}}{(x+z)\sqrt{z}} \frac{1}{r^2} (C - BY') dz dt \tag{21}$$

$$B = d\cos\Omega + z\sin\phi - X, \quad C = d\sin\Omega + z\cos\phi - Y \tag{22}$$

$$Z = \frac{1}{2} \frac{\tau^2 - R^2}{\tau + U}, \quad R = \sqrt{(U^2+V^2)} = \sqrt{[d^2 + X^2 + Y^2 - 2d(X\cos\Omega + Y\sin\Omega)]} \tag{23}$$

$$U = d\cos\psi - X\cos\phi - Y\sin\phi, \quad V = d\sin\psi - X\sin\phi + Y\cos\phi \tag{24}$$

where $t^* = s - R(t^*)$. The restrictions on $(D,\dot{D},Y)$ imply that $t^*=0$ for $s=d$ and $dt^*/ds \geq 0$, $0 \leq t^* \leq s$ for $s \geq d$. Figure 2 illustrates that $(x,y)=(U,V)$ and R are, respectively, the instantaneous dislocation edge position and instantaneous distance between the crack and dislocation edges. Thus, $R(0)=d$.

The z-integrand behaves as $0(z^{-2})$ for $|z| \to \infty$, has branch points at $(0,Z)$, simple poles at $-U \pm i|V|$ $(r^2=0)$, and a first-order singularity on the branch cut at $-x(x>0)$. These observations allow use of the Cauchy residue theorem to perform the z-integration. The ϕ and s-differentiations can then readily be carried out and it can be shown that for $x \to 0$, $s \geq d$

$$\frac{1}{\mu}\tau_{yc}(x,s) \sim \frac{K_c(t^*)}{2\sqrt{(xd)}} \tag{25}$$

$$\pi K_c(t^*) = \frac{-\dot{D}}{1-\dot{D}\cos(\omega-\theta)} \sqrt{\left(\frac{d}{R}\right)} \frac{dX}{dS} \sin(\omega-\theta)\sin\frac{\theta}{2} - \frac{1}{2d}\int_0^{t^*} \dot{D}\frac{dX}{dS}\sqrt{\left(\frac{d}{R}\right)^3} I(t)\,dt \quad (s \geq d) \tag{26}$$

$$I(t) = \cos\left(\phi - \frac{3\theta}{2}\right) + Y'\sin\left(\phi - \frac{3\theta}{2}\right) \tag{27}$$

$$\omega = \phi - \alpha, \quad \tan\theta = \frac{V}{U}, \quad \tan\alpha = Y' \ (|\theta| \leq \pi, |\alpha| \leq \pi/2) \tag{28}$$

Figure 2 shows that (R,θ) are the plane polar coordinates of the instantaneous dislocation edge position w.r.t. the crack edge, α is its instantaneous slope w.r.t. the initial dislocation plane, and $-\omega$ is the instantaneous slope w.r.t. the crack plane. Thus, $\theta(0)=\psi$ and $\omega(0)=\phi$. Again it is understood that $Y=Y(X)$, $X=X(D)$, while $(D,\dot{D})$ are functions of t. Upon introduction of the trajectory length integration variable

$$\int_0^{X[D(t)]} \sqrt{[1+(Y')^2]}\,du \tag{29}$$

in view of (2), (10b), and the restrictions on Y it can be shown that

Downloaded 02 May 2010 to 171.66.16.246. Redistribution subject to ASME license or copyright; see http://www.asme.org/terms/Terms_Use.cfm

$$\frac{1}{2d}\dot{D}\frac{dX}{dS}\sqrt{\left(\frac{d}{R}\right)^3}I(t)=\frac{d}{dN}\left[\sqrt{\left(\frac{d}{R}\right)}\sin\frac{\theta}{2}\right]$$

$$=\frac{d}{dS}\left[\sqrt{\left(\frac{d}{R}\right)}\cos\frac{\theta}{2}\right] \tag{30}$$

Then, equation (26) assumes the form

$$\pi K_c(t^*)=\cos\frac{\psi}{2}-\sqrt{\left(\frac{d}{R}\right)}\cos\frac{\theta}{2}$$

$$-\frac{\dot{D}}{1-\dot{D}\cos(\omega-\theta)}\sqrt{\left(\frac{d}{R}\right)}\sin(\omega-\theta)\sin\frac{\theta}{2}\quad(s\geq d) \tag{31}$$

An alternative form can be obtained by noting that

$$\sin(\omega-\theta)=-\frac{dR}{dN},\quad \cos(\omega-\theta)=-\frac{dR}{dS} \tag{32}$$

The form of K_c is independent of (29) so that, as indicated earlier, the single-valuedness restriction on the trajectory function Y can be dropped and the slope angle α can take on values $|\alpha|\leq\pi$. Equation (31) appropriately reduces to the results in [8] for rectilinear motion ($\alpha\equiv 0$).

In view of (5), the dynamic stress intensity factor K for the problem is obtained by superposing K_c on the equilibrium intensity factor K_0. It is readily shown [4] that πK_0 is the negative of the first term in (31) so that

$$\pi K(t^*)=-\sqrt{\frac{d}{R}}\frac{\cos\frac{\theta}{2}+\dot{D}\cos\left(\omega-\frac{\theta}{2}\right)}{1-\dot{D}\cos(\omega-\theta)} \tag{33}$$

Equation (33) is convenient for computational purposes. In the following analysis, however, alternative forms prove to be useful.

General Observations on K

Equation (33) shows that the dynamic stress intensity factor depends explicitly on the instantaneous dislocation position (R,θ), orientation (ω), and speed $(\dot{D})$. In Fig. 2 the angle β between the radial (R) and tangential (S) directions is defined as

$$\beta=\pi+(\omega-\theta)\,\mathrm{sgn}(\theta)\quad(0\leq\beta\leq\pi) \tag{34}$$

It should be noted that β, unlike the angles $(\theta, \psi, \phi, \alpha)$, is measured w.r.t. instantaneous directions and thus, for convenience, has no positive or negative sense in the xy-plane. In view of (31) and (34), equation (33) becomes

$$\pi K(t^*)=-\sqrt{\frac{d}{R}}\frac{\cos\frac{\theta}{2}+\dot{D}\cos\left(\beta+\left|\frac{\theta}{2}\right|\right)}{1+\dot{R}} \tag{35}$$

where $\dot{D}\sin\beta$ and $\dot{R}=\dot{D}\cos\beta$ are, respectively, the dislocation velocity components in the directions perpendicular and parallel to the R-direction. Equation (35) can itself be rewritten as

$$\pi K(t^*)=\sqrt{\frac{d}{R}}\left(-\cos\frac{\theta}{2}+\frac{\dot{D}\sin\beta}{1+\dot{R}}\sin\left|\frac{\theta}{2}\right|\right) \tag{36}$$

which shows that the intensity factor has two competing (of opposite sign) components. The first component depends on the dislocation position, while explicit orientation and speed dependence is coupled with positional dependence in the second component. Both components vary inversely with the distance between the dislocation and crack edge. However, while the first component varies directly with the angle between the distance line and the crack surface, variation of the second component is inverse. Thus, these components vanish, respectively, on the crack surface and directly ahead of the crack edge. The second component also vanishes when the dislocation moves directly toward or away from the crack edge ($\beta=0,\pi$). These observations imply that the intensity factor is finite except perhaps when the dislocation is at the crack edge ($R=0$) and may vanish for various combinations of dislocation position, orientation, and speed.

Figure 1 shows that the dislocation at some $t_a>0$ will radiate a shear wave that travels the distance $R(t_a)$ to subsequently reach the crack edge at $s_a=t_a+R(t_a)$. Similarly, the dislocation at some $t_b>t_a$ will radiate a shear wave that reaches the crack edge at $s_b=t_b+R(t_b)$. If $t_b=t_a+\epsilon$, $0<\epsilon<<d$, then from (23)

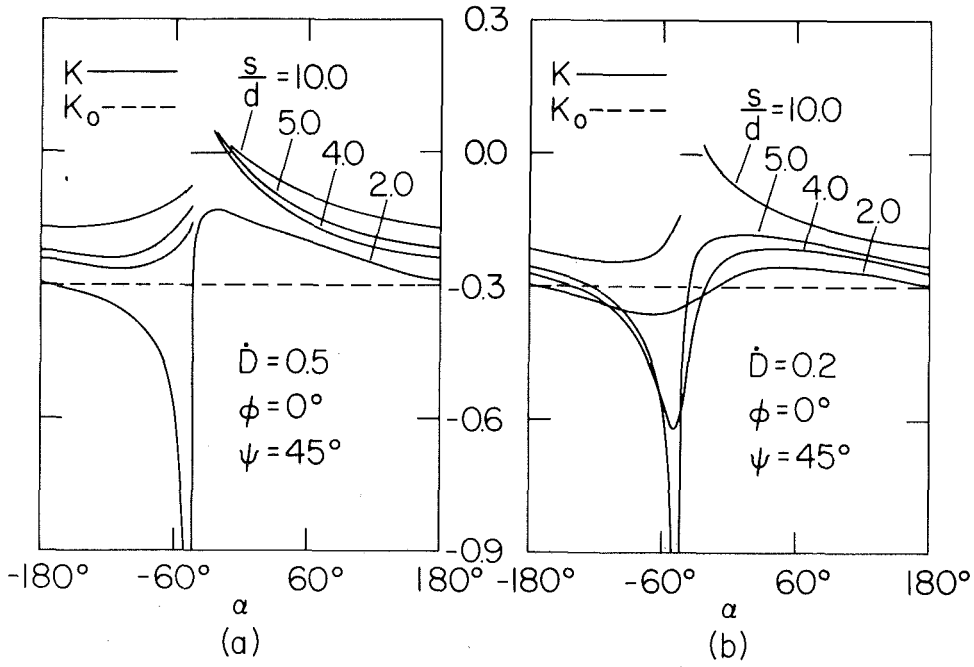

Fig. 3 (a) K versus α, $\dot{D}=0.5$; and (b) K versus α, $\dot{D}=0.2$

Downloaded 02 May 2010 to 171.66.16.246. Redistribution subject to ASME license or copyright; see http://www.asme.org/terms/Terms_Use.cfm

$$s_b - s_a = t_b - t_a + R(t_b) - R(t_a) \sim [1 + \dot{R}(t_a)]\epsilon,$$

$$\dot{R} = \frac{\dot{D}}{R}\frac{dX}{dS}[X - d\cos\Omega + Y'(Y - d\sin\Omega)] \tag{37}$$

The condition $\dot{D} < 1$ and (10*b*) guarantee that $|\dot{R}| < 1$, and the left-hand side of (37) is therefore positive. Thus, the order in which signals giving rise to K leave the dislocation is preserved, on their arrival at the crack edge.

With this in mind, we now consider dislocation motion discontinuities: Suppose that the dislocation speed undergoes a sudden change at $t = t_0$. Since $dt^*/ds \geq 0$, $0 < t^* < s$, we have $t^* = t_0$ at some subsequent instant $s_0 = t_0 + R(t_0)$. Since $\dot{D}$ is finite and the path is continuous, the first intensity factor component will be continuous at s_0. However, the second will instantaneously change unless $\beta = \pi/2$ and $\theta = 0$ at t_0, i.e., the dislocation was crossing directly ahead of the crack edge at right angles to the crack plane.

A related phenomenon occurs when the dislocation arrests or starts moving at t_0. The intensity factor will suffer a discontinuity as s_0 unless at t_0 $\beta = \pi/2$ and $\theta = 0$ or $\dot{D}$ vanishes continuously. If arrest occurs, only the first component remains and gives K the constant value

$$\pi K = -\sqrt{\frac{d}{R(t_0)}}\cos\frac{\theta_{(t0)}}{2} \quad (s > s_0) \tag{38}$$

Thus, once the dislocation arrest signal reaches the crack edge, the intensity factor assumes a new equilibrium value. Since $\theta(t_0) = \pm\pi$, the intensity factor vanishes for $s > s_0$ when arrest is at any crack surface point except the edge. More generally, comparison of (36) and (38) shows that the first intensity factor component is essentially a static contribution. The second is a correction for dislocation motion not directly toward or away from the crack edge.

Dislocation motion discontinuities can also occur due to the path itself, which is required to be continuous but only piecewise smooth. If at some $t = t_0$ the dislocation reaches a corner, equations (33) and (35) show that unless $\dot{D}$ vanishes continuously there, an intensity factor discontinuity will subsequently be manifested at s_0 through the parameters (α, β, ω).

In summary, then, discontinuities in dislocation speed and path slope cause discontinuities in the dynamic stress intensity factor. However, appropriate behavior by either quantity can also remove the discontinuity effect due to the other.

Dynamic Overshoot

Because two components compete during dislocation motion, the signal received at the crack edge from a given dislocation position triggers in the dynamic analysis an intensity factor that will either have a smaller magnitude than the static value or be of opposite sign. Only when

$$\frac{\dot{D}\sin\beta}{1 + \dot{R}} > 2\cot\left|\frac{\theta}{2}\right|, \tag{39}$$

will the latter instance produce a larger magnitude. Thus, unless (39) is satisfied, dynamic overshoot in the sense that the dynamic stress intensity factor at some instant exceeds its initial equilibrium value occurs due to the change in dislocation position, e.g., the dislocation moves closer to the crack edge.

Numerical Illustrations

To illustrate the effect of the implicit orientation parameter α, we consider the dislocation motion defined by $(\dot{D}, \alpha)$ constant. The parameter K is plotted in Fig. 3(*a*) versus α for $\psi = 45$ deg, $\phi = 0$ deg, $\dot{D} = 0.5$, and various values of $s/d > 1.0$. The discontinuities for $\alpha = -45$ deg indicate dislocation arrest at the crack edge, which occurs when $s/d = 2.0$. The other discontinuities and the constant behavior show the aforementioned effects of dislocation arrest at other crack surface locations. In general, the K-variation with α decreases as s/d becomes large. As implied earlier K temporarily vanishes at several values of α. Figure 3(*b*) presents a K-plot for the same situation, except that now $\dot{D} = 0.2$ and crack edge arrest occurs for $\alpha = -45$ deg when $s/d = 5.0$. The observations made for Fig. 3(*a*) are apparently again valid. The decrease in K-variation with α, however, seems to occur more slowly.

In view of the behavior near and away from the value $\alpha = -45$ deg, Fig. 3 shows the inverse variation of the dynamic stress intensity factor magnitude with the distance between the dislocaton and crack edge. This behavior is more clearly illustrated in Fig. 4(*a*), where K is plotted versus $s/d \geq 1.0$ for

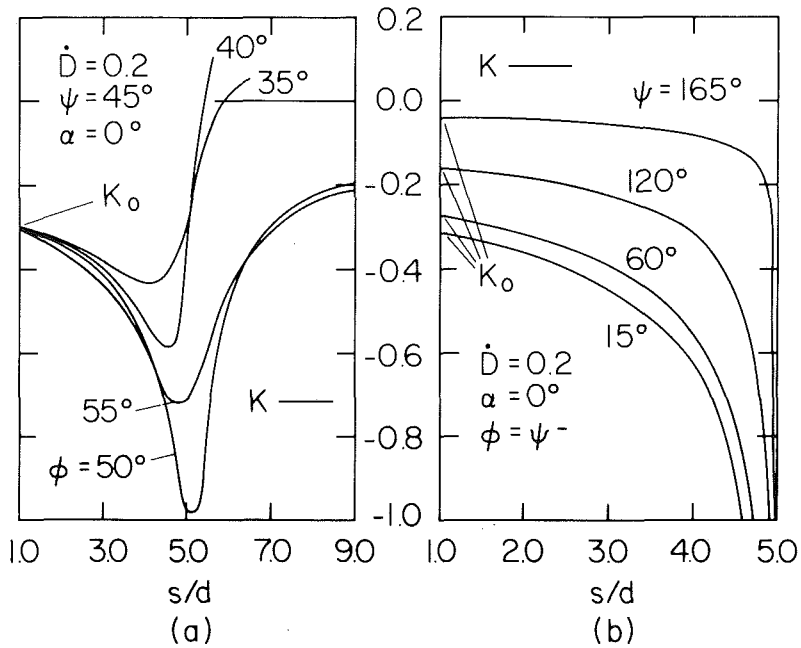

Fig. 4 (a) K versus s/d, $\psi = 45$ deg; and (b) K versus s/d, $\phi = \psi -$

Downloaded 02 May 2010 to 171.66.16.246. Redistribution subject to ASME license or copyright; see http://www.asme.org/terms/Terms_Use.cfm

$\dot{D}=0.2$, $\alpha=0$ deg, $\psi=45$ deg and $\phi=(35, 40, 50, 55$ deg). The intensity factor magnitude is seen to grow continuously until the dislocation nears its point of minimum distance to the crack edge. When the dislocation passes in front of the crack edge ($\phi=50, 55$ deg), the magnitude decreases asymptotically to zero. For the crack surface arrest cases ($\phi=35, 40$ deg) the intensity factor changes sign and then instantaneously vanishes when the arrest signals reach the crack edge.

As a third illustration, K is plotted in Fig. 4(*b*) versus $s/d \geq 1.0$ for $\dot{D}=0.2$, $\alpha=0$ deg and various values of ψ that define rectilinear paths which intersect the crack surface at the crack edge ($\phi=\psi^-$). Because $\beta \sim \pi$, the intensity factor motion component is negligible, and Fig. 4(*b*) shows the aforementioned characteristic that the static component varies inversely with the angle to the crack surface.

Application to Dynamic Fracture

Dynamic brittle fracture initiates at an existing crack under rapid loading conditions, such as stress wave diffraction at the crack edge [12]. If there are no other external stress fields, the crack in an ideal, homogeneous, isotropic solid is often treated as completely at rest prior to the stress wave arrival. In a real material, however, if a screw dislocation of strength h is located in equilibrium as in Fig. 1(*a*), and intensity factor k_0, where [4]

$$k_0 = -\frac{hK_0}{\sqrt{d}} = -\frac{h}{\pi\sqrt{d}}\cos\frac{\psi}{2} \tag{40}$$

will exist. An antiplane shear wave that subsequently ($s'=0$) diffracts at the crack edge will generate an additional intensity factor k_d. For the plane step-stress wave of magnitude σ in Fig. 5, it can be shown [13] that

$$g = \frac{k_d}{k_0} = \frac{\sigma}{\mu}\frac{d}{h}\frac{4\sqrt{(1-\sin\Phi)}}{\cos\frac{\psi}{2}}\sqrt{\frac{s'}{d}} \quad (s' \geq 0) \tag{41}$$

The dislocation strength is on the order of the atomic spacing in the cracked material. If it is argued that linear elasticity breaks down very near the dislocation or that the large dislocation force does not allow equilibrium dislocations to exist very near the crack edge [4], then $|d/h| >> 1$. On the other hand, we require that $|\sigma/\mu| << 1$ in the elastic range; e.g., $|\sigma/\mu| \sim 0.0075$ for a hot-rolled low carbon steel at yield. The ratio of trigonometric terms can take on any value between 0 and ∞. Equation (41) shows, therefore, that the dislocation stress field can concievably govern ($|g| < 1$) the crack edge for a finite period. If $\sigma/h > 0$, then diffraction merely intensifies the existing (dislocation) stress field. If $\sigma/h < 0$, however, diffraction initially relaxes the crack edge stress field and subsequently reverses its sign. That is, the dislocation temporarily shields the crack edge from the wave diffraction effects, and so postpones the onset of a stress level critical for fracture. A discussion of this shielding concept has been presented for static situations in [4, 5].

If the wave diffraction process also triggers dislocation motion, the results of previous sections would modify (41) to give

$$g = \frac{\sigma}{\mu}\frac{d}{h}\frac{4(1+\dot{R})\sqrt{(1-\sin\Phi)}}{\cos\frac{\theta}{2}+\dot{D}\cos\left(\beta+\left|\frac{\theta}{2}\right|\right)}\sqrt{\frac{R}{d}}\sqrt{\frac{s'}{d}} \quad (s'>0) \tag{42}$$

$$s' + s_c = t^* + R(t^*) \geq d \tag{43}$$

Here $|s_c|$ is the interval between the arrival of the plane wave at the crack edge and dislocation motion initiation. The force on an equilibrium dislocation such as in Fig. 1(*a*) varies inversely with d and always points to the crack edge [4]. Therefore, if we ignore effects such as grain distortion or the plane wave itself and assume that the dislocation moves directly to the crack edge, previous analysis shows that the governance ratio g reduces to

$$g = \frac{\sigma}{\mu}\frac{d}{h}\frac{4\sqrt{(1-\sin\Phi)}}{\cos\frac{\psi}{2}}\sqrt{\frac{R}{d}}\sqrt{\frac{s'}{d}} \quad (s'>0) \tag{44}$$

The g-behavior versus s'/d for both stationary and moving dislocations is shown in Fig. 5 for various combinations of

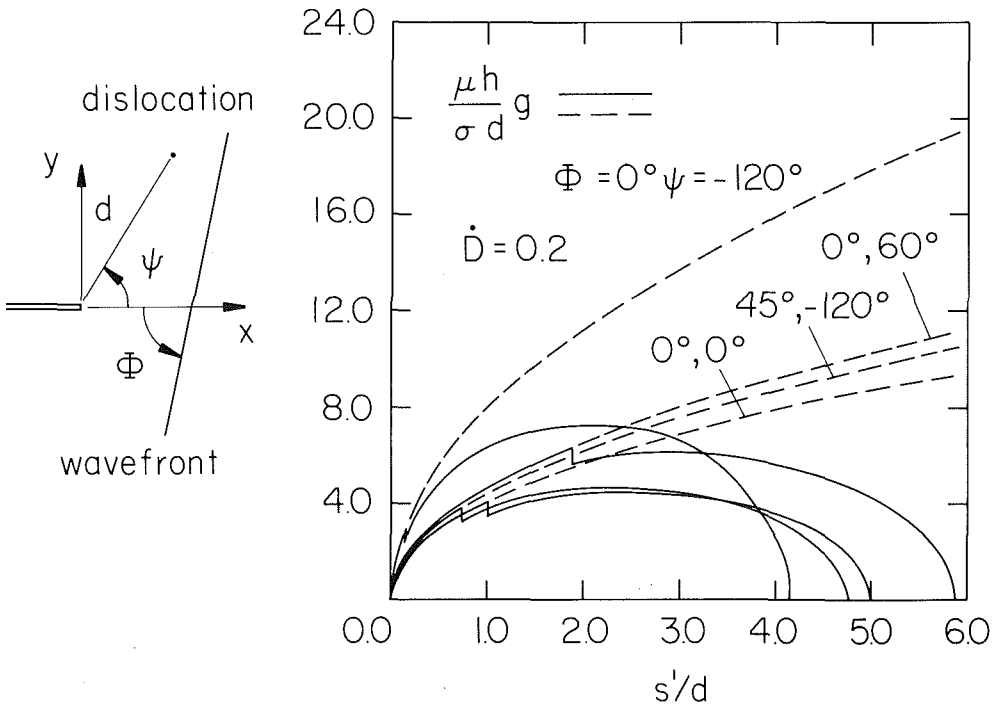

Fig. 5 *g* versus *s'/d*

Downloaded 02 May 2010 to 171.66.16.246. Redistribution subject to ASME license or copyright; see http://www.asme.org/terms/Terms_Use.cfm

(Φ,ψ). It is assumed that dislocation motion initiates on arrival of the wave pattern and proceeds at a constant speed $\dot{D}=0.2$. The discontinuities in Fig. 5 indicate the motion signal arrivals and the broken lines, the g-curves if no motion had occurred. The dislocation lies in the crack shadow when $\psi-\Phi>\pi/2$. Then, the diffracted cylindrical wave (see Figs. 1(b) and (c)) reaches the dislocation before the plane wave. If it is assumed that this wavefront has the same triggering effect, then $s_c=-d$ and $g=0$ for $s'/d<1.0$. The $(\Phi,\psi)-$ values chosen in Fig. 5 do not fall into this category.

Figure 5 shows that the stationary dislocation initially governs ($|g|<1$) the crack edge stress field. After a finite time that varies directly with $|\sigma d/\mu h|$ the wave diffraction governs ($|g|>1$) indefinitely, and to an ever-increasing degree. When dislocation motion occurs, however, the initial dislocation governance period may be increased while the wave diffraction governance interval is now finite, and may vanish entirely if $|\sigma d/\mu h|$ is large enough. Moreover, the degree of wave diffraction governance is lower than for the stationary dislocation at the same instant. In Fig. 5, the time intervals are on the order of the shear wave travel time d between the equilibrium dislocation and crack edge.

Figure 5 thus confirms the stationary dislocation observations. Because the dislocation-induced intensity factor itself increases with s' (inversely with R), Fig. 5 shows that these observations must be modified for the moving dislocation: For $\sigma/h>0$, the stress intensification process is accelerated, while for $\sigma/h<0$, the relaxation process might not occur ($|g|<1$) or will be briefer. Thus, a stress level critical for fracture will always be achieved sooner if the dislocation moves to the crack edge.

Since the time intervals arising here are on the order of shear wave travel times between the crack and equilibrium dislocation, the delay/acceleration effects for a single dislocation might not be readily detectable experimentally. However, a dislocation array might by superposition give measurable time intervals. On the other hand, the number of dislocations per grain has been estimated to be on the order of 10^{10}, which implies an unreasonably large k_0 total. However, this implication would follow from the assumption that h for each dislocation in the array is of the same sign. Finally, it should be noted that the results obtained here are for a dislocation existing initially in equilibrium. Wave excitation of the dislocation source itself involves the solution to the problem of the instantaneously appearing dislocation. This is related but not identical to the problem defined by (3) and (4).

Brief Summary

This paper first studied the dynamic stress intensity factor generated for a stationary crack by the motion of a screw dislocation of unit strength from an equilibrium position. The intensity factor was found to have two components of opposite sign. The first component depended on the instantaneous dislocation position. The second component also depended on the instantaneous dislocation speed and orientation, but vanished for the important case of a dislocation moving directly toward the crack edge. Discontinuities in the dislocation speed or a nonsmooth path were found to cause discontinuities in the intensity factor. However, appropriate behavior by either could remove the discontinuity effect due to the other. It was also found that dislocation arrest caused the intensity factor to instantaneously attain a new equilibrium value which, on the crack surface, vanishes.

More generally, the study showed that screw dislocation motion from rest near an otherwise undisturbed crack edge does not necessarily intensify or relax the stress field there. Stress field response depends on the dislocation path and speed, and how they affect the dislocation position in particular, the distance between the crack edge, and dislocation.

The study results were then used to consider a screw dislocation near a crack edge at which plane step-stress antiplane shear wave diffraction occurs. In terms of the combined intensity factor, it was found that, depending on the relation between the wave stress and the slip direction, a stationary screw dislocation can either accelerate or delay the onset of the stress level critical for crack edge fracture. If the wave pattern, however, also triggers dislocation motion into the crack edge, the delaying effect is diminished and the acceleration process accentuated. For a single dislocation, the time intervals involved are apparently on the order of the shear wave travel time between the equilibrium dislocation and the crack edge. The dimensionless quantity $\sigma d/\mu h$, the dislocation path angle ψ, and wavefront angle Φ are key parameters in determining these time intervals.

The results of this paper will form the basis for further studies of dynamic fracture in the presence of dislocations. In particular, future work will utilize more fully the path effect results obtained here; attempts to model the effects of crack edge and multiple dislocation interaction on the dislocation path in view of the dislocation force concept will be made. It is hoped, however, that the present results themselves will allow insight into this area.

References

1 Bilby, B. A., and Eshelby, J. D., "Dislocations and the Theory of Fracture," in: *Fracture*, Vol. 1, Liebowitz, H., ed. Academic Press, New York, 1968, Chapter 2.

2 Rice, J. R., and Thomson, R., "Ductile Versus Brittle Behaviour of Crystals," *Philosophical Magazine*, Vol. 29, 1974, pp. 73–97.

3 Tirosh, J., and McClintock, F. A., "Finding Elastoplastic Stress and Strain in Cracked Bars Under Torsion by Assembling Screw Dislocations," *Engineering Fracture Mechanics*, Vol. 11, 1979, pp. 563–572.

4 Majumdar, B. S., and Burns, S. J., "An Elastic Theory of Dislocation Arrays and Inclusions Near a Sharp Crack," Technical Report #2422-26, Department of Mechanical and Aerospace Sciences, University of Rochester, Rochester, N.Y., 1980.

5 Thomson, R. M., and Sinclair, J. E., "Mechanics of Cracks Screened by Dislocations," *Acta Metallurgica*, Vol. 30, 1982, pp. 1325–1334.

6 Johnston, W. G., and Gilman, J. J., "Dislocation Velocities, Dislocation Densities, and Plastic Flow in Lithium Fluoride Crystals," *Journal of Applied Physics*, Vol. 30, 1959, pp. 129–144.

7 Burridge, R., and Knopoff, L., "Body Force Equivalents for Seismic Dislocations," *Bulletin of the Seismological Society of America*, Vol. 54, 1964, pp. 1875–1888.

8 Brock, L. M., "The Dynamic Stress Intensity Factor for a Crack Due to Arbitrary Rectilinear Screw Dislocation Motion," *Journal of Elasticity*, to appear.

9 Sneddon, I. N., *The Use of Integral Transforms*, McGraw-Hill, New York, 1972.

10 deHoop, A. T., "A Modification of Cagniard's Method for Solving Seismic Pulse Problems," *Applied Scientific Research*, Vol. B8, 1960, pp. 349–356.

11 Kostrov, B. V., "Unsteady Propagation of Longitudinal Shear Cracks," *Prikladnaya Matem i Mekhanika*, Vol. 30, 1966, pp. 1241–1248 (English translation).

12 Achenbach, J. D., *Wave Propagation in Elastic Solids*, North-Holland, Amsterdam, 1973, Chapter 9.

13 Brock, L. M., "Effects of Secondary Diffractions on the Stress Intensity Factors Generated for a Finite Crack by a Shear Wave," *International Journal of Engineering Science*, Vol. 13, 1975, pp. 851–859.

Downloaded 02 May 2010 to 171.66.16.246. Redistribution subject to ASME license or copyright; see http://www.asme.org/terms/Terms_Use.cfm

The Determination of the Elastodynamic Fields of an Ellipsoidal Inhomogeneity

L. S. Fu
Associate Professor,
Department of Engineering Mechanics,
Ohio State University,
Columbus, Ohio 43210
Mem. ASME

T. Mura
Professor,
Department of Civil Engineering,
Northwestern University,
Evanston, Ill. 60201
Mem. ASME

Elastic fields of a single ellipsoidal inhomogeneity embedded in an infinite elastic matrix subjected to plane time-harmonic waves are studied by employing the concept of eigenstrain and the extended version of Eshelby's method of equivalent inclusion. Using the dynamic version of the Betti-Rayleigh reciprocal theorem, an integral representation of the displacement field, due to the presence of inhomogeneity, is given in terms of the eigenstrains. Two types of eigenstrains arise in the elastodynamic case. Expanding the eigenstrains and applied strains in the polynomial form in the position vector $\mathbf{r}$ *and satisfying the equivalence conditions at every point, the governing simultaneous algebraic equations for the unknown coefficients in the eigenstrain expansion are derived. Elastodynamic field outside an ellipsoidal inhomogeneity in a linear elastic isotropic medium is given as an example. The angular and frequency dependence of the induced displacement field, which is in fact the scattered displacement field, the differential and the total cross sections are formally given in series expansion form for the case of uniformly distributed eigenstrains.*

Introduction

The elastodynamic fields in the region outside a single ellipsoidal inhomogeneity (scatterer) embedded in an infinite medium are of fundamental importance in nondestructive evaluation (NDE). A comprehensive discussion of applications of elastic wave theory in NDE can be found in references [1-3]. This problem has been attacked by a variety of methods: the direct volume integral formulation [4, 5]; the matched asymtotic expansions [6]; the surface integral formulation [7]; and the polarization approach [8]. These solutions are appropriate at very long wavelength or very low frequency range, $ka << 1$, where k is the wave number and "a" is a typical geometric dimension of the scatterer.

It appears that Mal and Knopoff [4] were first in presenting a direct volume integral formulation where they gave the scattered displacements in terms of volume integrals involving the displacements and strains inside the scatterer. Since these fields are not known, successive approximations were obtained by using the incident wave field [9], or by using the static displacement field for a spherical scatterer [4], and for an ellipsoidal scatterer [10]. The latter approach greatly enhances the validity of the solution toward a higher dimensionless wave number, say ka of value near unity. Special cases wtihin the ellipsoidal system such as the cases of spheroids, cylinders, flat cracks, etc., can be easily studied. Due to the use of the static solution as a first approximation, the frequency structure of the solution is somehow limited and cannot easily be extended to medium frequency ranges, say, $1 < ka < 10$.

Using the equivalent inclusion method, Eshelby [11-13] studied the static elastic fields "inside" and "outside" an ellipsoidal inclusion or inhomogeneity embedded in an infinite isotropic elastic medium under applied tension. All through this paper, an "inhomogeneity" is referred to as a

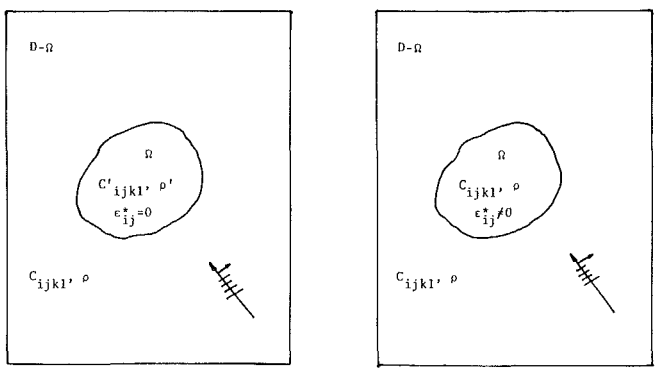

Fig. 1 (*a*) The inhomogeneity problem and (*b*) the inclusion problem

Contributed by the Applied Mechanics Division for presentation at the 1983 ASME Applied Mechanics, Bioengineering, and Fluids Engineering Conference, Houston, Texas, June 20-22, 1983 of THE AMERICAN SOCIETY OF MECHANICAL ENGINEERS.

Discussion on this paper should be addressed to the Editorial Department, ASME, United Engineering Center, 345 East 47th Street, New York, N.Y. 10017, and will be accepted until two months after final publication of the paper itself in the JOURNAL OF APPLIED MECHANICS. Manuscript received by ASME Applied Mechanics Division, June 1981; final revision, June, 1982. Paper No. 83-APM-19.

Copies will be available until February, 1984.

Copyright © 1983 by ASME
Downloaded 02 May 2010 to 171.66.16.246. Redistribution subject to ASME license or copyright; see http://www.asme.org/terms/Terms_Use.cfm

region of different elastic moduli and density compared with its surrounding medium and an "inclusion" is referred to as a region with the same elastic moduli and density as its surrounding medium but include in it a distribution of eigenstrains. Eigenstrains are strains that are not derived from mechanical loading. As examples we note that thermal strains and also the swelling strains due to the presence of moisture are special types of eigenstrains.

The method of equivalent inclusion is a method where the inhomogeneity is replaced by an inclusion such that solutions for the two problems are exactly the same. The basic concept is sketched in Fig. 1. Wheeler and Mura [14] first developed but did not apply a complete eigenstrain formulation to the dynamic case. They studied the dispersion of waves in fiber-reinforced and laminated composites. Since no treatment was given to the mismatch in mass density, their results are appropriate for the case such is absent. Subsequently, Fu presented a complete eigenstrain formulation to study the interaction problem [15] and the scattering problem [16].

The purpose of this study is to extend the method of equivalent inclusion to fully develop the equivalence conditions and to present a method for complete determination of the eigenstrains and/or their derivatives as appropriate. The equivalence conditions and the solutions to the elastodynamic fields, exterior to an inhomogeneity, in terms of eigenstrains and/or their derivatives are first developed. Agreement with other approaches is then easily seen. The formulation is general and both the inhomogeneity and the host medium can be anisotropic. The problem of an ellipsoidal inhomogeneity embedded in a linear elastic isotropic whole space subjected to plane time-harmonic wave is studied and the differential and total cross sections for a uniformly distributed eigenstrain are detailed and shown.

Equivalence Conditions

In this section, we develop the equivalence conditions by requiring that the displacement and stress fields obtained in the inclusion problem be identical to those for the inhomogeneity problem, Figs. 1(*a*) and 1(*b*).

The Inhomogeneity Problem (Problem *I*). Consider the problem of a single inhomogeneity occupying the region Ω in the infinitely extended region D-Ω subjected to applied incident wave field $u_j^{(i)}$, Fig. 1. Let the elastic moduli and the mass density be denoted by C'_{ijkl} and ρ' for the inhomogeneity, and by C_{ijkl} and ρ for the host medium, respectively.

The governing equations for the displacement field are:

$$C_{jkrs}\ u_{r,sk} + \Delta C_{jkrs} u_{r,sk} = \rho \ddot{u}_j + \Delta\rho\ \ddot{u}_j \quad \text{in} \quad D \tag{1}$$

in which we used

$$\sigma_{jk} = C_{jkrs}\ u_{r,s} + \Delta C_{jkrs}\ u_{r,s} \tag{2}$$

$$\Delta\rho = \begin{cases} 0 & \text{in} \quad D-\Omega \\ \rho' - \rho & \text{in} \quad \Omega \end{cases} \tag{3}$$

$$\Delta C_{jkrs} = \begin{cases} 0 & \text{in} \quad D-\Omega \\ C'_{jkrs} - C_{jkrs} & \text{in} \quad \Omega \end{cases} \tag{4}$$

Let the superscripts (i) and (m) denote fields associated with the "incident" wave, and the "mismatch' in mass density and elastic moduli, respectively. It is clear that

$$u_j = u_j^{(i)} + u_j^{(m)} \tag{5}$$

as in the absence of mismatch, $u_j^{(m)}$ disappears, and the total field is identical to the incident field.

The boundary conditions are that (1) the displacements and tractions at the intersection of the regions Ω and D-Ω must be continuous, and (2) the characteristics of outgoing wave field and that the stresses die out at infinity must be observed.

The Inclusion Problem (Problem *II*). Consider next an infinite elastic solid of homogeneous moduli C_{ijkl} and density ρ with distributed eigenstrains, denoted by ϵ^*_{ij}, in a region Ω, such that Ω is identical in shape and size to that in Problem *I*, and

$$\epsilon^*_{ij} = \begin{cases} 0 & \text{in} \quad D-\Omega \\ \epsilon^*_{ij} & \text{in} \quad \Omega \end{cases} \tag{6}$$

The total strain field is

$$\epsilon_{rs} = (u_{r,s} + u_{s,r})/2 = \epsilon^e_{rs} + \epsilon^*_{rs} \tag{7}$$

where

$$\sigma_{jk} = C_{jkrs}\ \epsilon^e_{rs} \tag{8}$$

Using equations (6) and (7) in the equations of motion, we easily obtain the governing equations for the total displacement field as follows:

$$C_{jkrs}\ u_{r,sk} = \rho\ \ddot{u}_j + C_{jkrs}\ \epsilon^*_{rs,k} \quad \text{in} \quad D \tag{9}$$

It is clear from equation (9) that

$$u_j = u_j^{(i)} + u_j^* \tag{10}$$

where u_j^* is the displacement field due to the presence of ϵ^*_{ij} and it disappears when ϵ^*_{ij} vanish. The only boundary conditions are those regular conditions at infinity and the radiation condition.

Equivalence Conditions. For a complete equivalence between Problem *I* and Problem *II*, we require that the displacement and stress fields in the two problems be identical. Hence, for equivalence in stress field, we require, from equations (2), (7), and (8),

$$(C_{jkrs}\ u_{r,s} + \Delta C_{jkrs}\ u_{r,s})_I = (C_{jkrs}(u_{r,s} - \epsilon^*_{rs}))_{II} \tag{11}$$

For equivalence in displacement fields we require that the equations (1) and (9) be identical, hence

$$(\Delta\rho\ \ddot{u}_j - \Delta C_{jkrs} u_{r,sk})_I = (C_{jkrs}\ \epsilon^*_{rs,k})_{II} \tag{12}$$

It is clear that equations (11) and (12) are automatically satisfied in the region D-Ω by observing the definitions given in equations (3), (4), and (6). It is convenient to split the right-hand side of equations (12) into two parts such that

$$C_{jkrs}\ \epsilon^{*(1)}_{rs,k} = -\Delta C_{jkrs}\ u_{r,sk} \tag{13a}$$

$$C_{jkrs}\ \epsilon^{*(2)}_{rs,k} = \Delta\rho\ \ddot{u}_j \tag{13b}$$

Employing equations (11)–(13) and equations (5) and (10) we obtain the equivalence conditions as:

$$\Delta C_{jkrs}\ u^{(m)}_{r,s}(\bar{\mathbf{r}},t) + C_{jkrs}\ \epsilon^{*(1)}_{rs}(\bar{\mathbf{r}},t) = -\Delta C_{jkrs}\ u^{(i)}_{r,s}\ (\bar{\mathbf{r}},t), \quad \text{in} \quad \Omega \tag{14a}$$

$$\Delta\rho\ \ddot{u}^{(m)}_j(\bar{\mathbf{r}},t) - C_{jkrs}\ \epsilon^{*(2)}_{rs,k}\ (\bar{\mathbf{r}},t) = -\Delta\rho\ \ddot{u}^{(i)}_j(\bar{\mathbf{r}},t) \quad \text{in} \quad \Omega \tag{14b}$$

These conditions can be used to determine the eigenstrain distribution that is necessary for the equivalence of Problems *I* and *II* provided that we can write $u_r^{(m)}$ in terms of the eigenstrains. One such method is given in [17]. It is of interest to note that equations (14*a*) are identical in form as the equivalence conditions in the static case and that only in equations (14*b*) the jth components of $C_{jkrs}\ \epsilon^{*(2)}_{rs,k}$ are needed for determining $u_j^{(m)}$. Further discussion on the determination of the eigenstrains will follow in the next few sections.

The Elastodynamic Fields Associated With an Inhomogeneity

Instead of finding the solution to the physical problem stated we seek the solution to the equivalent inclusion problem. The governing equations are equations (6)–(9). Let the incident wave field be plane time harmonic then the time-

Downloaded 02 May 2010 to 171.66.16.246. Redistribution subject to ASME license or copyright; see http://www.asme.org/terms/Terms_Use.cfm

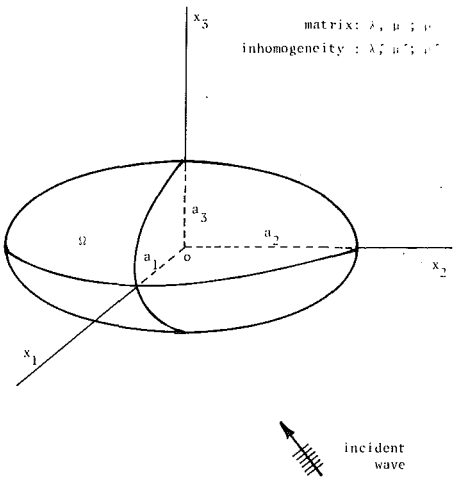

Fig. 2 An ellipsoidal inhomogeneity under incident wave

harmonic displacement and eigenstrain fields can be written as:

$$u_j^{(m)}(\bar{\mathbf{r}},t) = u_j^{(m)}(\bar{\mathbf{r}}) \exp(-i\omega t)$$
$$\epsilon_{rs}^*(\bar{\mathbf{r}},t) = \epsilon_{rs}^*(\bar{\mathbf{r}}) \exp(-i\omega t)$$

where ω is the frequency of the incident wave field and $i \cdot i = -1$. Using the dynamic version of the Betti-Rayleigh reciprocal theorem and suppressing the time dependence we obtain the displacement field as:

$$u_m(\bar{\mathbf{r}}') = u_m^{(i)}(\bar{\mathbf{r}}') - \iiint_V C_{jkrs}\, g_{jm}(\bar{\mathbf{r}},\bar{\mathbf{r}}')\epsilon_{rs,k}^*(\bar{\mathbf{r}})\, dV \tag{15}$$

or, upon employing Gauss' theorem,

$$u_m(\bar{\mathbf{r}}') = u_m^{(i)}(\bar{\mathbf{r}}') + \iiint_V C_{jkrs}\, g_{jm,k}(\bar{\mathbf{r}},\bar{\mathbf{r}}')\epsilon_{rs}^*(\bar{\mathbf{r}})\, dV \tag{16}$$

where $g_{jm}(\bar{\mathbf{r}},\bar{\mathbf{r}}')$ is the spatial part of the solution to the associated Green's function problem for equation (9). Note that the use of the Green's function preserves the characteristics of an outward propagating wave and satisfies the boundary condition on stress at infinity. Since there are two types of eigenstrains, we write the displacements as

$$u_m(\bar{\mathbf{r}}') = u_m^{(i)}(\bar{\mathbf{r}}') - \iiint_\Omega g_{jm}(\bar{\mathbf{r}},\bar{\mathbf{r}}')C_{jkrs}\,\epsilon_{rs,k}^{*(2)}(\bar{\mathbf{r}})\, dV - \iiint_\Omega g_{jm,k'}(\bar{\mathbf{r}},\bar{\mathbf{r}}')C_{jkrs}\,\epsilon_{rs}^{*(1)}(\bar{\mathbf{r}})\, dV \tag{17}$$

where equations (6), (15), and (16) are used. It is clear that only the jth component of $C_{jkrs}\,\epsilon_{rs,k}^{*(2)}$ are needed to determine the displacements. We can therefore view this as a vector quantity, say π_j^*, where

$$\pi_j^* = C_{jkrs}\,\epsilon_{rs,k}^{*(2)} \tag{18}$$

Substituting equation (18) in equation (17) we obtain the solution form given as equation (2.19) in reference [8, p. 291], for the time-harmonic case. If the equations (14) are substituted in equation (17), we find the solution form equation (12) in reference [4, p. 379], or equation (2.25) in reference [5, p. 2806].

The stress field that has arisen from the presence of mismatch or equivalently by the presence of eigenstrains can be obtained by using Hooke's law and equations (5), (10), and (17) as:

$$\sigma_{pq}^{(m)}(\bar{\mathbf{r}}') = -\frac{1}{2}C_{pqmn}\iiint_\Omega [(g_{jm,n'}(\bar{\mathbf{r}},\bar{\mathbf{r}}') + g_{jn,m'}(\bar{\mathbf{r}},\bar{\mathbf{r}}')]\pi_j^*(\bar{\mathbf{r}})\, dV - \frac{1}{2}C_{pqmn}\iiint_\Omega (g_{jm,k'n'} + g_{jn,k'm'})C_{jkrs}\,\epsilon_{rs}^{*(1)}(\bar{\mathbf{r}})\, dV \tag{19}$$

Quantities of interest such as the differential cross section $dP(\omega)/d\Omega$ defined as: [18, 5]

$$\frac{dP(\omega)}{d\Omega} = \lim_{r\to\infty} \frac{<r^2\, l_i\, \sigma_{ij}^s\, \dot{u}_i^s>}{<I^0>} \tag{20}$$

can be obtained in terms of the eigenstrains via equations (17)–(20), where I^0 is the incident power,

$$I^0 = n_i\, \sigma_{ij}^{(i)}\, \dot{u}_j^{(i)},$$

$<f(t)>$ denotes time averaging of a function

$$<f(t)> = \frac{1}{T}\int_0^T f(t)\, dt,$$

and l_i, n_i are direction cosines for $\bar{\mathbf{r}}$ and $\bar{n}$, respectively. The differential $d\Omega$ is the differential element of a solid angle. The total cross section is simply

$$p(\omega) = \int_{4\pi} \frac{dP(\omega)}{d\Omega} \cdot d\Omega \tag{21}$$

In what follows we give examples for the scattering of an isotropic smooth inhomogeneity in a linear isotropic infinite medium subjected to plane time-harmonic incident wave field.

Linear Elastic Isotropic Medium

For such a medium the spatial part of the Green's function is

$$g_{jm}(\bar{\mathbf{r}}-\bar{\mathbf{r}}') = \frac{1}{4\pi\rho\omega^2}\{\beta^2\,\delta_{jm}(\exp i\beta R)/R + [(\exp i\beta R)/R - (\exp i\alpha R)/R]_{,jm}\} \tag{22}$$

where

$$R = |\bar{\mathbf{r}}-\bar{\mathbf{r}}'|, \quad \alpha^2 = \frac{\omega^2}{v_L^2} = \frac{\rho\omega^2}{\lambda+2\mu}, \quad \beta^2 = \frac{\omega^2}{v_T^2} = \frac{\rho\omega^2}{\mu}$$

and λ, μ, v_L, and v_T are the Lame's constants, longitudinal wave speed, and transverse wave speed, respectively. Before we substitute equation (22) in equation (17), we expand the unknown quantities associated with the eigenstrains in form of a polynomial as [17, 19]:

$$\pi_j^*(\bar{\mathbf{r}}) = A_j + A_{jk}\, x_k + A_{jkl}\, x_k\, x_l + \ldots \tag{23}$$
$$\epsilon_{ij}^{*(1)}(\bar{\mathbf{r}}) = B_{ij} + B_{ijk}\, x_k + B_{ijkl}\, x_k\, x_l + \ldots \tag{24}$$

where A_j, A_{jk}, ..., B_{ij}, B_{ijk}, ... are constants. Substituting equations (22)–(24) with π_j^* defined by equation (18), we obtain

$$u_m^{(m)}(\bar{\mathbf{r}}) = u_m(\bar{\mathbf{r}}) - u_m^{(i)}(\bar{\mathbf{r}}) = f_{mj}(\bar{\mathbf{r}})A_j + f_{mjk}(\bar{\mathbf{r}})A_{jk} + \ldots + F_{mij}(\bar{\mathbf{r}})B_{ij} + F_{mijk}(\bar{\mathbf{r}})B_{ijk} + \ldots \tag{25a}$$

where

$$4\pi\rho\omega^2 f_{mj}(\bar{\mathbf{r}}) = -\beta^2\,\phi\,\delta_{mj} + \psi_{,mj} - \phi_{,mj} \tag{25b}$$
$$4\pi\rho\omega^2 f_{mjk}(\bar{\mathbf{r}}) = -\beta^2\,\phi_k\,\delta_{mj} + \psi_{k,mj} - \phi_{k,mj} \tag{25c}$$
$$\ldots$$
$$4\pi\rho\omega^2 F_{mij}(\bar{\mathbf{r}}) = -[\lambda\alpha^2\,\psi_{,m}\,\delta_{ij} + 2\mu\,\beta^2\,\phi_{,i}\delta_{mj} - 2\mu\,\psi_{,mij} + 2\mu\,\phi_{,mij}] \tag{25d}$$
$$4\pi\rho\omega^2 F_{mijk}(\bar{\mathbf{r}}) = -[\lambda\,\alpha^2\psi_{k,m}\,\delta_{ij} + 2\mu\,\beta^2\phi_{k,i}\,\delta_{mj} - 2\mu\,\psi_{k,mij} + 2\mu\,\phi_{k,mij}] \tag{25e}$$
$$\ldots$$

and

$$\phi(\bar{\mathbf{r}}) = \iiint_\Omega (\exp i\beta R)/R\, dV' \tag{26a}$$
$$\phi_k(\bar{\mathbf{r}}) = \iiint_\Omega x_k'\, (\exp i\beta R)/R\, dV' \tag{26b}$$
$$\ldots$$

Downloaded 02 May 2010 to 171.66.16.246. Redistribution subject to ASME license or copyright; see http://www.asme.org/terms/Terms_Use.cfm

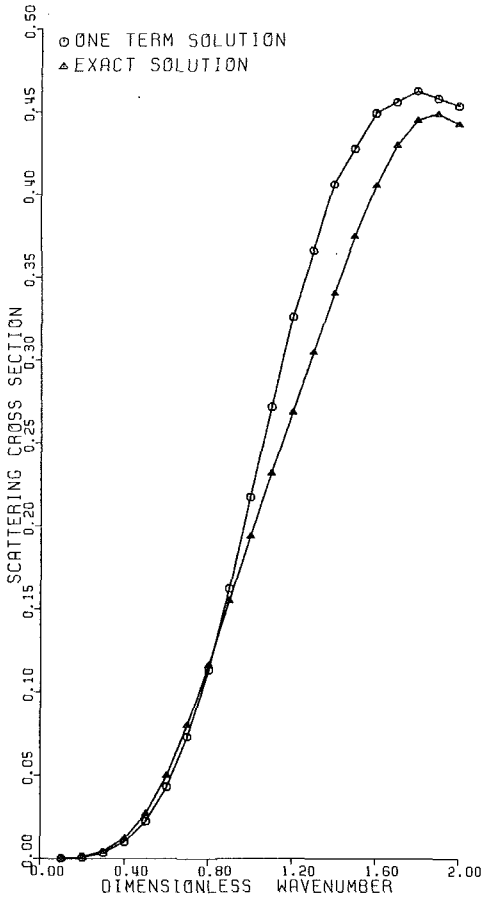

Fig. 3 Scattering cross section as a function of *ka*: aluminum sphere in germanium

$$\phi_{kl\ldots s}(\bar{\mathbf{r}}) = \iiint_{\Omega} x_k' \, x_l' \ldots x_s' \, (\exp i\beta R)/R \, dV' \tag{26c}$$

$$\psi(\bar{\mathbf{r}}) = \iiint_{\Omega} (\exp i\alpha R)/R \, dV' \tag{26d}$$

$$\psi_k(\bar{\mathbf{r}}) = \iiint_{\Omega} x_k' \, (\exp i\alpha R)/R \, dV' \tag{26e}$$

$$\ldots$$

$$\psi_{kl\ldots s}(\bar{\mathbf{r}}) = \iiint_{\Omega} x_k' \, x_l' \ldots x_s' \, (\exp i\alpha R)/R \, dV' \tag{26f}$$

The ϕ- and ψ-integrals given in equations (26) are the volume integrals associated with the inhomogeneous Helmholtz equation. They can be carried out for an ellipsoidal region by expanding $(\exp ikR)/R$ in Taylor series expansions with respect to $\bar{\mathbf{r}}'$, for $r > r'$ and with respect to $\bar{\mathbf{r}}$ for $r < r'$. Here k can be either α or β. Details are given in reference [20]. This type of expansion for the integrand is particularly useful in determining the coefficients of a "polynomial" distribution of π_j^* and $\epsilon_{ij}^{*(1)}$.

To determine the coefficients A_j, A_{jk}, ..., B_{jk}, B_{jkl}, ..., we substitute equations (18) and (23)–(25) in equations (14) and note that we are dealing with time-harmonic displacements. Since the π_j^* and $\epsilon_{ij}^{*(1)}$ are given in terms of polynomials we expand the $u_j^{(m)}(\bar{\mathbf{r}})$, $u_{r,s}^{(m)}(\bar{\mathbf{r}})$, and $u_{r,s}^{(i)}(\bar{\mathbf{r}})$ in Taylor series expansions with respect to the coordinate origin, by matching the coefficients of terms to the same power of x_i^0, x_i, $x_i x_j$, ..., we obtain a set of infinite number of algebraic equations for A_j, A_{jk}, ... B_{jk}, B_{jkl}, ... The scattering cross sections are given in terms of these coefficients by way of equations (17), (19), and (20).

Examples

Uniformly Distributed Eigenstrains. Let the region Ω be an ellipsoidal region of $2a_1$, $2a_2$, and $2a_3$ along the x, y, and z-axis, respectively, Fig. 2. We first expand the integrals and their derivatives in Taylor series for $r < r'$ and obtain the Taylor series for $u_j^{(m)}(\bar{\mathbf{r}})$ from equations (25). Substituting this series for $u_j^{(m)}(\bar{\mathbf{r}})$ and its derivatives in equations (14) with equations (23) and (24), and the Taylor series for $u_j^{(i)}(\bar{\mathbf{r}})$, we obtain the governing algebraic equations for A_j, A_{jk}, ..., B_{ij}, B_{ijk}, ... by comparing the order in the power series i.e., x_i^0, x_i, $x_i x_j$, etc. To save space these equations are not shown here. Once these coefficients are determined, we go back to equations (25) and find the scattered displacement field, which is $u_j^m(\bar{\mathbf{r}})$ when $r \to \infty$. By using formulas given in [20] the scattered displacement field is given in terms of a triple sum.

In what follows we consider the case for a plane time-harmonic wave propagating in the $+z$-direction, i.e.

$$u_j^{(i)}(\bar{\mathbf{r}}, t) = u_0 \exp i(\alpha z - \omega t) \tag{27}$$

For a given (ka) enough terms must be taken in determining the coefficients A's and B's in equations (23) and (24) from

$$\underset{mXm}{[f]} \quad \underset{mX1}{\{A\}} + \underset{mXm}{[F]} \quad \underset{mX1}{\{B\}} = \underset{mX1}{\{H\}}$$

$$\underset{mXm}{[d]} \quad \underset{mX1}{\{A\}} + \underset{mXm}{[D]} \quad \underset{mX1}{\{B\}} = \underset{mX1}{\{E\}}$$

where $[f]$ and $[F]$ are defined by the Taylor expansion of the f- and F-functions at $r = 0$, and $[d]$ and $[D]$ are the average of the symmetric part of $[f]$ and $[F]$. The right-hand side are obtained from the Taylor series expansion for $u_j^{(i)}$ and $\epsilon_{ij}^{(i)}$, respectively.

Using equations (12) and (17) in [20] and equation (25), we find that, for the lowest order of $\epsilon_{ij}^{*(1)}$ and π_j^* or $C_{jkrs}\epsilon_{rs,k}^{*(2)}$, i.e., keeping only the constant terms in equations (23) and (24) at a distance far away from the ellipsoid:

$$u_m^{(s)}(\bar{\mathbf{r}}, t) = u_m^{(m)}(\bar{\mathbf{r}}, t)|_{r\to\infty} = (4\pi\rho\omega^2)^{-1}$$

$$\sum_{n=0,2}^{\infty} \sum_{l=0}^{n} \sum_{k=0,2}^{n-l} \left[\frac{(-1)^n 4\pi a_1 a_2 a_3 \; a_1^l a_2^k a_3^{n-l-k} l_1^l l_2^k l_3^{n-l-k} (n/2)!}{(n+3)(n+1)n!(l/2)!(k/2)!(n-l-k)/2!} \right] \cdot$$

$$\cdot \left\{ \frac{\exp i\alpha r}{r} [-\alpha^2 (i\alpha)^n l_m l_j A_j - \lambda i\alpha^3 (i\alpha)^n l_m \delta_{kj} B_{kj} \right.$$

$$- 2\mu i\alpha^3 (i\alpha)^n l_m l_k l_j B_{kj}]$$

$$+ \frac{\exp i\beta r}{r} [\beta^2 (l_m l_j - \delta_{mj}) A_j - 2\mu i\beta^3 l_k B_{km}$$

$$\left. + 2\mu i\beta^3 l_m l_k l_j B_{kj}](i\beta)^n \right\} \exp(-i\omega t) \tag{28}$$

where the repeated subscripts must be summed from 1 to 3. Note that B_{kj} is nondimensional and is homogeneous in (αu_0) and A_j is of dimension $(\Delta\rho \cdot \omega^2 \cdot u_0)$. The first term in the expression, i.e., $n = 0$, gives the following:

$$\frac{u_m^{(s)}(\bar{\mathbf{r}})}{(\alpha a_1)^3 u_0} = \frac{\exp i\alpha r}{3\ \alpha r} G_m^0(\theta, \phi) + \frac{\exp i\beta r}{3\ \beta r} H_m^0(\theta, \phi) \tag{29a}$$

where (r, θ, ϕ) are spherical coordinates and

$$G_m^0(\theta, \phi) = -(a_2 a_3 / a_1 a_1)[l_m l_j A_j^*(\Delta\rho/\rho)$$

$$+ (1 - 2\alpha^2/\beta^2) l_m \; B_{jj}^* + 2 l_m l_k l_j \; B_{kj}^* (\alpha^2/\beta^2)] \tag{29b}$$

$$H_m^0(\theta, \phi) = (a_2 a_3 / a_1 a_1)[(\beta/\alpha)^3 (l_m l_j - \delta_{mj}) A_j^*(\Delta\rho/\rho)$$

$$- 2(\beta/\alpha)^2 l_k \; B_{km}^* + 2(\beta/\alpha)^2 l_m l_k l_j B_{kj}^*] \tag{29c}$$

Downloaded 02 May 2010 to 171.66.16.246. Redistribution subject to ASME license or copyright; see http://www.asme.org/terms/Terms_Use.cfm

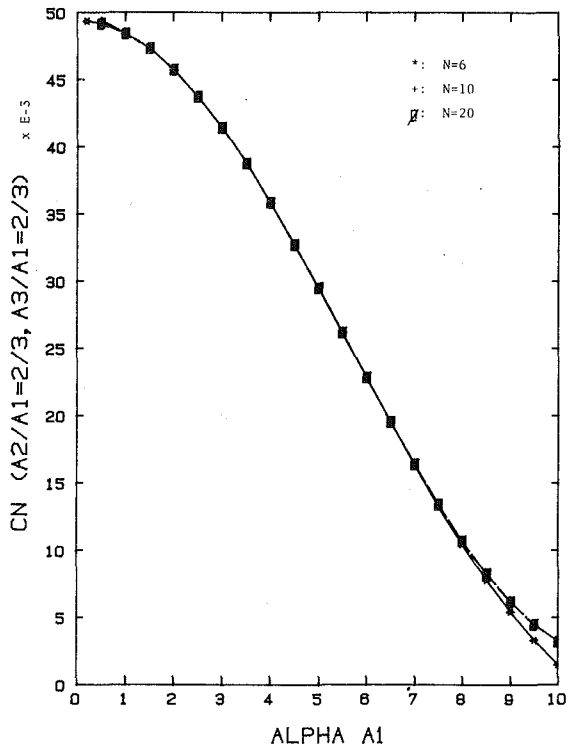

Fig. 4 Convergence of C_n as a function of αa_1: $a_2/a_1 = 2/3$; $a_3/a_1 = 2/3$

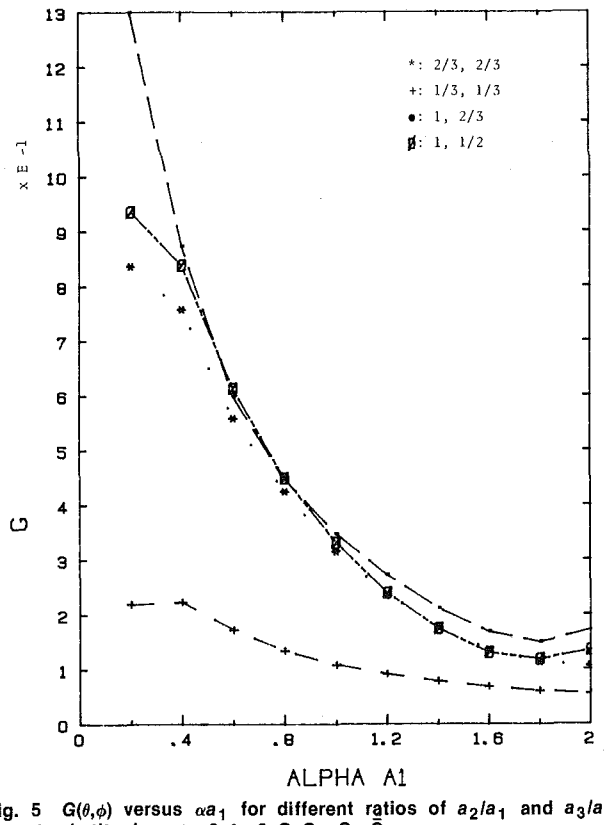

Fig. 5 $G(\theta,\phi)$ versus αa_1 for different ratios of a_2/a_1 and a_3/a_1: tungston in titanium, $\phi = 0$, $\theta = 0$, $G \cdot G = G_m \bar{G}_m$

in which

$$A_j^* = A_j / (\Delta\rho\omega^2 u_0) \tag{29d}$$

$$B_{kj}^* = -B_{kj} / (i\alpha u_0) \tag{29e}$$

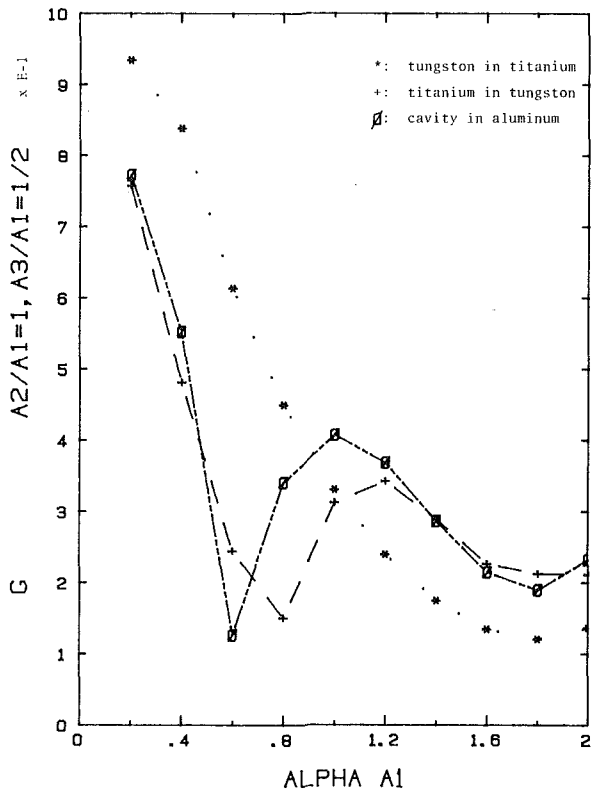

Fig. 6 $G(\theta,\phi)$ versus αa_1: $a_2/a_1 = 1$, $a_3/a_1 = 1/2$, $\phi = 0$, $\theta = 0$, $G \cdot G = G_m \cdot \bar{G}_m$

By using equations (20), (27), and (28) we obtain the differential scattering cross section, after manipulation, as

$$\frac{dP(\omega)}{d\Omega} = \sigma^P(\theta,\phi) + (\alpha/\beta)\,\sigma^S(\theta,\phi) \tag{30}$$

where

$$\alpha^2\ \sigma^P(\theta,\phi) = (\alpha a_1)^6 G_m^0(\theta,\phi)\ \bar{G}_m^0(\theta,\phi)\ (C_n \cdot \bar{C}_{n'})$$

$$\beta^2\ \sigma^S(\theta,\phi) = (\alpha a_1)^6 \cdot H_m^0(\theta,\phi)\ H_m^0(\theta,\phi)\ (D_n \cdot \bar{D}_{n'})$$

$$C_n = \sum_{n=0}^{\infty} \sum_{l=0}^{n} \sum_{k=0,2}^{n-l} \frac{(-i)^n (\alpha a_1)^n (a_2/a_1)^k (a_3/a_1)^{n-l-k} l_1^l l_2^k 1_3^{n-l-k} (n/2)!}{(n+3)(n+1)n!(l/2)!(k/2)!(n-l-k)/2!}$$

$$D_n = \sum_{n=0}^{\infty} \sum_{l=0}^{n} \sum_{k=0,2}^{n-l} \frac{(-i)^n (\beta a_1)^n (a_2/a_1)^{n-l-k} l_1^{\,l} l_2^{\,k} l_3^{\,n-l-k} (n/2)!(a_3/a_1)^k}{(n+3)(n+1)n!(l/2)!(k/2)!(n-l-k)/2!}$$

The super bar here denotes complex conjugate. The total differential cross section can be easily obtained as

$$P(\omega)/a_1{}^2 = (\alpha\ a_1)^4 \int_{\Sigma} G_m^0(\theta,\phi)\,\bar{G}_m^0(\theta,\phi)\,C_n \bar{C}_{n'}\,d\Omega$$

$$+ (\alpha/\beta)^3 (\alpha\ a_1)^4 \int_{\Sigma} H_m^0\,\bar{H}_m^0\,D_n \bar{D}_{n'}\,d\Omega \tag{31}$$

In Fig. 3[1], a comparison of the total cross section as a function of dimensionless wave number with exact solution for a spherical inhomogeneity is displayed. For an aluminum sphere embedded in a gemanium matrix the agreement is found to be within 5 percent, $ka < 2$. The comparison does depend on the material systems involved. In Figs. 4–8[2], results related to the scattered displacement field are shown. The frequency responses of the fields are contained in the

[1] A computer program that provides the output for exact solution originally given in [18] was kindly given to L. S. Fu by J. E. Gubernatis. Plotted by Y. C. Sheu.

[2] Plotted by Y. P. Hsu.

Downloaded 02 May 2010 to 171.66.16.246. Redistribution subject to ASME license or copyright; see http://www.asme.org/terms/Terms_Use.cfm

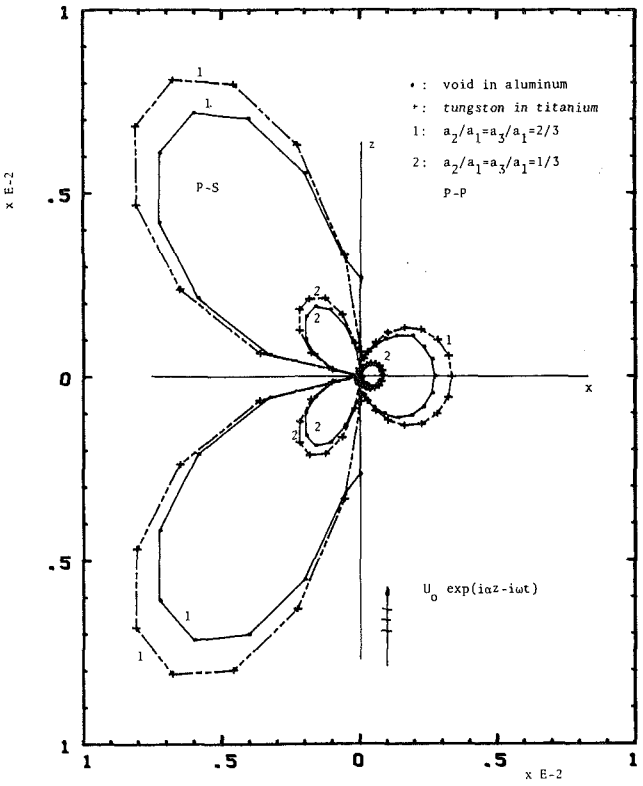

Fig. 7 Polar plots for the scattering amplitudes: $\alpha a_1 = 0.2$, $\phi = 0$

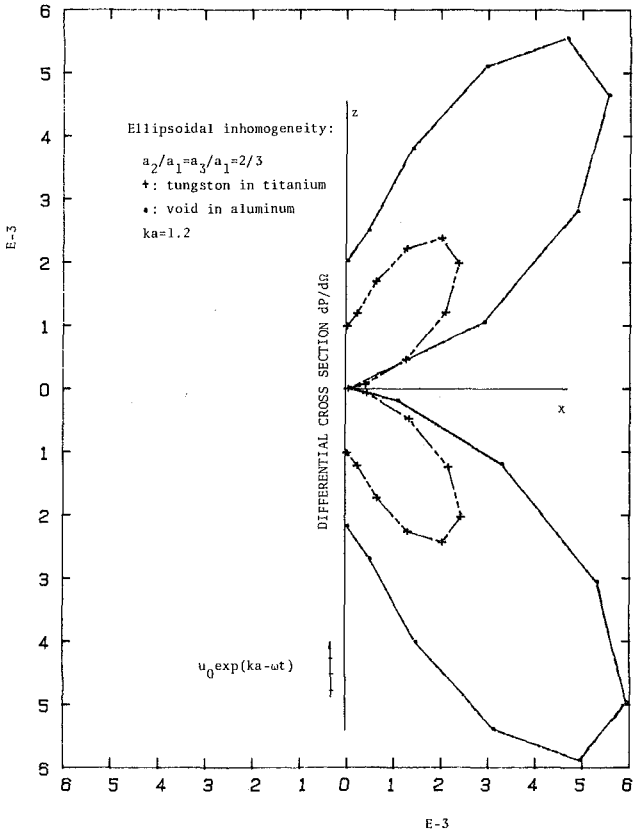

Fig. 8 Polar plots for the differential cross section

coefficients A_j, B_{kj}, C_n, and D_n. The series expansion for C_n or D_n converges very fast and is shown in Fig. 4. In Figs. 5 and 6 the absolute value of the reduced scattering amplitudes are displayed for different aspect ratios and material systems. Polar plots for the scattering amplitudes [21] and differential cross sections are sampled and displayed in Fig. 7 and Fig. 8, respectively. Numerical results were obtained by using the AMDAHL 470 computing system and peripheral equipment.

Discussion and Conclusion

The determination of the elastodynamic fields of an ellipsoidal inhomogeneity is studied in detail via the eigenstrain approach. A complete formulation and a treatment of both types of eigenstrains for equivalence between the inhomogeneity problem and the inclusion problem are given. This approach is shown to be mathematically identical to other approaches such as the direct volume integral formulation, references [4, 5, 8]. There are several advantages in using this approach: (1) the radiation condition for outgoing waves and the continuity conditions at the interface between the inhomogeneity and the matrix are automatically satisfied; (2) the frequency response of the field quantities are clearly identified; and (3) the solution for specialized geometry of the inhomogeneity, such as sphere, cylinder, disk, prolate, and oblate spheroids, etc., can be obtained by simply evaluating the associated integrals [20].

From the comparison with exact solution for a spherical inhomogeneity, the case of uniformly distributed eigenstrains gives accuracy within a few percent up to dimensionless wave number around two. Numerical results for an ellipsoidal inhomogeneity indicate similar trends as that given in [6] for very low dimensionless wave number, $ka << 1$, i.e., the reduced scattering amplitude tends to be proportional to the volume of the inhomogeneity.

As the dimensionless wave number ka increases, it is expected that the solution due to uniformly distributed eigenstrains becomes less accurate. It was observed, during the study for a spherical inhomogeneity that the total cross section vanishes at ka approximately equals to four. This suggests that there exists a frequency structure in the coefficients of the eigenstrain distributions, i.e., a certain distribution pattern may be predominant at a certain frequency range. Since the mismatch in mass density does not give rise to any eigenstrain in the static case, it appears that this solution should give better frequency representation than any other ones that use the static solution as a first approximation.

Acknowledgment

L. S. Fu is grateful for support by NASA Lewis Research Center through a grant to the Ohio State University Research Foundation, NSG 3269. He also thanks Y. P. Hsu and Y. C. Sheu for their assistance in production of the computed plots, and Marcia Andrews for typing the manuscript.

References

1 Pao, Y. H., ed., *Elastic Waves and Non-Destructive Testing of Materials*, AMD-Vol. 29, ASME, 1978.

2 Miklowitz, J., and Achenbach, J., eds., *Modern Problems in Elastic Wave Propagation*, Proc. IUTAM (1977); Wiley, New York, 1978.

3 Fu, L. S., "Mechanics Aspects of NDE by Sound and Ultrasound," feature article series, *Applied Mechanics Review*, Vol. 35, Aug. 1982, pp. 1047-1057.

4 Mal, A. K., and Knopoff, L., "Elastic Wave Velocities in Two-Component Systems," *J. Inst. Maths. Applics.*, Vol. 3, 1967, pp. 376-387.

5 Gubernatis, J. E., Domany, E., and Krumhansl, J. A., "Formal Aspects of the Theory of the Scattering of Ultrasound by Flaws in Elastic Materials," *J. Appl. Phys.*, Vol. 48, 1977, pp. 2804-2811.

6 Datta, S. K., "Diffraction of Plane Elastic Waves by Ellipsoidal Inclusions," *J. Acoust. Soc. Am.*, Vol. 61, 1977, pp. 1432-1437.

7 Pao, Y.-H., "The Transition Matrix for the Scattering of Acoustic Waves and for Elastic Waves," in reference [2], 1978, pp. 123-144.

Downloaded 02 May 2010 to 171.66.16.246. Redistribution subject to ASME license or copyright; see http://www.asme.org/terms/Terms_Use.cfm

8 Willis, J. R., "A Polarization Approach to the Scattering of Elastic Waves—I. Scattering by a Single Inclusion," *J. Mech. Phys. Solids*, Vol. 28, 1980, pp. 287–306.

9 Gubernatis, J. E., Domany, E., Krumhansl, J. A., and Huberman, M., "The Born Approximation in the Theory of the Scattering of Elastic Waves by Flaws," *J. Appl. Phys.*, Vol. 48, 1977, pp. 2812–2819.

10 Gubernatis, J. E., "Longwave Approximations for the Scattering of Elastic Waves From Flaws With Applications to Ellipsoidal Voids and Inclusions," *J. Appl. Phys.*, Vol. 50, 1979, pp. 4046–4058.

11 Eshelby, J. D., "Elastic Inclusions and Inhomogeneities," in: *Progress in Solid Mechanics*, Vol. 2, Sneddon, I. N., and Hill, R., eds., North-Holland, Amsterdam, 1961, pp. 89–140.

12 Eshelby, J. D., "The Determination of the Elastic Field of an Ellipsoidal Inclusion, and Related Problems," *Proc. Roy. Soc.*, Series A, Vol. 241, 1957, pp. 378–396.

13 Eshelby, J. D., "The Elastic Field Outside an Ellipsoidal Inclusion," *Proc. Roy. Soc.*, Series A, Vol. 252, 1959, pp. 561–569.

14 Wheeler, P., and Mura, T., "Dynamic Equivalence of Composite Material and Eigenstrain Problems," ASME JOURNAL OF APPLIED MECHANICS, Vol. 40, 1973, pp. 498–502.

15 Fu. L. S., "Method of Equivalent Inclusion in Dynamic Elasticity," *Review of Progress on Quantitative NDE*, Vol. 1, Plenum Press, 1982, pp. 145–156. Presented at Boulder, Colo., Aug. 1981.

16 Fu. L. S., "Fundamental Aspects in the Quantitative Ultrasound Determination of Fracture Toughness: The Scattering of a Single Inhomogeneity," Ohio State University Research Fdn. Technical Report #102, (NASA Grant NSG 3269), Feb. 1982; NASA Contractor Report #3625, Oct. 1982.

17 Fu. L. S., "Fundamental Aspects in the Quantitative Ultrasonic Determination of Fracture Toughness: General Equations," NASA Contractor Report 3445, July 1981.

18 Truell, R., Elbaum, C., and Chick, B. B., *Ultrasonic Methods in Solid State Physics*, Academic Press, New York, 1969.

19 Sendeckyj, G., "Ellipsoidal Inhomogeneity Problem," Ph.D. Dissertation, Northwestern University, 1967.

20 Fu. L. S., and Mura, T., "Volume Integrals of Ellipsoids Associated With the Inhomogeneous Helmholtz Equation," *Wave Motion*, Vol. 4, 1982, pp. 141–149.

21 Morse, P. M., and Feshbach, H., *Method of Theoretical Physics*, McGraw-Hill, New York, 1953.

Downloaded 02 May 2010 to 171.66.16.246. Redistribution subject to ASME license or copyright; see http://www.asme.org/terms/Terms_Use.cfm

Transient Response of an Elastic Medium to Torsional Loads on a Cylindrical Cavity

R. Parnes
Mem. ASME

L. Banks-Sills
Assoc. Mem. ASME

Department of Solid Mechanics, Materials and Structures, School of Engineering, Tel-Aviv University, Ramat-Aviv, Tel-Aviv, Israel 69978

The transient response of an elastic medium to torsional line loads acting as a step function in time on the surface of an infinite cylindrical bore is obtained. The solution is seen to be composed of a superposition of space-harmonic applied tractions. Integral representations of the resulting displacement and stress fields are derived and numerical results are presented. The behavior in the vicinity immediately behind the outward propagating S-wave fronts is studied and analytic expressions for the resulting singularities and jumps across the fronts are given. These solutions may be used as the Green's functions for more general spatial loading systems. The response is compared with the known static solution to determine the relative contribution of the transient effect.

1 Introduction

In the present investigation, we consider the transient response of an axisymmetric, circular, torsional line load applied to the surface of a cylindrical cavity as a step function in time. The prescribed torsional load corresponds, for example, to forces exerted on a bore hole as encountered in oil prospecting and drilling. It is also an approximate representation of frictional line forces which are due to twisting of a relatively rigid shaft situated with a tight fit within a hollow cylinder whose ratio of outer to inner radius is very large. The solutions obtained are the Green's functions in space from which the response to more general spatial loading patterns can be obtained. The application of a step function in time permits the determination of the response to forces with more general time dependencies by means of Duhamel integrals. Moreover, the analytic solutions presented in the following can be considered as limiting and check cases for numerical solutions to more complex loadings. The solution to the present problem also establishes regions in which the transient effects predominate in the response. Knowledge of the approximate delineation of such regions for the loading case considered can aid in predicting the corresponding region for the more significant but considerably more difficult case of transient radial pressures.

The response of a medium to applied tractions on the surface of a cylindrical bore has been the subject of several investigations. Tranter [1] first studied the effect of static radial pressure loadings over a finite segment of the bore surface. Jordan [2] later investigated the corresponding dynamic problem assuming an applied traction with a step load in time. The response to a moving pressure line load was given in [3] and a similar study for a torsional line load appears in [4]. The static response of applied tractions acting on a bore surface, including that of a torsional line loading, is given in [5]. Previous dynamic solutions for cylindrical edge loading conditions either usually omitted transient effects (e.g. the moving load problems [3, 4] were presented as steady-state solutions in a moving coordinate system attached to the traveling load) or were limited to plane-strain loading conditions. In this class, we cite, among others, the solutions of Selberg [6] and Miklowitz [7] who obtained the transient solutions to related plane-strain problems using integral transform techniques, and more recently the plane-strain solution given in [8] and derived using the method of characteristics.

Transform techniques, discussed extensively by Miklowitz [9] in the context of wave propagation problems, and which are particularly appropriate in obtaining transient solutions, are used. Integral representations of the displacement and stress field are obtained. In addition, analytic expressions for the behavior in the vicinity behind the wave fronts and for jumps across the wave fronts are derived. The response to the line load is observed to consist of a shear wave with an outward propagating toroidal wave front whose centerline lies on the circle of load application. The displacements at the front are seen to vanish. However, the stresses exhibit an infinite jump at the front, resulting in a singular stress behavior. The solution for large times is observed to approach the static solution previously derived. Numerical results for the displacement and stresses are presented and comparisons are made with the static solution.

Contributed by the Applied Mechanics Division for presentation at the 1983 ASME Applied Mechanics, Bioengineering, and Fluids Engineering Conference, Houston, Texas, June 20–22, 1983 of THE AMERICAN SOCIETY OF MECHANICAL ENGINEERS.

Discussion on this paper should be addressed to the Editorial Department, ASME, United Engineering Center, 345 East 47th Street, New York, N.Y. 10017, and will be accepted until two months after final publication of the paper itself in the JOURNAL OF APPLIED MECHANICS. Manuscript received by ASME Applied Mechanics Division, February, 1982; final revision, October, 1982. Paper No. 83-APM-29.

Copies will be available until February, 1984.

Copyright © 1983 by ASME
Downloaded 02 May 2010 to 171.66.16.246. Redistribution subject to ASME license or copyright; see http://www.asme.org/terms/Terms_Use.cfm

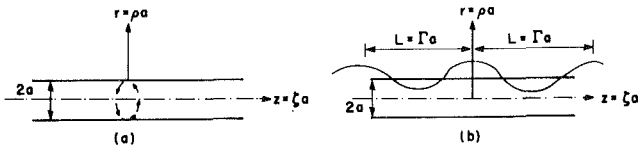

Fig. 1 Geometry of problem

2 General Formulation

Consider a linear isotropic elastic medium containing a cylindrical cavity of radius $r=a$ with a coordinate system (r,θ,z) as shown in Fig. 1(*a*), to which there corresponds a nondimensional coordinate system $\rho=r/a$, θ, $\zeta=z/a$. A line torque T is suddenly applied to the cylindrical surface $\rho=1$ at $z=0$ such that the stresses on the boundary are

$$\left.\begin{aligned}\sigma_{r\theta}&=\frac{T}{2\pi a^2}\,\delta(\zeta)H(t)\\ \sigma_{rr}&=\sigma_{rz}=0\end{aligned}\right\}\ \rho=1 \tag{1}$$

where $\delta(\zeta)$ is the Dirac-delta function and $H(t)$ is the step function in time t.

The medium is defined by the Lamé constants λ and μ and density ρ_D with $c_s=\sqrt{(\mu/\rho_D)}$ being the propagation velocity of shear waves. Introducing a nondimensional time coordinate $\tau=c_s t/a$, the equations of motion define a displacement field $\mathbf{u}=v(\rho,\zeta,\tau)\mathbf{e}_\theta$ where v, the circumferential displacement component, satisfies

$$\frac{\partial^2 v}{\partial\rho^2}+\frac{1}{\rho}\frac{\partial v}{\partial\rho}-\frac{v}{\rho^2}+\frac{\partial^2 v}{\partial\zeta^2}=\frac{\partial^2 v}{\partial\tau^2}. \tag{2}$$

The stresses in the medium, obtained from the linear elastic stress-strain relations, are then given by

$$\left.\begin{aligned}\sigma_{r\theta}&=\frac{\mu}{a}\left(\frac{\partial v}{\partial\rho}-\frac{v}{\rho}\right) &(a)\\ \sigma_{\theta z}&=\frac{\mu}{a}\frac{\partial v}{\partial\zeta} &(b)\\ \sigma_{rr}&=\sigma_{\theta\theta}=\sigma_{zz}=\sigma_{rz}=0. &(c)\end{aligned}\right\} \tag{3}$$

The last two boundary conditions of equation (1) are thus identically satisfied. Expressing the Dirac-delta function by means of its integral representation

$$\delta(\zeta)=\frac{1}{\pi}\int_0^\infty \cos\alpha\zeta\, d\alpha, \tag{4}$$

the remaining boundary condition may be written as

$$\left.\frac{\partial v}{\partial\rho}-\frac{v}{\rho}\right|_{\rho=1}=\frac{TH(\tau)}{2\pi^2 a\mu}\int_0^\infty \cos\alpha\zeta\, d\alpha. \tag{5}$$

Hence, equation (2) must be solved subject to the boundary condition of equation (5). It is recognized from equation (5) that the total solution is obtained as a superposition of solutions due to dynamic space-harmonic boundary stresses (Fig. 1(*b*))

$$\left.\sigma_{r\theta}\right|_{\rho=1}=\frac{TH(\tau)}{2\pi a^2}\cos\alpha\zeta \tag{6}$$

having wave length L, and represented by the aspect ratio $\Gamma=L/a=2\pi/\alpha$.

Therefore we first proceed with the solution to such space-harmonic applied boundary stresses and determine the response to the line torque in a subsequent section.

3 Response to Space-Harmonic Applied Torsional Loads

(A) General Inversion. The response is obtained from equation (2) subjected to the boundary condition, equation (6). Applying the Laplace transform

$$\bar f(s)=\mathcal{L}[f(\tau)]=\int_0^\infty f(\tau)e^{-s\tau}ds \tag{7}$$

and letting

$$\bar v(\rho,\zeta,s)=\bar\phi(\rho,s)\cos\alpha\zeta, \tag{8}$$

we obtain the transform equation

$$\frac{\partial^2\bar\phi}{\partial\rho^2}+\frac{1}{\rho}\frac{\partial\bar\phi}{\partial\rho}-\left[(\alpha^2+s^2)+\frac{1}{\rho^2}\right]\bar\phi=0 \tag{9}$$

while, applying the transformation to equation (3), the boundary condition on $\bar\phi(\rho,s)$ becomes

$$\left.\frac{\partial\bar\phi}{\partial\rho}-\frac{\bar\phi}{\rho}\right|_{\rho=1}=\frac{T}{2\pi\,\mu as}. \tag{10}$$

Solutions of equation (9) that decay as $\rho\to\infty$ are

$$\bar\phi(\rho,s)=A(s)K_1(\beta\rho) \tag{11}$$

where

$$\beta=(s^2+\alpha^2)^{1/2} \tag{12}$$

and where K_n is the modified Bessel function of the second kind of order n. Upon substituting in the boundary condition, equation (10), the undetermined constant $A(s)$ is obtained, from which

$$\bar v(\rho,\zeta,s)=-\frac{T}{2\pi a\mu}\frac{K_1(\beta\rho)}{s\beta\,K_2(\beta)}\cos\alpha\zeta. \tag{13}$$

The resulting transformed stresses, by equations (3) and (13), are then

$$\bar\sigma_{r\theta}(\rho,\zeta,s)=\frac{T}{2\pi a^2}\frac{K_2(\beta\rho)}{sK_2(\beta)}\cos\alpha\zeta \tag{14a}$$

$$\bar\sigma_{\theta z}(\rho,\zeta,s)=\frac{T}{2\pi a^2}\frac{\alpha K_1(\beta\rho)}{s\beta K_2(\beta)}\sin\alpha\zeta. \tag{14b}$$

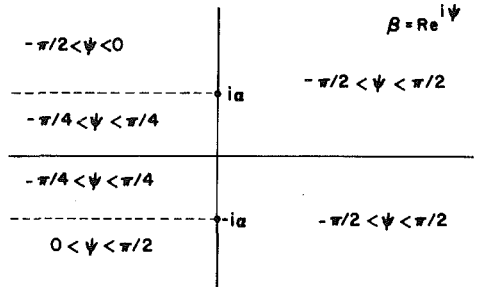

Fig. 2 Complex s-plane: arguments of parameter β

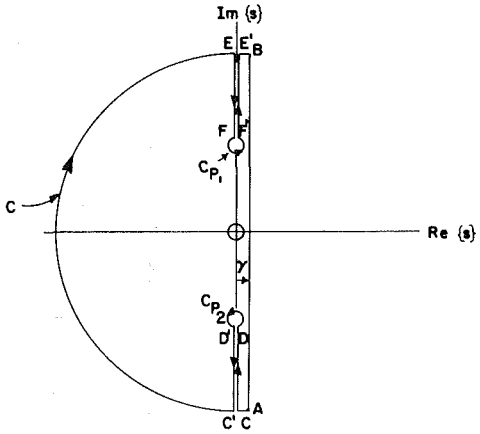

Fig. 3 Deformed integration contour (s-plane)

Downloaded 02 May 2010 to 171.66.16.246. Redistribution subject to ASME license or copyright; see http://www.asme.org/terms/Terms_Use.cfm

The displacement and stress components, in non-dimensional form, are now obtained by inversion using the standard Bromwich integral

$$\frac{\mu a v}{T}(\rho,\zeta,\tau)=\frac{\cos\alpha\zeta}{4\pi^2 i}\int_{\gamma-i\infty}^{\gamma+i\infty}\frac{-K_1(\beta\rho)}{s\beta K_2(\beta)}e^{s\tau}ds \tag{15a}$$

$$\frac{a^2\sigma_{r\theta}}{T}(\rho,\zeta,\tau)=\frac{\cos\alpha\zeta}{4\pi^2 i}\int_{\gamma-i\infty}^{\gamma+i\infty}\frac{K_2(\beta\rho)}{sK_2(\beta)}e^{s\tau}ds \tag{15b}$$

$$\frac{a^2\sigma_{z\theta}}{T}(\rho,\zeta,\tau)=\frac{\sin\alpha\zeta}{4\pi^2 i}\int_{\gamma-i\infty}^{\gamma+i\infty}\frac{\alpha K_1(\beta\rho)}{s\beta K_2(\beta)}e^{s\tau}ds. \tag{15c}$$

The preceding integrals may be evalutated by contour integration upon continuation into the complex s-plane. As a result of the multivalued nature of the K_n functions, branch cuts emanating from branch points at $\beta=0$, i.e., at $s=\pm i\alpha$, must be chosen. In addition, simple poles exist at $s=0$ and poles, defined by the roots of $K_2(\beta)=0$ are expected. However, upon choosing branch cuts extending from the branch points $s=\pm i\alpha$ to $\pm i\infty$, respectively (as shown in Fig. 2), these latter poles are seen to be nonexistent. Thus, if β as defined in equation (12) is represented by $\beta=Re^{i\psi}$, it is observed that for the choice of branch cuts, $-\pi/2<\psi<\pi/2$, the $Re\{\beta\}>0$ for all values of s in the complex plane. (Ranges of ψ in the various regions of the complex plane are shown in Fig. 2.) Moreover, since the zeros of $K_n(\beta)$ exist only in the region $Re\{\beta\}<0$[11,12], it follows that with these specified branch cuts, no poles will occur in the integrands of equations (15) due to a vanishing $K_2(\beta)$. Consequently, the only remaining pole of the integrands of equations (15) occurs at $s=0$. The Bromwich integrals of these equations, evaluated by residue theory upon deforming the contour to the left of the complex plane (Fig. 3), may be then written as

$$I_{(\ )}=2\pi i\, Res_{(\ )}+I_{B(\ )}+I_{p(\ )}+I_{c(\ )} \tag{16}$$

where

$I_{(\ )}=\int_A^B \bar{f}(\rho,s)e^{s\tau}\,ds$ represents the desired Bromwich integral,

$I_{B(\ )}=\int_C^D+\int_{D'}^{C'}+\int_E^F+\int_{F'}^{E'}$ represents the branch integral contribution,

$Res_{(\ )}$ represents the residue at $s=0$, and $I_{p(\ )}$ and $I_{c(\ )}$ represent, respectively, the branch point contributions, and the contribution along the large circular arcs as $R\to\infty$. In the foregoing (v) denotes the displacement and $(r\theta)$ and (θz) denote the stress component quantities $\sigma_{r\theta}$ and $\sigma_{\theta z}$, respectively.

The residues of equations (15) at $s=0$, upon noting that $\beta=\alpha$, are readily given by:

$$Res_{(v)}=\frac{-K_1(\alpha\rho)}{\alpha K_2(\alpha)},\quad Res_{(r\theta)}=\frac{K_2(\alpha\rho)}{K_2(\alpha)},$$

$$Res_{(z\theta)}=\frac{K_1(\alpha\rho)}{K_2(\alpha)} \tag{17}$$

while the branch integrals, evaluated along EF and $E'F'$ and along CD and $C'D'$ by setting $s=\pm i\xi$, respectively ($\xi>0$, real), become

$$I_{B(v)}=-4i\int_\alpha^\infty \frac{G_1(\eta,\rho)}{\xi\eta D(\eta)}\cos\xi\tau d\xi \tag{18a}$$

$$I_{B(r\theta)}=4i\int_\alpha^\infty \frac{G_2(\eta,\rho)}{\xi D(\eta)}\cos\xi\tau d\xi \tag{18b}$$

$$I_{B(\theta z)}=4i\int_\alpha^\infty \frac{\alpha G_1(\eta,\rho)}{\xi\eta D(\eta)}\cos\xi\tau d\xi \tag{18c}$$

where

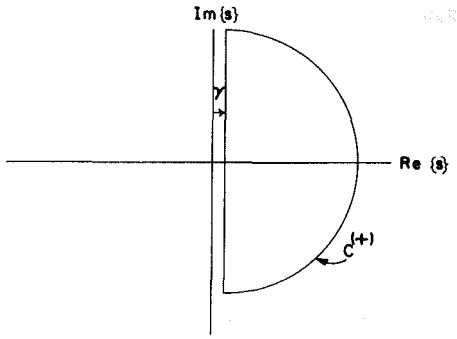

Fig. 4 Deformed integration path for wave front solution

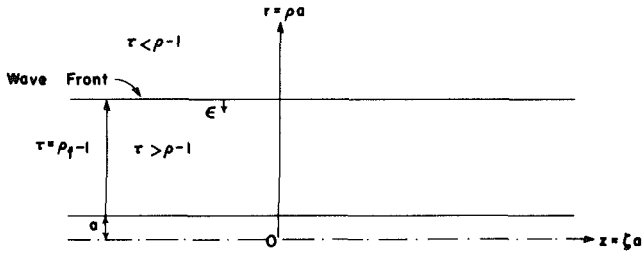

Fig. 5 Cylindrical wave front

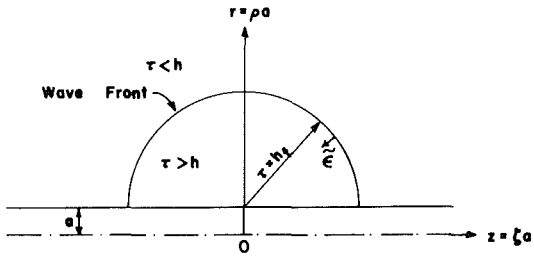

Fig. 6 Toroidal wave front

$$G_n(\eta,\rho)=J_n(\eta\rho)\,Y_2(\eta)-Y_n(\eta\rho)J_2(\eta),\ n=1,2 \tag{19a}$$

$$D(\eta)=J_2^2(\eta)+Y_2^2(\eta) \tag{19b}$$

and

$$\eta=\sqrt{(\xi^2-\alpha^2)},\quad \text{real}. \tag{20}$$

In the foregoing, the complex conjugate character of the K_n functions and the standard relationships between $K_n(i\xi)$ and $J_n(\xi)$ and $Y_n(\xi)$ have been used [13]. Considerable simplification of the expressions for the response at the boundary $\rho=1$ is achieved by use of the Wronskian relations [14]. The contributions I_p and I_c at the branch points $s=\pm i\alpha$ and along the large circular arcs are found to vanish by use of the small and large circle lemma and by expressing the K_n functions by their appropriate asymptotic expansions. Again, details are given in [14].

Finally then, the response to the space-harmonic applied tractions are expressed as:

$$\frac{\mu a v}{T}(\rho,\zeta,\alpha,\tau)=\frac{\cos\alpha\zeta}{2\pi}R_{H(v)} \tag{21a}$$

$$\frac{a^2\sigma_{r\theta}}{T}=\frac{\cos\alpha\zeta}{2\pi}R_{H(r\theta)} \tag{21b}$$

$$\frac{a^2\sigma_{z\theta}}{T}=\frac{\sin\alpha\zeta}{2\pi}R_{H(\theta z)} \tag{21c}$$

where

$$R_{H(\ )}\equiv Res_{(\ )}+\frac{1}{2\pi i}I_{B(\ )}. \tag{22}$$

Downloaded 02 May 2010 to 171.66.16.246. Redistribution subject to ASME license or copyright; see http://www.asme.org/terms/Terms_Use.cfm

(B) Behavior at the Wave Front and Long-Time Behavior. Although the inversions of the expressions of equation (15) have been formally obtained for all points throughout the medium for all $\tau>0$, a numerical integration is still required due to the form of the branch integrals. However, at the wave front, the behavior can be obtained in closed form.

To this end, we first deform the Bromwich path of integration to the path $C^{(+)}$ lying in the quadrants $Re\{s\}>0$ with $R\to\infty$, as shown in Fig. 4. Retaining the first term of the asymptotic expansion for $K_n(z)$,

$$K_n(z)=\sqrt{\left(\frac{\pi}{2z}\right)}\,e^{-z}\left\{1+\frac{a_n}{z}+\frac{b_n}{z^2}+\ldots\right\} \tag{23}$$

the inversion for the displacement integral, equation (15*a*), becomes

$$\frac{1}{2\pi i}\int_{C^{(+)}}\frac{K_1(\beta\rho)}{s\beta K_2(\beta)}e^{s\tau}ds\approx\frac{1}{2\pi i}\int_{C^{(+)}}\frac{\rho^{-1/2}e^{-(s^2+\alpha^2)^{1/2}(\rho-1)}e^{s\tau}ds}{s(s^2+\alpha^2)^{1/2}}. \tag{24}$$

Now, it is recognized that the integrand appearing in the last integral contains no singularities for $Re\{s\}>0$. Consequently, the Cauchy theorem may be applied, i.e., we may consider the value along the Bromwich integration path. Using [15, 5.6, No. 24][1], and the convolution theorem, we obtain

$$\frac{1}{2\pi i}\int_{C^{(+)}}\frac{K_1(\beta\rho)}{s\beta K_2(\beta)}e^{s\tau}ds\approx\rho^{-1/2}\int_0^{\tau}H[\eta-(\rho-1)]\cdot J_0\{\alpha[\eta^2-(\rho-1)^2]^{1/2}\}d\eta. \tag{25}$$

Thus, the integral is seen to vanish for $\tau<\rho-1$, i.e., for points ahead of the wave front (Fig. 5). For $\tau>\rho-1$, the displacement in the vicinity of the wave front becomes

$$\frac{\mu a v(\rho,\zeta,\tau)}{T}\approx-\frac{\cos\alpha\zeta}{2\pi}\rho^{-1/2}\cdot\int_{\rho-1}^{\tau}J_0\{\alpha[\eta^2-(\rho-1)^2]^{1/2}\}d\eta \tag{26}$$

Denoting the radial coordinate at the wave front as $\rho=\rho_f$, and noting that at the wave front $\tau=\rho_f-1$, it follows that

$$\frac{\mu a v(\rho,\zeta,\epsilon)}{T}\approx-\frac{\cos\alpha\zeta}{2\pi}\rho^{-1/2}\epsilon \tag{27}$$

where $\epsilon=\rho_f-\rho<<1$ represents the distance measured from the wave front. Thus $v(\rho_f)=0$, i.e., the displacement at the wave front vanishes. In addition, since ϵ is a measure of the distance from the wave front, we observe that the displacement varies linearly in the neighborhood of the wave front.

The stress components in the vicinity of the wave front are obtained similarly. Using [15, 5.6, No. 23], the stress $\sigma_{r\theta}$ is given as

$$\frac{a^2\sigma_{r\theta}}{T}(\rho,\zeta,\tau)\approx\frac{\cos\alpha\zeta}{2\pi}\rho^{-1/2}\left\{H[\tau-(\rho-1)]-\alpha(\rho-1)\cdot\int_{\rho-1}^{\rho_f-1}\frac{J_1\{\alpha[\eta^2-(\rho-1)^2]^{1/2}\}}{[\eta^2-(\rho-1)^2]^{1/2}}d\eta\right\}. \tag{28}$$

Noting that

$$\lim_{x\to0}\frac{J_1(\alpha x)}{x}=\alpha/2, \tag{29}$$

the stress in the vicinity of the wave front becomes

$$\frac{a^2\sigma_{r\theta}(\rho,\zeta,\epsilon)}{T}\approx\frac{\cos\alpha\zeta}{2\pi}\rho^{-1/2}\{1-1/2(\rho-1)\alpha^2\epsilon\}. \tag{30a}$$

Similarly, one obtains for the stress $\sigma_{z\theta}$

$$\frac{a^2\sigma_{\theta z}(\rho,\zeta,\epsilon)}{T}\approx\frac{\alpha\sin\alpha\zeta}{2\pi}\rho^{-1/2}\epsilon. \tag{30b}$$

Thus it is observed that at the wave front ($\epsilon=0$) there exists a jump in the stress $\sigma_{r\theta}$ given by

$$\frac{a^2}{T}[\sigma_{r\theta}]=\frac{\cos\alpha\zeta}{2\pi}\rho_f^{-1/2}. \tag{31}$$

The long-time solution throughout the medium, as $\tau\to\infty$, obtained from the final-value theorem [16] is seen to coincide with the residues as given by equations (17).[2] It is of interest to observe that for the case of a wave length $L\to\infty$ (i.e., $\alpha=0$), the long-time solution degenerates to

$$v(\rho)=-\frac{T}{4\pi a\mu\rho},\quad \sigma_{r\theta}(\rho)=\frac{T}{2\pi a^2\rho^2},\quad \sigma_{\theta z}(\rho)=0 \tag{32}$$

which corresponds to the static solution of a uniform torsional load T applied at the cavity boundary $\rho=1$.

4 Response to Line Torsional Loads

(A) General Inversion. It was observed in Section 2 that the response to a concentrated torque at $\zeta=0$, which we denote by $R_{c(\ )}(\rho,\zeta,\tau)$, can be obtained from the superposition of the response to the space harmonic loads. Thus

$$R_{c(\ )}(\rho,\zeta,\tau)=\frac{1}{2\pi^2}\int_0^{\infty}R_{H(\ )}(\rho,\zeta,\tau;\alpha)\begin{Bmatrix}\cos\alpha\zeta\\ \sin\alpha\zeta\end{Bmatrix}d\alpha \tag{33a}$$

where $R_{H(\ )}$ is a function that represents the space-harmonic response. Here, again, (v), (θr), and (θz) denote the various displacement and stress responses, respectively; $\cos\alpha\zeta$ is associated with v and θr, while $\sin\alpha\zeta$ is associated with θz. Using the appropriate expression for $R_{H(\ )}$ given by equation (22), the line torque responses are written as

$$R_{c(\ )}(\rho,\zeta,\tau)=\frac{1}{2\pi^2}\int_0^{\infty}\left[Res_{(\ )}+\frac{1}{2\pi i}I_{B(\ )}\right]\begin{Bmatrix}\cos\alpha\zeta\\ \sin\alpha\zeta\end{Bmatrix}d\alpha. \tag{33b}$$[3]

In principle, then, the response for all points throughout the medium can be evaluated. However, because of the complexity of the integrands, the required integrals cannot be determined analytically and the general response is therefore obtained by means of a numerical integration scheme.

(B) Behavior at the Wave Front and Long-Term Behavior. Although the desired response, in general, cannot be written in closed form, analytic expressions for the behavior in the vicinity of the wave front and long-time solutions may be derived. To this end, we note first that the complete expression for the displacement is given by

$$\frac{a\mu v}{T}=\frac{-1}{2\pi^2}\int_0^{\infty}\left(\frac{1}{2\pi i}\int_{Br}\frac{K_1(\beta\rho)}{s\beta K_2(\beta)}e^{s\tau}\,ds\right)\cos\alpha\zeta\,d\alpha \tag{34a}$$

which upon interchanging the integration processes, yields

$$\frac{a\mu v}{T}=-\frac{1}{2\pi^2}\frac{1}{2\pi i}\int_{Br}\frac{e^{s\tau}}{s}\left\{\int_0^{\infty}\frac{K_1(\beta\rho)}{\beta K_2(\beta)}\cos\alpha\zeta\,d\alpha\right\}ds. \tag{34b}$$

[1] Reference [15], given here and in the following, denotes reference, section no. and equation no., as appear in Erdelyi, et al.

[2] We note that the transient effect appears only in the branch integrals; indeed from equations (18), we observe that the time parameter τ appears only in these expressions.

[3] The first portion of equation (33*b*), consisting of the integral of the residue term, is seen to yield the static solution, while the latter yields the transient effect. See preceding footnote.

Downloaded 02 May 2010 to 171.66.16.246. Redistribution subject to ASME license or copyright; see http://www.asme.org/terms/Terms_Use.cfm

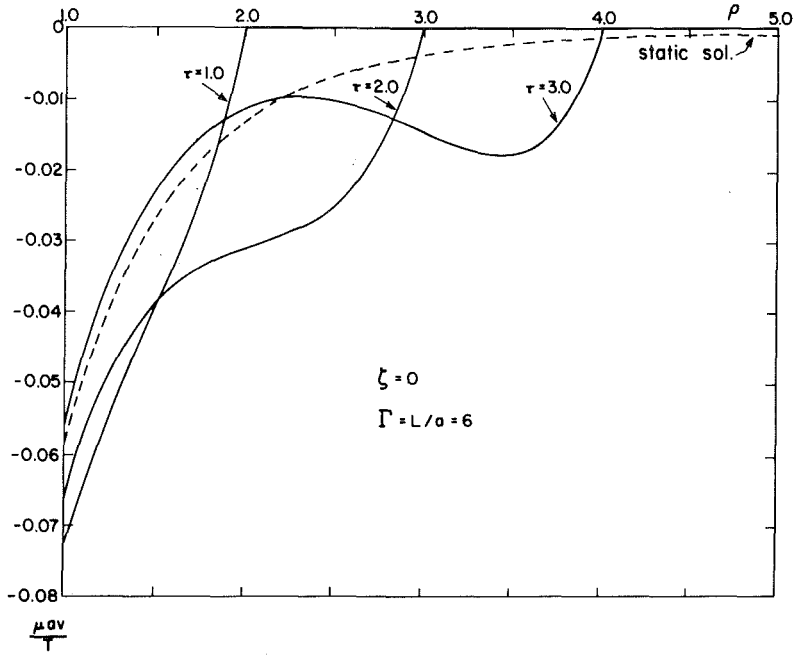

Fig. 7 Spatial distribution for displacement: space harmonic loading

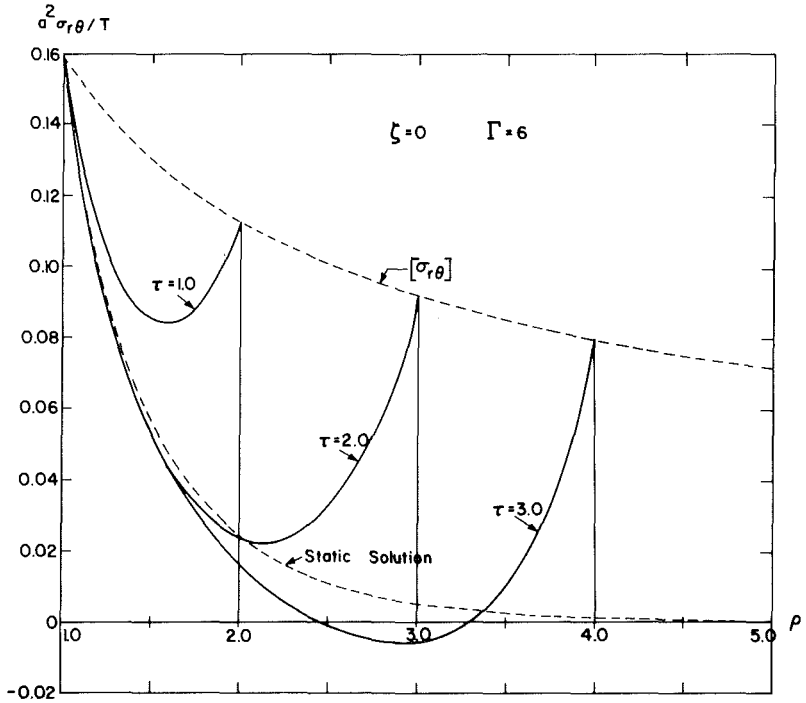

Fig. 8 Spatial distribution for stress $\sigma_{r\theta}$: space harmonic loading

Proceeding as in the preceding section, we deform the path of integration for $s>>1$ to the curve $C^{(+)}$ (Fig. 4) and, retaining the first term of the asymptotic expansion of K_n, equation (23), obtain

$$\frac{a\mu v}{T} \approx -\frac{\rho^{-1/2}}{2\pi^2} \cdot \frac{1}{2\pi i}\int_{C^{(+)}} \frac{e^{s\tau}}{s}\left[\int_0^\infty \frac{e^{-(s^2+\alpha^2)^{1/2}(\rho-1)}}{(s^2+\alpha^2)^{1/2}}\cos\alpha\zeta d\alpha\right] ds. \tag{35}$$

From [15, 1.4, No. 27], the inner integral is found to be

$$\int_0^\infty \frac{e^{-(s^2+\alpha^2)^{1/2}(\rho-1)}}{(s^2+\alpha^2)^{1/2}}\cos\alpha\zeta\, d\alpha = K_0(sh),\ \rho>1 \tag{36}$$

where $h=[(\rho-1)^2+\zeta^2]^{1/2}$.[4] Hence

$$\frac{a\mu v}{T} \approx -\frac{\rho^{-1/2}}{2\pi^2}\left\{\frac{1}{2\pi i}\int_{C^{(+)}} \frac{K_0(sh)e^{s\tau}}{s}\, ds\right\}. \tag{37}$$

Again, it is recognized that no singularities appear in the foregoing expression for $Re\{s\}>0$. Invoking the Cauchy

[4] Clearly, h represents a semicircle of radius h whose center is located at $(\rho=1,\ \zeta=0)$ (Fig. 6). This is recognized precisely as the wave front of waves traveling in time τ from the applied load. The semicircle of radius h thus appears as the locus of points of the wave front that intersects a longitudinal cross section of the cavity passing through the z-axis. The three-dimensional character of the wave front is hence described as the outer half of a torus whose center is at $\rho=0$, with a mean radius $\rho=1$ and with a varying core radius $h(\tau)$.

Downloaded 02 May 2010 to 171.66.16.246. Redistribution subject to ASME license or copyright; see http://www.asme.org/terms/Terms_Use.cfm

theorem, the preceding integral is seen to be equivalent to the integration along the Bromwich path. Noting that [15, 5.15, No. 9],

$$\mathcal{L}^{-1}\left[\frac{K_0(sh)}{s}\right]=\cosh^{-1}(\tau/h)H(\tau-h), \tag{38}$$

and proceeding as in the previous cases, we finally obtain the behavior for the displacement near the wave front as

$$\frac{a\mu v}{T}(\rho,\zeta,\epsilon)\approx-\frac{\sqrt{2}}{2\pi^2}\frac{1}{(\rho_f h_f)^{1/2}}\tilde{\epsilon}^{1/2} \tag{39}$$

where $\tau=h_f$ represents the wave front and where $\tilde{\epsilon}=h_f-h$ denotes the distance behind this front. Thus, the displacement exhibits no jump at the wave front and is seen to vary with the square root of the distance away from the front.

The stress behavior in the vicinity of the front is similarly determined. The stresses are seen to vanish ahead of the circular wave front; behind the front, for $\tau>h$, the stress components are given by

$$\frac{a^2\sigma_{r\theta}}{T}(\rho,\zeta,\tilde{\epsilon})\approx\frac{\sqrt{2}}{4\pi^2}\frac{\rho^{-1/2}(\rho-1)}{h^{3/2}}\tilde{\epsilon}^{-1/2},\quad \rho>1 \tag{40a}$$

and

$$\frac{a^2\sigma_{\theta z}}{T}(\rho,\zeta,\epsilon)\approx\frac{\sqrt{2}}{4\pi^2}\frac{\rho^{-1/2}\zeta}{h^{3/2}}\tilde{\epsilon}^{-1/2},\quad \rho>1. \tag{40b}$$

Here it is observed that, at the circular wave front, the stress components become singular as the inverse of the square root of the distance behind the front.

The long-time solution through the medium, as $\tau\to\infty$, obtained again from the final value theorem, is found to be identical to the corresponding static solution given in [5].

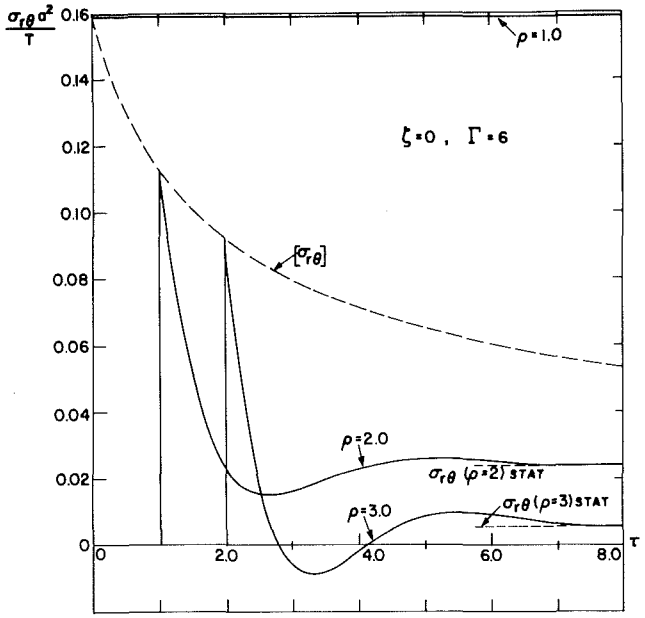

Fig. 9 Stress time history: space harmonic loading

5 Numerical Solution and Results

The general response of the medium to the space-harmonic load requires a numerical evaluation of the branch integrals appearing in equations (18) while the general response to the line loads, represented by the integrals of equation (33*b*) must also be determined numerically. Details of the numerical integration procedures used to evaluate the integrals are given in [14], where it is shown that a portion of the solution may be expressed in terms of the sine integral function. Similar numerical integration schemes for evaluation of infinite integrals have been used in [5]. Responses are presented for points along the radial line of symmetry, $\zeta=0$, in the form of space distributions for discrete times and time histories for prescribed points along the line.

(A) Space-Harmonic Applied Loading. Numerical results for this case are shown in Figs. 7–9 where typical results are presented for the case $\Gamma=L/a=6$. Results for other moderate values of Γ were found to exhibit similar behavior and consequently are not reproduced here.

In Figs. 7 and 8, the spatial distribution along the radial line $\zeta=0$ is given at several discrete times, $\tau=1.0$, 2.0, and 3.0 for the circumferential displacement and nonvanishing shear stress $\sigma_{r\theta}$. From Fig. 7, it is observed that the displacement $|v|$ reaches a maximum along the bore surface $\rho=1$ and

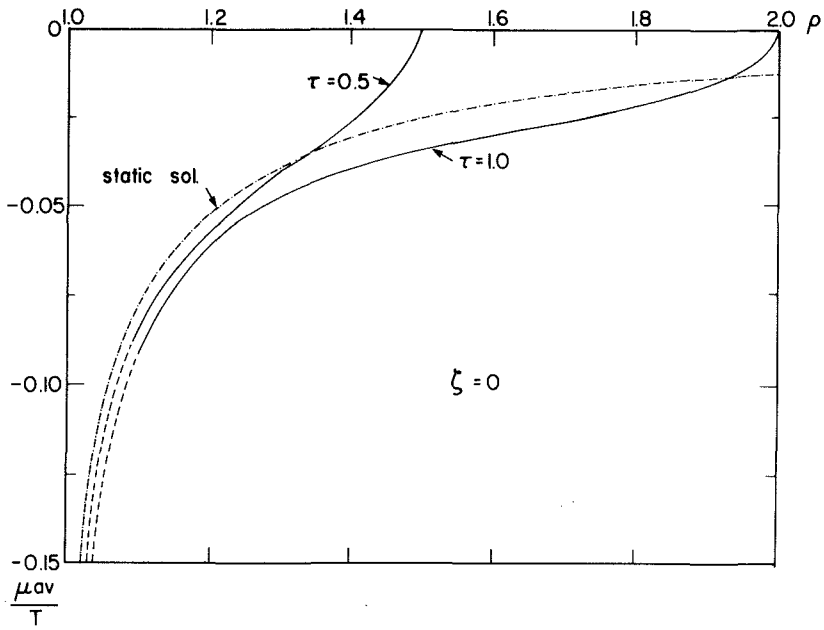

Fig. 10 Spatial distribution for displacement: line loading

Downloaded 02 May 2010 to 171.66.16.246. Redistribution subject to ASME license or copyright; see http://www.asme.org/terms/Terms_Use.cfm

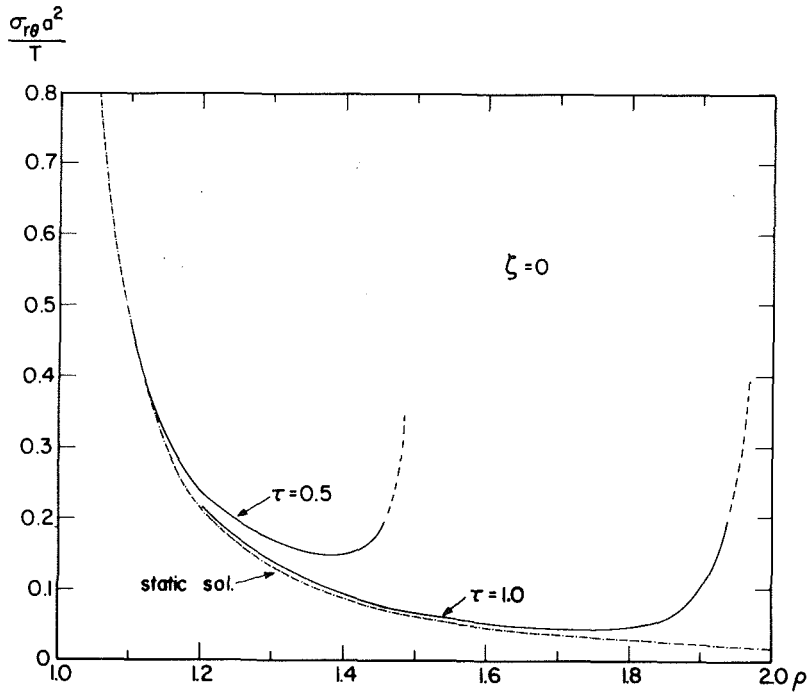

Fig. 11 Spatial distribution for stress $\sigma_{r\theta}$: line loading

vanishes, as expected, at the wave front. It is of interest to note that the spatial distribution of the displacements deviates increasingly from a linear variation with increasing time τ. This may be attributed to the fact that for small τ the inertial forces have insufficient time to react to the applied loadings.

From the spatial variation for the stress $\sigma_{r\theta}$ shown in Fig. 8, it is observed that at all times, a peak is reached at the wave front; this peak represents the jump at the wave front. The locus of these jumps, given by the simple analytic expression of equation (31) is shown in the figure by means of a broken line.[5] The static (long-time) response, obtained from [5] is also shown in Figs. 7 and 8. It is observed that at $\tau = 3.0$, the response at points more than two radial distances behind the wave front approaches the static solution. Thus the transient effect, as expected, is mainly confined to the region near the wave front.

Time histories for the stress $\sigma_{r\theta}$ at points $\rho = 1.0$, 2.0, and 3.0 are presented in Fig. 9 for time values $0 \leq \tau \leq 8$. The curves are seen to first exhibit an initial jump at the wave front undergoing oscillatory behavior about the static solution. Values of these jumps, as given by equation (31), are observed to be independent of Γ for points along the radial line $\zeta = 0$.

(B) Line Loading. As has been previously noted, the primary interest in the solutions for the line load resides in the transient response. Consequently, results for this case are presented here for early times, $\tau \leq 1.0$, i.e., for $\tau = 0.5$ and 1.0.

The spatial distribution of the displacement is given in Fig. 10. It is observed that the displacement $|v|$ is infinite at $\rho = 1$, the point of the load application, and decays to zero at the wave front. The singular behavior at $\rho = 1$ is a consequence of the nature of a point load representation by means of the Dirac-delta function as was the case in previous studies [4, 5]. (Numerical results in this region were not obtainable to the desired accuracy and are therefore shown as broken lines.) The static (long-time) solution is also shown, and it is observed that the transient solution in the region sufficiently behind the wave front follows the same monotonic spatial distribution pattern.

The $\sigma_{r\theta}$ shear stress variation is shown in Fig. 11 for the same time values. Again, at the boundary $\rho = 1$ the stresses are singular. In the region near the wave front, too, the stresses are singular [cf equation (40*a*)] and accurate results could not be obtained numerically. (As before, results in the foregoing two regions are therefore shown as broken lines.) Comparison with the static solution [5] shows, as in the case of the displacements, that the dynamic stresses, while always larger than the static stress, approach the latter at distances sufficiently far from the wave front. Thus, the transient effect is predominant only in the region in the immediate vicinity behind the wave front.

6 Conclusions

From the derived analytic expressions, it is observed, for the case of the space-harmonic loading, that the displacement and shear stresses, in the vicinity of the outgoing cylindrical *S*-front, decay as $\rho^{-1/2}$. While, for this case, the displacement v and stress $\sigma_{\theta z}$ vanish at the wave front, there exists a jump in $\sigma_{r\theta}$ across this wave front whose strength also decays as $\rho^{-1/2}$.

For the case of the line load, the displacement along the outward propagating toroidal *S*-front vanishes, while the stresses become singular as $\lim_{\tilde{\epsilon} \to 0} \tilde{\epsilon}^{-1/2}$, where $\tilde{\epsilon}$ represents the perpendicular distance from the toroidal wave front. In the vicinity behind the wave front, $0 < \tilde{\epsilon} << 1$, away from the singularity, we may also conclude from the derived expressions that the decay in the stresses, for a given value of ζ is $0(\rho^{-1})$. However, along the boundary $\rho = 1$, the displacement and shear stresses $\sigma_{\theta z}$ decay as $0(\zeta^{-1/2})$. Thus the decay in these quantities is observed to be stronger as the wave penetrates the medium compared to the decay with the distance from the point of load application along the surface of the cavity.

Finally, from the numerical results presented, we may also conclude, upon comparing with the long-time static response, that the transient effects are confined mainly to the region immediately behind the wave front.

[5] This provides an effective check on the accuracy of the numerical integration scheme which was used to obtain the general response.

Downloaded 02 May 2010 to 171.66.16.246. Redistribution subject to ASME license or copyright; see http://www.asme.org/terms/Terms_Use.cfm

References

1 Tranter, C. J., "On the Elastic Distortion of a Cylindrical Hole by a Localized Hydrostatic Pressure," *Q. Appl. Math.*, Vol. 4, 1946, pp. 298–302.

2 Jordan, D. W., "The Stress Wave From a Finite Cylindrical Explosive Source," *J. Math. and Mech.*, Vol. 11, No. 4, 1962, pp. 503–551.

3 Parnes, R., "Response of an Infinite Elastic Medium to Traveling Loads in a Cylindrical Bore," ASME JOURNAL OF APPLIED MECHANICS, Vol. 36, 1969, pp. 51–58.

4 Parnes, R., "Progressing Torsional Loads Along a Bore in an Elastic Medium," *Int. J. Solids & Struct.*, Vol. 16, 1980, pp. 653–670.

5 Parnes, R., "Applied Tractions on the Surface of an Infinite Cylindrical Bore," *Int. J. Solids & Struct.*, Vol. 19, 1982, pp. 165–177.

6 Selberg, W. L., "Transient Compression Waves From Spherical and Cylindrical Cavities," *Arkiv for Fysik*, Vol. 5, No. 7, 1952, pp. 97–108.

7 Miklowitz, J., "Plane Stress Unloading Waves Emanating From a Suddenly Punched Hole in a Stretched Elastic Plate," ASME JOURNAL OF APPLIED MECHANICS, Vol. 27, 1960, pp. 165–171.

8 Moodie, T. B., Haddow, J. B., Mioduchowski, A., and Tait, R. J., "Plane Elastic Waves Generated by Dynamic Loading Applied to Edge of Circular Hole," ASME JOURNAL OF APPLIED MECHANICS, Vol. 48, 1981, pp. 577–581.

9 Miklowitz, J., *The Theory of Elastic Waves and Waveguides*, North-Holland, Amsterdam, 1978.

10 Sneddon, I., *Fourier Transforms*, McGraw-Hill, New York, 1951.

11 Watson, G. N., *A Treatise on the Theory of Bessel Functions*, 2nd ed., Cambridge Univ. Press, 1966.

12 Parnes, R., "Complex Zeros of the Modified Bessel Functions $K_n(z)$," *Math. of Comput.*, Vol. 26, No. 120, Oct. 1972, pp. 949–953.

13 McLachlan, N. W., *Bessel Functions for Engineers*, Oxford, 1955.

14 Parnes, R., and Banks-Sills, L., "Torsional Loads on a Cylindrical Cavity—Transient Response," Tel-Aviv Univ. Report TAU/SOE-82/4, 1982.

15 Erdelyi, et al., *Tables of Integral Transforms*, McGraw-Hill, New York, 1954.

16 Churchill, R. V., *Operational Mathematics*, 3rd ed., McGraw-Hill, New York, 1972.

Downloaded 02 May 2010 to 171.66.16.246. Redistribution subject to ASME license or copyright; see http://www.asme.org/terms/Terms_Use.cfm

Reflection Coefficient for Plane Waves in a Fluid Incident on a Layered Elastic Half-Space

D. B. Bogy
Professor.
Mem. ASME

S. M. Gracewski
Graduate Student.

Department of Mechanical Engineering,
University of California,
Berkeley, Calif. 94720

The reflection coefficient is derived for an isotropic, homogeneous elastic layer of arbitrary thickness that is perfectly bonded to such an elastic half-space of a different material for the case when plane waves are incident from an inviscid fluid onto the layered solid. The derived function is studied analytically by considering several limiting cases of geometry and materials to recover previously known results. Approximate reflection coefficents are then derived using various plate models for the layer to obtain simpler expressions that are useful for small values of σd, where σ is the wave number and d is the layer thickness. Numerical results based on all the models for the propagation of interface waves localized near the fluid-solid boundary are obtained and compared. These results are also compared with some previously published experimental measurements.

1 Introduction

There are many industrial products and processes that employ structures containing a thin layer of one solid deposited on, or somehow otherwise adhering to, a different solid. One approach to testing the uniformity of quality of the bond of such layers is by the use of ultrasonic methods. It has been suggested by Maxfield [16] that nonspecularly reflected finite width beam profiles, which can occur in a water bath at critical angles of incidence, may provide a means for detecting variations in layer thickness or bond integrity.

This nonspecular reflection phenomenon, known as the Goos-Hänchen [17] effect in optics, was predicted, demonstrated, and partially explained by Schoh [4] for ultrasonic beams incident from a liquid onto a homogeneous solid at a critical angle of incidence. The phenomenon was first analyzed correctly, in this context, by Bertoni and Tamir [7]. The analogous problem for the case of a thin elastic plate immersed in a liquid was the topic of the doctoral thesis of Pitts [3]. The main results of this work were also presented in the paper by Pitts et al. [5]. The problem of nonspecular reflection of a bounded ultrasonic beam incident from a liquid onto a layered elastic half-space was recently considered by Nayfeh et al. [13].

The method of computation of the reflected beam profile, given the incident beam, is essentially the same for all the cases mentioned, and it was presented by Bertoni and Tamir [7]. It amounts to the evaluation of a Fourier integral of the product of the reflection coefficient times the incident beam profile at the interface. The zeros and poles of the reflection coefficient, which are closest to the real axis in a complex wave-number plane, determine the primary effect of the reflection coefficient. Therefore, a prerequisite for studying reflected beam profiles is the derivation of the reflection coefficient and the determination of the location of its poles and zeros. These poles and zeros also determine the propagation characteristics of the interface waves (analogous to Rayleigh waves or Stoneley waves).

In an effort to obtain the reflection coefficient for an elastic half-space with a different elastic layer, Nayfeh et al. [13] assumed the layer was relatively thin (compared to wavelength). They derived an approximate thin layer model from which they obtained a reflection coefficient, which they also used to predict the dependence of the phase velocity of the propagating surface wave on ωd, where ω is the frequency and d is the layer thickness. They compared their theoretical phase velocity with their own experimental results and found that the agreement was not very good. After our paper was submitted two papers by Chimenti et al. [18] and Chimenti and Nayfeh [19] were brought to our attention. In reference [18] the problem of reference [13] is reconsidered by use of the exact theory for the layer. The dispersion curve was obtained for the same materials (with some differences in material parameters), and it was found to agree much better with experimental results than the corresponding approximate curve of reference [13]. Reference [19] is similar to reference [18], but different materials were considered.

In this paper we derive the exact reflection coefficient for the liquid-solid layer-solid structure for a layer of arbitrary thickness. We also derive some approximate expressions for

Contributed by the Applied Mechanics Division for presentation at the 1983 ASME Applied Mechanics, Bioengineering, and Fluids Engineering Conference, Houston, Texas, June 20–22, 1983 of THE AMERICAN SOCIETY OF MECHANICAL ENGINEERS.

Discussion on this paper should be addressed to the Editorial Department, ASME, United Engineering Center, 346 East 47th Street, New York, N.Y. 10017, and will be accepted until two months after final publication of the paper itself in the JOURNAL OF APPLIED MECHANICS. Manuscript received by ASME Applied Mechanics Division, April, 1982; final revision, October, 1982. Paper No. 83-APM-17.

Copies will be available until February, 1984.

Copyright © 1983 by ASME
Downloaded 02 May 2010 to 171.66.16.246. Redistribution subject to ASME license or copyright; see http://www.asme.org/terms/Terms_Use.cfm

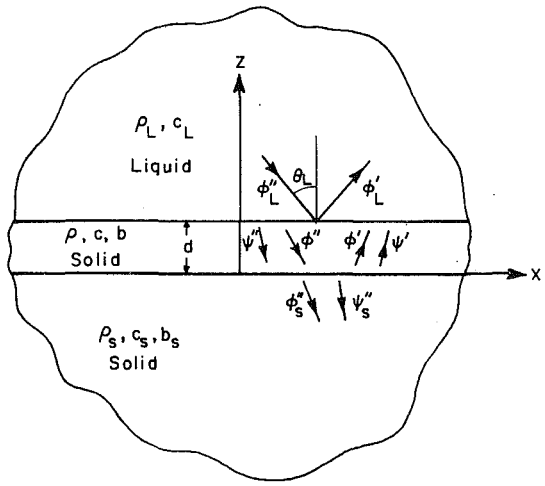

Fig. 1 Liquid-solid layer-solid structure with incident plane wave from liquid

the reflection coefficient using various plate theories for the layer. In Section 2 the exact reflection coefficient for this structure is derived. Its complicated functional form is studied in Section 3, where several limiting cases are considered to produce previously known results. In Section 4 the reflection coefficient is linearized in σd, where σ is the wave number, to obtain an approximation that is valid for small values of σd. Also reflection coefficients are derived there in which the layer is first considered as a classical (Kirchhoff) plate and then as a Cosserat plate. Finally, Nayfeh's et al. [13] thin layer model is used. Section 5 presents numerical results for the dependence of the surface wave speeds on ωd as predicted by the exact reflection coefficient as well as the various approximate expressions. These theoretical results are also compared with the experimental results presented in reference [13]. Finally, Section 6 presents a brief discussion and some conclusions.

2 Derivation of Exact Reflection Coefficient

We consider the layered structure composed of an isotropic elastic layer of thickness d perfectly bonded at its face $z = 0$ to an isotropic elastic half-space and in contact at its face $z = d$ with an inviscid fluid (see Fig. 1). The material parameters for the layer are ρ,c,b; those for the solid half-space (substrate) are ρ_S,c_S,b_S; and those for the fluid half-space are ρ_L,c_L, where ρ,c, and b denote density, longitudinal wave speed, and shear wave speed, respectively. The elastic wave speeds are related to the Lamé constants, λ and μ, by

$$\rho c^2 = \lambda + 2\mu, \quad \rho b^2 = \mu. \tag{1}$$

We consider the plane strain problem of a harmonic plane wave with wave potential ϕ''_L in the liquid incident on the liquid-layer interface at $z = d$ at the angle θ_L measured from the normal to the interface. Associated with this wave is a reflected longitudinal wave in the liquid with wave potential ϕ'_L, a set of longitudinal and shear waves in the layer with potentials ϕ',ψ' incident on the surface $z = d$, a set of longitudinal and shear waves in the layer with potentials ϕ'',ψ'' incident on the interface $z = 0$, and a set of longitudinal and shear waves that are transmitted into the substrate with potentials ϕ''_S,ψ''_S. Adopting the notation of Brekhovskikh [1], we represent the waves in the three media as follows:

$$\phi_L = (\phi'_L e^{i\alpha_L z} + \phi''_L e^{-i\alpha_L z}) e^{i(\alpha x - \omega t)} \tag{2}$$

in the liquid,

$$\phi = (\phi' e^{i\alpha z} + \phi'' e^{-i\alpha z}) e^{i(\alpha x - \omega t)},$$
$$\psi = (\psi' e^{i\beta z} + \psi'' e^{-i\beta z}) e^{i(\alpha x - \omega t)}, \tag{3}$$

in the layer, and

$$\phi_S = \phi''_S e^{-i\alpha_S z} e^{i(\alpha x - \omega t)}, \quad \psi_S = \psi''_S e^{-i\beta_S z} e^{i(\alpha x - \omega t)} \tag{4}$$

in the substrate, where

$$\alpha^2 = k^2 - \sigma^2, \quad \alpha_L^2 = k_L^2 - \sigma^2, \quad \alpha_S^2 = k_S^2 - \sigma^2,$$
$$\beta^2 = \kappa^2 - \sigma^2, \quad \beta_S^2 = \kappa_S^2 - \sigma^2, \tag{5}$$

and

$$\sigma = k \sin\theta = k_L \sin\theta_L = k_S \sin\theta_S = \kappa \sin\gamma = \kappa_S \sin\gamma_S. \tag{6}$$

Thus k,k_L, and k_s represent longitudinal wave numbers for wave vectors making acute angles θ,θ_L, and θ_s with the normal to the interfaces, and κ,κ_S represent shear wave numbers for shear waves with angles γ,γ_S. It will also be convenient to adopt the following abbreviated notation for certain trigonometric functions,

$$\mathcal{S}_\theta = \sin\theta, \quad \mathcal{C}_\theta = \cos\theta, \quad \mathcal{T}_\theta = \tan\theta, \quad \mathcal{C}t_\theta = \cot\theta.$$

If we used the identity

$$\mu^{-1}\lambda k^2 + 2\alpha^2 = \beta^2 - \sigma^2, \tag{7}$$

equation (6.4) of reference [1] can be used to write the plane components of velocity and traction amplitudes at the boundary $z = 0$ of the substrate in terms of ϕ''_S and ψ''_S as follows

$$\mathbf{f}^S(0) \equiv \begin{Bmatrix} v_x^S(0) \\ v_z^S(0) \\ Z_z^S(0) \\ Z_x^S(0) \end{Bmatrix}$$

$$= \begin{bmatrix} i\sigma & i\beta_S \\ -i\alpha_S & i\sigma \\ -i\mu_S\omega^{-1}(\beta_S^2 - \sigma^2) & i2\mu_S\omega^{-1}\sigma\beta_S \\ i2\mu_S\omega^{-1}\alpha_S\sigma & i\mu_S\omega^{-1}(\beta_S^2 - \sigma^2) \end{bmatrix} \begin{Bmatrix} \phi''_S \\ \psi''_S \end{Bmatrix} \tag{8}$$

or, in obvious matrix notation

$$\mathbf{f}^S(0) = B \begin{Bmatrix} \phi''_S \\ \psi''_S \end{Bmatrix}. \tag{9}$$

Likewise, equation (6.6) of reference [1] can be used to express the velocity-traction matrix $\mathbf{f}(d)$ at $z = d$ of the layer in terms of the velocity-traction matrix $\mathbf{f}(0)$ at $z = 0$ of the layer as follows

$$\mathbf{f}(d) = A\mathbf{f}(0), \tag{10}$$

where A is the matrix

$$A = \begin{bmatrix} a_{11} & a_{12} & a_{13} & (2\mu)^{-1}a_{14} \\ a_{21} & a_{22} & a_{23} & (2\mu)^{-1}a_{24} \\ a_{31} & a_{32} & a_{33} & (2\mu)^{-1}a_{34} \\ 2\mu a_{41} & 2\mu a_{42} & 2\mu a_{43} & a_{44} \end{bmatrix}, \tag{11}$$

and the elements a_{ij} are given on p. 64 of reference [1]. The

Downloaded 02 May 2010 to 171.66.16.246. Redistribution subject to ASME license or copyright; see http://www.asme.org/terms/Terms_Use.cfm

particular elements a_{ij} that will be needed here are also recorded in equation (A1) of the Appendix.

The condition of perfect bond at the interface $z = 0$ requires continuity of velocity and traction there and it can be written in our notation as

$$\mathbf{f}(0) = \mathbf{f}^S(0). \tag{12}$$

Equations (9), (10), and (12) yield

$$\mathbf{f}(d) = AB \begin{Bmatrix} \phi_S'' \\ \psi_S'' \end{Bmatrix} = C \begin{Bmatrix} \phi_S'' \\ \psi_S'' \end{Bmatrix}, \tag{13}$$

where

$$C = AB. \tag{14}$$

This expresses the velocity-traction matrix $\mathbf{f}(d)$ on the layer at $z = d$ in terms of the two wave potentials in the substrate. The four wave potentials in the layer have therefore been eliminated. The conditions to be satisfied at the liquid-solid interface, $z = d$, are continuity of normal velocity and normal traction and vanishing shearing traction. Setting ψ', ψ'', and μ equal to zero in equation (6.3) of reference [1] we obtain for the normal velocity and traction on the fluid at $z = d$

$$\begin{Bmatrix} v_z^L(d) \\ Z_z^L(d) \end{Bmatrix} = \begin{bmatrix} \alpha_L & -\alpha_L \\ -\lambda_L k_L^2 \omega^{-1} & -\lambda_L k_L^2 \omega^{-1} \end{bmatrix} \begin{Bmatrix} ie^{iP_L} \phi_L' \\ ie^{-iP_L} \phi_L'' \end{Bmatrix}. \tag{15}$$

In view of equations (13) and (15), the just-mentioned fluid-layer interface conditions at $z = d$ yield

$$\begin{aligned} &c_{21}\phi_S'' + c_{22}\psi_S'' = i\alpha_L e^{iP_L}\phi_L' - i\alpha_L e^{-iP_L}\phi_L'', \\ &c_{31}\phi_S'' + c_{32}\psi_S'' = -i\lambda_L k_L^2 \omega^{-1} e^{iP_L}\phi_L' - i\lambda_L k_L^2 \omega^{-1} e^{-iP_L}\phi_L'', \\ &c_{41}\phi_S'' + c_{42}\psi_S'' = 0. \end{aligned} \tag{16}$$

We next divide by ϕ_L'' to obtain three inhomogeneous linear equations for determining the three unknown ratios of potentials; ϕ_L'/ϕ_L'', the reflection coefficient; ϕ_S''/ϕ_L'', the longitudinal transmission coefficient; and ψ_S''/ϕ_L'', the shear transmission coefficient. Our interest here is in the reflection coefficient which can be expressed as

$$R_{LSS} = \phi_L'/\phi_L'' = e^{-i2P_L} \frac{\Delta_3 - \mathcal{Z}_{\theta_L}\Delta_2}{\Delta_3 + \mathcal{Z}_{\theta_L}\Delta_2} \tag{17}$$

in which we have used the following identities and definitions

$$P_L = \alpha_L d, \quad \frac{\alpha_L}{k_L} = \mathcal{C}_{\theta_L}, \quad \lambda_L = \rho_L c_L^2, \quad k_L = \omega/c_L,$$

$$\lambda_L k_L \omega^{-1} = \rho_L c_L, \quad \mathcal{Z}_{\theta_L} = \frac{\rho_L c_L}{\mathcal{C}_{\theta_L}}. \tag{18}$$

and where Δ_i, $i = 2,3$, are defined by

$$\Delta_i = c_{i1}c_{42} - c_{41}c_{i2}, \quad i = 2,3. \tag{19}$$

Using the definitions of A, B, and C in equations (8), (9), (11), and (14) we obtain for Δ_i

$$\begin{aligned} (\omega/\mu_S)\Delta_i &= (\omega/\mu_S)(\sigma^2 + \alpha_S\beta_S)2\mu(a_{i2}a_{41} - a_{i1}a_{42}) \\ &+ \beta_S(\beta_S^2 + \sigma^2)2\mu(a_{i3}a_{41} - a_{i1}a_{43}) \\ &+ [2\alpha_S\beta_S\sigma - \sigma(\beta_S^2 - \sigma^2)][(a_{i1}a_{44} - a_{i4}a_{41}) \\ &+ 2\mu(a_{i2}a_{43} - a_{i3}a_{42})] \\ &+ \alpha_S(\beta_S^2 + \sigma^2)(a_{i2}a_{44} - a_{i4}a_{42}) \\ &+ (\mu_S/\omega)[(\beta_S^2 - \sigma^2)^2 + 4\alpha_S\beta_S\sigma^2](a_{i3}a_{44} - a_{i4}a_{43}), \\ &i = 2,3. \end{aligned} \tag{20}$$

In the Appendix, the required expressions for a_{ij} are recalled from reference [1] and the indicated minors of A in equation (20) are listed. After substitution of these expressions into equation (20) we obtain for the reflection coefficient R_{LSS} defined in equation (17)

$$R_{LSS} = \phi_L'/\phi_L'' = e^{-i2P_L} N/D, \tag{21}$$

where

$$\begin{aligned} \begin{pmatrix} N \\ D \end{pmatrix} &= \{2r^2 \mathcal{S}_{2\theta}\mathcal{S}_{2\gamma}\mathcal{C}_{2\gamma}^2(1 - \mathcal{C}_P\mathcal{C}_Q) + (\mathcal{C}_{2\gamma}^4 + r^4\mathcal{S}_{2\theta}^2\mathcal{S}_{2\gamma}^2)\mathcal{S}_P\mathcal{S}_Q \\ &- (\pm)i(\mathcal{Z}_{\theta_L}/\mathcal{Z}_\theta)(\mathcal{C}_{2\gamma}^2\mathcal{C}_P\mathcal{S}_Q \\ &+ r^2\mathcal{S}_{2\theta}\mathcal{S}_{2\gamma}\mathcal{S}_P\mathcal{C}_Q)\}\mathcal{Z}_\theta\mathcal{Z}_\gamma(1 + \mathcal{T}_{\theta_S}\mathcal{T}_{\gamma_S}) \\ &+ \{i(\mathcal{C}_{2\gamma}^2\mathcal{C}_P\mathcal{S}_Q + r^2\mathcal{S}_{2\theta}\mathcal{S}_{2\gamma}\mathcal{S}_P\mathcal{C}_Q) \\ &- (\pm)(\mathcal{Z}_{\theta_L}/\mathcal{Z}_\theta)\mathcal{S}_P\mathcal{S}_Q\}\mathcal{Z}_\gamma\mathcal{Z}_{\theta_S} \\ &+ \{-[\mathcal{S}_{4\gamma}(\mathcal{C}_{2\gamma} - r^2\mathcal{T}_\theta\mathcal{S}_{2\theta})(1 - \mathcal{C}_P\mathcal{C}_Q) \\ &+ 2(r^2\mathcal{S}_{2\theta}\mathcal{S}_{2\gamma}^2 - \mathcal{T}_\theta\mathcal{C}_{2\gamma}^3)\mathcal{S}_P\mathcal{S}_Q] \\ &+ (\pm)i2\left(\frac{\mathcal{Z}_{\theta_L}}{\mathcal{Z}_\theta}\right)\left(\frac{\mathcal{Z}_\theta}{\mathcal{Z}_\gamma}\right)(r^2\mathcal{S}_{2\theta}\mathcal{S}_P\mathcal{C}_Q \\ &- \mathcal{T}_\gamma\mathcal{C}_{2\gamma}\mathcal{C}_P\mathcal{S}_Q)\}\mathcal{Z}_\gamma\mathcal{Z}_{\gamma_S}(\mathcal{S}_{2\gamma_S} - \mathcal{T}_{\theta_S}\mathcal{C}_{2\gamma_S}) \\ &+ \{i(\mathcal{C}_{2\gamma}^2\mathcal{S}_P\mathcal{C}_Q + r^2\mathcal{S}_{2\theta}\mathcal{S}_{2\gamma}\mathcal{C}_P\mathcal{S}_Q) \\ &+ (\pm)(\mathcal{Z}_{\theta_L}/\mathcal{Z}_\theta)\mathcal{C}_P\mathcal{C}_Q\}\mathcal{Z}_\theta\mathcal{Z}_{\gamma_S} \\ &+ \{-[4\mathcal{S}_\gamma^2\mathcal{C}_{2\gamma} + (\mathcal{C}_{2\gamma}^2 + 4\mathcal{S}_\gamma^4)\mathcal{C}_P\mathcal{C}_Q \\ &- (\mathcal{T}_\gamma\mathcal{T}_\theta\mathcal{C}_{2\gamma}^2 + r^2\mathcal{S}_{2\theta}\mathcal{S}_{2\gamma})\mathcal{S}_P\mathcal{S}_Q] \\ &- (\pm)i(\mathcal{Z}_{\theta_L}/\mathcal{Z}_\theta)(\mathcal{S}_P\mathcal{C}_Q + \mathcal{T}_\theta\mathcal{T}_\gamma\mathcal{C}_P\mathcal{S}_Q)\}\mathcal{Z}_{\gamma_S}\mathcal{Z}_{\theta_S}\Delta_S, \end{aligned} \tag{22}$$

in which

$$r = b/c, \quad \mathcal{Z}_\theta = \rho c/\mathcal{C}_\theta, \quad \mathcal{Z}_\gamma = \rho b/\mathcal{C}_\gamma, \tag{23}$$

and Δ_S is the Rayleigh function for the substrate, which can be written in the notation used here as

$$\Delta_S = \mathcal{C}_{2\gamma_S}^2 + r_S^2\mathcal{S}_{2\theta_S}\mathcal{S}_{2\gamma_S}. \tag{24}$$

The structure of the reflection coefficient as given by equations (21)–(24) requires some discussion. First we note that the entire effect of the liquid is revealed in equation (17) through the phase term e^{-i2P_L} and the impedance $\mathcal{Z}_{\theta_L}$. In the limit of vanishing impedance $\mathcal{Z}_{\theta_L}$ the expressions for N and D both become Δ_3 which can be obtained from equation (22) by setting $\mathcal{Z}_{\theta_L}$ equal to zero. The expression Δ_3 represents the determinant, which, when set to zero, defines the dispersion relation for surface waves in a layered half-space as studied, for example, by Farnell and Adler [2]. (More will be said about this later.) The expressions for N and D in equation (22) have five sets of terms in braces. The liquid impedance $\mathcal{Z}_{\theta_L}$ appears once in each of these braces right after the $(\pm)$ sign. The effect of the substrate is represented by terms with subscript "S" that multiply each of these braces on their right-hand sides. These terms are seen to be algebraically quite simple when compared to the terms that represent the effect of the layer, which do not carry a subscript. A thorough discussion of the various limiting expressions for R_{LSS} is presented in the next section.

3 Limiting Cases

Because of the complexity of the reflection coefficient, and since, to the authors' knowledge, it has not been obtained before, it is instructive to study its limiting forms to verify its

Downloaded 02 May 2010 to 171.66.16.246. Redistribution subject to ASME license or copyright; see http://www.asme.org/terms/Terms_Use.cfm

correctness and also to better understand its structure. For simplicity of reference and in keeping with notation used by Pitts [3] and others, we have denoted the reflection coefficient for the structure considered here by R_{LSS}, i.e., the liquid-solid layer-solid case. In the limit when the substrate becomes a different liquid we can obtain $R_{L'SL''}$, which is also given in Brekhovskikh [1]. In the further limit when the two liquids become the same we should recover R_{LSL} as derived first by Schoch [4], and studied subsequently by Brekhovskikh [1], Pitts [3], Pitts et al. [5], Fiorito et al. [6], and others.

In the limit $d \to 0$ or in the limit when the solid layer has the same properties as the substrate we should recover R_{LS}, the liquid-solid case, which has also been extensively studied by Bertoni and Tamir [7], Pitts [3], and others. We should also recover this result in the limit when the layer becomes the same as the liquid. In the limit $d \to \infty$ we should recover again R_{LS}, but we should also recover the Stoneley wave determinant Δ_{STONELEY} for interface waves propagating parallel to the interface of two joined elastic half-spaces.

As mentioned at the end of the preceeding section, when the liquid vanishes the reflection coefficient is no longer meaningful but we should recover an expression Δ_{SS} for surface wave propagation in a layered half-space having one solid layer of finite thickness d attached to a different elastic half-space substrate. This has been previously studied by Farnell and Adler [2] and others.

After realizing that all the foregoing limiting cases must result from R_{LSS}, one should not be surprised at its algebraic complexity as given in equations (21) and (22). The process of exacting the forementioned limits strongly suggests that a less complex form for R_{LSS} cannot be obtained.

(A) The Limit: Solid Substrate Becomes a Liquid. In this limit the shear waves in the substrate vanish. This limit is affected in equation (22) by setting

$$b_S = 0, \quad \gamma_S = 0, \quad \mathcal{Z}_{\gamma_S} = 0, \quad \mathfrak{Z}_{\gamma_S} = 0, \quad \mathcal{Z}_{\theta_S} = \mathcal{Z}_{\theta_{L''}} \tag{25}$$

so that equation (22) becomes

$$\begin{aligned}\begin{pmatrix} N \\ D \end{pmatrix} &= \{2r^2 \mathcal{S}_{2\theta}\mathcal{S}_{2\gamma}\mathcal{C}_{2\gamma}^2(1-\mathcal{C}_P\mathcal{C}_Q) \\ &\quad + (\mathcal{C}_{2\gamma}^4 + r^4\mathcal{S}_{2\theta}^2\mathcal{S}_{2\gamma}^2)\mathcal{S}_P\mathcal{S}_Q \\ &\quad - (\pm)i(\mathcal{Z}_{\theta_L'}/\mathcal{Z}_\theta)(\mathcal{C}_{2\gamma}^2\mathcal{C}_P\mathcal{S}_Q \\ &\quad + r^2\mathcal{S}_{2\theta}\mathcal{S}_{2\gamma}\mathcal{S}_P\mathcal{C}_Q)\}\mathcal{Z}_\theta\mathcal{Z}_\gamma \\ &\quad + \{i(\mathcal{C}_{2\gamma}^2\mathcal{C}_P\mathcal{S}_Q + r^2\mathcal{S}_{2\theta}\mathcal{S}_{2\gamma}\mathcal{S}_P\mathcal{C}_Q) \\ &\quad - (\pm)(\mathcal{Z}_{\theta_L'}/\mathcal{Z}_\theta)\mathcal{S}_P\mathcal{S}_Q\}\mathcal{Z}_\gamma\mathcal{Z}_{\theta_{L''}},\end{aligned} \tag{26}$$

where $\mathcal{Z}_{\theta_L'}$ and $\mathcal{Z}_{\theta_{L''}}$ denote the impedances of the upper and lower liquids, respectively. The reflection coefficient $R_{L'SL''}$ is obtained from equation (21) with N and D determined by equation (26).

In the further limit in which the two liquids become the same we obtain from equation (26) by setting

$$\mathcal{Z}_{\theta_{L''}} = \mathcal{Z}_{\theta_{L'}} = \mathcal{Z}_{\theta_L} \tag{27}$$

the result

$$\begin{aligned}N &= 2r^2\mathcal{S}_{2\theta}\mathcal{S}_{2\gamma}\mathcal{C}_{2\gamma}^2(1-\mathcal{C}_P\mathcal{C}_Q) \\ &\quad + [\mathcal{C}_{2\gamma}^4 + r^4\mathcal{S}_{2\theta}^2\mathcal{S}_{2\gamma}^2 - (\mathcal{Z}_{\theta_L}/\mathcal{Z}_\theta)^2]\mathcal{S}_P\mathcal{S}_Q, \\ D &= N + 2(\mathcal{Z}_{\theta_L}/\mathcal{Z}_\theta)^2\mathcal{S}_P\mathcal{S}_Q + i2(\mathcal{Z}_{\theta_L}/\mathcal{Z}_\theta)(\mathcal{C}_{2\gamma}^2\mathcal{C}_P\mathcal{S}_Q \\ &\quad + r^2\mathcal{S}_{2\theta}\mathcal{S}_{2\gamma}\mathcal{S}_P\mathcal{C}_Q).\end{aligned} \tag{28}$$

Since Schoch [4] was the first to consider the liquid-solid layer-liquid case we try to compare equation (28) with his results. He did not explicitly solve for the reflection coefficient but he did give the transmission coefficient. The denominator in his expression, equation (13) of reference [4], should be the same as D in equation (28). To make the comparison we note the correspondence in notation

$$(\theta,\alpha,\beta,\delta,\epsilon)_{\text{Schoch}} = \left(\theta_L,\theta,\gamma,\frac{P}{2}\frac{Q}{2}\right)_{\text{here}}. \tag{29}$$

With this the two denominators are found to be identical. Using the same notation as Schoch [4], Fiorito et al. [6] gave the reflection coefficient in their equations (1)-(5). Comparing equation (28) with their results, we find complete agreement in their reflection coefficient and the ratio N/D. Thus, in view of equation (21), it appears that our reflection coefficient for the liquid-solid layer-liquid case differs from that given in reference [6] by the factor e^{-i2P_L} which would alter the phase but not the amplitude of R_{LSL}. We note that the limit considered here provides a check on only the first two terms of N and D given in equation (22).

(B) The Limit: Layer of Zero Thickness. In the limit $d \to 0$ we obtain

$$P = 0, \quad Q = 0, \quad \mathcal{S}_P = 0, \quad \mathcal{S}_Q = 0, \quad \mathcal{C}_P = 1, \quad \mathcal{C}_Q = 1, \tag{30}$$

so equation (22) yields

$$\begin{pmatrix} N \\ D \end{pmatrix} \to (\pm)\mathcal{Z}_{\theta_L}\mathcal{Z}_{\gamma_S} - (4\mathcal{S}_\gamma^2\mathcal{C}_{2\gamma} + \mathcal{C}_{2\gamma}^2 + 4\mathcal{S}_\gamma^4)\mathcal{Z}_{\gamma_S}\mathcal{Z}_{\theta_S}\Delta_S \tag{31}$$

and hence equation (21) reduces to

$$R_{LSS} \to R_{LS} = \frac{\Delta_S - (\mathcal{Z}_{\theta_L}/\mathcal{Z}_{\theta_S})}{\Delta_S + (\mathcal{Z}_{\theta_L}/\mathcal{Z}_{\theta_S})}, \tag{32}$$

which agrees with previous authors. This provides a check on parts of the last two terms of equation (22).

(C) The Limit: Solid Plate Becomes a Liquid. We first consider the case for which the liquid half-space is identified by L' and the solid layer becomes a liquid identified by L''. This limit is obtained from equation (22) by setting

$$b = 0, \quad \gamma = 0, \quad \mathcal{Z}_\gamma = 0, \quad \mathcal{Z}_\theta = \mathcal{Z}_{\theta_{L''}}, \quad P_{L''} = d\alpha_{L''} \tag{33}$$

so that $\begin{pmatrix} N \\ D \end{pmatrix}$ becomes

$$\begin{aligned}\begin{pmatrix} N \\ D \end{pmatrix} &= \{i\mathcal{S}_{P_{L''}} \pm (\mathcal{Z}_{\theta_{L'}}/\mathcal{Z}_{\theta_{L''}})\mathcal{C}_{P_{L''}}\}\mathcal{Z}_{\theta_{L''}} \\ &\quad + \{-\mathcal{C}_{P_{L''}} \mp i(\mathcal{Z}_{\theta_{L'}}/\mathcal{Z}_{\theta_{L''}})\mathcal{S}_{P_{L''}}\}\mathcal{Z}_{\theta_S}\Delta_S.\end{aligned} \tag{34}$$

Therefore the reflection coefficient for the liquid-liquid-solid case is

$$R_{L'L''S} = e^{-i2P_{L'}}\, N/D, \tag{35}$$

with N and D given by equation (34). This is evidently a new result.

In the further limit when the two liquids become the same, equation (34) yields

$$\begin{pmatrix} N \\ D \end{pmatrix} = \{i\mathcal{S}_{P_L} \pm \mathcal{C}_{P_L}\}\mathcal{Z}_{\theta_L} + \{-\mathcal{C}_{P_L} \mp i\mathcal{S}_{P_L}\}\mathcal{Z}_{\theta_S}\Delta_S \tag{36}$$

so that

$$\frac{N}{D} = e^{i2P_L}\frac{\Delta_S - (\mathcal{Z}_{\theta_L}/\mathcal{Z}_{\theta_S})}{\Delta_S + (\mathcal{Z}_{\theta_l}/\mathcal{Z}_{\theta_S})}. \tag{37}$$

By using this result in equation (21) we recover equation (32). This analysis indicates that the e^{-i2P_L} phase factor in equation (21) is due to the fact that the liquid-solid layer interface is located at $z = d$. It vanishes when the interface is located at $z = 0$.

(D) The Limit: Layer of Very Large Thickness. Here we

Downloaded 02 May 2010 to 171.66.16.246. Redistribution subject to ASME license or copyright; see http://www.asme.org/terms/Terms_Use.cfm

consider the limit $d \to \infty$. The technique used is similar to that in Pitts [3]. First we divide both N and D in equations (21) and (22) by $\mathcal{S}_P \mathcal{S}_Q$. Then we consider complex wave numbers so that

$$P = \alpha d = (\alpha_R + i\alpha_I)d, \quad Q = \beta d = (\beta_R + i\beta_I)d, \tag{38}$$

and in the limit $d \to \infty$

$$\mathcal{C}t_P \to -i, \quad \mathcal{C}t_Q \to -i, \quad \frac{1}{\mathcal{S}_P} \to 0, \quad \frac{1}{\mathcal{S}_Q} \to 0. \tag{39}$$

With these results equation (22) yields the limiting result

$$\begin{pmatrix} N \\ D \end{pmatrix} \to \{\Delta - (\pm)(\mathcal{Z}_{\theta_L}/\mathcal{Z}_\theta)\}\Delta_{\text{STONELEY}} \tag{40}$$

where

$$\begin{aligned}\Delta_{\text{STONELEY}} &= \mathcal{Z}_\theta \mathcal{Z}_\gamma \Delta(1 + \mathcal{T}_{\gamma_S}\mathcal{T}_{\theta_S}) + \mathcal{Z}_\gamma \mathcal{Z}_{\theta_S} \\ &\quad - 2\mathcal{Z}_\gamma(\mathcal{S}_{2\gamma} - \mathcal{T}_\theta \mathcal{C}_{2\gamma})\mathcal{Z}_{\gamma_S}(\mathcal{S}_{2\gamma_S} - \mathcal{T}_{\theta_S}\mathcal{C}_{2\gamma_S}) \\ &\quad + \mathcal{Z}_\theta \mathcal{Z}_{\gamma_S} = (1 + \mathcal{T}_\theta \mathcal{T}_\gamma)\mathcal{Z}_{\theta_S}\mathcal{Z}_{\gamma_S}\Delta_S.\end{aligned} \tag{41}$$

Since Δ_{STONELEY} occurs in both N and D it can be canceled from the reflection coefficient, which from equation (21) becomes as $d \to \infty$

$$R_{LSS} \to e^{-i2P_L}\left(\frac{\Delta - \mathcal{Z}_{\theta_L}/\mathcal{Z}_\theta}{\Delta + \mathcal{Z}_{\theta_L}/\mathcal{Z}_\theta}\right). \tag{42}$$

Disregarding for the moment the fact that the limit of the phase factor e^{-i2P_L} does not exist as $d \to \infty$, we obtain R_{LS} for the liquid-solid with the interface at $z = d$. If this interface were at $z = 0$ the phase factor would not appear. This reflection coefficient is relevant to the limit $d \to \infty$ when one focuses on the liquid-solid interface where there is an incident wave. If instead we focus on the solid-solid interface the term Δ_{STONELEY} is relevant. Its zeros determine the interface wave dispersion relation for Stoneley waves, as can be verified by comparing it to the Stoneley equation (see Ewing et al. [8]). Also notice that if the liquid vanishes both N and D in equation (40) become $\Delta\Delta_{\text{STONELEY}}$. The Rayleigh function Δ determines the surface waves and Δ_{STONELEY} determines the interface waves. This limit provides a good check on the reflection coefficient in equation (21) and (22) since terms in all of the five braces in equation (22) contribute to equation (40).

(E) **The Limit: Vanishing Liquid.** First we observe from equation (32), which gives the reflection coefficient for the liquid-solid case, that in the limit when the liquid vanishes, so that $\mathcal{Z}_{\theta_L}$ vanishes, the reflection coefficient becomes unity as the numerator and denominator both approach Δ, the Rayleigh function for the solid. In a similar manner when $\mathcal{Z}_{\theta_L} \to 0$ in the reflection coefficient of the liquid-solid layer-solid case given by equations (21) and (22) we find that N and D again become identical functions. This function determines surface waves in a solid layer on a solid half-space and is given by Δ_{SS} where

$$\begin{aligned}\Delta_{SS} &= \{2r^2 \mathcal{S}_{2\theta}\mathcal{S}_{2\gamma}\mathcal{C}_{2\gamma}^2(1 - \mathcal{C}_P\mathcal{C}_Q) \\ &\quad + (\mathcal{C}_{2\gamma}^4 + r^4\mathcal{S}_{2\theta}^2\mathcal{S}_{2\gamma}^2)\mathcal{S}_P\mathcal{S}_Q\}\mathcal{Z}_\theta\mathcal{Z}_\gamma(1 + \mathcal{T}_{\theta_S}\mathcal{T}_{\gamma_S}) \\ &\quad + i(\mathcal{C}_{2\gamma}^2\mathcal{C}_P\mathcal{S}_Q + r^2\mathcal{S}_{2\theta}\mathcal{S}_{2\gamma}\mathcal{S}_P\mathcal{C}_Q)\mathcal{Z}_\gamma\mathcal{Z}_{\theta_S} \\ &\quad - [\mathcal{S}_{4\gamma}(\mathcal{C}_{2\gamma} - r^2\mathcal{T}_\theta\mathcal{S}_{2\theta})(1 - \mathcal{C}_P\mathcal{C}_Q) \\ &\quad + 2(r^2\mathcal{S}_{2\theta}\mathcal{S}_{2\gamma}^2 - \mathcal{T}_\theta\mathcal{C}_{2\gamma}^3)\mathcal{S}_P\mathcal{S}_Q]\mathcal{Z}_\gamma\mathcal{Z}_{\gamma_S}(\mathcal{S}_{2\gamma_S} - \mathcal{T}_{\theta_S}\mathcal{C}_{2\gamma_S}) \\ &\quad + i(\mathcal{C}_{2\gamma}^2\mathcal{S}_P\mathcal{C}_Q + r^2\mathcal{S}_{2\theta}\mathcal{S}_{2\gamma}\mathcal{C}_P\mathcal{S}_Q)\mathcal{Z}_\theta\mathcal{Z}_{\gamma_S} \\ &\quad - [4\mathcal{S}_\gamma^2\mathcal{C}_{2\gamma} + (\mathcal{C}_{2\gamma}^2 + 4\mathcal{S}_\gamma^4)\mathcal{C}_P\mathcal{C}_Q \\ &\quad - \mathcal{T}_\gamma\mathcal{T}_\theta\mathcal{C}_{2\gamma}^2 + r^2\mathcal{S}_{2\theta}\mathcal{S}_{2\gamma})\mathcal{S}_P\mathcal{S}_Q]\mathcal{Z}_{\gamma_S}\mathcal{Z}_{\theta_S}\Delta_S.\end{aligned} \tag{43}$$

The problem of surface waves on a layered half-space was studied extensively by Farnell and Adler [2]. They did not obtain a function corresponding to Δ_{SS} in equation (43) except in the form of a 6×6 determinant (equation (18) of reference [2]), which they studied numerically. To the authors' knowledge, the function given in equation (43) has not been explicitly obtained previously. A final observation in connection with the layered half-space result in equation (43) is that in the limit $d \to \infty$, Δ_{SS} becomes the same as the expression in equation (40) but with $\mathcal{Z}_{\theta_L}$ set equal to zero. Therefore, Δ_{SS} becomes in this limit the product of the Rayleigh function Δ for the layer and the Stoneley function Δ_{STONELEY} for the solid-solid interface.

(F) **The Limit: Solid Layer Same as Substrate.** If the solid layer is the same as the solid substrate we again have the liquid-solid case with the interface at $z = d$. Algebraically this is the most complicated of the special cases considered, but it is the best check on equation (22) because all terms are involved. To carry out this analysis, we simply drop the subscript "S" from the half-space terms in equation (22). After considerable algebra we obtain

$$\begin{aligned}\begin{pmatrix} N \\ D \end{pmatrix} &= (\Delta\mathcal{Z}_\theta\mathcal{Z}_\gamma \mp \mathcal{Z}_{\theta_L}\mathcal{Z}_\gamma)[\mathcal{S}_P\mathcal{S}_Q - \mathcal{C}_P\mathcal{C}_Q \\ &\quad + i(\mathcal{S}_P\mathcal{C}_Q + \mathcal{C}_P\mathcal{S}_Q)] \\ &= -(\Delta \mp \mathcal{Z}_{\theta_L}/\mathcal{Z}_\theta)\mathcal{Z}_\theta\mathcal{Z}_\gamma e^{-i(P+Q)}\end{aligned} \tag{44}$$

so that the reflection coefficient in equation (21) becomes

$$R_{LS} = e^{-i2P_L}\left(\frac{\Delta - \mathcal{Z}_{\theta_L}/\mathcal{Z}_\theta}{\Delta + \mathcal{Z}_{\theta_L}/\mathcal{Z}_\theta}\right). \tag{45}$$

4 Reflection Coefficients for Some Thin Layer Models

Because of the complexity of the reflection coefficient presented in equations (21) and (22), and since for some applications the layer thickness d is much less than the wavelengths of interest, we present in this section several approximate reflection coefficients. First we linearize N and D in equation (22) to obtain their $0(d)$ approximations, and then we obtain the $0(d)$ approximation for R_{LSS} given in equation (21). We then consider various plate models for the thin layer. In particular, we derive the reflection coefficients for the cases where the layer is modeled as a classical Kirchhoff plate and a first-order Cosserat plate. (The complete development of Cosserat plate theory is contained in Naghdi [9]. Also included there is a thorough discussion of the relationship of this plate theory to the Reissner [10], Mindlin [11], and the classical (Kirchhoff [12]) plate theories.) We also examine a different approximate reflection coefficient derived by Nayfeh et al. [13] that is based on their thin layer assumptions. We compare analytically the various approximate reflection coefficients with the $0(d)$ approximation of R_{LSS}. In the next section numerical results based on all of these approximations are compared with numerical results based on R_{LSS}.

(A) **Thin Layer Approximation of R_{LSS}.** The layer thickness d is represented in N and D, given in equation (22), entirely through P and Q, which are defined in the Appendix as

$$P = \alpha d, \quad Q = \beta d. \tag{46}$$

Using the series expansions for $\mathcal{S}_P$, $\mathcal{S}_Q$, $\mathcal{C}_P$, $\mathcal{C}_Q$ and simplifying the results through various identities, we obtain from equation (21) in the limit of small αd

Downloaded 02 May 2010 to 171.66.16.246. Redistribution subject to ASME license or copyright; see http://www.asme.org/terms/Terms_Use.cfm

$$R_{LSS}=R_{LS}-i(\sigma d)\,\mathcal{C}t_{\theta_L}R_{LS}+i(\sigma d)\,(N'/D')+0(\sigma^2d^2), \quad (47)$$

where R_{LS} is the liquid-solid reflection coefficient defined in equation (32) and N',D' are given by

$$\begin{pmatrix}N'\\D'\end{pmatrix}=-\mathcal{C}t_\theta\Big\{\frac{\mathcal{Z}_\theta}{\mathcal{Z}_{\theta_S}}+(\mathcal{C}_{2\gamma}^2+r^4\mathcal{S}_{2\theta}^2)\Big[\frac{\mathcal{Z}_\theta}{\mathcal{Z}_{\gamma_S}}$$
$$\mp\frac{\mathcal{Z}_{\theta_L}\mathcal{Z}_\theta}{\mathcal{Z}_{\gamma_S}\mathcal{Z}_{\theta_S}}(1+\mathcal{T}_{\theta_S}\mathcal{T}_{\gamma_S})\Big]\Big\}\pm\Big\{(\mathcal{C}t_\theta+\mathcal{T}_\theta)\frac{\mathcal{Z}_{\theta_L}}{\mathcal{Z}_\theta}\Delta_S$$
$$-2(r^2\mathcal{S}_{2\theta}\mathcal{C}t_\theta-\mathcal{C}_{2\gamma})\frac{\mathcal{Z}_{\theta_L}}{\mathcal{Z}_{\theta_S}}(\mathcal{S}_{2\gamma_S}-\mathcal{T}_{\theta_S}\mathcal{C}_{2\gamma_S})\Big\}. \quad (48)$$

(B) Reflection Coefficient for Classical (Kirchhoff) Plate. Plate theories are two-dimensional models of a three-dimensional layer. Mathematically, the plate equations are two-dimensional, but the layer thickness enters through various moduli in the theory. For many applications the thickness of the layer can otherwise be ignored. However, when the plate model is used as part of a layered medium the continuity conditions imposed at the faces of the plate must also take into account the face locations that are determined by the thickness. The equations for a classical (Kirchhoff) plate with tractions on the faces can be found, for example, in Naghdi [9] and they can be written as

$$Cu_{,xx}-\rho d\ddot{u}=-\sigma_{zx}^+ +\sigma_{zx}^- \quad (49)$$

and

$$Bw_{,xxxx}+\rho d\ddot{w}=\sigma_{zz}^+-\sigma_{zz}^-+\frac{d}{2}(\sigma_{zx,x}^+ +\sigma_{zx,x}^-). \quad (50)$$

Equation (49) is the extensional equation, C is the extension modulus, u is the extensional (in-plane) displacement, subscripted x's after a comma denote partial differentiation, and $\sigma_{zx}^+,\sigma_{zx}^-$ denote the face shears on the positive and negative faces of the plate, respectively. Equation (50) is the bending equation, B is the flexure modulus, w is the flexural (transverse) displacement and $\sigma_{zz}^+,\sigma_{zz}^-$ denote the face normal stresses. The moduli C and B are defined in terms of Young's modulus E and Poisson's ratio ν by

$$C=Ed/(1-\nu^2), \quad B=Cd^2/12. \quad (51)$$

The appropriate interface conditions are

$$u=u_x^S(0), \quad w=u_z^L(d)=u_z^S(0), \quad (52)$$

$$\sigma_{zx}^+=0, \quad \sigma_{zx}^-=\sigma_{zx}^S(0), \quad \sigma_{zz}^+=\sigma_{zz}^L(d), \quad \sigma_{zz}^-=\sigma_{zz}^S(0). \quad (53)$$

Recalling that the x,t dependence of the waves is $e^{i(\alpha x-\omega t)}$ and using equations (52) and (53), we obtain from equations (49) and (50), after noting that $\mathbf{u}^S=i\mathbf{v}^S/\omega$

$$i\omega^{-1}\bar{C}v_x^S(0)=Z_x^S(0), \quad (54)$$

$$i\omega^{-1}\bar{B}v_z^S(0)+\frac{1}{2}\sigma d\omega^{-1}\bar{C}v_x^S(0)=Z_z^L(d)-Z_z^S(0), \quad (55)$$

where

$$\bar{C}=\rho d\omega^2-\frac{E\sigma^2 d}{1-\nu^2}, \quad \bar{B}=\frac{Ed^3\sigma^4}{12(1-\nu^2)}-\rho d\omega^2. \quad (56)$$

The second of equations (52) together with equations (54) and (55) provide, with use of equations (8) and (15), the following equations for determining the reflection and transmission coefficients:

$$\alpha_L e^{iP_L}\phi_L'+\alpha_S\phi_S''-\sigma\psi_S''=\alpha_L e^{-iP_L}\phi_L'',$$
$$(2\mu_S\alpha_S\sigma-i\sigma\bar{C})\phi_S''+[\mu_S(\beta_S^2-\sigma^2)-i\beta_S\bar{C}]\psi_S''=0,$$
$$\lambda_L k_L^2 e^{iP_L}\phi_L'-\Big[\mu_S(\beta_S^2-\sigma^2)+i\alpha_S\bar{B}-\frac{1}{2}\sigma^2 d\bar{C}\Big]\phi_S''$$
$$+\Big[2\mu_S\beta_S\sigma+i\sigma\bar{B}+\frac{1}{2}\sigma d\beta_S\bar{C}\Big]\psi_S''=-\lambda_L k_L^2 e^{-iP_L}\phi_L''. \quad (57)$$

The solution of this system yields

$$R_{LSS}^K=\frac{\phi_L'}{\phi_L''}=e^{-i2P_L}\frac{\Delta_{11}-\omega\mathcal{Z}_{\theta_L}\Delta_{13}}{\Delta_{11}+\omega\mathcal{Z}_{\theta_L}\Delta_{13}} \quad (58)$$

where

$$\Delta_{11}=d_{22}d_{33}+d_{32}d_{23}, \quad \Delta_{13}=\alpha_S d_{23}+\sigma d_{22},$$
$$d_{22}=2\mu_S\alpha_S\sigma-i\sigma\bar{C}, \quad d_{23}=\mu_S(\beta_S^2-\sigma^2)-i\beta_S\bar{C},$$
$$d_{32}=\mu_S(\beta_S^2-\sigma^2)+i\alpha_S\bar{B}-\frac{1}{2}\sigma^2 d\bar{C},$$
$$d_{33}=2\mu_S\beta_S\sigma+i\sigma\bar{B}+\frac{1}{2}\sigma d\beta_S\bar{C}. \quad (59)$$

Using the plate wave results

$$\rho\omega^2=\bar{E}k_P^2, \quad k_P=\omega/c_P, \quad c_P=\sqrt{\bar{E}/\rho}, \quad \bar{E}=E/(1-\nu^2) \quad (60)$$

so that

$$\bar{C}=\bar{E}d\alpha_P^2, \quad \bar{B}=-\bar{E}dk_P^2+\frac{\bar{E}d^3}{12}\sigma^4, \quad (61)$$

we can write the $0(d)$ approximation of R_{LSS}^K in the form

$$R_{LSS}^K=R_{LS}-i(\sigma d)\,\mathcal{C}t_{\theta_L}R_{LS}+i(\sigma d)\,\bar{N}/\bar{D}+0(\sigma^2d^2), \quad (62)$$

where

$$\begin{pmatrix}\bar{N}\\\bar{D}\end{pmatrix}=-\mathcal{C}t_{\theta_P}\Big\{\frac{\mathcal{Z}_{\theta_P}}{\mathcal{Z}_{\theta_S}}+$$
$$\mathcal{C}_{\theta_P}^2\Big[\frac{\mathcal{Z}_{\theta_P}}{\mathcal{Z}_{\gamma_S}}\mp\frac{\mathcal{Z}_{\theta_L}}{\mathcal{Z}_{\gamma_S}}\frac{\mathcal{Z}_{\theta_P}}{\mathcal{Z}_{\theta_S}}(1+\mathcal{T}_{\theta_S}\mathcal{T}_{\gamma_S})\Big]\Big\} \quad (63)$$

and where R_{LS} is defined in equation (32).

(C) Reflection Coefficient for Cosserat Plate. The theory of a Cosserat plate is contained in Naghdi [9]. The application of this plate theory to layered composites is presented in Green and Naghdi [14]. This theory includes effects of transverse shear deformation, transverse normal deformation, as well as rotatory inertia. None of these effects are included in the Kirchhoff plate theory. In the context used here for plane strain, there are two displacement-type equations for extension in the extensional variables u and δ, where u is the in-plane displacement and δ is the thickness change. Likewise, there are two equations for flexure in the flexural variables w and ϕ, where w is the transverse displacement and ϕ is the rotation. (We let x,z replace x_1,x_3 in reference [14]; also u,δ replace u_1,δ_3 and w,ϕ replace u_3,δ_1.) The equations appropriate to a plate with face loadings, as obtained from reference [9], are

Extension:

$$Cu_{,xx}+\frac{\nu C}{1-\nu}\delta_{,x}-\frac{(1-2\nu)}{(1-\nu)^2}\rho d\ddot{u}=-\frac{(1-2\nu)}{(1-\nu)^2}(\sigma_{zx}^+-\sigma_{zx}^-),$$
$$B\delta_{,xx}-\frac{20}{7}\frac{(1-\nu)B}{(1-2\nu)\alpha'}\delta-\frac{20}{7}\frac{\nu\ B}{(1-2\nu)\alpha'}u_{,x}$$
$$-\frac{20\,\alpha'}{7(1-\nu)}\rho d\ddot{\delta}=-\frac{10d}{7(1-\nu)}(\sigma_{zz}^+ +\sigma_{zz}^-), \quad (64)$$

Downloaded 02 May 2010 to 171.66.16.246. Redistribution subject to ASME license or copyright; see http://www.asme.org/terms/Terms_Use.cfm

Flexure:

$$B\phi_{,xx} - \frac{5\mu d}{6}(\phi + w_{,x}) - \rho d\alpha' \ddot{\phi} = -\frac{d}{2}(\sigma_{zx}^{+} + \sigma_{zx}^{-}),$$

$$\frac{5\mu d}{6}(w_{,xx} + \phi_{,x}) - \rho d\ddot{w} = -(\sigma_{zz}^{+} - \sigma_{zz}^{-}), \tag{65}$$

where C and B are defined in equation (51) and $\alpha' = d^2/12$. The interface conditions for the problem at hand are

$$u^{-} = u_x^S(0), \quad w^{+} = u_z^L(d), \quad w^{-} = u_z^S(0),$$

$$\sigma_{zx}^{+} = 0, \quad \sigma_{zx}^{-} = \sigma_{zx}^S(0), \quad \sigma_{zz}^{+} = \sigma_{zz}^L(d), \quad \sigma_{zz}^{-} = \sigma_{zz}^S(0), \tag{66}$$

where (see also reference [14] for interface conditions for Cosserat plates used in layered composites)

$$u^{-} = u - \frac{d}{2}\phi, \quad w^{+} = w + \frac{d}{2}\delta, \quad w^{-} = w - \frac{d}{2}\delta. \tag{67}$$

Next assume the harmonic wave solution

$$u = \hat{u}e^{i(\alpha x - \omega t)}, \quad \delta = \hat{\delta}e^{i(\alpha x - \omega t)},$$
$$w = \hat{w}e^{i(\alpha x - \omega t)}, \quad \phi = \hat{\phi}e^{i(\alpha x - \omega t)}, \tag{68}$$

Substitute these expressions into equations (64) and (65) and obtain, after use of the last four of equation (66)

$$e_{11}\hat{u} + e_{12}\hat{\delta} = d^{-1}h_1 Z_x^S(0),$$
$$e_{21}\hat{u} + e_{22}\hat{\delta} = h_2[Z_z^L(d) + Z_z^S(0)], \tag{69}$$

and

$$f_{11}\hat{w} + f_{12}\hat{\phi} = k_1 Z_x^S(0),$$
$$f_{21}\hat{w} + f_{22}\hat{\phi} = d^{-1}k_2[Z_z^L(d) - Z_z^S(0)], \tag{70}$$

in which

$$e_{11} = -\sigma^2 C' + \frac{(1-2\nu)}{(1-\nu)^2}\rho\omega^2/\mu, \quad e_{12} = i\frac{\nu\sigma}{1-\nu}C',$$

$$h_1 = \frac{1-2\nu}{(1-\nu)^2}\mu^{-1}, \quad e_{21} = -i\frac{20}{7}\frac{\nu}{(1-2\nu)}\sigma C',$$

$$e_{22} = \frac{20}{7}\alpha'\frac{1}{1-\nu}\frac{\rho\omega^2}{\mu} - C'\alpha'\sigma^2 - \frac{20}{7}\left(\frac{1-\nu}{1-2\nu}\right)C', \tag{71}$$

$$h_2 = -\frac{10}{7}\frac{1}{(1-\nu)\mu}, \quad C' = C/\mu d;$$

and

$$f_{11} = -10i\sigma, \quad f_{12} = -10 - d^2(\sigma^2 C' - \rho\omega^2/\mu), \quad k_1 = -6/\mu,$$
$$f_{21} = \mu^{-1}\rho\omega^2 - \frac{5}{6}\sigma^2, \quad f_{22} = i\frac{5}{6}\sigma, \quad k_2 = -\mu^{-1}. \tag{72}$$

Upon solving equations (69) and (70) and substituting the solution into the first two, as well as the second minus the third, of the continuity conditions in equation (66), we obtain, with the use of equation (67)

$$\begin{Bmatrix} du_x^S(0) \\ du_z^S(0) \\ u_z^L(d) - u_z^S(0) \end{Bmatrix} = \begin{bmatrix} l_{11} & l_{12} & l_{13} \\ l_{21} & l_{22} & l_{23} \\ l_{31} & l_{32} & l_{33} \end{bmatrix} \begin{Bmatrix} Z_x^S(0) \\ Z_z^L(d) \\ Z_z^S(0) \end{Bmatrix}, \tag{73}$$

where

$$l_{11} = \frac{e_{22}h_1}{\Delta_e} + \frac{d^2 f_{21}k_1}{2\Delta_f}, \quad \begin{pmatrix} l_{12} \\ l_{13} \end{pmatrix} = -\frac{de_{21}h_2}{\Delta_e}(\mp)\frac{df_{11}k_2}{2\Delta_f},$$

$$l_{21} = \frac{df_{22}k_1}{\Delta_f} + \frac{de_{21}h_1}{2\Delta_e}, \quad \begin{pmatrix} l_{22} \\ l_{23} \end{pmatrix} = (\mp)\frac{f_{12}k_2}{\Delta_f} - \frac{d^2 e_{11}h_2}{2\Delta_e},$$

$$l_{31} = -\frac{e_{21}h_1}{\Delta_e}, \quad l_{32} = l_{33} = \frac{de_{11}h_2}{\Delta_e}, \tag{74}$$

in which

$$\Delta_e = e_{11}e_{22} - e_{21}e_{12}, \quad \Delta f = f_{11}f_{22} - f_{21}f_{12}. \tag{75}$$

Finally, use $\mathbf{u} = i\mathbf{v}/\omega$ and equations (8) and (15) in equations (73) to obtain

$$\begin{bmatrix} G_{11} & G_{12} & G_{13} \\ G_{21} & G_{22} & G_{23} \\ G_{31} + i\alpha_L & G_{32} & G_{33} \end{bmatrix} \begin{Bmatrix} e^{iP_L}\phi_L' \\ \phi_S'' \\ \psi_S'' \end{Bmatrix}$$
$$= e^{-iP_L}\phi_L'' \begin{Bmatrix} -G_{11} \\ -G_{21} \\ -G_{31} + i\alpha_L \end{Bmatrix}, \tag{76}$$

where G_{ij}, $i = 1,2,3$ are listed in equation (A3). The solution of this system yields for the reflection coefficient

$$R_{LSS}^C = \frac{\phi_L'}{\phi_L''} = e^{-i2P_L}\frac{M_{31} - \mathcal{Z}_{\theta_L}M}{M_{31} + \mathcal{Z}_{\theta_L}M} \tag{77}$$

where

$$M = -\frac{i}{\rho_L\omega}[G_{11}M_{11} - G_{21}M_{21} + G_{31}M_{31}], \tag{78}$$

$$M_{11} = G_{22}G_{33} - G_{23}G_{32}, \quad M_{21} = G_{12}G_{33} - G_{13}G_{32},$$
$$M_{31} = G_{12}G_{23} - G_{13}G_{22}. \tag{79}$$

***(D)* Reflection Coefficient for Thin Layer Approximation of Nayfeh et al. [13].** In an investigation of the same problem as that of interest here Nayfeh et al. [13] derived an approximate model for the case of a thin layer. They did not use an existing plate theory but, instead, they made assumptions based on intuitive arguments for thin layers. In the notation and coordinates used here their equations (25) and (26) appear as

$$d(\lambda + 2\mu)u_{,xx} - \rho d\ddot{u} = \sigma_{zx}^S(0), \tag{80}$$

and

$$-d\mu w_{,xx} + \rho d\ddot{w} = \sigma_{zz}^L(0) - \sigma_{zz}^S(0). \tag{81}$$

These two equations should be compared with equations (49) and (50) of the Kirchhoff plate theory. Given that $\sigma_{zx}^{+} = 0$ in equation (49), it agrees with equation (80) except the extension modulus C is replaced by $(\lambda + 2\mu)d$. This means that longitudinal waves will propagate in the layer at the longitudinal wave speed of an infinite medium $(\lambda + 2\mu/\rho)^{1/2}$, rather than the plate wave speed $(C/\rho d)^{1/2}$. Equation (81) differs from equation (50) in two respects. The face shear gradients $\sigma_{zx,x}$ are missing in equation (81) and $Bw_{,xxxx}$ of equation (50) is replaced by $-\mu d w_{,xx}$ in equation (81). This means that equation (81) predicts flexural waves in the layer propagate at the shear wave speed of an infinite medium, $(\mu/\rho)^{1/2}$, rather than at the dispersive flexural wave speed, $(E/12(1-\nu^2)\rho)^{1/2}\sigma d$, predicted by equation (50). Also observe that $\sigma_{zz}L(0)$ appears in equation (81) in place of $\sigma_{zz}^L(d)$. This difference will lead to a difference in phase in the reflection coefficient.

The continuity conditions in reference [13] were given as

Downloaded 02 May 2010 to 171.66.16.246. Redistribution subject to ASME license or copyright; see http://www.asme.org/terms/Terms_Use.cfm

(there is evidently a misprint) in equation (24) of reference [13] in setting $u_0 = u_f$)

$$u = u_x^S(0), \quad w = u_z^S(0) = u_z^L(0), \tag{82}$$

which are different from equation (52) in that $u_z^L(0)$ replaces $u_z^L(d)$.

We can obtain the reflection coefficient for the layer model represented by equations (80)–(82) from the Kirchhoff result in equations (58) and (59) by setting

$$P_L = 0, \quad \bar{C} = \rho d\omega^2 - (\lambda + 2\mu)\sigma^2 d, \quad \bar{B} = \mu d\sigma^2 - \rho d\omega^2, \tag{83}$$

and deleting the $\bar{C}$ terms from the third of equation (57). Then we obtain

$$R_{LSS}^N = \frac{\phi_L'}{\phi_L''} = \frac{\Delta_{11}' - \omega \mathcal{Z}_{\theta_L} \Delta_{13}'}{\Delta_{11}' + \omega \mathcal{Z}_{\theta_L} \Delta_{13}'}, \tag{84}$$

where

$$\Delta_{11}' = d_{22}' d_{33}' + d_{32}' d_{23}', \quad \Delta_{13}' = \alpha_S d_{23}' + \sigma d_{22}',$$
$$d_{22}' = 2\mu_S \alpha_S \sigma - i\sigma \bar{C}, \quad d_{23}' = \mu_S(\beta_S^2 - \sigma^2) - i\beta_S \bar{C},$$
$$d_{32}' = \mu_S(\beta_S^2 - \sigma^2) + i\alpha_S \bar{B}, \quad d_{33}' = 2\mu_S \beta_S \sigma + i\sigma \bar{B}. \tag{85}$$

Using the results

$$\rho\omega^2 = (\lambda + 2\mu)k^2 = \mu\kappa^2 \tag{86}$$

so that

$$\bar{C} = (\lambda + 2\mu) d\alpha^2, \quad \bar{B} = -\mu d\beta^2, \tag{87}$$

we can write the $0(d)$ approximation of R_{LSS}^N in the form

$$R_{LSS}^N = R_{LS} + i(\sigma d)\tilde{N}/\tilde{D} + 0(\sigma^2 d^2), \tag{88}$$

where

$$\begin{pmatrix} \tilde{N} \\ \tilde{D} \end{pmatrix} = -\mathcal{C}t_\theta \left\{ \frac{\mathcal{Z}_\theta}{\mathcal{Z}_{\theta_S}} \mathcal{C}_\gamma^2 + \mathcal{C}_\theta^2 \left[\frac{\mathcal{Z}_\theta}{\mathcal{Z}_{\gamma_S}} \mp \frac{\mathcal{Z}_{\theta_L}}{\mathcal{Z}_{\gamma_S}} \frac{\mathcal{Z}_\theta}{\mathcal{Z}_{\theta_S}} (1 + \mathfrak{I}_{\theta_S} \mathfrak{I}_{\gamma_S}) \right] \right\}, \tag{89}$$

and where R_{LS} is defined in equation (32). (There is evidently a misprint in equations (30) and/or (31) of reference [13] as the reflection coefficient defined there does not reduce to R_{LS} when the thickness h is set equal to zero.) Equations (84), (88), and (89) should be compared to equations (58), (62), and (63) of the Krichhoff plate result.

5 Poles of Reflection Coefficient-Interface Wave Speeds

A study of the zeros and poles of the reflection coefficient R_{LSS} given in equations (21)–(24) will be presented in a subsequent paper, reference [15], in which the reflection coefficient is shown graphically as a function of incidence angle for many different material combinations. Here we limit the numerical computations to those necessary for a comparison of R_{LSS} with the approximate model reflection coefficients R_{LSS}^K, R_{LSS}^C, and R_{LSS}^N derived in the preceding section. To also compare with experimental results in reference [13] we compute the liquid-layer interface phase velocity c_I as a function of $q = d\omega/b_S$. The procedure for these computations is essentially as follows. The existence of the propagating wave is associated with a pole of R_{LSS} in a complex σ-plane. This pole is determined by a zero of D given in equation (22). If σ^* denotes this zero, so that

$$D(\sigma^*) = 0, \tag{90}$$

then the interface phase velocity c_I is given by

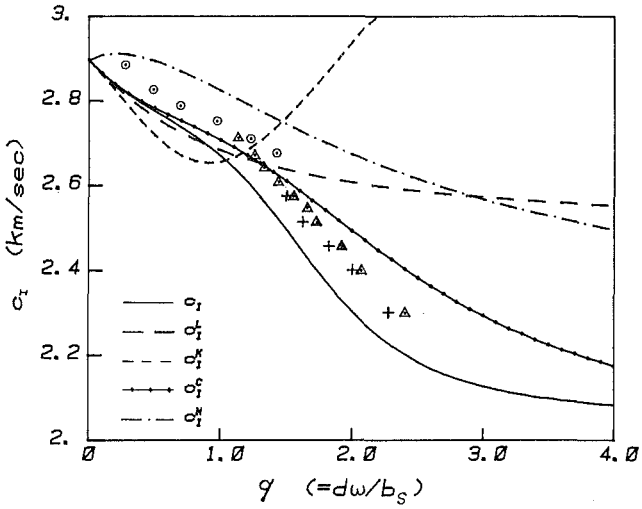

Fig. 2 Liquid-solid interface wave speed for water-copper-stainless steel as a function of q for the exact theory and several approximate models for the layer. Experimental points are from Nayfeh et al. [13]. Material parameters used: (densities, kg/m^3; velocities, km/sec) water-copper-stainless steel. $\rho_L = 1, c_L = 1.49, \rho = 8.93, c = 4.76, b = 2.2, \rho_S = 7.9, c_S = 5.69, b_S = 3.13.$

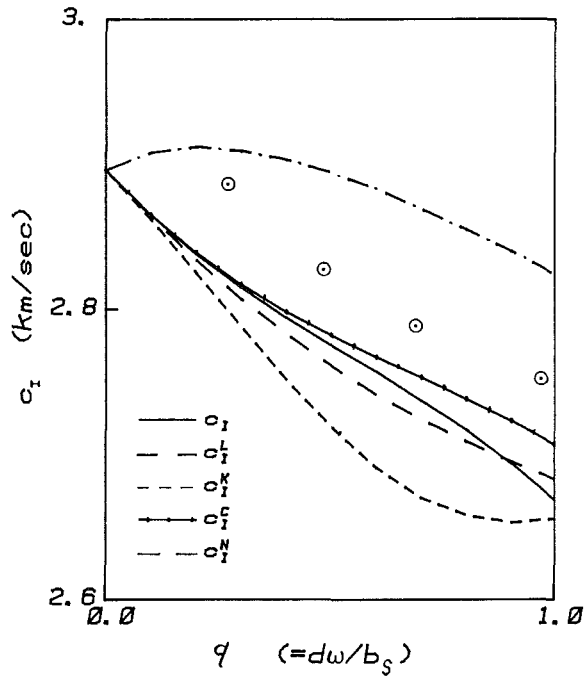

Fig. 3 Same as Fig. 2 except for scale

$$c_I = \omega/Re(\sigma^*). \tag{91}$$

First we choose the material parameters $\rho_L, c_{L\rho}, c, b, \rho_S, c_S$, and b_S and then choose the layer thickness d and the wave frequency ω. $D(\sigma)$ is then computed at points along a closed circuit in the σ-plane. Using the principle of the argument in complex function theory we can determine from this computation the number of zeros minus the number of poles of $D(\sigma)$ contained within the circuit. By systematically subdividing the circuit into smaller ones and repeating the calculations, we locate the zero, σ^*, corresponding to the lowest Rayleigh mode. (This zero lies on the real axis when $\mathcal{Z}_{\theta_L}$ in D vanishes.) The phase velocity is calculated according to equation (91) and plotted as a function of $q = d\omega/b_S$.

Figure 2 shows c_I based on R_{LSS} as a function of q for the

Downloaded 02 May 2010 to 171.66.16.246. Redistribution subject to ASME license or copyright; see http://www.asme.org/terms/Terms_Use.cfm

materials considered in reference [13], which are water, copper layer, and stainless steel substrate. Also shown are the corresponding approximate c_l based on (*i*) the $0(d)$ approximation of R_{LSS} (this curve is designated R^L_{LSS}) given in equation (47); (*ii*) the Krichhoff plate reflection coefficient R^K_{LSS} in equation (58); (*iii*) Cosserat plate reflection coefficient R^C_{LSS} given in equation (77); and (*iv*) thin layer model result of Nayfeh et al. [13] in equation (84). Figure 3 presents the same curves on an expanded scale for better comparison near $q = 0$.

The values of c_l at $q = 0$ for all of the models agree with the Rayleigh velocity for the substrate. As q becomes large the exact result approaches the Rayleigh velocity for a half-space of the layer material. The $0(d)$ approximate curve c^L_l is in good agreement with the exact result for $0 \leq q < 1$, then deviates seriously from c_l for $q > 1$. The Cosserat plate result, c^C_l, is also a good approximation in $0 \leq q < 1$ and indeed is the best approximation considered over the entire range of q. The result based on the Kirchhoff plate is a poor approximation for all $q > 0.2$, and Nayfeh et al. [13] thin layer approximation is the least accurate approximation considered. It is the only one of the approximate curves with the incorrect slopes at $q = 0$ as seen in Fig. 3. It should be noted that our calculation of the c^N_l curve is not entirely in agreement with the corresponding curve in Fig. 4 of reference [13]. The latter shows the c^N_l curve has almost zero slope for $0 < q < 0.5$. For larger values of q the curve presented there appears to agree with our c^N_l curve in Fig. 2.

The experimental results presented in Fig. 4 of reference [13] have also been plotted in our Fig. 2. Here we see that the exact curve parallels the experimental results, but the latter appear to be displaced about 10 to 15 percent above. There is no obvious explanation for this discrepancy. In reference [18] the dispersion curve based on the exact theory is presented along with experimental results, again for a copper layer on a stainless steel substrate. There the theoretical and experimental curves are in close agreement. The shear wave speed used for copper in the theoretical calculation in reference [18] was 2.32 km/sec rather than the value 2.2 km/sec used in reference [13]. We recalculated the exact curve in Fig. 2 for the 2.32 value and obtained a result that is in agreement with reference [18]. The experimental results reported in reference [13] are somewhat different from those in reference [18], and the latter are in better agreement with exact theory.

6 Summary and Conclusions

In this paper we have derived the reflection coefficient for plane harmonic waves incident from a fluid onto a layered elastic solid half-space. The layer and substrate are considered to be different isotropic, homogeneous elastic solids and the fluid is inviscid. The layer thickness is arbitrary. The structure of this reflection coefficient is revealed, and its relation to several previously studied special cases is obtained, by considering the appropriate limits. The reflection coefficient is linearized for the case of thin layers. Also, approximate reflection coefficients are derived using various thin layer models. In particular, the layer is modeled as a classical Kirchhoff plate and a Cosserat plate. In addition a thin layer model presented in Nayfeh et al. [13] is examined.

The poles of the reflection coefficients are obtained numerically and the resulting interface phase velocity curves (based on each model) as a function of $q = \omega d/b_S$ are presented. It is found that none of the approximate results are reliable for $q > 1$. Only the linearized result based on the exact theory and the Cosserat plate result have the useful range $0 \leq q < 1$. The Kirchhoff plate result provides a good approximation in the range $0 \leq q < 0.2$, but the Nayfeh et al. [13] model did not yield very useful results for any range of $q > 0$ for the particular materials considered.

The procedure for obtaining the zeros of the various reflection coefficients was the same, i.e., no computational simplification was associated with the approximations except that fewer terms needed to be programmed and computed. It is therefore recommended that the exact reflection coefficient be used rather than any of the approximations whenever applications require the use of R_{LSS}, provided computer time is not an overriding concern.

Acknowledgment

This problem was first brought to the attention of the authors by Dr. Bruce Maxfield of the Lawrence Livermore National Laboratory. We are grateful to Ms. H.-J. Yang for independently verifying the correctness of equations (21) and (22). One of us, S.M.G., would like to acknowledge support by an IBM Predoctoral Fellowship. This work was also partially supported by the National Science Foundation under Grant CME-8017840 to the University of California, Berkeley.

References

1 Brekhovskikh, L. M., *Waves in Layered Media*, Academic Press, New York, 1960.

2 Farnell, G. W., and Adler, E. L., "Elastic Wave Propagation in Thin Layers," in *Physical Acoustics*, Vol. 9, Academic Press, New York, 1972, pp. 35–127.

3 Pitts, L. E., "A Unified Theoretical Description of Ultrasonic Beam Reflections From a Solid Plate in a Fluid," Ph.D. Thesis, Georgetown University, 1976.

4 Schoch, A., "Der Schalldurchgang Durch Platten," *Acoustica*, Vol. 2, 1952, pp. 1–17.

5 Pitts, L. E., Plona, T. J., and Mayer, W. G., "Theory of Nonspecular Reflection Effects for an Ultrasonic Beam Incident on a Solid Plate in a Liquid," IEEE Trans. *Sonics and Ultrasonics*, Vol. SU-24, 1977, pp. 101–108.

6 Fiorito, R., Madigosky, W., and Überall, H., "Resonance Theory of Acoustic Waves Interacting With an Elastic Plate," *J. Acoust. Soc. Amer.*, Vol. 66, 1979, pp. 1857–1866.

7 Bertoni, H. L., and Tamir, T., "Unified Theory of Rayleigh-Angle Phenomena for Acoustic Beams at Liquid-Solid Interfaces," *Appl. Phys.*, Vol. 2, 1973, pp. 157–172.

8 Ewing, W. M., Jardetzky, M. C., and Press, F., *Elastic Waves in Layered Media*, McGraw-Hill, New York, 1957.

9 Naghdi, P. M., "The Theory of Shells and Plates," in Flügge's *Handbuch der Physik*, Vol. VIa/2, Truesdell, C., ed., Springer-Verlag, Berlin, Heidelberg, New York, 1972, pp. 425–640.

10 Reissner, E., "The Effect of Transverse Shear Deformation on the Bending of Elastic Plates," ASME JOURNAL OF APPLIED MECHANICS, Vol. 12, 1945, A-69–77.

11 Mindlin, R. D., "Influence of Rotatory Inertia and Shear on Flexural Vibrations of Isotropic, Elastic Plates," ASME JOURNAL OF APPLIED MECHANICS, Vol. 18, 1951, pp. 31–38.

12 Kirchhoff, G., "Uber das Gleichgewicht und die Bewegung Einer Elastischen Scheibe," *Crelles J.*, Vol. 40, 1850, pp. 51–88.

13 Nayfeh, A. H., Chimenti, D. E., Adler, L., and Crane, R. L., "Ultrasonic Leaky Waves in the Presence of a Thin Layer," *J. Appl. Phys.*, Vol. 52, 1981, pp. 4985–4994.

14 Green, A. E., and Naghdi, P. M., "A Theory of Laminated Composite Plates and Rods," University of California, Berkeley Report UCB/AM-81-3, May 1981.

15 Bogy, D. B., Gracewski, S. M., "On the Plane Wave Reflection Coefficient and Nonspecular Reflection of Bounded Beams For Layered Half Spaces Under Water," *J. Acoust. Soc. Amer.*, to appear.

16 Maxfield, B., Lawrence Livermore National Laboratory, private communication.

17 Goos, F., and Hänchen, H., "Ein Neuer und Fundamentaler Versuch zur Totalreflexion," *Ann. Phys.* (Leipzig), Vol. 1, 1947, pp. 333–346.

18 Chimenti, D. E., Nayfeh, A. H., and Butler, D. L., "Leaky Rayleigh Waves on a Layered Halfspace," *J. Appl. Phys.*, Vol. 53, 1982, pp. 170–176.

19 Chimenti, D. E., and Nayfeh, A. H., "Leaky Rayleigh Waves at a Layered Halfspace—Fluid Interface," Proc. *IEEE Ultrasonics Symposium*, 1981, pp. 291–294.

APPENDIX

The expressions for a_{ij} needed in equation (11) are given in reference [1], p. 64 as

Downloaded 02 May 2010 to 171.66.16.246. Redistribution subject to ASME license or copyright; see http://www.asme.org/terms/Terms_Use.cfm

$$a_{21} = i\left(\frac{b\mathcal{C}_\theta}{c\mathcal{C}_\gamma}\mathcal{S}_{2\gamma}\mathcal{S}_P - \mathcal{J}_\gamma\mathcal{C}_{2\gamma}\mathcal{S}_Q\right), \quad a_{22} = \mathcal{C}_{2\gamma}\mathcal{C}_P + 2\mathcal{S}_\gamma^2\mathcal{C}_Q,$$

$$a_{23} = -\frac{i}{\rho c}(\mathcal{C}_\theta\mathcal{S}_P + \mathcal{J}_\gamma\mathcal{S}_\theta\mathcal{S}_Q), \quad a_{24} = 2b\mathcal{S}_\gamma(\mathcal{C}_Q - \mathcal{C}_P),$$

$$a_{31} = 2\rho b\mathcal{S}_\gamma\mathcal{C}_{2\gamma}(\mathcal{C}_Q - \mathcal{C}_P),$$

$$a_{32} = -i\rho\left(\frac{c\mathcal{C}_{2\gamma}^2}{\mathcal{C}_\theta}\mathcal{S}_P + 4b\mathcal{C}_\gamma\mathcal{S}_\gamma^2\mathcal{S}_Q\right),$$

$$a_{33} = \mathcal{C}_{2\gamma}\mathcal{C}_P + 2\mathcal{S}_\gamma^2\mathcal{C}_Q, \quad a_{34} = 2i\rho b^2(\mathcal{C}_{2\gamma}\mathcal{J}_\theta\mathcal{S}_P - \mathcal{S}_{2\gamma}\mathcal{S}_Q),$$

$$a_{41} = -i\left(\frac{2}{c}\mathcal{C}_\theta\mathcal{S}_\gamma^2\mathcal{S}_P + \frac{\mathcal{C}_{2\gamma}^2}{2b\mathcal{C}_\gamma}\mathcal{S}_Q\right),$$

$$a_{42} = \frac{1}{c}\mathcal{S}_\theta\mathcal{C}_{2\gamma}(\mathcal{C}_Q - \mathcal{C}_P),$$

$$a_{43} = \frac{i}{2\rho}\left(\frac{\mathcal{S}_{2\theta}}{c^2}\mathcal{S}_P - \frac{\mathcal{C}_{2\gamma}}{b^2}\mathcal{J}_\gamma\mathcal{S}_Q\right), \quad a_{44} = 2\mathcal{S}_\gamma^2\mathcal{C}_P + \mathcal{C}_{2\gamma}\mathcal{C}_Q, \tag{A1}$$

in which $P = \alpha d$, $Q = \beta d$, and where the notation has been defined in Section 2. Using these results we obtain for the minors of the matrix A listed in equation (20) the following:

$$a_{22}a_{41} - a_{21}a_{42} = -i\left(\frac{\mathcal{C}_{2\gamma}^2}{2b\mathcal{C}_\gamma}\mathcal{C}_P\mathcal{S}_Q + \frac{2}{c}\mathcal{C}_\theta\mathcal{S}_\gamma^2\mathcal{S}_P\mathcal{C}_Q\right),$$

$$a_{32}a_{41} - a_{31}a_{42} = -\rho\left[4\mathcal{S}_\gamma^2\mathcal{C}_{2\gamma}^2(1 - \mathcal{C}_P\mathcal{C}_Q) + \left(\frac{c}{2b}\frac{\mathcal{C}_{2\gamma}^4}{\mathcal{C}_\theta\mathcal{C}_\gamma} + \frac{8b}{c}\mathcal{C}_\theta\mathcal{C}_\gamma\mathcal{S}_\gamma^4\right)\right],$$

$$a_{23}a_{41} - a_{21}a_{43} = -\frac{1}{2\rho bc}\frac{\mathcal{C}_\theta}{\mathcal{C}_\gamma}\mathcal{S}_P\mathcal{S}_Q,$$

$$a_{33}a_{41} - a_{31}a_{43} = a_{22}a_{41} - a_{21}a_{42},$$

$$(a_{21}a_{44} - a_{24}a_{41}) + 2\mu(a_{22}a_{43} - a_{23}a_{42}) = i\left(2\frac{b^2}{c^2}\mathcal{S}_{2\theta}\mathcal{S}_P\mathcal{C}_Q - 2\mathcal{J}_\gamma\mathcal{C}_{2\gamma}\mathcal{C}_P\mathcal{S}_Q\right),$$

$$(a_{31}a_{44} - a_{34}a_{41}) + 2\mu(a_{32}a_{43} - a_{33}a_{42}) = 2\rho b\left[2\mathcal{S}_\gamma\mathcal{C}_{2\gamma}(\mathcal{C}_{2\gamma} - 2\mathcal{S}_\gamma^2)(1 - \mathcal{C}_P\mathcal{C}_Q) + \left(\frac{4b}{c}\mathcal{C}_\theta\mathcal{S}_\gamma^2\mathcal{S}_{2\gamma} - \mathcal{J}_\theta\frac{\mathcal{C}_{2\gamma}^3}{\mathcal{C}_\gamma}\right)\mathcal{S}_P\mathcal{S}_Q\right],$$

$$a_{22}a_{44} - a_{24}a_{42} = \mathcal{C}_P\mathcal{C}_Q,$$

$$a_{32}a_{44} - a_{34}a_{42} = -i\rho\left(c\frac{\mathcal{C}_{2\gamma}^2}{\mathcal{C}_\theta}\mathcal{S}_P\mathcal{C}_Q + 2b\mathcal{S}_{2\gamma}\mathcal{S}_\gamma\mathcal{S}_Q\mathcal{C}_P\right),$$

$$a_{23}a_{44} - a_{24}a_{43} = -\frac{i}{\rho c}(\mathcal{C}_\theta\mathcal{S}_P\mathcal{C}_Q + \mathcal{S}_\theta\mathcal{J}_\gamma\mathcal{C}_P\mathcal{S}_Q),$$

$$a_{33}a_{44} - a_{34}a_{43} = 4\mathcal{S}_\gamma^2\mathcal{C}_{2\gamma} + (\mathcal{C}_{2\gamma}^2 + 4\mathcal{S}_\gamma^4)\mathcal{C}_P\mathcal{C}_Q - \left(\mathcal{J}_\gamma\mathcal{J}_\theta\mathcal{C}_{2\gamma}^2 + \frac{b^2}{c^2}\mathcal{S}_{2\theta}\mathcal{S}_{2\gamma}\right)\mathcal{S}_P\mathcal{S}_Q. \tag{A2}$$

The expressions G_{ij}, $i = 1,2,3$ in equation (76) are defined by

$$G_{11} = \lambda_L k_L^2 l_{12}, \quad G_{12} = i\sigma - 2l_{11}\mu_S\alpha_S\sigma + l_{13}\mu_S(\beta_S^2 - \sigma^2),$$
$$G_{13} = i\beta_S - l_{11}\mu_S(\beta_S^2 - \sigma^2) - 2l_{13}\mu_S\sigma\beta_S,$$
$$G_{21} = \lambda_L k_L^2 l_{22}, \quad G_{22} = -i\alpha_S - 2l_{21}\mu_S\alpha_S\sigma + l_{23}\mu_S(\beta_S^2 - \sigma^2),$$
$$G_{23} = i\sigma - l_{21}\mu_S(\beta_S^2 - \sigma^2) - 2l_{23}\mu_S\sigma\beta_S,$$
$$G_{31} = \lambda_L k_L^2 l_{32}, \quad G_{32} = i\alpha_S - 2l_{31}\mu_S\alpha_S\sigma + l_{33}\mu_S(\beta_S^2 - \sigma^2),$$
$$G_{33} = -i\sigma - l_{31}\mu_S(\beta_S^2 - \sigma^2) - 2l_{33}\mu_S\sigma\beta_S, \tag{A3}$$

where l_{ij} are defined by equations (71), (72), and (74).

Downloaded 02 May 2010 to 171.66.16.246. Redistribution subject to ASME license or copyright; see http://www.asme.org/terms/Terms_Use.cfm

W. D. Iwan
Professor of Applied Mechanics,
California Institute of Technology,
Pasadena, Calif.
Mem. ASME

C. M. Krousgrill Jr.
Assistant Professor of
Mechanical Engineering,
Purdue University,
West Lafayette, Ind.

Equivalent Linearization for Continuous Dynamical Systems

An approximate method is presented for determining the dynamical response of certain continuous nonlinear systems. In the proposed method, the system equation is linearized in the time domain prior to generation of a solution in the spatial domain. The approach is particularly suited to problems with complex boundary conditions which make selection of realistic global, spatial, domain comparison functions difficult. The approach is ideally suited to problems where discretization using finite elements is appropriate. The transverse response of a nonlinear rectangular plate is examined by way of the application of the proposed method.

Introduction

Many continuous dynamical systems may be represented by partial differential equations of the form

$$\mathfrak{D}(w,\mathbf{x},t) \equiv \nabla \cdot \mathbf{D}(w,\mathbf{x}) + cm(\mathbf{x})\dot{w} + m(\mathbf{x})\ddot{w} - p(\mathbf{x},t) = 0 \quad (1)$$

where $w(\mathbf{x},t)$ is the dependent variable of the spatial coordinates $\mathbf{x}$ and time t, $\mathbf{D}$ is a differential operator in the spatial domain, $m(\mathbf{x})$ is a positive distributed mass, c is a damping coefficient, and $p(\mathbf{x},t)$ is the distributed dynamical load. The statement of the problem is completed by the addition of appropriate boundary and initial conditions. An equation of the form of (1) may be used when there is a *set* of dependent variables w, by generalizing the notation so that $\mathfrak{D}$ is a vector.

Systems that are capable of being represented by equations of the form of (1) include most second-order systems, such as rods, strings, and membranes, and most fourth-order systems such as beam, plates, and some shells. The precise definition of the terms in equation (1) will change for each different physical problem, but the basic structure of the equation will remain the same.

Usually, dynamical systems of the type described by equation (1) will be approximately linear for small amplitudes of response. However, for large amplitudes of response, the system will often exhibit important nonlinear effects. When the system is nonlinear, it will be assumed that $\mathbf{D}$ can be separated into a linear and a nonlinear component, as

$$\mathbf{D}(w,\mathbf{x}) = \mathbf{D}_l(w,\mathbf{x}) + \mathbf{D}_{nl}(w,\mathbf{x}) \quad (2)$$

$\mathbf{D}_l$ may contain both stiffness and damping-like terms. However, it will be assumed that the linear part of the operator contains only "classical" or Rayleigh-type damping terms, and that the damping terms in $\mathbf{D}_{nl}$ are functions of w and it spatial derivatives only. It will further be assumed that $\mathbf{D}_{nl}$ is in some sense "small" with respect to $\mathbf{D}_l$ so that the deviation of the system from linearity is at most of first order in some parameter $\epsilon < 1$. The undamped, linearized system ($\mathbf{D}_{nl} = 0$) will be assumed to be both positive-definite and self-adjoint.

Generally speaking, analytical techniques for treating the nonlinear problem are based on separation of the problem into a spatial problem (usually taken to be linear) and a temporal problem (usually containing the nonlinear effects). The spatial problem is usually first discretized by some technique such as modal decomposition, the Ritz-Galerkin method, or the finite element method, and the resulting nonlinear time domain problem is solved by such techniques as equivalent linearization, harmonic balance, perturbation, Galerkin's method, general asymptotic expansions, or numerical integration.

This paper presents a new approach to the problem in which the system equation is linearized in the time domain *before* a solution is attempted in the spatial domain. This is accomplished by defining an "equivalent linear" analog for the system equation. The resulting linear problem may then be solved by any convenient technique. The approach is easily mechanized and is particularly suited to problems where complex boundary conditions or other complications make selection of realistic global, spatial, domain comparison functions difficult. The approach is ideally suited to problems where discretization of the continuum into finite elements is appropriate, since the system may be linearized on an element consistent basis prior to application of the finite-element solution algorithm.

Formulation

Let the nonlinear system under consideration be described by a partial differential equation of the form of equation (1) with appropriate boundary and initial or periodicity conditions. According to the general equivalent linearization approach, an associated linear system is sought such that the "difference" between the two systems is minimized. Then, the solution of the associated linear system is taken as an approximation to the solution of the original problem.

Contributed by the Applied Mechanics Division for presentation at the 1983 ASME Applied Mechanics, Bioengineering, and Fluids Engineering Conference, Houston, Texas, June 20–22, 1983 of THE AMERICAN SOCIETY OF MECHANICAL ENGINEERS.

Discussion on this paper should be addressed to the Editorial Department, ASME, United Engineering Center, 345 East 47th Street, New York, N.Y. 10017, and will be accepted until two months after final publication of the paper itself in the JOURNAL OF APPLIED MECHANICS. Manuscript received by ASME Applied Mechanics Division, November, 1981; final revision, September, 1982. Paper No. 83-APM-30.

Copies will be available until February, 1984.

Copyright © 1983 by ASME
Downloaded 02 May 2010 to 171.66.16.246. Redistribution subject to ASME license or copyright; see http://www.asme.org/terms/Terms_Use.cfm

Associated Linear System. Let the associated linear system for the nonlinear system of equation (1) be

$$\mathfrak{D}_a(w,\mathbf{x},t) = \nabla \cdot \mathbf{D}_a(w,\mathbf{x}) + cm(\mathbf{x})\dot{w} + m(\mathbf{x})\ddot{w} - p(\mathbf{x},t) = 0 \tag{3}$$

with the same boundary and initial conditions as specified for equation (1). w, m, and c are as defined for equation (1) and $\mathbf{D}_a$ is a linear operator which depends on a number of scalar parameter functions. In particular, let $\mathbf{D}_a$ depend on the parameters $\alpha(\mathbf{x})$ and $\beta(\mathbf{x})$, where

$$\mathbf{D}_a(w,x) = \mathbf{K}_a(w,\mathbf{x},\alpha(\mathbf{x})) + \mathbf{C}_a(w,\mathbf{x},\beta(\mathbf{x})) \tag{4}$$

It will be assumed that the operator $\mathbf{K}_a$ contains only stiffness-like terms and the operator $\mathbf{C}_a$ only damping-like terms, where

$$\mathbf{C}_a(w,\mathbf{x},\gamma) = \mathbf{K}_a(\dot{w},\mathbf{x},\gamma) \tag{5}$$

In other words, $\mathbf{C}_a$ is a Rayleigh-type damping operator.

It is assumed that the solutions of the associated linear system (3) are members of some known class $\mathcal{C}$ of functions of $\mathbf{x}$ and t. A particular member of this class is identified once the parameters α and β are specified. For the method of equivalent linearization, these parameters are specified by requiring that some measure of the difference between equations (1) and (3) be minimized *for all members of the class of solutions* $\mathcal{C}$.

Difference Definition. There are many possible definitions for the difference between the systems represented by equations (1) and (3). Herein, three possible differences will be considered. These differences do not depend on the particular form of the operator $\mathbf{D}$ which may be of either second or fourth order. Later, two additional difference definitions will be introduced which have meaning only for fourth-order systems.

Let $\Delta^{(i)}$ denote the system difference for definition i, where this quantity may be at most a vector. Then, the first difference will be defined as

$$\text{Diff. Dfn. 1: } \Delta^{(1)} \equiv \mathfrak{D} - \mathfrak{D}_a \tag{6}$$

This is simply the difference between the two equations over the class of solutions of equation (3).

The second difference will be defined as

$$\text{Diff. Dfn. 2: } \Delta^{(2)} \equiv \nabla w \cdot (\mathbf{D} - \mathbf{D}_a) \tag{7}$$

If the boundary conditions are selected appropriately for the self-adjoint problem, it will be noted that when $\Delta^{(2)}$ and $\Delta^{(1)}$ are scalar, they are related as

$$\int \Delta^{(2)} dv = -\int w \Delta^{(1)} dv \tag{8}$$

where the integral is carried out over the domain of the problem. Difference Definition 2 may therefore be thought of as a weighted equation difference.

The third difference will be defined as

$$\text{Diff. Dfn. 3: } \Delta^{(3)} = \mathbf{D} - \mathbf{D}_a \tag{9}$$

This vector difference is a type of integrated equation difference.

As stated in the foregoing, $\Delta^{(1)}$ is the straightforward equation difference usually employed in equivalent linearization. For cases considered herein, it will be a scalar. This difference will involve derivatives of the solution up to order n, the order of the system. The other two difference definitions will involve only derivatives of order up to $n-1$. This feature makes the second two definitions more desirable since they demand lower-order continuity of shape functions thereby making their use more computationally efficient.

For a second-order system, it may be shown that Difference Definition 2 corresponds to an energy difference and Difference Definition 3 corresponds to a "stress" difference. There is no analogous correspondence in the case of the fourth-order system. For the fourth-order system, a second integration by parts is required to obtain an energy difference from Difference Definition 2, and a similar integration of Difference Definition 3 gives a "moment" difference. These difference definitions will be considered later in an example. The three difference definitions stated herein have been found to be adequate in application to a wide range of physical problems.

Difference Measure. Consistent with the method of equivalent linearization, the difference $\Delta^{(i)}$ is to be minimized for all members of the class of solutions $\mathcal{C}$ of equation (3). Minimization of this difference on a point-by-point (collocation) basis will generally overconstrain the parameters α and β. Hence, an average measure of the difference will be employed.

Let $\mathfrak{A}_{tx}$ represent an averaging operation over both the spatial and temporal variables of the problem. Then, the measure of the difference will be defined by

$$\mathfrak{A}_{tx}\|\Delta^{(i)}\|^2 \equiv \underset{\forall t}{\text{Average}}\left[\int \|\Delta^{(i)}\|^2 dv\right] \tag{10}$$

where the norm is taken to be either the simple scalar magnitude or the Euclidean norm, depending on the dimension of $\Delta^{(i)}$. The time average may take on different forms depending on the nature of the excitation and response processes. The averaging operation will be assumed to be time invariant, linear, and positive-definite, as defined in reference [1].

Minimization of the Difference. Minimization of the system difference measure may be accomplished in a number of ways. One approach would be to use variational calculus directly on $\mathfrak{A}_{tx}$ after substitution for $\Delta^{(i)}$. This would lead to a set of associated Euler partial differential equations for α and β which could, it is hoped, be solved by some analytical or numerical technique. As an alternative, the linear system parameters may be discretized and the problem reduced to an ordinary minimization problem. This approach will be adopted herein.

Let α and β be represented as

$$\alpha(\mathbf{x}) = \sum_{k=1}^{M} \phi_k(\mathbf{x})\hat{\alpha}_k$$

$$\beta(\mathbf{x}) = \sum_{k=1}^{M} \phi_k(\mathbf{x})\hat{\beta}_k \tag{11}$$

where $\hat{\alpha}_k$ and $\hat{\beta}_k$ are constants to be determined, and ϕ_k is a locally defined set of linearly independent shape functions. Then, sufficient conditions for the minimization of $\mathfrak{A}_{tx}$ will be

$$\frac{\partial \mathfrak{A}_{tx}\|\Delta^{(i)}\|}{\partial \hat{\alpha}_k} = 0$$

$$\frac{\partial \mathfrak{A}_{tx}\|\Delta^{(i)}\|}{\partial \hat{\beta}_k} = 0 \tag{12}$$

Implementation of the minimization defined by equation (12) will be facilitated if the difference $\Delta^{(i)}$ is factored into component parts. For this purpose, let

$$\Delta^{(i)} \equiv \eta^{(i)} - \mathbf{L}_K^{(i)}(\alpha(x)) - \mathbf{L}_C^{(i)}(\beta(\mathbf{x})) \tag{13}$$

where η, $\mathbf{L}_K$, and $\mathbf{L}_C$ are defined according to the particular difference definition as

Downloaded 02 May 2010 to 171.66.16.246. Redistribution subject to ASME license or copyright; see http://www.asme.org/terms/Terms_Use.cfm

Diff. Dfn. 1: $\eta = \nabla \cdot \mathrm{D}_{nl}$; $\mathfrak{L}_K = \nabla \cdot \mathbf{K}_a$; $\mathfrak{L}_C = \nabla \cdot \mathbf{C}_a$

Diff. Dfn. 2: $\eta = \nabla W \cdot \mathrm{D}_{nl}$; $\mathfrak{L}_K = \nabla W \cdot \mathbf{K}_a$; $\mathfrak{L}_C = \nabla W \cdot \mathbf{C}_a$

Diff. Dfn. 3: $\eta = \mathbf{D}_{nl}$; $\mathbf{L}_K = \mathbf{K}_a$; $\mathbf{L}_C = \mathbf{C}_a$ (14)

Furthermore, let

$$\hat{\alpha} = (\hat{\alpha}_1, \hat{\alpha}_2, \ldots, \hat{\alpha}_M); \quad \hat{\beta} = (\hat{\beta}_1, \hat{\beta}_2, \ldots \hat{\beta}_M) \tag{15}$$

Then, application of the minimization conditions (14) leads to a set of algebraic equations for $\hat{\alpha}$ and $\hat{\beta}$ of the form

$$\mathbf{A}\hat{\alpha} + \mathbf{B}\hat{\beta} = \mathbf{G}$$

$$\mathbf{B}^T\hat{\alpha} + \mathbf{C}\hat{\beta} = \mathbf{H} \tag{16}$$

where

$$A_{ij} = \mathfrak{A}_{tx}(\mathbf{L}_K(\phi_i(\mathbf{x})) \cdot \mathfrak{L}_K(\phi_j(\mathbf{x})))$$

$$B_{ij} = \mathfrak{A}_{tx}(\mathbf{L}_K(\phi_i(\mathbf{x})) \cdot \mathfrak{L}_C(\phi_j(\mathbf{x})))$$

$$C_{ij} = \mathfrak{A}_{tx}(\mathbf{L}_C(\phi_i(\mathbf{x})) \cdot \mathfrak{L}_C(\phi_j(\mathbf{x})))$$

$$G_i = \mathfrak{A}_{tx}(\eta \cdot \mathbf{L}_K(\phi_i(\mathbf{x}))); \; H_i = \mathfrak{A}_{tx}(\eta \cdot \mathbf{L}_C(\phi_i(\mathbf{x}))) \tag{17}$$

It may be shown

$$\mathbf{B} = \mathbf{0}; \quad \text{for Diff. Dfns. 1 and 3} \tag{18}$$

Therefore, the system of equations for $\hat{\alpha}$ and $\hat{\beta}$ are uncoupled for this case. By a judicious selection of the ϕ_i, these equations may also be uncoupled for Difference Definition 2, but this will not generally be the case.

Solution of the Associated Linear System. Once the parameters α and β have been determined by the minimization condition, the associated linear system may be solved by any appropriate technique. Because closed-form solutions are seldom available for even linear problems with distributed parameters, resort will usually be made to some form of appropriate analysis. One of the most natural approaches is to expand $w(\mathbf{x},t)$ in terms of a set of shape functions $\psi_i(\mathbf{x})$ as

$$w(\mathbf{x},t) = \sum_{i=1}^{N} \psi_i(\mathbf{x}) u_i(t) \tag{19}$$

where $u_i(t)$ are coefficient functions that depend only on time. The shape functions $\psi_i(\mathbf{x})$ may be defined globally, leading to a Ritz-Galerkin type solution, or locally, leading to a finite-element type solution. The latter approach is particularly attractive when the functions α and β have been discretized on a localized element basis.

Discretization of the auxiliary equation leads to a problem statement of the form

$$\mathbf{M}\,\ddot{\mathbf{u}}(t) + \mathbf{\Gamma}\dot{\mathbf{u}}(t) + \mathbf{K}\,\mathbf{u}(t) = \mathbf{f}(t) \tag{20}$$

which can be solved by any number of analytical or numerical techniques. It should be noted, however, that the coefficient matrices $\mathbf{\Gamma}$ and $\mathbf{K}$ in equation (20) will depend on $\hat{\alpha}$ and $\hat{\beta}$ which, in turn, depend on the solution itself through equations (16). Hence, an iterative solution process will normally be required. In spite of this fact, the linearization scheme outlined in the foregoing will generally result in a considerable computational saving over straight numerical integration, particularly for problems of steady-state or stationary response.

Properties of the Solution. Given the properties of the averaging operation $\mathfrak{A}_{tx}$ and the Euclidean norm, it may be shown that the solution obtained from equations (12) represents a global minimum. Note, however, that this does not preclude the possibility of the existence of more than one set $\hat{\alpha}$ and $\hat{\beta}$ which minimizes $\mathfrak{A}_{tx}$.

Since the matrix B vanishes for Difference Definitions 1 and 3, the existence of unique solutions for $\hat{\alpha}$ and $\hat{\beta}$ for this case will depend on the invertability of matrices $\mathbf{A}$ and $\mathbf{C}$. It may be shown [1] that both $\mathbf{A}$ and $\mathbf{C}$ are positive definite for all difference definitions considered in the foregoing. Hence, solutions for $\hat{\alpha}$ and $\hat{\beta}$ using Difference Definitions 1 and 3 always exist for nonzero displacements, and are unique. If the functions ϕ_i selected for use with Difference Definition 2 cause equations (16) to be uncoupled, solutions will likewise exist and be unique. However, it is not readily shown that solutions will exist or be unique for the general case of Difference Definition 2.

Steady-State Harmonic Oscillation

Let

$$p(\mathbf{x},t) = h(\mathbf{x}) \cos \omega t \tag{21}$$

where ω is the excitation frequency. Furthermore, let the nonlinearity be symmetric so that the response is not biased. Then, the class of solutions of the associated linear system equation (3) is a family of harmonic functions and $u_i(t)$ may be represented as

$$u_i(t) = a_i \cos \omega t + b_i \sin \omega t \tag{22}$$

Substituting from equation (22) into equation (20), and equating coefficients of sine and cosine terms, yields a set of algebraic equations for a_i and b_i of the form

$$[-\omega^2\mathbf{M} + \mathbf{K}(\hat{\alpha})]\mathbf{a} + \omega\mathbf{\Gamma}(\hat{\beta})\mathbf{b} = \mathbf{f}$$

$$-\omega\mathbf{\Gamma}(\hat{\beta})\mathbf{a} + [-\omega^2\mathbf{M} + \mathbf{K}(\hat{\alpha})]\mathbf{b} = \mathbf{0} \tag{23}$$

where

$$\mathbf{a} = (a_1, a_2, \ldots, a_N)^T; \quad \mathbf{b} = (b_1, b_2, \ldots, b_N)^T \tag{24}$$

As indicated in equations (23), the matrices $\mathbf{K}$ and $\mathbf{\Gamma}$ depend explicitly on $\hat{\alpha}$ and $\hat{\beta}$. The specific form of these matrices and the vector $\mathbf{f}$ will of course depend on the details of the discretization employed.

Since the steady-state solution of the associated linear system is periodic with period $T = 2\pi/\omega$, the time average for all time in equation (10) is merely the average over one cycle of oscillation. The elements of the matrices $\mathbf{A}$, $\mathbf{B}$, and $\mathbf{C}$, and vectors $\mathbf{G}$ and $\mathbf{H}$ may be evaluated in terms of $\mathbf{a}$ and $\mathbf{b}$ from equations (17). As an example of the form of the resulting equations, consider the case for Difference Definition 3. Let U and V be defined as

$$U = \sum_{i=1}^{N} \psi_i a_i$$

$$V = \sum_{i=1}^{N} \psi_i b_i \tag{25}$$

Then

$$A_{ij} = \frac{\pi}{\omega}\int [\mathbf{D}_a(U,\mathbf{x},\phi_i) \cdot \mathbf{D}_a(U,\mathbf{x},\phi_j) + \mathbf{D}_a(V,\mathbf{x},\phi_i) \cdot \mathbf{D}_a(U,\mathbf{x},\phi_j)]dv$$

$$C_{ij} = \omega^2 A_{ij}$$

$$G_{ij} = \frac{\pi}{\omega}\int_0^{2\pi} [\mathbf{E} \cdot \mathbf{D}_a(U,\mathbf{x},\phi_i) + \mathbf{F} \cdot \mathbf{D}_a(V,\mathbf{x},\phi_i)]dv$$

$$H_{ij} = \pi\int_0^{2\pi} [\mathbf{E} \cdot \mathbf{D}_a(U,\mathbf{x},\phi_i) - \mathbf{F} \cdot \mathbf{D}_a(V,\mathbf{x},\phi_i)]dv \tag{26}$$

where

$$\mathbf{E} = \mathbf{E}(U,V) = \frac{1}{\pi}\int_0^{2\pi} \mathbf{D}_{nl}(\mathfrak{U}\cos\theta + V\sin\theta, \mathbf{x}) \cos\theta \, d\theta$$

Downloaded 02 May 2010 to 171.66.16.246. Redistribution subject to ASME license or copyright; see http://www.asme.org/terms/Terms_Use.cfm

$$\mathbf{F} = \mathbf{F}(U,V) = \frac{1}{\pi}\int_0^{2\pi} \mathbf{D}_{nl}(\mathcal{U}\cos\theta + V\sin\theta, \mathbf{x})\sin\theta\, d\theta$$

The form of the result is similar for Difference Definition 1, but is considerably more complex for Difference Definition 2 containing integrals of products with $\cos 3\theta$ and $\sin 3\theta$.

It should be noted that in solving for $\hat{\alpha}$ and $\hat{\beta}$ only one matrix, **A**, need be computed and inverted. Thus, a saving of computation effort is realized for the steady-state analysis.

Forced Oscillation. The approximate response $w(\mathbf{x},t)$ will be given by the solution of equation (23) constrained by equations (16). A secant method might appear to be a logical procedure for solving these equations. That is, for a given value of ω and an initial guess for **a** and **b**, $\hat{\alpha}$ and $\hat{\beta}$ may be determined from (16). This approximation may then be used to obtain a next approximation for **a** and **b** in (23), and so on, until convergence is obtained. It has been found, however, that such an iterative scheme is unstable, especially for the case of small damping.

Equations (23) and (16) together are nonlinear. Hence, the Newton-Raphson method can be used to obtain a nonlinear frequency response curve. In the case where a good initial guess is difficult to obtain, a hybrid technique such as the Levenberg/Marquardt method [2] may be used.

Free Oscillation. In the case of conservative systems, the free harmonic response may be found from the homogeneous form of equation (23)

$$[-\omega^2\mathbf{M} + \mathbf{K}(\hat{\alpha})]\mathbf{a} = \mathbf{0} \tag{28}$$

along with the constraint equation

$$\mathbf{A}\,\hat{\alpha} = \mathbf{G} \tag{29}$$

Inclusion of the constraint introduces a dependence of the frequency on amplitude of response. To determine this dependence, an iterative scheme may be employed.

For problems other than steady-state harmonic oscillation, a different form of time average must be employed. If the response process is random and assumed to be ergodic, the time average may be replaced by an ensemble average and the approach proceeds in a manner similar to standard stochastic equivalent linearization [3]. This particular subject will not be pursued in the present paper, but is discussed in reference [1].

Example—Nonlinear Plate

A customary assumption employed in analysis of the vibration of thin plates governed by the Poisson-Kirchhoff theory is that the amplitude of response is small in comparison to the thickness of the plate. This assumption permits the use of a linear equation of motion. However, when the deflection is of the same order of magnitude as the thickness, the coupling that exists between the membrane and bending stresses can no longer be ignored.

The nonlinear theory used in this example is based on the so-called Berger approximation to the coupled nonlinear Von Karman equations for static analysis. Berger's analysis, which originally appeared in reference [4], includes the effect of membrane stresses but neglects the strain energy due to the second invariant of the middle surface. Under these conditions, the nonlinear equations of motion for the transverse displacements become uncoupled from those of the inplane displacements. The work presented in reference [5] extended the Berger approximation to the dynamic form of the equation of motion, and these equations are used in this example.

The differential equation of motion for a harmonically excited nonlinear plate can be written in index notation as

$$M_{\gamma\delta,\gamma\delta}(D,w) - \mu\left[\int_v w_{,\gamma}w_{,\gamma}dv\right]w_{,\delta\delta} + c\dot{w} + \rho\ddot{w} = p(\mathbf{x})\cos\omega t \tag{33}$$

where

$$\mu = \frac{6D}{Ah^2}$$

$$M_{11} = D(w_{,11} + \nu w_{,22})$$

$$M_{12} = M_{21} = D(1-\nu)w_{,12}$$

$$M_{22} = D(\nu w_{,11} + w_{,22})$$

$$w_{,\gamma} = \frac{\delta w}{\delta x_\gamma};\quad \gamma = 1,2 \tag{34}$$

$w = \mathbf{w}(x,t)$ is the transverse displacement of the plate, D is the flexural rigidity, ν is Poisson's ratio, c is a mass proportional damping coefficient, ρ is the mass per unit area, A is the surface area of the plate, h is the plate thickness, $p(\mathbf{x})$ is a distributed force/unit area, and ω is the frequency of the harmonic excitation. The usual subscript convention is implied.

The nonlinearity in the equation of motion (33) lies in the second term. This term accounts for the coupling between the membrane and bending stresses of the deformed plate. In defining the linear associated system, this nonlinear term will be replaced by the divergence of the linear shear force, or

$$M_{\gamma\delta,\gamma\delta}(D,w) + M_{\gamma\delta,\gamma\delta}(\alpha,w) + c\dot{w} + \rho\ddot{w} = p(\mathbf{x})\cos\omega t \tag{35}$$

where the equation parameter $\alpha = \alpha(x)$ is to be taken as the associated linear flexural rigidity. It is this parameter that will be adjusted in the equivalent linearization procedure. The nonlinearity of equation (33) is stiffness related and hence the associated linear damping parameter β does not appear in equation (35).

Solution to the associated linear equation (35) can readily be accomplished by the finite element method. If displacements w are written as in equation (19), the finite element equations become (20) with $\mathbf{f}(t)$ a harmonic function of time. One sufficient condition for the convergence of the finite element method is the continuity of the m-1 derivatives of the shape functions, where m is the highest order derivative of the strain energy integral, **K**. **K** contains up to two spatial derivatives; consequently the continuity requirement specifies the need for continuous first derivatives across element boundaries. The analysis presented herein uses a set of shape functions developed in reference [6] that were constructed from Hermite cubic functions, and hence satisfy the continuity requirement. Using these shape functions, the unknown parameters at each node are w, $\partial w/\partial x_1$, $\partial w/\partial x_2$, $\partial^2 w/\partial x_1 \partial x_2$ for a total of 16 degrees of freedom for quadrilateral elements.

For the nonlinear plate, the shape functions ϕ_i will be constant across the domain of the finite-element shape functions. The terms $\mathbf{D}_{nl}$ and $\mathbf{D}_a$ in equations (13) and (14) that comprise **A** and **G** in equation (16) therefore take the form

$$(D_{nl})_\gamma = -\mu\left[\int_v w_{,\gamma}w_{,\gamma}dv\right]w_{,\gamma}$$

$$(D_a)_\gamma = M_{\gamma\delta,\delta} \tag{36}$$

In addition to the three difference definitions given in the body of the paper, it is instructive to consider two additional difference definitions for the case of the nonlinear plate problem. These will be defined as

$$\text{Diff. Dfn. 4: } \Delta^{(4)} \equiv M_{\gamma\delta}w_{,\gamma\delta} - \tfrac{1}{2}\mu A(w_{,\gamma}w_{,\gamma})^2 \tag{37}$$

$$\text{Diff. Dfn. 5: } \Delta^{(5)} \equiv M_{\gamma\delta} + \mu[\textstyle\int w_{,\eta}w_{,\eta}dv]w\delta_{\gamma\delta} \tag{38}$$

Downloaded 02 May 2010 to 171.66.16.246. Redistribution subject to ASME license or copyright; see http://www.asme.org/terms/Terms_Use.cfm

Difference Definition 4 corresponds to a difference in energy density functions between the associated linear and nonlinear equations while Difference Definition 5, a matrix, corresponds to a moment difference.

Typical results for the first nonlinear mode of vibration of a simply supported square plate are shown in Figs. 1 and 2 for two mesh sizes using Difference Definitions 1–5. The frequency of response has been normalized by the first natural frequency λ_1 of the linear equations. Also shown are the results from a standard one-term Galerkin approximation and from direct numerical integration of the nonlinear spatially discretized equations. The Galerkin approximation was constructed using the lowest eigenfunction of the linearized problem while the numerical integration was performed with a fourth-order Runge-Kutta algorithm.

It is clear from Figs. 1 and 2 that the choice of difference definition significantly affects the results. For the nine degree-of-freedom finite element mesh in Fig. 1, the use of Difference Definition 3 and the Galerkin formulation produce the most satisfactory results in comparison with the numerical

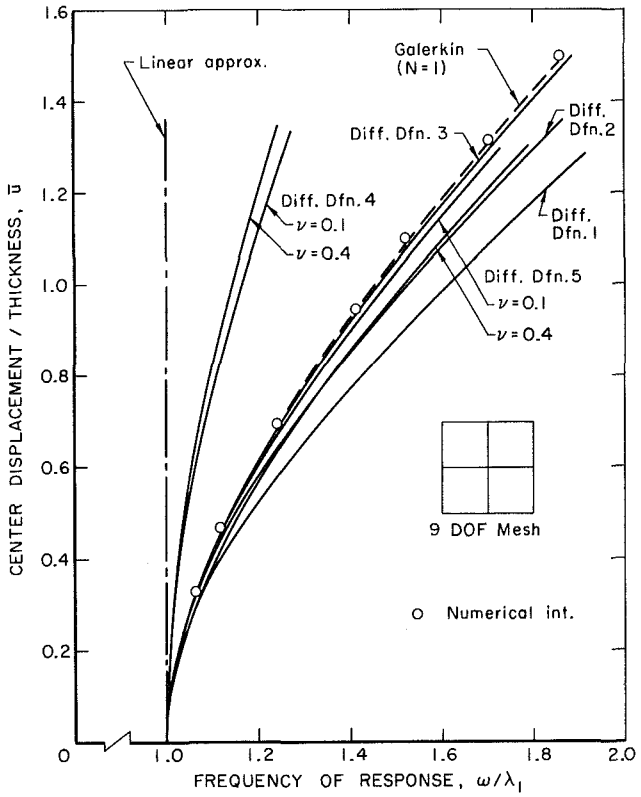

Fig. 1 First mode-free response amplitude; simply supported square plate

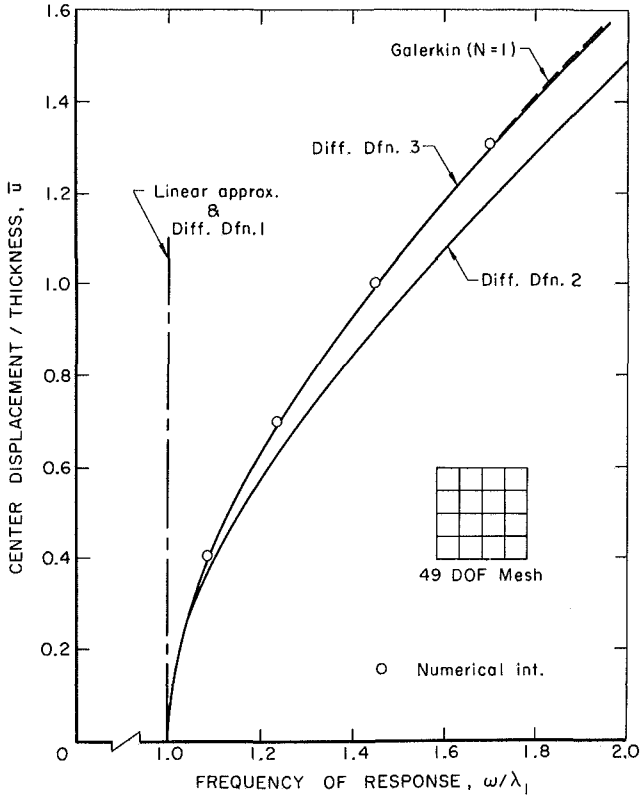

Fig. 2 First mode-free response amplitude; simply supported square plate

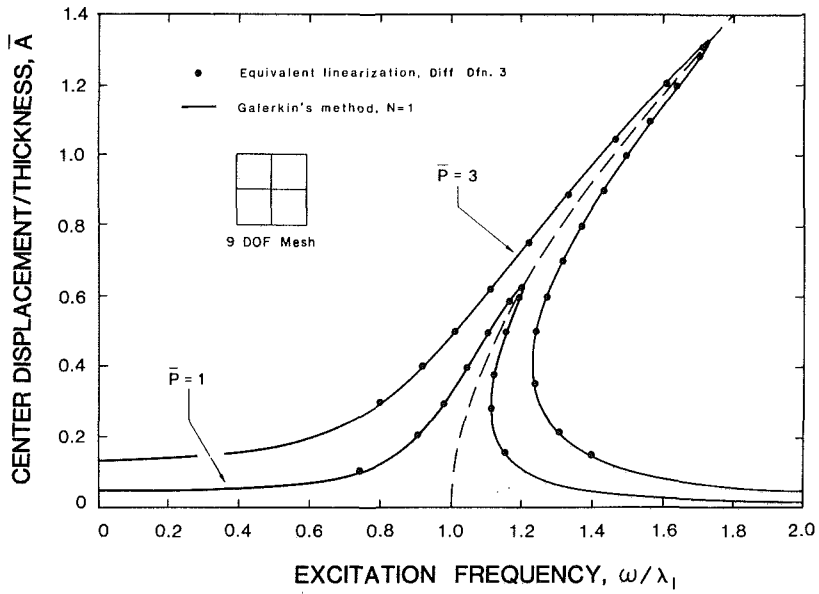

Fig. 3 Forced response at simply supported square plate. Viscous damping of 3 percent.

Downloaded 02 May 2010 to 171.66.16.246. Redistribution subject to ASME license or copyright; see http://www.asme.org/terms/Terms_Use.cfm

integration solutions. Difference Definitions 1, 2, and 5 predict a stiffer response while Difference Definition 4 produces a significantly softer response than that obtained by numerical integration. For the more refined mesh in Fig. 2 similar results are shown for all difference definitions except Difference Definition 1. It can be seen that Difference Definition 1 produces a totally nonphysical result of the frequency of response being independent of amplitude. Inspection of this difference definition shows that it contains fourth-order spatial derivatives of the displacements. Therefore, the norm of such a difference will be singular at the element boundaries for cubic shape functions. It is suspected that the use of higher-order shape functions for the displacements and for the flexural rigidity would enable Difference Definition 1 to perform better as the mesh is refined. This, of course, would be accomplished at the expense of computational efficiency.

The forced response of a simply supported plate with internal damping is shown in Fig. 3 for Difference Definition 3. Shown are the equivalent linearization and one-term Galerkin response curves for a spatially constant load $p(\mathbf{x}) = p_0$ with $\bar{p} = 1$ and 3 where

$$\bar{p} = \frac{p_0 A^2}{Eh^2} \tag{39}$$

A value of damping of 3 percent in the first mode of linear response is included. Again, Difference Definition 3 produces results very similar to the Galerkin formulation.

Often the maximum or resonant amplitude of response for a given level of excitation is of more interest than the detailed nature of the response curve. Reference [1] discusses an efficient technique for obtaining lightly damped resonant response directly from the free-vibration response.

Summary and Conclusions

A method has been presented for analyzing dynamical systems governed by a class of nonlinear equations of motion. With this approach, the nonlinear continuous system is modeled by an associated continuous linear system equation containing stiffness and energy dissipation parameters that can be adjusted to minimize a difference measure. A number of specific difference measures have been considered.

A nonlinear plate example demonstrates that the linearization approach is capable of providing useful solutions to such problems. Use of an integrated equation difference measure produces the best results for this example system. Results from the new method are quite similar to those obtained from a one-term Galerkin approximation. The close agreement with Galerkin's method is also observed for other second-order systems not considered herein. For some second-order systems, the integrated-equation difference measure approach gives identical results to Galerkin's method in the limit as the mesh is refined.

It appears that the equivalent linearization approach holds promise for use in the dynamic analysis of continuous nonlinear systems. In most cases considered, the accuracy of the method can be made comparable to numerical integration while the computational saving is significant. Galerkin's method can readily be used on problems with simple boundaries. However, for complex boundary conditions, the selection of reasonable spatial comparison becomes difficult and the Galerkin formation is not easily implemented. On the other hand, the equivalent linearization procedure used in conjunction with the finite element method can easily handle complicated boundary conditions. By using local shape functions for the equivalent linear parameters, the method can readily be incorporated into existing finite element codes.

Acknowledgments

This investigation was sponsored by Grant No. PFR77-23687 from the National Science Foundation. Any opinions, findings, and conclusions or recommendations expressed in this paper are those of the authors and do not necessarily reflect the views of the National Science Foundation.

References

1 Krousgrill, C. M., Jr., "A Linearization Technique for the Dynamic Response of Nonlinear Continua," Ph.D. Thesis, California Institute of Technology, Pasadena, Calif., 1980.

2 Powell, M. J. D., "A Hybrid Method for Nonlinear Equations," in *Numerical Methods for Nonlinear Algebraic Equations*, Rabinowitz, P., ed., Gordon and Breach, 1970, pp. 87–114.

3 Iwan, W. D., "Application of Nonlinear Analysis Techniques," in *Applied Mechanics in Earthquake Engineering*, W. D. Iwan, ed., ASME Symposium, AMD Vol. 8, 1974, pp. 135–161.

4 Berger, H. M., "A New Approach to the Analysis of Large Deflection of Plates," ASME JOURNAL OF APPLIED MECHANICS, Vol. 22, 1955, pp. 465–472.

5 Nash, W. A., and Modeer, J. R., "Certain Approximate Analysis of Nonlinear Behavior of Plates and Shallow Shells," *Proceedings of the Symposium on the Theory of Thin Elastic Shells*, Delft, The Netherlands, Aug. 1959.

6 Bogner, F. K., Fox, R. L., and Schmidt, L. A., "The Generation of Interelement-Compatible Stiffness and Mass Matrices by the Use of Interpolation Formulae," *Proceedings of the Conference on Matrix Methods in Structural Mechanics*, Air Force Institute of Technology, Wright Patterson A.F. Base, Ohio, Oct. 1965.

Downloaded 02 May 2010 to 171.66.16.246. Redistribution subject to ASME license or copyright; see http://www.asme.org/terms/Terms_Use.cfm

M. P. Paidoussis
Professor and Chairman.
Mem. ASME

K. N. El Barbir
Research Assistant.

M. R. Genadry[1]
Research Assistant.

J.-P. Chaubernard[2]
Research Assistant

Department of Mechanical Engineering,
McGill University,
Montreal, Quebec, Canada

Dynamics of a Cluster of Flexibly Interconnected Cylinders

Part 1: In Vacuum

This paper presents an analytical model for the dynamics of a cluster of flexible cylinders, the extremities of which are structurally interconnected, e.g., through "end plates" or other kinds of structural connectors. These connectors are modeled by sets of translational and rotational springs, such that resistance to both in-plane and out-of-plane deformation of the connectors is fully taken into account. The dynamics of the system ***in vacuum*** *is examined here, and especially the effect of varying the different spring stiffnesses on the system eigenfrequencies. This provides a reference base and the necessary analytical tools for the study of the system* ***in axial flow****, which is presented as Part 2 of this work.*

Introduction

Arrays of cylinders subjected to flow are commonly found in many structures associated with power generation. Thus, they are an essential component of most types of heat exchangers, boilers, and steam generators, in the form of tube banks; also, in most nuclear reactors, they are present in the form of clusters of fuel rods; in electricity transmission they appear in the form of bundles of wire conductors; and so on.

In all cases, the cylinders are neither totally unconnected to one another, nor are they supported by utterly rigid frames; rather, they are normally interconnected by flexible, and occasionally flimsy, structural elements. Thus in the case of nuclear fuel rods, the cylinders are sometimes supported at their extremities by thin "end plates," as shown, for example, in Fig. 1. Heat exchanger tubing is commonly supported at the ends by fairly rigid "tube sheets," but the cylinders are interconnected at intermediate points by relatively flexible baffle plates, lacing rods, or spacer bars [1]. Finally, high-tension electrical wire conductors are separated by spacers, some designs of which are purposely made to be quite flexible.

Although, in all cases, designers and researchers alike are aware that these relatively flexible connections between the cylinders imply a fair degree of structural coupling in cylinder motions, it is only in the area of electrical conductor dynamics that this matter has been studied in detail, e.g., [2, 3]. One previous study exists for the effect of structural coupling in nuclear fuel rod bundles [4], and the matter is also beginning to find its way in the literature of heat-exchanger tube vibration [5, 6].

In the present paper, the dynamics of an array of cylinders is investigated, where the ends of the cylinders are interconnected by slender beam-like elements, resembling but not necessarily modeling those of Fig. 1(a,b). Rather than studying a specific type of intercylinder connector, the problem has been generalized as follows: the extremities of the cylinders are considered to be interconnected by sets of translational and rotational springs, modeling the resistance of the connectors to in-plane extension and bending and to out-of-plane flexure and torsion. The principal concern of this paper is to study the effect of stiffness of these springs on the dynamics of the system, as compared to various limiting cases representing, say, ideally clamped or ideally pinned ends.

It is realized, of course, that this simplified model cannot deal with all possible kinds of intercylinder structural coupling. One such limitation is that these connectors exist only at cylinder extremities. However, generalization of the model to overcome such limitations is, in principle, not difficult.

This paper, Part 1 of the study, examines the dynamics of the system in vacuum. Thus, in the absence of interstitial fluid, hydrodynamic coupling in cylinder motions, which might otherwise be present, is totally absent, and hence the effect of pure structural coupling may conveniently be studied. Part 2 of the study [7] examines the dynamics of the system in the presence of axial flow.

The System Under Consideration

The system consists of N identical uniform cylinders within

[1] Presently with Jaros, Baum & Bolles, 345 Park Ave., New York, N.Y., 10022.

[2] Presently with TECHNIP, 170 place Henri Regnault, La Defense, 92090 Paris, France.

Contributed by the Applied Mechanics Division for presentation at the 1983 Applied Mechanics, Bioengineering, and Fluids Engineeirng Conference, Houston, Texas, June 20-22, 1983 of THE AMERICAN SOCIETY OF MECHANICAL ENGINEERS.

Discussion on this paper should be addressed to the Editorial Department, ASME United Engineering Center, 345 East 47th Street, New York, N.Y. 10017, and will be accepted until two months after final publication of the paper itself in the JOURNAL OF APPLIED MECHANICS. Manuscript received by ASME Mechanics Division, January, 1982, final revision, October, 1982. Paper No. 83-APM-24.

Copies will be available until February, 1984.

Copyright © 1983 by ASME
Downloaded 02 May 2010 to 171.66.16.246. Redistribution subject to ASME license or copyright; see http://www.asme.org/terms/Terms_Use.cfm

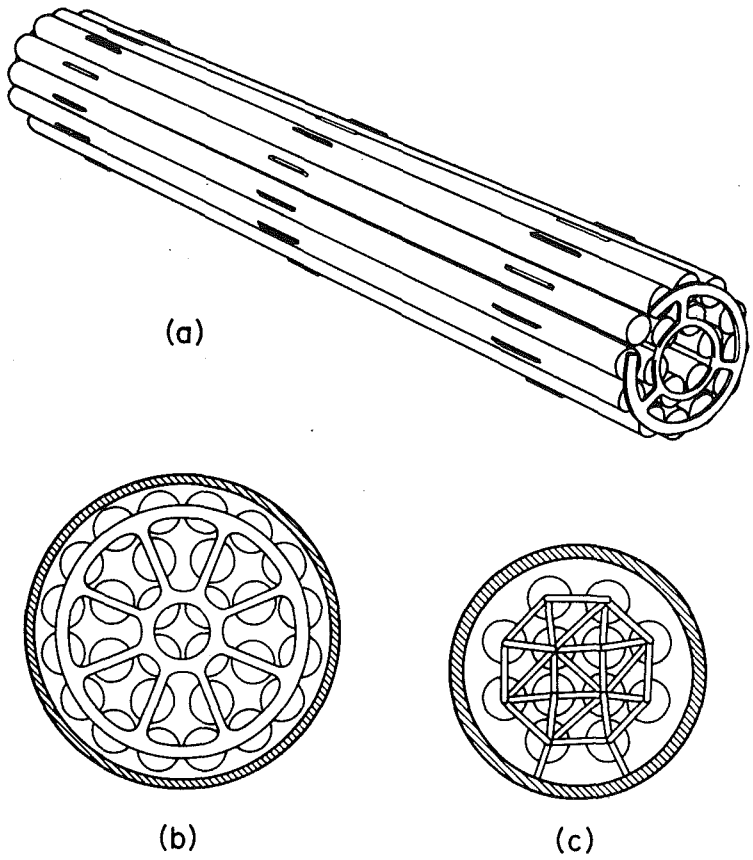

Fig. 1 *(a)* **Typical fuel element "bundle" used in CANDU-type nuclear reactors;** *(b)* **end view of the plate to which the ends of the cylinders are attached, showing also the channel containing the coolant flow; and (c) idealized system showing intercylinder and cylinder-to-channel connectors**

a rigid cylindrical container (to be referred to as the "channel"), which in Part 2 [7] of the study will be filled with fluid, but is here considered to be evacuated. When at rest, the cylinders are positioned so that their long axes lie parallel to the axis of the channel, which is defined as the x-axis. The ends of each cylinder are connected to those of its neighbors by beam-like connecting elements (henceforth to be simply referred to as "connectors"), and some of the outermost cylinders may similarly be connected to the rigid container, as shown in Fig. 1(*c*).

Resistance of the connectors to deformation of all kinds will be modeled by sets of springs, assumed to be the same at both ends. Considering first in-plane deformation—i.e., in the plane of Fig. 1(*c*)—it may be seen in Fig. 2 that two kinds of springs may be defined: (*a*) translational springs resisting stretching (or compression) of the connectors along their long axis, of stiffness K_{ij} and (*b*) springs resisting in-plane flexure of the connectors, of stiffness K'_{ij}.

Of course, for general cylinder motions, the connectors will also deform out of plane. Their resistance to out-of-plane flexure and torsion will be modeled by rotational springs with spring constants C_{ij} and C'_{ij}, respectively, as shown in Fig. 3. In general, torsional motions of individual cylinders about their long axes will also occur, because of differential rotation of the top and bottom of the cylinders; however, as the associated frequencies will be much higher than the flexural frequencies for slender cylinders, these motions will not be considered here.[3]

[3] By the same argument, longitudinal vibrations of individual cylinders are not considered. These are simplifying assumptions, not universally valid for all systems: e.g., if the cylinders are very stiff in comparison to the end supports.

In the analysis, motions of the system will be such that the displacements $v_i(x,t)$, $w_i(x,t)$ of an arbitrary cylinder (Fig. 2) and the angles ν_{ij}, μ_{ij} (Fig. 3) are sufficiently small for the springs to be considered linear and for the cylinders to be modeled as Euler-Bernoulli beams. Moreover, all inertial and dissipative effects associated with the connectors, and hence with the springs, will be neglected. Internal dissipation in the cylinders, for the purposes of this study, is similarly ignored.

To facilitate the general formulation of the problem, the equations of motion will be derived as if each cylinder were connected to *all* other cylinders, as well as to the channel. Of course, once the equations have been formulated, the more realistic model of Fig. 1(*c*) may be retrieved by setting to zero all spring constants associated with missing connectors.

The Equations of Motion

Recognizing that the interconnecting springs will affect only the boundary conditions, the equations of motion of the system are given by a set of beam equations

$$EI\frac{\partial^4 v_i}{\partial x^4}+m\frac{\partial^2 v_i}{\partial t^2}=0, \quad EI\frac{\partial^4 w_i}{\partial x^4}+m\frac{\partial^2 w_i}{\partial t^2}=0, \qquad i=1,2,\ldots N, \tag{1}$$

where EI is the flexural rigidity of each cylinder, and m its mass per unit length; $v_i(x,t)$ and $w_i(x,t)$ are the lateral displacements of the ith cylinder in the y and z-directions, respectively, as shown in Fig. 2(*c*).

Although it would appear from equations (1) that motions of each cylinder in each of the two directions are uncoupled, it is through the boundary conditions that coupling will

Downloaded 02 May 2010 to 171.66.16.246. Redistribution subject to ASME license or copyright; see http://www.asme.org/terms/Terms_Use.cfm

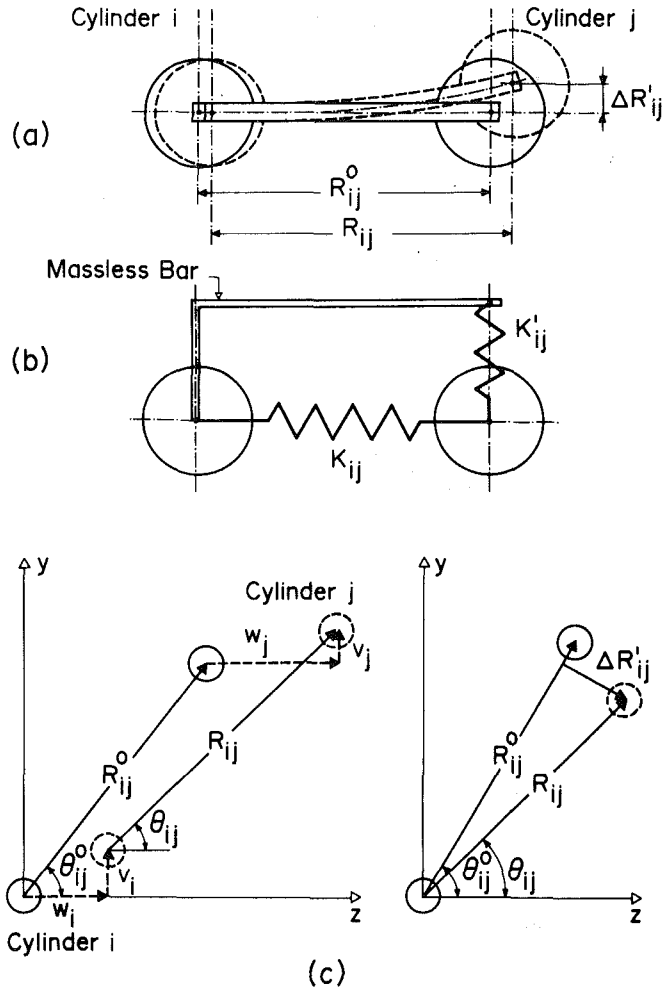

Fig. 2 (a) In-plane deformation of a connector, involving in-plane stretching and bending; (b) definition of the springs of stiffnesses K_{ij} and K'_{ij} resisting stretching and bending, respectively; and (c) diagrams defining various quantities used in the analysis of in-plane deformation of the connector

manifest itself, as will become obvious in the following section.

The Boundary Conditions

The boundary conditions may be obtained in a straightforward manner by a balance of forces and moments at the extremities of a typical cylinder, say cylinder i, in conjunction with motions of cylinder i itself and an adjacent cylinder j.

Considering the force balance first, it is recognized that the cylinder will be subjected to forces of magnitude

$$F_{ij}=K_{ij}(R_{ij}-R^0_{ij}) \quad \text{and} \quad F'_{ij}=K'_{ij}\Delta R'_{ij}, \quad j\neq i, \tag{2}$$

due to the effect of the translational springs connecting cylinders i and j, where R_{ij}, R^0_{ij}, and $\Delta R'_{ij}$ are defined in Fig. 2; the cylinder will also be subjected to forces

$$F_{ii}=K_{ii}(R_{ii}-R^0_{ii}) \quad \text{and} \quad F'_{ii}=K'_{ii}\Delta R'_{ii} \tag{3}$$

due to springs connecting cylinder i to the channel. These forces may be decomposed along the y and z-directions to give

$$\begin{aligned}
\mathbf{F}_{ij}&=K_{ij}(R_{ij}-R^0_{ij})\{\sin\theta_{ij}\mathbf{j}+\cos\theta_{ij}\mathbf{k}\},\\
\mathbf{F}'_{ij}&=K'_{ij}\Delta R'_{ij}\{-\cos\theta_{ij}\mathbf{j}+\sin\theta_{ij}\mathbf{k}\},\\
\mathbf{F}_{ii}&=K_{ii}(R_{ii}-R^0_{ii})\{\sin\theta_{ii}\mathbf{j}+\cos\theta_{ii}\mathbf{k}\},\\
\mathbf{F}'_{ii}&=K'_{ii}\Delta R'_{ii}\{\cos\theta_{ii}\mathbf{j}-\sin\theta_{ii}\mathbf{k}\},
\end{aligned} \tag{4}$$

where $\mathbf{j}$ and $\mathbf{k}$ are unit vectors in the y and z-direction, respectively; θ_{ij} is defined in Fig. 2(c), and θ_{ii} is similarly defined for cylinder-to-channel connections.

The quantities $R_{ij}-R^0_{ij}$, $\Delta R'_{ij}$, etc., may be obtained with the aid of Fig. 2(c). For instance, it may easily be seen that

$$R_{ij}\cos\theta_{ij}=R^0_{ij}\cos\theta^0_{ij}-w_i+w_j, \quad R_{ij}\sin\theta_{ij}=R^0_{ij}\sin\theta^0_{ij}-v_i+v_j,$$

which yield

$$R_{ij}-R^0_{ij}=\cos\theta^0_{ij}(-w_i+w_j)+\sin\theta^0_{ij}(-v_i+v_j), \tag{5}$$

to first-order approximation. In a similar manner, it is found that

$$\begin{aligned}
\Delta R'_{ij}&=\sin\theta^0_{ij}(-w_i+w_j)-\cos\theta^0_{ij}(-v_i+v_j),\\
R_{ii}-R^0_{ii}&=-\cos\theta^0_{ii}w_i-\sin\theta^0_{ii}v_i, \Delta R'_{ii}=\sin\theta^0_{ii}w_i-\cos\theta^0_{ii}v_i.
\end{aligned} \tag{6}$$

Substituting equations (5) and (6) into (4), forces balances at the two extremities of the cylinder, $x=0$ and $x=L$, in the y-direction yield, to first-order approximation,

$$\begin{aligned}
&\epsilon EI\frac{\partial^3 v_i}{\partial x^3}-\sum_{j=1}^{N}K_{ij}\sin^2\theta^0_{ij}\{v_i-(1-\delta^i_j)v_j\}\\
&\quad-\sum_{j=1}^{N}(K_{ij}-K'_{ij})\sin\theta^0_{ij}\cos\theta^0_{ij}\{w_i-(1-\delta^i_j)w_j\}\\
&\quad-\sum_{j=1}^{N}K'_{ij}\cos^2\theta^0_{ij}\{v_i-(1-\delta^i_j)v_j\}=0,
\end{aligned} \tag{7}$$

where δ^i_j is Kronecker's delta, and $\epsilon=-1$ at $x=0$ and $\epsilon=1$ at $x=L$; similarly, force balances in the z-direction yield

$$\begin{aligned}
&\epsilon EI\frac{\partial^3 w_i}{\partial x^3}-\sum_{j=1}^{N}K_{ij}\cos^2\theta^0_{ij}\{w_i-(1-\delta^i_j)w_j\}\\
&\quad-\sum_{j=1}^{N}(K_{ij}-K'_{ij})\sin\theta^0_{ij}\cos\theta^0_{ij}\{v_i-(1-\delta^i_j)v_j\}\\
&\quad-\sum_{j=1}^{N}K'_{ij}\sin^2\theta^0_{ij}\{w_i-(1-\delta^i_j)w_j\}=0.
\end{aligned} \tag{8}$$

Considering next moment balances at the extremities of the ith cylinder, it is recognized (Fig. 4) that there will be moments

$$\begin{aligned}
\mathfrak{M}_{i1}&=-C_{ij}(\nu_{ij}+\nu_{ji})\mathbf{u}_{\theta_{ij}+\frac{1}{2}\pi},\\
\mathfrak{M}'_{i1}&=-C'_{ij}(\mu_{ij}+\mu_{ji})\mathbf{u}_{\theta_{ij}}, \quad j\neq i,
\end{aligned} \tag{9}$$

due to the action of the rotational springs connecting cylinder i to cylinder j, and

$$\mathfrak{M}_{i2}=-C_{ii}\nu_{ii}\mathbf{u}_{\theta_{ii}+\frac{1}{2}\pi}, \quad \mathfrak{M}'_{i2}=-C'_{ii}\mu_{ii}\mathbf{u}_{\theta_{ii}} \tag{10}$$

due to the action of the corresponding springs connecting cylinder i to the channel. The angles μ and ν and the unit vectors $\mathbf{u}_\theta$, $\mathbf{u}_{\theta+\frac{1}{2}\pi}$ are defined in Fig. 4. In the foregoing, application of $\mathfrak{M}_{i1}$ moves M_iP_i to M_iQ_i and M_jP_j to M_jQ_j; then, application of $\mathfrak{M}'_{i1}$ results in the displacements from M_iQ_i and M_jQ_j to, respectively, M_iR_i and M_jR_j. In this connection, it is realized that the latter operation actually puts Q_i to R'_i rather than R_i, and may actually also induce in-plane displacements. If these latter are neglected, it may be shown that R'_i lies on the parabola given by the intersection of the plane $(P_iQ_iS_i)$ and the cone described by M_iQ_i during the rotation about $\mathbf{u}_{\theta_{ij}}$. Moreover, it may be shown that

$$(\overrightarrow{S_iR'_i})^2=(\overrightarrow{S_iR_i})^2+\tan^2\mu_{ij}\tan^2\nu_{ij}(\overrightarrow{M_iP_i})^2,$$

so that the approximation $R'_i\to R_i$ holds up to fourth order of small quantities.

Downloaded 02 May 2010 to 171.66.16.246. Redistribution subject to ASME license or copyright; see http://www.asme.org/terms/Terms_Use.cfm

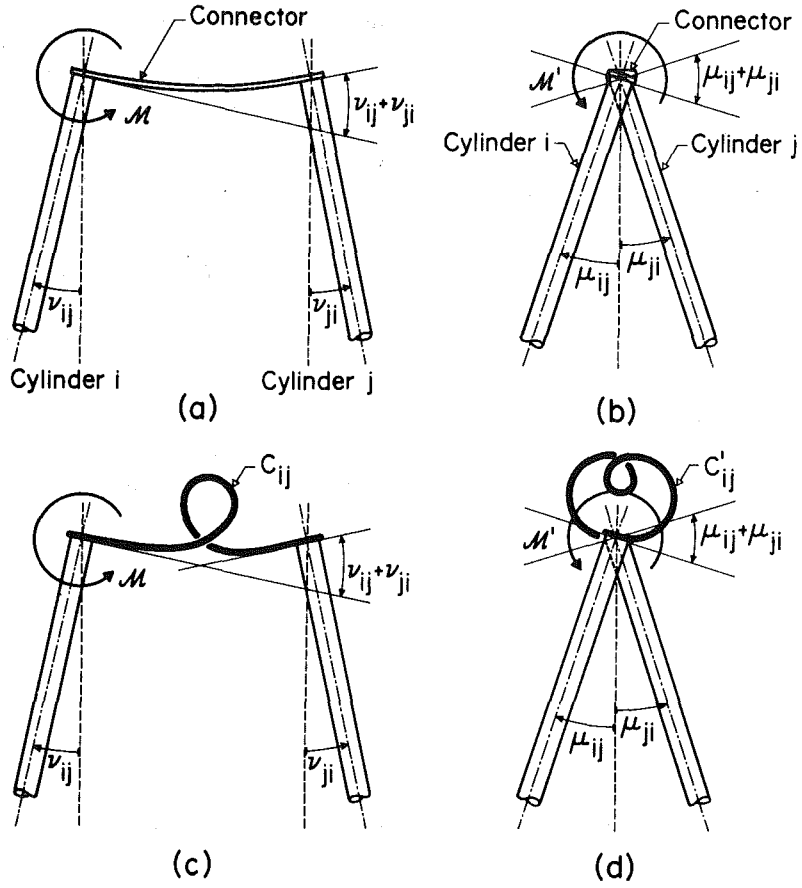

Fig. 3 (*a*) Out-of-plane bending and (*b*) torsion of the connector; (*c*) and (*d*) definition of rotational springs resisting out-of-plane bending and torsion, respectively

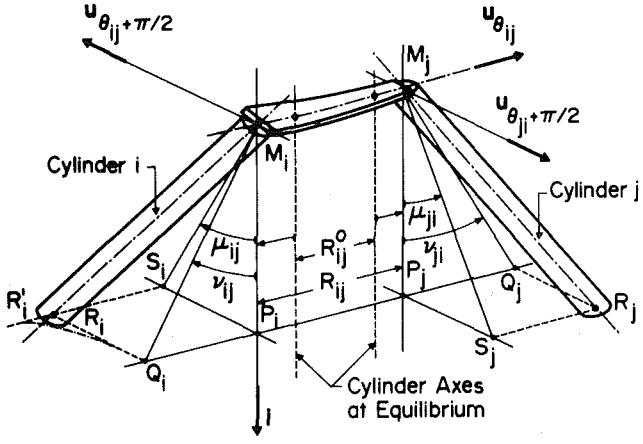

Fig. 4 Diagram showing combined out-of-plane bending and torsion of the connector (as well as in-plane stretching) and defining the quantities used in the analysis of out-of-plane deformation of the connector

Now, the evaluation of the angles ν_{ij}, μ_{ij} requires exertion of some care. The derivations to be presented here will proceed without imposing the restriction, initially at least, that these angles be small. The procedure will be illustrated here for the former of the two. It may be seen in Fig. 4 that

$$\cos\nu_{ij} = \{\vec{M_iP_i} \cdot \vec{M_iQ_i}\} / \{ |\vec{M_iP_i}| \ |\vec{M_iQ_i}| \}. \tag{11}$$

In terms of the coordinate system $(\mathbf{i}, \mathbf{u}_{\theta_{ij}})$, where $\mathbf{i}$ is the unit vector in the x-direction, one may write

$$\vec{M_iP_i} = dx\,\mathbf{i} \quad \text{and} \quad \vec{M_iQ_i} = dx\,\mathbf{i} + \vec{P_iQ_i},$$

where

$$\vec{P_iQ_i} = B\mathbf{u}_{\theta_{ij}} = \vec{S_iR_i},$$

in which B is to be determined. To this end, it is noted that

$$\vec{S_iR_i} \cdot \vec{S_iM_i} = 0$$

or

$$\{B\mathbf{u}_{\theta_{ij}}\} \cdot \{B\mathbf{u}_{\theta_{ij}} - dx\,\mathbf{i} + dv_i\mathbf{j} + dw_i\mathbf{k}\} = 0,$$

where dv_i and dw_i represent the differential displacements of the cylinder in the distance dx, so that $\partial v_i/\partial x$ and $\partial w_i/\partial x$ are the slopes of the cylinder at its extremities. From the foregoing relationships, considering that $\mathbf{u}_{\theta_{ij}}$ is at an angle θ_{ij} with $\mathbf{k}$, one obtains

$$B = -\sin\theta_{ij}dv_i - \cos\theta_{ij}dw_i.$$

Replacing these terms into equation (11) leads to

$$\cos\nu_{ij} = \left\{1 + \left\{\frac{\partial v_i}{\partial x}\sin\theta_{ij} + \frac{\partial w_i}{\partial x}\cos\theta_{ij}\right\}^2\right\}^{-1/2},$$

which, by series expansion, yields the first-order approximation:

$$\nu_{ij} = \sin\theta_{ij}\frac{\partial v_i}{\partial x} + \cos\theta_{ij}\frac{\partial w_i}{\partial x}. \tag{12}$$

Similarly, μ_{ij} may be determined, and it is found that

$$\mu_{ij} = -\cos\theta_{ij}\frac{\partial v_i}{\partial x} + \sin\theta_{ij}\frac{\partial w_i}{\partial x}. \tag{13}$$

Noting now that $\theta_{ji} = \theta_{ij} + \pi$ and that $\theta_{ij} \simeq \theta^0_{ij}$, the final formulation of the angles in equations (9) is as follows:

Downloaded 02 May 2010 to 171.66.16.246. Redistribution subject to ASME license or copyright; see http://www.asme.org/terms/Terms_Use.cfm

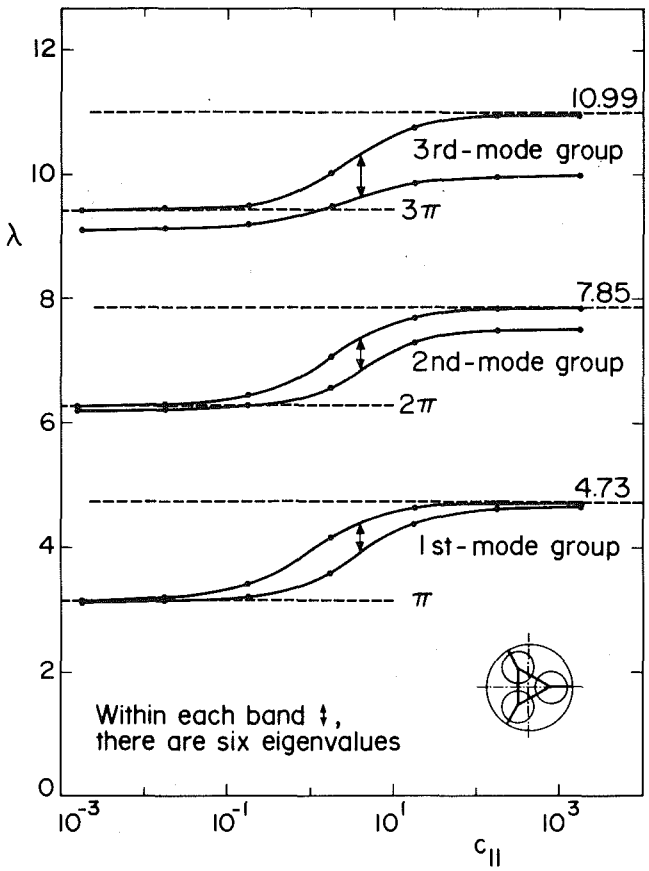

Fig. 5 Evolution of the three lowest groups of eigenvalues of the system shown, for large, constant, in-plane stiffnesses [$k_{ij} \sim 0(10^4)$, $k'_{ij} \sim 0(10^2)$] and varying c_{ij} and c'_{ij}, all of which are of the order of magnitude of c_{11} (See Table A.1)

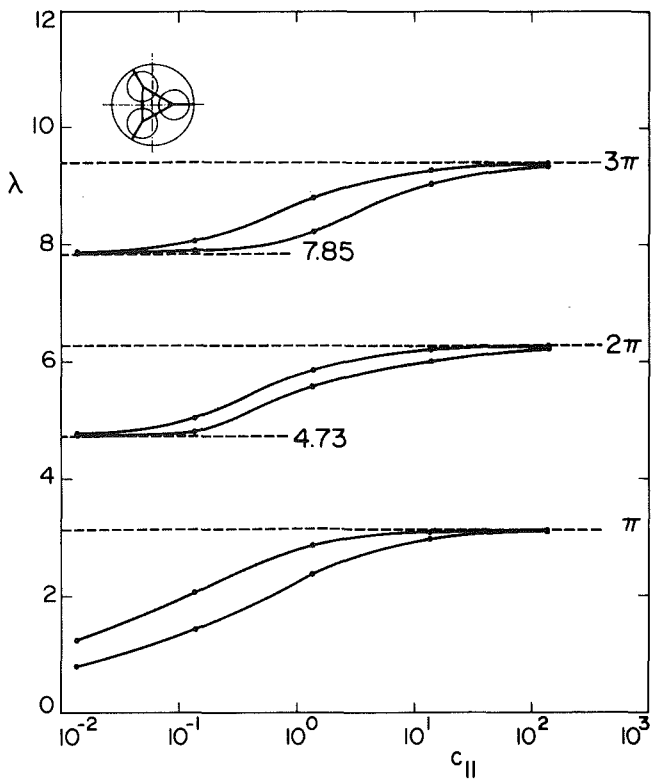

Fig. 6 Evolution of the three lowest groups of eigenvalues of the system shown, for small, constant, in-plane stiffnesses [k_{ij}, $k'_{ij} \sim 0$ (10^{-4})] and varying c_{ij}, c'_{ij}, all of which are of the order of magnitude of c_{11} (See Table A.2)

$$\nu_{ij}+\nu_{ji}=\sin\theta^0_{ij}\{\partial(v_i-v_j)/\partial x\}+\cos\theta^0_{ij}\{\partial(w_i-w_j)/\partial x\},$$
$$\mu_{ij}+\mu_{ji}=-\cos\theta^0_{ij}\{\partial(v_i-v_j)/\partial x\}+\sin\theta^0_{ij}\{\partial(w_i-w_j)/\partial x\}, \tag{14}$$

with similar expressions for ν_{ii} and μ_{ii}.

Next, referring to Fig. 4 and recalling once more that $\mathbf{u}_{\theta_{ij}}$ and $\mathbf{u}_{\theta_{ij}}+\frac{1}{2}\pi$ are at angles θ_{ij} and $\theta_{ij}+\frac{1}{2}\pi$, respectively, one may write

$$\mathbf{u}_{\theta_{ij}}=\sin\theta_{ij}\mathbf{j}+\cos\theta_{ij}\mathbf{k},$$
$$\mathbf{u}_{\theta_{ij}+\frac{1}{2}\pi}=\cos\theta_{ij}\mathbf{j}-\sin\theta_{ij}\mathbf{k}. \tag{15}$$

Then, neglecting second-order terms in the moment approximation, equations (9) and (10) may be rewritten as follows:

$$\mathfrak{M}_{i1}=-C_{ij}(\nu_{ij}+\nu_{ji})(\cos\theta^0_{ij}\mathbf{j}-\sin\theta^0_{ij}\mathbf{k}),$$
$$\mathfrak{M}_{i2}=-C_{ii}\nu_{ii}(\cos\theta^0_{ii}\mathbf{j}-\sin\theta^0_{ii}\mathbf{k}),$$
$$\mathfrak{M}'_{i1}=-C'_{ij}(\mu_{ij}+\mu_{ji})(\sin\theta^0_{ij}\mathbf{j}+\cos\theta^0_{ij}\mathbf{k}), \tag{16}$$
$$\mathfrak{M}'_{i2}=-C'_{ii}\mu_{ii}(\sin\theta^0_{ii}\mathbf{j}+\cos\theta^0_{ii}\mathbf{k}),$$

where the approximation $\theta_{ij}\simeq\theta^0_{ij}$ was once more introduced.

Finally, the total bending moment in the foregoing must formally be equated to the resisting flexural bending moment exerted by cylinder i, at either $x=0$ or $x=L$, i.e.,

$$\mathfrak{M}_{i1}+\mathfrak{M}_{i2}+\mathfrak{M}'_{i1}+\mathfrak{M}'_{i2}$$
$$=\epsilon\{EI(\partial^2 w_i/\partial x^2)|_{x=0,L}\mathbf{j}-EI(\partial^2 v_i/\partial x^2)|_{x=0,L}\mathbf{k}\}, \tag{17}$$

where $\epsilon=-1$ or 1 accordingly as $x=0$ or $x=L$. Hence, making use of equations (14)–(17), the remainder of the boundary conditions may be formulated as follows:

$$\epsilon EI\frac{\partial^2 v_i}{\partial x^2}+\sum_{j=1}^{N}C_{ij}\sin^2\theta^0_{ij}\frac{\partial}{\partial x}\{v_i-(1-\delta^i_j)v_j\}$$
$$+\sum_{j=1}^{N}(C_{ij}-C'_{ij})\sin\theta^0_{ij}\cos\theta^0_{ij}\frac{\partial}{\partial x}\{w_i-(1-\delta^i_j)w_j\}$$
$$+\sum_{j=1}^{N}C'_{ij}\cos^2\theta^0_{ij}\frac{\partial}{\partial x}\{v_i-(1-\delta^i_j)v_j\}=0,$$
$$\epsilon EI\frac{\partial^2 w_i}{\partial x^2}+\sum_{j=1}^{N}C_{ij}\cos^2\theta^0_{ij}\frac{\partial}{\partial x}\{w_i-(1-\delta^i_j)w_j\} \tag{18}$$
$$+\sum_{j=1}^{N}(C_{ij}-C'_{ij})\sin\theta^0_{ij}\cos\theta^0_{ij}\frac{\partial}{\partial x}\{v_i-(1-\delta^i_j)v_j\}$$
$$+\sum_{j=1}^{N}C'_{ij}\sin^2\theta^0_{ij}\frac{\partial}{\partial x}\{w_i-(1-\delta^i_j)w_j\}=0.$$

Nondimensionalization

The equations of motion and boundary conditions may be nondimensionalized by the introduction of the dimensionless quantities

$$\eta_i=\frac{w_i}{L},\quad \eta_{N+i}=\frac{v_i}{L},\quad \xi=\frac{x}{L},\quad \tau=\left\{\frac{EI}{m}\right\}^{1/2}\frac{t}{L^2},$$
$$k_{ij}=\frac{L^3}{EI}K_{ij},\quad k'_{ij}=\frac{L^3}{EI}K'_{ij},\quad c_{ij}=\frac{L}{EI}C_{ij},\quad c'_{ij}=\frac{L}{EI}C'_{ij}. \tag{19}$$

Hence, the equations of motion may be written, in matrix form, as follows:

$$\frac{\partial^4\boldsymbol{\eta}}{\partial\xi^4}+\frac{\partial^2\boldsymbol{\eta}}{\partial\tau^2}=\mathbf{0}, \tag{20}$$

Downloaded 02 May 2010 to 171.66.16.246. Redistribution subject to ASME license or copyright; see http://www.asme.org/terms/Terms_Use.cfm

where $\eta = \{\eta_1, \eta_2, \ldots, \eta_{2N}\}^T$ is a $2N$ vector. Similarly, the boundary conditions may be written as follows:

$$\epsilon(\partial^3\eta_i/\partial\xi^3) - \sum_{j=1}^{N}(g_{ij}+f'_{ij})\{\eta_i - (1-\delta_j^i)\eta_j\} - \sum_{j=1}^{N}(h_{ij}-h'_{ij})\{\eta_{N+i} - (1-\delta_j^i)\eta_{N+j}\} = 0,$$

$$\epsilon(\partial^3\eta_{N+i}/\partial\xi^3) - \sum_{j=1}^{N}(f_{ij}+g'_{ij})\{\eta_{N+i} - (1-\delta_j^i)\eta_{N+j}\} - \sum_{j=1}^{N}(h_{ij}-h'_{ij})\{\eta_i - (1-\delta_j^i)\eta_j\} = 0, \tag{21}$$

and

$$\epsilon(\partial^2\eta_i/\partial\xi^2) + \sum_{j=1}^{N}a_{ij}(\partial/\partial\xi)\{\eta_i - (1-\delta_j^i)\eta_j\} + \sum_{j=1}^{N}d_{ij}(\partial/\partial\xi)\{\eta_{N+i} - (1-\delta_j^i)\eta_{N+j}\} = 0,$$

$$\epsilon(\partial^2\eta_{N+i}/\partial\xi^2) + \sum_{j=1}^{N}b_{ij}(\partial/\partial\xi)\{\eta_{N+i} - (1-\delta_j^i)\eta_{N+j}\} + \sum_{j=1}^{N}d_{ij}(\partial/\partial\xi)\{\eta_i - (1-\delta_j^i)\eta_j\} = 0, \tag{22}$$

at $\xi = 0$ and $\xi = 1$, where $\epsilon = -1$ and 1, respectively, for $i = 1,2, \ldots, N$; in the preceding equations, f_{ij}, g_{ij}, etc., stand for

$$\begin{aligned}
&f_{ij} = k_{ij}\sin^2\theta_{ij}^0, \quad g_{ij} = k_{ij}\cos^2\theta_{ij}^0, \quad h_{ij} = k_{ij}\sin\theta_{ij}^0\cos\theta_{ij}^0,\\
&f'_{ij} = k'_{ij}\sin^2\theta_{ij}^0, \quad g'_{ij} = k'_{ij}\cos^2\theta_{ij}^0, \quad h'_{ij} = k'_{ij}\sin\theta_{ij}^0\cos\theta_{ij}^0,\\
&a_{ij} = c_{ij}\cos^2\theta_{ij}^0 + c'_{ij}\sin^2\theta_{ij}^0, \quad b_{ij} = c_{ij}\sin^2\theta_{ij}^0 + c'_{ij}\cos^2\theta_{ij}^0,\\
&d_{ij} = (c_{ij} - c'_{ij})\sin\theta_{ij}^0\cos\theta_{ij}^0
\end{aligned} \tag{23}$$

and will be constants for a given system.

Solution of the Equations of Motion

The solution of the system equations is given by

$$\eta(\xi,\tau) = \sum_{k=1}^{\infty}\phi_k(\xi)e^{i\omega_k\tau}, \tag{24}$$

where

$$\phi_k = \{\phi_k^1, \phi_k^2, \ldots, \phi_k^{2N}\}^T \tag{25}$$

and ω_k are the system dimensionless eigenfrequencies. Moreover, in view of the form of equation (20), the eigenfunctions ϕ_k^l will be

$$\phi_k^l = a_k^l\cos\lambda_k\xi + b_k^l\sin\lambda_k\xi + c_k^l\cosh\lambda_k\xi + d_k^l\sinh\lambda_k\xi, \tag{26}$$

where the constants a_k^l to d_k^l are to be determined, such that the ϕ_k^l satisfy the boundary conditions. Here the superscript l is associated with a specific cylinder and direction of motion, while the subscript k is associated with mode order.

Substituting equation (26) into (21) and (22), a system of $8N$ linear equations is obtained, not given here for brevity, which may be written as

$$[F(\lambda_k)]\{a_k^1, \ldots, a_k^{2N}; b_k^1, \ldots, b_k^{2N}; c_k^1, \ldots, c_k^{2N}; d_k^1, \ldots, d_k^{2N}\}^T = \{0\},$$

from which, by setting

$$\det[F(\lambda_k)] = 0, \tag{27}$$

the eigenvalues λ_k may be determined. Then, by evaluating the coefficients a_k^l to d_k^l, the corresponding eigenfunctions may be found. It is noted that eigenvalues and dimensionless eigenfrequencies are related as for a simple beam, i.e., $\omega_k = \lambda_k^2$.

Although this part of the paper is presented in highly abridged form, the computational aspect of the problem proved not to be trivial, especially because groups of eigenvalues were often found to be numerically very closely spaced. Hence, great care and some ingenuity had to be exercised in solving equation (27) in order to determine all the λ_k to the requisite precision.

It should finally be remarked that in Part 2, where flow will be imposed on the system, the eigenfunctions (26) will serve as suitable comparison functions in the Galerkin solution to be employed [7].

Calculations and Results

The main aim of the calculations was the study of the dynamical characteristics of the system with varying dimensionless spring constants. Of special interest was the study of the evolution of system eigenfrequencies with changing spring constants, and their comparison to various limiting cases, where the cylinders become effectively uncoupled: e.g., when all spring constants are sufficiently large to approach the ideally clamped boundary conditions.

It was generally found that the eigenvalues are clustered in groups of $2N$, corresponding to N cylinders and two independent lateral directions. Within each group, the (axial) mode of deformation of the cylinders is sensibly the same; the mode shapes differ from one another in terms of the relative motions of the cylinders, as may most easily be visualized in any given cross-sectional plane: i.e., the cylinders may all move together toward the center of the channel in one mode, while they move in other cross-sectional patterns in the other modes of the same mode group. Thus, in this respect, structural and hydrodynamic coupling have similar effects on the dynamics of the system—cf. [8, 9].

All results to be presented here are for a geometrically symmetric system of three interconnected cylinders, each of which is also attached to the channel, shown diagrammatically inset in Fig. 5. Mainly to minimize computational difficulties associated with the occurrence of repeated eigenvalues, but also to reflect more closely the real case (Fig. 1), not all spring constants of a kind were taken to be equal, but merely of the same order of magnitude; thus, $c_{21}/c_{11} = 8/5$, $c_{31}/c_{11} = 1$, and so on, for the results of Fig. 5, where these ratios were chosen arbitrarily and are given in full in the Appendix.

In the first set of calculations, k_{ij} and k'_{ij} were kept constant and large [$k_{ij} \sim 0(10^4)$, $k'_{ij} \sim 0(10^3)$], while the out-of-plane stiffnesses were varied. The effect on the eigenvalues is shown in Fig. 5. (It is realized, of course, that this independent variation of some of the spring stiffnesses, while others are kept constant, is for analytical convenience and that it is not physically realistic.) The abscissa in Fig. 5 is c_{11}, but, as may be seen in Table A.1, all the c_{ij} and c'_{ij} are varied proportionately to c_{11}. Moreover, in the figure only the *band* of the lowest three groups of eigenvalues is shown; i.e., in each case the curves depict the evolution of the lowest and highest λ within each mode group.

It is seen that for very small c_{ij}, c'_{ij}, the six first-mode eigenvalues are essentially coincident and equal to the classical value of π for an ideally pinned-pinned cylinder. Similarly, the second and third-mode groups are clustered about 2π and 3π, respectively, but the eigenvalues are in-

Downloaded 02 May 2010 to 171.66.16.246. Redistribution subject to ASME license or copyright; see http://www.asme.org/terms/Terms_Use.cfm

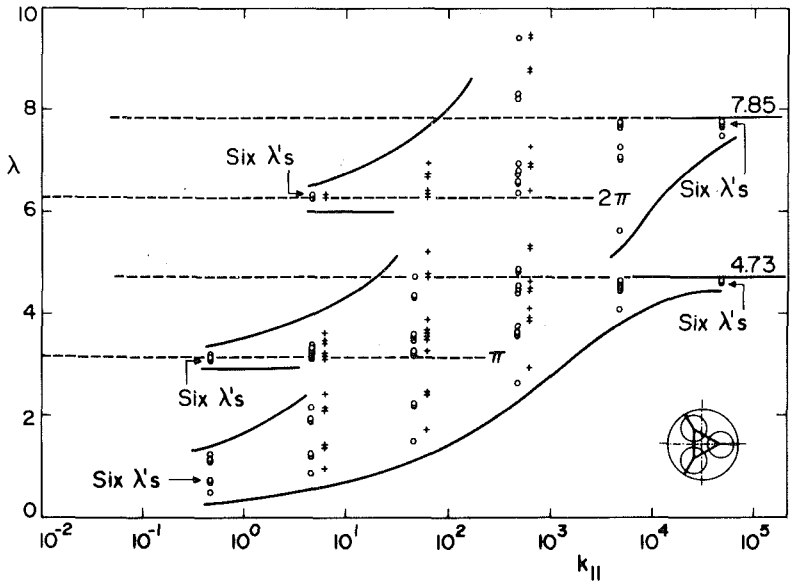

Fig. 7 Evolution of the three lowest groups of eigenvalues of the system shown, for fairly large constant c_{ij}, c'_{ij} [c_{ij}, $c'_{ij} \sim 0(10^2)$] and variable k_{ij}, all of which are of the order of magnitude of k_{11}, and k'_{ij} which are two orders of magnitude smaller. o: stiffnesses as given in Table A.1; +: stiffnesses as given in Table A.3.

creasingly spread out for these higher mode groups; this is physically reasonable, as higher axial modal shapes imply larger end moments, so that even very weak out-of-plane springs do not have a negligible effect on the coupled dynamical behavior of the system.

With increasing c_{ij}, c'_{ij}, the band of each group of eigenvalues spreads out, which characterizes stronger intercylinder coupling—cf. [8]. For large enough c_{ij}, c'_{ij}, the system eigenvalues approach those of an ideally clamped-clamped beam. Once more, those in the first-mode group are almost coincident, while the eigenvalues of the third-mode group are quite far apart, indicating that fairly strong coupling still exists in the higher modes. Here it should be remarked that, although all spring constants at this point are quite large, they are nevertheless not quite infinitely large.

Similar results are shown in Fig. 6, where in-plane stiffnesses are now very low [k_{ij} and $k'_{ij} \sim 0(10^{-4})$]. It is seen here that if the c_{ij}, c'_{ij} are large, the eigenvalues approach those of a beam with ideally "sliding" end conditions [10], i.e., zero slope and no constraint to lateral movement. Hence, in addition to those shown, there is an additional group of six nearly *null* eigenvalues, lying essentially on the c_{11}-axis, corresponding to rigid-body motions of the cylinders, parallel to the x-axis. They will further be discussed later.

At the left-hand end of Fig. 6, all springs are very weak, and the three groups of eigenvalues approach those of a free-free beam, namely 0, 4.73, and 7.85 [10]. The group of eigenvalues approaching zero is associated with the other six possible rigid-body modes of free-free beams, involving rigid-body rotation about the cylinder midpoint; these clearly evolve from the corresponding mode shapes of a sliding-sliding beam, which are half-sinusoids with a midspan node. (The formerly discussed parallel motion rigid-body modes are of course still there, with nearly null eigenvalues.) It is remarked that the first-mode eigenvalues shown are still somewhat away from zero at $c_{ij} \sim 0(10^{-2})$, but the progression to zero cannot but be very gradual, as c'_{ij}, c_{ij}, k_{ij}, and k'_{ij}, although small, are still finite. Once more, it is noted that intermediate values of c_{ij}, c'_{ij} give the broadest band of system eigenvalues for each mode group, i.e., they are associated with maximum coupling in cylinder motions.

A more interesting set of results is shown in Fig. 7, where c_{ij}, c'_{ij} are fixed at fairly high values, while the k_{ij} are varied from $\sim 0(10^{-1})$ to $\sim 0(10^4)$, and the k'_{ij} proportionately but two orders of magnitude smaller. Thus, Fig. 7 may be thought of as the continuation of Fig. 6, in the sense that it shows the evolution of the eigenvalues, with increasing in-plane spring stiffnesses from the state represented by the right-hand side of Fig. 6 to high k_{ij} and k'_{ij}. For small k_{ij}, k'_{ij}, it is noted that, in addition to the eigenvalues clustered about π and 2π (those about 3π are not shown), there now appears a new set lying between $\lambda = 0.4$ and 1.2 which were absent in Fig. 6. Noting that k'_{ij} and k_{ij} at the extreme left of Fig. 7 are, respectively, one and three orders of magnitude higher than those at the extreme right of Fig. 6; these "new" eigenvalues may be identified as the evolution of the set of null eigenvalues formerly lying on the abscissa.

At the extreme right of Fig. 7, once more all the spring constants are high and, predictably, the eigenvalues tend to cluster around those of a clamped-clamped beam. The most interesting part of this figure, however, lies in the middle range of in-plane stiffnesses. Thus, whereas for lower k_{ij} the three groups of eigenvalues are quite distinct, for $k_{ij} > 0(50)$ approximately, the first and second-mode groups become intertwined into a single group of 12 eigenvalues. Similarly, for $k_{ij} > 0(5 \times 10^2)$ all three groups of eigenvalues become interspersed. On the other hand, as the k_{ij} are further increased the eigenvalues once more begin to separate into distinct mode packets: for $k_{ij} \sim 0(5 \times 10^3)$ there is a clearly distinguishable first-mode group; for higher k_{ij}, the second and then the higher-mode groups, become once more distinct. This unusual evolutionary behavior of the system eigenvalues may be considered to be analogous to that of Fig. 5 where, for the middle range of c_{ij}, the lowest two eigenvalue bands are widest; the results of Fig. 7 may be viewed as a case where the eigenvalue bands become so wide as to intersect one another.

The results of Fig. 7, apart from their intrinsic interest, also explain the paradoxical behavior noted but not explained in the work of reference [4], where it had been found that the number of modes in particular mode groups varied with changing parameters.

Conclusions

The work presented here indicates that the eigenvalues and

Downloaded 02 May 2010 to 171.66.16.246. Redistribution subject to ASME license or copyright; see http://www.asme.org/terms/Terms_Use.cfm

hence the eigenfrequencies of the system display a very intricate and interesting dependence on the kind and strength of intercylinder structural coupling. For intermediate ranges of stiffnesses of the springs modeling intercylinder connections, coupling effects are strong and the eigenfrequencies become widely separated; indeed the groups of $2N$ modes with distinct axial mode shapes may lose their cohesiveness and become suffused into larger groupings, as shown in Fig. 7. On the other hand, as the various spring stiffnesses become either vanishingly small or very large, then the modes become neatly grouped once more, and the eigenfrequencies become clustered about the values associated with the four idealized sets of boundary conditions: free-free, sliding-sliding, pinned-pinned, and clamped-clamped. The eigenfunctions of the system, although discussed qualitatively here, will actually be presented in Part 2 of this study [7].

The main conclusions of this work, as well as the Acknowledgments, will also be presented in Part 2, after the behavior of the sytem in flowing fluid will have been discussed [7].

References

1 Paidoussis, M. P., "Flow-Induced Vibrations in Nuclear Reactors and Heat Exchangers: Practical Experiences and State of Knowledge," in: *Practical Experiences With Flow-Induced Vibration*, Naudascher, E., and Rockwell, D., eds., Springer-Verlag, Berlin, 1980, pp. 1–81.

2 Simpson, A., "Wake Induced Flutter of Circular Cylinders: Mechanical Aspects," *The Aeronautical Quarterly*, Vol. XXIII, 1971, pp. 101–118.

3 Allnut, J. G., Price, S. J., and Tunstall, M. J., "The Control of Sub-Span Oscillation of Multi-Conductor Bundled Transmission Lines," Paper 22-01, *Cigré International Conference on Large High Voltage Electric Systems*, Paris, Aug.-Sept., 1980.

4 Jagannath, D. V., and Paidoussis, M. P., "Solid-Fluid Interactions in the Vibration of Nuclear Fuel Bundles," Paper 1.2, *Proceedings BNES International Conference on Vibration in Nuclear Plant*, Keswick, U.K., May 1978.

5 Whiston, G. S., and Thomas, G. D., "Whirling Instabilities of Heat Exchanger Tube Arrays," *Journal of Sound and Vibration*, Vol. 81, 1982, pp. 1–31.

6 Price, S. J., and Paidoussis, M. P., "Fluidelastic Instability of an Infinite Double Row of Circular Cylinders Subject to Cross Flow," ASME Paper 81-DET-24, *ASME Journal of Vibration, Stress, and Reliability in Design*, Vol. 105, 1983, pp. 59–66.

7 Paidoussis, M. P., Chaubernard, J.-P., El Barbir, K. N., and Genadry, M. R., "Dynamics of a Cluster of Flexibly Interconnected Cylinders. Part 2: In Axial Flow," ASME JOURNAL OF APPLIED MECHANICS, Vol. 50, 1983, pp.

8 Paidoussis, M. P., Suss, S., and Pustejovsky, M., "Free Vibration of Cylinders in Liquid-Filled Channels," *Journal of Sound and Vibration*, Vol. 55, 1977, pp. 443–459.

9 Paidoussis, M. P., and Suss, S., "Stability of a Cluster of Flexible Cylinders in Bounded Axial Flow," ASME JOURNAL OF APPLIED MECHANICS, Vol. 44, 1977, pp. 401–408.

10 Bishop, R. E. D., and Johnson, D. C., *The Mechanics of Vibration*, Cambridge University Press, 1960.

APPENDIX

The Tables below give the spring stiffnesses utilized in the calculations.

Table $A.1$ The spring stiffnesses used in some of the calculations. For Fig. 5: $k_{11}=4.77\times10^{4}$, $k'_{11}=1.13\times10^{3}$, and c_{11} is variable. For Fig. 7: $c_{11}=1.73\times10^{2}$, $k'_{11}=2.36\times10^{-2}k_{11}$, and k_{11} is variable.

i, j:	1, 1	1, 2	1, 3	2, 2	2, 3	3, 3
$5\,c_{ij}/c_{11}$:	5	8	5	8	5	5
$5\,c'_{ij}/c_{11}$:	5	9	6	9	6	7
$11\,k_{ij}/k_{11}$:	11	5	5	10	5	10
$13\,k'_{ij}/k'_{11}$:	13	6.3	6.3	12	6.3	12

Table $A.2$ The spring stiffnesses used in the calculations of Fig. 6; $k_{11}=3.46\times10^{-4}$, $k'_{ij}=k_{ij}$, and c_{11} is still variable.

i, j:	1, 1	1, 2	1, 3	2, 2	2, 3	3, 3
$4\,c_{ij}/c_{11}$:	4	7	4	7	4	4
$4\,c'_{ij}/c_{11}$:	5	8	5	8	5	5
$4\,k_{ij}/k_{11}$:	4	5	4	5	4	4

Table $A.3$ The spring stiffnesses used in some of the calculations of Fig. 7; $c_{11}=1.73\times10^{2}$, $k'_{11}=2.54\times10^{-2}k_{11}$, and k_{11} is variable.

i, j:	1, 1	1, 2	1, 3	2, 2	2, 3	3, 3
$5\,c_{ij}/c_{11}$:	5	8	5	8	5	5
$5\,c'_{ij}/c_{11}$:	5	9	6	9	6	7
$15k_{ij}/k_{11}$:	15	9	9	14	9	14
$19k'_{ij}/k'_{11}$:	19	11	11	18	11	18

In these Tables, as $[c_{ij}]$, $[k_{ij}]$, etc., are symmetric matrices, only the upper half of the matrix elements need be given.

Downloaded 02 May 2010 to 171.66.16.246. Redistribution subject to ASME license or copyright; see http://www.asme.org/terms/Terms_Use.cfm

M. P. Paidoussis
Professor and Chairman.
Mem. ASME

J.-P. Chaubernard[1]
Research Asistant.

M. R. Genadry[2]
Research Asistant.

K. N. El Barbir
Research Asistant.

Department of Mechanical Engineering,
McGill University,
Montreal, Québec, Canada

Dynamics of a Cluster of Flexibly Interconnected Cylinders

Part 2: In Axial Flow

In this paper the dynamical characteristics are discussed of a cluster of cylinders, the extremities of which are interconnected by beam-like connectors, modeled here by sets of linear springs as formulated in Part 1 of this study; resistance to both in-plane and out-of-plane deformation of the connectors is taken into account. The cylinders are subjected to axial flow, and hydrodynamic coupling in cylinder motions is taken into account. The system eigenfrequencies and modal shapes are calculated for different conditions of structural and hydrodynamic coupling. The effect of increasing flow on the dynamics of the system is also studied, up to and beyond the threshold of fluid-elastic instabilities.

Introduction

Clusters of closely spaced cylinders subjected to nominally axial flow may be found in certain types of heat exchangers and nuclear reactors [1]. Axial flow, in contrast to cross flow, usually induces rather small amplitude vibration of the cylinders, which would normally be considered negligible [2], were it not for the very tight spacing of the cylinders; hence, even small amplitude vibration may cause intercylinder impact, resulting in fretting wear of the cylinders and failure of the system. For sufficiently high flow velocities, axial flow may induce fluid-elastic instabilities [2, 3], namely divergence and flutter of the system, involving coupled motions of the cylinders, which are of considerable fundamental interest.

Although hydrodynamic coupling has been taken into account when studying the dynamics of such systems, e.g., references [3, 4], intercylinder structural coupling has been ignored, despite the fact that the cylinders are often interconnected by fairly flexible structural elements. In Part 1 of this study [1] a mathematical model was formulated for taking into account these flexible connections. To this end, each connector, assumed to exist only at the cylinder extremities, was replaced by a set of translational and rotational springs modeling resistance to in-plane and out-of-plane deformation of the connector. The effect of structural coupling on the dynamics of the system *in vacuum* was then examined [1]. Here, utilizing the same mathematical model for the connectors, the dynamics of the structurally coupled system is studied *in axial flow*.

The Equations of Motion and Boundary Conditions

The equations of motion of a cluster of cylinders in axial flow have been derived previously [4] and will, therefore, be given here directly, without repeating the derivation. For a system of N identical cylinders of flexural rigidity EI, cross-sectional area A, diameter D, length L, and mass per unit length m, in fluid of density ρ, flowing with velocity U along the x-axis, i.e., parallel to the long axis of the cylinders, the equations of motion of an arbitrary cylinder, say the ith, in two mutually perpendicular lateral directions y and z, involving displacements $v_i(x,t)$ and $w_i(x,t)$, respectively, are given by

$$EI\frac{\partial^4 v_i}{\partial x^4}+\rho A\sum_{l=1}^{N}\left\{\kappa'_{il}\frac{D^2 w_l}{Dt^2}+\kappa_{il}\frac{D^2 v_l}{Dt^2}\right\}$$

$$+\frac{1}{2}\rho DUC_f\sum_{l=1}^{N}\left\{\sigma'_{il}\frac{Dw_l}{Dt}+\sigma_{il}\frac{Dv_l}{Dt}\right\}$$

$$-\frac{1}{2}\rho DU^2C_f(1+D/D_h)\frac{\partial}{\partial x}\left[\left(\frac{1}{2}L-x\right)\frac{\partial v_i}{\partial x}\right]$$

$$-[\bar{T}+(1-2\nu)\bar{p}A]\frac{\partial^2 v_i}{\partial x^2}+m\frac{\partial^2 v_i}{\partial t^2}=0,$$

$$EI\frac{\partial^4 w_i}{\partial x^4}+\rho A\sum_{l=1}^{N}\left\{\epsilon_{il}\frac{D^2 w_l}{Dt^2}+\epsilon'_{il}\frac{D^2 v_l}{Dt^2}\right\}$$

[1] Presently with TECHNIP, 170 Place Henri Regnault, La Defense, 92090, Paris, France.

[2] Presently with Jaros, Baum & Bolles, 345 Park Ave., New York, N.Y., 10022.

Contributed by the Applied Mechanics Division for presentation at the 1983 ASME Applied Mechanics, Bioengineering, and Fluids Engineering Conference, Houston, Texas, June 20-22, 1983 of THE AMERICAN SOCIETY OF MECHANICAL ENGINEERS.

Discussion on this paper should be addressed to the Editorial Department, ASME United Engineering Center, 345 East 47th Street, New York, N.Y. 10077, and will be accepted until two months after final publication of the paper itself in the JOURNAL OF APPLIED MECHANICS. Manuscript received by ASME Applied Mechanics Division, January, 1982; final revision, October, 1982. Paper No. 83-APM-25.

Copies will be available until February, 1984.

Copyright © 1983 by ASME
Downloaded 02 May 2010 to 171.66.16.246. Redistribution subject to ASME license or copyright; see http://www.asme.org/terms/Terms_Use.cfm

$$+\frac{1}{2}\rho DUC_f\sum_{l=1}^{N}\left\{\zeta_{il}\frac{Dw_l}{Dt}+\zeta'_{il}\frac{Dv_l}{Dt}\right\}$$

$$-\frac{1}{2}\rho DU^2C_f(1+D/D_h)\frac{\partial}{\partial x}\left[\left(\frac{1}{2}L-x\right)\frac{\partial w_i}{\partial x}\right]$$

$$-[\bar{T}+(1-2\nu)\bar{p}A]\frac{\partial^2 w_i}{\partial x^2}+m\frac{\partial^2 w_i}{\partial t^2}=0,$$

$$i=1,2,\ldots,N, \qquad (1)$$

where $D/Dt\equiv(\partial/\partial t)+U(\partial/\partial x)$ is the convective derivative, C_f is the fluid frictional coefficient, D_h the hydraulic diameter of the flow in the channel containing the cluster, $\bar{T}$ is the externally applied tension on the cylinders, if any, $\bar{p}$ is the mean pressurization in the channel, and ν Poisson's ratio; κ_{il}, κ'_{il}, ϵ_{il}, ϵ'_{il} are the elements of the virtual ("hydrodynamic") mass matrix, which defines the inviscid hydrodynamic coupling in cylinder motions, and σ_{il}, σ'_{il}, ζ_{il}, ζ'_{il} are the corresponding elements of the viscous coupling matrix [4].

It is noted that equations (1) are a simplified version of those derived in reference [4], arrived at by neglecting internal dissipation in the cylinder, neglecting the effect of gravity (operative in vertical systems), assuming that the overall length of the cylinders between supports remains constant (no axial sliding), and by introducing some other minor simplifications. Without implying that they are always all negligible, these effects will not be included, simply because their inclusion would not have appreciably added to the significance of the results to be presented here.

It is remarked that in vacuum, where $\rho=0$, $\bar{p}=0$, if additionally $\bar{T}=0$, equations (1) reduce to simple Euler-Bernoulli beam equations, retrieving those of Part 1. In still fluid, on the other hand, some of the terms survive, but it is noted that D/Dt is replaced by $\partial/\partial t$.

The equations may be nondimensionalized through the use of the following dimensionless terms:

$$\eta_i=\frac{w_i}{L},\quad \eta_{N+i}=\frac{v_i}{L},\quad \xi=\frac{x}{L},\quad \tau=\left\{\frac{EI}{m+\rho A}\right\}^{1/2}\frac{t}{L^2},$$

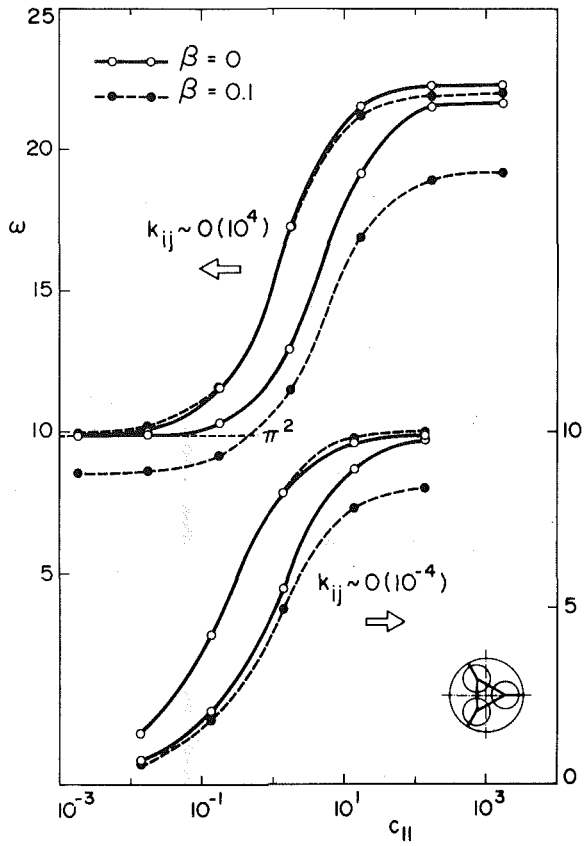

Fig. 1 The band of eigenfrequencies of the lowest mode group in vacuum ($\beta=0$) and in still fluid ($\beta=0.1$) as c_{ij} and c'_{ij} are varied, proportionately to c_{11}. Upper figure: the in-plane stiffnesses are large [$k_{ij}\sim O(10^4)$, $k'_{ij}\sim O(10^2)$, vide Table A.1 of Part 1]; lower figure: the in-plane stiffnesses are small [k_{ij}, $k'_{ij}\sim O(10^{-4})$, vide Table A.2 of Part 1]. Other system parameters: $\Gamma=\bar{\Pi}=u=0$, $G_c=G_w=1/4$.

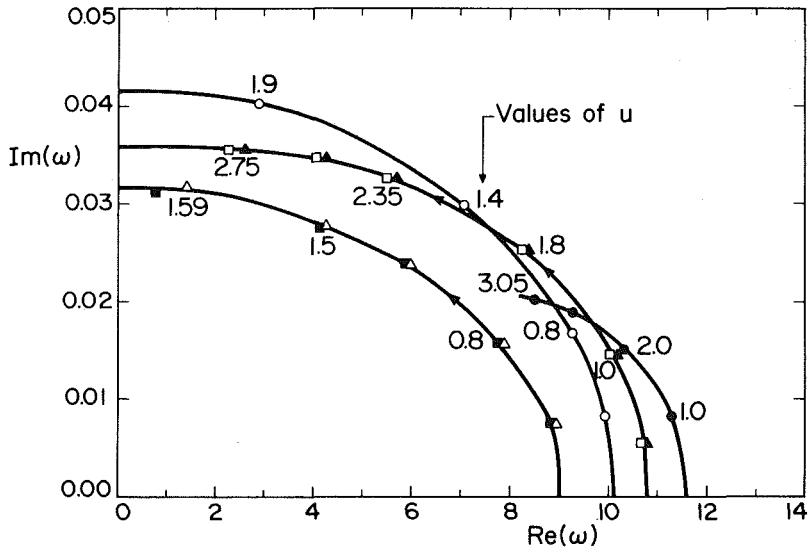

Fig. 2 The evolution of the six lowest eigenfrequencies with increasing u, shown as an Argand diagram, for a three-cylinder system with low out-of-plane stiffnesses and high in-plane stiffnesses [c_{ij}, $c'_{ij}\sim O(10^{-1})$; $k_{ij}\sim O(10^4)$, $k'_{ij}\sim O(10^2)$, as given in Table A.1 of Part 1, with $c_{11}=1.73\times10^{-1}$]. Other system parameters: $\beta=0.1$, $\Gamma=\bar{\Pi}=0$, $\epsilon c_f=0.25$, $h=1.26$, $G_c=G_w=1/4$.

Downloaded 02 May 2010 to 171.66.16.246. Redistribution subject to ASME license or copyright; see http://www.asme.org/terms/Terms_Use.cfm

$$\beta=\frac{\rho A}{m+\rho A},\quad \Gamma=\frac{\bar{T}L^2}{EI},\quad \epsilon=\frac{L}{D},\quad \Pi=\frac{\bar{p}AL^2}{EI},$$

$$c_f=\frac{4}{\pi}C_f,\quad h=\frac{D}{D_h},\quad u=\left\{\frac{\rho A}{EI}\right\}^{1/2}UL. \tag{2}$$

Substitution into equation (1) yields a dimensionles set of equations, which may be written in matrix form as follows:

$$\mathbf{I}\frac{\partial^4\eta}{\partial\xi^4}+\mathbf{E}\frac{\partial^2\eta}{\partial\xi^2}+\mathbf{F}\xi\frac{\partial^2\eta}{\partial\xi^2}+\mathbf{C}\frac{\partial^2\eta}{\partial\xi\partial\tau}+\mathbf{G}\frac{\partial\eta}{\partial\xi}+\mathbf{H}\frac{\partial\eta}{\partial\tau}+\mathbf{M}\frac{\partial^2\eta}{\partial\tau^2}=\mathbf{O}, \tag{3}$$

where

$$\mathbf{C}=2\beta^{1/2}u\mathbf{M}_v,$$
$$\mathbf{E}=u^2\mathbf{M}_v-[\Gamma+(1-2\nu)\Pi+\tfrac{1}{4}\epsilon c_f u^2(1+h)]\mathbf{I},$$
$$\mathbf{G}=\tfrac{1}{2}\epsilon c_f u^2\mathbf{C}_v+\tfrac{1}{2}\epsilon c_f u^2 h\mathbf{I},\quad \mathbf{F}=\tfrac{1}{2}\epsilon c_f u^2(1+h)\mathbf{I}, \tag{4}$$
$$\mathbf{H}=\tfrac{1}{2}\epsilon c_f\beta^{1/2}u\mathbf{C}_v,\quad \mathbf{M}=\beta\mathbf{M}_v+(1-\beta)\mathbf{I},$$
$$\eta=\{\eta_1,\eta_2,\ldots,\eta_{2N}\}^T,$$

and $\mathbf{I}$, $\mathbf{M}_v$, and $\mathbf{C}_v$ are, respectively, the identity matrix, the virtual mass matrix, and viscous coupling matrix, all of order $2N\times 2N$, the latter two being of the form

$$\mathbf{M}_v=\begin{bmatrix}[\epsilon_{il}]&[\epsilon'_{il}]\\ [\kappa'_{il}]&[\kappa_{il}]\end{bmatrix},\quad \mathbf{C}_v=\begin{bmatrix}[\zeta_{il}]&[\zeta'_{il}]\\ [\sigma'_{il}]&[\sigma_{il}]\end{bmatrix}. \tag{5}$$

If the cylinders are very far apart from one another and from the channel, then $\kappa_{ii}\to 1$, $\epsilon_{ii}\to 1$, and all off-diagonal terms of $\mathbf{M}_v$ tend to zero, reflecting weak coupling; otherwise all elements of $\mathbf{M}_v$ are generally nonzero, and $\kappa_{ii}>1$, $\epsilon_{ii}>1$. Similar relationships hold for $\mathbf{C}_v$ [3, 4].

The cylinders are connected to one another and to the channel by sets of springs, modeling the effect of the beam-like connectors, as developed in Part 1 of this study. Thus, resistance to in-plane stretching of the connector between cylinders i and j is represented by a spring of stiffness K_{ij}; in-plane bending is similarly modeled by a spring of stiffness K'_{ij}. Out-of-plane flexure and torsion are modeled by springs of stiffnesses C_{ij} and C'_{ij}, respectively. The boundary conditions involving these springs have been derived in Part 1. It will be assumed that they are unaffected by fluid flow and will, therefore, hold for this analysis as well. The following nondimensional stiffness parameters

$$k_{ij}=K_{ij}L^3/EI,\quad k'_{ij}=K'_{ij}L^3/EI,$$
$$c_{ij}=C_{ij}L/EI,\quad c'_{ij}=C'_{ij}L/EI \tag{6}$$

are necessary to render the boundary conditions also dimensionless [1].

Finally, the degree of spatial "tightness" of the geometrically symmetric systems to be considered here may be characterized by the following two parameters:

$$G_c = \text{(smallest intercylinder gap)/(cylinder radius)},$$
$$G_w = \text{(smallest cylinder-to-channel gap)/(cylinder radius)}. \tag{7}$$

Outline of the Method of Solution

Equations (3) will be solved by Galerkin's method. Hence, the solutions will have the form

$$\eta(\xi,\tau)=\sum_{k=1}^{Q}\phi_k(\xi)p_k(\tau), \tag{8}$$

where

$$\phi_k=\{\phi_k^1,\phi_k^2,\ldots,\phi_k^{2N}\}^T \tag{9}$$

are vectors of the comparison functions ϕ_k^j, j being associated with a specific cylinder and direction of motion and k with the order of the mode; $p_k(\tau)$ are the associated generalized coordinates. The eigenfunctions of the system in vacuum which were determined in Part 1 satisfy the same boundary conditions as those applying to this problem, and may therefore serve as a suitable set of comparison functions. Rewriting then (8) in matrix form,

$$\eta=\Phi\ \mathbf{p} \tag{10}$$

where

$$\Phi=[\phi_1,\phi_2,\ldots,\phi_Q],\quad \mathbf{p}=\{p_1,p_2,\ldots,p_Q\}^T; \tag{11}$$

then substituting into equation (3) and applying the procedures of Galerkin's method, one obtains

$$\left\{\int_0^1\Phi^T\mathbf{M}\Phi\,d\xi\right\}\ddot{\mathbf{p}}+\left\{\int_0^1\Phi^T\left\{\mathbf{C}\frac{\partial}{\partial\xi}+\mathbf{H}\right\}\Phi\,d\xi\right\}\dot{\mathbf{p}}$$
$$+\left\{\int_0^1\Phi^T\left\{\mathbf{I}\frac{\partial^4}{\partial\xi^4}+\mathbf{E}\frac{\partial^2}{\partial\xi^2}+\xi\mathbf{F}\frac{\partial^2}{\partial\xi^2}+\mathbf{G}\frac{\partial}{\partial\xi}\right\}\Phi\,d\xi\right\}\mathbf{p}=\mathbf{O}; \tag{12}$$

the comparison functions involve trigonometric and hyperbolic terms, and hence all the definite integrals in (12) may easily be evaluated, yielding an equation of the form

$$\mathbf{A}\ddot{\mathbf{p}}+\mathbf{B}\dot{\mathbf{p}}+\mathbf{L}\mathbf{p}=\mathbf{O}. \tag{13}$$

It should be stressed that the comparison functions, and hence **A**, **B**, **L** also, are functionally dependent on the spring stiffnesses k_{ij}, k'_{ij}, c_{ij}, and c'_{ij}. Equation (13) may easily be transformed into a standard eigenvalue problem, from which the eigenvalues, and hence the eigenfrequencies, and the eigenvectors of the system may be determined numerically. For the sake of brevity the computational aspects of the problem will not be elaborated here.

The Eigenfrequencies and Stability of the System

In Part 1, calculations were conducted in which the in-plane springs were kept constant and out-of-plane springs were varied, or vice-versa, and the effect on the system eigenvalues studied. Some of the results, in vacuum, are reproduced in Fig. 1, where they are compared to those calculated here for the same system in still fluid. As described in Part 1 (vide also references [3, 4]) the eigenvalues, and hence the eigenfrequencies shown in Fig. 1, occur in groups of six ($2N$) for this three-cylinder system ($N=3$); the frequency band of only the lowest group is shown for the two cases in the figure.

In the first case (upper part of Fig. 1), the in-plane stiffnesses are large [$k_{ij}\sim 0(10^4)$, $k'_{ij}\sim 0(10^2)$].[3] As c_{11}, and all the other c_{ij} and c'_{ij} proportionately, become small, the eigenfrequencies are seen to be clustered about the value of π^2, which is the dimensionless eigenfrequency of the first mode of a beam with pinned ends. For the system in still fluid, however, the eigenfrequency band is far broader, and they are mostly lower than those in vacuum, as expected (cf. [3, 4]). At the other end of the scale, where c_{ij} and c'_{ij} are large, the eigenfrequencies are in the neighborhood of those of a beam with clamped ends ($\omega\simeq 4.73^2$). For intermediate c_{ij}, c'_{ij}, the main effect of the presence of the fluid is to render the eigenfrequency band wider.

Similar effects are noted in the case where the k_{ij}, k'_{ij} are vanishingly small [k_{ij}, $k'_{ij}\sim 0(10^{-4})$]. In this case, if the c_{ij} and c'_{ij} are also small, the eigenfrequencies tend toward zero, approximating free-free boundary conditions, and if they are large they tend toward π^2, approximating sliding-sliding boundary conditions [1]. hence, the principal effects of the

[3] As discussed in Part 1, all stiffnesses of a kind (e.g., all c_{ij}) were taken to be of the same order of magnitude, but not exactly equal. The exact values used are given in tabular form in the Appendix of Part 1 [1].

Downloaded 02 May 2010 to 171.66.16.246. Redistribution subject to ASME license or copyright; see http://www.asme.org/terms/Terms_Use.cfm

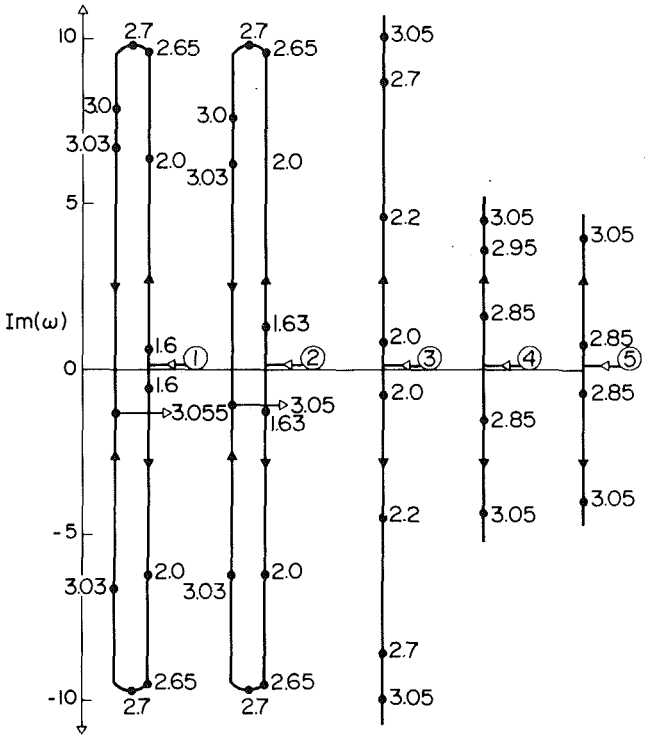

Fig. 3 The loci of the lowest five of the six eigenfrequencies of Fig. 2 whilst on the $Im(\omega)$-axis, drawn here off the axis and separated from one another for clarity

presence of hydrodynamic coupling in addition to structural coupling are (*i*) to render wider the frequency band within which the eigenfrequencies lie, and (*ii*) to maintain the separation between the eigenfrequencies even in the limiting cases at the extreme left and right of the figure. In connection with this last point, if only structural coupling is present, then the cylinders in the cluster behave almost as if they were independently supported—i.e., coupling effects become rather small.

The effect of flow on the dynamics of the system is studied next. Figures 2 and 3 show the evolution of the eigenfrequencies of the first-mode group, with increasing dimensionless flow velocity u, for a system with rather low out-of-plane stiffnesses but high in-plane stiffnesses. It is seen that two pairs of the eigenfrequencies are almost coincident, for any given u; had all the spring stiffnesses of a kind been taken equal, then the system would have been completely symmetric and there would have been two repeated eigenfrequencies (cf. [4]).

Discussion of the results of Figs. 2 and 3 will be aided by the realization that for a given complex eigenfrequency, ω_j,

$$\eta(\xi,\tau)\propto\exp(i\omega_j\tau)=\exp[iRe(\omega_j)\tau]\exp[-Im(\omega_j)\tau].$$

Hence, $Re(\omega_j)$ corresponds to the dimensionless frequency of oscillation in that mode, which is related to the dimensional radian frequency, Ω_j, by $\omega_j=\{(\rho A+m)/EI\}^{1/2}\Omega_j L^2$. Similarly, $Im(\omega_j)$, if positive, is related to damping, so that the damping ratio is $\zeta_j=Im(\omega_j)/Re(\omega_j)$; if $Im(\omega_j)<0$, this corresponds to negative damping, or amplification, of motions in that mode.

It is now seen in Fig. 2 that, with increasing flow, the $Re(\omega)$ are diminished, while the $Im(\omega)$ become finite and positive, indicating the existence of flow-induced damping in all the modes. At sufficiently high u, $Re(\omega)$ vanishes and the locus bifurcates on the $Im(\omega)$-axis, first for the lowest mode, and then successively for the others. The continuation of the loci on the $Im(\omega)$-axis is shown diagrammatically and separately in Fig. 3. It is seen that the locus of one of the branches of the lowest mode eventually crosses the origin, at $u\simeq 1.6$, indicating the onset of amplified motion; in this case, as $Re(\omega)=0$ at that point, this is the onset of divergence (buckling). The higher-mode loci behave in a similar manner. At $u\simeq 3.055$, the two branches of the first mode coalesce and leave the $Im(\omega)$-axis; at this point $Re(\omega)\neq 0$ and $Im(\omega)<0$, so that this point corresponds to the onset of oscillatory instability, or flutter. Similar results may be obtained for the second-mode group, the eigenfrequencies of which, at small u, are clustered about $4\pi^2$.

The results of Figs. 2 and 3 are similar to those previously found in references [3, 4] in the absence of structural coupling. This is not surprising, as the spring stiffnesses are such as to imply minimum structural coupling, the boundary conditions resembling those of cylinders with pinned-pinned ends.

On the other hand, for another range of spring constants, where structural coupling is much more pronounced, the results become far less "regular," as shown in Fig. 4. (The in-plane and out-of-plane stiffnesses in this case correspond to the middle range of the results shown in Fig. 7 of Part 1.) In this case the first and second-mode groups become intertwined, and one may distinguish one grouping of three modes which, for low u, lie in the range $3<Re(\omega)<6$, another grouping of six modes in the range $10.5<Re(\omega)<14$, both of which are shown in Fig. 4, and three other modes at higher $Re(\omega)$; the third-mode group remains distinct. The nature of these modes is rather perplexing, and will be discussed further when the eigenfunctions of the system are examined.

Another interesting and unusual feature of the results of Fig. 4 is that the mode loci can no longer be considered to be one family of curves, all of which behave alike with increasing flow. Thus, buckling in the first mode does not occur first with increasing flow, to be followed by buckling in the second, third, et seq modes; instead buckling occurs first in the *second* mode.

Comparing the flow velocities for the first onset of instability, u_{cb}, between Figs. 2 and 4, it is evident that they are dependent on the spring stiffnesses involved, which makes sense on physical grounds. The dependence of u_{cb} on the out-of-plane spring stiffnesses for a system with large in-plane stiffnesses is shown in Fig. 5. The two limiting cases of c_{ij}, $c'_{ij}\sim 0(10^{-3})$ and $\sim 0(10^3)$ compare well with those previously found [4] for the same system with (independently) ideally pinned and clamped ends, respectively. For intermediate values of the c_{ij} there is a smooth transition. The only noteworthy point that may be made here is that, so far as the values of u_{cb} are concerned, c_{ij}, $c'_{ij}<0(10^{-1})$ give sensibly the same results as for $c_{ij}=c'_{ij}\simeq 0$, and for c_{ij}, $c'_{ij}>0(10^2)$ one obtains almost the results corresponding to $c_{ij}=c'_{ij}\simeq\infty$.

The Eigenfunctions of the System

For a system of N independently supported (uncoupled) cylinders, one obtains $2N$ modes with basically the same axial modal shape, which corresponds to that of the first flexural mode of a beam with the same boundary conditions; these modes differ from one another in that the relative motions between the cylinders are distinctly different, i.e., they are associated with different "cross-sectional" modal patterns. Similarly, there is a group of $2N$ modes of second beam-mode axial modal shape, but with essentially the same cross-sectional modal patterns as those of the first-mode group; and so on. Here we shall examine the case of structurally coupled cylinders.

The modal shapes of a system with large in-plane stiffnesses and rather small out-of-plane stiffnesses are shown in Fig.

Downloaded 02 May 2010 to 171.66.16.246. Redistribution subject to ASME license or copyright; see http://www.asme.org/terms/Terms_Use.cfm

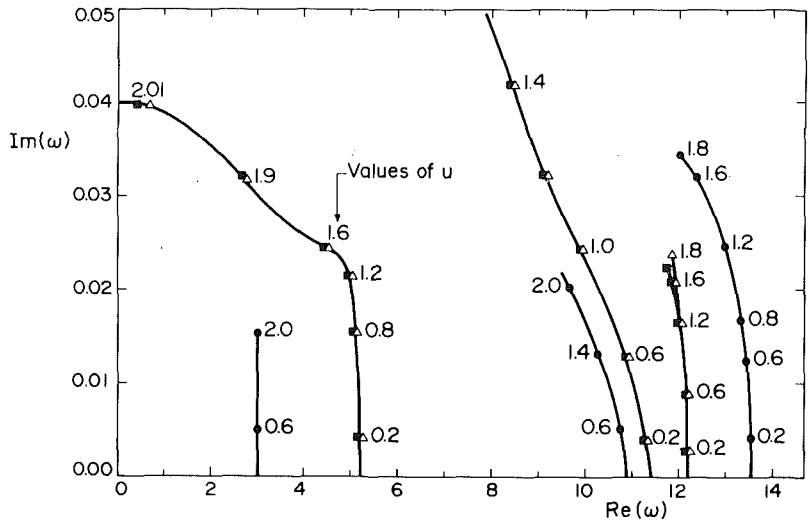

Fig. 4 The evolution of the nine lowest eigenfrequencies with increasing u, shown as an Argand diagram for a system with quite low in-plane stiffnesses and intermediate out-of-plane stiffnesses [$k_{ij} \sim 0(10)$, $k'_{ij} \sim 0(10^{-2})$, $c_{ij}, c'_{ij} \sim 0(10^{2})$, as given in Table A.3 of Part 1, with $k_{11} = 6.50$]. Other system parameters: $\beta = 0.1$, $\Gamma = \Pi = 0$, $\epsilon c_f = 0.25$, $h = 1.26$, $G_c = G_w = 1/4$.

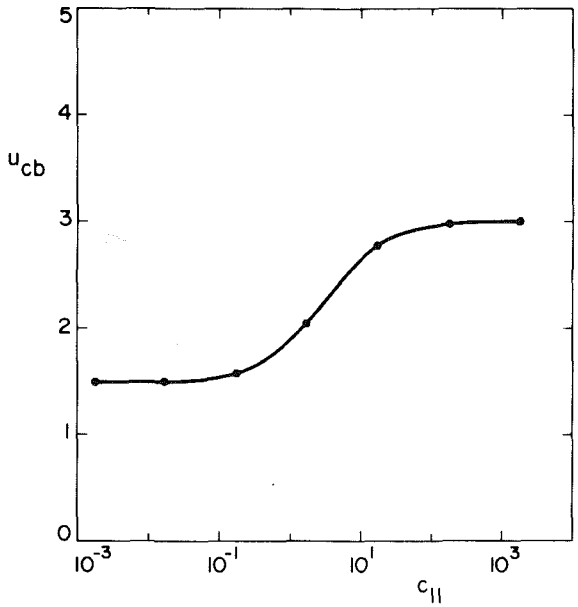

Fig. 5 The variation of the lowest dimensionless flow velocity, u_{cb}, for the onset of buckling for a system with large in-plane stiffnesses and variable out-of-plane stiffnesses. All the system parameters are the same as in Fig. 2.

6—for basically the system of Fig. 2, with $u = 0.5$. In Fig. 6(*a*) are shown the six distinctive cross-sectional modal patterns, which remain essentially the same for the first and second-mode groups, the animated axial mode shapes of which are shown in Figs. 6(*b*) and 6(*c*), respectively. These latter, in view of the spring stiffnesses involved, resemble those of a pinned-pinned beam.

Several points should be made. First, the cross-sectional modal patterns of Fig. 6(*a*) are closely similar to, and ordered in the same sequence as those of an ideally pinned-pinned system (cf. Fig. 3 of reference [4]). However, the angles between the vectors are not identical. Thus, for the ideally pinned system, the third-mode "implosion-explosion" pattern involves exactly equal vectors, disposed to one another at 120 deg; similarly, the sixth-mode pattern involves pure rotary motion about the center of the channel. In the case of Fig. 6(*a*), on the other hand, these ideal patterns are almost, but not quite, reproduced. This is so, simply because the spring stiffnesses c_{12}, c_{13}, c_{23} are not equal, nor c_{11}, c_{22}, and c_{33} (and similarly for the c'_{ij}); hence, the system is not truly symmetric, albeit geometrically symmetric.

A second point of interest is that there is no true node at the midpoint of the cylinder in Fig. 6(*c*). This is a well-known flow-induced phenomenon, associated with traveling wave components in the vibrations of the cylinders. Such effects become more pronounced with increasing flow.[4]

We turn next to the study of modal shapes of the system of Fig. 4, where the first and second-mode groups of eigenfrequencies are not separated, but rather appear to form a single group of 12 modes—vide also the eigenvalues in the middle range of Fig. 7 of Part 1 and the discussion pertaining thereto. The modal shape characteristics of the lowest 12 modes of this system are shown in Figs. 7 and 8. Here, unlike Fig. 6, the axial mode shape of Fig. 7(*b*) is associated with only the first three modes, while that of Fig. 7(*c*) with the next three; similarly, Fig. 8(*b*) is associated with modes 7, 8, and 9, while Fig. 8(*c*) with modes 10 to 12. Hence, this is an "unusual" system in many ways, deserving special attention.

Two important observations may be made. First, within each of Figs. 7 and 8, the upper three cross-sectional modal patterns are the same as the lower three. Second, the axial modal shapes of Figs. 7(*b*) and 8(*b*) are essentially similar, as are those of Figs. 7(*c*) and 8(*c*). Based on these two considerations, it may be said that the first three modes of Fig. 7 and those of Fig. 8 (i.e., modes 1, 2, 3, 7, 8, 9) form one modally cohesive group, and similarly modes 4 to 6 and 10 to 12 constitute another such group.

Consider next the form of the axial modal shapes. In view of the spring stiffnesses involved, these should resemble the modal shapes of a beam with sliding-sliding boundary conditions. This is verified by the modal shapes shown. Thus, the modal shapes of Figs. 7(*b*) and 8(*b*) resemble that of the first, or "null," rigid-body mode of a sliding-sliding beam, where the cylinders move essentially parallel to their long axes, while the modal shapes of Figs. 7(*c*) and 8(*c*) are similar to those of the second mode (first flexural mode) of a sliding-sliding beam.

[4] The calculations in Figs. 6–9 were purposely conducted with a small u to highlight mostly the structural coupling effects on system behavior.

Downloaded 02 May 2010 to 171.66.16.246. Redistribution subject to ASME license or copyright; see http://www.asme.org/terms/Terms_Use.cfm

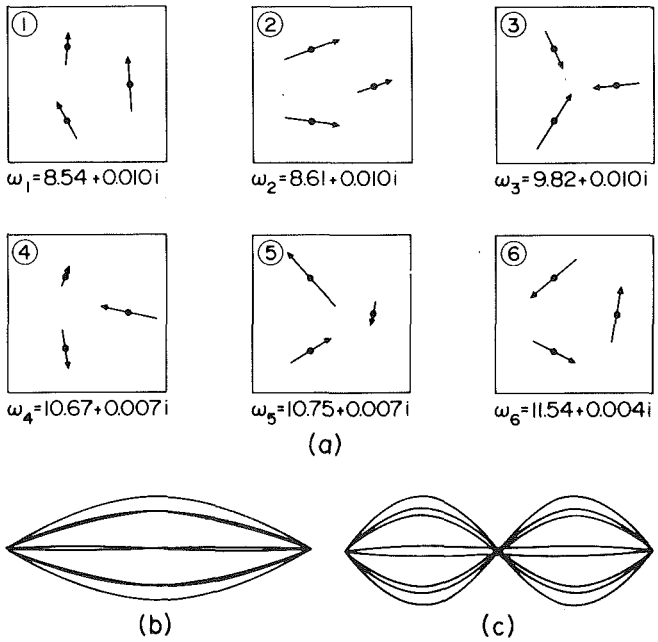

Fig. 6 Modal shapes of a system of three cylinders with large in-plane and small out-of-plane stiffnesses, corresponding to the parameters of Fig. 2 and $u = 0.5$. (*a*) Cross-sectional modal patterns of the first mode group; (*b*) and (*c*) typical axial modal shapes of the first and second-mode groups, respectively.

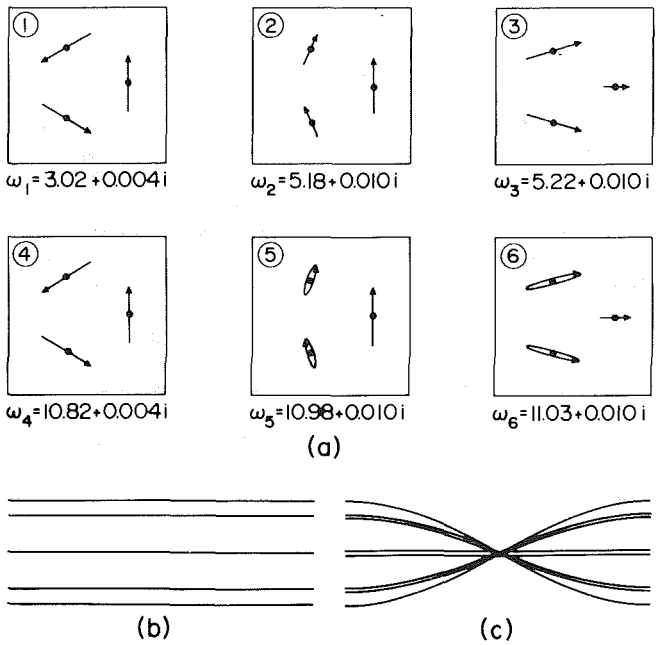

Fig. 7 The modal shapes of the six lowest modes of a system with quite low in-plane stiffnesses and intermediate out-of-plane stiffnesses [$k_{ij} \sim 0(10)$, $k'_{ij} \sim 0(10^{-2})$, c_{ij}, $c'_{ij} \sim 0(10^{2})$, as in Fig. 4]; system parameters as in Fig. 4, and $u = 0.5$. (*a*) Cross-sectional modal patterns; (*b*) and (*c*) typical axial modal shapes for the lowest three modes and the other three, respectively.

Hence, the discussion of the foregoing two paragraphs makes it obvious that one may distinguish a first-mode group consisting of modes 1 to 3 and 7 to 9, and a second-mode group consisting of modes 4 to 6 and 10 to 12. Thus, although the two groups of modes are intertwined and the highest eigenfrequency of the first-mode group is not lower than the lowest eigenfrequency of the second, one may nevertheless still distinguish individual mode groups. The preceding discussion also reinforces the view expressed in Part 1 that what happens in circumstances where both the c_{ij}, c'_{ij} and the k_{ij}, k'_{ij} are neither very small nor very large, the bands of first and second-mode eigenfrequencies become so wide as to intersect (vide Fig. 7 of Part 1).

A final point of interest in Figs. 7 and 8 is that in some cases orbital, rather than planar motion may be observed, e.g., in the cross-sectional patterns of the fifth and sixth modes in Fig. 7(*a*). Such patterns had been observed before in conjunction with repeated eigenvalues [3, 4]. Here, however, it is believed that this likely arises because of the differences that exist, in these cases, in the axial modal shapes in the y and z-directions; thus, although they are all similar to those shown here, the axial mode shapes for some of the cylinders are appreciably different in the two directions, e.g., in one direction they may be as in Fig. 7(*c*), while in the other the quasi-node at the cylinder midpoint is much more diffuse.

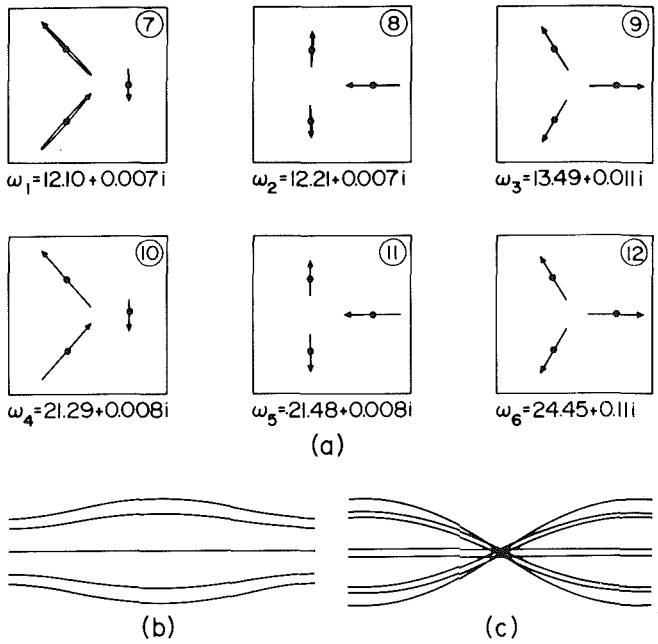

Fig. 8 The modal shapes of the six next to lowest modes of the system of Fig. 7. (*a*) Cross-sectional modal patterns; (*b*) and (*c*) typical axial modal shapes for, respectively, modes 7 to 9 and modes 10 to 12.

Figure 9 shows the modal shapes of a system with vanishingly small in-plane spring stiffnesses and out-of-plane stiffnesses relatively higher, but still one order of magnitude smaller than those in Figs. 7 and 8; thus, one might expect the system to behave similarly to one of free-free beams. Here the modes occur once more in distinct mode-groups; thus, the real parts of the first-mode group eigenfrequencies range from 7.37 to 9.72, while those of the second-mode group are clustered two decades higher. Moreover, once more the cross-sectional modal patterns of the first group of six modes, shown in Fig. 9(*a*) and associated with the axial mode shape of Fig. 9(*b*), are essentially identical to those of the second mode group (not shown) which have the axial mode shape shown in Fig. 9(*c*). Here it is also noted that Fig. 9(*b*) is the evolution of the modal pattern of Figs. 7(*c*) and 8(*c*). The "first-mode" group, associated with Figs. 7(*b*) and 8(*b*) still exists in this case, with essentially the modal shape of Fig. 7(*b*), but the associated eigenfrequencies become vanishingly small—i.e., as the spring stiffnesses tend to zero, that group is transformed into what might be called the "null-mode" group. In this connection the reader is referred to the discussion of Figs. 6 and 7 of Part 1 [1].

Conclusion

Various aspects of the dynamics of a system of cylinders were examined in this two-part study, where the cylinder

Downloaded 02 May 2010 to 171.66.16.246. Redistribution subject to ASME license or copyright; see http://www.asme.org/terms/Terms_Use.cfm

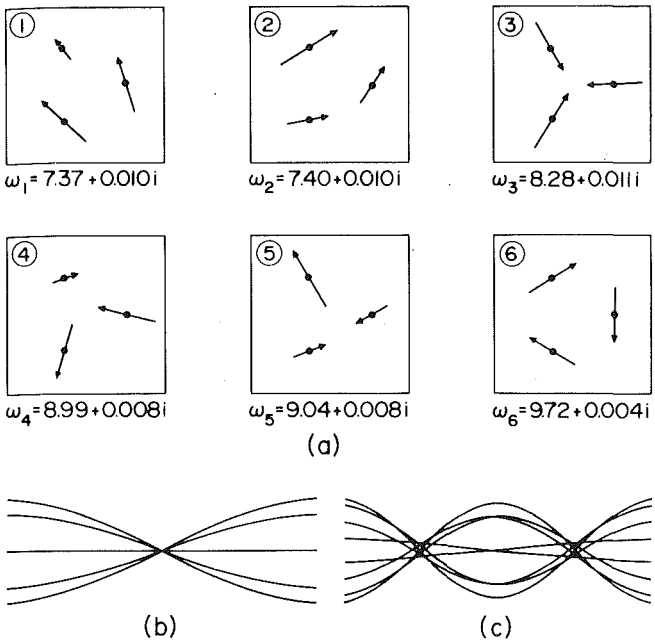

Fig. 9 The modal shapes of a system with vanishing in-plane and relatively higher out-of-plane stiffnesses [k_{ij}, $k'_{ij} \sim 0(10^{-4})$, c_{ij}, $c'_{ij} \sim 0(10)$, as given in Table A.2 of Part 1, with $c_{11} = 13.9$]; other parameters: $\beta = 0.1$, $\Gamma = \Pi = 0$, $\epsilon c_f = 0.25$, $h = 1.26$, $G_c = G_w = 1/4$, $u = 0.5$. (a) Cross-sectional modal patterns of the first-mode group; (b) and (c) typical axial modal shapes of the first and second-mode groups, respectively.

extremities were interconnected by a number of in-plane and out-of-plane springs, modeling physical connectors at these points. In Part 1 [1] the dynamics of the system were examined in vacuum, while the present paper was devoted to the study of the system in axial flow.

It was found that, provided that either the in-plane spring constants or the out-of-plane ones are either small or large, the system behavior is similar, but not identical, to that of a system of independently supported (structurally uncoupled) cylinders. Thus, the characteristics of the system in vacuum tend toward those of solitary beams with the appropriate boundary conditions, as in such cases there is effectively little intercylinder coupling of any kind; similarly, in axial flow, system behavior is similar to that of systems studied previously [3, 4], where structural coupling was not considered, but hydrodynamic coupling was. Indeed, in the limit of either very small or very large stiffnesses of the different types of springs involved, the system eigenfrequencies and modal characteristics approach those of systems with independent and ideal clamped, pinned, sliding, or free boundary conditions.

The foregoing are as one might expect. When one set of spring stiffnesses, however, is of intermediate magnitude, then structural coupling effects become pronounced, as may be seen in Fig. 1 (and in Figs. 5 and 6 of Part 1), and the frequency bands of the so-called mode groups become considerably broader; but, these mode groups remain distinct from one another. This broadening of the frequency band becomes more pronounced in the presence of fluid (Fig. 1), and more so in the presence of flow (Figs. 2 and 4). The relative importance of hydrodynamic and structural coupling depends on the fluid density and "tightness" of the cylinder geometry, as well as on the magnitude of the spring stiffnesses, all of which have been characterized by appropriate dimensionless numbers in the mathematical model developed here.

The most interesting case arises when all kinds of springs are of intermediate strength. Then the curious phenomenon occurs, where the first and second-mode groups, or even all the lowest three mode groups, merge. As shown here this may be thought to be a manifestation of extreme widening of the frequency bands of the different mode groups, leading to intertwining of the eigenfrequencies. One may still identify sets of $2N$ modes as belonging to distinct mode groups, but the ordering of the modes becomes irregular: as shown in conjunction with Figs. 7 and 8, the first mode group there consists of the first, second, third, seventh, eighth, and ninth modes of the system, where these modes have been numbered in ascending order of the eigenfrequencies.

The stability of the system was also examined—vide Figs. 2–5. For the systems studied, stability was lost by divergence, although it is expected that for different sets of spring stiffnesses, flutter may be the most critical mode of instability. The reason for not pursuing this latter point further is that in these circumstances the geometry of the leading and trailing ends of the cylinders becomes important from the fluid mechanics viewpoint [5], while these effects are not taken into account in this mathematical model. Nevertheless, for systems with firmly supported ends (i.e., fairly large k_{ij}, k'_{ij}), the transition from one limit of spring stiffnesses to the other is smooth (Fig. 5), and one may consider the pinned-pinned system as giving the most conservative estimate of the critical flow velocity.

All calculations presented were for three-cylinder clusters, in the interests of economy; systems of two cylinders have also been studied. Even so, the expenditure in terms of computational cost was considerable. This arises because, unlike the case of independently supported, structurally uncoupled systems (*i*) the comparison functions here involve *all* the cylinders, rather than just one, and (*ii*) the comparison functions are functionally dependent on the spring stiffnesses, so that they change as these latter are varied.

Finally, it should be noted that, in the calculations presented, the spring stiffnesses were varied arbitrarily, as if one were dealing with individual physical springs—which is justified in this type of fundamental study. However, for a real system, as one changes the thickness or width of the connectors, the spring stiffnesses would of course all be affected together. It is obvious that for a given physical system these stiffnesses may be estimated analytically. Better still, a simple finite-element model for the interconnecting structure may be constructed that would directly give the pertinent equivalent stiffnesses, and this is now being done, as an aid to designers.

Acknowledgments

The authors gratefully acknowledge the financial support that has made this research possible, under a research contract from the Whiteshell Nuclear Research Establishment of Atomic Energy of Canada Ltd. They also acknowledge Le Conseil des Arts du Canada for a scholarship to one of the authors.

References

1 Paidoussis, M. P., El Barbir, K. N., Genadry, M. R., and Chaubernard, J.-P., "Dynamics of a Cluster of Flexibly Interconnected Cylinders. Part 1: In Vacuum," ASME JOURNAL OF APPLIED MECHANICS, Vol. 50, 1983, pp. 421–428.

2 Paidoussis, M. P., "Fluidelastic Vibration of Cylinder Arrays in Axial and Cross Flow: State of the Art," *Journal of Sound and Vibration*, Vol. 76, 1981, pp. 329–360.

3 Paidoussis, M. P., "The Dynamics of Flexible Cylinders in Axial Flow: Theory and Experiments," *Journal of Sound and Vibration*, Vol. 65, 1979, pp. 391–417.

4 Paidoussis, M. P., and Suss, S., "Stability of a Cluster of Flexible Cylinders in Bounded Axial Flow," ASME JOURNAL OF APPLIED MECHANICS, Vol. 44, 1977, pp. 401–408.

5 Paidoussis, M. P., "Dynamics of Flexible Slender Cylinders in Axial Flow. Part 1: Theory," *Journal of Fluid Mechanics*, Vol. 26, 1966, pp. 717–736.

Downloaded 02 May 2010 to 171.66.16.246. Redistribution subject to ASME license or copyright; see http://www.asme.org/terms/Terms_Use.cfm

Application of Wiener-Hermite Expansion to Nonstationary Random Vibration of a Duffing Oscillator

A. Jahedi
Department of Mechanical Engineering,
Shiraz University,
Shiraz, Iran

G. Ahmadi
Department of Mechanical and
Industrial Engineering,
Clarkson College,
Potsdam, N.Y. 13676

Nonstationary random vibration of a Duffing oscillator is considered. The method of Wiener-Hermite series expansion of an arbitrary random function is reviewed and applied to the analysis of the response of a Duffing oscillator. Deterministic integral equations for the Wiener-Hermite kernel functions are derived and discussed. For the special case of a shaped white-noise excitation, the system of integral equations are solved by an iterative scheme and the mean square responses of a Duffing oscillator for various values of nonlinearity strength and damping coefficient are calculated and the results are elaborated in several graphs.

1 Introduction

Analysis of the response of linear and nonlinear systems subjected to random excitations is of considerable interest to the fields of mechanical and structural engineering.

When the amplitude of vibration is large or when the system undergoes a plastic deformation, nonlinear analysis must be employed. The development of the mathematical theory of nonlinear vibrations was started at the end of the last century by the work of Poincare [1] who laid the foundation of topological and perturbation methods for the study of weakly nonlinear systems.

Studies undertaken by Duffing [2] brought important contributions to the theory of nonlinear vibrations and drew attention to the importance of this theory in physics and engineering.

Response of linear systems subjected to stationary random excitations was investigated by several investigators as summarized for instance by Eringen [3], Crandall and Mark [4], Clough and Penzien [5], and Lin [6].

The problem of nonlinear random vibration has been considered in the past two decades. The common techniques for approximate analysis of nonlinear random systems are the method of equivalent linearization [7] and the perturbation technique [8]. The exact method of the Fokker-Planck equation [9] can only be used when the response is a Markov process [10].

An excellent review of the literature on the response of nonlinear systems to random excitation was provided by Caughey [11]. Analysis of the response of nonlinear plates to stationary random excitation was considered by Ahmadi, Tadjbakhsh, and Farshad [12]. Nonlinear strings and beams subjected to stationary random excitation were studied by Caughey [13] and Srinivasan and Vasudevan [14], respectively.

Progress in the theory of nonlinear random oscillation is reported by Spano and Iwan [15, 16], Spano [17, 18], and Roberts [19]. Recently, response of nonlinear systems under nonstationary random excitations was investigated by Ahmadi [20–22], Kaul and Penzien [23], Iwan and Mason [24], Wen [25], and Baber and Wen [26, 27]. An excellent review is provided by Spanos [28].

In the present study, the method of truncated Wiener-Hermite expansion is employed for analysis of the response of a Duffing nonlinear oscillator subjected to some nonstationary random excitations. The Wiener-Hermite series expansion method was developed by Cameron and Martin [29] and Wiener [30]. It was applied to a time invariant nonlinear system with white-noise input by Barret [31]. Meecham and Siegel [32] and Meecham and Jeng [33] applied the Wiener-Hermite method to the closure problem of Navier-Stokes turbulence. Recently, this technique was used in the analysis of strong electrostatic plasma turbulence by Ahmadi [34]. Wiener-Hermite expansion was also employed to represent the random ground acceleration during an earthquake by Ahmadi [35].

In the present analysis both the forcing function and the response of the Duffing oscillator are expanded on the random, statistically orthogonal Wiener-Hermite set. The series are truncated after the third terms. Deterministic equations for the time development of the Wiener-Hermite Kernel functions are derived and discussed. For the special case of a modulated, nonstationary white-noise excitation, the nonlinear integral equation for the first-order kernel function is solved by an iterative technique. The mean square responses of the Duffing oscillator are obtained for various

Contributed by the Applied Mechanics Division for publication in the JOURNAL OF APPLIED MECHANICS.

Discussion on this paper should be addressed to the Editorial Department, ASME, United Engineering Center, 345 East 47th Street, New York, N.Y. 10017, and will be accepted until two months after final publication of the paper itself in the JOURNAL OF APPLIED MECHANICS. Manuscript received by ASME Applied Mechanics Division, March, 1983; final revision, January, 1983.

Copyright © 1983 by ASME
Downloaded 02 May 2010 to 171.66.16.246. Redistribution subject to ASME license or copyright; see http://www.asme.org/terms/Terms_Use.cfm

ranges of values for damping coefficient and strength of nonlinearity. The results are presented in several figures.

2 Formulation

The basic equation for vibration of a nonlinear Duffing oscillator subjected to a random force $f(t)$ is given by

$$\ddot{x}+2\zeta\omega_0\dot{x}+\omega_0^2x+\epsilon\omega_0^2x^3=f(t), \tag{1}$$

where ω_0 is the natural frequency of the corresponding linear system, ζ is the damping coefficient, and ϵ is the strength of nonlinearity. Duffing equation (1) is encountered in the vibration of nonlinear plates as discussed for instance by Ahmadi [20] and Jahedi and Ahmadi [36].

To analyze the response of equation (1) to an arbitrary random force $f(t)$, the Wiener-Hermite expansion method is employed. The Wiener-Hermite is a complete set of statistically orthogonal random functions which was developed by Cameron and Martin [29] and Wiener [30]).

The first few terms of the Wiener-Hermite series are:

$$\begin{aligned}
&H^{(0)}=1,\\
&H^{(1)}(t)=n(t),\\
&H^{(2)}(t_1,t_2)=n(t_1)n(t_2)-\delta(t_1-t_2),\\
&H^{(3)}(t_1,t_2,t_3)=n(t_1)n(t_2)n(t_3)-n(t_1)\delta(t_2-t_3)\\
&\qquad -n(t_2)\delta(t_3-t_1)-n(t_3)\delta(t_1-t_2),
\end{aligned} \tag{2}$$

where $n(t)$ is a white-noise process with the following statistical properties

$$\begin{aligned}
&<n(t)>=0,\\
&<n(t_1)n(t_2)>=\delta(t_1-t_2),
\end{aligned} \tag{3}$$

and $\delta(\ )$ is the Dirac delta function. $<>$ stands for the expected value (ensemble average) operator. Elements of the Wiener-Hermite set are random variables with zero mean with the exception of the zeroth-order term, i.e.,

$$<H^{(i)}(t_1,t_2,\ldots t_i)>=0 \quad \text{for} \quad i\neq 0. \tag{4}$$

The Wiener-Hermite set is also an orthogonal set, i.e.,

$$<H^{(i)}(t_1,t_2,\ldots t_i)H^{(j)}(t_1',t_2',\ldots t_j')>=0 \quad \text{for} \quad i\neq j. \tag{5}$$

Furthermore, as shown by Wiener [30], the Wiener-Hermite set is a complete set in the sense that any arbitrary random function can be expanded in terms of a Wiener-Hermite set and the expansion converges to the original random function with probability one. Further properties of the Wiener-Hermite set is described in Appendix A.

The basic method for the use of the Wiener-Hermite expansion in the analysis of the response of a nonlinear system is the following: both the forcing and the response are expanded in terms of the Wiener-Hermite set. From the original governing equation deterministic equations are derived for the dynamics of the unknown kernel functions of the Wiener-Hermite expansion of the response, which involves the known kernels of the corresponding series for the forcing function. The Wiener-Hermite expansion series for the response must be truncated after a few terms. As discussed in Appendix A, the zeroth-order term in the Wiener-Hermite series corresponds to the mean value, the first-order term corresponds to the Gaussian part, and the second and higher-order terms correspond to the non-Gaussian part of the random function. Therefore, it is clear that the Wiener-Hermite method is capable of considering the non-Gaussian response of a nonlinear structure subjected to random load.

To analyze the response of a Duffing oscillator as given by equation (1), the functions $f(t)$ and $x(t)$ are expanded in terms of the Wiener-Hermite set. These are given by

$$\begin{aligned}
f(t)=&\int_{-\infty}^{+\infty}F^{(1)}(t,t_1)H^{(1)}(t_1)dt_1\\
&+\int_{-\infty}^{+\infty}\int_{-\infty}^{+\infty}F^{(2)}(t,t_1,t_2)H^{(2)}(t_1,t_2)dt_1dt_2+\ldots,
\end{aligned} \tag{6}$$

and

$$\begin{aligned}
x(t)=&\int_{-\infty}^{+\infty}A^{(1)}(t,t_1)H^{(1)}(t_1)dt_1\\
&+\int_{-\infty}^{+\infty}\int_{-\infty}^{+\infty}A^{(2)}(t,t_1,t_2)H^{(2)}(t_1,t_2)dt_1dt_2+\ldots,
\end{aligned} \tag{7}$$

where the mean values are taken to be zero and the higher-order terms are neglected. $F^{(1)}$ and $F^{(2)}$ are known deterministic kernel functions.

Employing (6) and (7) into equation (1), neglecting the second and third-order power of $A^{(2)}(t, t_1, t_2)$ and multiplying both sides of the equation by $H^{(1)}(t_5)$, taking the expected value, and using orthogonality properties of the Wiener-Hermite set, we find

$$\begin{aligned}
&\ddot{A}^{(1)}(t,t_5)+2\zeta\omega_0\dot{A}^{(1)}(t,t_5)+\omega_0^2A^{(1)}(t,t_5)\\
&\quad+<\epsilon\omega_0^2\int_{-\infty}^{+\infty}\int_{-\infty}^{+\infty}\int_{-\infty}^{+\infty}A^{(1)}(t,t_1)A^{(1)}(t,t_2)A^{(1)}(t,t_3)\\
&\qquad H^{(1)}(t_1)H^{(1)}(t_2)H^{(1)}(t_3)H^{(1)}(t_5)dt_1dt_2dt_3>\\
&\quad+<3\epsilon\omega_0^2\int_{-\infty}^{+\infty}\int_{-\infty}^{+\infty}\int_{-\infty}^{+\infty}\int_{-\infty}^{+\infty}A^{(1)}(t,t_1)A^{(1)}(t,t_2)\\
&\qquad A^{(2)}(t,t_3,t_4)H^{(1)}(t_1)H^{(1)}(t_2)H^{(1)}(t_5)H^{(2)}(t_3,t_4)\\
&\qquad dt_1dt_2dt_3dt_4>=F^{(1)}(t,t_5).
\end{aligned} \tag{8}$$

Employing equations (A-3) and (A-6) of Appendix A, after some algebra, equation (8) reduces to

$$\begin{aligned}
&\ddot{A}^{(1)}(t,t_1)+2\zeta\omega_0\dot{A}^{(1)}(t,t_1)+\omega_0^2A^{(1)}(t,t_1)\\
&\quad+2\epsilon\omega_0^2A^{(1)}(t,t_1)\int_{-\infty}^{+\infty}[A^{(1)}(t,t_2)]^2dt_2=F^{(1)}(t,t_1).
\end{aligned} \tag{9}$$

Now if equation (1) in which $x(t)$ and $f(t)$ are replaced by their respective series expansions as given by equations (7) and (8), are multiplied by $H^{(2)}(t_2, t_1)$, after taking the expected value and using orthogonality properties of the Wiener-Hermite polynomials, the result is

$$\begin{aligned}
&2\ddot{A}^{(2)}(t,t_1,t_2)+4\zeta\omega_0\dot{A}^{(2)}(t,t_1,t_2)+2\omega_0^2A^{(2)}(t,t_1,t_2)\\
&+<3\epsilon\omega_0^2\int_{-\infty}^{+\infty}\int_{-\infty}^{-\infty}\int_{-\infty}^{+\infty}\int_{-\infty}^{+\infty}A^{(1)}(t,t_5)A^{(1)}(t,t_6)A^{(2)}(t,t_3,t_4)\\
&H^{(1)}(t_5)H^{(1)}(t_6)H^{(2)}(t_1,t_2)H^{(2)}(t_3,t_4)>\\
&\qquad=F^{(2)}(t,t_1,t_2).
\end{aligned} \tag{10}$$

Simplifying the fourth term in equation (10) by the use of equation (A-6), we find

$$\begin{aligned}
&\ddot{A}^{(2)}(t,t_1,t_2)+2\zeta\omega_0\dot{A}^{(2)}(t,t_1,t_2)+\omega_0^2A^{(2)}(t,t_1,t_2)\\
&\quad+6\epsilon\omega_0^2A^{(1)}(t,t_1)\int_{-\infty}^{+\infty}A^{(1)}(t,t_3)A^{(2)}(t,t_2,t_3)dt_3\\
&\quad+6\epsilon\omega_0^2A^{(1)}(t,t_2)\int_{-\infty}^{+\infty}A^{(1)}(t,t_3)A^{(2)}(t,t_1,t_3)dt_3\\
&+6\epsilon\omega_0^2A^{(2)}(t,t_1,t_2)\int_{-\infty}^{+\infty}(A^{(1)}(t,t_3))^2dt_3=F^{(2)}(t,t_1,t_2).
\end{aligned} \tag{11}$$

Equations (9) and (11) are two deterministic equations for finding the two unknown kernel functions $A^{(1)}$ and $A^{(2)}$. It is observed that for the present case of a Duffing oscillator,

Downloaded 02 May 2010 to 171.66.16.246. Redistribution subject to ASME license or copyright; see http://www.asme.org/terms/Terms_Use.cfm

equation (9) for $A^{(1)}$ is decoupled from equation (11) and can be solved independently. The solution for $A^{(1)}$ may then be employed in equation (11) and the unknown function $A^{(2)}$ may then be calculated. This decoupling simplifies the numerical calculations to a considerable extent. When $A^{(1)}$ and $A^{(2)}$ are known, equation (7) gives the Wiener-Hermite representation of the nonlinear response. From the series (7) all the statistical properties of the random process $x(t)$ could be calculated. For instance the variance of $x(t)$ is given by

$$\sigma^2(t) = \langle x^2(t) \rangle = \int_{-\infty}^{+\infty} [A^{(1)}(t,t_1)]^2 dt_1 + 2\int_{-\infty}^{+\infty}\int_{-\infty}^{+\infty} [A^2(t,t_1,t_2)]^2 dt_1 dt_2. \tag{12}$$

The formulation given by equations (9) and (11) are quite general and could be used for analysis of the response of the Duffing oscillator subjected to an arbitrary, stationary, or nonstationary Gaussian or non-Gaussian random excitation. These equations are exact up to the second-order terms in the Wiener-Hermite series. Considerations of third and higher-order terms would of course lead to more accurate results.

3 Response to Modulated White-Noise Excitations

In this section, the special case, when the excitation $f(t)$ is a modulated white-noise process is considered. The expansion of $f(t)$ in terms of the Wiener-Hermite set is given by

$$f(t) = \int_{-\infty}^{+\infty} F(t,t_1) H^{(1)}(t_1) dt_1, \tag{13}$$

where its mean value and non-Gaussian parts are zero. Now let the Kernel $F(t, t_1)$ be given by

$$F(t,t_1) = e(t_1)\delta(t-t_1), \tag{14}$$

where $e(t_1)$ is a deterministic envelope function. In this special case the explicit form of the excitation given by equation (13) becomes

$$f(t) = e(t) H^{(1)}(t) = e(t) n(t). \tag{15}$$

For solving equation (9) with $F(t, t_1)$ being given by equation (14) it is assumed that

$$A^{(1)}(t,t_1) = \begin{cases} e(t_1)a(t-t_1) & t \geq t_1 \\ 0 & t < t_1 \\ 0 & t_1 < 0. \end{cases} \tag{16}$$

Since $F^{(2)}$ is identically equal to zero, equation (11) satisfies the trivial solution

$$A^{(2)}(t,t_1,t_2) = 0. \tag{17}$$

Employing equations (14) and (16) into equation (9), and measuring time from the origin of t_1, we find

$$\ddot{a}(t) + 2\zeta\omega_0 \dot{a}(t) + \omega_0^2 a(t) + 3\epsilon\omega_0^2 a(t) \int_0^t e^2(t') a^2(t-t') dt' = \delta(t). \tag{18}$$

The variance of $x(t)$ as given by equation (12) now becomes

$$\sigma^2(t) = \int_{-\infty}^{+\infty} e^2(t-\theta) a^2(\theta) d\theta. \tag{19}$$

When $a(t)$ is found from the solution of equation (18), equation (19) gives the variance of the response for an arbitrary envelope function $e(t)$.

Some envelope functions of interest are considered here.

(*a*) If $e(t)$ is a unit step function

$$e(t) = \begin{cases} 1 & t \geq 0 \\ 0 & t < 0 \end{cases} \tag{20}$$

then from equation (19), it follows that

$$\sigma^2(t) = \int_0^t a^2(\theta) d\theta. \tag{21}$$

(*b*) If $e(t)$ is unity for a finite time duration t_0, i.e.,

$$e(t) = \begin{cases} 1 & 0 \leq t \leq t_0, \\ 0 & \text{otherwise}, \end{cases} \tag{22}$$

the expression for the response variance then becomes

$$\sigma^2(t) = \begin{cases} \int_0^t a^2(\theta) d\theta & 0 \leq t \leq t_0, \\ \int_{t-t_1}^t a^2(\theta) d\theta & t > t_0. \end{cases} \tag{23}$$

(*c*) If $e(t)$ is a decaying exponential function

$$e(t) = \begin{cases} e^{-\gamma t} & t \geq 0, \\ 0 & t < 0, \end{cases} \tag{24}$$

the expression for the response variance then becomes

$$\sigma^2(t) = \begin{cases} \int_0^t \exp\{-2\gamma(t-\theta)\} a^2(\theta) d\theta \; t \geq 0, \\ 0 \qquad\qquad t < 0. \end{cases} \tag{25}$$

Several other envelope functions could be employed. However, these examples show the procedure and some of the most used envelope functions.

In the absence of nonlinearity, equation (18) reduces to

$$\ddot{a}(t) + 2\zeta\omega_0 \dot{a}(t) + \omega_0^2 a(t) = \delta(t), \tag{26}$$

the solution of which is given by

$$a(t) = \frac{1}{\omega_D} e^{-\zeta\omega_0 t} \sin(\omega_D t), \tag{27}$$

where

$$\omega_D = \omega_0 \sqrt{1-\zeta^2}. \tag{28}$$

For a unit-step envelope function, substituting for $a(t)$ from equation (28) into equation (21) and neglecting the second-order terms in damping coefficient, the mean square response becomes

$$\sigma^2(t) = \frac{1}{4\zeta\omega_0^3}(1 - e^{-2\zeta\omega_0 t}) - \frac{1}{8\omega_D^4}[2\omega_D \sin 2\omega_D t - 2\zeta\omega_D \cos 2\omega_D t) e^{-2\zeta\omega_0 t} + 2\zeta\omega_0]. \tag{29}$$

If the second bracket of equation (29) which is small with respect to the first term is neglected, it reduces to

$$\sigma^2(t) = \frac{1}{4\zeta\omega_0^3}(1 - e^{-2\zeta\omega_0 t}). \tag{30}$$

Downloaded 02 May 2010 to 171.66.16.246. Redistribution subject to ASME license or copyright; see http://www.asme.org/terms/Terms_Use.cfm

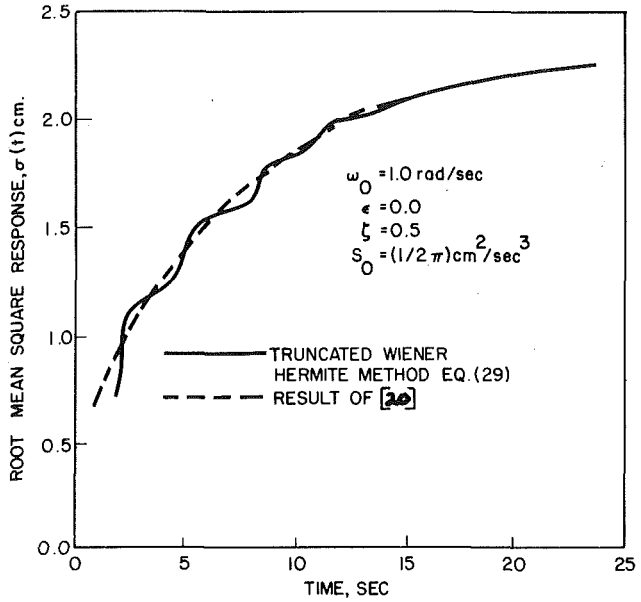

Fig. 1 Root mean square response of a Duffing oscillator for a white noise excitation with a unit step envelope function

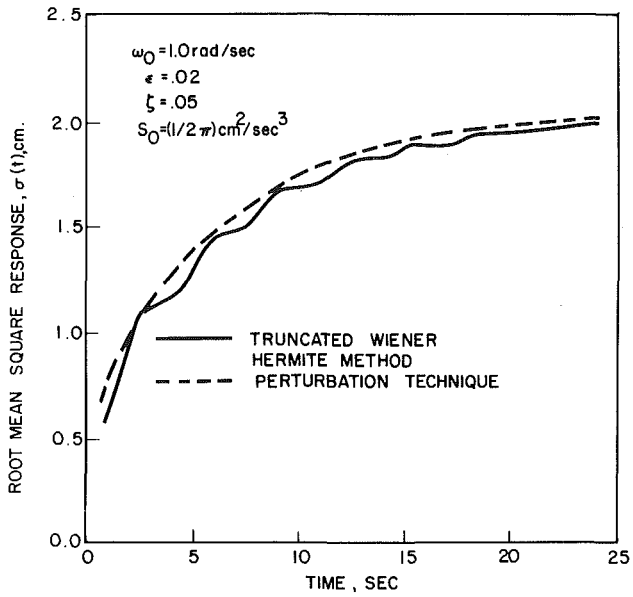

Fig. 2 Root mean square response of a Duffing oscillator for a white noise excitation with a unit step envelope function

Equation (30) is the same equation as found by Ahmadi [20] for the zeroth-order perturbation of the same problem. The second bracket of (29) was neglected in [20].

Figure 1 shows the standard deviations of the response of a linear system to a modulated white noise (envelope function being a unit step function) as predicted by equations (29) and (30). It is observed that the results are very close and the slight difference is due to the terms neglected in [20].

For the original nonlinear Duffing equation, the nonlinear integrodifferential equation given by (18) must be solved. An iterative scheme for the solution is adapted here. First, equation (18) for the case of a unit-step envelope function is rewritten as

$$\ddot{a}(t)+2\zeta\omega_0\dot{a}(t)+\omega_0^2 a(t)=\delta(t)-3\epsilon\omega_0^2 a(t)\int_0^t a^2(t)\,dt. \tag{31}$$

The iteration scheme starts by neglecting the nonlinear term on the right-hand side of equation (31) in the zeroth-order iteration. The solution of the resulting linear equation, which is identical to equation (26) for $a(t)$, is given by equation (27). In the first-order iteration the approximate value of the nonlinear term is found by using the previously calculated estimate of $a(t)$. Then, in the next iteration it is treated as a part of the excitation of the right-hand side of equation (31). The new estimate $a_1(t)$ of the response is found by numerical evaluation of the convolusion integral

$$a_1=\int_0^t h(t-\tau)f(\tau,a_0(\tau))\,d\tau, \tag{32}$$

where $h(t)$ is the impulse response of the linearized equation (26) given by equation (27).

The iteration is continued by replacing a_0 on the right-hand side of equations (31) and (32) by a_1 and evaluating a_2 by numerical integration of (32). For the present problem the iteration was continued until at two successive iterations the absolute values of the differences of $a_n(t)$ with the previous iteration $a_{n-1}(t)$ became less than one-thousandth of the absolute value of a_{n-1} for all the time steps considered. A simple Simpson rule of integration is employed throughout for numerical evaluation of the integrals. The final solution $a_n(t) = a(t)$ is used in equation (21) for evaluation of the mean square response of the Duffing oscillator.

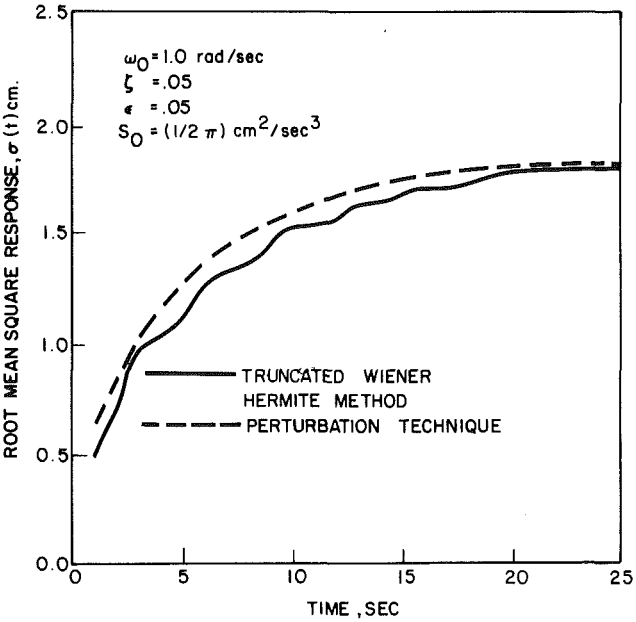

Fig. 3 Root mean square response of a Duffing oscillator for a white noise excitation with a unit step envelope function

Some examples of the results of the present analysis together with those obtained by the perturbation method in [20] are shown in Figs. 2 and 3. It is observed that the differences of the standard deviations as found by these two methods increases slightly as the strength of nonlinearity increases. However, the values of the root mean square responses as found by the present truncated Wiener-Hermite method remain slightly less than the corresponding ones found by the perturbation method all the time. The time variations of the calculated standard deviations for different natural frequencies are plotted in Fig. 4. It is observed that, as the natural frequency increases, the value of the root mean square response of the Duffing oscillator decreases. This is because the square of natural frequency appears as the coefficient of nonlinearity in equation (1). An example of the

Downloaded 02 May 2010 to 171.66.16.246. Redistribution subject to ASME license or copyright; see http://www.asme.org/terms/Terms_Use.cfm

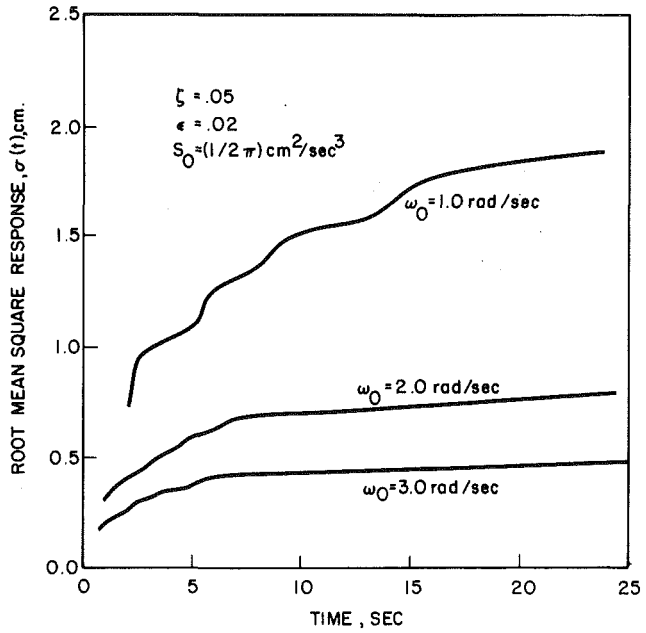

Fig. 4 Root mean square response for different natural frequencies

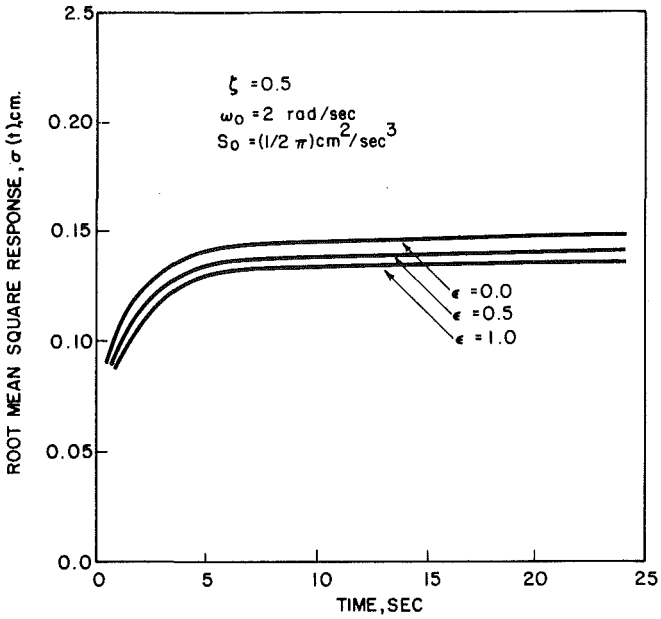

Fig. 6 Root mean square response for different nonlinearity coefficients

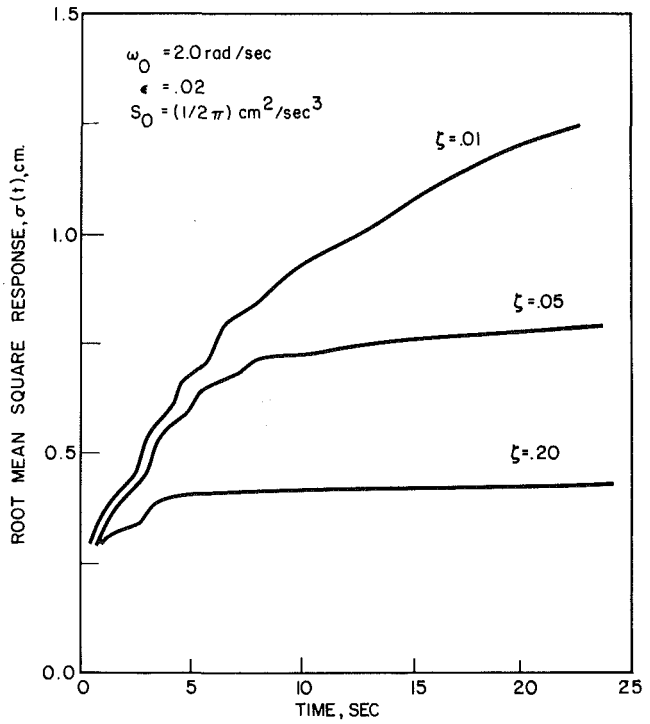

Fig. 5 Root mean square response for different damping coefficients

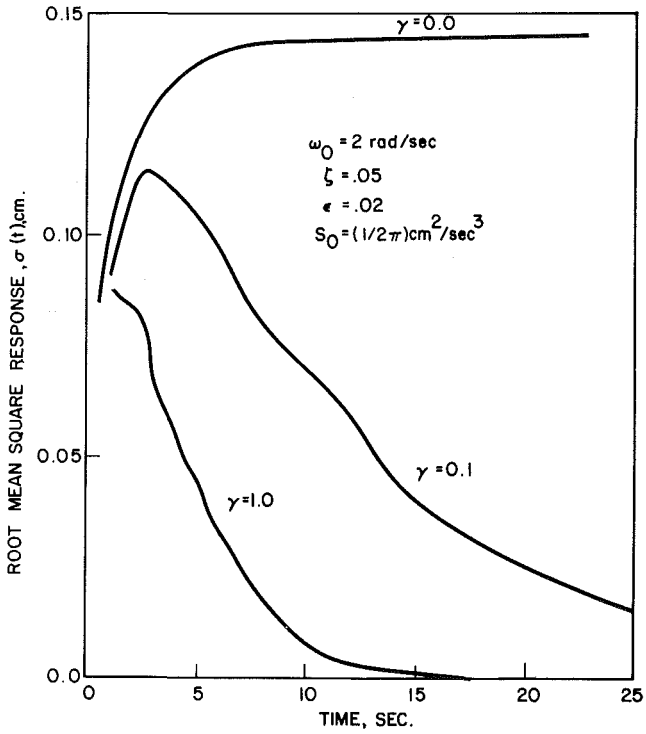

Fig. 7 Root mean square response for a white noise excitation with an exponential envelope function

effect of damping coefficient on the response of the Duffing oscillator is shown in Fig. 5.

Figure 6 shows the effect of nonlinearity strength on the root mean square response. It is observed that the magnitude of the standard deviation of the response decreases with an increase in the nonlinearity strength, as is expected for the hardening spring of the Duffing oscillator.

All the results presented in Figs. 1-6 correspond to a unit-step envelope function. When the envelope function is a decaying exponential, the value of the mean square response should be calculated by using equation (25). The method of numerical calculation is almost the same as that discussed for the case of a unit-step envelope function. Figure 7 shows the time variations of the standard deviation of the response for various levels of nonlinearity for the case of an exponential envelope function given by equation (24). It is observed that when γ is zero, root mean square response increases rapidly to a constant level in agreement with the results obtained for the unit-step envelope function. But when γ is finite, the response curves increase to a maximum point and then decrease to zero gradually. For the example shown in Fig. 7, the maximum of the curve of the root mean square response for $\gamma = 0.1$ occurs at 2.5 sec, and the maximum of root mean square response for $\gamma = 1.0$ occurs at 1 sec.

Downloaded 02 May 2010 to 171.66.16.246. Redistribution subject to ASME license or copyright; see http://www.asme.org/terms/Terms_Use.cfm

4 Conclusion and Discussion

Mean square responses of a Duffing equation are found by the truncated Wiener-Hermit method for the cases when the excitation is a modulated white noise with unit-step or exponential envelope functions. It is shown that, for slightly nonlinear systems, the results of the truncated Wiener-Hermite method are the same as those found by the perturbation technique. It is observed that, for nonlinear systems with large nonlinearities, the values of the variance of the response found by the present truncated Wiener-Hermite method are less than the corresponding ones found by the perturbation technique. Also it is observed that, as the nonlinearity strength increases, the magnitude of the differences of the results of these two methods increases to an extent. The effects of damping coefficient, natural frequency, and nonlinearity strength on the root mean square response of Duffing equation are shown in several plots. It is observed that the increase of these three parameters cause the values of the variances of the system response to decrease.

It is concluded that the present method is a useful technique for analyzing nonlinear systems with large nonlinearities where the perturbation method is no longer applicable. A truncated Wiener-Hermite method could also be employed in the analysis of nonlinear systems with general non-Gaussian excitations where the well-known technique of the Fokker-Planck equation is no longer applicable.

The method is also superior to the most common technique of equivalent linearization by its capability of inclusion of non-Gaussianity of the response statistics. However, these advantages are at the expense of complexity encountered in dealing with integrodifferential equations. The iteration scheme employed in this study appears to work reasonably well for single-degree-of-freedom systems. But for multidegree-of-freedom structures some suitable numerical schemes should be developed. Such studies are under consideration and the results will be reported in the near future.

Acknowledgments

This work is based on the MS thesis of the first author which was carried out at the Department of Mechanical Engineering, Shiraz University, Shiraz, Iran.

References

1 Poincare, H., *Les Methods Nouvelles de la Mecanique Celeste*, Vols. 1-3, Gauthier Villars, Paris, 1899.

2 Duffing, G., "Erzwungene Schwgungen bei veranderlicher Eigenfrequenz und ihre technische Bedeutung," PhD. Thesis, Summlung Vieweg, Braunschweig, 1918.

3 Eringen, A. C., *Hand Book of Mechanical Engineering Science*, Flugge, ed., McGraw-Hill, New York, 1962.

4 Crandall, S. H., and Mark, W. D., *Random Vibration in Mechanical Systems*, Academic Press, New York, 1963.

5 Clough, R. W., and Penzien, J., *Dynamics of Structure*, McGraw-Hill, New York, 1975.

6 Lin, Y. K., *Probabilistic Theory of Structural Dynamics*, McGraw-Hill, New York, 1967.

7 Caughey, T. K., "Equivalent Linearization Techniques," *J. Acoust. Soc. Am.*, Vol. 35, 1963, pp. 1706-1711.

8 Crandall, S. H., "Perturbation Techniques for Random Vibration of Nonlinear Systems," *J. Acoust. Soc. Am.*, Vol. 35, 1963, pp. 1700-1705.

9 Caughey, T. K., "Derivation and Application of the Fokker-Planck Equation to Discrete Nonlinear Dynamic Systems Subjected to White Random Excitation," *J. Acoust. Am.*, Vol. 35, 1963, pp. 1683-1692.

10 Papoulis, A., *Probability, Random Processes and Stochastic Process*, McGraw-Hill, New York, 1965.

11 Caughey, T. K., "Nonlinear Theory of Random Vibration," *Advances in Applied Mechanics*, Yih, C. H., ed., Vol. 11, Academic Press, New York, 1971.

12 Ahmadi, G., Tadjbakhsh, I., and Farshad, M., "On the Response of Nonlinear Plate to Random Load," *Acoustica*, Vol. 48, 1978, pp. 316-322.

13 Caughey, T. K., "Response of Nonlinear String to Random Load," ASME JOURNAL OF APPLIED MECHANICS, Vol. 26, 1959, pp. 341-344.

14 Srinivasan, S. K., and Vasudevan, R. V., *Introduction to Random Differential Equation and Their Application*, Elsevier, New York, 1971.

15 Spano, P-T. D., and Iwan, W. D., "The Existence and Uniqueness of Solution Generated by Equivalent Linearization," *Int. J. Nonlinear Mech.*, Vol. 13, 1978, pp. 71-78.

16 Iwan, W. D., and Spano, P-T. D., "Response Envelope Statistics for Nonlinear Oscillators with Random Excitation," ASME JOURNAL OF APPLIED MECHANICS, Vol. 45, 1978, pp. 170-174.

17 Spano, P-T. D., "Stochastic Analysis of Oscillator With Nonlinear Damping," *Int. J. Nonlinear Mech.*, Vol. 13, 1978, pp. 249-259.

18 Spano, P-T. D., "Hysteretic Structural Vibrations Under Random Load," *J. Acoust. Soc. Am.*, Vol. 65, 1979, pp. 404-410.

19 Roberts, J. B., "The Energy Envelope of a Randomly Excited, Nonlinear Oscillator," *J. Sound Vibration*, Vol. 60, 1978, pp. 177-185.

20 Ahmadi, G., "Earthquake Response of Nonlinear Plates," *Nuclear Engineering and Design*, Vol. 54, 1979, pp. 407-417.

21 Ahmadi, G., "Mean Square Response of a Duffing Oscillator to a Modulated White Noise Excitation by the Generalized Method of Equivalent Linearization," *J. Sound Vibration*, Vol. 71, 1980, pp. 9-15.

22 Ahmadi, G., "Nonstationary Random Vibration of a Nonlinear System With a Set-Up Spring," *Acoustica*, Vol. 48, 1981, pp. 50-53.

23 Kaul, M. K., and Penzien, J., "Stochastic Seismic Analysis of Yielding Offshore Towers," *J. Eng. Mech. Div.*, ASCE, Vol. 100, 1974, pp. 1025-1037.

24 Iwan, W. D., and Mason, B., "Equivalent Linearization for Systems Subjected to Nonstationary Random Excitation," *Int. J. Nonlinear Mech.*, Vol. 15, 1980, pp. 71-82.

25 Wen, Y. K., "Equivalent Linearization for Hysteretic Systems Under Random Excitation," ASME JOURNAL OF APPLIED MECHANICS, Vol. 47, 1980, pp. 150-154.

26 Baber, T. T., and Wen, Y. K., "Random Vibration of Hysteretic Degrading Systems," *J. Eng. Mech. Div.*, ASCE, Vol. 107, 1981, pp. 1069-1087.

27 Baber, T. T., and Wen, Y. K., "Stochastic Response of Multistory Yielding Frames," *Earthquake Eng. Struct. Dynamics*, Vol. 10, 1982, pp. 403-416.

28 Spanos, P. T. D., "Stochastic Linearization in Structural Dynamics," *Appl. Mech. Review*, Vol. 34, 1981, pp. 1-8.

29 Cameron, R. H., and Martin, W. T., "The Orthogonal Development of Nonlinear Functionals in Series of Furier-Hermite Functionals," *J. Ann. Math.*, Vol. 48, 1947, pp. 385-392.

30 Wiener, N., *Nonlinear Problem in Random Theory*, Wiley, New York, 1958.

31 Barret, J. F., "Hermite Functional Expansions and Calculation of Output Autocorrelation and Spectrum for any Time Invariant Nonlinear System With White Noise Input," *Nonlinear Stochastic Control System*, Fuller, A. T., ed., Taylor and Francis Ltd., 1963.

32 Meecham, W. C., and Siegel, A., "Wiener-Hermite Expansion in Model Turbulence at Large Reynolds Numbers," *Physics Fluid*, Vol. 7, 1964, pp. 1178-1190.

33 Meecham, W. C., and Jeng, D. T., "Use of Wiener-Hermite Expansion for Nearly Normal Turbulence, *J. Fluid Mech.*, Vol. 32, 1968, pp. 225-249.

34 Ahmadi, G., "Wiener-Hermite Closure Method in Strong Plasma Turbulence," Presented in the 35th Meeting of the American Physical Society, Division of Fluid Mechanics, Rutgers University, Nov. 21-23, 1982.

35 Ahmadi, G., "A Note on the Wiener-Hermite Representation of the Earthquake Ground Acceleration," *Mech. Research Comm.*, Vol. 7, 1980, pp. 7-11.

36 Jahedi, A., and Ahmadi, G., "Applications of Truncated Wiener-Hermite Expansion to Nonlinear Vibration With Application to Nonlinear Plates," Shiraz University, Mech. Eng. Research Report 80-1, 1980.

APPENDIX A

The Wiener-Hermite polynomials satisfy the following relationships

$$H^{(1)}(t_1)H^{(1)}(t_2)=H^{(2)}(t_1,t_2)+\delta(t_1-t_2),$$

$$H^{(1)}(t_1)H^{(2)}(t_2,t_3)=H^{(3)}(t_1,t_2,t_3)+\delta(t_1-t_2)H^{(1)}(t_3)+\delta(t_2-t_3)H^{(1)}(t_1)+\delta(t_1-t_3)H^{(1)}(t_2), \quad (A\text{-}1)$$

$$H^{(1)}(t_1)H^{(3)}(t_2,t_3,t_4)=H^{(4)}(t_1,t_2,t_3,t_4)+\delta(t_1-t_2)H^{(2)}(t_3,t_4)+\delta(t_1-t_3)H^{(2)}(t_2,t_4)+\delta(t_1-t_4)H^{(2)}(t_2,t_3), \quad (A\text{-}2)$$

$$H^{(2)}(t_1,t_2)H^{(2)}(t_3,t_4)=H^{(4)}(t_1,t_2,t_3,t_4)+\delta(t_1-t_3)\times H^{(2)}(t_2,t_4)+\delta(t_1-t_4)H^{(2)}(t_2,t_3)+\delta(t_2-t_3)\times H^{(2)}(t_1,t_4)+\delta(t_2-t_4)H^{(2)}(t_1,t_3)+\delta(t_1-t_3)\times\delta(t_2-t_4)+\delta(t_1-t_4)\delta(t_2-t_3). \quad (A\text{-}3)$$

Downloaded 02 May 2010 to 171.66.16.246. Redistribution subject to ASME license or copyright; see http://www.asme.org/terms/Terms_Use.cfm

The Wiener-Hermite polynomials satisfy the following statistical properties:

$$<H^{(0)}H^{(0)}>=1, \tag{A-4}$$

$$<H^{(1)}(t_1)H^{(1)}(t_2)>=\delta(t_1-t_2),$$

$$<H^{(2)}(t_1,t_2)H^{(2)}(t_3,t_4)>=\delta(t_1-t_3)\delta(t_2-t_4),$$

$$+\delta(t_1-t_4)\delta(t_2-t_3), \tag{A-5}$$

$$<H^{(2)}(t_1,t_2)H^{(2)}(t_3,t_4)H^{(1)}(t_5)H^{(1)}(t_6)>=$$

$$\delta(t_1-t_3)\delta(t_5-t_2)\delta(t_6-t_4)$$

$$+\delta(t_1-t_3)\delta(t_5-t_4)\delta(t_6-t_2)$$

$$+\delta(t_1-t_4)\delta(t_5-t_2)\delta(t_6-t_3)$$

$$+\delta(t_1-t_4)\delta(t_6-t_2)\delta(t_5-t_3)$$

$$+\delta(t_2-t_3)\delta(t_1-t_5)\delta(t_4-t_6)$$

$$+\delta(t_2-t_3)\delta(t_1-t_6)\delta(t_5-t_4)$$

$$+\delta(t_2-t_4)\delta(t_5-t_1)\delta(t_6-t_3)$$

$$+\delta(t_2-t_4)\delta(t_6-t_1)\delta(t_5-t_3)$$

$$+\delta(t_5-t_6)\delta(t_1-t_3)\delta(t_2-t_1)$$

$$+\delta(t_5-t_6)\delta(t_1-t_4)\delta(t_2-t_3). \tag{A-6}$$

A random function $g(t)$ could be expanded in terms of a Wiener-Hermit set, i.e.,

$$g(t)=G^{(0)}(t)H^{(0)}+\int_{\infty}^{\infty}G^{(1)}(t,t_1)H^{(1)}(t_1)dt_1$$

$$+\int_{-\infty}^{\infty}\int_{-\infty}^{\infty}G^{(2)}(t,t_1,t_2)H^{(2)}(t_1,t_2)dt_1dt_2$$

$$+\int_{\infty}^{-\infty}\int_{-\infty}^{\infty}\int_{-\infty}^{\infty}G^{(3)}(t,t_1,t_2,t_3)H^{(3)}(t_1,t_2t_3)dt_1dt_2dt_3,$$

$$+\ldots\ldots \tag{A-7}$$

where $G^{(0)}(t)$ is the mean of $g(t)$. The second term is the Gaussian part and the rest of the terms are non-Gaussian parts of $g(t)$. The deterministic function $G^{(i)}(t, t_1, t_2, \ldots)$ are the statistical projection of $g(t)$ on ith Wiener-Hermite base function, i.e.,

$$G^{(i)}(t,t_1,t_2,\ldots t_i)=<g(t)H^{(i)}(t_1,t_2,\ldots t_i)>. \tag{A-8}$$

Downloaded 02 May 2010 to 171.66.16.246. Redistribution subject to ASME license or copyright; see http://www.asme.org/terms/Terms_Use.cfm

The Radially Flexible Pendulum Subjected to a High-Frequency Excitation

B. A. Schmidt
Department of Mathematics,
Central Michigan University,
Mount Pleasant, Mich. 48859

A high-frequency harmonic excitation is applied to a pendulum that is flexible in the radial direction. Approximate equilibrium positions are found when the excitation is in a general and fixed direction. An approximate stable motion is found when the direction of the excitation changes constantly and slowly. It is found that the excitation causes a reduction of the radius.

1 Introduction

Pendulums with oscillating base motions have been the subject of many investigations. Stephenson [1] considered the plane pendulum subjected to a vertical oscillation. He presented an explanation of the inverted position. Lowenstern [2] investigated the spherical pendulum with an oscillating base. Phelps and Hunter [3] presented a thorough study of the plane pendulum subjected to a vertical oscillation at an unrestricted frequency. Miles [4] considered the stability of the downward vertical position of the spherical pendulum subjected to a horizontal oscillation. Sethna and Hemp [5] analyzed the gyroscopic pendulum subjected to a high-frequency vertical oscillation. Several authors including Howe [6], Bogdanoff and Citron [7], Mitchell [8], and Hemp and Sethna [9] have investigated the plane pendulum subjected to nonharmonic oscillations. Ryland and Meirovitch [10] considered stability of the vertical position of the plane flexible pendulum with a vertical harmonic oscillation at an unrestricted frequency. Schmidt [11, 12] presented variations of pendulums with oscillating base motions.

In this paper, we consider a radially flexible pendulum. The pendulum is shown in Fig. 1. The pendulum is made up of a mass, a spring, and a pivoted weightless rod. The mass is allowed to move along the rod under the influence of the spring. The mass is not allowed to move rotationally with respect to the rod. A small-amplitude harmonic excitation is applied to the pivot. The excitation is along a line in the plane of the pendulum. The frequency of the excitation is large with respect to the natural frequency of the rotational motion of the pendulum under the influence of gravity. The frequency of the excitation is not large with respect to the natural frequency of the motion of the mass along the rod under the influence of the spring.

In Section 2, the method of averaging [13] is used to replace the equations of motion by differential equations which provide the first approximation of the motion. Equilibrium solutions are found in a special case in which the direction of the excitation is fixed. In another special case, equilibrium solutions are found when gravity is zero and the direction of the excitation is moving constantly and slowly. In Section 3, the method of averaging is used to obtain the improved first approximation. The direction of the excitation is allowed to be either fixed or moving as in Section 2. An interesting effect is shown.

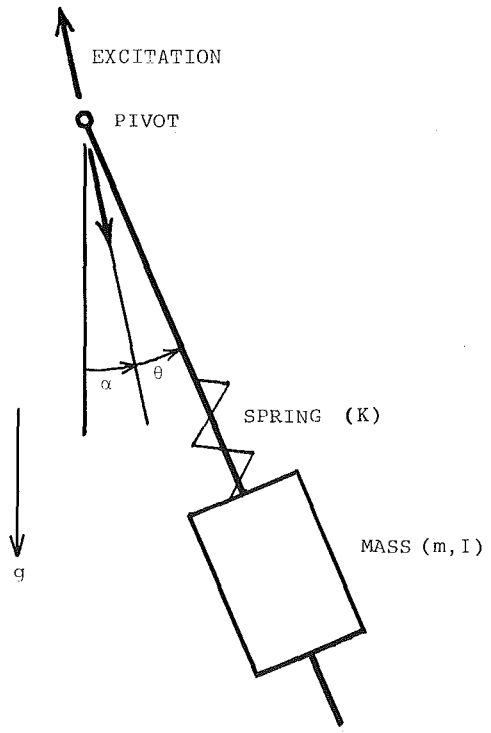

Fig. 1 The pendulum

Contributed by the Applied Mechanics Division for publication in the JOURNAL OF APPLIED MECHANICS.

Discussion on this paper should be addressed to the Editorial Department, ASME, United Engineering Center, 345 East 47th Street, New York, N.Y. 10017, and will be accepted until two months after final publication of the paper itself in the JOURNAL OF APPLIED MECHANICS. Manuscript received by ASME Applied Mechanics Division, January, 1981; final revision, January, 1982.

Copyright © 1983 by ASME
Downloaded 02 May 2010 to 171.66.16.246. Redistribution subject to ASME license or copyright; see http://www.asme.org/terms/Terms_Use.cfm

2 The First Approximation

The excitation is applied at an angle α measured from vertical. The angular position of the pendulum is given by θ measured from the line of the excitation. The equations of motion are

$$(I+mr^2)(\ddot{\theta}+\ddot{\alpha})+2mr\dot{r}(\dot{\theta}+\dot{\alpha})+mrg\sin(\theta+\alpha)+mA\nu^2 r\sin\theta\cos\nu t-2mA\nu r\dot{\alpha}\cos\theta\sin\nu t+mAr\ddot{\alpha}\cos\theta\cos\nu t+mAr\dot{\alpha}^2\sin\theta\cos\nu t+C_1(\dot{\theta}+\dot{\alpha})=0$$

and

$$m\ddot{r}-mr\dot{\theta}^2-2mr\dot{\theta}\dot{\alpha}-mr\dot{\alpha}^2+K(r-r_o)-mg\cos(\theta+\alpha)-mA\nu^2\cos\theta\cos\nu t-2mA\nu\dot{\alpha}\sin\theta\sin\nu t+mA\ddot{\alpha}\sin\theta\cos\nu t-mA\dot{\alpha}^2\cos\theta\cos\nu t+C_2\dot{r}=0$$

where m is the mass, I is the moment of inertia of the mass with respect to the center, r is the distance from the pivot to the center of the mass, r_o is the value of r when the spring is not strained, g is the gravitational constant, A is the amplitude of the excitation, ν is the frequency of the excitation, K is the spring constant, c_1 and c_2 are the damping coefficients, t is time, and the dot indicates differentiation with respect to time.

The excitation is restricted so that the frequency is large and the amplitude is small. The smallness of some terms is indicated by a small and positive parameter $\epsilon = \nu^{-1}$. To represent the problem in dimensionless variables and parameters, let $\epsilon=\nu^{-1}$, $x=r/r_e$, $x_0=r_o/r_e$, $\epsilon\gamma=A/r_e$, $\epsilon^2\delta=g(r_e\nu^2)^{-1}$, $\tau=\nu t$, $k^2=K(\nu^2 m)^{-1}$, $\epsilon a_1=C_1(mr_e^2\nu)^{-1}$, $\epsilon\alpha_2=C_2(m\nu)^{-1}$, and let the prime indicate differentiation with respect to τ. r_e is the radius of gyration of the mass. Also, let α be slowly varying, i.e., $\alpha=h(\epsilon\tau)$. If third-order terms are discarded, the equations of motion become

$$(1+x^2)\ddot{\theta}+2x\dot{x}\dot{\theta}+\epsilon^2\delta x\sin(\theta+h)+\epsilon\gamma x\sin\theta\cos\tau+\epsilon^2(1+x^2)\frac{d^2h}{d(\epsilon\tau)^2}+2\epsilon x\dot{x}\frac{dh}{d(\epsilon\tau)}-2\epsilon^2\gamma x\frac{dh}{d(\epsilon\tau)}\cos\theta\sin\tau+\epsilon a_1\left(\dot{\theta}+\epsilon\frac{dh}{d(\epsilon\tau)}\right)=0$$

$$\ddot{x}-x\dot{\theta}^2-2\epsilon x\dot{\theta}\frac{dh}{d(\epsilon\tau)}-\epsilon^2 x\left(\frac{dh}{d(\epsilon\tau)}\right)^2+k^2(x-x_0)-\epsilon^2\delta\cos(\theta+h)-\epsilon\gamma\cos\theta\cos\tau-2\epsilon^2\gamma\frac{dh}{d(\epsilon\tau)}\sin\theta\sin\tau+\epsilon a_2\dot{x}=0. \qquad (1a, b)$$

The parameters δ, k, x_0, a_1, and a_2 are positive and independent of ϵ. Further restrictions are made. (1) k^2 is not near 1 or 4, i.e., k^2-4 are independent of ϵ, and (2) $x(0)-x_0$ and $x'(0)$ are of order ϵ.

To change the equations of motion (1) into four equations in the standard form for the method of averaging, the following transformation is made. Let

$$\dot{\theta}=\epsilon\phi-\epsilon\gamma x_o(1+x_o^2)^{-1}\sin\theta\sin\tau$$

$$x=x_o+\xi u\sin k\tau+\epsilon v\cos k\tau-\epsilon\gamma(1-k^2)^{-1}\cos\theta\cos\tau$$

$$\dot{x}=\epsilon uk\cos k\tau-\epsilon vk\sin k\tau+\epsilon\gamma(1-k^2)^{-1}\dot{\theta}\sin\theta\cos\tau+\epsilon\gamma(1-k^2)^{-1}\cos\theta\sin\tau. \qquad (2a, b, c)$$

The choice of (2) is motivated by the assumption that θ is made up of a slow term plus a small fast term and that x is made up of a constant, x_o, plus a first-order solution of (1b) using variation of parameters. Differentiation of (2a) and substitution of (1a) and (2a–c) gives a first-order differential equation for ϕ'. Variation of parameters with (2b) and (2c) and substitution of (1a), (1b), and (2a–c) gives an equation for u' and an equation for v'. Then, if (2a) is included, there are four first-order equations in the standard form for the method of averaging. They are

$$\dot{\theta}=\epsilon\phi-\epsilon\gamma x_o(1+x_o^2)^{-1}\sin\theta\sin\tau$$

$$\dot{\phi}=\epsilon\Big[-\gamma x_o(1+x_o^2)^{-1}(1+k^2)(1-k^2)^{-1}(\phi-\gamma x_o(1+x_o^2)^{-1}\sin\theta\sin\tau)\cos\theta\sin\tau-2x_o(1+x_o^2)^{-1}(uk\cos k\tau-v k\sin k\tau)(\phi-\gamma x_o(1+x_o^2)^{-1}\sin\theta\sin\tau)-\delta x_o(1+x_o^2)^{-1}\sin(\theta+h)-\frac{d^2h}{d(\epsilon\tau)^2}+\gamma(1+x_o^2)^{-2}(x_o^2-1)(u\sin k\tau+v\cos k\tau)\sin\theta\cos\tau-\gamma^2(1+x_o^2)^{-2}(x_o^2-1)(1-k^2)^{-1}\cos\theta\sin\theta\cos^2\tau-2x_o(1+x_o^2)^{-1}(uk\cos k\tau-vk\sin k\tau+\gamma(1-k^2)^{-1}\cos\theta\sin\tau)\frac{dh}{d(\epsilon\tau)}+2\gamma x_o(1+x_o^2)^{-1}\frac{dh}{d(\epsilon\tau)}\cos\theta\sin\tau-a_1(1+x_o^2)^{-1}\left(\phi-\gamma x_o(1+x_o^2)^{-1}\sin\theta\sin\tau+\frac{dh}{d(\epsilon\tau)}\right)\Big]$$

$$\dot{u}=\frac{\epsilon}{k}\Big[\gamma^2 x_o(1+x_o^2)^{-1}(1-k^2)^{-1}\sin^2\theta(\cos^2\tau-2\sin^2\tau)+2\gamma(1-k^2)^{-1}\phi\sin\theta\sin\tau+x_o(\phi-\gamma x_o(1+x_o^2)^{-1}\sin\theta\sin\tau)^2+2x_o(\phi-\gamma x_o(1+x_o^2)^{-1}\sin\theta\sin\tau)\frac{dh}{d(\epsilon\tau)}+x_o\left(\frac{dh}{d(\epsilon\tau)}\right)^2+\delta\cos(\theta+h)+2\gamma\frac{dh}{d(\epsilon\tau)}\sin\theta\sin\tau-a_2(uk\cos k\tau-vk\sin k\tau+\gamma(1-k^2)^{-1}\cos\theta\sin\tau\Big]\cos k\tau$$

$$\dot{v}=-\frac{\epsilon}{k}\Big[\gamma^2 x_o(1+x_o^2)^{-1}(1-k^2)^{-1}\sin^2\theta(\cos^2\tau-2\sin^2\tau)+2\gamma(1-k^2)^{-1}\phi\sin\theta\sin\tau+x_o(\phi-\gamma x_o(1-x_o^2)^{-1}\sin\theta\sin\tau)^2+2x_o(\phi-\gamma x_o(1+x_o^2)^{-1}\sin\theta\sin\tau)\frac{dh}{d(\epsilon\tau)}+x_o\left(\frac{dh}{d(\epsilon\tau)}\right)^2+\delta\cos(\theta+h)+2\gamma\frac{dh}{d(\epsilon\tau)}\sin\theta\sin\tau-a_2(uk\cos k\tau-vk\sin\tau+\gamma(1-k^2)^{-1}\cos\theta\sin\tau)\Big]\sin k\tau. \qquad (3a, b, c, d)$$

Downloaded 02 May 2010 to 171.66.16.246. Redistribution subject to ASME license or copyright; see http://www.asme.org/terms/Terms_Use.cfm

Averaging equations (3) gives

$$\dot{\Theta} = \epsilon\Phi$$

$$\dot{\Phi} = -\epsilon B\sin 2\Theta - \epsilon C\sin(\Theta + h) - \epsilon D\left(\Phi + \frac{dh}{d(\epsilon\tau)}\right) - \epsilon\frac{d^2h}{d(\epsilon\tau)^2}$$

$$\dot{U} = -\epsilon\frac{1}{2}a_2 U$$

$$\dot{V} = -\epsilon\frac{1}{2}a_2 V, \qquad (4a, b, c, d)$$

where $B = 1/4\,\gamma^2(1+x_o^2)^{-2}(k^2x_o^2+1)(k^2-1)^{-1}$, $C = \delta x_o(1+x_o^2)^{-1}$, $D = a_1(1+x_o^2)^{-1}$, and Θ, Φ, U, and V are the averaged variables corresponding to θ, ϕ, u, and v. $h(\epsilon\tau)$ is held constant in the averaging process.

For the first approximation, equations (4) are analyzed for two cases. (*A*) $h(\epsilon\tau)$ is constant, and (*B*) δ is zero and $h(\epsilon\tau)$ is slowly and constantly varying, i.e., $h(\epsilon\tau) = h_o + \epsilon h_1\tau$, where h_0 and h_1 are constants independent of ϵ. In Case *B*, δ is chosen to be zero to ease the analysis and because a nonzero δ is not expected to add any feature of particular interest. That δ is zero implies the pendulum is confined to a horizontal plane. In this investigation, the equilibrium solutions of (4) are presented. Other solutions, for example, solutions near the equilibrium solutions, could be found. They are not treated here.

In both Cases *A* and *B*, we may refer to a theorem of Balachandra and Sethna [14] to provide validity to our results. This theorem applies to the first approximation of the method of averaging for a more general problem and for a more general set of hypotheses than occur in this problem. By means of this theorem, we may state that there exists a solution to (3) that approaches an equilibrium solution to (4) as $\epsilon \to 0$, for all τ. The equilibrium solutions in Case *A* and *B* are valid in this sense.

For both Cases *A* and *B*, equations (4*c*) and (4*d*) can be solved. Attention is restricted to the equilibrium solutions. They are

$$U = 0$$

and

$$V = 0. \qquad (5, a, b)$$

These solutions are stable.

Consider Case *A*. In this case, $h(\epsilon\tau) = h_0$, where h_0 is a constant and $0 \le h_0 \le \pi/2$. This interval is sufficient. A larger interval causes effects that are similar in an obvious way. Equations (4*a*) and (4*b*) become

$$\dot{\Theta} = \epsilon\Phi$$

$$\dot{\Phi} = -\epsilon B\sin 2\Theta - \epsilon C\sin(\Theta + h) - \epsilon D\Phi. \qquad (6a, b)$$

Equations (6*a*) and (6*b*) indicate the following about equilibrium and stability. In all cases of equilibrium $\Phi = 0$. If $k^2 > 1$, Θ always has a stable equilibrium value Θ_{e1} and an unstable equilibrium value Θ_{e2} and Θ sometimes (as specified in the following) has a stable equilibrium value Θ_{e3} and an unstable equilibrium value Θ_{e4}. These equilibrium values have these properties:

1. $-h_0 \le \Theta_{e1} \le 0$, $1/2\pi \le \Theta_{e2} \le \pi - h_0$.
2. If $1/2\,C < B \le C$ and $h_0 < h_0^*$ or $h_0 > \pi/2 - h_0^*$, Θ_{e3} and Θ_{e4} occur with $\pi \le \Theta_{e3} < \Theta^*$ and $\Theta^* < \Theta_{e4} \le 3/2\pi$. Θ^* is the third quadrant angle obtained by eliminating h_0 from

$$B\sin 2\Theta + C\sin(\Theta + h_0) = 0$$

and

$$2B\cos 2\Theta + C\cos(\Theta + h_0) = 0, \qquad (7a, b)$$

and h_0^* is the first quadrant angle obtained by eliminating Θ from (7*a*) and (7*b*).

3. If $B > C$, Θ_{e3} and Θ_{e4} occur with $\pi \le \Theta_{e3} < \Theta_{e4} \le 3/2\pi$.
4. If gravity is made smaller, i.e., if δ is diminished, Θ_{e1}, Θ_{e2}, Θ_{e3}, and Θ_{e4} become closer to 0, $1/2\pi$, π, and $3/2\pi$, respectively.

If $k^2 < 1$, Θ sometimes (as specified in the following) has an unstable equilibrium value Θ_{e1} and a stable equilibrium value Θ_{e2} and Θ always has an unstable equilibrium value θ_{e3} and a stable equilibrium value Θ_{e4}. These equilibrium values have these properties:

1. If $B > C$, Θ_{e1} and Θ_{e2} occur with $0 \le \Theta_{e1} < \Theta_{e2} \le 1/2\pi$.
2. If $1/2C < B \le C$ and $h_0 < h_0^*$ or $h_0 > 1/2\pi - h_0^*$, Θ_{e1} and Θ_{e2} occur with $0 \le \Theta_{e1} < \Theta^*$ and $\Theta^* < \Theta_{e2} \le 1/2\pi$. Θ^* is the first quadrant angle obtained by eliminating h_0 from (7*a*) and (7*b*) and h_0^* is the first quadrant angle obtained by eliminating Θ from (7*a*) and (7*b*).
3. $\pi - h_0 \le \Theta_{e3} \le \pi$, $3/2\pi \le \Theta_{e4} \le 2\pi - h_0$.
4. If gravity is made smaller, i.e., δ is diminished, Θ_{e1}, Θ_{e2}, Θ_{e3}, and Θ_{e4} become nearer to 0, $1/2\pi$, π, and $3/2\pi$, respectively.

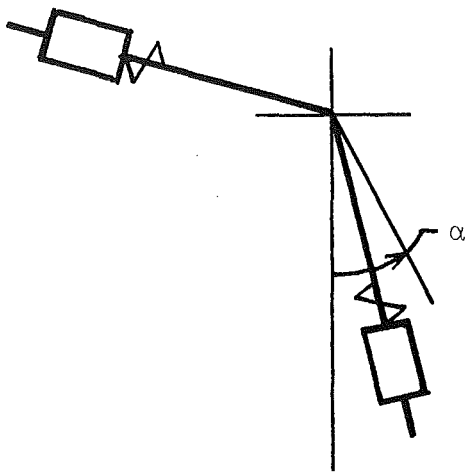

Fig. 2(a) ($K^2 > 1$)

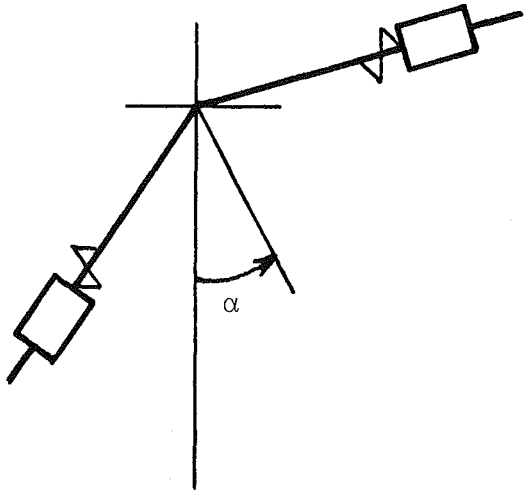

Fig. 2(b) ($K^2 < 1$)

Fig. 2 Typical stable equilibrium positions

Downloaded 02 May 2010 to 171.66.16.246. Redistribution subject to ASME license or copyright; see http://www.asme.org/terms/Terms_Use.cfm

The equilibrium solutions are Θ_{ei} ($i = 1, 2, 3, 4$), $\Phi = 0$, $U = 0$, and $V = 0$. From the theorem of Balachandra and Sethna we can conclude that solutions exist for equations (3) that are near these equilibrium solutions (for all τ) if ϵ is near zero. Using equation (2*b*), corresponding solutions for θ and x can be constructed. They are

$$\theta = \Theta_{ei}$$

$$x = x_o - \epsilon\gamma(1-k^2)^{-1}\cos\Theta_{ei}\cos\tau \qquad (8a, b)$$

where Θ_{ei} are the four equilibrium solutions described by equations (6*a*, *b*).

Equations (8*a*, *b*) along with the conclusions about Θ_{ei} allow the following summary. When $k^2 > 1$, the excitation creates a moment that tends to align the pendulum along the line of the excitation (in either direction). The moment caused by gravity tends to move the pendulum to the downward vertical position. The two moments create the two stable equilibrium positions shown in Fig. 2(*a*). These equilibrium positions coincide with those that would occur if the pendulum were rigid. This is described by Hemp and Sethna [9]. When $k^2 < 1$, the excitation causes a moment that tends to move the pendulum to either of two positions perpendicular to the line of the excitation. This, along with gravity, causes the stable equilibrium positions shown in Fig. 2(*b*).

For Case *B*, δ is zero and $h(\epsilon\tau) = h_0 + h_1\epsilon\tau$, where h_0 and h_1 are constant and $h_1 > 0$. If h_1 were negative, the motion would be different in an obvious and uninteresting way. These conditions mean that the pendulum is restricted to move in a horizontal plane and the direction of the excitation is slowly and constantly changing. As in Case *A*, equations (4*c*) and (4*d*) have stable equilibrium solutions as given by equations (5*a*) and (5*b*), i.e., $U = 0$ and $V = 0$. In Case *B*, equations (4*a*) and (4*b*) become

$$\Theta' = \epsilon\Phi$$

and

$$\Phi' = -\epsilon B\sin 2\Theta - \epsilon D(\Phi + h_1) \qquad (9a, b)$$

Equations (9*a*, *b*) indicate the following about equilibrium and stability. In all cases of equilibrium $\Phi = 0$. If $k^2 > 1$, equations (9*a*, *b*) indicate that Θ has equilibrium values Θ_{e1}, Θ_{e2}, Θ_{e3}, and θ_{e4} when $Dh_1 < B$. These equilibrium values have these properties:

1. $-\frac{\pi}{4} < \Theta_{e1} < 0, \frac{1}{2}\pi < \Theta_{e2} < \frac{3}{4}\pi,$

   $\frac{3}{4}\pi < \Theta_{e3} < \pi, \frac{3}{2}\pi < \Theta_{e4} < \frac{7}{4}\pi.$

2. Θ_{e1} and Θ_{e3} are stable. Θ_{e2} and Θ_{e4} are unstable.

3. $\Theta_{e1} \to 0$ as $D \to 0$, $\Theta_{e2} \to \frac{\pi}{2}$ as $D \to 0$,

   $\Theta_{e3} \to \pi$ as $D \to 0$, $\Theta_{e4} \to \frac{3}{2}\pi$ as $D \to 0$.

4. $\Theta_{e1} \to -\frac{\pi}{4}$ as $Dh_1 \to B$, $\Theta_{e2} \to \frac{3}{4}\pi$ as $Dh_1 \to B$,

   $\Theta_{e3} \to \frac{3}{4}\pi$ as $Dh_1 \to B$, $\Theta_{e4} \to \frac{7}{4}\pi$ as $Dh_1 \to B$.

If $k^2 < 1$, equations (9*a*, *b*) indicate that Θ has equilibrium values Θ_{e1}, Θ_{e2}, Θ_{e3}, and Θ_{e4} when $Dh_1 < -B$. These equilibrium values have the properties:

1. $0 < \Theta_{e1} < \frac{\pi}{4}, \frac{1}{4}\pi < \Theta_{e2} < \frac{1}{2}\pi, \pi < \Theta_{e3} < \frac{5}{4}\pi,$

   $\frac{5}{4}\pi < \Theta_{e4} < \frac{3}{2}\pi.$

2. Θ_{e1} and Θ_{e3} are unstable. Θ_{e2} and Θ_{e4} are stable.

3. $\Theta_{e1} \to 0$ as $D \to 0$, $\Theta_{e2} \to \frac{\pi}{2}$ as $D \to 0$,

   $\Theta_{e3} \to \pi$ as $D \to 0$, $\Theta_{e4} \to \frac{3}{2}\pi$ as $D \to 0$.

4. $\Theta_{e1} \to \frac{\pi}{4}$ as $Dh_1 \to -B$, $\theta_{e2} \to \frac{\pi}{4}$ as $Dh_1 \to -B$

   $\Theta_{e3} \to \frac{5}{4}\pi$ as $Dh_1 \to -B$, $\theta_{e4} \to \frac{5}{4}\pi$ as $Dh_1 \to -B$.

Using the equilibrium solutions for Θ, U, and V and equation (2*b*), corresponding approximate solutions for θ and x can be constructed. They are:

$$\theta = \Theta_{ei}$$

and

$$x = x_o - \epsilon\gamma(1-k^2)^{-1}\cos\Theta_{ei}\cos\tau, \qquad (10a, b)$$

where Θ_{ei} are the four equilibrium values described by (9*a*, *b*).

We can make this summary. When $k^2 > 1$, the excitation tends to align the pendulum along the line of the excitation, i.e., $\theta = 0, \pi$. When $k^2 < 1$ the excitation tends to align the pendulum along a line perpendicular to the excitation, i.e., $\theta = \pi/2, 3/2\pi$. The damping moment causes the pendulum to lag these positions in such a way that the moment caused by the excitation balances the moment caused by the damping. The pendulum rotates following the rotation of the line of the excitation.

3 Improved First Approximation

The improved first approximation (described by Bogoliuboff and Mitropolskiy [15]) reveals an interesting effect of the excitation: the excitation causes an average reduction of the radius of the pendulum.

The theorem of Balachandra and Sethna does not pertain to the improved first approximation so the validity that it attaches to the first approximation is not useful here. However, the improved first approximation is still useful at least in a conjectural sense. It can also be said that the differential equations (3) are more fully satisfied by the improved first approximation. It might also be noted that the improved first approximation gives a solution to equations (1) which satisfies equation (1*b*) through second-order terms but does not satisfy equation (1*a*) through second-order terms. This occurs because of the nature of the transformation (2). If the second-order solution to (1) were desired, the second approximation of equations (3*a*) would be needed while the improved first approximation of (3*b*, *c*, *d*) would suffice. The feature of interest is shown by the improved first approximation. It is presented here.

In the improved first approximation, each of the variables θ, ϕ, u, and v are assumed to be the sum of a slow term and a small fast term, i.e.,

$$\theta = \Theta + \epsilon\theta_1,$$

$$\phi = \Phi + \epsilon\phi_1,$$

$$u = U + \epsilon u_1,$$

and

$$v = V + \epsilon v_1, \qquad (11a, b, c, d)$$

where Θ, Φ, U, and V are the slow variables and θ_1, ϕ_1, u_1, and v_1 are the fast variables. The variables Θ, Φ, U, and V are described by the averaged equations (4*a*, *b*, *c*, *d*) and the fast variables are described by equations formed in this way: $\epsilon\,\partial\theta_1/\partial\tau$, $\epsilon\,\partial\phi_1/\partial\tau$, $\epsilon\,\partial u_1/\partial\tau$, and $\epsilon\,\partial v_1/\partial\tau$ are, respectively, set equal to the right-hand sides of equations (3*a*–*d*) with the

Downloaded 02 May 2010 to 171.66.16.246. Redistribution subject to ASME license or copyright; see http://www.asme.org/terms/Terms_Use.cfm

averaged parts deleted and with the variables θ, ϕ, u, and v replaced by the slow variables Θ, Φ, U, and V. θ_1, ϕ_1, u_1 and v_1 are then found by integrating these equations while holding Θ, Φ, U, and V constant. $h(\epsilon\tau)$ is treated as are the slow variables, i.e., it is held constant during the integrations.

Following this procedure and imposing the equilibrium values for the slow variables $\Phi = U = V = 0$ and $\Theta = \Theta_{ei}$, as described in Section 2 (for either Case A or B), we obtain:

$$\theta_1 = \gamma x_o (1+x_o^2)^{-1} \sin\Theta_{ei} \cos\tau$$

$$\phi_1 = (2k^2 \gamma x_o (1+x_o^2)^{-1}(1-k^2)^{-1} \frac{dh}{d(\epsilon\tau)} \cos\Theta_{ei} - a_1 \gamma x_o (1+x_o^2)^{-2} \sin\Theta_{ei}) \cos\tau - \frac{1}{4}\gamma^2 (1-k^2)^{-1}(1+x_o^2)^{-2}(2x_o^2 + k^2 x_o^2 - 1) \sin\Theta_{ei}\cos\Theta_{ei}\sin 2\tau$$

$$u_1 = k^{-1}\Big[\Big(-\frac{1}{2}\gamma^2 x_o (1+x_o^2)^{-2}(1-k^2)^{-1}(1+k^2x_o^2)\sin^2\Theta_{ei} + x_o\Big(\frac{dh}{d(\epsilon\tau)}\Big)^2 + \delta\cos(\Theta_{ei}+h)\Big) k^{-1}\sin k\tau + \gamma^2 x_o (1+x_o^2)^{-2}(1-k^2)^{-1}(3+2x_o^2+k^2x_o^2)(4-k^2)^{-1} \sin^2\Theta_{ei}\Big(\cos k\tau \sin 2\tau - \frac{1}{2}k\sin k\tau\cos 2\tau\Big) - 2\gamma(1+x_o^2)^{-1}\sin\Theta_{ei}\frac{dh}{d(\epsilon\tau)} - a_2\gamma(1-k^2)^{-1}\cos\Theta_{ei})(1-k^2)^{-1}(\cos k\tau\cos\tau + k\sin k\tau\sin\tau)\Big]$$

$$v_1 = -k^{-1}\Big[-\Big(-\frac{1}{2}\gamma^2 x_o (1+x_o^2)^{-2}(1-k^2)^{-1}(1+k^2x_o^2)\sin^2\Theta_{ei} + x_o\Big(\frac{dh}{d(\epsilon\tau)}\Big)^2 + \delta\cos(\Theta_{ei}+h)\Big) k^{-1}\cos k\tau + \gamma^2 x_o (1+x_o^2)^{-2}(1-k^2)^{-1}(3+2x_o^2+k^2x_o^2)(4-k^2)^{-1} \sin^2\Theta_{ei}\Big(\sin k\tau \sin 2\tau + \frac{1}{2}k\cos k\tau\cos 2\tau\Big) + (2\gamma(1+x_o^2)^{-1}\sin\Theta_{ei}\frac{dh}{d(\epsilon\tau)} - a_2\gamma(1-k^2)^{-1}\cos\Theta_{ei})(1-k^2)^{-1}(-\sin k\tau\cos\tau + k\cos k\tau\sin\tau)\Big] \qquad (12a, b, c, d)$$

Combining (12c), (12d), (11c), (11d), and (2b) (with $U = V = 0$) and also combining (12a), (11a), and (2a) (with $\Theta = \Theta_{ei}$), approximate solutions for θ and x are obtained. They are

$$\theta = \Theta_{ei} + \epsilon\gamma x_o (1+x_o^2)^{-1}\sin\Theta_{ei}\cos\tau$$

$$x = x_o - \epsilon\gamma(1-k^2)^{-1}\cos\Theta_{ei}\cos\tau + \epsilon^2 k^{-2}\Big(-\frac{1}{2}\gamma^2 x_o (1+x_o^2)^{-2}\sin^2\Theta_{ei} + x_o\Big(\frac{dh}{d(\epsilon\tau)}\Big)^2 + \delta\cos(\Theta_{ei}+h)\Big) + \epsilon^2\frac{1}{2}\gamma^2 x_o (1+x_o^2)^{-2}(1+2x_o^2)(4-k^2)^{-1}\sin^2\Theta_{ei}\cos 2\tau - \epsilon^2 2\gamma(1-k^2)^{-1}(1+x_o^2)^{-1}\frac{dh}{d(\epsilon\tau)}\sin\Theta_{ei}\sin\tau + \epsilon^2 a_2\gamma(1-k^2)^{-2}\cos\Theta_{ei}\sin\tau.$$

Equations (13a, b) give the approximate solutions for θ and x which correspond to the improved first approximation of equations (3). Θ_{ei} is any of the equilibrium values in Cases A and B in Section 2. $h(\epsilon\tau)$ is either of the functions described in Cases A or B. When equations (13a, b) pertain to case B, δ must be set equal to zero.

For the most part, equations (13a, b) reveal nothing unexpected. However, the term $-\epsilon^2 1/2 k^{-2}\gamma^2 x_o (1+x_o^2)^{-2}\sin^2\Theta_{ei}$ in equation (13b) is surprising. This term shows that the excitation of the pendulum causes an average reduction of the radius except when $\Theta_{ei} = 0$ or π. Some thought might suggest that the excitation creates an inertia force in the negative radial direction.

4 Conclusions and Remarks

The first approximation shows that the excitation creates new equilibrium points when the direction of the excitation is fixed. The position of the equilibrium points depend on the amplitude and frequency and direction of the excitation. If the frequency is less than $\sqrt{K/m}$ the pendulum acts much the same as the rigid pendulum. If the amplitude were large enough or if the frequency were near enough to $\sqrt{K/m}$, the excitation would cause two stable equilibrium positions near the line of the excitation and nearly 180 deg apart. The stable equilibrium points would be displaced from the line of excitation toward the downward vertical. If the amplitude or frequency were reduced, the stable equilibrium points would be moved further toward the downward vertical. Typical equilibrium positions are shown in Fig. 2(a). If the frequency of the excitation were greater than $\sqrt{K/m}$, the equilibrium positions would be different. If the amplitude were large enough or if the frequency were near enough to $\sqrt{K/m}$, there would be two stable equilibrium positions near the line perpendicular to the line of the excitation and nearly 180 deg apart. The stable equilibrium points would be displaced from the perpendicular line toward the downward vertical. Typical equilibrium positions are shown in Fig. 2(b). If the amplitude were reduced or if the frequency were increased, the stable equilibrium points would be moved further toward the downward vertical.

When the direction of the excitation is constantly rotating, the pendulum follows the rotation. In this analysis, the gravity was restricted to be zero and the excitation was restricted to be slowly and constantly rotating. It was shown that the pendulum would follow the rotation of the excitation. If the frequency of the excitation were smaller than $\sqrt{K/m}$, the pendulum would follow but lag the line of the excitation. If the frequency of the excitation were larger than $\sqrt{K/m}$, the pendulum would follow but lag the line perpendicular to the line of the excitation. The lag is caused by the damping.

The solution obtained by using the improved first approximation, equations (13a, b), shows that an unexpected average reduction of the radius can occur because of the excitation. This effect is shown by the term $-\epsilon^2 1/2 k^{-2}\gamma^2 x_o (1+x_o^2)^{-2}\sin^2\Theta_{ei}$ in equation (13b). This term indicates a reduction of the radius. The terms $\epsilon^2 k^{-2} x_o (dh/d(\epsilon\tau))^2$ and $\epsilon^2 k^{-2}\delta\cos(\Theta_{ei}+h)$ in equation (13b) show average changes in the radius but they are not surprising. The former is the increase in radius caused by a centrifugal force associated with the rotation of the pendulum and the latter is the change in radius caused by gravity.

An understanding of the physical situation can be gained if it is understood that the excitation causes small amplitude oscillations in θ and x at the frequency of the excitation. This is shown in the solutions (13a, b). Because of this, the terms $x^2\dot{\theta}$, $2x\dot{x}\dot{\theta}$, and $\epsilon x\gamma\sin\theta\cos\tau$ in equation (1a) will have slow parts that are the rectifications of the products of the oscillatory parts of θ and x. These inertia moments cause the equilibrium points mentioned in Section 2. Also because of

Downloaded 02 May 2010 to 171.66.16.246. Redistribution subject to ASME license or copyright; see http://www.asme.org/terms/Terms_Use.cfm

these oscillations in θ and x, the terms $-x\dot{\theta}^2$ and $-\epsilon\gamma\cos\theta\cos\tau$ in equation (1*b*) will have slow parts. These inertia forces cause the reduction of the radius shown in (13*b*).

References

1 Stephenson, A., "On a New Type of Dynamical Stability," *Memoirs and Proceedings of the Manchester Literary and Philosophical Society*, Vol. 52, 1907, pp. 1–10.

2 Lowenstern, E. R., "The Stabilizing Effect of Imposed Oscillations of High Frequency on a Dynamical System," *Philosophical Magazine*, Vol. 13, 1932, pp. 458–486.

3 Phelps, F. M. III, and Hunter, J. H. Jr., "An Analytical Solution of the Inverted Pendulum," *American Journal of Physics*, Vol. 33, 1965, pp. 285–295.

4 Miles, J. W., "Stability of Forced Oscillations of a Spherical Pendulum," *Quarterly of Applied Mathematics*, Vol. 20, No. 1, 1962, pp. 21–32.

5 Sethna, P. R., and Hemp, G. W., "Nonlinear Oscillations of a Gyroscopic Pendulum With an Oscillating Point of Suspension," *Proc. Colloq. International du Center National de la Rercherche Scientifique*, N-148, Les Vibrations Forcees dans les Systems Non-Lineares, 1964, pp. 375–392.

6 Howe, M. S., "The Mean Square Stability of an Inverted Pendulum Subject to Ramdon Parametric Excitation," *Journal of Sound and Vibration*, Vol. 32, No. 3, 1974, pp. 407–421.

7 Bogdanoff, J. L., and Citron, S. J., "Experiments With an Inverted Pendulum Subject to Random Parametric Excitation," *Journal of the Acoustical Society of America*, Vol. 38, 1965, pp. 447–452.

8 Mitchell, R., "Stability of the Inverted Pendulum Subjected to Almost Periodic and Stochastic Base Motion—An Application of The Method of Averaging," *Journal of Sound and Vibration*, Vol. 32, No. 3, 1974, pp. 101–123.

9 Hemp, G. W., and Sethna, P. R., "On Dynamical Systems With High Frequency Parametric Excitation," *International Journal of Mechanics*, Vol. 3, 1968, pp. 351–365.

10 Ryland, G. II, and Meirovitch, L., "Stability Boundaries of a Swinging Spring With Oscillatiory Support," *Journal of Sound and Vibration*, Vol. 51, No. 4, 1977, pp. 547–560.

11 Schmidt, B. A., "Vibrated Pendulum With a Mass Free to Move Radially," ASME JOURNAL OF APPLIED MECHANICS, Vol. 47, 1980, pp. 428–430.

12 Schmidt, B. A., "Pendulum With a Rotational Vibration," ASME JOURNAL OF APPLIED MECHANICS, Vol. 48, 1981, pp. 200–203.

13 Bogoliuboff, N. M., and Mitropolskiy, Yu. A., *Asymptotic Methods in the Theory of Nonlinear Oscillations*, Gordon and Breach, 1962.

14 Balachandra, M., and Sethna, P. R., "A Generalization of the Method of Averaging for Systems With Two Time Scales," *Archive for Rational Mechanics and Analysis*, Vol. 58, No. 3, 1975, pp. 261–283.

15 Bogoliuboff, N. M., and Mitropolskiy, Yu. A., *Asymptotic Methods in the Theory of Nonlinear Oscillations*, Gordon and Breach, 1962, p. 394.

Downloaded 02 May 2010 to 171.66.16.246. Redistribution subject to ASME license or copyright; see http://www.asme.org/terms/Terms_Use.cfm

Journal of Applied Mechanics

Design Data and Methods

Natural Frequencies of In-Plane Vibration of Arcs

T. Irie,[1] G. Yamada[1] and K. Tanaka[1]

The natural frequencies of in-plane vibration are presented for uniform arcs with circular cross section under all combinations of boundary conditions.

Previously, the natural frequencies of out-of-plane vibration of elastic arcs have been present by the same authors [1]. The Design Data present the natural frequencies (the dimensionless frequency parameters) of in-plane vibration for arcs with the same dimensions and the same boundary conditions as in reference [1]. Although the free in-plane vibration of arcs has been studied by many researchers [2–18], there have been not sufficient engineering data for practical use. Here, the Timoshenko beam theory is used for the calculation, because it presents accurate values for beams or arcs of considerably thick cross section.

Consider a uniform arc of radius of curvature of the neutral axis R. With the angular coordinate denoted by θ and the opening angle by α, the X, Y, and Z-axes are taken in radial, transverse, and tangential directions, respectively. The Timoshenko equations of in-plane vibration of an arc are written as

$$\frac{dQ_x^*}{d\theta} + N^* + \rho AR\omega^2(1+k^2)u^* = 0$$

$$\frac{dM_y^*}{Rd\theta} + Q_x^* + \rho AR\omega^2(k_1^2 w^* + k_2^2 R\psi) = 0$$

$$\frac{dN^*}{d\theta} - Q_x^* + \rho AR\omega^2\{(1+k^2)w^* + k_1^2 R\psi\} = 0 \qquad (1)$$

where ρ is the mass density, A is the cross-sectional area, and ω is the frequency in radians/second. The quantities k^2, k_1^2, and k_2^2 are the dimensionless parameters defined as

$$k^2 = -\frac{1}{A}\iint_A \zeta\xi dA, \quad k_1^2 = -\frac{1}{A}\iint_A \xi(1-\xi)dA$$

$$k_2^2 = \frac{1}{A}\iint_A \xi^2(1-\xi)dA \qquad (2)$$

where $x = R\xi$ denotes the length measured from the neutral axis in radial direction. The distance between the neutral axis and the centroid of cross section is calculated by

$$\iint_A \frac{\xi}{1-\xi} dA = 0 \qquad (3)$$

The shearing force Q_x^*, the bending moment M_y^*, and the tensile force N^*, respectively, are expressed as

$$Q_x^* = \kappa GA\left(\frac{1}{R}w^* + \frac{du^*}{Rd\theta} - \psi\right)$$

$$M_y^* = EARk^2\frac{d\psi}{d\theta}, \quad N^* = EA\left(\frac{dw^*}{Rd\theta} - \frac{1}{R}u^*\right) \qquad (4)$$

in terms of the displacements u^* and w^* in radial and tangential directions and the slope ψ due to pure bending. The variables u^*, ψ, w^*, Q_x^*, M_y^*, and N^* are defined to be positive sign in the X, Y, and Z-directions. Here, E and G are Young's modulus and shear modulus, respectively, and κ is the numerical factor depending on the shape of the cross section, which is 0.85 for rectangular cross section and 0.89 for circular cross section, respectively, for an arc of Poisson's ratio $\nu = 0.3$.

The boundary conditions of an arc are given by

$$\begin{aligned} Q_x^* &= M_y^* = N^* = 0 && \text{at free edge} \\ u^* &= w^* = M_y^* = 0 && \text{at hinged edge} \\ u^* &= \psi = w^* = 0 && \text{at clamped edge} \end{aligned} \qquad (5)$$

Upon eliminating the variables Q_x^*, M_y^* and N^*, equation (1) can be written as

$$\frac{\kappa}{2(1+\nu)}u'' - \left(1 - \lambda^2\frac{1+k^2}{s_y^2}\right)u - \frac{\kappa}{2(1+\nu)}\psi' + \left\{1 + \frac{\kappa}{2(1+\nu)}\right\}w' = 0$$

$$\frac{\kappa}{2(1+\nu)}u' + k^2\psi'' - \left\{\frac{\kappa}{2(1+\nu)} - \lambda^2\frac{k_2^2}{s_y^2}\right\}\psi + \left\{\frac{\kappa}{2(1+\nu)} + \lambda^2\frac{k_1^2}{s_y^2}\right\}w = 0$$

$$\left\{1 + \frac{\kappa}{2(1+\nu)}\right\}u' - \left\{\frac{\kappa}{2(1+\nu)} + \lambda^2\frac{k_1^2}{s_y^2}\right\}\psi - w'' + \left\{\frac{\kappa}{2(1+\nu)} - \lambda^2\frac{1+k^2}{s_y^2}\right\}w = 0 \qquad (6)$$

[1] Professor, Associate Professor, and Instructor of Mechanical Engineering, respectively, Faculty of Engineering, Hokkaido University, Kita-13, Nishi-8, Sapporo, 060 Japan.

Manuscript received by ASME Applied Mechanics Division, September, 1982.

Copyright © 1983 by ASME
Downloaded 02 May 2010 to 171.66.16.246. Redistribution subject to ASME license or copyright; see http://www.asme.org/terms/Terms_Use.cfm

Table 1 Frequency equations of in-plane vibration of arcs

Free-free

$$\begin{vmatrix} T_{41} & T_{42} & T_{43} \\ T_{51} & T_{52} & T_{53} \\ T_{61} & T_{62} & T_{63} \end{vmatrix}_{(\alpha)} = 0$$

Free-hinged

$$\begin{vmatrix} T_{11} & T_{12} & T_{13} \\ T_{31} & T_{32} & T_{33} \\ T_{51} & T_{52} & T_{53} \end{vmatrix}_{(\alpha)} = 0$$

Free-clamped

$$\begin{vmatrix} T_{11} & T_{12} & T_{13} \\ T_{21} & T_{22} & T_{23} \\ T_{31} & T_{32} & T_{33} \end{vmatrix}_{(\alpha)} = 0$$

Hinged-hinged

$$\begin{vmatrix} T_{12} & T_{14} & T_{16} \\ T_{32} & T_{34} & T_{36} \\ T_{52} & T_{54} & T_{56} \end{vmatrix}_{(\alpha)} = 0$$

Hinged-clamped

$$\begin{vmatrix} T_{12} & T_{14} & T_{16} \\ T_{22} & T_{24} & T_{26} \\ T_{32} & T_{34} & T_{36} \end{vmatrix}_{(\alpha)} = 0$$

Clamped-clamped

$$\begin{vmatrix} T_{14} & T_{15} & T_{16} \\ T_{24} & T_{25} & T_{26} \\ T_{34} & T_{35} & T_{36} \end{vmatrix}_{(\alpha)} = 0$$

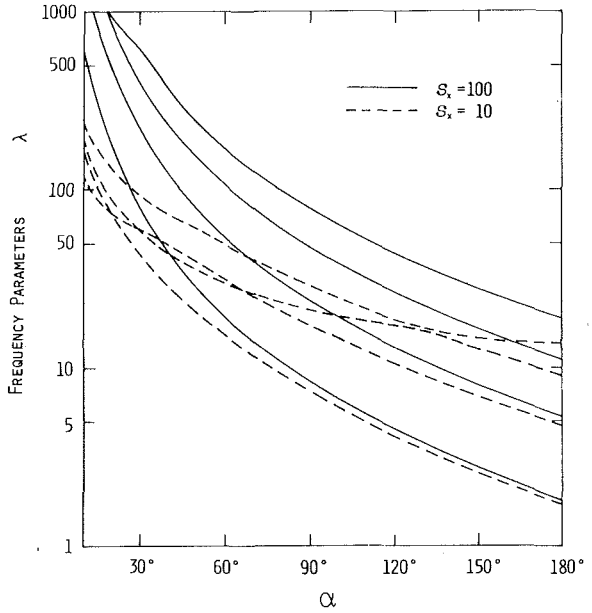

Fig. 1(*a*) Free-free arcs

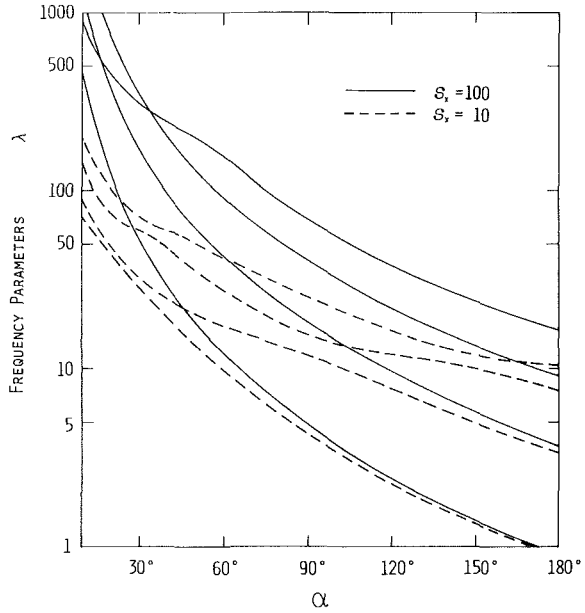

Fig. 1(*b*) Free-hinged arcs

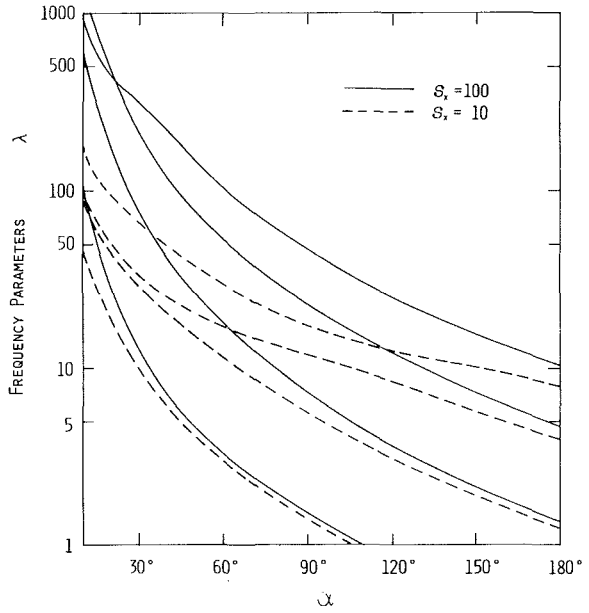

Fig. 1(*c*) Free-clamped arcs

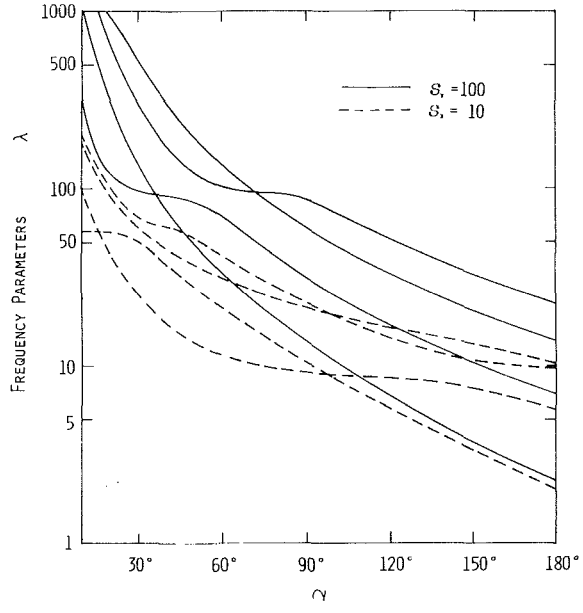

Fig. 1(*d*) Hinged-hinged arcs

Downloaded 02 May 2010 to 171.66.16.246. Redistribution subject to ASME license or copyright; see http://www.asme.org/terms/Terms_Use.cfm

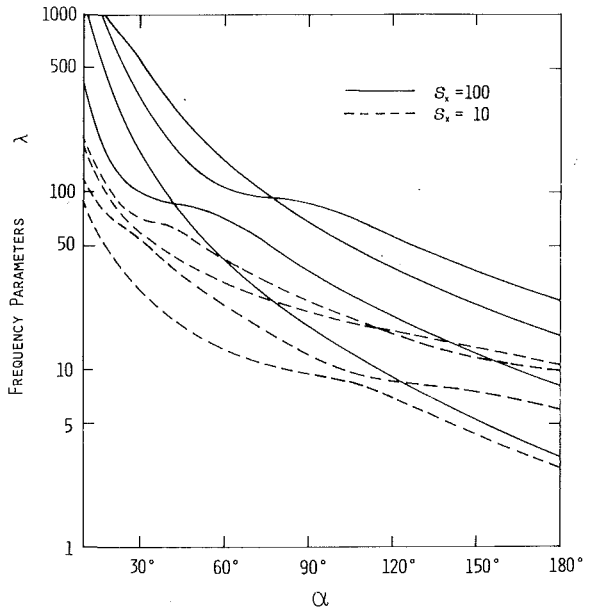

Fig. 1(e) Hinged-clamped arcs

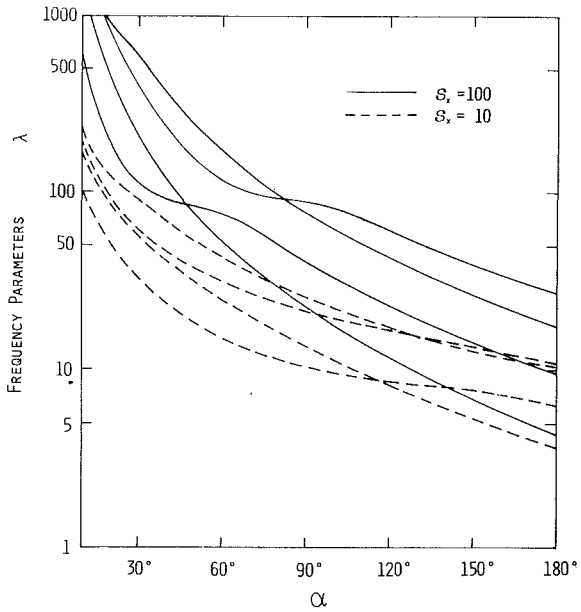

Fig. 1(f) Clamped-clamped arcs

Fig. 1 Frequency parameter λ_n of arcs of circular cross section; $\nu = 0.3$

Table 2 The frequency parameters λ_n of clamped-clamped arcs with rectangular and circular cross sections; $\nu = 0.3$

		Rectangular cross section			Circular cross section		
s_y	n	$\alpha = 60$ deg	120 deg	180 deg	$\alpha = 60$ deg	120 deg	180 deg
20	1	23.70	12.57	4.143	23.75	10.61	4.151
	2	38.73	15.17	8.519	39.05	15.19	8.542
	3	62.35	24.63	15.40	62.38	24.72	15.46
	4	69.97	30.38	17.90	70.71	30.47	17.91
100	1	52.78	11.79	4.374	52.82	11.79	4.374
	2	75.98	23.24	9.602	76.01	23.25	9.603
	3	117.8	42.35	17.81	117.9	42.37	17.81
	4	170.8	61.39	27.21	171.1	61.43	27.22

Here, for simplicity of the analysis, the following dimensionless variables have been introduced:

$$(u,w) = \frac{1}{R}(u^*,w^*)$$

$$(Q_x,M_y,N) = \frac{1}{EA}\left(Q_x^*,\frac{1}{R}M_y^*,N^*\right)$$

$$s_y^2 = \frac{AR^2}{I_y}, \quad \lambda^2 = \frac{\rho AR^4\omega^2}{EI_y} \tag{7}$$

where I_y is the second moment of area, s_y is the slenderness ratio of the arc, and λ is a frequency parameter.

With the variables taken as $u = Ce^{p\theta}$, $\psi = -Cqe^{p\theta}$ and $w = Cre^{p\theta}$, equations (6) are written as the matrix equation,

$$\begin{bmatrix} \frac{\kappa}{2(1+\nu)}p^2 - 1 + \lambda^2\frac{1+k^2}{s_y^2} & \frac{\kappa}{2(1+\nu)}p & \left\{1+\frac{\kappa}{2(1+\nu)}\right\}p \\ \frac{\kappa}{2(1+\nu)}p & -k^2p^2 + \frac{\kappa}{2(1+\nu)} - \lambda^2\frac{k_2^2}{s_y^2} & \frac{\kappa}{2(1+\nu)} + \lambda^2\frac{k_1^2}{s_y^2} \\ \left\{1+\frac{\kappa}{2(1+\nu)}\right\}p & \frac{\kappa}{2(1+\nu)} + \lambda^2\frac{k_1^2}{s_y^2} & -p^2 + \frac{\kappa}{2(1+\nu)} - \lambda^2\frac{1+k^2}{s_y^2} \end{bmatrix} \begin{Bmatrix} 1 \\ q \\ r \end{Bmatrix} = 0 \tag{8}$$

The parameter p is determined by calculating numerically the eigenvalues of (8), and the parameters q and r are determined by calculating the eigenvectors corresponding to the eigenvalues. The state vector $\{z(\theta)\} = \{u\psi wQxMyN\}^T$ of the arc is expressed as

$$\{Z(\theta)\} = [T(\theta)]\{z(0)\} \tag{9}$$

by using the transfer matrix

$$[T(\theta)] = [M(\theta)][M(0)]^{-1} \tag{10}$$

where

Downloaded 02 May 2010 to 171.66.16.246. Redistribution subject to ASME license or copyright; see http://www.asme.org/terms/Terms_Use.cfm

$$[M(\theta)] = \begin{bmatrix} e^{p_1\theta} & \cdots & e^{p_6\theta} \\ -q_1 e^{p_1\theta} & \cdots & -q_6 e^{p_6\theta} \\ r_1 e^{p_1\theta} & \cdots & r_6 e^{p_6\theta} \\ \frac{\kappa}{2(1+\nu)}(p_1+q_1+r_1)e^{p_1\theta} & \cdots & \frac{\kappa}{2(1+\nu)}(p_6+q_6+r_6)e^{p_6\theta} \\ -k^2 p_1 q_1 e^{p_1\theta} & \cdots & -k^2 p_6 q_6 e^{p_6\theta} \\ -(1-p_1 r_1)e^{p_1\theta} & \cdots & -(1-p_6 r_6)e^{p_6\theta} \end{bmatrix} \tag{11}$$

The substitution of (9) into a given set of the boundary conditions (5) derives the frequency equations with only the elements of $[T(\alpha)]$ necessary for the calculation, as shown in Table 1. The frequency parameters λ of arcs are determined by calculating the eigenvalues of the equations.

Figures 1 present the frequency parameters λ of arcs with uniform circular cross section under all combinations of the boundary conditions. For an arc with circular cross section of diameter d, the parameters k^2, k_1^2, k_2^2 and s_y are written as

$$k^2 = (d/4R)^2, \quad k_1^2 = k^2(1+k^2), \quad k_2^2 = k^2(1+4k^2+k^4)$$
$$s_y = (4R/d)\ [1+(d/4R)^2]^{-1/2} \tag{12}$$

In general, the frequency parameters become smaller with an increase of the opening angle α and with a decrease of the slenderness ratio s_y.

In Table 2, the frequency parameters of rectangular cross-section arcs are compared with those of circular cross-section arcs under clamped-clamped edge conditions. For an arc with rectangular cross section of height h, the parameters k^2, k_1^2, k_2^2, and s_y are expressed as

$$k^2 = \frac{h}{2R}\coth\left(\frac{h}{2R}\right) - 1, \quad k_1^2 = k^2(1+k^2) + \frac{1}{3}\left(\frac{h}{2R}\right)^2$$
$$k_2^2 = k^2\left\{k^2 + k^4 + \left(\frac{h}{2R}\right)^2\right\} + \frac{1}{3}\left(\frac{h}{2R}\right)^2$$
$$s_y = [k^4 + (1/3)(h/2R)^2]^{-1/2} \tag{13}$$

independent of the breadth of the cross section. Although the frequency parameters of rectangular cross-section arcs are generally smaller than those of circular cross-section arcs, the difference between them is very small.

The natural frequencies of arcs can be calculated numerically by

$$\omega = (EI_y/\rho AR^4)^{1/2}\lambda \tag{14}$$

using the dimensionless frequency parameters λ presented here.

References

1 Irie, T., Yamada, G., and Tanaka, K., "Natural Frequencies of Out-of-Plane Vibration of Arcs," ASME JOURNAL OF APPLIED MECHANICS, Vol. 49, 1982, pp. 910–913.

2 Den Hartog, J. P., "The Lowest Natural Frequency of Circular Arcs," *Philosophical Magazine*, Series 7, Vol. 5, 1928, pp. 400–408.

3 Waltking, F. W., "Schwingungszahlen und Schwingungsformen von Kreisbogenträgern," *Ingenieur-Archiv*, Col. 5, 1934, pp. 429–449.

4 Archer, R. R., "Small Vibrations of Thin Incomplete Circular Rings," *International Journal of Mechanical Sciences*, Vol. 1, 1960, pp. 45–56.

5 Volterra, E., and Morell, J. D., "A Note on the Lowest Natural Frequency of Elastic Arcs," ASME JOURNAL OF APPLIED MECHANICS, Vol. 27, 1960, pp. 744–746.

6 Volterra, E., and Morell, J. D., "Lowest Natural Frequencies of Elastic Hinged Arcs," *The Journal of the Acoustical Society of America*, Vol. 33, 1961, pp. 1787–1790.

7 Morley, L. S. D., "Elastic Waves in a Naturally Curved Rod," *Quarterly Journal of Mechanics and Applied Mathematics*, Vol. 14, 1961, pp. 155–172.

8 Nelson, F. C., "In-Plane Vibration of a Simply Supported Circular Ring Segment," *International Journal of Mechanical Sciences*, Vol. 4, 1962, pp. 517–527.

9 Hammoud, A. S., and Archer R. R., "On the Free Vibration of Complete and Incomplete Rings," *Developments in Mechanics 2*, 1963, pp. 489–524.

10 Takahashi, S., "Vibration of a Circular Arc Bar in its Plane (Both Ends Built-in)," *Bulletin of the JSME*, Vol. 6, 1963, pp. 666–673.

11 Ojalvo, I. U., and Newman, M., "Natural Frequencies of Clamped Ring Segments," *Machine Design*, Vol. 36, 1964, pp. 219–222.

12 Ojalvo, I. U., and Newman, M., "Natural Frequencies of Cantilevered Ring Segments," *Machine Design*, Vol. 37, 1965, pp. 191–195.

13 Petyt, M., and Fleischer, C. C., "Free Vibration of a Curved Beam," *Journal of Sound and Vibration*, Vol. 18, 1971, pp. 17–30.

14 Dawe, D. J., "The Transverse Vibration of Shallow Arches Using the Displacement Method," *International Journal of Mechanical Sciences*, Vol. 13, 1971, pp. 713–720.

15 Veletsos, A. S., Austin, W. J., Pereira, C. A. L., and Wung, S. -j., "Free In-Plane Vibration of Circular Arches," *Journal of Engineering Mechanics Division*, ASCE, Vol. 98, 1972, pp. 311–329.

16 Davis, R., Henshell, R. D., and Warburton, G. B., "Constant Curvature Beam Finite Elements for In-Plane Vibration," *Journal of Sound and Vibration*, Vol. 25, 1972, pp. 561–576.

17 Nagaya, K., and Hirano, Y., "In-Plane Vibration of Viscoelastic Circular Rod With Consideration of Shearing Deformation and Rotatory Inertia," *Bulletin of the JSME*, Vol. 20, 1977, pp. 539–547.

18 Blevins, R. D., *Formulas for Natural Frequency and Mode Shape*, Van Nostrand Reinhold, New York, 1979, pp. 203–223.

Downloaded 02 May 2010 to 171.66.16.246. Redistribution subject to ASME license or copyright; see http://www.asme.org/terms/Terms_Use.cfm

Journal of Applied Mechanics

Brief Notes

A Brief Note is a short paper that presents a specific solution of technical interest in mechanics but which does not necessarily contain new general methods or results. A Brief Note should not exceed 1500 words *or equivalent* (a typical one-column figure or table is equivalent to 250 words; a one line equation to 30 words). Brief Notes will be subject to the usual review procedures prior to publication. After approval such Notes will be published as soon as possible. The Notes should be submitted to the Technical Editor of the JOURNAL OF APPLIED MECHANICS. Discussions on the Brief Notes should be addressed to the Editorial Department, ASME, United Engineering Center, 345 East 47th Street, New York, N. Y. 10017, or to the Technical Editor of the JOURNAL OF APPLIED MECHANICS. Discussions on Brief Notes appearing in this issue will be accepted until two months after publication. Readers who need more time to prepare a Discussion should request an extension of the deadline from the Editorial Department.

A Note on Broken Pencil Points

S. C. Cowin[1]

A stress analysis of a pencil writing tip at fracture is presented. It is an interesting illustration of combined axial and bending loading.

Cronquist [1] pointed out that broken-off pencil points (BOPP's) are almost all the same size and shape. He suggested that the mechanism for fracture of the lead near the writing tip is the tensile stress due to a bending moment. He analyzed the stress state near the writing tip by idealizing the tip as a tapered caltilever beam subject to a transverse end load. This analysis predicted that the pencil lead would fail in tension at the distance from the writing tip where the lead had a diameter 1.5 times the lead diameter at the writing tip. Walker [2] gave a popular presentation of Conquist's result and introduced a convenient dimensionless geometric parameter for BOPP's analyze the data from his own pencil-point breaking experiments. This dimensionless geometric parameter is denoted here by N and it is the ratio of the length of a BOPP (measured from the writing tip to the closest point on the fracture surface, along the slanted conical surface of the BOPP) to the diameter of the writing tip. According to Cronquist's analysis N should be equal to 0.25 (cos α) ctnα where α is one-half the apex angle of the BOPP if it were a pointed cone rather than a truncated cone. Walker's data showed a value N of 2.5 for pencils with an apex angle of 12 deg broken by pressing the pencil down on a tabletop. As the pencil was pressed down on the tabletop an angle 45 deg between the plane of the tabletop and the long axis of the pencil was maintained. Cronquist's analysis predicts a value of 2.37 for N when α is 6 deg. This agreement between theory and experiment is satisfactory. However Cronquist's stress analysis of a pencil writing tip neglected the axial force in the pencil and the frictional force between the paper and the pencil. This Note extends the analysis of Cronquist to include these two forces.

The problem of breaking pencil points has several features of interest. First, the location of the fracture site is independent of the exact value of the tensile strength of the pencil lead and dependent only on pencil lead being a brittle material weaker in tension than compression. The results of this analysis are therefore applied to any brittle material. Second, a consequence of the analysis is the prediction of the dimensionless geometric parameter N of the BOPP independent of all material properties except, possibly, the coefficient of friction between the writing tip and the writing surface. N is experimentally determined from a BOPP using a micrometer. A significant feature of the stress analysis presented is that most of the results are obtained from strictly geometric parameters and are independent of material properties.

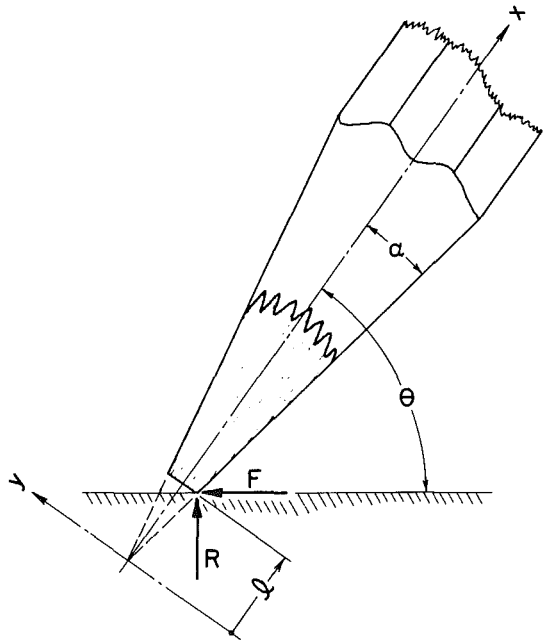

Fig. 1 This figure illustrates the geometry of the idealized writing tip of a pencil and the forces the writing surface exert on the pencil

An analysis of the stress state near the writing tip that includes the axial force in the pencil and the frictional force between the writing surface and the pencil as well as the bending moment will now be presented. The geometry of the writing tip and the forces that act on it are illustrated in Fig. 1. The apex angle of the pencil point is 2α and the sharpness length is l. Small values of l correspond to sharp points and larger values of l to dull points. The angle between the plane

[1] Professor, Department of Biomedical Engineering, Tulane University, New Orleans, La. 70118. Fellow ASME

Manuscript received by ASME Applied Mechanics Division, June, 1982; final revision October, 1982.

Copyright © 1983 by ASME
Downloaded 02 May 2010 to 171.66.16.246. Redistribution subject to ASME license or copyright; see http://www.asme.org/terms/Terms_Use.cfm

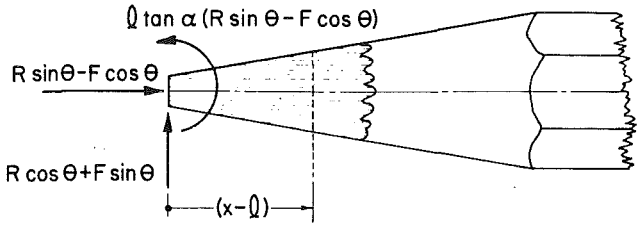

Fig. 2 This figure illustrates the forces at the writing tip resolved in an axial component, a transverse of shearing component, and a bending moment

of the writing surface and the long axis of the pencil is denoted by θ. The normal force between the pencil and the writing surface is denoted by R and the friction force is denoted by F. If the pencil is moving relative to paper, $F=\mu_d R$ where μ_d is the coefficient of dynamic friction. If the pencil is not moving, but motion is impending, then $F=\mu R$ where μ is the coefficient of static friction. If motion is not impending, then $F<\mu R$. The friction force is taken to lie in the plane that is perpendicular to the writing surface and contains the long axis of the pencil. This orientation for the friction force is chosen because it is the orientation in which the friction force makes the largest contribution to the tensile stresses induced by bending. It is assumed that that pencil point will break on the downstroke in writing, or by statically pressing the point down on a flat surface while maintaining a fixed value θ less than 90 deg and greater than 0 deg.

The forces acting in the writing tip can be resolved into an axial force, a shearing force, and a bending moment applied at the tip. The results of this resolution are illustrated in Fig. 2. The axial force P, the shear force V, and the bending moment M in the pencil at a distance $(x-l)$ from the writing tip are given by

$$\begin{aligned} P &= -R\sin\theta + F\cos\theta, \\ V &= -R\cos\theta - F\sin\theta, \quad \text{and} \\ M &= (x-l)(R\cos\theta - F\sin\theta) - l\tan\alpha(R\sin\theta - F\cos\theta), \end{aligned} \tag{1}$$

respectively. The bending moment is taken to be positive if it bends the beam concave upward. The maximum axial stress σ_x in the writing tip is given by the standard formula for combined axial and bending stresses, namely

$$\sigma_x = \frac{P}{A} - \frac{Mc}{I} \tag{2}$$

where A is the cross-sectional area of the beam, I is the moment of inertia of the cross-sectional area bout the neutral axis, and c is the distance from the neutral axis to the outermost fiber of the cross section. Because of the taper of the pencil point A, I, and c are all functions of x and α;

$$A=\pi r^2=\pi x^2\tan^2\alpha \quad I=\frac{\pi r^4}{4}=\frac{\pi x^4}{4}\tan^4\alpha, \quad c=-x\tan\alpha, \tag{3}$$

where r is the radius of the cross section which is equal to $x\tan\alpha$. The distance c is negative so that it corresponds to the fiber in which the tensile stress is maximum. The substitution of (1) and (3) into (2) yields a formula for the maximum tensile stress σ_x at any cross section as a function of x:

$$\begin{aligned} \sigma_x = \frac{\cos\theta}{\pi\tan^3\alpha}[&(R(4-\tan\alpha\tan\theta)+F(4\tan\theta+\tan\alpha))x^{-2} \\ &-(R(1+\tan\alpha\tan\theta)+F(\tan\theta-\tan\alpha))6lx^{-3}]. \end{aligned} \tag{4}$$

An interesting feature of equation (4) is the fact that term proportional to x^{-2} is opposite in sign from the term proportional to x^{-3}. Thus, there will be a maximum value for σ_x as a function of x for some finite value of x. This value of x is determined by computing the first derivative of σ_x and setting it equal to zero. The value of x for which $\sigma_x(x)$ given by (4) takes on a maximum value is denoted by $x_{\max}$ and given by

$$x_{\max}\frac{6l(R(1+\tan\alpha\tan\theta)+F(\tan\theta-\tan\alpha))}{R(4-\tan\alpha\tan\theta)+F(4\tan\theta+\tan\alpha)}. \tag{5}$$

This result shows that the location of the tensile fracture site is independent of the tensile strength of the material and dependent only on the geometric parameters l and α and the ratio of the forces F and R. When the pencil point is moving or when its motion is impending, the ratio of F to R is a coefficient of friction. Recall that α is one-half of the apex angle of the perfectly sharp pencil point and l is the sharpness length of the pencil point. As l tends to zero, $x_{\max}$ tends to zero and the mode of failure of the pencil point changes. As one can see from equation (4) the stress becomes proportional to x^{-2} as l tends to zero indicating a crushing failure mode at the writing tip. Thus, a very sharp pencil will tend to crush rather than form a BOPP.

The dimensionless geometric parameter N of a BOPP will now be computed in terms of the geometric parameters l and α and the ratio of F to R. Recall that N is the ratio of the slanted length of the BOPP to its writing tip diameter. The slanted length is measured from the writing tip to the nearest point on the fracture surface along the conical face of the BOPP. Using trigonometry it is easy to show that N is given by

$$N=\frac{(x_{\max}-l)\cos\alpha}{2l\tan\alpha} \tag{6}$$

and, substituting (5) into (6), the desired result is obtained,

$$N=\frac{\cos\alpha}{2\tan\alpha}\left[\frac{R(2+7\tan\theta\tan\alpha)+F(2\tan\theta-7\tan\alpha)}{R(4-\tan\theta\tan\alpha)+F(4\tan\theta+\tan\alpha)}\right]. \tag{7}$$

If the dependence of N on θ and F is suppressed, the value of N becomes 0.25 $(\text{ctn}\alpha)\cos\alpha$ as suggested by the analysis of Cronquist [1]. If friction only is neglected, then

$$N_0=\lim_{F\to 0} N=\frac{\cos\alpha}{2\tan\alpha}\left[\frac{2+7\tan\alpha\tan\alpha}{4-7\tan\theta\tan\alpha}\right], \tag{8}$$

however, the limit of N for infinite friction is also finite,

$$N_\infty=\lim_{F\to\infty} N=\frac{\cos\alpha}{2\tan\alpha}\left[\frac{2\tan\alpha-7\tan\alpha}{4\tan\theta+\tan\alpha}\right]. \tag{9}$$

In order for a BOPP to form, N must be greater than zero. From (7), (8), and (9) it is easy to show that a necessary and sufficient condition for N to be positive for all values of the friction force F is that the angle θ the long axis of the pencil makes with the table satisfy the condition

$$\frac{4}{7\tan\alpha}>\tan\theta>\frac{7}{2}\tan\alpha. \tag{10}$$

With these results concerning N it is interesting to consider again the pencil-point breaking results reported by Walker [2]. Walker used several No. 2 pencils with a half apex angle of 6 deg. He held the pencils at a θ of 45 deg while pressing the writing tip downward on a tabletop. In order for a BOPP to form for a pencil with a half apex angle of 6 deg, the angle θ must be between 20 and 80 deg. These restrictions on θ follow from equation (10). For $\alpha=6$ deg and $\theta=45$ deg, N_0 and N_∞ are 3.32 and 1.46, respectively, thus N is restricted to the range

$$1.46\le N\le 3.32. \tag{11}$$

Walker reported an N of 2.5 which is almost the central point in this range.

References

1 Cronquist, D., "Broken Off Pencil Points," *American Journal of Physics*, Vol. 47, No. 7, July 1979, pp. 653-655.

2 Walker, J., "The Amateur Scientist," *Scientific American*, Vol. 240, No. 2, Feb. 1979, pp. 158-166.

Downloaded 02 May 2010 to 171.66.16.246. Redistribution subject to ASME license or copyright; see http://www.asme.org/terms/Terms_Use.cfm

Microscales and Correlation Tensors in the Viscous Turbulent Sublayer

P. S. Bernard[1] and B. S. Berger[1]

Introduction

G. I. Taylor originally defined a microscale, $\lambda_f^2(X_N)$, [1], as the minimum radius of curvature of a parabolic approximation to the two-point velocity correlation function evaluated at X_N. The Taylor and other closely related microscales, based on various normalizations of the correlation function, have subsequetly been extensively studied [2-4, 7]. Physical interpretations of microscales are given in [1] and [7].

In the following, two-point velocity correlation tensors, R_{IJ}, are defined in curvilinear coordinates. The microscale associated with each component of R_{IJ}, for a particular direction and in rectangular Cartesian coordinates, is given for various normalizations. Power series expansions of the correlation tensors are derived utilizing Taylor's series representations of the velocity fluctuations. Expressions for the microscales are found in terms of the normalizing function and the coefficient of the quadratic terms in the expansion of the correlation tensor. The microscales were numerically evaluated in the sublayer of a channel flow through least square polynomial fits of $<u^2>^{1/2}/u_\tau$ and the more complex quantity $Q(y)$ as measured in [5]. The Taylor microscale is shown to be essentially constant for $1.5 \le y \le 8.0$ where y is in wall units.

Correlation Tensors

The two-point velocity correlation tensor may be defined at X_N by

$$R_{IJ}(X_N,x_n) = <u_I(X_N)u_j(x_n)>g_J{}^j/\Phi \tag{1}$$

where X_N and x_n are the coordinates of two points in the same curvilinear coordinate system, $\mathbf{X}_N$, $u_I(X_N) \equiv$ covariant components of the velocity fluctuation vector evaluated at point X_N, $u_j(x_n) \equiv$ covariant components of the velocity fluctuation vector at point x_n, $\Phi \equiv$ a scalar function of $u_I(X_N)$ and $u_j(x_n)$, and $<f> \equiv$ the average of f in some sense, [7]. $g_J{}^j \equiv \delta_K^k\, \partial x^j/\partial z^k\, \partial Z^K/\partial X^J$ where $\mathbf{Z}^K = \mathbf{Z}^K(\mathbf{X}_N)$ is the coordinate transformation that defines the curvilinear coordinates $\mathbf{X}_N$ in terms of the rectangular Cartesian coordinates $\mathbf{Z}_K$, δ_K^k is the Kronecker delta, $\partial x^j/\partial z^k$ is evaluated at z_n, and $\partial Z^K/\partial X^J$ is evaluated at X_N. The shifters, $g_J{}^j$, shift covariant vectors from point x_k to point X_N, [6], and appear in (1) because of the necessity of expressing $u_j(x_n)$ in terms of curvilinear base vectors defined at X_N. The scalar Φ is an arbitrary nomalizing factor, [7]. If $\mathbf{X}_N$ is taken to coincide with the rectangular Cartesian coordinate system $\mathbf{Z}_N$, then $g_J{}^j = \delta_J{}^j$ and (1) becomes

$$R_{IJ}(Z_N,z_n) = <u_I(Z_N)u_J(z_n)>/\Phi \tag{2}$$

For a given coordinate system $\mathbf{Z}_K$, consider all points such that $z_I = Z_I + \delta_{I(M)}r_{(M)}$, no sum on M, where r_M is chosen so that z_I is a point of the flow. Substituting into (2) gives

$$R_{IJ}(Z_N,r_M) = <u_I(Z_N)u_J(r_M)>/\Phi \tag{3}$$

where $u_J(r_M)$ is a spatial function of the Z_N and r_M. For $M = 2$, $z_1 = Z_1$, $z_2 = Z_2 + r_2$, $z_3 = Z_3$, which when substituted into (3) gives $R_{IJ}(Z_N, r_2)$. In the notation of [3] $R_{IJ}(Z_N, r_2) \equiv R_{IJ}(Z_N, 0, r, 0)$.

Microscales

The microscales introduced by G. I. Taylor and others, [1-4], are generally defined as the minimum radius of curvature of a parabolic approximation of one of the diagonal components of (3), $R_{(I)(I)}$, no sum on I. Substituting the Taylor's series expansion $u_J(r_M) = u_J + ru_{J,M} + (r^2/2)u_{J,(M)(M)} + \ldots$ into (3) gives

$$R_{IJ}(Z_N,r_M) = (<u_Iu_J> + r<u_Iu_{J,M}> + \frac{r^2}{2}<u_Iu_{J,(M)(M)}> + \ldots)/\Phi \tag{4}$$

where $r \equiv r_M$, u_J and its derivatives are evaluated at Z_N and Φ is a function of Z_N only. The radius of curvature of the parabolic approximation, $R_{IJ}(Z_N,r_M) \simeq a_1r^2 + b_1r + c_1$, is given by $\rho = |(1 + (2a_1r + b_1)^2)^{3/2}/(2a_1)|$ which has a minimum, $\rho_{\min.} = |1/(2a_1)|$, for $r_{\min.} = -b_1/(2a_1)$. From (4) it follows that $\rho_{\min.} = |\Phi/<u_Iu_{J,(M)(M)}>|$ and therefore the microscale $\lambda_1(Z_N,I,J,M)$ may be defined as

$$\lambda_1{}^2(Z_N) = |\Phi/<u_Iu_{J,(M)(M)}>| \tag{5}$$

The Taylor microscale, λ_f^2, is a special case of (5) for which $I = J$, $b_1 = 0$ in the parabolic approximation and $\Phi = 2<u_I^2>$, [1]. Since the Φ so defined is not a scalar function of u_J it follows that the associated correlation function (3) is not a tensor quantity. The tensor form for R_{IJ} would be retained if $\Phi = f(<u_Iu_J>)$ for example.

A normalization of (3) in which Φ is a function of both Z_N and r_M or z_n is given by $\Phi = (<u_I(Z_N)u_I(Z_N)>)^{1/2}(<u_k(r_M)u_k(r_M)>)^{1/2}$. Expanding $u_k(r_M)$ in a power series about Z_N gives $(<u_k(r_M)u_k(r_M)>)^{-1/2} = a_2{}^{-1/2}(1 + 2b_2r/a_2 + c_2r^2/a_2 + \ldots)^{-1/2}$ where $a_2 = <u_ku_k>$, $b_2 = <u_ku_{k,M}>$, and $c_2 = <u_ku_{k,(M)}>$, $_{(M)}$ are evaluated at Z_N. The Taylor's expansion about $r = 0$ of the factor $(1 + 2b_2r/a_2 + \ldots)^{-1/2} = 1 - b_2r/a_2 - c_2r^2/2a_2 + (3/8)(4\, b_2^2r^2/a_2^2 + \ldots)$. Substituting into Φ and then into (3) gives

$$R_{IJ}(Z_N,r_M) \simeq a_1r^2 + b_1r + c_1 \tag{6}$$

where $c_1 = <u_Iu_J>/a_2$

$$b_1 = (<u_Iu_{J,M}> - (b_2/a_2)<u_Iu_J>)/a_2 \tag{6a}$$

$$a_1 = ((1/2)<u_Iu_{J,(M)(M)}> + (3b_2^2/2a_2^2 - c_2/2a_2)<u_Iu_J> - (b_2/a_2)<u_Iu_{J,M}>)/a_2 \tag{6b}$$

From (6b) and the definition of the microscale it follows that

$$\lambda_2^2(Z_N) = |1/2a_1| \tag{7}$$

Channel Flow

Consider a turbulent channel flow in which $\mathbf{Z}_1$ is the streamwise coordinate, $\mathbf{Z}_2$ is perpendicular to the channel wall, and $\mathbf{Z}_3$ is orthogonal to $\mathbf{Z}_1$ and $\mathbf{Z}_2$. Assume that the origin of $\mathbf{Z}_N$ is on a wall with $M = 2$ so that $z_1 = 0$, $z_2 = Z_2 + r_2$, and $z_3 = 0$ corresponds to points in the flow. Let $u \equiv u_1/u_{1\tau}$, $y \equiv Z_2u_{1\tau}/\nu$, $u^1 \equiv <u_1{}^2>^{1/2}/u_{1\tau}$, $u_{1\tau} \equiv (\nu u_{1,2}(0))^{1/2}$, and $Q(y) = <u,_Y(0)u(y)>/(u^1(y)<u^2,_Y(0)>^{1/2})$ where $\nu \equiv$ kinematic viscosity and $u,_Y(0)$ is evaluated at the wall, $y = 0$. Expanding u in a power series about the origin gives $u(y) = u,_Y(0)y + u,_{YY}(0)y^2/2 + \ldots$, since $u(0) = 0$. Then $<u^2(y)> = a^2y^2 + by^3 + (c/4 + d/3)y^4 + (e/12 + f/6)y^5 + \ldots$, $<(u,_Y)^2> = a^2 + 2by + (c+d)y^2 + (e/3 + f)y^3 + \ldots$, $<uu,_{YY}> = by + (c/2+d)y^2 + (e/2 + 2f/3)y^3 + \ldots$,

$$u^1(y) = ay + (b/2a)y^2 + (c/8a + d/6a - b^2/8a^3)y^3 + ((e+2f)/24a - b(c/4 + d/3)/4a^3 + b^3/16a^5)y^4 + \ldots \tag{8}$$

[1] Assistant Professor and Professor, respectively, Department of Mechanical Engineering, University of Maryland, College Park, Md. 20742. Mems. ASME.

Manuscript received by ASME Applied Mechanics Division, February, 1982, final revision, September 1982.

Copyright © 1983 by ASME
Downloaded 02 May 2010 to 171.66.16.246. Redistribution subject to ASME license or copyright; see http://www.asme.org/terms/Terms_Use.cfm

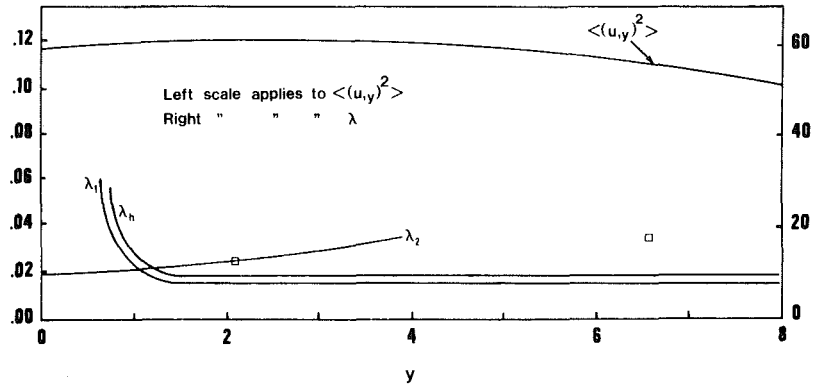

Fig. 1 Microscales and $< (u,_y)^2 >$ in the sublayer

$$Q(y) = 1 + (b^2/8a^4 - c/8a^2)y^2 + (-f/12a^2 + b(c/2 + d)/4a^4 - b^3/16a^6)y^3 + \ldots \quad (9)$$

where $a \equiv <(u,_Y)^2>^{1/2}$, $b \equiv <u,_Yu,_{YY}>$, $c \equiv <(u,_{YY})^2>$, $d \equiv <u,_Yu,_{YYY}>$, $e \equiv <u,_Yu,_{YYYY}>$, and $f \equiv <u,_{YY}u,_{YYY}>$, all evaluated at $y = 0$.

Experimental values of $u^1(y)$ and $Q(y)$, as given in [5], provided the basis for least square polynomial approximations of the form

$$u^1 \simeq \sum_{i=1}^{K} A_i y^i, K=4 \text{ and } Q = 1 + \sum_{i=2}^{N} B_i y^i, N=3.$$

The upper bounds on K and N were set by the limited amount of data available, 28 values for u^1 and 18 for Q. It was found that, for u^1, $A_1 = 0.34465$, $A_2 = 0.0037876$, $A_3 = -0.0015635$, and $A_4 = 0.000040629$ while for Q, $B_2 = -0.0050066$ and $B_3 = 0.0015642$. The percentage of variation explained by the approximation was 99.76 percent for u^1 and 99.21 percent for Q. The six coefficients A_i and B_i were equated to the coefficients of the corresponding powers of y in (8) and (9), providing six equations which when solved gave $a = 0.345$, $b = 0.0026$, $c = 0.0048$, $d = -0.0068$, $e = 0.0012$, and $f = -0.00051$. These values were used to compute λ_h, λ_1, and λ_2, with $I = J = 1$ and $M = 2$ in (5) and (7), and $<(u,_Y)^2>$. Insufficient data precluded the calculation of c_2, $M = 2$, for the general case of $K = 1, 3$. It was therefore necessary, for computation, to redefine ϕ in λ_2, equation (7), as $\phi = <u_1{}^2(Z_N)^{1/2}><u_1{}^2(r_M)>^{1/2}$, which is not a scalar function. For this normalization, with $I = J = 1$ and $M = 2$, (7) becomes

$$\lambda_2^2(Z_N) = <u_1^2>^2/|<u_1{}^2><(u_{1,2})^2> - (<u_1{}^2>_{,2})^2/4| \quad (10)$$

Numerical Results

Figure 1 shows $<(u,_Y)^2>$ as a function of y. The function reaches a maximum at $y \simeq 2.5$. The Taylor microscale λ_h and the closely related λ_1 microscale, equation (5), are both shown to be nearly constant, in Fig. 1, for $1.5 \leq y \leq 8$. The Taylor miscoscale, λ_h, is defined by (4) and (5) for nonhomogeneous turbulence for which $<u_1u_{1,2}>$ and therefore b_1 and $r_{\min.}$ do not vanish everywhere. Both λ_h and λ_1 are undefined at $y = 0.614$ since $<u_1u_{1,22}> = 0$ there. For $0 < y < 0.614$, both $a_1 = (<u_1u_{1,22}>/2\Phi) > 0$ and $b_1 = (<u_1u_{1,2}>/\Phi) > 0$ and $r_{\min.} = -b/2a_1$, the position of the point of minimum radius of curvature relative to y, is found to be outside of the flow region, to the left of the origin at the wall. It follows that λ_h and λ_1 are undefined for $0 < y < 0.614$. The microscales λ_1 and λ_h are defined, as shown in Fig. 1 for $0.614 < y < 8$ since $(<u_1u_{1,22}>) > 0$ and $(<u_1u_{1,2}>) > 0$ in that region.

The differencing required in the computation of the demoninator of λ_2 caused error sensitivity that invalidated results for $y > 2.6$. The upper bound on y could, presumably, be raised as more data becomes available. The normalization associated with the simplified form of λ_2, equation (10), corresponds to an $R_{IJ}(Z_N, r_M)$, equation (6), for which $b_1 = 0$ and therefore $r_{\min.} = 0$. λ_2 is therefore defined at the wall, Fig. 1. The quantity, $<u_1{}^2><(u_{1,2})^2> - (<u_1{}^2>_{,2})^2/4$, which appears in the denominator of (10) is always ≥ 0 since $(<u_1{}^2>_{,2})^2/4 = (<u_1u_{1,2}>)^2$ and $(<u_1u_{1,2}>)^2 \leq |<u_1{}^2>| \cdot |<(u_{1,2})^2>|$ by the Schwarz inequality. The two data points indicated by small squares, in Fig. 1, are values of λ_h found in [2] by independent means. The promixity of these values to those found here, to some extent, support the validitity of the series approximations.

Acknowledgment

The authors wish to express their appreciations to Dr. James Wallace and Dr. Oscar Manley for their encouragment. The work was supported by the Department of Energy, under project number DE-AS05-81ER10809.A000.

References

1 Taylor, G. I., "Statistical Theory of Turbulence, Part 1," *Proc. of the Royal Society, London, Series A*, Vol. 151, 1935, pp. 421-444.

2 Laufer, J., "Investigation of Turbulent Flow in a Two-Dimensional Channel," NACA Rept. No., 1053, 1950.

3 Townsend, A. A., *The Structure of Turbulent Shear Flow*, Cambridge University Press, 1956.

4 Lawn, C. J., "The Determination of the Rate of Dissipation in Turbulent Pipe Flow," *Journal of Fuid Mechanics*, Vol. 48, Part 3, 1971, pp. 477-505.

5 Eckelmann, H. J., "The Structure of the Viscous Sublayer and the Adjacent Wall Region in a Turbulent Channel Flow," *Journal of Fluid Mechanics*, Vol. 65, 1974, pp. 439-459.

6 Ericksen, J. L., "Principles of Classical Mechanics and Field Theory," Section 16, Tensor Fields, *Encyclopedia of Physics*, Vol. 3, Springer-Verlag, New York, 1960.

7 Hinze, J. O., *Turbulence*, McGraw-Hill, New York, 1975.

The Numerical Integration of Green's Functions

B. S. Berger[1] and P. S. Bernard[1]

Introduction

Expressions requiring the numerical integration of products

[1] Professor, and Assistant Professor, respectively, Department of Mechanical Engineering, University of Maryland, College Park, Md. 20742. Mems. ASME.

Manuscript received by ASME Applied Mechanics Division, May, 1982; final revision, November, 1982.

Downloaded 02 May 2010 to 171.66.16.246. Redistribution subject to ASME license or copyright; see http://www.asme.org/terms/Terms_Use.cfm

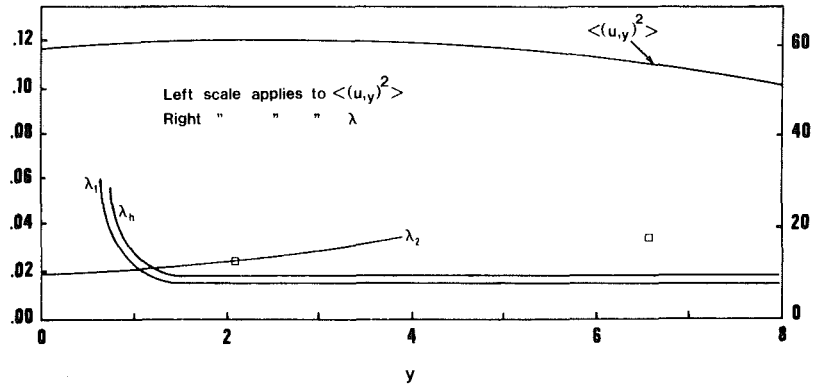

Fig. 1 Microscales and $< (u_{,y})^2 >$ in the sublayer

$$Q(y) = 1 + (b^2/8a^4 - c/8a^2)y^2 + (-f/12a^2 + b(c/2 + d)/4a^4 - b^3/16a^6)y^3 + \ldots \quad (9)$$

where $a \equiv <(u_{,Y})^2>^{1/2}$, $b \equiv <u_{,Y}u_{,YY}>$, $c \equiv <(u_{,YY})^2>$, $d \equiv <u_{,Y}u_{,YYY}>$, $e \equiv <u_{,Y}u_{,YYYY}>$, and $f \equiv <u_{,YY}u_{,YYY}>$, all evaluated at $y = 0$.

Experimental values of $u^1(y)$ and $Q(y)$, as given in [5], provided the basis for least square polynomial approximations of the form

$$u^1 \simeq \sum_{i=1}^{K} A_i y^i, K=4 \text{ and } Q = 1 + \sum_{i=2}^{N} B_i y^i, N=3.$$

The upper bounds on K and N were set by the limited amount of data available, 28 values for u^1 and 18 for Q. It was found that, for u^1, $A_1 = 0.34465$, $A_2 = 0.0037876$, $A_3 = -0.0015635$, and $A_4 = 0.000040629$ while for Q, $B_2 = -0.0050066$ and $B_3 = 0.0015642$. The percentage of variation explained by the approximation was 99.76 percent for u^1 and 99.21 percent for Q. The six coefficients A_i and B_i were equated to the coefficients of the corresponding powers of y in (8) and (9), providing six equations which when solved gave $a = 0.345$, $b = 0.0026$, $c = 0.0048$, $d = -0.0068$, $e = 0.0012$, and $f = -0.00051$. These values were used to compute λ_h, λ_1, and λ_2, with $I = J = 1$ and $M = 2$ in (5) and (7), and $<(u_{,Y})^2>$. Insufficient data precluded the calculation of c_2, $M = 2$, for the general case of $K = 1, 3$. It was therefore necessary, for computation, to redefine ϕ in λ_2, equation (7), as $\phi = <u_1^2(Z_N)^{1/2}><u_1^2(r_M)>^{1/2}$, which is not a scalar function. For this normalization, with $I = J = 1$ and $M = 2$, (7) becomes

$$\lambda_2^2(Z_N) = <u_1^2>^2/|<u_1^2><(u_{1,2})^2> - (<u_1^2>_{,2})^2/4| \quad (10)$$

Numerical Results

Figure 1 shows $<(u_{,Y})^2>$ as a function of y. The function reaches a maximum at $y \simeq 2.5$. The Taylor microscale λ_h and the closely related λ_1 microscale, equation (5), are both shown to be nearly constant, in Fig. 1, for $1.5 \leq y \leq 8$. The Taylor miscoscale, λ_h, is defined by (4) and (5) for nonhomogeneous turbulence for which $<u_1u_{1,2}>$ and therefore b_1 and $r_{\min.}$ do not vanish everywhere. Both λ_h and λ_1 are undefined at $y = 0.614$ since $<u_1u_{1,22}> = 0$ there. For $0 < y < 0.614$, both $a_1 = (<u_1u_{1,22}>/2\Phi) > 0$ and $b_1 = (<u_1u_{1,2}>/\Phi) > 0$ and $r_{\min.} = -b/2a_1$, the position of the point of minimum radius of curvature relative to y, is found to be outside of the flow region, to the left of the origin at the wall. It follows that λ_h and λ_1 are undefined for $0 < y < 0.614$. The microscales λ_1 and λ_h are defined, as shown in Fig. 1 for $0.614 < y < 8$ since $(<u_1u_{1,22}>) > 0$ and $(<u_1u_{1,2}>) > 0$ in that region.

The differencing required in the computation of the demoninator of λ_2 caused error sensitivity that invalidated results for $y > 2.6$. The upper bound on y could, presumably, be raised as more data becomes available. The normalization associated with the simplified form of λ_2, equation (10), corresponds to an $R_{IJ}(Z_N, r_M)$, equation (6), for which $b_1 = 0$ and therefore $r_{\min.} = 0$. λ_2 is therefore defined at the wall, Fig. 1. The quantity, $<u_1^2><(u_{1,2})^2> - (<u_1^2>_{,2})^2/4$, which appears in the denominator of (10) is always ≥ 0 since $(<u_1^2>_{,2})^2/4 = (<u_1u_{1,2}>)^2$ and $(<u_1u_{1,2}>)^2 \leq |<u_1^2>| \cdot |<(u_{1,2})^2>|$ by the Schwarz inequality. The two data points indicated by small squares, in Fig. 1, are values of λ_h found in [2] by independent means. The promixity of these values to those found here, to some extent, support the validitity of the series approximations.

Acknowledgment

The authors wish to express their appreciations to Dr. James Wallace and Dr. Oscar Manley for their encouragment. The work was supported by the Department of Energy, under project number DE-AS05-81ER10809.A000.

References

1 Taylor, G. I., "Statistical Theory of Turbulence, Part 1," *Proc. of the Royal Society, London, Series A*, Vol. 151, 1935, pp. 421-444.

2 Laufer, J., "Investigation of Turbulent Flow in a Two-Dimensional Channel," NACA Rept. No., 1053, 1950.

3 Townsend, A. A., *The Structure of Turbulent Shear Flow*, Cambridge University Press, 1956.

4 Lawn, C. J., "The Determination of the Rate of Dissipation in Turbulent Pipe Flow," *Journal of Fuid Mechanics*, Vol. 48, Part 3, 1971, pp. 477-505.

5 Eckelmann, H. J., "The Structure of the Viscous Sublayer and the Adjacent Wall Region in a Turbulent Channel Flow," *Journal of Fluid Mechanics*, Vol. 65, 1974, pp. 439-459.

6 Ericksen, J. L., "Principles of Classical Mechanics and Field Theory," Section 16, Tensor Fields, *Encyclopedia of Physics*, Vol. 3, Springer-Verlag, New York, 1960.

7 Hinze, J. O., *Turbulence*, McGraw-Hill, New York, 1975.

The Numerical Integration of Green's Functions

B. S. Berger[1] and P. S. Bernard[1]

Introduction

Expressions requiring the numerical integration of products

[1] Professor, and Assistant Professor, respectively, Department of Mechanical Engineering, University of Maryland, College Park, Md. 20742. Mems. ASME.

Manuscript received by ASME Applied Mechanics Division, May, 1982; final revision, November, 1982.

Copyright © 1983 by ASME
Downloaded 02 May 2010 to 171.66.16.246. Redistribution subject to ASME license or copyright; see http://www.asme.org/terms/Terms_Use.cfm

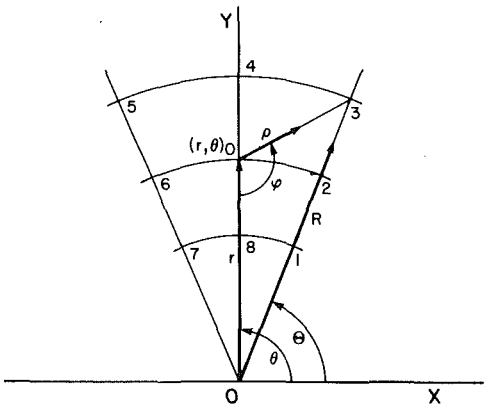

Fig. 1

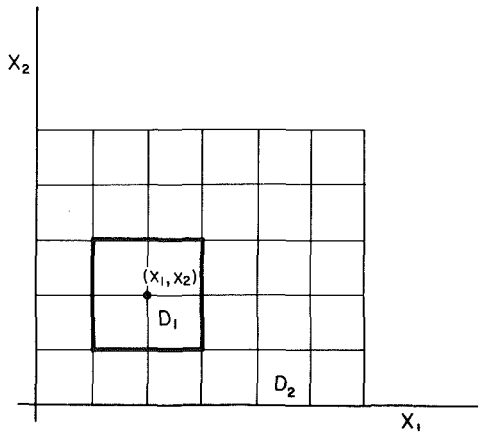

Fig. 2

of Green's functions, or their derivatives with nonsingular functions, arise in both solid and fluid mechanics (references [1-4]). A comprehensive discussion of Green's functions for linear elastodynamics, together with some examples, is given in [1]. It is shown that once Green's function is found for a given geometry, often a difficult task, the solution of a large class of boundary-initial value problems is reduced to the evaluation of definite multiple integrals. For a study of integration formulas for multidimensional singular integrals see [11]. For an incompressible viscous fluid the velocity vector potential may be expressed as the integral of the product of Green's function with the vorticity, [2]. While F.F.T. methods may provide more efficient algorithms for this computation, when cast in partial differential equation form (reference [4]) there are related problems arising in turbulence computations for which the corresponding differential equation form is not known, (reference [5]). In this and other cases for which a numerical evaluation of an integral formulation may be required, the singularities associated with the Green's function constitute a significant computational difficulty.

The technique given here for the numerical integration of products of Green's functions, G, with nonsingular functions, w, is applied to the Poisson equation for the region, D, exterior to a circle. Domain D is subdivided into domains D_1 and D_2 such that D_1 contains the singular point of the integrand and D_2 is covered by a global polar coordinate system. The integral over D_1 is expressed as the sum of a nonsingular integral and the product of the nonsingular function, w, with the integral of Green's function. A transformation to local polar coordinates removes the singularity of Green's function, yielding a nonsingular double integral over an irregular domain which is reduced to a single integral through exact methods. N-dimensional integrals are evaluated with N-dimensional forms of Simpson's rule. The nonsingular function, w, need be defined only at the nodes of the mesh associated with D_2. If a finer mesh than the global is required in D_1, then w may be interpolated in D_1 from the given nodal values in D_2. For the exterior problem, an asymptotic form of the Green's function is employed for $R >$ exp.(8).

Comparisons between exact and numerical results are in excellent agreement. The technique is applicable to both two and three-dimensional geometries. Algorithms for the integration of singular functions defined on the real line (reference [6]) do not entirely reflect the computational difficulties associated with the N-dimensional integration of products of Green's functions with nonsingular functions defined at nodal points.

Green's Functions

Consider the velocity vector potential, $B(x_1, x_2)$, and vorticity vector $w(X_1, X_2)$ which satisfy (reference [2])

$$\nabla^2 B = -w \tag{1}$$

for the region exterior to the unit circle where $R = \exp X_1$, $r = \exp x_1$, $X_2 = \Theta$, $x_2 = \theta$ and R, Θ, r, θ are polar coordinates, see Fig. 1. The x_1, X_1 coordinates are introduced in applications to expand the R, Θ grid step size as R increases for a constant step size in X_1. The Green's function for (1) with the given geometry is known to be

$$G(r,\theta;R,\Theta) = (-1/4\pi)\log(N/M) \tag{2}$$

where $N = r^2 - 2rR\cos(\theta-\Theta) + R^2$ and $M = 1 - (2/rR)\cos(\theta-\Theta) + 1/(rR)^2$, [7]. Then

$$B(x_1,x_2) = \int\int_D G(x_1,x_2;X_1,X_2)w(X_1,X_2)dA \tag{3}$$

where $dA = RdRd\Theta = \exp(2X_1)dX_1dX_2$ and the integration is over the region, D, exterior to the circle (reference [3]). Since (x_1,x_2) or (r,θ) are coordinates of a point in D it follows that the arguments X_1,X_2 of $G(x_1,x_2;X_1,X_2)$ in (3) will always take on the value $X_1 = x_1$ and $X_2 = x_2$ or $R = r$ and $\Theta = \theta$. From (2) and the definition of N and M it follows that $N/M = 0$ for this point and therefore that $G(r,\theta;R,\Theta)$ will be unbounded. The existence of a singularity for $G(x_n;X_n)$ at $x_n = X_n$ is a property of Green's functions, (reference [3]).

Therefore the domain D is taken to be the sum of two subdomains D_1 and D_2 such that D_1 contains the singular point (x_1,x_2), Fig. 2. Then (3) may be evaluated by any of the standard cubature formulas (references [8,9]) over the subdomain D_2. The integration of (3) over D_1 may be accomplished by letting

$$\int\int_{D_1} G(x_1,x_2;X_1,X_2)w(X_1,X_2)dA$$

$$= \int\int_{D_1} G(x_1,x_2;X_1,X_2)(w(X_1,X_2) - w(x_1,x_2))dA$$

$$+ w(x_1,x_2)\int\int_{D_1} G(x_1,x_2;X_1,X_2)dA \tag{4}$$

For a large class of functions $w(X_1,X_2)$ including those that possess a convergent power series expansion, in the neighborhood of (x_1,x_2), the first integrand on the right side of (4) vanishes at the singular point $(x_1 = X_1, x_2 = X_2)$ of $G(x_1,x_2;X_1,X_2)$ (reference [10]). It follows, therefore, that this integral may be evaluated by any of the standard cubature formulas. The second integral on the right side of (4) may be written

$$\int\int_{D_1} G(x_1,x_2;X_1,X_2)dA = (-1/4\pi)\int\int_{D_1} \log N dA$$

$$+ (1/4\pi)\int\int_{D_1} \log M dA \tag{5}$$

Downloaded 02 May 2010 to 171.66.16.246. Redistribution subject to ASME license or copyright; see http://www.asme.org/terms/Terms_Use.cfm

where $\log M$ is well behaved in D_1. It follows that the second integral on the right side of (5) may be evaluated by the standard methods. The singularity of $\log N$ occurring in the first integral on the right side of (5) may be removed through a coordinate transformation to the local polar coordinates ρ and ϕ with origin at the singularity $R = r$, $\Theta = \theta$, Fig. 1, which gives

$$(-1/4\pi)\int\int_{D_1} \log N dA = (-1/2\pi)\int\int_{D_1} (\log\rho)\rho d\rho d\phi \qquad (6)$$

Note that $\lim(\rho\log\rho) = 0$ for $\rho = 0$. It is seen from Figs. 1 and 2 that the boundaries of D_1, which are coordinate lines in X_1 and X_2, do not coincide with the coordinate lines of the local ρ, ϕ coordinates. Thus the limits of integration for (6) are variable in ρ and ϕ. For Green's functions possessing singularities of greater complexity, the evaluation of the expression corresponding to (6) could be accomplished through the application of the adaptive formula for numerical integration over an irregular region given in [12]. However, for the example considered here, equation (6) may be integrated exactly with respect to ρ to give

$$\int\int_{D_1} (\log\rho)\rho d\rho d\phi = \frac{1}{2}\int_{D_1} (\rho^2\log\rho - \frac{1}{2}\rho^2)d\phi \qquad (7)$$

where $\rho = \rho(\phi)$ is given by $\rho = r(\sin\theta - a\cos\theta)/(a\sin\phi + \cos\phi)$ over the radial lines defined by Θ constant, with $a = \tan^{-1}(\theta - \Delta\Theta)$, $\Delta\Theta = \Delta X_2$ = step size in X_2 and by $\rho = -r\sin(\phi - \theta) \pm (r^2\sin^2(\phi-\theta) + (R_o^2 - r^2))^{1/2}$ over a given circular arc $R = R_0$, Fig. 1. It follows that (7) may be evaluated by standard methods and therefore that (5) may be computed to as high a degree of accuracy as required, for a given grid. If the evaluation of (3) is part of an iteration, over the same grid for various $w(X_1,X_2)$ then (5) and $G(x_1,x_2;X_1,X_2)$ need be computed only once. In this and subsequent computations the symmetry of the Green's function $G(x_1,x_2;X_1,X_2) = G(X_1,X_2;x_1,x_2)$, significantly reduces computer storage requirements (reference [3]). An alternative method for the evaluation of the left side of (4) involves its transformation to the local cylindrical coordinates ρ, ϕ and the double integration of the resulting nonsingular integrand over a domain with irregular boundaries using [12]. This is a disadvantage if the evaluation of (3) is part of an iteration over the same grid for various $w(X_1,X_2)$. Furthermore, since the alternative method involves the evaluation of $w(X_1,X_2)$ at other than the grid points, a double interpolation would be required for a $w(X_1,X_2)$ defined only over the grid points. The method developed here requires the integration of only the Green's function over the irregular domain, equations (5) and (6).

Numerical Results

The following exact solution of (1), $w = (2/r^3) - (4/r^4)$ and $B = (1/r^2) - (2/r)$, was used as a test of the accuracy and computational utility of the method. Note that $\partial B(r,\theta)/\partial\theta = 0$ for $r = 1$ as is required by (2) and (3) and that w is such that the integral in (3) exists for the region exterior to the unit circle. Although the test function, $w(R)$, is a function of R only, all integrands are functions of both R and Θ, X_1 and X_2, since the Green's function is a function of R and Θ. The domain D in (3) was defined as $0 \le X_1 \le 8$ and $0 \le X_2 \le 2\pi$ which corresponds to $1 \le R \le \exp.(8)$ and $0 \le \Theta \le 2\pi$. A grid was taken over D_2 with a grid spacing of $\Delta X_1 = 0.0875$ and $\Delta X_2 = 0.75\pi$. The domain D_1 was defined as $0.8 \le X_1 \le 1.6$ and $0.4\pi \le X_2 \le 0.6\pi$, Fig. 2. A uniform $N \times N$ grid was taken over D_1 for which $N = 2, 4, 8$ where $N \equiv$ number of intervals. Double integrations over D_1 and D_2 were carried out using a two-dimensional generalization of Simpson's rule (references [8,9]). Computations showed that the evaluations of the first integral on the right side of (4) and the second integral on the right side of (5) changed only in the fifth digit for $N = 4$ and $N = 8$. The evaluation of the first integral on the right side of (5) over the irregular region, Fig. 1, using (6) and (7) was accomplished using a one dimensional Simpson's rule subroutine, SIAMINI, with automatic step-size reduction. The relative error specified was $(1.0)10^{-4}$. $B(x_1,x_2)$ was evaluated for the three points, $x_2 = 0$ and $x_1 = 0.4$, 0.8, and 1.2. The differences between the exact and numerical results were found to be -0.006 to three digits for each point. An asymptotic form of (2) for $R >> r$ may be derived by taking $\lim R \to +\infty$ which gives $G(r,\theta;R,\Theta) \simeq (-1/4\pi)\log R^2$. Substituting into (3) yields

$$\Delta B(r,\theta) = (-1/4\pi)\int_0^{2\pi}\int_\alpha^\infty \log R^2 w(R,\Theta) R dR d\Theta \qquad (8)$$

where $\alpha = \exp(8.0)$ and $\Delta B(r,\theta)$ is the contribution to $B(r,\theta)$ from (3) for the region $R > \exp.(8.0)$. The evaluation of (8), which may be done exactly for the test function, gives $\Delta B(r,\theta) = -0.006036$. Adding $\Delta B(r,\theta)$ to the results of the numerical integrations over D_1 and D_2 gives $B(r,\theta) = -0.891316$, -0.696753, and -0.511654 for $x_1 = 0.4$, 0.8, and 1.2. The exact values for $B(r,\theta) = -0.891311$, -0.696761, and -0.511671, respectively. The numerical and the exact solutions differ only in the fifth or sixth significant digit.

The method may be applied to the three-dimensional case and to partial differential equations other than (1). In the general case the Green's function, equation (2) may be written as the sum of a singular and a nonsingular function such that (3) holds over a volume (references [1,3]). It follows that (4) is valid over a volume and that the decomposition given by (5) is always possible. The singularity occurring in the Green's function is such that a transformation to local spherical coordinates will remove it (references [1,3]). Therefore the integrand on the right side of (6) will be nonsingular for the general case. The integral over the irregular three-dimensional region may be evaluated by methods given in [8]. For the Poisson and related equations an exact integration in ρ may be used to reduce the dimensionality of the integration.

Conclusion

A technique has been developed for the numerical integration of products of Green's functions with nonsingular functions which is applicable to two and three-dimensional geometries. Comparisons between exact and numerical solutions for the Poisson equation, in the region exterior to the circle, show excellent agreement. For the exterior problem, an asymptotic form of the Green's function was used for the region R > exp. (8). This could be dispensed with for the interior problem. The level of accuracy attained indicates that integration in terms of local coordinates that remove the singularity but introduce irregular boundaries in terms of the global coordinates, may be accomplished efficiently and with a high degree of accuracy.

Acknowledgments

The authors wish to express their appreciation to Drs. Oscar Manley and James Wallace for their encouragement. The work was supported by the Department of Energy, under project number DE-AS05-81ER10809.A000.

References

1 Eringen, A. C., and Suhubi, E. S., *Elastodynamics*, Vol. II, Academic Press, New York, 1975.

Downloaded 02 May 2010 to 171.66.16.246. Redistribution subject to ASME license or copyright; see http://www.asme.org/terms/Terms_Use.cfm

2 Batchelor, G. K., *An Introduction to Fluid Dynamics*, Cambridge University Press, 1967.
3 Morse, P. M., and Feshbach, H., *Methods of Theoretical Physics*, Parts I and II, McGraw-Hill, New York, 1953.
4 Roache, P. J., *Computational Fluid Dynamics*, Hermosa Pub., Albuquerque, N.Mex., 1976.
5 Bernard, P. S., and Berger, B. S., "A Method For Computing Three-Dimensional Turbulent Flows," *SIAM Jour. of Applied Math*, June, 1982.
6 Isaacson, E., and Keller, H. B., *Analysis of Numerical Methods*, Wiley, New York, 1966.
7 Milne, Thomson, L. M., *Theoretical Hydrodynamics*, MacMillan, New York, 1950.
8 Davis, P. J., and Rabinowitz, P., *Methods of Numerical Integration*, Academic Press, New York, 1975.
9 Engels, H., *Numerical Quadrature and Cubature*, Academic Press, New York, 1980.
10 Mayers, D. F., "Quadrature Methods for Fredholm Equations of the Second Kind, Numerical Solution of Integral Equations," Delves, L., and Walsh, J., eds., Oxford, 1974, pp. 64–96.
11 Gabdulkhaev, R. G., "Cubature Formulas for Multi-dimensional Singular Integrals," II, *Izvestiya Vysshikh Uchebnykh Zavedenii, Matematika*, Vol. 19, No. 4, 1975, pp. 3–13.
12 Ichida, K., and Kiyono, T., "Numerical Integration in the Irregular Region," *Computing*, Vol. 12, 1974, pp. 9–15.

The Effects of Finite Amplitude on the Behavior of Antisymmetric Waves on Two-Dimensional Liquid Sheets

R. Y. Tam[1] and M. S. Cramer[2]

Introduction

In many industrial processes liquids are sprayed in the form of thin sheets. Well-known examples include the spraying of liquid fuels [1], film coating processes, and the spraying of paints and insecticides. The dynamics of both radially flowing and two-dimensional sheets have been examined by a number of authors; see, for example, [2–7]. The disintegration of these sheets and resultant droplet formation is frequently associated with the stability of waves that propagate relative to the fluid. These waves are driven by surface tension and can be of two distinct modes. The first corresponds to a pure thickness variation which leaves the centerline undisturbed and the second is a constant thickness mode in which the centerline is displaced. We will follow Taylor [4] and refer to these as the symmetric and antisymmetric modes, respectively. With the exception of Clark and Dombrowski [6] and the steady flow analysis of Kinnersley [8] all previous investigations have been restricted to linear analyses. The purpose of this Note is to extend these results to include the effect of finite amplitude on the propagation of antisymmetric waves.

Formulation

We employ a Cartesian coordinate system in which the flow direction of the undisturbed sheet is the $\bar{x}$ direction and which moves with the velocity of the undisturbed fluid. The free surfaces of the undisturbed and disturbed sheet are given by $\bar{y} = \pm h$ and $\bar{y} = \pm h + \eta^{\pm}(\bar{x}, \bar{t})$, respectively, where $\bar{t}$ is the time, and the upper and lower signs denote the upper and lower surfaces. Here we will assume the flow is irrotational and ignore the effects of the surrounding gas and gravity. As a result, the exact nondimensional equations of motion are

$$\phi_{xx} + \phi_{yy} = 0 \quad \text{for} \quad -1 + \epsilon\eta^{-} \le y \le 1 + \epsilon\eta^{+} \tag{1}$$

where, on $y = \pm 1 + \epsilon\eta^{\pm}$,

$$\phi_y = \eta_t^{\pm} + \epsilon\eta_x^{\pm}\phi_x \tag{2}$$

and

$$\phi_t + \frac{\epsilon}{2}[\phi_x^2 + \phi_y^2] = \pm[1 + \epsilon^2\eta_x^{\pm 2}]^{-3/2}\eta_{xx}^{\pm}, \tag{3}$$

where $\phi(x,y,t;\epsilon)$ is the nondimensional velocity potential and the dimensional quantities $\bar{\eta}^{\pm}, \bar{\phi}, \bar{y}, \bar{x}$, and $\bar{t}$ are related to their nondimensional counterparts by:

$$\bar{\eta}^{\pm} = \epsilon h\eta^{\pm}, \quad \bar{\phi} \equiv \epsilon\left(\frac{Th}{\rho}\right)^{1/2}\phi, \quad \bar{x} \equiv hx,$$

$$\bar{y} \equiv hy \quad \text{and} \quad \bar{t} \equiv h\left(\frac{\rho h}{T}\right)^{1/2} t.$$

The quantities T and ρ are the surface tension and liquid density, respectively. The first equation is recognized as the usual continuity equation for incompressible irrotational flow, the second is the kinematic boundary condition, and the third is the unsteady Bernoulli equation evaluated at the free surfaces.

In the small amplitude limit, equations (1)–(3) admit lowest order wave-train solutions of the form $Aexpi\mu(x-ct)$ where μ is a nondimensional wave number such that the length of the wave is given by $h\mu^{-1}$ and the phase speed c is given by either $(\mu\tanh\mu)^{1/2}$ or $\mu^{1/2}\tanh\mu^{-1/2}$ which corresponds to the symmetric and antisymmeric modes, respectively. In the linear theory, these modes are completely uncoupled and can propagate independently of each other.

Because of the nonlinear terms appearing in (1)–(3), the linear solution is only expected to be valid over relatively short times. We have therefore used the method of multiple scales to analyze the long time behavior of antisymmetric waves as they propagate on these sheets and in this Note will simply record the main results.

Because of the symmetry of the symmetric mode, its behavior is exactly that of a capillary wave on water of constant depth. The nonlinear results for pure symmetric waves may therefore be extracted from the extensive literature on gravity-capillary waves if we set the gravitational acceleration g identically equal to zero and simultaneously require that the wave number μ be fixed.

Results and Discussion

Our analysis has shown that the disturbance function $\eta^{\pm}(x,t;\epsilon)$ is given by

$$\eta^{\pm} = Ae^{i\theta} \mp \frac{\epsilon}{2}\mu\tanh\mu A^2 e^{i2\theta} + \epsilon[BA^3 e^{i3\theta} \pm DAA_x e^{i2\theta}] + 0(\epsilon^3), \tag{4}$$

where $B = B(\mu)$, $D = D(\mu;\epsilon)$, $\theta \equiv \mu x - \omega t$ and $\omega = (\mu)^{3/2}\tanh\mu^{-1/2}$. The quantities B and D are somewhat complicated and, in order to save space, we will simply note that they are bounded for all values of $\mu \ge 0$. When x and t are of order ϵ^{-2}, we find that the foregoing expansion for $\eta^{\pm}$ is valid only if A satisfies

$$A_t + \omega' A_x = \frac{i\omega''}{2}A_{xx} + \frac{i\epsilon^2\alpha}{4}A^2A^*, \tag{5}$$

where A^* denotes the complex conjugate of A, and $\omega' \equiv d\omega/d\mu$, $\omega'' \equiv d^2\omega/d\mu^2$ and $\alpha \equiv \mu^2\omega(7\tanh^2\mu - 6)$.

Equation (5) is the well-known cubic Schrödinger equation first discussed in connection with nonlinear wave propagation

[1] Graduate Student, Department of Theoretical and Applied Mechanics, Cornell University, Ithaca, N.Y.
[2] Assistant Professor, Department of Engineering Science and Mechanics, Virginia Polytechnic Institute and State University, Blacksburg, Va. 24060.
Manuscript received by ASME Applied Mechanics Division, June, 1982; final revision, September, 1982.

Downloaded 02 May 2010 to 171.66.16.246. Redistribution subject to ASME license or copyright; see http://www.asme.org/terms/Terms_Use.cfm

2 Batchelor, G. K., *An Introduction to Fluid Dynamics*, Cambridge University Press, 1967.
3 Morse, P. M., and Feshbach, H., *Methods of Theoretical Physics*, Parts I and II, McGraw-Hill, New York, 1953.
4 Roache, P. J., *Computational Fluid Dynamics*, Hermosa Pub., Albuquerque, N.Mex., 1976.
5 Bernard, P. S., and Berger, B. S., "A Method For Computing Three-Dimensional Turbulent Flows," *SIAM Jour. of Applied Math*, June, 1982.
6 Isaacson, E., and Keller, H. B., *Analysis of Numerical Methods*, Wiley, New York, 1966.
7 Milne, Thomson, L. M., *Theoretical Hydrodynamics*, MacMillan, New York, 1950.
8 Davis, P. J., and Rabinowitz, P., *Methods of Numerical Integration*, Academic Press, New York, 1975.
9 Engels, H., *Numerical Quadrature and Cubature*, Academic Press, New York, 1980.
10 Mayers, D. F., "Quadrature Methods for Fredholm Equations of the Second Kind, Numerical Solution of Integral Equations," Delves, L., and Walsh, J., eds., Oxford, 1974, pp. 64–96.
11 Gabdulkhaev, R. G., "Cubature Formulas for Multi-dimensional Singular Integrals," II, *Izvestiya Vysshikh Uchebnykh Zavedenii, Matematika*, Vol. 19, No. 4, 1975, pp. 3–13.
12 Ichida, K., and Kiyono, T., "Numerical Integration in the Irregular Region," *Computing*, Vol. 12, 1974, pp. 9–15.

The Effects of Finite Amplitude on the Behavior of Antisymmetric Waves on Two-Dimensional Liquid Sheets

R. Y. Tam[1] and M. S. Cramer[2]

Introduction

In many industrial processes liquids are sprayed in the form of thin sheets. Well-known examples include the spraying of liquid fuels [1], film coating processes, and the spraying of paints and insecticides. The dynamics of both radially flowing and two-dimensional sheets have been examined by a number of authors; see, for example, [2–7]. The disintegration of these sheets and resultant droplet formation is frequently associated with the stability of waves that propagate relative to the fluid. These waves are driven by surface tension and can be of two distinct modes. The first corresponds to a pure thickness variation which leaves the centerline undisturbed and the second is a constant thickness mode in which the centerline is displaced. We will follow Taylor [4] and refer to these as the symmetric and antisymmetric modes, respectively. With the exception of Clark and Dombrowski [6] and the steady flow analysis of Kinnersley [8] all previous investigations have been restricted to linear analyses. The purpose of this Note is to extend these results to include the effect of finite amplitude on the propagation of antisymmetric waves.

Formulation

We employ a Cartesian coordinate system in which the flow direction of the undisturbed sheet is the $\bar{x}$ direction and which moves with the velocity of the undisturbed fluid. The free surfaces of the undisturbed and disturbed sheet are given by $\bar{y} = \pm h$ and $\bar{y} = \pm h + \eta^{\pm}(\bar{x}, \bar{t})$, respectively, where $\bar{t}$ is the time, and the upper and lower signs denote the upper and lower surfaces. Here we will assume the flow is irrotational and ignore the effects of the surrounding gas and gravity. As a result, the exact nondimensional equations of motion are

$$\phi_{xx} + \phi_{yy} = 0 \quad \text{for} \quad -1 + \epsilon\eta^{-} \le y \le 1 + \epsilon\eta^{+} \tag{1}$$

where, on $y = \pm 1 + \epsilon\eta^{\pm}$,

$$\phi_y = \eta_t^{\pm} + \epsilon\eta_x^{\pm}\phi_x \tag{2}$$

and

$$\phi_t + \frac{\epsilon}{2}[\phi_x^2 + \phi_y^2] = \pm[1 + \epsilon^2\eta_x^{\pm 2}]^{-3/2}\eta_{xx}^{\pm}, \tag{3}$$

where $\phi(x,y,t;\epsilon)$ is the nondimensional velocity potential and the dimensional quantities $\bar{\eta}^{\pm}, \bar{\phi}, \bar{y}, \bar{x}$, and $\bar{t}$ are related to their nondimensional counterparts by:

$$\bar{\eta}^{\pm} = \epsilon h\eta^{\pm}, \quad \bar{\phi} \equiv \epsilon\left(\frac{Th}{\rho}\right)^{1/2}\phi, \quad \bar{x} \equiv hx,$$

$$\bar{y} \equiv hy \quad \text{and} \quad \bar{t} \equiv h\left(\frac{\rho h}{T}\right)^{1/2} t.$$

The quantities T and ρ are the surface tension and liquid density, respectively. The first equation is recognized as the usual continuity equation for incompressible irrotational flow, the second is the kinematic boundary condition, and the third is the unsteady Bernoulli equation evaluated at the free surfaces.

In the small amplitude limit, equations (1)–(3) admit lowest order wave-train solutions of the form $Aexpi\mu(x-ct)$ where μ is a nondimensional wave number such that the length of the wave is given by $h\mu^{-1}$ and the phase speed c is given by either $(\mu\tanh\mu)^{1/2}$ or $\mu^{1/2}\tanh\mu^{-1/2}$ which corresponds to the symmetric and antisymmeric modes, respectively. In the linear theory, these modes are completely uncoupled and can propagate independently of each other.

Because of the nonlinear terms appearing in (1)–(3), the linear solution is only expected to be valid over relatively short times. We have therefore used the method of multiple scales to analyze the long time behavior of antisymmetric waves as they propagate on these sheets and in this Note will simply record the main results.

Because of the symmetry of the symmetric mode, its behavior is exactly that of a capillary wave on water of constant depth. The nonlinear results for pure symmetric waves may therefore be extracted from the extensive literature on gravity-capillary waves if we set the gravitational acceleration g identically equal to zero and simultaneously require that the wave number μ be fixed.

Results and Discussion

Our analysis has shown that the disturbance function $\eta^{\pm}(x,t;\epsilon)$ is given by

$$\eta^{\pm} = Ae^{i\theta} \mp \frac{\epsilon}{2}\mu\tanh\mu A^2 e^{i2\theta} + \epsilon[BA^3 e^{i3\theta} \pm DAA_x e^{i2\theta}] + 0(\epsilon^3), \tag{4}$$

where $B = B(\mu)$, $D = D(\mu;\epsilon)$, $\theta \equiv \mu x - \omega t$ and $\omega = (\mu)^{3/2}\tanh\mu^{-1/2}$. The quantities B and D are somewhat complicated and, in order to save space, we will simply note that they are bounded for all values of $\mu \ge 0$. When x and t are of order ϵ^{-2}, we find that the foregoing expansion for $\eta^{\pm}$ is valid only if A satisfies

$$A_t + \omega' A_x = \frac{i\omega''}{2}A_{xx} + \frac{i\epsilon^2\alpha}{4}A^2A^*, \tag{5}$$

where A^* denotes the complex conjugate of A, and $\omega' \equiv d\omega/d\mu$, $\omega'' \equiv d^2\omega/d\mu^2$ and $\alpha \equiv \mu^2\omega(7\tanh^2\mu - 6)$.

Equation (5) is the well-known cubic Schrödinger equation first discussed in connection with nonlinear wave propagation

[1] Graduate Student, Department of Theoretical and Applied Mechanics, Cornell University, Ithaca, N.Y.
[2] Assistant Professor, Department of Engineering Science and Mechanics, Virginia Polytechnic Institute and State University, Blacksburg, Va. 24060.
Manuscript received by ASME Applied Mechanics Division, June, 1982; final revision, September, 1982.

Copyright © 1983 by ASME
Downloaded 02 May 2010 to 171.66.16.246. Redistribution subject to ASME license or copyright; see http://www.asme.org/terms/Terms_Use.cfm

by Benney and Newell [9]. Since then a number of studies have examined its behavior; an excellent review which includes extensions to higher dimensions has been provided by Yuen and Lake [10]. A useful feature of this equation is that it can describe the modulational stability of the simple constant amplitude solutions obtained in the linear theories mentioned in the foregoing. For $t = 0(\epsilon^{-2})$ the solution for A corresponding to these wave trains is

$$A = a_0 \exp \frac{i\alpha a_0^2 \epsilon^2}{4} t$$

and can be recognized as the analog of a Stokes wave in the theory of surface gravity waves. The stability of this wave train to small perturbations depends on the relative signs of α and ω''. In this problem, $\omega'' > 0$ for all μ but α changes sign at $\mu = \mu_c$, where

$$\mu_c \equiv \frac{1}{2} ln\left[\frac{\sqrt{7}+\sqrt{6}}{\sqrt{7}-\sqrt{6}}\right] \approx 1.628.$$

If we apply a simple linear stability analysis to (5), see, e.g., [11], we can show that this wave train is stable to all small disturbances provided $0 < \mu < \mu_c$ and, if $\mu > \mu_c$, it will be stable to perturbations having a wave number greater than $\epsilon a_0[\alpha/\omega'']^{1/2}$ but unstable to longer perturbations. In the latter case, we expect both the complex and simple recurrence phenomena described by Yuen and Ferguson [12]. The fact that sufficiently long antisymmetric waves are unconditionally stable to two-dimensional disturbances contrasts with the corresponding results for the symmetric mode. There, all wave trains may become unstable if the modulation is sufficiently long.

We have also examined the possibility of wave-wave interaction in the system (1)–(3). The usual kinematic analysis [13] shows that although no interaction is possible between waves of the same mode, simple two wave interactions do appear possible between a symmetric and antisymmetric mode. However, the authors have conducted the appropriate multiple scales analysis of (1)–(3) and found that the interaction coefficients are identically zero; this, of course, could have been anticipated from the fact that the expansion (4) was seen to be nonsingular. Thus, although the dispersion relations satisfy the appropriate resonance conditions, equations (1)–(3) preclude any such interaction. As a result, we conclude that when the interaction with the surrounding gas is ignored, there can be no significant energy exchange between modes.

References

1 Williams, A., *Combustion of Sprays of Liquid Fuels*, Elek Science, 1976, London.

2 Squire, H. B., "Investigation of the Instability of a Moving Liquid Film," *British J. Appl. Phys.*, Vol. 4, 1953, pp. 167–169.

3 Hagerty, W. W., and Shea, J. F., "A Study of the Stability of Plane Fluid Sheets," ASME JOURNAL OF APPLIED MECHANICS, 1955, pp. 509–514.

4 Taylor, G. I., "The Dynamics of Thin Sheets of Fluid II. Waves on Fluid Sheets," *Proc. R. Soc.*, Series A, Vol. 253, 1959, pp. 296–312.

5 Huang, J. C. P., "The Break-up of Axisymmetric Liquid Sheets," *J. Fluid Mech.*, Vol. 43, 1970, pp. 305–319.

6 Clark, G. J., and Dombrowski, N., "Aerodynamic Instability and Disintegration of Inviscid Liquid Sheets," *Proc. R. Soc.*, Series A, Vol. 329, 1972, pp. 467–478.

7 Weihs, D., "Stability of Thin Radially Moving Liquid Sheets," *J. Fluid Mech.*, Vol. 87, 1978, pp. 289–298.

8 Kinnersley, W., "Exact Large Amplitude Capillary Waves on Sheets of Fluid," *J. Fluid Mech.*, Vol. 77, 1976, pp. 229–241.

9 Benney, D. J., and Newell, A. C., "The Propagation of Nonlinear Wave Envelopes," *J. Math. Phys.*, 1967, Vol. 46, pp. 133–139.

10 Yuen, H. C., and Lake, B. M., "Nonlinear Dynamics of Deep-Water Gravity Waves," *Advances Appl. Mech.*, Vol. 22, 1982, pp. 67–229.

11 Hasimoto, H., and Ono, H., "Nonlinear Modulation of Gravity Waves," *J. Phys. Soc. Japan*, 1972, Vol. 33, pp. 805–811.

12 Yuen, H. C., and Ferguson, W. E., Jr., "Relationship Between Benjamin-Feir Instability and Recurrence in the Nonlinear Schrodinger Equation," *Phys. Fluids*, Vol. 21, 1978, pp. 1275–1278.

13 Phillips, O. M., *The Dynamics of the Upper Ocean*, Cambridge University Press, London, 1977.

Analysis of Photoelastic Fringes in Wave Propagation Problems

A. J. Durelli[1] and A. Shukla[2]

Introduction

Attention has been called, in another paper [1], to the stumbling block that exists at present for the photoelastic analysis of some wave propagation problems. The high-fringe density and the high-fringe orders present in isochromatic patterns associated with waves make it so difficult in many cases to identify the fringe orders that frequently no quantitative analysis is conducted and comments are limited to the evaluation of the type of waves that seem likely to correspond to some portions of the patterns. In the previous paper guidelines were given which permit the numbering of the fringes in most cases of practical interest. Those guidelines are based on topological properties of the patterns, and also require a particular observation of their time derivatives.

In this note, the application of the suggested procedures will be illustrated with the analysis of a complicated problem of interaction of several types of waves. No quantitative analysis of this type of problem had previously been attempted, due to the great complexity of the pattern and a lack of guidelines to properly number the fringe orders.

Review of Basic Guidelines

Some of the guidelines of numbering isochromatic fringes in dynamic problems will be briefly reviewed. (1) Outward square corners on free boundaries are points of zero τ_{max} as required by equilibrium; (2) At points of maximum (peaks) or minimum (valleys) τ_{max} value, the space derivative of τ_{max} in a direction perpendicular to the direction of the fringe, is zero. The gradient in that direction, of the curve representing the fringe order is zero at those points. The distance between fringes close to those points is therefore larger than the distance between fringes further removed from those points. (3) It can also be observed that the width of the fringes is related to the gradient. The sharper the gradient the thinner the fringe. Wider fringes indicate lower gradients. (4) Where fringes of the same order cross (saddle) the transition fringes divide the field in four zones. Moving away from the saddle point the fringe order increases in two of the opposite zones, and decreases in the other two. (5) Shades of gray connecting two fringes indicate that their order is the same. (6) The edge, or Rayleigh-type wave fringes, moving along a boundary exhibit two peaks separated by a zero, and another peak and two other zeros in the subsurface.

Example Illustrating the Use of Guidelines

The example presented here is of a wave propagation in a thin square plate subjected to an explosion at one of its

[1] Professor, Department of Mechanical Engineering, College of Engineering, University of Maryland, College Park, Md. 20742. Fellow ASME.

[2] Resident Student, Civil Engineering Department, IIT Kanpar 208016, India.

Manuscript received by ASME Applied Mechanics Division, March, 1982; final revision, June, 1982.

Downloaded 02 May 2010 to 171.66.16.246. Redistribution subject to ASME license or copyright; see http://www.asme.org/terms/Terms_Use.cfm

by Benney and Newell [9]. Since then a number of studies have examined its behavior; an excellent review which includes extensions to higher dimensions has been provided by Yuen and Lake [10]. A useful feature of this equation is that it can describe the modulational stability of the simple constant amplitude solutions obtained in the linear theories mentioned in the foregoing. For $t = 0(\epsilon^{-2})$ the solution for A corresponding to these wave trains is

$$A = a_0 \exp \frac{i\alpha a_0^2 \epsilon^2}{4} t$$

and can be recognized as the analog of a Stokes wave in the theory of surface gravity waves. The stability of this wave train to small perturbations depends on the relative signs of α and ω''. In this problem, $\omega'' > 0$ for all μ but α changes sign at $\mu = \mu_c$, where

$$\mu_c \equiv \frac{1}{2} ln\left[\frac{\sqrt{7}+\sqrt{6}}{\sqrt{7}-\sqrt{6}}\right] \approx 1.628.$$

If we apply a simple linear stability analysis to (5), see, e.g., [11], we can show that this wave train is stable to all small disturbances provided $0 < \mu < \mu_c$ and, if $\mu > \mu_c$, it will be stable to perturbations having a wave number greater than $\epsilon a_0[\alpha/\omega'']^{1/2}$ but unstable to longer perturbations. In the latter case, we expect both the complex and simple recurrence phenomena described by Yuen and Ferguson [12]. The fact that sufficiently long antisymmetric waves are unconditionally stable to two-dimensional disturbances contrasts with the corresponding results for the symmetric mode. There, all wave trains may become unstable if the modulation is sufficiently long.

We have also examined the possibility of wave-wave interaction in the system (1)–(3). The usual kinematic analysis [13] shows that although no interaction is possible between waves of the same mode, simple two wave interactions do appear possible between a symmetric and antisymmetric mode. However, the authors have conducted the appropriate multiple scales analysis of (1)–(3) and found that the interaction coefficients are identically zero; this, of course, could have been anticipated from the fact that the expansion (4) was seen to be nonsingular. Thus, although the dispersion relations satisfy the appropriate resonance conditions, equations (1)–(3) preclude any such interaction. As a result, we conclude that when the interaction with the surrounding gas is ignored, there can be no significant energy exchange between modes.

References

1 Williams, A., *Combustion of Sprays of Liquid Fuels*, Elek Science, 1976, London.

2 Squire, H. B., "Investigation of the Instability of a Moving Liquid Film," *British J. Appl. Phys.*, Vol. 4, 1953, pp. 167–169.

3 Hagerty, W. W., and Shea, J. F., "A Study of the Stability of Plane Fluid Sheets," ASME JOURNAL OF APPLIED MECHANICS, 1955, pp. 509–514.

4 Taylor, G. I., "The Dynamics of Thin Sheets of Fluid II. Waves on Fluid Sheets," *Proc. R. Soc.*, Series A, Vol. 253, 1959, pp. 296–312.

5 Huang, J. C. P., "The Break-up of Axisymmetric Liquid Sheets," *J. Fluid Mech.*, Vol. 43, 1970, pp. 305–319.

6 Clark, G. J., and Dombrowski, N., "Aerodynamic Instability and Disintegration of Inviscid Liquid Sheets," *Proc. R. Soc.*, Series A, Vol. 329, 1972, pp. 467–478.

7 Weihs, D., "Stability of Thin Radially Moving Liquid Sheets," *J. Fluid Mech.*, Vol. 87, 1978, pp. 289–298.

8 Kinnersley, W., "Exact Large Amplitude Capillary Waves on Sheets of Fluid," *J. Fluid Mech.*, Vol. 77, 1976, pp. 229–241.

9 Benney, D. J., and Newell, A. C., "The Propagation of Nonlinear Wave Envelopes," *J. Math. Phys.*, 1967, Vol. 46, pp. 133–139.

10 Yuen, H. C., and Lake, B. M., "Nonlinear Dynamics of Deep-Water Gravity Waves," *Advances Appl. Mech.*, Vol. 22, 1982, pp. 67–229.

11 Hasimoto, H., and Ono, H., "Nonlinear Modulation of Gravity Waves," *J. Phys. Soc. Japan*, 1972, Vol. 33, pp. 805–811.

12 Yuen, H. C., and Ferguson, W. E., Jr., "Relationship Between Benjamin-Feir Instability and Recurrence in the Nonlinear Schrodinger Equation," *Phys. Fluids*, Vol. 21, 1978, pp. 1275–1278.

13 Phillips, O. M., *The Dynamics of the Upper Ocean*, Cambridge University Press, London, 1977.

Analysis of Photoelastic Fringes in Wave Propagation Problems

A. J. Durelli[1] and A. Shukla[2]

Introduction

Attention has been called, in another paper [1], to the stumbling block that exists at present for the photoelastic analysis of some wave propagation problems. The high-fringe density and the high-fringe orders present in isochromatic patterns associated with waves make it so difficult in many cases to identify the fringe orders that frequently no quantitative analysis is conducted and comments are limited to the evaluation of the type of waves that seem likely to correspond to some portions of the patterns. In the previous paper guidelines were given which permit the numbering of the fringes in most cases of practical interest. Those guidelines are based on topological properties of the patterns, and also require a particular observation of their time derivatives.

In this note, the application of the suggested procedures will be illustrated with the analysis of a complicated problem of interaction of several types of waves. No quantitative analysis of this type of problem had previously been attempted, due to the great complexity of the pattern and a lack of guidelines to properly number the fringe orders.

Review of Basic Guidelines

Some of the guidelines of numbering isochromatic fringes in dynamic problems will be briefly reviewed. (1) Outward square corners on free boundaries are points of zero τ_{max} as required by equilibrium; (2) At points of maximum (peaks) or minimum (valleys) τ_{max} value, the space derivative of τ_{max} in a direction perpendicular to the direction of the fringe, is zero. The gradient in that direction, of the curve representing the fringe order is zero at those points. The distance between fringes close to those points is therefore larger than the distance between fringes further removed from those points. (3) It can also be observed that the width of the fringes is related to the gradient. The sharper the gradient the thinner the fringe. Wider fringes indicate lower gradients. (4) Where fringes of the same order cross (saddle) the transition fringes divide the field in four zones. Moving away from the saddle point the fringe order increases in two of the opposite zones, and decreases in the other two. (5) Shades of gray connecting two fringes indicate that their order is the same. (6) The edge, or Rayleigh-type wave fringes, moving along a boundary exhibit two peaks separated by a zero, and another peak and two other zeros in the subsurface.

Example Illustrating the Use of Guidelines

The example presented here is of a wave propagation in a thin square plate subjected to an explosion at one of its

[1] Professor, Department of Mechanical Engineering, College of Engineering, University of Maryland, College Park, Md. 20742. Fellow ASME.

[2] Resident Student, Civil Engineering Department, IIT Kanpar 208016, India.

Manuscript received by ASME Applied Mechanics Division, March, 1982; final revision, June, 1982.

Copyright © 1983 by ASME

Downloaded 02 May 2010 to 171.66.16.246. Redistribution subject to ASME license or copyright; see http://www.asme.org/terms/Terms_Use.cfm

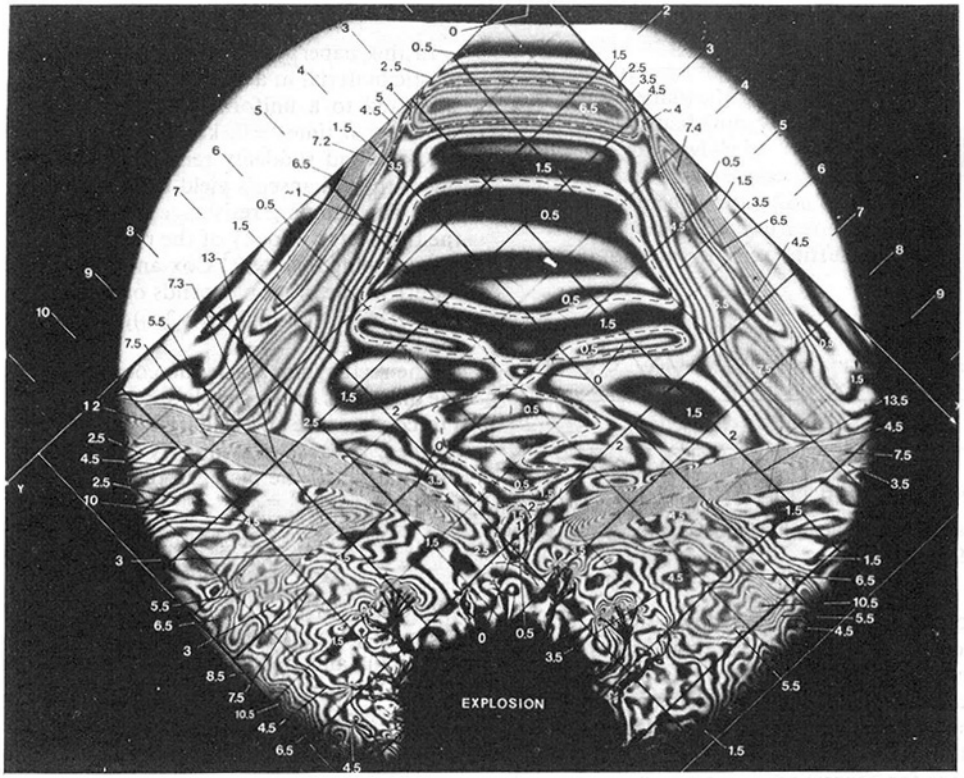

Fig. 1 Isochromatics produced by an explosion, near a square corner

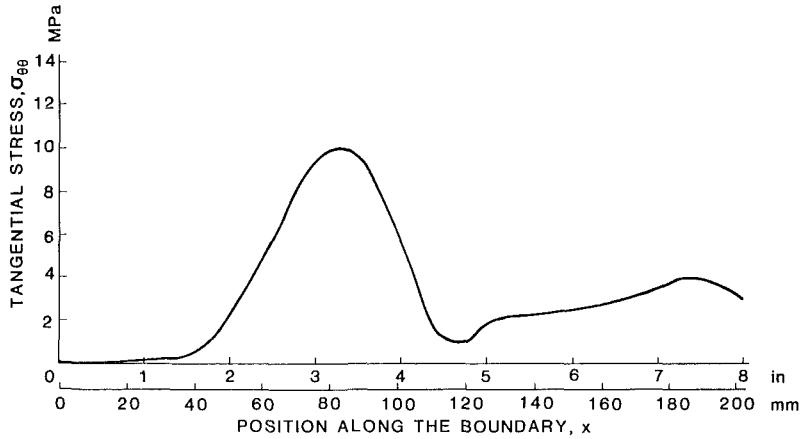

Fig. 2 Stress tangential to the free boundaries of a sqaure corner, subjected to an explosion

corners. The explosion generates a complicated system of waves as shown in Fig. 1. This system of fringes associated with these waves was analyzed completely using the following steps.

Starting at the top square corner of the photograph one finds by equilibrium that the fringe order must be zero. Traveling along the axis of symmetry, the fringe order at point $x=y=1.5$ is 6.5. The width of this fringe, and the distance from fringe 5.5 to fringe 6.5 suggests that 6.5 is a maximum. This is confirmed by the existence of a transition fringe of order approximately 4 near the boundary at $x=3.2$ where a saddle point indicates that orders increase more or less horizontally, inward, and decrease upward along the boundary. Another saddle point of order ~ 5 at a position slightly below the previous one and closer to the boundary, indicates that the order increases to a maximum of $\sim$ 7.4 on the right half, and $\sim$ 7.2 on the left half of the body. The second digit in these fringe orders is an estimate obtained from the width and the intensity of the fringe at the point where maximum occurs. For instance, it is obvious that at the point on the left mentioned in the foregoing, the fringe of order 7.5 has not developed yet. On the other hand, the order at the point at the right is closer to 7.5 and comparing the fringe at this point to the fringe present at point $x=8$ and $y\sim 1.8$, it is estimated that the order is about 7.4.

The observation of this last saddle may not be completely clear. The results can be confirmed the following way. From the maximum fringe order 6.5 at $x=y=1.5$, going down along the axis of symmetry, the order decreases to 1.5 (which encloses an island) and then to 0.5 (which encloses two islands). The order goes up then again to 1.5 and through a transition order (represented dotted) of value $\sim$ 1, down to 0.5 and to a point of value $\sim$ 0. Then it oscillates, rather erratically from 0.5 to $\sim$ 1, goes up to 1.5, passes through

Downloaded 02 May 2010 to 171.66.16.246. Redistribution subject to ASME license or copyright; see http://www.asme.org/terms/Terms_Use.cfm

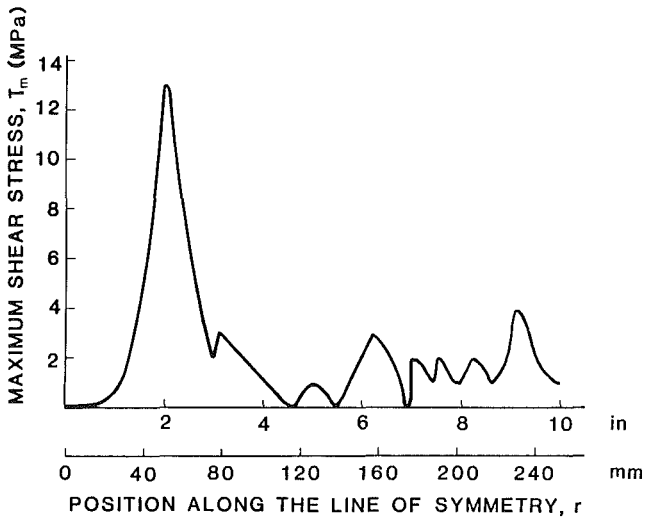

Fig. 3 Maximum shear stress along the line of symmetry of a square corner, subjected to an explosion

another transition value of ~ 2 and down again to ~ 0. Therefore, on the symmetry axis there are two points at which the maximum shear is zero. Continuing this process a third one can be noticed very near the zone blackened by the explosion. This analysis indicates the existence of a saddle at point $x \sim 8.5$ and $y \sim 3$, the value of which is ~ 2 and indicates that orders increase for generic point moving away from the saddle, parallel to y axis, toward the right. These values reach a maximum of 7.5 at the center of an island. The orders so obtained verify the one obtained previously.

Another observation may sometimes be helpful. Fringes of order 0.5 and 1.5, and to less extent of order 2.5 and 3.5, look darker in the photograph than higher order fringes. This is proably due to the different spectrum associated with different orders, which are all filtered by the same filter, giving a somewhat different appearance in the photograph.

Thus the whole field of fringes in Fig. 1 was completely identified. In this figure the fringe of order one was represented with dotted lines. It happens to be a "transition" isochromatic, crossing itself at several "saddle" points which, a shown in the foregoing are very important in the process of identifying the order of the fringes.

The normal sresses along the boundaries are shown in Fig. 2. Moreover, since the maximum shear stress τ_m is known in the whole field it has been plotted as a function of position along the line of symmetry in Fig. 3.

References

1 Durelli, A. J., and Shukla, A., "Identification of Isochromatic Fringes," to be published in *Exp. Mech.*

Dynamic Response of Rigid-Plastic Square Plates in a Damping Medium

A. Kumar[1] and M. Hedge[2]

[1]Assistant Professor, Civil Engineering Department, IIT Kanpur, Kanpur-208016, India.

[2]Design Engineer, Engineering Consultants (India), New Delhi-110024, India.

Manuscript received by ASME Applied Mechanics Division, June, 1982; final revision, December, 1982

Introduction

In this paper, the motion of a thin square plate of rigid-plastic material in a damping medium is studied. The plate is subjected to a uniformly distributed load which is applied suddenly at time $t=0$, kept constant at an intensity p during $0<t<\tau$, and suddenly removed at $t=\tau$. The plate material obeys the Johansen's yield criterion and the associated flow rule. The damping resistance is taken to be $f=\alpha V$ where V is the transverse velocity of the plate and α is a constant. When the damping is absent, Cox and Morland [1] found that the nature of the motion depends on whether the load is medium ($p_0<p<2p_0$) or high ($p>2p_0$), where p_0 is the static limit load.

The rectangular Cartesian coordinates x, y are taken along the diagonals of the simply supported square plate of side $2L$. For convenience an auxiliary coordinate $z=(x+y)/\sqrt{2}L$ is also defined. Because of symmetry it is only necessary to consider one quarter of the plate. In the present case, the equation of motion is

$$\frac{\partial^2 M_{xx}}{\partial x^2}+\frac{2\partial^2 M_{xy}}{\partial x \partial y}+\frac{\partial^2 M_{yy}}{\partial y^2}+p=\mu\ddot{w}+\alpha\dot{w}$$

where M_{xx}, M_{yy}, $M_{xy}=M_{yx}$ are the moment components, μ is the mass per unit area of the middle surface whose deflection is $w(x,y)$, and dots indicate differentiation with respect to time. Following the method outlined in [1], the results are summarized in the following.

Medium Load

Phase 1 ($0 < t < \tau$). The moment distribution is

$$\begin{aligned} M_{xx} &= M_0+x^2 f_1(z) \\ M_{yy} &= M_0+y^2 f_1(z) \\ M_{xy} &= xy f_1(z) \end{aligned} \tag{2}$$

where M_0 is the fully plastic moment and the function $f_1(z)$ is given by

$$f_1(z)=(\mu\ddot{W}+\alpha\dot{W})(2-z)/12-p/6 \tag{3}$$

in which the central plate deflection W is

$$W(t)=\frac{2}{\alpha}\left(p-\frac{6M_0}{L^2}\right)\left[t+\frac{\mu}{\alpha}\left\{\exp\left(-\frac{\alpha t}{\mu}\right)-1\right\}\right] \tag{4}$$

Phase 2 ($\tau < t < T$). The plate comes to rest at time T given by

$$T=\frac{\mu}{\alpha}\log\left[\frac{p}{p_0}\left\{\exp\left(\frac{\alpha\tau}{\mu}\right)-1\right\}+1\right] \tag{5}$$

The final central deflection is

$$W(T)=\frac{2}{\alpha}(p\tau-p_0 T) \tag{6}$$

The moment distribution is given by (2) with $f_1(z)$ replace by $f_2(z)$ where

$$f_2(z)=(\mu\ddot{W}+\alpha\dot{W})(2-z)/12 \tag{7}$$

High Load

Phase 1 ($0 < t < \tau$). The central plate deflection is

$$W(t)=\frac{p}{\alpha}\left[t+\frac{\mu}{\alpha}\left\{\exp\left(-\frac{\alpha t}{\mu}\right)-1\right\}\right] \tag{8}$$

In the region $0 \le z \le \theta_0$, $M_{xx}=M_{yy}=M_0$ and $M_{xy}=0$. In the region $\theta_0 \le z \le 1$, the moment distribution is expressed by (2) with $f_1(z)$ replaced by $f_3(z)$ such that

Downloaded 02 May 2010 to 171.66.16.246. Redistribution subject to ASME license or copyright; see http://www.asme.org/terms/Terms_Use.cfm

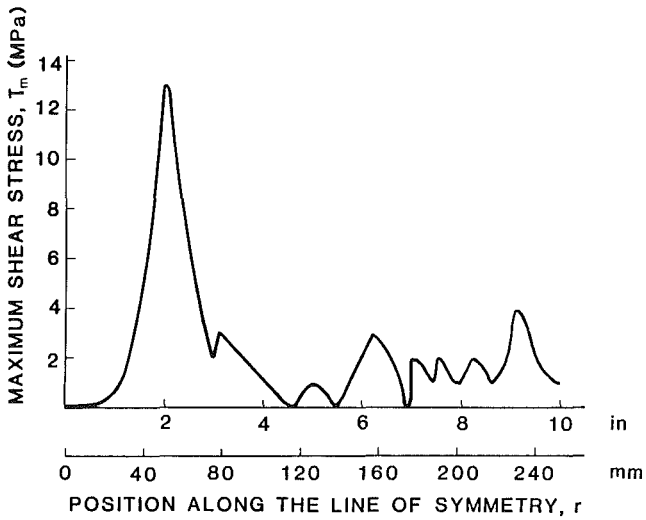

Fig. 3 Maximum shear stress along the line of symmetry of a square corner, subjected to an explosion

another transition value of ~ 2 and down again to ~ 0. Therefore, on the symmetry axis there are two points at which the maximum shear is zero. Continuing this process a third one can be noticed very near the zone blackened by the explosion. This analysis indicates the existence of a saddle at point $x \sim 8.5$ and $y \sim 3$, the value of which is ~ 2 and indicates that orders increase for generic point moving away from the saddle, parallel to y axis, toward the right. These values reach a maximum of 7.5 at the center of an island. The orders so obtained verify the one obtained previously.

Another observation may sometimes be helpful. Fringes of order 0.5 and 1.5, and to less extent of order 2.5 and 3.5, look darker in the photograph than higher order fringes. This is proably due to the different spectrum associated with different orders, which are all filtered by the same filter, giving a somewhat different appearance in the photograph.

Thus the whole field of fringes in Fig. 1 was completely identified. In this figure the fringe of order one was represented with dotted lines. It happens to be a "transition" isochromatic, crossing itself at several "saddle" points which, a shown in the foregoing are very important in the process of identifying the order of the fringes.

The normal sresses along the boundaries are shown in Fig. 2. Moreover, since the maximum shear stress τ_m is known in the whole field it has been plotted as a function of position along the line of symmetry in Fig. 3.

References

1 Durelli, A. J., and Shukla, A., "Identification of Isochromatic Fringes," to be published in *Exp. Mech.*

Dynamic Response of Rigid-Plastic Square Plates in a Damping Medium

A. Kumar[1] and M. Hedge[2]

Introduction

In this paper, the motion of a thin square plate of rigid-plastic material in a damping medium is studied. The plate is subjected to a uniformly distributed load which is applied suddenly at time $t=0$, kept constant at an intensity p during $0<t<\tau$, and suddenly removed at $t=\tau$. The plate material obeys the Johansen's yield criterion and the associated flow rule. The damping resistance is taken to be $f=\alpha V$ where V is the transverse velocity of the plate and α is a constant. When the damping is absent, Cox and Morland [1] found that the nature of the motion depends on whether the load is medium ($p_0<p<2p_0$) or high ($p>2p_0$), where p_0 is the static limit load.

The rectangular Cartesian coordinates x, y are taken along the diagonals of the simply supported square plate of side $2L$. For convenience an auxiliary coordinate $z=(x+y)/\sqrt{2}L$ is also defined. Because of symmetry it is only necessary to consider one quarter of the plate. In the present case, the equation of motion is

$$\frac{\partial^2 M_{xx}}{\partial x^2}+\frac{2\partial^2 M_{xy}}{\partial x \partial y}+\frac{\partial^2 M_{yy}}{\partial y^2}+p=\mu\ddot{w}+\alpha\dot{w}$$

where M_{xx}, M_{yy}, $M_{xy}=M_{yx}$ are the moment components, μ is the mass per unit area of the middle surface whose deflection is $w(x,y)$, and dots indicate differentiation with respect to time. Following the method outlined in [1], the results are summarized in the following.

Medium Load

Phase 1 ($0 < t < \tau$). The moment distribution is

$$\begin{aligned} M_{xx} &= M_0+x^2 f_1(z) \\ M_{yy} &= M_0+y^2 f_1(z) \\ M_{xy} &= xy f_1(z) \end{aligned} \tag{2}$$

where M_0 is the fully plastic moment and the function $f_1(z)$ is given by

$$f_1(z)=(\mu\ddot{W}+\alpha\dot{W})(2-z)/12-p/6 \tag{3}$$

in which the central plate deflection W is

$$W(t)=\frac{2}{\alpha}\left(p-\frac{6M_0}{L^2}\right)\left[t+\frac{\mu}{\alpha}\left\{\exp\left(-\frac{\alpha t}{\mu}\right)-1\right\}\right] \tag{4}$$

Phase 2 ($\tau < t < T$). The plate comes to rest at time T given by

$$T=\frac{\mu}{\alpha}\log\left[\frac{p}{p_0}\left\{\exp\left(\frac{\alpha\tau}{\mu}\right)-1\right\}+1\right] \tag{5}$$

The final central deflection is

$$W(T)=\frac{2}{\alpha}(p\tau-p_0 T) \tag{6}$$

The moment distribution is given by (2) with $f_1(z)$ replace by $f_2(z)$ where

$$f_2(z)=(\mu\ddot{W}+\alpha\dot{W})(2-z)/12 \tag{7}$$

High Load

Phase 1 ($0 < t < \tau$). The central plate deflection is

$$W(t)=\frac{p}{\alpha}\left[t+\frac{\mu}{\alpha}\left\{\exp\left(-\frac{\alpha t}{\mu}\right)-1\right\}\right] \tag{8}$$

In the region $0 \le z \le \theta_0$, $M_{xx}=M_{yy}=M_0$ and $M_{xy}=0$. In the region $\theta_0 \le z \le 1$, the moment distribution is expressed by (2) with $f_1(z)$ replaced by $f_3(z)$ such that

[1]Assistant Professor, Civil Engineering Department, IIT Kanpur, Kanpur-208016, India.
[2]Design Engineer, Engineering Consultants (India), New Delhi-110024, India.

Manuscript received by ASME Applied Mechanics Division, June, 1982; final revision, December, 1982

Copyright © 1983 by ASME
Downloaded 02 May 2010 to 171.66.16.246. Redistribution subject to ASME license or copyright; see http://www.asme.org/terms/Terms_Use.cfm

$$f_3(z) = \frac{p}{12(1-\theta_0)}\left[2\theta_0 - z - \frac{2\theta_0^3}{z^2} + \frac{\theta_0^4}{z^3}\right] \tag{9}$$

where θ_0 is given by

$$(1+\theta_0)(1-\theta_0)^2 = 2p_0/p \tag{10}$$

Phase 2 ($\tau < t < T_1$). The central square region $0 \le z \le \theta_0$ shrinks to zero at time T_1 given by

$$T_1 = \frac{\mu}{\alpha}\log\left[1 + \frac{p}{2p_0}\left\{\exp\left(\frac{\alpha\tau}{\mu}\right) - 1\right\}\right] \tag{11}$$

At that instant, the central plate deflection is

$$W(T_1) = \frac{p}{\alpha}\left[\tau - \frac{\mu}{\alpha}\left\{\exp\left(-\frac{\alpha\tau}{\mu}\right) - 1\right\}\exp\left(-\frac{\alpha T_1}{\mu}\right)\right] \tag{12}$$

Phase 3 ($T_1 < t < T_2$). The plate comes to rest at $t = T_2$:

$$T_2 = \frac{\mu}{\alpha}\log\left[1 + \frac{p}{p_0}\left\{\exp\left(\frac{\alpha\tau}{\mu}\right) - 1\right\}\right] \tag{13}$$

The final central deflection is

$$W(T_2) = \frac{p\tau}{\alpha} + \frac{2p_0}{\alpha}(T_1 - T_2) \tag{14}$$

Discussions

The variation of moments is found to be independent of damping during the motion. However, the plate deflection is affected by damping force. When the damping coefficient tends to zero, it is found that the present solutions reduce to those obtained by Cox and Morland [1].

The results for an impulse I_0 can now be obtained easily. Let τ tend to zero and p/p_0 tend to infinity such that $p\tau$ tends to a finite value I_0. Then, equations (11) and (13) become

$$T_1 = \frac{\mu}{\alpha}\log\left[\frac{\alpha}{\mu}\frac{I_0}{2p_0} + 1\right] \tag{15}$$

$$T_2 = \frac{\mu}{\alpha}\log\left[\frac{\alpha}{\mu}\frac{I_0}{p_0} + 1\right] \tag{15}$$

The corresponding final central deflection is

$$W(T_2) = \frac{I_0}{\alpha} - \frac{2p_0}{\alpha^2}\log\left[\frac{(\alpha I_0/\mu p_0) + 1}{(\alpha I_0/2\mu p_0) + 1}\right] \tag{17}$$

If α tends to zero in (17), then

$$W(T_2) = \frac{3I_0^2}{4p_0\mu} \tag{19}$$

which is the same as obtained in [1].

One of the important observations is that the expressions for the deflection (and for the velocity field) are identical to ones derived for simply supported circular plates in a damping medium [2]. The final central deflection in two cases is the same but, of course, not the deformed shape of the plate. However, if the deflections are plotted in the plane $y = 0$ or in $x = 0$, the curves will again be similar to the one drawn along a diameter of the circular plate. The conclusion is, therefore, that the permanent central deflection of a simply supported square plate is the same, for a given impulse per unit area, as that for a simply supported circular plate inscribed to the square, since under these circumstances the yield-point pressure p_0 is the same. The same conclusion holds in the absence of damping also [1].

While the rigid-plastic theory is fairly successful in predicting the final deformation, certain discrepencies still remain between the results of experiments and those predicted by the theory. Many of these are attributed to the effect of the rate of strain on the material response. A constitutive relation that includes a strain-rate term is necessary. The inclusion of the effect of transverse shear and rotary inertia, in a manner similar to one adopted in [3], in the present analysis is also desirable. Alternatively, one can follow the continuum approach of Batra and Dubey [4].

It may be worthwhile to extend the present study to plates clamped along the periphery. An unfinished attempt has revealed that the determination of the central plate deflection itself is not a straightforward exercise; it requires solving two coupled, nonlinear, ordinary differential equations.

References

1 Cox, A. D., and Morland, L. W., "Dynamic Plastic Deformations of Simply Supported Square Plates," *J. Mech. Phy. Solids*, Vol. 7, 1959, pp. 229-241.

2 Kumar, A., and Hegde, M., "Dynamic Response of Rigid-Plastic Circular Plates in a Damping Medium," ASME JOURNAL OF APPLIED MECHANICS, Vol. 49, 1982, pp. 240-241.

3 Jones, N., and Gomes de Oliveira, "Dynamic Plastic Response of Circular Plates With Transverse Shear and Rotary Inertia," ASME JOURNAL OF APPLIED MECHANICS, Vol. 47, 1980, pp. 27-34.

4 Batra, R. C., and Dubey, R. N., "Impulsively Loaded Circular Plates," *Int. J. Solids Structures*, Vol. 7, 1971, pp. 965-968.

Bending of a Free Beam on an Elastic Foundation

A. P. Gallagher[1]

Introduction

The bending, due to a concentrated load at the center, of a uniform weightless finite beam resting on a foundation, which is treated as a two-dimensional, frictionless, elastic half space, is considered. Various foundation models have been used (see Kerr [1], Lentini [2]). Biot [3] used the two-dimensional model for the infinitely long beam, as well as the three-dimensional one. Conway and Farnham [4] solved this problem assuming uniform pressure and deflection but their results appear to be in error since they indicate increasing deflection with increasing foundation stiffness. Weitsman [5] applied a variational approach to the infinite beam but his results contain an error as was pointed out by Gladwell [6], who solved this problem using the two-dimensional model. Gladwell's results are in good agreement with those of Keer et al. [7] and with the present ones. The method used here (see Gallagher [8]) expresses the problem as an integro-differential equation. The contact length is found to be independent of the load, a particular case of the more general result proved by Dundurs [9]. Good agreement is obtained with the experimental results of Vesic [10].

Statement of Equations

Assuming no friction is present at the beam-foundation interface and that the weight of the beam is negligible in comparison with the load P, then the Bernoulli-Euler law gives

$$E_B I\frac{d^4y}{dx^4} = P\delta(x) - W(x), \quad |x| \le a \tag{1}$$

with $y(\pm a) = y''(\pm a) = 0$.

[1] Senior Lecturer, Department of Engineering Mathematics, The Queen's University of Belfast, Northern Ireland.

Manuscript received by ASME Applied Mechanics Division, March 1981; final revision, August, 1981.

Downloaded 02 May 2010 to 171.66.16.246. Redistribution subject to ASME license or copyright; see http://www.asme.org/terms/Terms_Use.cfm

$$f_3(z) = \frac{p}{12(1-\theta_0)}\left[2\theta_0 - z - \frac{2\theta_0^3}{z^2} + \frac{\theta_0^4}{z^3}\right] \tag{9}$$

where θ_0 is given by

$$(1+\theta_0)(1-\theta_0)^2 = 2p_0/p \tag{10}$$

Phase 2 ($\tau < t < T_1$). The central square region $0 \le z \le \theta_0$ shrinks to zero at time T_1 given by

$$T_1 = \frac{\mu}{\alpha}\log\left[1 + \frac{p}{2p_0}\left\{\exp\left(\frac{\alpha\tau}{\mu}\right) - 1\right\}\right] \tag{11}$$

At that instant, the central plate deflection is

$$W(T_1) = \frac{p}{\alpha}\left[\tau - \frac{\mu}{\alpha}\left\{\exp\left(-\frac{\alpha\tau}{\mu}\right) - 1\right\}\exp\left(-\frac{\alpha T_1}{\mu}\right)\right] \tag{12}$$

Phase 3 ($T_1 < t < T_2$). The plate comes to rest at $t = T_2$:

$$T_2 = \frac{\mu}{\alpha}\log\left[1 + \frac{p}{p_0}\left\{\exp\left(\frac{\alpha\tau}{\mu}\right) - 1\right\}\right] \tag{13}$$

The final central deflection is

$$W(T_2) = \frac{p\tau}{\alpha} + \frac{2p_0}{\alpha}(T_1 - T_2) \tag{14}$$

Discussions

The variation of moments is found to be independent of damping during the motion. However, the plate deflection is affected by damping force. When the damping coefficient tends to zero, it is found that the present solutions reduce to those obtained by Cox and Morland [1].

The results for an impulse I_0 can now be obtained easily. Let τ tend to zero and p/p_0 tend to infinity such that $p\tau$ tends to a finite value I_0. Then, equations (11) and (13) become

$$T_1 = \frac{\mu}{\alpha}\log\left[\frac{\alpha}{\mu}\frac{I_0}{2p_0} + 1\right] \tag{15}$$

$$T_2 = \frac{\mu}{\alpha}\log\left[\frac{\alpha}{\mu}\frac{I_0}{p_0} + 1\right] \tag{15}$$

The corresponding final central deflection is

$$W(T_2) = \frac{I_0}{\alpha} - \frac{2p_0}{\alpha^2}\log\left[\frac{(\alpha I_0/\mu p_0)+1}{(\alpha I_0/2\mu p_0)+1}\right] \tag{17}$$

If α tends to zero in (17), then

$$W(T_2) = \frac{3I_0^2}{4p_0\mu} \tag{19}$$

which is the same as obtained in [1].

One of the important observations is that the expressions for the deflection (and for the velocity field) are identical to ones derived for simply supported circular plates in a damping medium [2]. The final central deflection in two cases is the same but, of course, not the deformed shape of the plate. However, if the deflections are plotted in the plane $y = 0$ or in $x = 0$, the curves will again be similar to the one drawn along a diameter of the circular plate. The conclusion is, therefore, that the permanent central deflection of a simply supported square plate is the same, for a given impulse per unit area, as that for a simply supported circular plate inscribed to the square, since under these circumstances the yield-point pressure p_0 is the same. The same conclusion holds in the absence of damping also [1].

While the rigid-plastic theory is fairly successful in predicting the final deformation, certain discrepencies still remain between the results of experiments and those predicted by the theory. Many of these are attributed to the effect of the rate of strain on the material response. A constitutive relation that includes a strain-rate term is necessary. The inclusion of the effect of transverse shear and rotary inertia, in a manner similar to one adopted in [3], in the present analysis is also desirable. Alternatively, one can follow the continuum approach of Batra and Dubey [4].

It may be worthwhile to extend the present study to plates clamped along the periphery. An unfinished attempt has revealed that the determination of the central plate deflection itself is not a straightforward exercise; it requires solving two coupled, nonlinear, ordinary differential equations.

References

1 Cox, A. D., and Morland, L. W., "Dynamic Plastic Deformations of Simply Supported Square Plates," *J. Mech. Phy. Solids*, Vol. 7, 1959, pp. 229-241.

2 Kumar, A., and Hegde, M., "Dynamic Response of Rigid-Plastic Circular Plates in a Damping Medium," ASME JOURNAL OF APPLIED MECHANICS, Vol. 49, 1982, pp. 240-241.

3 Jones, N., and Gomes de Oliveira, "Dynamic Plastic Response of Circular Plates With Transverse Shear and Rotary Inertia," ASME JOURNAL OF APPLIED MECHANICS, Vol. 47, 1980, pp. 27-34.

4 Batra, R. C., and Dubey, R. N., "Impulsively Loaded Circular Plates," *Int. J. Solids Structures*, Vol. 7, 1971, pp. 965-968.

Bending of a Free Beam on an Elastic Foundation

A. P. Gallagher[1]

Introduction

The bending, due to a concentrated load at the center, of a uniform weightless finite beam resting on a foundation, which is treated as a two-dimensional, frictionless, elastic half space, is considered. Various foundation models have been used (see Kerr [1], Lentini [2]). Biot [3] used the two-dimensional model for the infinitely long beam, as well as the three-dimensional one. Conway and Farnham [4] solved this problem assuming uniform pressure and deflection but their results appear to be in error since they indicate increasing deflection with increasing foundation stiffness. Weitsman [5] applied a variational approach to the infinite beam but his results contain an error as was pointed out by Gladwell [6], who solved this problem using the two-dimensional model. Gladwell's results are in good agreement with those of Keer et al. [7] and with the present ones. The method used here (see Gallagher [8]) expresses the problem as an integro-differential equation. The contact length is found to be independent of the load, a particular case of the more general result proved by Dundurs [9]. Good agreement is obtained with the experimental results of Vesic [10].

Statement of Equations

Assuming no friction is present at the beam-foundation interface and that the weight of the beam is negligible in comparison with the load P, then the Bernoulli-Euler law gives

$$E_B I\frac{d^4y}{dx^4} = P\delta(x) - W(x), \quad |x| \le a \tag{1}$$

with $y(\pm a) = y''(\pm a) = 0$.

[1] Senior Lecturer, Department of Engineering Mathematics, The Queen's University of Belfast, Northern Ireland.

Manuscript received by ASME Applied Mechanics Division, March 1981; final revision, August, 1981.

Copyright © 1983 by ASME
Downloaded 02 May 2010 to 171.66.16.246. Redistribution subject to ASME license or copyright; see http://www.asme.org/terms/Terms_Use.cfm

In the preceding equation E_B is the Young's modulus of the beam; I is the moment of inertia per unit width; P is the load per unit width; $W(x)$ is the contact pressure; x is distance measured along the beam; y is downward deflection; $\delta(x)$ is the delta function and $2a$ is the contact length.

If the slope of the deflection of the interface is assumed to be the same as that of the neutral axis of the beam, the pressure may be taken using the formulation given by Muskhelishvili [11], namely

$$W(x) = -\frac{E(a^2-x^2)^{1/2}}{2\pi(1-\sigma^2)} \int_{-a}^{a} \frac{y'(t)}{(a^2-t^2)^{1/2}(a-x)}\,dt, \quad |x| \le a, \tag{2}$$

where E and σ are the Young's modulus and Poisson's ratio of the foundation.

Equations (1) and (2) are made nondimensional by letting $\xi = x/a$, $\eta = y/\alpha a$, $\tau = t/a$, $\bar{\delta}(\xi) = a\delta(x)$, $\alpha = Pa^2/E_B I$ and $\lambda = Ea^3/(1-\sigma^2)E_B I$ where α and λ are nondimensional parameters.

The dimensionless form of (1) and (2) is

$$\frac{d^4\eta}{d\xi^4} - \frac{\lambda(1-\xi^2)^{1/2}}{2\pi}\int_{-1}^{+1} \frac{\eta'(\tau)}{(1-\tau^2)^{1/2}(\tau-\xi)}\,d\tau = \bar{\delta}(\xi), \quad |\xi| \le 1, \tag{3}$$

with $\eta(\pm 1) = \eta''(\pm 1) = 0$. The unknown quantity λ must be determined from the condition that the total reaction and the load must balance. Denoting this value by λ_0, the solution to the problem is given by the following:

$$\text{half contact length} \quad a = \{\lambda_0(1-\sigma^2)E_B I/E\}^{1/3}, \tag{4a}$$

$$\text{deflection} \quad y(x) = \lambda_0 P(1-\sigma^2)\eta(\xi)/E, \quad |x| \le a, \tag{4b}$$

$$\text{bending moment per unit width} \quad -E_B I y''(x) = -Pa\eta''(\xi), \quad |x| \le a, \tag{4c}$$

$$\text{pressure} \quad W(x) = P\omega(\xi)/a, \quad |x| \le a, \tag{4d}$$

$$\text{where} \quad \omega(\xi) = (\lambda(1-\xi^2)^{1/2}/2\pi)\int_{-1}^{+1} \frac{\eta'(\tau)\,d\tau}{(1-\tau^2)^{1/2}(\tau-\xi)}.$$

These expressions show that the contact length is independent of the load P, while the maximum deflection, which clearly occurs at $x = 0$, is independent of the flexural rigidity $E_B I$ of the beam. It may also be noted that the deflection, bending moment, and pressure at a point are all directly proportional to the load [9].

For values of x for which $|x| > a$, the deflection of the beam may be taken as a straight line with slope $y'(\pm a)$.

Solution of the Dimensionless Beam Equation

The method of solution of (3) is to expand the slope in a series of Chebyshev polynomials of the first kind thus

$$\eta'(\xi) = \sum_{n=1}^{\infty} a_{2n-1} T_{2n-1}(\xi), \quad |\xi| \le 1, \tag{5}$$

where only odd polynomials are used since $\eta(\xi)$ is obviously even because of the symmetry of the problem.

Substituting (5) into (3) and assuming validity of termwise differentiation and utilizing

$$\int_{-1}^{+1} \{T_n(\tau)/(1-\tau^2)^{1/2}(\tau-\xi)\}\,d\tau = \pi U_{n-1}(\xi), \; n \ge 1, \; |\xi| \le 1,$$

where U_n is the Chebyshev polynomial of the second kind, one obtains

$$\sum_{n=1}^{\infty} a_{2n-1} T_{2n-1}^{(4)}(\xi)$$

Table 1 The dimensionless functions $\eta(\xi)$, $\eta''(\xi)$, and $\omega(\xi)$ at intervals of 0.1 for $\lambda = 22.0$

ξ	$\eta(\xi)$	$\eta''(\xi)$	$\omega(\xi)$
0	0.037	−0.176	−0.894
0.1	0.036	−0.133	−0.851
0.2	0.034	−0.095	−0.771
0.3	0.031	−0.066	−0.679
0.4	0.027	−0.043	−0.584
0.5	0.023	−0.027	−0.492
0.6	0.019	−0.015	−0.406
0.7	0.014	−0.007	−0.326
0.8	0.009	−0.002	−0.247
0.9	0.005	−0.000	−0.164
1	0.000	−0.000	0.000

Table 2

	Experimental	(*i*)	(*ii*)
Deflection at center (mm)	9	18	11
Half contact length (mm)	787	908	782
Maximum bending moment/ unit width (kN)	20.5	28.9	24.9
Maximum contact pressure (kN/m^2)	221	178	207

(*i*) using $W(x)$ (equation (2))
(*ii*) using $W_{av}(x)$ (equation (11))

$$-(\lambda/2)(1-\xi^2)^{1/2}\sum_{n=1}^{\infty} a_{2n-1} U_{2n-2}(\xi) = \bar{\delta}(\xi). \tag{6}$$

The end conditions become

$$\sum_{n=1}^{\infty} (2n-1)^2 a_{2n-1} = 0. \tag{7}$$

Multiplying by U_{2m-1}, $m = 1,2,3, \ldots$ and integrating, making use of the orthogonality of the polynomials, equation (6) becomes

$$\sum_{n=1}^{\infty} \{I_{mn} - (3\pi\lambda/8)\delta_{mn}\} a_{2n-1} = 1.5(-1)^{m-1}, \quad m = 1, 2, 3, \ldots, \tag{8}$$

$$\text{where } I_{mn} = \int_{-1}^{+1} U_{2m-2} T_{2n-1}^{(4)}\,d\xi = I_{mn}^{(1)} + I_{mn}^{(2)},$$

$$\text{and } I_{mn}^{(1)} = (2m-1)(2n-1)^4, \; m, n \ge 1,$$

$$I_{mn}^{(2)} = 0, \; m = 1 \text{ or } n = 1,$$

$$I_{mn}^{(2)} = 192(2n-1)\sum_{r=1}^{m-1}\sum_{s=1}^{n-1}\sum_{t=1}^{s} \frac{r^2 s}{(2t-1)^2 - 4r^2}, \; m, n \ge 2,$$

$$\delta_{nn} = 1 \text{ and } \delta_{mn} = 0 \text{ if } m \ne n.$$

Equation (7) has been used in calculating $I_{mn}^{(1)}$. The method of solution of equations (8) was the usual one of truncating the coefficient matrix to a finite square one of size N and increasing N until no change is observed in the coefficients a_n. A further term of the form $\pm (2m-1)^p \sum_{n=1}^{\infty} (2n-1)^2 a_{2n-1}$ $m = 1, 2, 3, \ldots$, was added to the mth equation, where p and the sign were chosen so that maximum accuracy was obtained in the case where the exact solution was known, namely $\lambda = 0$. This corresponds to a beam with no foundation but simply supported at $x = \pm a$. It was found that $p = 4.3$ and the minus sign gave maximum accuracy, the error

Downloaded 02 May 2010 to 171.66.16.246. Redistribution subject to ASME license or copyright; see http://www.asme.org/terms/Terms_Use.cfm

in each coefficient being less than 2×10^{-9}, while the error in $\eta(0)$ was 8×10^{-8} and in $\eta''(0)$ was 3×10^{-3}.

The value of λ_0 was determined by the fact that the load and the total reaction of the foundation must balance. Using the expression for the total reaction given in [11], this implies

$$-\frac{E}{2(1-\sigma^2)}\int_{-a}^{a}\frac{ty'(t)}{(a^2-t^2)^{1/2}}\,dt=P. \tag{9}$$

Using (4) and (5) the equation in λ_0 becomes $\lambda_0 = -4/\pi a_1$.

Equations (8) were solved with different values of λ until this condition was satisfied. The value of λ_0 was found to be 22.0. This is to be compared with the value 22.14 obtained in [6]. To conform with the present notation the shear modulus G used in that paper must be replaced by $E/2(1+\sigma)$ and the flexural rigidity D by E_BI. The values of $\eta(\xi)$, $\eta''(\xi)$, and $\omega(\xi)$ for $\lambda = \lambda_0$ are given in Table 1 at intervals of 0.1.

Modification Using Average Pressure

The value for the contact pressure as given by the two-dimensional model is too small since it does not allow for the large values in contact pressure near the faces $z = \pm b$, where z is the transverse coordinate and b is the half-width of the beam. This increase in contact pressure can be allowed for, and better agreement with experimental results expected, if a widthwise average pressure $W_{av}(x)$ is used instead. This can be estimated from the expression for the contact pressure under a rigid stamp of width $2b$, [11], namely

$$\frac{2bW_{av}(x)}{\pi\sqrt{b^2-z^2}}, \quad |z| \le b. \tag{10}$$

If $W(x)$ is equated with the value of (10) at the center line of the beam, $z = 0$, one obtains

$$W_{av}(x) = \frac{\pi}{2}W(x). \tag{11}$$

Comparison With Experiment

Vesic [10] obtained experimental results with a beam and foundation with the following values for the parameters: $P = 181$ kN/m, $E_BI = 282$ kNm, $E/(1-\sigma^2) = 8274$ kN/m^2. The beam was 2.54 cm (1 in.) thick, 20.32 cm (8 in.) wide, and 182.9 cm (72 in.) long. The comparison with these experimental results is shown in Table. 2. It will be noted that while the results using $W(x)$ as given in (2) are in fair agreement with the experimental ones, there is considerable improvement in those obtained using $W_{av}(x)$, particularly in the value for the contact length which is in error by only 0.6 percent as compared with 15 percent for that obtained using (2).

Comparison With the Winkler Theory

If the Winkler theory is correct, then the ratio of contact pressure to deflection should be constant, i.e., $W/y = K$ where K is a constant. From (4) it is found that

$$K = C(\xi)\{E/(1-\sigma^2)\}^{4/3}\{1/E_BI\}^{1/3} \tag{12}$$

where $C(\xi)$ lies between 0.344 and 0.563 for $0 \le \xi \le 0.9$ so that the assumption of the Winkler theory is approximately satisfied. Biot obtained a similar expression to (12) with $C = 0.3$ for the infinite beam on the two-dimensional foundation, by equating the maximum bending moments of the two theories. It should be noted that the foundation modulus is $k = 2bK$, where $2b$ is the width of the beam. If the average pressure under the beam is used then $C(\xi)$ must be multiplied by $(\pi/2)^{4/3} = 1.83$.

Conclusion

The foregoing method can be applied to similar problems, for example, to nonfree beams, to different loading conditions, and to the case where friction is present. The latter problem is being investigated and it is hoped that the results will be published shortly.

Acknowledgment

The author wishes to thank the referees for providing some important references.

References

1 Kerr, A. D., "Elastic and Viscoelastic Foundation Models," ASME Journal of Applied Mechanics, Vol. 31, 1964, pp. 491-498.

2 Lentini, M., "Numerical Solution of Beam Equation With Nonuniform Foundation Coefficient," ASME Journal of Applied Mechanics, Vol. 46, 1979, pp. 901-904.

3 Biot, M. A., "Bending of an Infinite Beam on an Elastic Foundation," ASME Journal of Applied Mechanics, Vol. 59, 1937, pp. A1-A7.

4 Conway, H. D., and Farnham, K. A., "Bending of a Finite Beam in Bonded and Unbonded Contact With an Elastic Foundation," *Int. J. Mech. Sci.*, Vol. 12, 1970, pp. 997-1005.

5 Weitsman, Y., "A Tensionless Contact Between a Beam and an Elastic Half-Space," *International Journal of Engineering Science*, Vol. 10, 1972, pp. 73-81.

6 Gladwell, G. M. L., "On Some Unbonded Contact Problems in Plane Elasticity Theory," ASME Journal of Applied Mechanics, Vol. 43, 1976, pp. 263-267.

7 Keer, L. M., Dundurs, J., and Tsai, K. C., "Problems Involving a Receding Contact Between a Layer and Half Space," ASME Journal of Applied Mechanics, Vol. 39, 1972, pp. 1115-1120.

8 Gallagher, A. P., "Buckling of a Beam Under Axial Compression With Elastic Support," *Studies in Numerical Analysis*, Scaife, B. K. P., ed., Academic Press, London and New York, 1974.

9 Dundurs, J., "Properties of Elastic Bodies in Contact," *The Mechanics of Contact Between Deformable Bodies*, de Pater, A. D., and Kalker, J. J., eds., Delft University Press, Holland, 1975.

10 Vesic, A. B., "Beams on Elastic Subgrade and the Winkler Hypothesis," *Proceedings, Fifth Internatl. Conf. on Soil Mech. and Foundation Eng.*, Paris, 1961, pp. 845-850.

11 Muskhelishvili, W. I., *Some Basic Problems of the Mathematical Theory of Elasticity*, Noordhoff, Groningen, 1963.

Viscoplastic Modeling With Strain Rate-History Dependency

H. Ghoneim,[1] S. Matsouka,[1] and Y. Chen[2]

The strain rate-history effect on the plastic behavior of some classes of viscoplastic materials is incorporated into the power formula of Bodner's model by adopting an integral-memory type equation for the "hardening" state variable. The modified model is incorporated into a finite element program. Results on uniaxial loading-unloading-reloading at different rates as well as jump tests show the capability of this modified model in simulating the strain rate-history effects on the yield stress and the plastic hardening for some viscoplastic materials.

Introduction

In modeling viscoplastic materials, the effect of the strain rate-history on plastic behavior, yield stress, and strain hardening has been gaining growing interest. Extension of the classical theory of plasticity to incorporate strain rate-history

[1] Plastic Research and Development Department, Bell Laboratories, Murray Hill, N.J. 07974.

[2] Professor, Department of Mechanics and Materials Science, College of Engineering, Rutgers, The State University of New Jersey, P.O. Box 909, Piscataway, N.J. 08854. Fellow ASME.

Manuscript received by ASME Applied Mechanics Division, June, 1982; final revision, October, 1982.

Downloaded 02 May 2010 to 171.66.16.246. Redistribution subject to ASME license or copyright; see http://www.asme.org/terms/Terms_Use.cfm

in each coefficient being less than 2×10^{-9}, while the error in $\eta(0)$ was 8×10^{-8} and in $\eta''(0)$ was 3×10^{-3}.

The value of λ_0 was determined by the fact that the load and the total reaction of the foundation must balance. Using the expression for the total reaction given in [11], this implies

$$-\frac{E}{2(1-\sigma^2)}\int_{-a}^{a}\frac{ty'(t)}{(a^2-t^2)^{1/2}}\,dt=P. \tag{9}$$

Using (4) and (5) the equation in λ_0 becomes $\lambda_0 = -4/\pi a_1$.

Equations (8) were solved with different values of λ until this condition was satisfied. The value of λ_0 was found to be 22.0. This is to be compared with the value 22.14 obtained in [6]. To conform with the present notation the shear modulus G used in that paper must be replaced by $E/2(1+\sigma)$ and the flexural rigidity D by E_BI. The values of $\eta(\xi)$, $\eta''(\xi)$, and $\omega(\xi)$ for $\lambda = \lambda_0$ are given in Table 1 at intervals of 0.1.

Modification Using Average Pressure

The value for the contact pressure as given by the two-dimensional model is too small since it does not allow for the large values in contact pressure near the faces $z = \pm b$, where z is the transverse coordinate and b is the half-width of the beam. This increase in contact pressure can be allowed for, and better agreement with experimental results expected, if a widthwise average pressure $W_{av}(x)$ is used instead. This can be estimated from the expression for the contact pressure under a rigid stamp of width $2b$, [11], namely

$$\frac{2bW_{av}(x)}{\pi\sqrt{b^2-z^2}}, \quad |z| \le b. \tag{10}$$

If $W(x)$ is equated with the value of (10) at the center line of the beam, $z = 0$, one obtains

$$W_{av}(x) = \frac{\pi}{2}W(x). \tag{11}$$

Comparison With Experiment

Vesic [10] obtained experimental results with a beam and foundation with the following values for the parameters: $P = 181$ kN/m, $E_BI = 282$ kNm, $E/(1-\sigma^2) = 8274$ kN/m^2. The beam was 2.54 cm (1 in.) thick, 20.32 cm (8 in.) wide, and 182.9 cm (72 in.) long. The comparison with these experimental results is shown in Table. 2. It will be noted that while the results using $W(x)$ as given in (2) are in fair agreement with the experimental ones, there is considerable improvement in those obtained using $W_{av}(x)$, particularly in the value for the contact length which is in error by only 0.6 percent as compared with 15 percent for that obtained using (2).

Comparison With the Winkler Theory

If the Winkler theory is correct, then the ratio of contact pressure to deflection should be constant, i.e., $W/y = K$ where K is a constant. From (4) it is found that

$$K = C(\xi)\{E/(1-\sigma^2)\}^{4/3}\{1/E_BI\}^{1/3} \tag{12}$$

where $C(\xi)$ lies between 0.344 and 0.563 for $0 \le \xi \le 0.9$ so that the assumption of the Winkler theory is approximately satisfied. Biot obtained a similar expression to (12) with $C = 0.3$ for the infinite beam on the two-dimensional foundation, by equating the maximum bending moments of the two theories. It should be noted that the foundation modulus is $k = 2bK$, where $2b$ is the width of the beam. If the average pressure under the beam is used then $C(\xi)$ must be multiplied by $(\pi/2)^{4/3} = 1.83$.

Conclusion

The foregoing method can be applied to similar problems, for example, to nonfree beams, to different loading conditions, and to the case where friction is present. The latter problem is being investigated and it is hoped that the results will be published shortly.

Acknowledgment

The author wishes to thank the referees for providing some important references.

References

1 Kerr, A. D., "Elastic and Viscoelastic Foundation Models," ASME Journal of Applied Mechanics, Vol. 31, 1964, pp. 491-498.

2 Lentini, M., "Numerical Solution of Beam Equation With Nonuniform Foundation Coefficient," ASME Journal of Applied Mechanics, Vol. 46, 1979, pp. 901-904.

3 Biot, M. A., "Bending of an Infinite Beam on an Elastic Foundation," ASME Journal of Applied Mechanics, Vol. 59, 1937, pp. A1-A7.

4 Conway, H. D., and Farnham, K. A., "Bending of a Finite Beam in Bonded and Unbonded Contact With an Elastic Foundation," *Int. J. Mech. Sci.*, Vol. 12, 1970, pp. 997-1005.

5 Weitsman, Y., "A Tensionless Contact Between a Beam and an Elastic Half-Space," *International Journal of Engineering Science*, Vol. 10, 1972, pp. 73-81.

6 Gladwell, G. M. L., "On Some Unbonded Contact Problems in Plane Elasticity Theory," ASME Journal of Applied Mechanics, Vol. 43, 1976, pp. 263-267.

7 Keer, L. M., Dundurs, J., and Tsai, K. C., "Problems Involving a Receding Contact Between a Layer and Half Space," ASME Journal of Applied Mechanics, Vol. 39, 1972, pp. 1115-1120.

8 Gallagher, A. P., "Buckling of a Beam Under Axial Compression With Elastic Support," *Studies in Numerical Analysis*, Scaife, B. K. P., ed., Academic Press, London and New York, 1974.

9 Dundurs, J., "Properties of Elastic Bodies in Contact," *The Mechanics of Contact Between Deformable Bodies*, de Pater, A. D., and Kalker, J. J., eds., Delft University Press, Holland, 1975.

10 Vesic, A. B., "Beams on Elastic Subgrade and the Winkler Hypothesis," *Proceedings, Fifth Internatl. Conf. on Soil Mech. and Foundation Eng.*, Paris, 1961, pp. 845-850.

11 Muskhelishvili, W. I., *Some Basic Problems of the Mathematical Theory of Elasticity*, Noordhoff, Groningen, 1963.

Viscoplastic Modeling With Strain Rate-History Dependency

H. Ghoneim,[1] S. Matsouka,[1] and Y. Chen[2]

The strain rate-history effect on the plastic behavior of some classes of viscoplastic materials is incorporated into the power formula of Bodner's model by adopting an integral-memory type equation for the "hardening" state variable. The modified model is incorporated into a finite element program. Results on uniaxial loading-unloading-reloading at different rates as well as jump tests show the capability of this modified model in simulating the strain rate-history effects on the yield stress and the plastic hardening for some viscoplastic materials.

Introduction

In modeling viscoplastic materials, the effect of the strain rate-history on plastic behavior, yield stress, and strain hardening has been gaining growing interest. Extension of the classical theory of plasticity to incorporate strain rate-history

[1] Plastic Research and Development Department, Bell Laboratories, Murray Hill, N.J. 07974.

[2] Professor, Department of Mechanics and Materials Science, College of Engineering, Rutgers, The State University of New Jersey, P.O. Box 909, Piscataway, N.J. 08854. Fellow ASME.

Manuscript received by ASME Applied Mechanics Division, June, 1982; final revision, October, 1982.

Copyright © 1983 by ASME
Downloaded 02 May 2010 to 171.66.16.246. Redistribution subject to ASME license or copyright; see http://www.asme.org/terms/Terms_Use.cfm

effects presents difficulties, as pointed out by Naghdi [1], and complicates the applicability of the theory to numerical solution for boundary value problems [2]. Consequently, other approaches have been developed among which are: the endochronic theory of Valanis [3], the fracture entropy of Matsuoka [4], and the "state variable" theories.

The internal or state variable theories utilize state variables which, in turn, relate to microstructural changes of the material to provide for the history-dependent behavior. In many of these theories, two internal state variables are used, one to simulate isotropic hardening and a second to simulate kinematic hardening [5]. These state variables are generally governed by differential equations following a work hardening-recovery format.

This paper is concerned with modeling viscoplastic materials of which yield stress and work hardening are strain rate-history dependent. The basic idea is to let the hardening state variable be strain rate-history dependent via an integral-memory type equation. The present paper does not aim at developing a new viscoplastic model, nor does it aim at quantitative modeling of a specific material. Rather it is intented to investigate the influence of introducing such integral-memory type equation on the behavior of an existing viscoplastic model. Because of its mathematical simplicity and the lucidity of its material constants, the power formula of Bodner's model [6] is chosen.

The modified model is implemented via a finite element program. Numerical results of loading-unloading-reloading and stepwise jump tests are presented. The results demonstrate the capacity of the modified model in depicting some of the rate-history dependent phenomena exhibited by some viscoplastic materials.

Mathematical Model

Based on Bodner's model, at all stages of loading history, the total deformation rate tensor $\mathbf{d}$ is assumed to be separable into elastic $\mathbf{d}^e$ and plastic $\mathbf{d}^p$ components, i.e.,

$$\mathbf{d} = \mathbf{d}^e + \mathbf{d}^p \tag{1}$$

the plastic component is assumed to be governed by the flow rule, i.e., $\mathbf{d}^p = \lambda \mathbf{S}$, or upon squaring,

$$\mathbf{d}^p = \left(\frac{D_2^p}{J_2}\right)^{1/2} \mathbf{S} \tag{2}$$

where J_2 is the second invariant of the deviatoric stress tensor $\mathbf{S}$, and D_2^p is the second invariant of the plastic deformation rate. In addition, D_2^p is assumed to be defined by the relation,

$$D_2^p = F(J_2, T, Z_k) \tag{3}$$

where T is the temperature and Z_k are internal state variables. If the power formula is adopted for (3), for isothermal infinitesimal deformation, equation (2) can be written as

$$\dot{\epsilon}^p = C\left(\frac{\tau^E}{Z}\right)^n \frac{\mathbf{S}}{\tau^E} \tag{4}$$

where $\dot{\epsilon}^p$ is the plastic strain rate tensor, τ^E is the effective stress ($\tau^E = \sqrt{3J_2}$), n and Z are two material parameters, and C is a scalar factor. Analysis of (4) shows that n can be considered as a strain rate-sensitivity factor. Increasing n decreases the rate sensitivity. Also, Z can be considered as the "equivalent yield stress," or the threshold beyond which the plastic deformation becomes more pronounced [6]. In fact, as n tends to infinity, the power formula of Bodner degenerates to the elastic-perfectly plastic model of the inviscid theory of plasticity with Z as the yield stress. It should be pointed out that (4) can be considered as a special case of the internal state variable theories, where the kinematic hardening state variable is dropped and Z is the isotropic hardening state variable.

Since Z can be viewed as the equivalent yield stress and/or the isotropic hardening variable, and since experimental evidences, for some viscoplastic materials [7, 8], show strain rate-history dependency of the yield stress and plastic hardening, Z is taken to be functional of the strain rate-history,

$$Z = \mathfrak{F}\left\{\int_{\tau=0}^{\tau=t} \dot{\epsilon}(s)\right\} \tag{5}$$

where s is a measure of the length of a "convenient" parameter from a past time τ to the present time t,

$$s = s_t - s_\tau$$

where s_t and s_τ are the values of the s at the present time t and the past time τ, respectively. The parameter s can be taken as time, deformation, entropy, or any other variable that may yield meaningful result. In this paper, s, is taken as a measure of deformation,

$$s = \tfrac{1}{2} tr \epsilon^2 = \tfrac{1}{2} tr(\epsilon_{ij}\epsilon_{ij})$$

Consequently, the equivalent yield stress Z becomes dependent on the strain rate-history of deformation.

Upon adopting the integral-memory type equation for the functional, $\mathfrak{F}$, for isotropic case, equation (5) can be written as

$$Z = y + \int_0^{s_t} g(s_\tau)\dot{\bar{\epsilon}}(s)\, ds_\tau \tag{6}$$

where y stands for the static yield stress, $\dot{\bar{\epsilon}}$ is the equivalent strain rate ($\dot{\bar{\epsilon}} = \tfrac{1}{2}\dot{\epsilon}_{ij}\dot{\epsilon}_{ij}$), and g is a weighting function. Abiding by the principle of fading memory, a simple form of $g(s)$ can be written as

$$g(s) = g_0 e^{s/s_0} \tag{7}$$

where s_0 is a relaxation constant which determines the length of the memory of the equivalent yield Z, and g_0 is a material constant that controls the strain rate sensitivity of Z.

Equations (1), (4), (6), and (7) complete the constitutive equation of the modified model. Evaluation of the modified model is exercised by incorporating the constitutive equation into a finite element program and running some uniaxial tests as will be demonstrated in the following sections.

Numerical Solution

The constitutive equation of the modified model can be written as,

$$\dot{\sigma} = [D]\dot{\epsilon} - \dot{\sigma}^* \tag{8}$$

where σ is the stress tensor expressed in a vector form, $[D]$ is the elastic matrix, and σ^* is a stress term analogous to the initial stress and is referred to as the "equivalent initial stress,"

$$\dot{\sigma}^* = [D](\dot{\epsilon}^v + \dot{\epsilon}^p) \tag{9}$$

where $\dot{\epsilon}^v$ is a viscous strain rate added to make up for the diminishing rate sensitivity of the model as high values of n are chosen. Generally speaking, upon adopting Kelvin model to represent the viscous part, $\dot{\epsilon}^v$ can be expressed as

$$\dot{\epsilon}^v = \alpha_1 \sigma - \alpha_2 \epsilon^v \tag{10}$$

where α_1 and α_2 are two material constants.

Adopting the displacement method [9] for the development of the finite element program, the general equilibrium equation is

$$\int_v [B]^T \dot{\sigma} dv = \dot{\mathbf{R}} \tag{11}$$

where $[\ ]^T$ stands for the transpose of the matrix, $\mathbf{R}$ is the nodal force vector, and $[B]$ is the strain-displacement matrix,

Downloaded 02 May 2010 to 171.66.16.246. Redistribution subject to ASME license or copyright; see http://www.asme.org/terms/Terms_Use.cfm

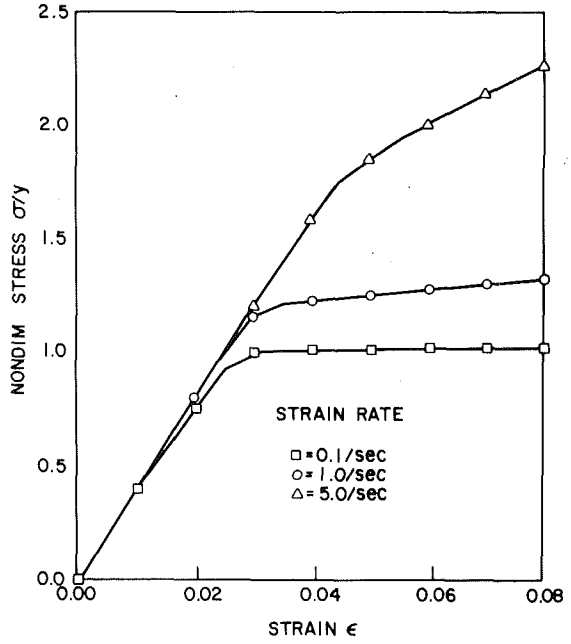

Fig. 1 Effect of strain rate on the stress-strain curve

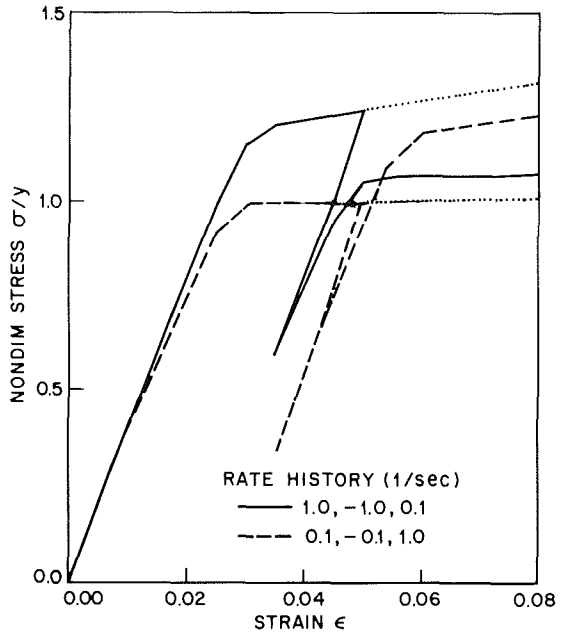

Fig. 2 Loading-unloading-reloading at different strain rates

$$[B] = [L][N]$$

where $[L]$is a linear differential operator matrix, and $[N]$ is the shape function matrix. Substituting from (8) into (11) and making use of $\dot{\epsilon} = [B]\dot{\mathbf{u}}$, where $\mathbf{u}$ is the nodal displacement vector, we get

$$[K]\dot{\mathbf{u}} = \dot{\mathbf{f}}^* + \dot{\mathbf{R}} \tag{12}$$

where $[K]$ is the global stiffness matrix,

$$[K] = \int_v [B]^T[D][B]dv \tag{13}$$

and $\mathbf{f}^*$ is a force term, will be referred to as the "equivalent initial load,"

$$\mathbf{f}^* = \int_v [B]^T \sigma^* dv \tag{14}$$

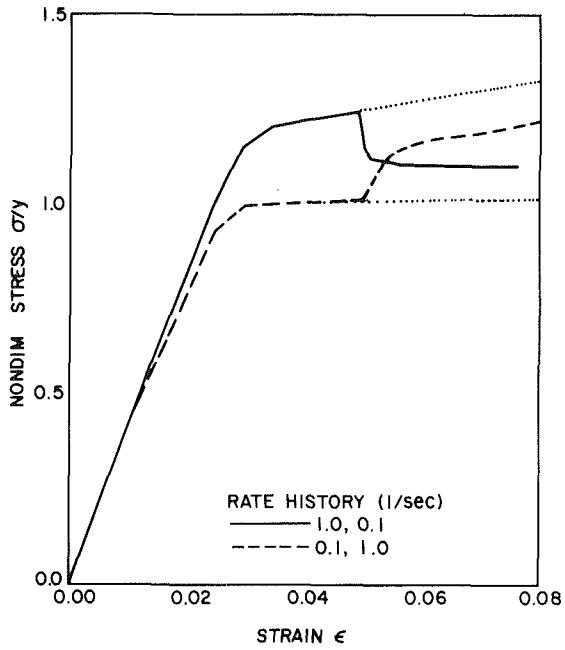

Fig. 3 Jump test

The finite element algorithm involves the simultaneous solution of both equation (8) at each element (local level), and the global equilibrium equation (12). The corresponding incremental forms of (8) and (12), which are appropriate for the step-by-step solution strategy, are

$$\Delta\sigma = [D]\Delta\sigma + \Delta\sigma^* \tag{15}$$

and

$$[K]\Delta\mathbf{u} = \Delta\mathbf{f}^* + \Delta\mathbf{R} \tag{16}$$

where

$$\Delta\mathbf{f}^* = \int_v [B]^T \Delta\sigma^* dv$$

and

$$\Delta\sigma^* = [D](\Delta\epsilon^v + \Delta\epsilon^p)$$

Clearly, (4) and (10) have to be numerically integrated in order to find $\Delta\epsilon^p$ and $\Delta\epsilon^v$, respectively. The rectangular rule and the General Implicit methods are adopted for the quadratures of (4) and (10), respectively, which give,

$$\Delta\epsilon^p = \Delta t c\left\{\left(\frac{\tau^E}{Z}\right)^n \left(\frac{\mathbf{S}}{\tau^E}\right)\right\}_{j+1/2} \tag{17}$$

and

$$\Delta\epsilon^v = \beta_1[\Theta\sigma_{j+1} + (1-\Theta)\sigma_j] - \beta_2\epsilon_j{}^v \tag{18}$$

where

$$\beta_1 = \frac{\Delta t\alpha_1}{1+\Delta t\Theta\alpha_2}, \quad \text{and} \quad \beta_2 = \frac{\Delta t\alpha_2}{1+\Delta t\Theta\alpha_2}$$

where Δt is the time increment ($\Delta t = t_{j+1} - t_j$), and Θ is a weighing parameter ($0 \le \Theta \le 1$). The subscript j stands for the step number.

From (17) and (18), solution of (15) and (16) is implicit and requires an iteration algorithm. At each loading step, guessed values of σ_{j+1} and $\dot{\epsilon}_{j+1/2}$ have to be assumed and improved via successive iteration. Isoparametric quadratic elements are used in this program. Also, it should be pointed out that evaluation of the integration (6) is necessary to complete the finite element solution at each step. This integration is evaluated using Guassian quadrature. First, the integration limits in (6) are to be changed such that,

$$Z = y + \frac{s_t}{2}\int_{-1}^{1} g\left\{\frac{s_t}{2}(1+x)\right\}\dot{\epsilon}\left\{\frac{s_t}{2}(1-x)\right\}dx$$

Downloaded 02 May 2010 to 171.66.16.246. Redistribution subject to ASME license or copyright; see http://www.asme.org/terms/Terms_Use.cfm

and upon applying Guassian quadrature,

$$Z = y + \frac{s_l}{2} \sum_{i=1}^{m} g\left\{\frac{s_l}{2}(1+x_i)\right\} \dot{\epsilon}\left\{\frac{s_l}{2}(1-x_i)\right\} W_i$$

The number of integration points m depends on the nature of the strain rate history $\dot{\epsilon}(s)$ and the lengths of s_l. The more intermittent $\dot{\epsilon}(s)$ and the longer s_l are, the more integration points are required to get good numerical results.

Numerical Examples

Uniaxial loading at different rates, loading-unloading-reloading, and jump tests are selected for the investigation of the response of the modified model. The following material constants are chosen for those numerical examples,

$$\begin{aligned} E &= 4.137 \times 10^5 \text{KPa}, \nu = 0.45, \alpha_1 \\ &= 2.417 \times 10^{-6} (\text{KPa sec})^{-1}, \\ \alpha_2 &= 1.0, C = 0.1 \text{ sec}^{-1}, n = 20, s_0 = 0.5, \\ y &= 1.034 \times 10^4 \text{KPa, and } g_0 = 3.447 \times 10^4 \text{KPa} \end{aligned}$$

Young's modulus E, Poisson ratio ν, and y are obtained from the tensile mechanical properties of Polytetrafluoroethylen (PTFE) [10], a material that exhibits plastic strain rate-history dependency and consequently is foreseen as an appropriate material to be represented by the present modified model. Pending experimental works, the other material constants are determined via numerical exercises, and consequently no qualitative comparison is presented. Figure 1 presents the strain rate effect on the stress-strain curve. It is clear that increasing the strain rate, in general, increases the yield stress and plastic hardening.

Loading-unloading-reloading results are shown in Fig. 2. In these figures, the upper and lower dotted curves represent the constant-rate stress-strain curves at 1.0 and 0.1 sec^{-1}, respectively. And the solid as well as the dashed curve represents the loading-unloading-reloading stress response. Dotted curves are plotted for the sake of comparison. Clearly, on reloading at a different rate from that of loading-unloading, the reloading stress yields at values that are influenced by the previous strain rate of loading-unloading.

The jump test, results where the strain rate is suddenly changed, are displayed in Fig. 3. As in loading-unloading-reloading, the jump test results reveal the strain rate-history dependency inherited in the modified model. Upon decreasing the strain rate from 1.0 to 0.1 sec^{-1} (solid line) the stress drops to values higher than that of the constant-rate loading at 0.1 sec^{-1} (lower dotted curve). This is because the response after the jump is influenced by the previous strain rate of loading before the jump (1.0 sec^{-1}). Similarly, when the strain rate is increased from 0.1 to 1.0 sec^{-1} (dashed line) the stress response rises to values lower than that of the constant-rate loading at 1.0 sec^{-1} (upper dotted curve).

Conclusion

The power formula of Bodner's viscoplastic model is modified to account for the strain rate-history effect on the plastic behavior, yield stress, and hardening of the model. Modification is accomplished by adopting an integral-memory type of equation for the "hardening" state variable. Results from uniaxial simulation reveal the capability of the modified model not only in simulating the strain-rate effect on the stress-strain curve, but also in depicting the rate-history dependency of the plastic behavior exhibited by some viscoplastic materials, as illustrated by loading-unloading-reloading and jump tests.

The apparent success of the modified model suggests the extension of the modification to other types of state variable models which include kinematic hardening, temperature, and pressure effects, to solving nonisothermal-large deformation problems, and to experimental verification of the behavior of the modified model.

References

1 Naghdi, P. M., and Murch, S. A., "On the Mechanical Behavior of the Viscoelastic/Plastic Solids," ASME JOURNAL OF APPLIED MECHANICS, Vol. 30, No. 3, 1963, pp. 321-328.

2 Ghoneim, H., and Chen, Y., "A Viscoelastic-Viscoplastic Constitutive Equation And Its Finite Element Implementation," *Journal of Computers and Structures*, to appear.

3 Valanis, K. C., "A Theory of Viscoplasticity Without a Yield Surface," *Archives Mechanics*, Vol. 23, No. 4, 1971, pp. 517-551.

4 Matsuoka, S., and Bair, H. E., "The Temperature Drop in Glasy Polymers During Deformation," *Journal of Applied Physics*, Vol. 48, No. 10, 1977, pp. 4058-4062.

5 Miller, A. K., "Modeling of Cyclic Plasticity With Unified Constitutive Equations: Improvement in Simulating Normal and Anomalous Bauschinger Effects," ASME *Journal of Engineering Materials and Technology*, Vol. 102, 1980, pp. 215-222.

6 Bodner, S. R., and Partom, Y., "A Large Deformation Elastic-Viscoplastic Analysis of Thick-Walled Spherical Shell," ASME JOURNAL OF APPLIED MECHANICS, Vol. 39, 1972, pp. 751-757.

7 Duffy, J., "Testing Technique and Material Behavior at High Rates of Strain," *Mechanical Properties at High Rates of Strain*, Hardening, J., ed., 1979, pp. 1-15.

8 Ghoneim, H., "Constitutive Modeling of Viscoelastic-Viscoplastic Materials And Their Finite Element Implementation," Ph.D. thesis, Rutgers University, 1981, pp. 109-115.

9 Zienkiewicz, O. C., *The Finite Element Method*, Third Edition, McGraw-Hill (UK), 1977.

10 Sauer, J. A., and Pae, K. D., "Introduction to Polymer Science and Technology," Kaufman, H. S., and Falcetta, J. J., eds., Wiley, New York, Chapter 7, 1977, p. 334.

Postbuckling Analysis of Moderately Thick Elastic Circular Plates

K. Kanaka Raju[1] and G. Venkateswara Rao[1]

Introduction

Postbuckling behavior of thin elastic circular plates has been studied using contiuum [1] and finite element methods [2]. Recently, the authors presented a simplified finite element formulation [3] and obtained very accurate results for the postbuckling behavior of thin elastic circular plates. In this Note, the simple finite element formulation developed by the authors [3] is modified to consider the effects of shear deformation to obtain the axisymmetric postbuckling behavior of moderately thick circular plates.

Finite Element Formulation

The strain-displacement relations for a moderately thick circular plate of radius a under axisymmetric conditions are given by

$$\epsilon_r = \frac{\partial u}{\partial r} + \frac{1}{2}\left(\frac{\partial w}{\partial r}\right)^2$$

$$\epsilon_\theta = \frac{u}{r}$$

[1] Scientist/Engineer, Aerospace Structures Division, Vikram Sarabhai Space Centre, Trivandrum-695 022, India.

Manuscript received by ASME Applied Mechanics Division, July, 1982.

Downloaded 02 May 2010 to 171.66.16.246. Redistribution subject to ASME license or copyright; see http://www.asme.org/terms/Terms_Use.cfm

and upon applying Guassian quadrature,

$$Z = y + \frac{s_t}{2} \sum_{i=1}^{m} g\left\{\frac{s_t}{2}(1+x_i)\right\} \dot{\epsilon}\left\{\frac{s_t}{2}(1-x_i)\right\} W_i$$

The number of integration points m depends on the nature of the strain rate history $\dot{\epsilon}(s)$ and the lengths of s_t. The more intermittent $\dot{\epsilon}(s)$ and the longer s_t are, the more integration points are required to get good numerical results.

Numerical Examples

Uniaxial loading at different rates, loading-unloading-reloading, and jump tests are selected for the investigation of the response of the modified model. The following material constants are chosen for those numerical examples,

$$\begin{aligned} E &= 4.137 \times 10^5 \text{KPa}, \nu = 0.45, \alpha_1 \\ &= 2.417 \times 10^{-6} (\text{KPa sec})^{-1}, \\ \alpha_2 &= 1.0, C = 0.1 \text{ sec}^{-1}, n = 20, s_0 = 0.5, \\ y &= 1.034 \times 10^4 \text{KPa, and } g_0 = 3.447 \times 10^4 \text{KPa} \end{aligned}$$

Young's modulus E, Poisson ratio ν, and y are obtained from the tensile mechanical properties of Polytetrafluoroethylen (PTFE) [10], a material that exhibits plastic strain rate-history dependency and consequently is foreseen as an appropriate material to be represented by the present modified model. Pending experimental works, the other material constants are determined via numerical exercises, and consequently no qualitative comparison is presented. Figure 1 presents the strain rate effect on the stress-strain curve. It is clear that increasing the strain rate, in general, increases the yield stress and plastic hardening.

Loading-unloading-reloading results are shown in Fig. 2. In these figures, the upper and lower dotted curves represent the constant-rate stress-strain curves at 1.0 and 0.1 sec^{-1}, respectively. And the solid as well as the dashed curve represents the loading-unloading-reloading stress response. Dotted curves are plotted for the sake of comparison. Clearly, on reloading at a different rate from that of loading-unloading, the reloading stress yields at values that are influenced by the previous strain rate of loading-unloading.

The jump test, results where the strain rate is suddenly changed, are displayed in Fig. 3. As in loading-unloading-reloading, the jump test results reveal the strain rate-history dependency inherited in the modified model. Upon decreasing the strain rate from 1.0 to 0.1 sec^{-1} (solid line) the stress drops to values higher than that of the constant-rate loading at 0.1 sec^{-1} (lower dotted curve). This is because the response after the jump is influenced by the previous strain rate of loading before the jump (1.0 sec^{-1}). Similarly, when the strain rate is increased from 0.1 to 1.0 sec^{-1} (dashed line) the stress response rises to values lower than that of the constant-rate loading at 1.0 sec^{-1} (upper dotted curve).

Conclusion

The power formula of Bodner's viscoplastic model is modified to account for the strain rate-history effect on the plastic behavior, yield stress, and hardening of the model. Modification is accomplished by adopting an integral-memory type of equation for the "hardening" state variable. Results from uniaxial simulation reveal the capability of the modified model not only in simulating the strain-rate effect on the stress-strain curve, but also in depicting the rate-history dependency of the plastic behavior exhibited by some viscoplastic materials, as illustrated by loading-unloading-reloading and jump tests.

The apparent success of the modified model suggests the extension of the modification to other types of state variable models which include kinematic hardening, temperature, and pressure effects, to solving nonisothermal-large deformation problems, and to experimental verification of the behavior of the modified model.

References

1 Naghdi, P. M., and Murch, S. A., "On the Mechanical Behavior of the Viscoelastic/Plastic Solids," ASME JOURNAL OF APPLIED MECHANICS, Vol. 30, No. 3, 1963, pp. 321-328.

2 Ghoneim, H., and Chen, Y., "A Viscoelastic-Viscoplastic Constitutive Equation And Its Finite Element Implementation," *Journal of Computers and Structures*, to appear.

3 Valanis, K. C., "A Theory of Viscoplasticity Without a Yield Surface," *Archives Mechanics*, Vol. 23, No. 4, 1971, pp. 517-551.

4 Matsuoka, S., and Bair, H. E., "The Temperature Drop in Glasy Polymers During Deformation," *Journal of Applied Physics*, Vol. 48, No. 10, 1977, pp. 4058-4062.

5 Miller, A. K., "Modeling of Cyclic Plasticity With Unified Constitutive Equations: Improvement in Simulating Normal and Anomalous Bauschinger Effects," ASME *Journal of Engineering Materials and Technology*, Vol. 102, 1980, pp. 215-222.

6 Bodner, S. R., and Partom, Y., "A Large Deformation Elastic-Viscoplastic Analysis of Thick-Walled Spherical Shell," ASME JOURNAL OF APPLIED MECHANICS, Vol. 39, 1972, pp. 751-757.

7 Duffy, J., "Testing Technique and Material Behavior at High Rates of Strain," *Mechanical Properties at High Rates of Strain*, Hardening, J., ed., 1979, pp. 1-15.

8 Ghoneim, H., "Constitutive Modeling of Viscoelastic-Viscoplastic Materials And Their Finite Element Implementation," Ph.D. thesis, Rutgers University, 1981, pp. 109-115.

9 Zienkiewicz, O. C., *The Finite Element Method*, Third Edition, McGraw-Hill (UK), 1977.

10 Sauer, J. A., and Pae, K. D., "Introduction to Polymer Science and Technology," Kaufman, H. S., and Falcetta, J. J., eds., Wiley, New York, Chapter 7, 1977, p. 334.

Postbuckling Analysis of Moderately Thick Elastic Circular Plates

K. Kanaka Raju[1] and G. Venkateswara Rao[1]

Introduction

Postbuckling behavior of thin elastic circular plates has been studied using contiuum [1] and finite element methods [2]. Recently, the authors presented a simplified finite element formulation [3] and obtained very accurate results for the postbuckling behavior of thin elastic circular plates. In this Note, the simple finite element formulation developed by the authors [3] is modified to consider the effects of shear deformation to obtain the axisymmetric postbuckling behavior of moderately thick circular plates.

Finite Element Formulation

The strain-displacement relations for a moderately thick circular plate of radius a under axisymmetric conditions are given by

$$\epsilon_r = \frac{\partial u}{\partial r} + \frac{1}{2}\left(\frac{\partial w}{\partial r}\right)^2$$

$$\epsilon_\theta = \frac{u}{r}$$

[1] Scientist/Engineer, Aerospace Structures Division, Vikram Sarabhai Space Centre, Trivandrum-695 022, India.

Manuscript received by ASME Applied Mechanics Division, July, 1982.

Copyright © 1983 by ASME

Downloaded 02 May 2010 to 171.66.16.246. Redistribution subject to ASME license or copyright; see http://www.asme.org/terms/Terms_Use.cfm

$$\epsilon_{rz} = -\zeta \tag{1}$$

$$\chi_r = -\left(\frac{\partial^2 w}{\partial r^2} + \frac{\partial \zeta}{\partial r}\right)$$

$$\chi_\theta = -\frac{1}{r}\left(\frac{\partial w}{\partial r} + \zeta\right)$$

where u, w are the inplane and transverse displacements, ζ is the shear rotation, r, θ, and z are the radial, circumferential, and normal directions, respectively. Assuming the circular plate to be discretized into a set of annular plate elements, the strain energy of an element bounded by radii r_1 and r_2 is given by

$$U = \frac{1}{2}\int_0^{2\pi}\int_{r_1}^{r_2}\left\{C(\epsilon_r^2 + \epsilon_\theta^2 + 2\nu\epsilon_r\epsilon_\theta) + D(\chi_r^2 + \chi_\theta^2 + 2\nu\chi_r\chi_\theta + \frac{5}{6}Gh\epsilon_{rz}^2\right\} r dr d\theta \tag{2}$$

where h is the thickness of the plate, $C = Eh/(1-\nu^2)$ and $D = Eh^3/12(1-\nu^2)$, E being Young's modulus and ν Poisson's ratio (chosen as 0.3 in the present study). G is the shear modulus given by$E/2(1+\nu)$.

The work done on the element by the uniform compressive load N_r per unit length at the boundary is given by

$$W = \frac{1}{2}\int_0^{2\pi}\int_{r_1}^{r_2}\bar{N}_r\left(\frac{\partial w}{\partial r}\right)^2 r dr d\theta \tag{3}$$

where $\bar{N}_r$ is the radial load distribution per unit length in the element.

Following standard principles, with cubic polynomials in r assumed for u, w, and ζ the final matrix equation governing the postbuckling phenomenon is obtained as

$$[K]\{\delta\} + \lambda[G]\{\delta\} = 0 \tag{4}$$

where $[K]$ and $[G]$ are the assembled stiffness and geometric stiffness matrices, respectively. $\{\delta\}$ is the eigenvector and λ is the eigenvalue. The iterative numerical method of [3] is used to evaluate the nonlinear stiffness matrix K and to solve the equation (4) to obtain the linear buckling load parameter $\lambda_L = N_{r_{cr}} a^2/D$, where $N_{r_{cr}}$ is the critical radial load and the nonlinear radial load parameter λ_{NL} $(N_r a^2/D)$ for various ratios of central deflection (c) to thickness (h) with the thickness ratio (h/a) varying between 0.001 (thin plate) and 0.2.

Table 1 $\lambda_L, \bar{a}, \bar{b}$ values for moderately thick circular plates

	Simply supported						Clamped					
h/a	0.001	0.05	0.1	0.15	0.2	0.001	0.05	0.1	0.15	0.2
4 elements										
λ_L	4.1978	4.1853	4.1481	4.0875	4.0056	14.6894	14.5353	14.0941	13.4176	12.5736
$\bar{a}$	0.2702	0.2709	0.2734	0.2774	0.2830	0.2026	0.2046	0.2109	0.2214	0.2361
$\bar{b}$	0.004676	0.004726	0.005194	0.005962	0.007146	0.005703	0.005996	0.006896	0.008623	0.011298
8 elements										
λ_L	4.1978	4.1852	4.1481	4.0874	4.0056	14.6825	14.5299	14.0910	13.4159	12.5725
$\bar{a}$	0.2702	0.2710	0.2734	0.2775	0.2830	0.2028	0.2049	0.2112	0.2217	0.2364
$\bar{b}$	0.004647	0.004797	0.005246	0.006136	0.007205	0.005836	0.006097	0.007065	0.008784	0.011529

Results and Discussion

With the preceding formulation, the results obtained for moderately thick circular plates are presented in Table 1 in the form of linear buckling load parameter λ_L and the coefficients $\bar{a}$, $\bar{b}$ of an empirical formula for the radial load ratio, $\gamma = N_r/N_{r_{cr}} = \lambda_{NL}/\lambda_L$ in the postbuckling range. The coefficients $\bar{a}$, $\bar{b}$ of the empirical formula for γ given by

$$\gamma = 1 + \bar{a}(c/h)^2 - \bar{b}(c/h)^4 \tag{5}$$

are obtained through a least square curve fitting technique from the nonlinear radial load parameter, λ_{NL}, values obtained for c/h values ranging from 0.0 to 1.0 in steps of 0.2 from equation (4).

The results for various h/a values for four and eight element idealizations of the plate with simply supported and clamped boundary conditions are given in Table 1. The convergence can be seen to be very good and an eight element solution gives very accurate results.

λ_L values can be seen to decrease with increasing thickness, whereas the values of γ increase with the thickness indicating that as the plates become thicker, the radial load ratio increases (as $\bar{a}$ is increasing and $\bar{b}$ is sufficiently small). In other words, the effect of nonlinearity increases as the plate

Downloaded 02 May 2010 to 171.66.16.246. Redistribution subject to ASME license or copyright; see http://www.asme.org/terms/Terms_Use.cfm

thickness increases which consequently includes the effect of shear deformation. The effect of shear deformation can be seen to increase the γ values by about 4 percent in the simply supported case and by about 14 percent in the clamped case over the thin plate results ($h/a=0.001$). The present results for thin plates ($h/a=0.001$) are in excellent agreement up to $(c/h)^2$ term in the empirical formula with the continuum solutions [1]. All the present results are further accurate up to $(c/h)^4$ terms.

Concluding Remarks

Results for the axisymmetric postbuckling behavior of moderately thick circular plates are presented. The simplified finite element formulation developed by the authors to study postbuckling behavior is extendable to plates of other shapes.

References

1 Thompson, J. M. T., and Hunt, G. W., *A General Theory of Elastic Stability*, Wiley, London, 1973, pp. 160-178.

2 Carter Wellford, Jr., L., and Ghanan M., Dib., "Finite Element Methods for Nonlinear Eigenvalue Problems and the Post-Buckling Behavior of Elastic Circular Plates," *Computers and Structures*, Vol. 6, 1976, pp. 413-418.

3 Kanaka Raju, K., and Venkateswara Rao, G., "Finite Element Analysis of Post-Buckling Behavior of Cylindrically Orthotropic Circular Plates," Communicated for publication to Fibre Science and Technology.

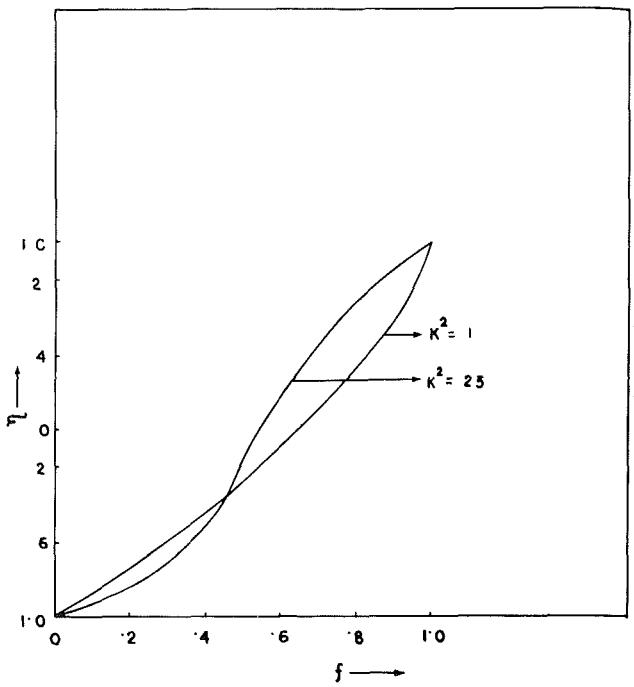

Fig. 1 Variation of f for various k^2

Magnetohydrodynamic Flow Between Two Horizontal Plates in a Rotating System, the Lower Plate Being a Stretching Sheet

B. Banerjee[1]

Introduction

Fluid flow through porous media is of fundamental importance to a wide range of disciplines in various branches of natural science and technology. Chakravorty and Gupta [1] have studied the MHD flow and heat transfer over a stretching sheet. Borkakati and Bharali [2] have discussed the MHD flow and heat transfer between two horizontal plates, the lower plate being a stretching sheet. The theoretical study of fluid flow problems taking into account the simultaneous effects of hydromagnetic and Coriolis forces is very useful in understanding various geophysical and astrophysical problems. The purpose of the present Note is to study the effect of rotation on the hydromagnetic flow between two parallel plates where the upper plate is porous and solid and the lower plate is a stretching sheet. We believe that our study will find application in metallurgy and polymer technology.

Formulation and Solution of the Problem

We consider the steady flow of an electrically conducting fluid between two horizontal parallel plates $y=\pm h$, when the fluid and the plates rotate in unison about an axis normal to the plates with an angular velocity Ω. We consider that the x axis is along the plate, the y axis is perpendicular to it, and the z axis is normal to the xy plane. The origin is considered at the center of the channel. The lower plate is being stretched by introducing two equal and opposite forces so that the position of the point $(0, -h)$ remains unchanged. A uniform magnetic

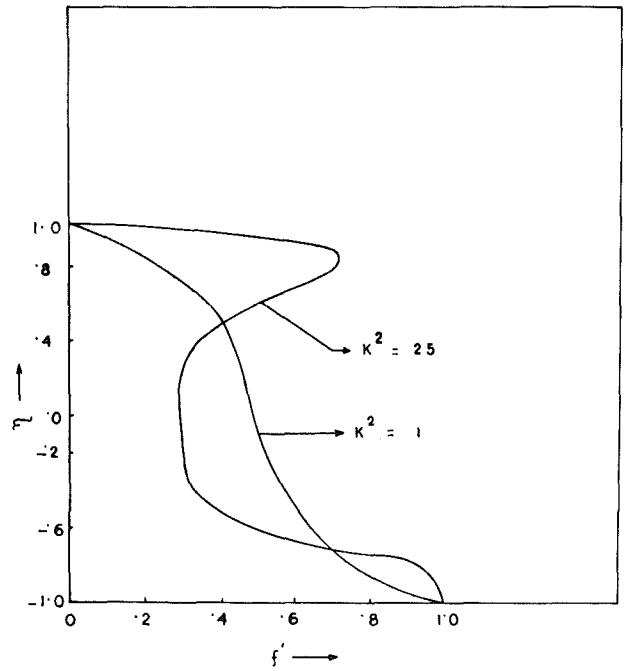

Fig. 2 Variation of f' for various k^2

flux density B_0 is acting along y axis about which the system is rotating. The upper plate is subjected to a constant wall injection with a velocity V_0

The boundary conditions of the problem are

$$u=E\,x,\ v=0,\ w=0 \quad \text{at} \quad y=-h$$
$$u=0,\ v=-v_0,\ w=0 \quad \text{at} \quad y=+h \qquad (1)$$

Using the substitution

$$\eta=\frac{y}{h},\ u=E\,x\,f'(\eta),\ v=-E\,h\,f(\eta), w=E\,x\,g(\eta) \qquad (2)$$

where a prime denotes differentiation with respect to η. The equations of motion in a rotating frame of reference are

[1] Lecturer in Mathematics, Dibrugarh University, Assam, India 786004.

Manuscript received by ASME Applied Mechanics Division, April, 1982; final revision, September, 1982.

Downloaded 02 May 2010 to 171.66.16.246. Redistribution subject to ASME license or copyright; see http://www.asme.org/terms/Terms_Use.cfm

thickness increases which consequently includes the effect of shear deformation. The effect of shear deformation can be seen to increase the γ values by about 4 percent in the simply supported case and by about 14 percent in the clamped case over the thin plate results ($h/a=0.001$). The present results for thin plates ($h/a=0.001$) are in excellent agreement up to $(c/h)^2$ term in the empirical formula with the continuum solutions [1]. All the present results are further accurate up to $(c/h)^4$ terms.

Concluding Remarks

Results for the axisymmetric postbuckling behavior of moderately thick circular plates are presented. The simplified finite element formulation developed by the authors to study postbuckling behavior is extendable to plates of other shapes.

References

1 Thompson, J. M. T., and Hunt, G. W., *A General Theory of Elastic Stability*, Wiley, London, 1973, pp. 160-178.

2 Carter Wellford, Jr., L., and Ghanan M., Dib., "Finite Element Methods for Nonlinear Eigenvalue Problems and the Post-Buckling Behavior of Elastic Circular Plates," *Computers and Structures*, Vol. 6, 1976, pp. 413-418.

3 Kanaka Raju, K., and Venkateswara Rao, G., "Finite Element Analysis of Post-Buckling Behavior of Cylindrically Orthotropic Circular Plates," Communicated for publication to Fibre Science and Technology.

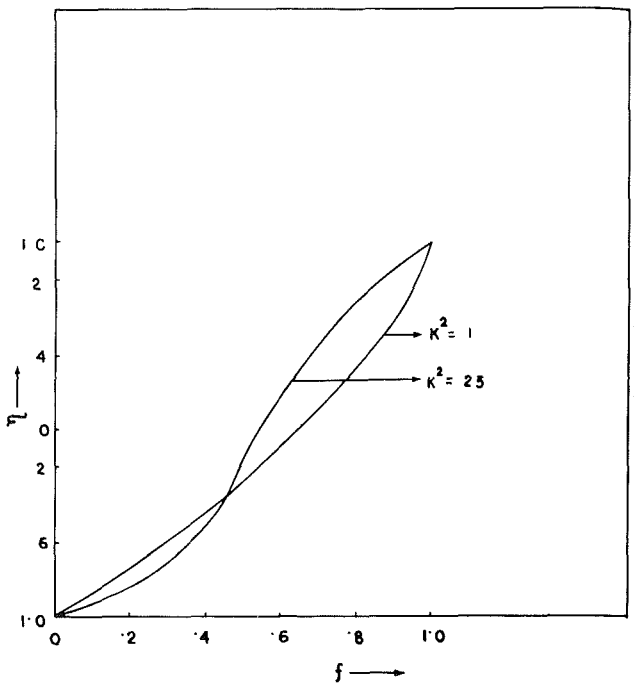

Fig. 1 Variation of f for various k^2

Magnetohydrodynamic Flow Between Two Horizontal Plates in a Rotating System, the Lower Plate Being a Stretching Sheet

B. Banerjee[1]

Introduction

Fluid flow through porous media is of fundamental importance to a wide range of disciplines in various branches of natural science and technology. Chakravorty and Gupta [1] have studied the MHD flow and heat transfer over a stretching sheet. Borkakati and Bharali [2] have discussed the MHD flow and heat transfer between two horizontal plates, the lower plate being a stretching sheet. The theoretical study of fluid flow problems taking into account the simultaneous effects of hydromagnetic and Coriolis forces is very useful in understanding various geophysical and astrophysical problems. The purpose of the present Note is to study the effect of rotation on the hydromagnetic flow between two parallel plates where the upper plate is porous and solid and the lower plate is a stretching sheet. We believe that our study will find application in metallurgy and polymer technology.

Formulation and Solution of the Problem

We consider the steady flow of an electrically conducting fluid between two horizontal parallel plates $y=\pm h$, when the fluid and the plates rotate in unison about an axis normal to the plates with an angular velocity Ω. We consider that the x axis is along the plate, the y axis is perpendicular to it, and the z axis is normal to the xy plane. The origin is considered at the center of the channel. The lower plate is being stretched by introducing two equal and opposite forces so that the position of the point $(0, -h)$ remains unchanged. A uniform magnetic

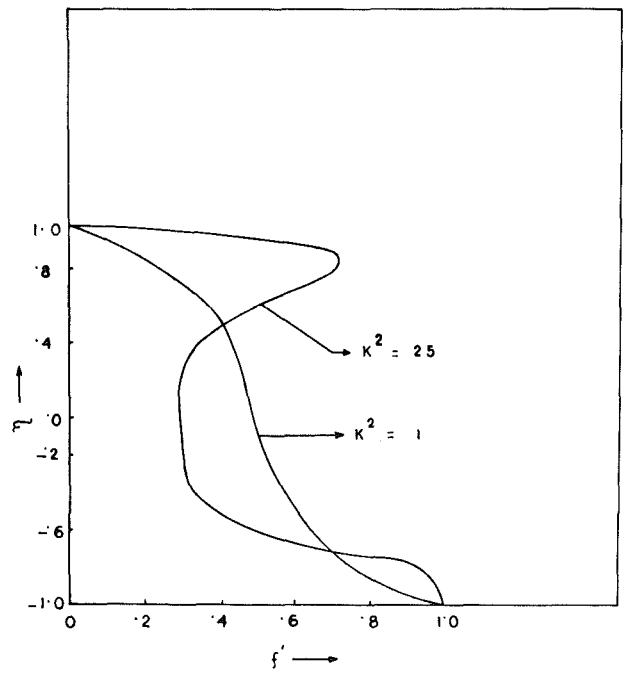

Fig. 2 Variation of f' for various k^2

flux density B_0 is acting along y axis about which the system is rotating. The upper plate is subjected to a constant wall injection with a velocity V_0

The boundary conditions of the problem are

$$u=E\,x,\ v=0,\ w=0 \quad \text{at} \quad y=-h$$
$$u=0,\ v=-v_0,\ w=0 \quad \text{at} \quad y=+h \qquad (1)$$

Using the substitution

$$\eta=\frac{y}{h},\ u=E\,x\,f'(\eta),\ v=-E\,h\,f(\eta), w=E\,x\,g(\eta) \qquad (2)$$

where a prime denotes differentiation with respect to η. The equations of motion in a rotating frame of reference are

[1] Lecturer in Mathematics, Dibrugarh University, Assam, India 786004.

Manuscript received by ASME Applied Mechanics Division, April, 1982; final revision, September, 1982.

Copyright © 1983 by ASME
Downloaded 02 May 2010 to 171.66.16.246. Redistribution subject to ASME license or copyright; see http://www.asme.org/terms/Terms_Use.cfm

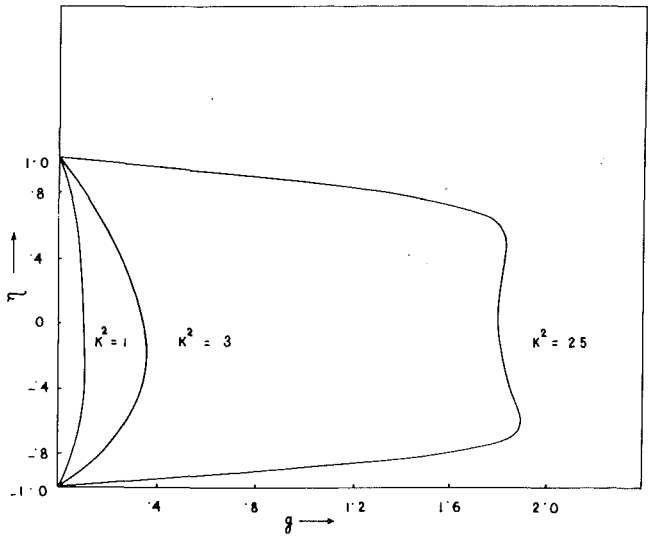

Fig. 3 Variation of g for various K^2

$$-\frac{1}{\rho}\frac{\partial p^*}{\partial x} = E^2 x\left[f'^2 - ff'' - \frac{f'''}{R} + \frac{M^2}{R}f' + \frac{2K^2}{R}g\right] \quad (3)$$

$$-\frac{1}{\rho h}\frac{\partial p^*}{\partial \eta} = E^2 h\left[ff' + \frac{1}{R}f''\right] \quad (4)$$

$$g'' - R[f'g - fg'] + 2K^2 f' - M^2 g = 0 \quad (5)$$

where p^* is the modified fluid pressure including centrifugal force and

$$R = \frac{Eh^2}{\nu},\quad M^2 = \frac{6B_0^2 h^2}{\rho\nu},\quad K^2 = \frac{\Omega h^2}{\nu} \quad (6)$$

Equation (3) with the help of (4) can be written as

$$f''' - R[f'^2 - ff''] - 2K^2 g - M^2 f' = A \quad (7)$$

where A is a constant.

Because an exact solution to the equations (5) and (7) cannot be obtained, a perturbation technique has been applied by expanding f, g, and A in powers of R, by considering R to be small. We have not presented the solution but the results have been discussed numerically.

Results and Discussion

To gain an insight into the patterns of flow f, f' and g have been plotted against η for different values of the rotation parameter K^2 with $M = 3$ and $\lambda(V_0/_{Eh}) = 1$ in Figs. 1-3. Figure 1 shows that f increases steadily for low K^2 where as for high value of K^2, f increases near the plates and decreases near the center of the channel. Figure 2 reveals that f' decreases near the stretching sheet and increases near the porous plate for low K^2 where as for high K^2, f' increases near the porous plate and decreases at the center of the channel. Also, the rotation of the channel brings humps near the porous plate, indicating the occurrence of a boundary layer near the porous plate. For high K^2 the Coriolis force and the magnetic field that act against the pressure gradient, causes reversal of the flow. Figure 3 shows that the transverse velocity g increases as the rotation parameter K^2 increases and the maximum of g occurs near the stretching sheet for low K^2 and for high K^2, the profile is depressed at the center of the channel, and nearly symmetrical about the center line of the channel.

References

1 Chakravorty, A., and Gupta, A. S., "Hydromagnetic Flow and Heat Transfer Over a Stretching Sheet," *Quart. Appl. Math.*, Vol. 37, 1979, pp. 73-78.

2 Borkakati, A. K., and Bharali, A., "Hydromagnetic Flow and Heat Transfer Between Two Horizontal Plates, the Lower Plate Being a Stretching Sheet, to appear in *Quart. Appl. Math.*

Downloaded 02 May 2010 to 171.66.16.246. Redistribution subject to ASME license or copyright; see http://www.asme.org/terms/Terms_Use.cfm

Journal of Applied Mechanics

Discussion

Extended Kane's Equations for Nonholonomic Variable Mass System[1]

Y. Pironneau[2]. The paper presents a generalization of Kane's equations to nonholonomic variable mass systems. The authors claim that the new equations are simpler than any of the others and give an illustrative example.

However it seems to the writer that even for the simple system of Fig. 1 the method leads to more complicated results. The (ideal) constraint

$$x^2 + y^2 = a^2$$

gives

$$x\dot{x} + y\dot{y} = 0.$$

Following Kane's method we add the linear relation

$$\alpha\dot{x} + \beta\dot{y} = u$$

supposedly to simplify that α and β are (arbitrary) constants. We have to calculate $\dot{x}$, $\dot{y}$, $\ddot{x}$, $\ddot{y}$ and

$$\mathbf{F}(P)\cdot\hat{\mathbf{V}}(P) = -mg\times(\beta x - \alpha y)^{-1}\hat{u}$$

$$ma(P)\cdot\hat{\mathbf{V}}(P) = m(\ddot{x}\dot{x} + \ddot{y}\dot{y}) = m[\ \ldots\ ]\hat{u}.$$

Finally we obtain the equation of motion

$$(x^2 + y^2)(\beta x - \alpha y)^{-1}[\dot{u} + (\alpha x + \beta y)(\beta x - \alpha y)^{-2}u^2] + gx = 0.$$

(The result is more complicated of α and β are considered to be functions of x and y.)

This does not seem simpler than the equation obtained when using, for instance, Lagrange's multiplier

$$m\ddot{x} = \lambda x$$

$$m\ddot{y} = -mg + \lambda y$$

and, eliminating λ,

$$y\ddot{x} - x\ddot{y} = gx.$$

For a system with n generalized coordinates $q(q_i, i = 1, \ldots, n)$ and m ideal constraints represented by m linear nonholonomic equations

$$a_{si}(q,t)\dot{q}_i = b_s(q,t) \quad (s = 1, \ldots, m) \tag{1}$$

we can choose $p = n - s$ coordinates q_α as principal, the s others designated by q_j being secondary. The equations (1) can be written in the matrix form

$$A(q_\alpha, q_j, t)\dot{\underline{q}}^{(j)} + B(q_\alpha, q_j, t)\dot{\underline{q}}^{(\alpha)} = \underline{b}(q_\alpha, q_j, t) \tag{2}$$

$$\dot{\underline{q}}^{(j)} = -A^{-1}B\dot{\underline{q}}^{(\alpha)} + A^{-1}\underline{b} \tag{3}$$

The Euler-Lagrange equation of motion is

$$(E_i - Q_i - C_i)\hat{\dot{q}} = 0 \quad (i = 1, \ldots, n) \tag{4}$$

where

$$E_i\dot{q} \triangleq \Sigma\mathbf{a}(P)m(P)\cdot\frac{\partial\mathbf{P}}{\partial q_i}\dot{q}_i,$$

$Q_i\hat{\dot{q}}_i$ is the virtual power of the given forces, and

$C_i\hat{\dot{q}}_i$ is the virtual power of the constraining forces, with

$$C_i\hat{\dot{q}}_i = C_\alpha\hat{\dot{q}} + C_j\hat{\dot{q}}_j.$$

This quantity is equal to zero if, after (3),

$$\hat{\underline{q}}^{(j)} = -A^{-1}B\hat{\underline{q}}^{(\alpha)} \tag{5}$$

In this case (4) can be rewritten

$$[\underline{E}^{(\alpha)} - \underline{Q}^{(\alpha)}]^T\hat{\underline{q}}^{(\alpha)} + [\underline{E}^{(j)} - \underline{Q}^{(j)}]^T[-A^{-1}B\hat{\underline{q}}^{(\alpha)}] = \underline{0} \tag{6}$$

and we obtain $p = n - m$ equations of motion

$$\underline{E}^{(\alpha)} - \underline{Q}^{(\alpha)} - [A^{-1}B]^T(\underline{E}^{(j)} - \underline{Q}^{(j)}) = \underline{0} \tag{7}$$

which, using (3), gives p differential equations of the second order in q_α whose coefficients are functions of q_α, q_j, and t. In some particular and very interesting cases these coefficients are only functions of q_α and t.

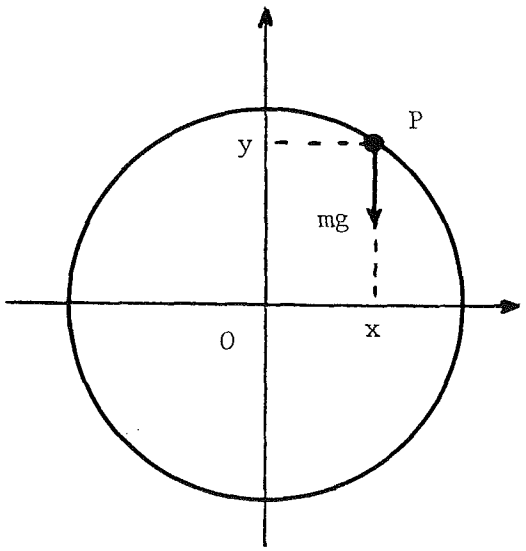

Fig. 1

[1] By Z. M. Ge and Y. H. Cheng, and published in the June, 1982 issue of the ASME Journal of Applied Mechanics, Vol. 49, pp. 429–431.

[2] Professor of Mechanics, Ecole Nationale Süperieure de Mécanique, Nantes University, Nantes, France.

Copyright © 1983 by ASME
Downloaded 02 May 2010 to 171.66.16.246. Redistribution subject to ASME license or copyright; see http://www.asme.org/terms/Terms_Use.cfm

According to Kane's method, we have to add to the relations (2) p linear equations in order to obtain

$$\left|\begin{array}{c|c} A & B \\ \hline X & Y \end{array}\right| \left|\begin{array}{c} \dot{q}^{(j)} \\ \hline \dot{q}^{(\alpha)} \end{array}\right| = \left|\begin{array}{c} b \\ \hline u \end{array}\right| \tag{8}$$

or

$$\dot{\underline{q}}^{(j)} = -A^{-1}B\dot{\underline{q}}^{(\alpha)} + A^{-1}\underline{b} \tag{9}$$

$$\dot{\underline{q}}^{(\alpha)} = [Y - XA^{-1}B]^{-1}[u - XA^{-1}b], \tag{10}$$

and, for virtual velocities,

$$\hat{\underline{q}}^{(\alpha)} = [Y - XA^{-1}B]^{-1}\hat{\underline{u}} \tag{11}$$

$$\dot{\underline{q}}^{(j)} = -A^{-1}B[Y - XA^{-1}B]^{-1}\hat{\underline{u}}. \tag{12}$$

Then the relations (6) become

$$[(\underline{E}^{(\alpha)} - \underline{Q}^{(\alpha)})^T + (\underline{E}^{(j)} - \underline{Q}^{(j)})^T(-A^{-1}B)][Y - XA^{-1}B]^{-1}\hat{\underline{u}} = \underline{0} \tag{13}$$

and we obtain p equations of motion

$$[(Y - XA^{-1}B)^{-1}]^T[\underline{E}^{(\alpha)} - \underline{Q}^{(\alpha)} - (A^{-1}B)^T(\underline{E}^{(j)} - Q^{(j)})] = \underline{0} \tag{14}$$

which, using (9) and (10), give p differential equations of the first order in u but with coefficient functions of q_α, q_j and t. It seems difficult to consider (14) as simpler than (7).

For the example given in (1) there are eight parameters but only two, q_3 and q_4, appear explicitely in the six constraint equations (2). The authors choose two complementary equations

$$\dot{q}_4 = u_1 \tag{15}$$

$$\cos(q_3 + q_4)\dot{q}_1 + \mathrm{Sin}(q_3 + q_4)\dot{q}_2 = u_2 \tag{16}$$

and obtain two differential equations of the first order in u_1 and u_2 with coefficient functions of q_3 and q_4.

In fact (16) can be rewritten (L being a constant) as

$$L(\sin\ q_4)^{-1}\cdot\dot{q}_3 = u_2. \tag{17}$$

Taking $q_1{}^{(\alpha)} = q_3$ and $q_2{}^{(\alpha)} = q_4$, the relations (15) and (17) correspond in (8) to

$$X = 0 \text{ and } Y = \left|\begin{array}{cc} L(\sin q_4)^{-1} & 0 \\ 0 & 1 \end{array}\right|.$$

It would have been simpler to take $X = 0$ and $Y = 1$, which is exactly the Lagrange method.

Authors' Closure

The Kane's equation and its derivation in Pironneau's simple example are wrong, since the coordinates used in Kane's equation are generalized coordinates that were mistaken for the mutually dependent Cartesian coordinates in the example. The correct procedure of the formulation of Kane's equation for this example is as follows. Let the radius of the ring be r and the angle between the OP and x axis be θ which is taken as a generalized coordinate.

$$\dot{q} = \dot{\theta} = u \tag{1}$$

$$\mathbf{V}^P = u(-r\sin\theta\,\mathbf{i} + r\cos\theta\,\mathbf{j}) \tag{2}$$

The partial velocity

$$\mathbf{V}_p^P = -r\sin\theta\,\mathbf{i} + r\cos\theta\,\mathbf{j} \tag{3}$$

$$\mathbf{a}^P = r(-\dot{u}\sin\theta - u^2\cos\theta)\mathbf{i} + r(\dot{u}\cos\theta - u^2\sin\theta)\mathbf{j} \tag{4}$$

The generalized active force

$$F = \mathbf{V}_p^P \cdot \mathbf{R} = -rmg\cos\theta \tag{5}$$

The generalized inertia force

$$F^* = \mathbf{V}_p^P \cdot (-m\mathbf{a}^P) = -r^2m\dot{u} = -r^2m\ddot{\theta} \tag{6}$$

The Kane's equation is

$$F + F^* = 0 \tag{7}$$

$$r\ddot{\theta} + g\cos\theta = 0 \tag{8}$$

It is true that for such a simple example, the method of Lagrange's multiplier is simpler than Kane's equation and Lagrange's equation. Furthermore, in this case, the most convenient method is not the method of Lagrange's multiplier but the Newton's equation of motion. By taking the projection of Newton's equation on the tangent line of the circle at P, we can immediately obtain (8). However, this fact has not presented an obstacle to the superiority of Lagrange's equations over Newton's equations and the method of Lagrange's multiplier for complicated problems, just as it cannot present an obstacle to the superiority of Kane's equations over other methods in many cases of complicated problems.

Both (14) and the derivation are far from Kane's equations and their derivation, although for specific problems the final equations of motion obtained by (14) and by Kane's equations may be the same, just as the same equation (8) can be obtained by several methods. The original contribution of Kane's method lies in the introduction of partial velocities, generalized active forces, and generalized inertia forces, which all disappeared in the derivation of (14), and the application of D'Alembert's principle as the foundation without the use of virtual displacements (or velocities), while the foundation of (14) is D'Alembert-Lagrange's principle, which had been miscalled Euler-Lagrange equation of motion in Pironneau's statement, with the concept of virtual velocities used. By the statement "it would have been simpler to take $X = 0$ and $Y = 1$, which is exactly the *Lagrange method*," the lead author has reason to say that (7) in the statement is the varied and unfinished form of Woronetz's equations of motion [1] and (14) the varied and unfinished form of Hamel's equations of motion [2, 3], which was compared with the former.

Equation (16) is superior to (17) in that the physical significance of the former, of which left side is the velocity (projection) of Q, is more apparent than (17). Equations (15) and (16) are superior to $u_1 = \dot{q}_4$, $u_2 = \dot{q}_3$ in that first, the final equations obtained are simpler; and second, they have very interesting practical importance *together*. Let $u_1 = \dot{q}_4 = \dot{\phi}$, $u_2 = v$, the equations of motion in our paper may be rewritten as

$$\left.\begin{array}{c} L\ddot{\phi} + v\,\dot{\phi}\cos\phi + \dot{v}\sin\phi = 0 \\ \sigma\,\ddot{\phi}\sin\phi + \pi\,v\,\dot{\phi}\sin\phi\cos\phi \\ +(\tau + \tau_1\sin^2\phi + \tau_2^2\cos^2\phi)\dot{v} + C(t)\dot{m}\cos\phi = 0 \end{array}\right\} \tag{9}$$

We have two equations of two variables ϕ, v, where ϕ is the turning angle of the car and v the velocity of the car which, taken together, properly characterize the motion of the car and in which we are most interested.

The choice of generalized speeds affords an opportunity to select the parameters of practical interest as the generalized speeds that can be often described by closed system of differential equations (in our case, two equations of two variables) so that the specific problem can be greatly simplified. This is also an advantage of Kane's method. Although the calculation of accelerations is an additional task, yet as a

Downloaded 02 May 2010 to 171.66.16.246. Redistribution subject to ASME license or copyright; see http://www.asme.org/terms/Terms_Use.cfm

whole, Kane's method is simpler than other methods in many cases of complicated problems.

References

1 Woronetz, P. V., "On the Equations of Motion for Nonholonomic Systems" (Russian), *Matem. Sb. T.*, Vol. 22, No. 4, 1901.

2 Hamel, G., "Die Lagrange-Eulerschen Gleichungen der Mechanik," *Zeitschrift für Mathematik und Physik*, Bd. 50, 1904.

3 Ge, Z.-M., "Equations of Motion for Nonholonomic Variable Mass Systems and Their Application to a Control System," *Journal of Shanghai Jiaotong University*, No. 4, 1979, pp. 1–22.

Downloaded 02 May 2010 to 171.66.16.246. Redistribution subject to ASME license or copyright; see http://www.asme.org/terms/Terms_Use.cfm

Journal of Applied Mechanics

Book Reviews

An Album of Fluid Motion. By M. Van Dyke. Parobolic Press, Stanford, Calif. 1982. 176 Pages. Price $20.00, Clothbound; $10.00, paperback.

REVIEWED BY S. WIDNALL[1]

This book is a unique publishing event in the field of fluid mechanics. Since its arrival, I have seen many small clusters of enraptured graduate students work through its rich offerings. The book contains 166 pages of photographs of fluid motion displaying a wide variety of phenomena, utilizing many different flow-visualization techniques. The only text beyond a short introduction are the figure captions, which contain a description of the phenomenon, an interpretation, and a reference to the original work or a credit.

The phenomena include low Reynolds number flows, separation, vortices, flow instability, turbulence, free-surface flow, convection, subsonic flow, shock waves, and supersonic flow. The book has the power to excite and inform students about the complexity of possible fluid motions, arising even in simple geometries. Its price is low and its quality is so high that instructors can recommend it without reservation as a supplemental text or for independent study at both the undergraduate and graduate level. No faculty member who teaches fluid mechanics should be without a copy.

The clothbound version would make an ideal gift or coffee-table book for any one with an interest in the natural sciences. The high artistic quality of many of the photographs will also appeal to those of a more general audience who chance to come upon this book.

One unfortunate feature is the absence of color photographs. Although there are many such photos available, which would have added to the appeal of the book, it is clear that they would have increased the cost well beyond the current price. This book, at this price, is certainly to be recommended.

Entropy Generation Through Heat and Fluid Flow. By A. Bejan. Wiley, New York, 1982. 248 Pages. Price $39.95.

REVIEWED BY J. KESTIN[2]

It is fair to assume that readers of the JOURNAL OF APPLIED MECHANICS are unaware of the existence of Public Law 95-619-Nov. 9, 1978 entitled *National Energy Conservation Policy Act*. There, on page 3287, we read:

SEC. 683. SECOND LAW EFFICIENCY STUDY.

(a) Study.—(1) The Secretary of Energy, in consultation with the Director of the National Bureau of Standards and such other agencies as he deems necessary, shall conduct a study of the relevance to energy conservation programs of the use of the concept of energy efficiency as being the ratio of the minimum available work necessary for accomplishing a given task to the available work in the actual fuel used to accomplish that task.

Never mind that the ratio of the *actual* available work employed by a device to either the available energy residing in the fuel or to the minimum available work necessary for accomplishing a given task would be more appropriate measures. The fact remains that in 1978, as distinct from 1983, the country was genuinely concerned about its energy future. A. Bejan's book is the outgrowth of that concern in 1978 and earlier. In a number of well-known papers Bejan made the concept of available energy (otherwise known as exergy) accessible in detail to practicing engineers. The present book is a connected and thoughtful restatement of Bejan's very useful contributions.

The basics of the subject are clearly presented in Chapters 1 and 2. Chapters 3 and 5—10 contain applications to fluid flow, convective heat transfer, heat-transfer enhancement, heat exchangers, storage and low temperature. Chapter 11 contains an accurate application of so-called second-law analysis to solar energy which corrects many erroneous earlier analyses and convincingly demonstrates the "high-temperature" nature of solar radiation. In this the author is right, contrary opinions expressed by certain popularizers notwithstanding. Throughout the book, good use is made of the Gouy-Stodola theorem which connects entropy production to losses in available energy (exergy).

Chapter 4, entitled "Theory of Turbulent Flow," constitutes a surprising anomaly. In it the author rejects what most of use have learned, and learned to accept, about the origin of turbulence. He rejects the relevance of the theory of hydrodynamic stability and makes the astonishing statement:

> "It seems that by focusing on the transition regime as a way of explaining the nature of turbulence, researchers have complicated their work beyond need. First let us agree on what a "transition regime" is. It is simply that domain in which *two* different and competing mechanisms fight one another for dominance.

No. We do not agree. Neither do we accept the role the author assigns to the "buckling property of inviscid layers." Chapter 4 should never have been included in this book because, even if it were revealingly correct, its topic is irrelevant to the eminently useful message contained in the remainder of the book.

The last chapter, Chapter 12, by Mary Bejan discusses energy policy in more sociological terms; it is a very good basis for thinking about this aspect of the subject.

[1] Professor, Department of Aeronautic and Astronautics, Massachusetts Institute of Technology, Cambridge, Mass. 02139.

[2] Professor, Division of Engineering, Brown University, Providence, R. I. 02912.

Copyright © 1983 by ASME
Downloaded 02 May 2010 to 171.66.16.246. Redistribution subject to ASME license or copyright; see http://www.asme.org/terms/Terms_Use.cfm

Finite Elements in Biomechanics. By R. H. Gallagher, B. R. Simon, P. C. Johnson, and J. F. Gross. Wiley, New York, 1982. pp. xiv–404. Price $48.50.

REVIEWED BY R. D. CROWNINSHIELD[3]

The First International Conference on Finite Elements in Biomechanics was held in Tucson, Ariz. February 18–20, 1980. This conference, which was sponsored by the United States National Science Foundation and the College of Engineering of the University of Arizona, contained about 60 presentations which covered a wide variety of finite element applications in biomechanics. The conference organizers (editors of this book) invited the authors of 18 of these presentations to prepare manuscripts for publication in this book.

The book starts with the introduction of a clinician's view and then a finite element specialist view of the method. G. T. Rab presents his views on the finite element method, special model problems with biologic materials, and problem of clinician-engineer collaboration. O. C. Zienkiewicz and D. W. Kelley then present the basic outline of the finite element process, its historical development, present trends, and its impact on the field of bioengineering.

The remainder of the book presents a diverse array of finite element applications in biomechanics. Two chapters address the mechanics of biologic fluid flow. Normal mechanics of capillary flow, arterial flow, blood cell deformation, and peristaltic flow are discussed. Special problems of pulsatile flow through a stenosis and through an aneurysm are also considered.

The application of the finite element method in soft tissue mechanics is demonstrated in an introductory chapter and a subsequent series of chapters dealing with the mechanics of the lungs and heart. Analyses of the role of interfacial forces in lung deformation, lung parenchyma, and the heart's left ventricle are discussed.

The remainder of the book, and by far the most indepth treatment of a subject, is devoted to the finite element method applied to solid mechanics, predominantly orthopaedic problems. After a survey chapter on the role of finite element models in orthopaedics, subsequent chapters address specific orthopaedic applications. An application of the finite method to external fracture fixation devices is followed by studies of stress-morphology relationships in trabecular bone, stress distributions in the femoral head, intervertebral disk function, the mechanics of artificial joint fixation, cement-bone failure, the function of femoral endoprostheses, and head and neck injury mechanisms.

This book assembles the highlights of what was a very interesting biomechanics conference. The presentations chosen for inclusion in this book survey well the diverse application of the finite element method to biomechanics problems and illustrate important problems unique to finite element modeling of biologic systems. The reader is introduced to problems associated with biologic variability, growth and maturation, nonlinear materials, anisotropic materials, incompressible materials, viscoelastic materials, and structural pathology. The book as a whole serves as an excellent introduction for the experienced finite element programmer to the applications and special problems of biologic system modeling. The individual chapters present new data, discussion, and reference useful to the reader with interest in one or more of the specific subject areas.

[3] Associate Professor, Department of Orthopaedic Surgery, The University of Iowa Hospitals and Clinics, Biomechanics Laboratory, The University of Iowa, Iowa City, Iowa 52242.

Optimality in Parametric Systems. By T. L. Vincent and W. J. Grantham. Wiley, New York, 1982. 243 Pages. Price $34.50.

REVIEWED BY W. STADLER[4]

If optimization methods are ever to become standard tools of analysis in industry, they must be introduced on a regular basis at an undergraduate level. The present book is very readable and could be used as an undergraduate text. With the exception of some supplements on differential calculus and cones in R^n, the needed mathematical background should include differential equations and linear algebra, a level usually attained by seniors in engineering.

Only about 30 pages of the book pertain to optimality in parametric systems, about half of the book concerns nonlinear programming, and the remainder is devoted to gametheoretic concepts. Throughout, it is generally assumed that the criterion functions and the constraint functions are differentiable as needed, resulting in theorems and proofs that are relatively easy to apply and follow, respectively.

With the exception of three examples and their various treatments, all of the examples are academic and there are no direct applications to mechanics. However, in mechanics, as well as in other areas, there is a need for a formal treatment of optimization problems involving the simultaneous "minimization" of several criteria. This requires some new notions of optimality. Although such concepts as Pareto optimality have been around in economics for nearly 100 years and game theory was conceived by Borel in 1921, they have only found their way into the engineering literature within the last 20 years. The authors provide a fairly detailed treatment of Pareto optimality as the optimality concept for the "vector maximum problem" and they treat Nash-equilibrium, min-max, and Stackelberg Leader-Follower solutions in a gametheoretic context. The authors, as well as others, usually introduce these concepts as possible resolutions between antagonistic "rational" players; however, they can also serve as optimality concepts for the vector maximum problem. Thus, min-max clearly is suited for worst case design, and the Nash-equilibrium concept could be used when one might wish to assure that one criterion maintain a lower bound when one of the design variables is changed with all others remaining fixed at the optimal design. Collectively, all of the games may be viewed as "games against nature" played by a single decision maker.

In summary, the book provides a needed transition from the treatment of these topics in monographs and in a research context to possible classroom use.

Theory of Dislocations (2nd ed.). By J. P. Hirth and J. Lothe. Wiley, New York, 1982. pp. xii–857. Price $72.95.

REVIEWED BY T. MURA[5]

This book is based on the lecture notes developed by the authors for courses on the theory of dislocations at Carnegie Institute of Technology, The Ohio State University, and Oslo University. The first edition of this book was published by McGraw-Hill, in 1968. The present major revision is made in the sections related to elastic theory of dislocations. Accordingly, the works of Willis, Barnett, and Asaro, among

[4] Associate Professor, Division of Engineering, San Francisco State University, San Francisco, Calif. 94132.

[5] Professor, Department of Civil Engineering, The Technological Institute, Northwestern University, Evanston, Ill. 60201.

Copyright © 1983 by ASME
Downloaded 02 May 2010 to 171.66.16.246. Redistribution subject to ASME license or copyright; see http://www.asme.org/terms/Terms_Use.cfm

others whose names did not appear in the first edition, are introduced in the second edition. These people advocated the importance of the line integral expressions for the elastic field of a dislocation loop. There is also added coverage of atomic calculations and new material on advanced anisotropic elastic theory and grain boundary dislocations. However, very little coverage is found in the area of continuous distributions of dislocations developed by K. Kondo, Bilby and Kröner, among others.

This book consists of four parts. Part 1 focuses on the fundamentals of dislocations (elastic theory of dislocations in isotropic continua); Part 2 on effects of crystal structure on dislocations (the Peiels-Nabarro dislocation model, partial dislocations, kinks, and anisotropy of crystals); Part 3 on dislocation-point defect interactions (thermal kinks and jogs, pinning and drag of Cottrell, Snoek, and Suzuki's atmospheres); and Part 4 focuses on groups of dislocations (dislocation models of grain boundaries, dislocation sources, pileups and twinning).

Compared with Nabarro's book (*Theory of Crystal Dislocations*, Oxford 1967), this book provides sufficient detail for the book to be effectively used as an undergraduate text, as well as extended treatments of specific problems to stimulate advanced graduate students and scientists.

Micromechanics of Defects in Solids. By T. Mura. Martinus Nijhoff, The Hague, 1982. pp. x–494. Price $98.00.

REVIEWED BY D. M. BARNETT[6]

Much of what might be termed advances in the mathematical treatment of defects (inclusions, inhomogeneities, dislocations, and cracks) in solids tends to be scattered throughout the journal literature; as a result, the researcher intent on entering this field faces the rather formidable task of deciding on the best way in which to begin learning about the theory of defects. Prior to the appearance of Professor Mura's monograph, *the* single outstanding text available to such a researcher was *Theory of Dislocations* by J. P. Hirth and J. Lothe, now available in its second edition. The Hirth and Lothe book is, in my opinion, a beautiful exposition of great lasting value. Nonetheless, I have long had the feeling that it is more easily digested by one trained in solid state physics or materials science than by one whose primary bent is solid mechanics; in addition, Hirth and Lothe devote very little space to J. D. Eshelby's famous "transformation strain" problem, whose solution and attendent results should be in the "bag of tricks" carried by every Ph.D. materials scientist. Professor Mura's book more than adequately fills both gaps. Over one-third of the book is devoted to the treatment of inclusions and inhomogeneities in isotropic and anisotropic linear elastic solids, and the development of the subject matter should please readers familiar with either solid mechanics or applied mathematics.

The first chapter introduces the notion of eigenstrains and emphasizes in a self-contained way the use of elastic Green's functions to represent the solution to eigenstrain problems. The next three chapters provide a most complete survey of inclusion and inhomogeneity problems and contain a wealth of formulas which should prove most useful to those requiring solutions to this class of problems. Cracks and dislocations in elastic solids receive a reasonably complete treatment in chapters 5 and 6. The final chapter emphasizes the use of techniques and solutions introduced previously to model phenomena of importance to mechanical metallurgists, including work-hardening of dispersion strengthened alloys, stress relaxation via diffusion, and polycrystal plasticity.

In summary, Professor Mura's book may be heartily recommended to those interested in either applying or learning to apply the methods of continuum mechanics to treat defects in the solid state. This monograph could serve as the perfect text for a second-level graduate course with the same title as that of the book.

Advanced Engineering Analysis. By J. N. Reddy and M. L. Rasmussen. Wiley, New York, 1982. pp. xiv–488. Price $39.95.

REVIEWED BY L. WHEELER[7]

The aim of this book is to present a unified treatment of three topics, namely vector and tensor analysis, functional analysis, and the calculus of variations for an audience of students in engineering and applied science. It is based on class notes used by the authors in teaching seniors and first-year graduate students, and for the most part, its level and style reflect these origins. Exercises are included. They are well chosen and suitably placed.

The subject of functional analysis is important to much of modern science and I believe that a useful purpose is served by bringing it to a wider audience. An initiate to this field faces a rather bland literature which might seem merely to proliferate abstract function spaces. Here the authors have something to offer. They have put together a concise introductory treatment where a student can pick up the basic concepts.

The remaining two parts of the book do not seem to measure up to the part on functional analysis. While the treatment of the calculus of variations benefits slightly from the emphasis placed on methods of approximation and computation, I am disappointed to see it so weakly linked to the functional analysis that precedes it in the book.

A major goal of the vector and tensor part is evidently to ease the student into functional analysis. While it might also be intended to furnish mathematical preliminaries for such subjects as modern continuum mechanics, this purpose is hindered by the notation, level, and style of the presentation. In particular, I fail to see why portions of it are so elementary.

I recommend this book as a course book to those who teach functional analysis and variational methods to students interested in applications. Further, it is written so that students in need of outside reading should find it helpful. It would deserve serious attention as a textbook, but I doubt whether many institutions offer a course to which it is closely suited.

Spacecraft Dynamics. By T. R. Kane, P. W. Likins, and D. A. Levinson. McGraw-Hill, New York, 1982. 436 Pages. Price $49.50.

REVIEWED BY R. L. HUSTON[8]

This book is a welcome addition to the literature on spacecraft dynamics and on dynamics itself. It is basically a textbook, but it will undoubtedly become a reference for engineers and designers as well. Although the book has only

[6] Professor, Department of Materials Science, Stanford University, Stanford, Calif., 94305.

[7] Professor, Department of Mechanical Engineering, University of Houston, Houston, Texas 77004.

[8] Professor, Department of Mechanical and Industrial Engineering, University of Cincinnati, Cincinnati, Ohio 45221.

Copyright © 1983 by ASME
Downloaded 02 May 2010 to 171.66.16.246. Redistribution subject to ASME license or copyright; see http://www.asme.org/terms/Terms_Use.cfm

four chapters, there is a vast range of topics covered in depth in its 436 pages.

The first chapter on kinematics contains an excellent analysis and discussion of rigid body orientation and angular velocity – subjects that are often poorly treated in standard texts and are thus confusing to students. The chapter includes discussions of Euler parameters, Rodrigues parameters, and screw motion – topics of increasing interest in modern dynamical analyses. In the reviewer's opinion, purchase of the text could be justified solely on the basis of this first chapter.

The second chapter is more specialized; it deals with gravitational forces as they affect spacecraft. However, it is perhaps the most extensive and exhaustive treatment of this subject at one place in the literature.

The third chapter discusses simple spacecraft dynamics. A "simple spacecraft" is a single rigid body or simple gyrostat. Dynamical equations are formulated using the angular momentum principle. Knowledge of inertia principles is assumed.

The final chapter extends the discussion to complex spacecraft with multiple degrees of freedom and with elastic parts. Particular emphasis is given to formulaton of the dynamical equations. A system of equations called "Kane's dynamical equations" are shown to be especially convenient for this formulation – particularly as the complexity of the spacecraft increases. The chapter concludes with a discussion on the use of the finite element method for constructing modal functions.

Four sets of problems are provided at the end of the text covering the subject matter of the respective chapters. (The reviewer believes it would be pedagogically more efficient to have these at the end of the chapters themselves.) The problems are good, but *all* need to be solved to cover the subject material. That is, there is little overlap in the problems – a possible disadvantage for classroom instructors.

The book is eloquently set in a lucid style. It should be of interest and use to students, engineers, and researchers, and it is highly recommended by this reviewer.

Theory of Thin Elastic Shells. By M. Dikman. Pitman, Marshfield, Mass., 1982, pp. xii–364. Price $59.95.

REVIEWED BY J. L. SANDERS, JR.[9]

This monograph is the eighth in a series of surveys and reference works in mathematics offered by the publisher. Both as a reference work and as a survey the volume is superb. An early chapter on the differential geometry of surfaces and nearby space (i.e., the shell space) developed by means of tensor calculus introduces the notation and takes care of most of the purely mathematical aspects of the subject.

The book is devoted wholly to the theory of elastic thin shells. There is essentially no material on applications, methods of solution, or inelastic behavior. There is a strong emphasis on the nature of the problem: to arrive at a satisfactory and usable approximate two-dimensional theory for real shells that are three-dimensional objects. The author recognizes two principal approaches to the problem which lead to two classes of theories termed "derived" and "direct." Derived theories involve a descent from three dimensions and, at least in an intermediate stage, involve an infinite system of equations or rather a hierarchy of systems of equations. In this case the problem is how to decide where to leave off. The direct approach is two-dimensional from the outset, and involves defining the objects of shell theory (displacement measures, stress measures, etc.) over the surface, and postulating constitutive relations. In this case the problem is to justify the relation of the defined objects and postulated equations to the real world. The direct approach occupies much less space in the book, perhaps because it is the more efficient, or as the author maintains the two approaches complement each other. The ideas of the many researchers who have contributed to the subject are smoothly woven into the text. Copious references are supplied.

In addition to the material on the foundations of shell theory there are chapters on stability, dynamics, and stochastic problems. A chapter each is devoted to the state of knowledge on error estimation and existence. Missing is a chapter dealing specifically with the significant advances made in recent years on the geometrically nonlinear theory.

Perhaps some readers, like the reviewer, might wish to see a more definite choice among alternatives at a number of places in the book. Some questions are, I believe, rather more definitely settled than the author indicates. However, no axes are ground, and on the whole the author has produced an excellent book, unique in its field.

Classical Mechanics, Vol. I an Vol. II. By E. A. Desloge. Wiley, New York, 1982. 991 Pages. Price: Vol. I, $40.00; Vol. II, $49.50.

REVIEWED BY R. H. RAND[10]

This lengthy two-volume work consists of some 93 chapters and 32 appendices spread over 991 pages. Volume I treats Newtonian particle and rigid body dynamics, and offers a brief introduction to Lagrange's and Hamilton's equations. Volume II treats Lagrangian and Hamiltonian dynamics in detail and includes a discussion of special relativity. The appendices contain brief summaries of mathematical topics.

The author's style is clear and readable, and there are many solved examples and homework problems (with solutions at the back of the book). In terms of current engineering education, volume I would be suitable for text in a senior level or beginning graduate course in intermediate dynamics, while volume II could serve as a text for a graduate course in advanced dynamics.

Volume II offers an unusually good treatment of the following topics: Noether's theorem for obtaining first integrals; the use of group representations for solving linear vibrations problems with symmetry; the Gibbs-Appell equations; and special relativity. On the other hand, the following topics are regrettably missing: differential forms and exterior calculus, which provide an elegant and concise condition for a transformation to be canonical; KAM theory and related results on the breakup of invariant tori in nonintegrable systems; and canonical perturbation theory, e.g., Lie series or von Zeipel's method.

These books, especially volume II, would be a useful reference for a researcher in applied mechanics, particularly a specialist in dynamics. However, the importance of Desloge's Classical Mechanics as a reference work is eclipsed by the existence of many other excellent and established works covering the same material (e.g., those by Goldstein, Lanczos, and Pars).

---

[9] Professor, Division of Applied Sciences, Harvard University, Cambridge, Mass. 02138.

[10] Professor, Department of Theoretical and Applied Mechanics, Cornell University, Ithaca, N.Y. 14853

Copyright © 1983 by ASME
Downloaded 02 May 2010 to 171.66.16.246. Redistribution subject to ASME license or copyright; see http://www.asme.org/terms/Terms_Use.cfm